Ore-forming processes of hydrothermal vein-type deposits, SW Germany

Dissertation

der Mathematisch-Naturwissenschaftlichen Fakultät
der Eberhard Karls Universität Tübingen
zur Erlangung des Grades eines
Doktors der Naturwissenschaften
(Dr. rer. nat.)

vorgelegt von
M.Sc. Mathias Burisch
aus Karlsruhe

Tübingen
2016

Gedruckt mit Genehmigung der Mathematisch-Naturwissenschaftlichen Fakultät der Eberhard Karls Universität Tübingen.

Tag der mündlichen Qualifikation:	24.08.2016
Dekan:	Prof. Dr. Wolfgang Rosenstiel
1. Berichterstatter:	Prof. Dr. Gregor Markl
2. Berichterstatter:	PD. Dr. Thomas Wenzel
3. Berichterstatter:	Prof. Dr. Jens Gutzmer

Danksagung

Ich möchte mich sehr herzlich bei Prof. Dr. Gregor Markl für die Finanzierung und Betreuung dieser Arbeit, für unzählige konstruktive, hilfreiche, geistreiche und motivierende Gespräche und die unglaublich zeitnahe Bearbeitung meiner Manuskripte bedanken. Des Weiteren möchte ich mich für meine intensive wissenschaftliche Förderung und für die vielen Sachen, die ich von ihm während meiner Promotion gelernt habe, aufrichtig bedanken. Solch eine erstklassige Ausbildung ist nicht selbstverständlich und das rechne ich ihm sehr hoch an.

Ich möchte mich auch sehr herzlich bei PD. Dr. Thomas Wenzel für die Zweitbetreuung, die zahlreichen Diskussionen und die erheiternden Gespräche bedanken. Bei PD. Dr. Michael Marks und Dr. Udo Neumann möchte ich mich aufrichtig für viele gute Diskussionen und ihre fortwährende Hilfsbereitschaft bedanken.

Bei Herrn Prof. Dr. Jens Gutzmer möchte ich mich für die Drittbegutachtung meiner Dissertation bedanken. Für die Unterstützung der im Zuge diese Dissertation entstandenen Publikationen möchte ich allen Koautoren: Prof. Dr. Gregor Markl, PD. Dr. Michael Marks, Dr. Udo Neumann, Dr. Benjamin Walter, Dr. Axel Gerdes, Prof. Dr. Marcus Nowak, Dr. Markus Wälle und Michael Fettel danken. Dr. Kurt Bucher, Dr. Antonin Richard, Dr. Richard Tosdal, Dr. Kåre Kullerud und den anonymen Gutachtern für ihre konstruktiven und hilfreichen Anmerkungen zu den Manuskripten danken.

Bei Gabi Stoschek, Dr. Melanie Keuper, Bernd Steinhilber, Linda Marko, Barbara Maier, Dagmar Kost und Dorothea Muehlbayer-Renner möchte ich mich für die Unterstützung bei analytischen Angelegenheiten bedanken.

Für das Korrekturlesen dieser Dissertation danke ich Marguerita Duchoslav, Dr. Udo Neumann, Johannes Giebel und Benjamin Walter.

Meinen Arbeitskollegen Dr. Benjamin Walter, Marguerita Duchoslav, Dr. Tobias Fußwinkel, Dr. Holger Teiber, Dr. Susanne Göb, Petya Atanasova, Maximilian Keim, Stefan Kreißl, Johannes Giebel und Rainer Babiel möchte ich für die gute Arbeitsatmosphäre danken.

Mein besonderer Dank für ihre bedingungslose Unterstützung gilt meiner Familie: Veronika Berner, Elisa-Marie Hassel, Bernd Kreisel, Stephanie, Viktoria, Valentin und Jens Burlefinger, Semra, Lucas und Axel Burisch, Marcus Hamm sowie meinen engsten Freunden: Gisa Wörlein, Jörg Uehlin, Jonas Doussal, Can Yapici, Peter Bichler, Hannes Schaffrick. Danke dass ihr immer an mich geglaubt habt.

ABSTRACT

This thesis focuses on ore-forming processes and the provenance of involved fluids, solutes and gases of epithermal to mesothermal Pb-Zn-(Cu)-fluorite-quartz and Ag/Bi-Ni-Co-(Fe)-As-(U)-calcite vein-type deposits of the Schwarzwald and the Odenwald, SW Germany. These veins occur across basement-cover unconformities due to mixing of two or more chemically contrasting fluids. A fluid component (fluid-type A), which originates from deeper crustal levels (high salinity; low Cl/Br (by mass)) of the upper crust is invariably recognised in the ore fluids, while the other fluid component is of basinal, sedimentary and/or meteoric origin (fluid-type B). Although extensive data is available for unconformity-related hydrothermal veins, several important aspects are still poorly constrained. These aspects include a precise understanding of the processes that result in the observed compositions of deep-seated crustal fluids, alteration processes in root zones (below actual vein), regional and temporal variations in the composition of the ore fluids of the Schwarzwald and the genesis of the enigmatic five-element veins of the Odenwald, SW Germany. To attain a better understanding of the presented aspects, we carried out leaching experiments on common igneous, metamorphic and sedimentary rocks including their mineral separates at variable temperatures (25 to 350°C), pressures (0.01 to 1.9 kbar), grain-size fractions and fluid/rock ratios. Leachates were analysed by ion chromatography and total reflexion X-ray fluorescence (TXRF). The samples were characterized prior to the experiments by X-ray fluorescence, microthermometry, electron microprobe analyses, pyrohydrolysis and TXRF. Furthermore, numerous hydrothermal veins of the Schwarzwald and the Odenwald were characterized with respect to their ore geology, vein mineralogy, mineral chemistry, fluid inclusion composition (microthermometry, crush-leach, LA-ICPMS and Raman spectroscopy), stable isotopic composition and radiogenic isotopic composition. This comprehensive analytical and experimental approach yields new and profound insights into processes relevant for hydrothermal vein-type deposits.

Halogens fractionate during fluid-rock interaction, since they are distributed between two reservoirs in the rock: as highly soluble phases and as low soluble phases. Lowest Cl/Br ratios, similar to natural basement brines are obtained by short leaching of medium- to fine-grained rock. Still, the maximum salinities that can be obtained by selective leaching of the low soluble phases are limited to ~10 wt.%. Consequently, at least an additional chlorine source is required for natural basement fluids having high

salinities (~26 wt.%) and low Cl/Br ratios. Furthermore, the experiments confirm that substantial amounts of Pb, Zn, Cu, Ni, As and W are released by alteration of common rock-forming minerals.

Time resolved trace element, Rb/Cs and Cl/Br variations of vein-hosted fluid inclusions of the Jurassic Brandenberg vein near Todtnau (Germany) were used to monitor alteration processes that occur in cataclastic root zones below the actual hydrothermal vein.

On the other hand, the sedimentary aquifers involved in ore-forming processes and their associated fluids are inhomogeneous in their composition on the scale of the Schwarzwald. The combined study of the regional geology, basement brines, sedimentary brines and the ore fluids (mixture) of different vein-types and ages enabled a reconstruction of the evolution and origin of the involved fluids during the last 300 million years.

A new genetic model for five-element veins is proposed, which seems to be universally valid for most occurrences of five-element veins. Five-element veins form where strongly reducing methane or methane-bearing fluids are introduced into an active hydrothermal sulphide system. This is the first genetic model for five-element veins, which is in total agreement with all textural and chemical features that are typical of five-element veins.

KURZZUSAMMENFASSUNG

Diese Dissertation befasst sich mit den Erz bildenden Prozessen und der Herkunft beteiligter Fluide, gelöster Feststoffe und Gase von epithermalen bis mesothermalen Pb-Zn-(Cu)-Fluorit-Quarz- und Ag/Bi-Ni-Co-(Fe)-As-(U)-Kalzit-Gängen des Schwarzwaldes und des Odenwaldes, Südwestdeutschland. Diese Gänge bilden sich im Bereich der Grundgebirgs-Deckgebirgsdiskordanz durch Mischung von zwei oder mehr, chemisch unterschiedlicher Fluide. Das Erzfluid enthält stets eine Fluidkomponente (Fluidtyp A: hohe Salinitäten; niedrige Cl/Br Verhältnisse), die ursprünglich aus tieferen Krustenbereichen stammt und eine Fluidkomponente (Fluidtyp B), die aus basinalen, sedimentären und/oder meteorischen Fluiden besteht. Obwohl bereits viel an Diskordanz-gebundenen hydrothermalen Gängen geforscht wurde, sind einige wichtige Aspekte der Genese immer noch nicht genau verstanden. Diese offenen Fragen beinhalten das Verständnis der Prozesse die zu der beobachteten Fluidzusammensetzung von Tiefenfluiden beitragen, Alterationsprozesse in der Wurzelzone (unter dem eigentlichen Gang), regionale und zeitliche Veränderungen in der Zusammensetzung der Erzfluide des Schwarzwaldes sowie die Genese der Fünfelementgänge des Odenwaldes, in Südwestdeutschland. Zur Klärung dieser Fragen wurden Laugungsexperimente an gewöhnlichen magmatischen, metamorphen und sedimentären Gesteinen, sowie deren Mineralseparate (Feldspat, Quarz und Biotit) bei verschiedenen Temperaturen (25 bis 350°C), Drücken (0.01 bis 1.9 kbar), Korngrößen und Fluid/Gesteins Verhältnissen durchgeführt. Die Versuchslösungen wurden mittels Ionenchromatographie und Totalreflektionsröntgenfluoreszens (TXRF) analysiert. Die Gesteinsproben wurden vor den Laugungsversuchen mittels Röntgenfluoresenz, Mikrothermometrie, Elektronenstrahlmikrosonde, Pyrohydrolyse und TXRF charakterisiert. Des Weiteren wurden zahlreiche hydrothermale Gänge des Schwarzwaldes und des Odenwaldes hingehend ihrer Erzgeologie, Mineralogie, Mineralchemie, Fluideinschlusszusammensetzung, stabiler Isotopenverhältnisse und radiogener Isotopenverhältnisse untersucht. Dieser umfassende analytische und experimentelle Ansatz liefert neue und tiefgreifende Erkenntnisse über Prozesse die bei der Bildung hydrothermale Ganglagerstätten eine wichtige Rolle spielen.

Halogene fraktionieren durch Gesteins-Wasserwechselwirkung, da sie in zwei unterschiedlichen Reservoiren - leichtlösliche Phasen und schwerlösliche Phasen - im Gestein anzutreffen sind. Die niedrigsten Cl/Br-Werte, welche natürlichen Werten in

Tiefenfluiden entsprechen, können durch kurze Laugungszeiten von fein- bis mittelkörnigem Gestein erzielt werden. Jedoch kann das selektive Laugen der leichtlöslichen Phasen nicht zu Salinitäten oberhalb von ~10 Gew.% führen. Eine zusätzliche Quelle für Chlor ist notwendig, um hochsalinare Fluide mit niedrigen Cl/Br zu erlangen. Des Weiteren haben die Experimente gezeigt, dass beträchtliche Mengen an Pb, Zn, Cu, Ni, As und W durch die Alteration von gesteinsbildenden Mineralen freigesetzt werden.

Zeitlich auflösbare Variationen von Spurenelementen, Rb/Cs und Cl/Br in Fluideinschlüssen des Brandenbergganges bei Todtnau (Deutschland) wurden verwendet um Alterationsprozesse, die in den kataklastischen Wurzelzonen, unterhalb der eigentlichen Gänge ablaufen, nachzuverfolgen.

Andererseits unterscheiden sich die bei der Erzbildung beteiligten sedimentären Fluide und ihre zugehörigen Aquifere innerhalb des Schwarzwaldes stark in ihrer Zusammensetzung. Eine übergreifende Studie der regionalen Geologie, Tiefenfluide, sedimentären Fluide und Erzfluide ermöglicht eine detaillierte Rekonstruktion der Entwicklung und der Herkunft der beteiligten Fluidkomponenten in den letzten 300 Millionen Jahren.

Ein neues Bildungsmodell für Fünfelementgänge wird vorgeschlagen, welches universell für die meisten aller Fünfelementgänge weltweit gültig zu sein scheint. Fünfelementgänge bilden sich dort, wo Methan oder methanführende Fluide in ein bestehendes, sulfidisches Hydrothermalsystem einströmen. Dieses Model ist das erste Bildungsmodell für Fünfelementgänge, das alle texturellen und chemischen Beobachtungen dieses Gangtypus berücksichtigt.

Table of content

1. INTRODUCTION

This compilation of studies focuses on the formation mechanisms and the source of fluids, solutes and gases involved in the formation of hydrothermal Pb-Zn-(Cu)-fluorite-quartz veins and Ag/Bi-Ni-Co-(Fe)-As-(U)-calcite veins (five-element veins). As a case study Pb-Zn-(Cu)-fluorite-quartz veins of the Schwarzwald and five-element veins of the Odenwald crystalline windows, SW Germany were investigated.

The Pb-Zn-(Cu) veins of the Schwarzwald were extensively mined for silver during medieval times (Markl, 2015). Nowadays fluorite and to a lesser extend barite are mined as major ore at the Clara mine near Oberwolfach, but silver is still mined as a by-product (Markl, 2015). The increasing economic importance of rare elements like In, Ga and Ge due to their rising demand for high-tech applications uncloses new perspectives on sphalerite (and other sulphides) as potential sources for these elements (Frenzel et al., 2016). Five-element veins are exploited as Ag-, (Au-), Bi-, Co-, Ni- and often U-ores (Kissin, 1992). Insufficient trace element data is available of minerals of the five-element assemblage. Therefore the potential of five-element deposits as source of rare elements is not yet explored.

Although the mineralogy of these vein-types is rather different, they have in common that they formed due to mixing of two or more chemically contrasting fluids (Sverjensky, 1981; Marshall et al., 1993; Fußwinkel et al., 2013a). This mixing occurs where fluids from different crustal levels are introduced into the same fracture, which can only happen if deep-seated fluids (fluid-type A) are efficiently mobilised from deep crustal levels. Potential processes that cause this ascend are seismic pumping (Sibson et al., 1975), magmatic-driven fluid convection (Gleeson et al., 2001), topographic fluid-flow (Appold and Garven, 1999) or extension-driven dewatering (Staude et al., 2009). During their simultaneous ascend (Bons et al., 2014), these fluids mix with basinal or sedimentary fluids (fluid-type B) at shallower crustal levels. Depending on whether mixing of these fluids occurs below or above the unconformity, the hydrothermal veins form within the range of around 3 km below to around 1 km above the unconformity (Andrews et al., 1986; Franklin et al., 1986; Kissin, 1992; Munz et al., 1995; Staude et al., 2012b).

Deep-seated basement brines (fluid-type A) occur invariably as major constituent in ore fluids, trapped in fluid inclusions of vein minerals from various localities and deposit-

types such as e.g. Mississippi-Valley-Type-, unconformity-related U-, five-element- and Pb-Zn-sulphide deposits. (Sverjensky, 1981; Gleeson et al., 2001; Yardley, 2005; Ahmed et al., 2009; Pfaff et al., 2010; Richard et al., 2011; Staude et al., 2012b; Fußwinkel et al., 2013a; Richard et al., 2016). This fluid-type is characterised by high salinities of 25 to 28 wt.%, temperatures around 200 to 350°C and low Cl/Br ratios (typically 80 to 140, by mass) (Frape et al., 1984; Behr and Gerler, 1987; Möller et al., 2005; Stober and Bucher, 2005; Fußwinkel et al., 2013a). While the major anion is invariably Cl, the dominant cation may be Na or Ca, depending on temperature and plagioclase composition of the host rock in the source region of the fluids (Orville, 1972). In contrast, the composition of fluid-type B is controlled by the composition of its sedimentary aquifer, and therefore might strongly vary in its chemistry. Still, the majority of sedimentary fluids recognized in ore fluids of Pb-Zn-(Cu) and Ag/Bi-Ni-Co-(Fe)-As veins are moderate to high salinity (14 to 27 wt.%), Na-dominated, high Cl/Br (2000 to 10000) fluids with temperatures between 50 and 210°C (Lüders et al., 2012; Fußwinkel et al., 2013a; Stober et al., 2013).

Many authors suggest that the metal source of these hydrothermal deposits lies within the crystalline basement (O'Keeffe, 1986; Gleeson et al., 2001; Yardley, 2005; Ahmed et al., 2009; Fußwinkel et al., 2013a). The idea is that metals are leached from large volumes of crystalline rocks and subsequently transported as chloro-complexes along with the basement brine (Holland, 1972; Wood and Samson, 1998). Importantly, the metal-rich basement brine needs to be nominally free of reduced sulphur, since solubility of e.g. galena, chalcopyrite and sphalerite is very low in the presence of aqueous sulphide (not compulsory aqueous sulphate), which would inhibit an effective mobilisation of the metals. Zink and Pb (II)-bisulfide complexes are not relevant for such fluids, since they are only relevant at low chloride concentrations, low temperatures and very high pH conditions (Wood and Samson, 1998 and references therein). Deposition and concentration in hydrothermal veins with relatively small volumes (compared to the source volume) is related to sudden changes in the physio-chemical properties of the ore fluid. Particularly, mixing with a sedimentary fluid results potentially in a drastic change of the pH, temperature, redox state and/or activity of relevant ligands (e.g. reduced sulphur or chlorine) in the ore fluid. Other relevant processes that might result in ore deposition in hydrothermal systems are boiling and fluid-rock interaction (proximal to the ore deposition), but they do not seem to play an important role regarding the formation of the Pb-Zn-(Cu) and Ag/Bi-Ni-Co-(Fe)-As veins considered in this study (Kissin, 1992; Marshall et al., 1993; Fußwinkel et al., 2013a).

Although much is known about the formation of the hydrothermal Pb-Zn-(Cu) veins of the Schwarzwald, still several aspects are poorly constrained. Thus, the first part (chapter 3.1 to 3.3) of this thesis focuses on:

- The precise source of halogens and their behaviour during fluid-rock interaction (study a, chapter 3.1).
- The precise provenance of the metals and their mobility during fluid-rock interaction (study a, chapter 3.1).
- Root zones of hydrothermal veins, and how they govern the metal and trace element budget of the involved basement brine (study b, chapter 3.2).
- The chemical and hydrogeological evolution of the Schwarzwald hydrothermal system with time (~300 Ma until present) (study c, chapter 3.3.1).
- Regional systematics and/or variations of the sedimentary fluid component related to compositional inhomogeneity of the sedimentary aquifers (study d, chapter 3.3.2).
- The evolution of the hydrothermal system after the opening of the Upper Rhine Graben and concomitant tectonic disturbance of the sedimentary cover (study e, chapter 3.3.3).

In contrast to Pb-Zn-(Cu) veins, modern analytical data of five-element veins is only sparsely available. The mineralisation-type occurs as ore shoots (Otto, 1967; Gross, 1975) within Pb-Zn veins and as large-scale vein systems (Bugge, 1931; Changkakoti et al., 1986; Ondrus et al., 2003b; Ahmed et al., 2009). Typically of these veins is the occurrence of native metals encapsulated by massive Co-, Ni- and Fe-arsenides, which may form aggregates of up to several dm. To shed light on these long unattended but not less fascinating veins, the second part (chapter 3.4) of this thesis focuses on:

- Textural, mineralogical and chemical characterization of five-element veins (study f and g, chapter 3.4).
- Detailed characterisation of the ore fluid (study g, chapter 3.4).
- Timing of the ore formation (study g, chapter 3.4).
- The spatial and temporal relationship between Pb-Zn and five-element veins (study f and g, chapter 3.4).

- A general genetic model, which can be applied to the majority of five-element veins on a global scale (study f and g, chapter 3.4).
- Thermodynamic modelling and mass balance considerations (study f, chapter 3.4).
- Formation processes that cause a secondary Ag and Hg enrichment (study g, chapter 3.4).

2. REGIONAL GEOLOGY

Both, the Schwarzwald and the Odenwald are deeply eroded crystalline windows in SW Germany, which consist dominantly of Variscan metamorphic and igneous rock suites. Although the Odenwald (Saxothuringian) and the Schwarzwald (Moldanubian) mostly originate from two different terrains (Geyer et al., 2011), their geological history is quite similar from a simplified point of view (which is good enough for this study). Both consist of dominantly felsic syn- and post-collisional plutonic rocks (Variscan orogeny/subduction), and amphibolite facies metamorphic rocks of various protoliths (Stein, 2001; Geyer et al., 2011). One important exception is the occurrence of mafic igneous rock units of the Frankenstein-pluton in the northern Odenwald (Stein, 2001). To the west these basement rocks are restricted by the Upper Rhine Graben, while to the east the crystalline rocks are successively covered by Paleozoic and Mesozoic sediments. After the Variscan orogeny, the basement rocks were eroded. Detritic rock material was deposited in proximal troughs, forming arkoses and conglomerates of the Rotliegend with thicknesses of up to 400 m (Geyer et al., 2011). Mostly felsic volcanics occur locally at the same time. The Lower Triassic units are composed of clay, sandstone and conglomerates, which are up to 600 m thick in the Odenwald and successively become thinner to around 50 m in the southern Schwarzwald (Nickel, 1975; Stein, 2001; Geyer et al., 2011). Formation and migration of methane in Permo-Triassic organic-rich sediments due to the thermal decomposition of organic matter during basin subsidence is documented in fluid inclusions of fracture minerals in the Northern German Basin (Lüders et al., 2005). As a consequence of ongoing subsidence during the Middle Triassic, marine limestones, clays and evaporites prevailed. Especially the evaporites vary strongly in their distribution and thickness, according to the paleo-depth and geometry of the marine basins, where they were deposited (Geyer et al., 2011). Thus, thicknesses of halite can reach locally up to 100 m, whereas elsewhere they are entirely

absent. Total thicknesses of the Middle Triassic sediments typically do not exceed 250 m. These units are covered by 100 to 300 m thick Upper Triassic formations, which consist of dominantly fine-grained clastic sediments. The Jurassic chemical and clastic sediments reach thicknesses of up to 1200 m. During the Cretaceous no sediments are deposited in SW Germany. In total the thicknesses of the entire sedimentary cover is between 1200 and 2200 m (Nickel, 1975; Stein, 2001; Geyer et al., 2011). The extensive stress field related to the alpine orogeny in the Paleogene induced rifting and concomitant uplift of the rift shoulders on both sides of the rift. Subsequent erosion led to the exposure of the deep crystalline units. While the basement block of the Odenwald was uplifted almost homogeneously (Zienert, 1957; Nickel, 1975), the uplift in the Schwarzwald happened asymmetrically (Geyer et al., 2011). Consequently, the veins nowadays exposed at the surface record different depths of formation. The veins exposed in the northern Odenwald were originally formed at depths ~200 m below the basement-cover unconformity, while the veins in the southern Odenwald formed at ~100 m below the basement-cover unconformity (Zienert, 1957). In the northern Schwarzwald the veins are within sedimentary host rocks (200-500 m above the unconformity), while the outcropping veins in the southern Schwarzwald were formed at depth of ~2000 m below the unconformity (Geyer et al., 2011).

3. INDIVIDUAL STUDIES

In the following section the research focus, the most important results and conclusions are presented in a qualitative manner for each individual study (a-g). For further details, please refer to the publications attached to the appendix.

3.1 Halogen and trace metal systematics in deep-seated crustal fluids

Title of publication:
The effect of temperature and cataclastic deformation on the composition of upper crustal fluids — An experimental approach, Chemical Geology (study a)

Fluids with high salinity (~26 wt.% NaCl equivalent) appear to occur ubiquitous in the middle and lower parts of the upper continental crust (Lodemann et al., 1997; Stober and Bucher, 1999a; Frape et al., 2003). These deep-seated fluids represent a large

halogen reservoir and influence the redistribution of metals in the crust significantly (Yardley, 2005). Consequently, deep-seated fluids are invoked to be an essential element source for various hydrothermal vein-type deposits such as e.g. Mississippi-Valley-Type-, unconformity-related U-, five-element and Pb-Zn-sulphide deposits (Gleeson et al., 2001; Yardley, 2005; Ahmed et al., 2009; Pfaff et al., 2010; Staude et al., 2012b; Fußwinkel et al., 2013a; Richard et al., 2016). The dominant anion is invariably Cl, while the dominant cation might be Na or Ca. Deep-seated fluids have relatively high Br concentrations, yielding low Cl/Br ratios (Cl/Br is given as mass ratio), below the seawater ratio of 288 (Frape et al., 2003). At shallow crustal depths, however, fluids are typically Ca- and HCO_3^--rich (Frape et al., 2003), except for fluids derived from halite dissolution in evaporite-bearing aquifers. Theses halite-dissolution brines have also high Na and Cl concentrations (Stober et al., 2013), but very low Br concentrations (Stober and Bucher, 1999b), since halite incorporates only very small amounts of Br (Cl/Br ~2000–10,000; (Stober and Bucher, 1999b; Siemann and Schramm, 2000)). Hence, the Cl/Br ratio is often used to discriminate between halite dissolution brines of mostly shallow origin (high Cl/Br) and deep-seated brines (low Cl/Br) (Chi and Savard, 1997; Savoye et al., 1998; Stober and Bucher, 1999b; Leisen et al., 2012; Fußwinkel et al., 2013a), without particularly knowing why these low Cl/Br ratios occur in deep crustal fluids. Similarly, the processes causing the extreme chlorinities combined with low Cl/Br and Na/Cl ratios are not well constrained.

Furthermore, as mentioned above basement brines are often invoked as an important source of metals such as Pb, Zn, Cu, Co, Ni, U or Ag, for hydrothermal vein-type deposits (Wilkinson et al., 2005; Yardley, 2005; Gleeson and Turner, 2007; Boiron et al., 2010; Fußwinkel et al., 2013a). Nevertheless, it is poorly constrained by which mineral phase each metal is preferentially hosted, and which processes efficiently release the metals to the fluid.

Therefore, the potential of common igneous, metamorphic and sedimentary rocks to facilitate the geochemical evolution of continental basement brines and to serve as a metal source for hydrothermal ore deposits is tested under controlled laboratory conditions. Leaching experiments on these lithologies, including their mineral separates (feldspar, quartz and biotite) were performed at variable temperatures (25, 180, 275 and 350 °C), pressures (ambient pressure, 0.9, 1.4 and 1.9 kbar), grain-size fractions (<0.01 mm, 0.063–0.125 mm and 2–4 mm) and variable fluid/rock ratios (10 to 1.1) with ultra-pure water and 25 wt.% NaCl solution as solvents. Leachates were analysed

by ion chromatography and total reflexion X-ray fluorescence (TXRF). The samples were characterized prior to the experiments using X-ray fluorescence, microthermometry, electron microprobe analyses, pyrohydrolysis and TXRF. Although leaching experiments using different kinds of crustal rocks of the Schwarzwald were already carried out by Bucher and Stober (2002), their experimental setup was extensively expanded with respect to parameters like temperature, pressure, grain-size, starting materials and duration of experimental runs.

In summary, the grain-size strongly affects fluid modification during water–rock interaction: leachates (using pure H_2O) of fine-grained rock powders have lower Na/Cl and Cl/Br ratios but much higher chlorinities (by a factor of up to 40) compared to leachates using coarse-grained rock powders. All leachates have lower Cl/Br ratios than the respective Cl/Br ratio of the whole-rock. Time integrated and whole-rock normative halogen release to the fluid shows that F, Cl and Br are assigned in variable abundances to two distinctly different reservoirs. These reservoirs are: (A) highly soluble phases (HSP) such as halogens adsorbed (e.g., halides) to the surface of minerals (Hellmann et al., 2012) and present as fluid inclusions and (B) Low soluble phases (LSP) in which halogens are structurally bound (e.g., mica, amphibole, apatite). HSP and LSP response differently to parameters like grain-size, temperature and reaction time. Especially, the proportion of each halogen present as HSP and LSP controls the degree of halogen fractionation between the fluid and the host rock due to selective leaching. Lowest Cl/Br ratios (highest fractionation) can be observed at fine to medium grain-sizes, lower temperatures and short reaction times, since these conditions promote selective leaching of the LSP. Selective leaching of LSP results in Cl/Br and Na/Cl ratios similar to those observed in natural basement brines, which indicates that cataclastic deformation within deeper parts of the upper continental crust is a key parameter controlling the composition of these fluids. Nevertheless, the maximum salinity that can be reached by leaching LSP is dictated by the composition of the LSP, which is difficult to constrain precisely, but most likely it can hardly exceed 8-10 wt.% of total salinity (Nordstrom et al., 1989; Simon, 1990). Mass balance considerations show that the Br enrichment in such moderately saline fluids is sufficiently high to maintain low Cl/Br ratios even after potential mixing with a high salinity, high Cl/Br halite-dissolution brine. In other words, mixing of relatively small volumes (~10 to 30 vol.%) of a 27 wt.% salinity and high Cl/Br (10000) fluid with a 8.5 wt.% salinity and low Cl/Br (65) fluid, results in high salinities and low Cl/Br (~100-200) ratios of the mixed fluid. Consequently, the Cl/Br

ratio should be evaluated critically and if possible combined with other chemical tracers when used as a reservoir tracer.

The leaching experiments showed that, Pb, Zn, Cu and W are released by felsic minerals, while biotite alteration releases Ni, As and additional Zn and Cu. This confirms that crystalline rocks may serve as metal source for hydrothermal ore deposits. Remarkably, substantial amounts of Zn are present in leachates using felsic minerals, although the felsic minerals have low absolute Zn contents.

This broad analytical and experimental approach yields new and important insights into global processes that essentially control the major and trace element composition of deep-seated fluids.

3.2 Root zones of unconformity-related veins

Title of publication:

Tracing fluid migration pathways in the root zone below unconformity-related hydrothermal veins: Insights from trace element systematics of individual fluid inclusions, Chemical Geology (study b)

The temporal evolution of fracture networks below the actual hydrothermal vein (root zones) and their impact on fluid chemistry, vein mineralogy and ore formation is insufficiently understood for hydrothermal vein-systems, such as the common epithermal to mesothermal sediment-, unconformity- and basement- hosted Pb–Zn-, U-,MVT- and five-element deposits. Although a large amount of data on the actual hydrothermal veins are available, only few studies have addressed feeder systems (root zones): Richardson et al. (1987) and Everett et al. (1999) describe alteration and concomitant metal depletion of the wall rock in large-scale fracture root zones below volcanogenic massive sulphide and Irish-type deposits. If, however, this interconnected network is a juvenile fracture system related to recent/local tectonics, or if this system has been previously active over a relatively long time and discontinuously feeds into reactivated veins, is completely unknown. Heretofore, no approach has been proposed to track the temporal evolution of root zones. Consequently, this is what we try to address in the present contribution by proposing an innovative geochemical tool, which allows us to monitor the degree of host rock alteration in the root zone of fracture systems. The degree of alteration in the root zone provides indirect evidence of the life-

time of such fracture meshes below the actual veins since extensive host rock alteration only happens if new fractures with fresh reactive rock material are generated in depth. In contrast, fracture networks, which already persisted for some time, interact significantly less with perfusing fluids, due to the decreased amount of fresh rock. As metals and other trace elements are mobilized during water–rock interaction of highly saline brines with basement rocks (Yardley, 2005), the evolution of these fracture zones might potentially be directly related to episodes of ore formation in the actual hydrothermal vein..

LA-ICPMS microanalyses of individual, texturally well-characterized fluid inclusions were carried out. The fluid inclusions are hosted by fluorite and quartz of the Jurassic–Cretaceous Brandenberg Pb-Zn-(Cu)-fluorite–barite–quartz vein near Todtnau, Schwarzwald, SW Germany. The ore is predominantly associated with the fluorite, which is overgrown by euhedral, younger quartz. The analysed fluid inclusion assemblages (FIAs) have unambiguous age relationships. Therefore, major and trace element systematics in their fluid composition reflect a temporal variation of the ore fluid.

Fluid mobile elements (Rb, Cs, Li, W, Ba, Zn and Pb), show a distinct decrease in their concentration from old to young FIAs. These elements are preferentially released by the alteration of primary rock-forming minerals and are hence potential process tracer for ongoing host rock alteration in the root zone. No systematic variation of Cl/Br ratio, major element chemistry, homogenisation temperatures and a very intense dilution of trace elements of up to a factor of ~0.001 from the oldest FIA in fluorite to the youngest analysed FIA in quartz can be observed. This clearly indicates that these variations in trace elements of the ore fluid are truly caused by processes within the root zone and not by e.g. different mixing proportions of the involved fluids.

Although data is partly overlapping, the maximum and mean values of the Rb/Cs ratio and the Rb, Cs, Li, Pb, Zn, W, and Ba concentrations decrease with time (from early fluorite to late quartz). When juvenile fluid migration paths are established first (fracture opening), abundant fresh reactive mineral surfaces are present along the fracture walls, which immediately react with the percolating fluid. Therefore, first-generation fracture fluids are strongly enriched in Rb, Cs and other fluid mobile trace elements released by feldspar and mica (W, Pb, Zn, Li, Zn, and Ba).

Lower values of Rb, Cs, W, Pb, Zn, Li, and Ba in later quartz indicate that later fluid batches migrated along the same fracture networks (during fluorite and quartz precipitation), rather than establishing new fracture systems. With each consecutive

fluid pulse, the abundance of fresh rock material decreases, and subsequently causes a decrease in the trace element load of the ascending fluid.

Since Rb is incorporated into the clay mineral structure while Cs is only adsorbed onto surfaces of these clay minerals and residual mica (Göb et al., 2013 and references therein), leaching the absorbed Cs results in lower Rb/Cs ratios compared to entirely unaltered rock. The observation of distinctly decreasing of mean Rb/Cs ratios and absolute Rb and Cs concentrations from early fluorite to late quartz indicates progressive rock alteration in the root zone.

Empirical data of granitic and sedimentary fluids (Aquilina et al., 1997; Göb et al., 2013) combined with data of this study were used to model an entire cycle of a hydrothermal fracture system, governed by tectonic processes that promote host rock alteration in the root zone. Assuming closed-system conditions, the Rb/Cs ratio should increase successively after all fresh rock has been altered, trending towards a steady-state with crystalline rocks (Rb/Cs ~2; Aquilina et al. (1997); Göb et al. (2013)). Whether the system obtains steady-state is governed by the timing of the generation of new fractures in the root zone. Assuming open-system conditions, a sedimentary fluid (high Rb/Cs) or a fluid in steady-state with crystalline rocks (Rb/Cs ~2) might be introduced into the newly formed fractures of the root zone. For all of these open- and closed-system possibilities, the Rb/Cs drastically decreases after fresh reactive rock is produced by cataclastic deformation at the beginning of each cycle.

Maximum concentration of trace elements in the fluid and also ore formation occurs preferentially in the initial phase of a fracture root system, directly after new migration paths are established. Later fluid pulses migrate along pre-existing fractures, decreasing the amount of fresh reactive rock material progressively with each fluid pulse. As a consequence, multiple generations of ore minerals seem to preferably occur if new fracture branches are forming in the root zone of hydrothermal veins. Therefore, cataclastic zones below hydrothermal veins appear to control the fertility of a hydrothermal fluid essentially. Their tectonically induced dynamics seems to be one key parameter that governs the temporal interval of ore precipitation in the overlying hydrothermal vein.

3.3 Temporal and regional variation in fluid composition of hydrothermal veins of the Schwarzwald, SW Germany

3.3.1 The temporal evolution of ore fluids in the Schwarzwald

Title of publication:
Long-term chemical evolution and modification of continental basement brines – a field study from the Schwarzwald, SW Germany, Geofluids (study c)

Previous studies showed that the variety of hydrothermal vein-type deposits in the Schwarzwald can be classified into five groups, which are based on their mineralogy and the temporal episode of ore formation:

(i) Late-magmatic W-Sn-quartz-tourmaline veins of the Carbonaceous.
(ii) Metamorphic Sb-Au-quartz veins of the Permian.
(iii) Hematite-quartz veins occurring at the Triassic-Jurassic boundary.
(iv) Jurassic-Cretaceous Pb-Zn-Cu-Ag-fluorite-quartz-(calcite) or Ag/Bi-Ni-Co-(Fe)-As-(U)-calcite-barite veins.
(v) Post-Cretaceous Pb±Zn±Ag± Cu±barite±quartz±carbonate±fluorite veins.

Besides their different ages, distinct differences in their fluid composition (microthermometry and crush-leach analyses) can be recognized. Low salinity, high temperature and volatile-rich ore fluids (vein-type i) are related to W-Sn-quartz-tourmaline veins, which occur in the Carbonaceous in close proximity to granitic intrusions (Marks et al., 2013). During the Permian, late metamorphic low salinity and high temperature fluids (vein-type ii) are present in low-grade Au-Sb-quartz veins (Wagner and Cook, 2000). Hematite-quartz veins (vein type iii) occur since the Triassic-Jurassic boundary (Brander, 2000). These veins comprise a variety of fluid types including primary fluids of low and moderate salinities, which alternate on the scale of growth zones and have intermediate temperatures. The Jurassic-Cretaceous veins (vein-type iv) are characteristically Pb-Zn-Cu-Ag-fluorite-quartz-(calcite) or to a lesser extent Ag/Bi-Ni-Co-(Fe)-As-(U)-calcite-baryte veins, which are related to the opening of the North Atlantic (Boiron et al., 2010). In contrast to vein-types i to iii, the associated ore fluid of vein-type iv is invariably of high salinity and moderate temperature (Behr and Gerler, 1987; Baatartsogt et al., 2007; Staude et al., 2009; Staude et al., 2011; Staude et al., 2012a; Staude et al., 2012b). Post-Cretaceous Pb-Zn-(Cu)-fluorite-barite-calcite-

quartz veins are related to the Upper Rhine Graben rifting. Due to the complex graben-related tectonic and hydrogeological setting, these veins comprise a great variability in fluid composition and mineralogy.

In the following these distinct temporal changes in fluid composition of the trapped ore fluid are related to the regional geological history, which has undeniably a substantial influence on the composition of the ore fluids (fluid sources, aquifer composition, hydrogeology, precipitation mechanism and fluid mobilisation).

After late magmatic (vein-type i) and metamorphic (vein-type ii) high temperature, low salinity and Na-dominated fluids prevailed from the Carbonaceous until the Permian, the first occurrence of highly saline fluids can be recognized at the Triassic-Jurassic boundary (vein-type iii). Importantly, these highly saline fluids alternate with low salinity fluids, but mixing between these fluids cannot be observed (e.g. intermediate salinities) at that stage (vein-type iii). The highly saline fluids show low Ca/(Ca+Na) (molar) and low Cl/Br ratios (weight) and are most likely residual brines derived from evaporitic basins (Richard et al., 2011; Fußwinkel et al., 2013a), where the formation of halite is well documented (Geyer et al., 2011). These highly saline residual fluids (bittern brines) are strongly enriched in Br (since halite does not incorporate Br, (Siemann and Schramm, 2000)) and descend subsequently into deeper crustal levels due to desiccation processes within the crystalline basement (Stober and Bucher, 2004; Bons et al., 2014). In the Jurassic, the extensive tectonic setting, induced by the opening of the North Atlantic, resulted in mixing of two contrasting fluids on large-scale fractures, which formed the Jurassic hydrothermal veins (iv). The bittern brine already recognized in vein type (iii), has been extensively modified by fluid-rock interaction with the igneous and metamorphic rocks of the basement. Thus, metal concentrations and the Ca/(Ca+Na) ratio increased, while the low Cl/Br ratio inherited from the original bittern brine remains (iv). Rifting related, large-scale fluid migration results in mixing of this modified bittern brine and a sedimentary fluid (halite-dissolution: high Cl/Br ratio, high salinity and very low Ca/(Na+Ca) ratio) during their simultaneous ascend (Bons et al., 2014). Large-scale mixing occurred also at post-Cretaceous times, but stronger compositional variations of ore fluids (v) can be observed, which are related to the tectonic displacement of the crystalline and sedimentary aquifers caused by the Upper Rhine Graben rifting.

In summary, the first occurrence of highly saline brines, which are necessary for efficient metal transportation, is closely related to the formation of halite in marine basins at the

sub-surface. During its percolation of these bittern brines through basement rocks, they are substantially modified with respect to their major and trace element chemistry as a consequence of fluid-rock interaction. Mixing happens only, if the hydrogeological/tectonic setting is suitable to release fluids from different crustal levels/aquifers synchronically into large-scale fractures. A comparison of these criteria with similar vein-type deposits from the Harz and the Spessart mountains (SW Germany) emphasis even more the importance of satisfying these prerequisites for effective ore deposition: the first deposition of halite in the sedimentary units happened in the Harz and the Spessart already in the Zechstein (Upper Permian), which is the reason why the first occurrence of highly saline fluids and ore-bearing hydrothermal veins can be recognized earlier (lower Triassic) than in the Schwarzwald (Lüders and Möller, 1992; Fußwinkel et al., 2013b).

3.3.2. A refined geochemical model for the Jurassic-Cretaceous veins of the Schwarzwald - The relationship between paleo-topography and the composition of hydrothermal ore fluids

Title of submitted manuscript:
Major element and trace metal systematics of fluid inclusions in hydrothermal veins: metal provenance and the reconstruction of eroded sedimentary units, submitted to Mineralium Deposita (study d)

Study d focuses on the Jurassic-Cretaceous veins (iv) and refines the simplified genetic model presented in study c with additional details. As mentioned earlier the Jurassic-Cretaceous veins formed due to binary mixing of a deep-seated basement fluid (low Cl/Br mass ratios) and a sedimentary/basinal brine (high Cl/Br ratios) (Fußwinkel et al., 2013a).
Therefore, regional compositional variations of the ore fluids that are ascribed to compositional differences of the involved sedimentary fluid might be used to reconstruct regional differences in the composition of the yet eroded sedimentary rock units.
Actually, compositional variations with respect to the Ca/(Ca+Na) molar ratio, sulphate concentrations, and the Cl/Br ratio can be observed in ore fluids from the northern, central and southern Schwarzwald. While fluids from the northern and southern

Schwarzwald show very variable Cl/Br and Ca/(Ca+Na) ratios, the analysed fluids of the central Schwarzwald show invariably low Cl/Br, relatively higher Ca/(Ca+Na) ratios as well as dissolved aqueous sulphate. This agrees with the distribution of Middle Triassic halite in the sedimentary units, which is predominantly present in the northern and southern Schwarzwald (Geyer et al., 2011). While the topography of the paleo-marine basin enhanced halite precipitation in the northern and in the southern Schwarzwald, the evaporitic sequence in the central Schwarzwald did not exceed the anhydrite stage. Consequently, in the northern and in the southern the analysed ore fluids consist of mixtures of basement brines and halite-dissolution brines, while in the central Schwarzwald the ore fluid consists of mixtures of basement brines and sulphate-dissolution brines.

It has been shown that important information about the composition of the involved sedimentary paleo-aquifer, which is yet entirely eroded is archived in fluid inclusions of hydrothermal veins.

3.3.3 Multicomponent mixing in post-Cretaceous hydrothermal veins of the Schwarzwald

Title of manuscript:

Multi-reservoir fluid mixing processes in rift-related hydrothermal vein-type deposits, in preparation (study e)

This study focuses on post-Cretaceous Pb-Zn-Cu-fluorite-quartz-calcite-barite veins (v) related to the Upper Rhine Graben rifting. These veins are characterized by a great diversity of their mineralogy and fluid chemistry. In contrast to the Jurassic-Cretaceous veins (iv), fluid inclusion data (microthermometry, crush-leach and LA-ICPMS) of the post-Cretaceous veins show that more than two fluids are involved in ore formation (multi-component mixing). While the basement brine component is invariably present in these ore fluids (like in vein type iv), two or more other involved fluids can be recognized, which are of sedimentary, basinal and/or meteoric origin. This multi-component mixing can be recognized on the regional scale, the scale of one single vein and even on the scale of one single fluid inclusion assemblage. This variation is caused by intense tectonic movement related to Paleogene rifting, resulting in complex

displacement of the involved aquifers. Consequently, fluids from different sedimentary aquifers locally mix with each other. The resulting fluid composition is very diverse, depending on which aquifers hydraulically interact with each other. A precise identification of fluid sources other than the involved basement fluid is difficult, since the composition of the sedimentary aquifers changes with time due to e.g. progressive fluid-rock interaction, subsidence or uplift. Still geochemical mixing models with inferred fluid compositions indicate that fluids from the Middle Triassic, halite-bearing limestone, the Bunter Sandstone aquifer and diluted meteoric fluids participate in variable proportions in vein formation.

In summary, the observed multi-component fluid mixing is caused by the rift related tectonic disturbance of the crustal stack, which is accompanied by the generation of complex hydrogeological fluid migration pathways. Depending on the source and composition of the involved fluids, the mineralogy of the veins varies substantially.

3.4 The genesis of five-element veins

Title of publication and submitted manuscript:

a.) *Natural fracking and the genesis of five-element veins*, Mineralium Deposita (study f)

b.) *Methane and the origin of five-element veins: mineralogy, age, fluid inclusion chemistry and ore forming processes in the Odenwald, SW Germany*, submitted to Ore Geology Reviews (study g)

Five-element veins (Ag, Bi, Co, Ni, As) have been valuable mineral deposits since medieval to contemporary times. The characteristic occurrence of fascinating, large aggregates of native metals enclosed by a succession of arsenides and carbonates makes this vein-type attractive for the mining industry, museums and private mineral collectors. Some of the best studied and well-known deposits are Schneeberg/Germany (Lipp and Flach, 2003), Jachymov/Czech Republic (Ondrus et al., 2003a; Ondrus et al., 2003b; Ondrus et al., 2003c), Kongsberg-Modum/Norway (Bugge, 1931), Cobalt-Gowganda/Canada (Andrews et al., 1986), Thunder Bay/Canada (Franklin et al., 1986), Batopilas/Mexico (Wilkerson et al., 1988), Imiter/Morocco (Cheilletz et al., 2002) and Bou Azzer/Morocco (Ahmed et al., 2009). But with a few exceptions (Ondrus et al., 2003a; Ahmed et al., 2009; Staude et al., 2012b) the majority of this literature does not comprise modern analytical data.

Hydrothermal five-element veins occur below, across and above the basement-cover unconformity (Kissin, 1992). The ambient host lithologies are very variable and include igneous, metamorphic and sedimentary rocks. Formation temperatures range from ~150 to 450°C, and hence the mode of host rock alteration is also variable (Kissin, 1992; Staude et al., 2012b). All five-element veins have very similar mineral assemblages and ore textures, which implies that all these deposits are genetically related, though formation temperature, fluid salinity, host rock and alteration type may strongly vary for each occurrence (Kissin, 1992; Staude et al., 2012b).

Despite of the great diversity, but also controversy of existing genetic theories, the enigmatic formation process of these specific vein-type was long poorly constrained. These genetic theories include a magmatic, hydrothermal and metamorphic origin (Kissin, 1992). However, these models do not consider the textural details, and the precise precipitation mechanism, which are included in the genetic model presented in this thesis (study f and g).

All mineralogical varieties (Ag-, As- and Bi-dominated) of the five-element veins in the Odenwald (SW Germany) were analysed in terms of ore textures, mineral chemistry, fluid inclusion composition (microthermometry and Raman spectroscopy), stable isotopes (C, O and S) and radiogenic isotope composition (U-Pb) as a profound database for the genetic model.

Pb-Zn-Cu-sulphide-calcite veins and arsenide-free Ag-Hg-barite veins occur besides the five-element veins and have also been examined in this study.

Characteristically, the ore textures of five-element veins have in common that up to dm-sized, often dendritic native metals are overgrown by a succession of arsenides, followed by carbonate and finally sulphides. The succession of arsenides typically comprises rammelsbergite, skutterudite, safflorite and loellingite, which results in a distinct chemical trend from Ni- to Co- and finally Fe-dominated phases (old to young). In contrast, spatially closely related Ag-Hg-barite veins consist of almost mono-mineralic amalgam inter-grown with barite and calcite.

The five-element veins of the Odenwald precipitated at 170 to 180 Ma from Na-Ca-Cl fluids at 290°C, 0.1-0.3 kbar, salinities of ~27 wt.% and Ca/(Ca+Na) ratios of 0.30 to 0.35. This age clearly relates the relevant fluid migration to extension and crustal thinning caused by the opening of the North Atlantic (Mitchell and Halliday, 1976). This is the first time that U-Pb dating of nominally U-free gangue minerals (calcite and prehnite) was applied to ore deposits. Mixing of deep-seated metal- and arsenic-rich

basement brines (fluid-type A), sulphide-bearing basinal/sedimentary brines (fluid-type B) and methane-dominated fluids/gases (fluid-type C) induced ore formation (for further details on the origin of the involved fluids, solutes and gases refer to study g in the appendix). The encounter of such chemically contrasting fluids results in a strong chemical disequilibrium of the mixed fluid, which potentially leads to rapid precipitation of native metals and arsenides forming these specific ore textures. In contrast, sulphide-bearing calcite veins formed under similar P-T-conditions, but the ore fluid consists only of fluid-type A and B, while fluid-type C is absent.

An internally consistent model shows that the oxidation of relatively small amounts of methane is sufficient to maintain suitable low fO_2 conditions to precipitate native metals and arsenides. Besides the decrease of fO_2, the simultaneous precipitation of native metals and oxidation of methane causes a drastic decrease of the pH. The predicted reaction path that related to methane influx crosses the skutterudite predominance field before some of the native metal is dissolved due to the decreasing pH. As soon as the majority of the methane is oxidized, the pH increases, which leads to the subsequent precipitation of safflorite and loellingite and finally calcite. The trend of increasing pH is caused by the consumption of methane and the subsequent transition from a methane-buffered to a rock-buffered system. This hydro-chemical model is in absolute agreement with all textural observations (even the dissolution textures of native metals). A compositional trend of Ni, Co and Fe seems to occur in all five-element veins (Kissin, 1992; Ondrus et al., 2003c; Ahmed et al., 2009; Staude et al., 2012b). This trend is caused by decreasing stabilities from Ni to Co and finally Fe chloro complexes with increasing pH at low fO_2. According to this model, concentrations of 30 mg/l methane in fluid BC are sufficient to precipitate the observed amounts of native metals, arsenides and carbonates. Furthermore, stable C-isotopes of analysed calcites show relatively low $\delta^{13}C$ values, which are in the range of the predicted isotopic composition including both involved C-sources: the calculated amount of HCO_3^- derived by methane oxidation and the inferred amount of inorganic HCO_3^- already present in fluid A (Frape et al., 2003).

Although methane could be detected in a few fluid inclusions of the analysed veins and the importance as a reducing agent could be clearly shown, it is noteworthy that its presence in the ore fluids is often cryptic, due to its oxidation and dissolution to HCO_3^-.

Methane production and migration is well documented (Lüders et al., 2005; Lüders et al., 2012) in the North German Basin, and therefore the source of methane is presumably within the organic-rich Permo-Triassic sediments, which were also present above the

hydrothermal veins prior to erosion. The release and uptake of isolated methane by migrating sedimentary fluids (B) is closely related to tectonically active episodes, which promote the formation of inter-connected fracture networks (Sibson, 1996) triggering indirectly the formation of the five-element assemblage.

Introduction of methane into an active hydrothermal Pb-Zn-Cu-sulphide system, and concomitant reduction of the ore fluid has a substantial effect on the species present in the fluid. Particularly, dissolved arsenic typically present as As^{3+} at moderate fO_2 and pH conditions (Wood and Samson, 1998) is reduced to $As^{1-/2-}$, which is crucial for arsenide precipitation. Furthermore, the direct observation of sulphides occurring temporarily before and after the formation of native metals and arsenides (Ramdohr, 1975) indicates that the five-element assemblage is restricted to a narrow temporal interval ("arsenide window") within a sulphide-dominated hydrothermal background system. Chemically, this arsenide window is most likely controlled by the As^{1-}/S^{2-} ratio, which is directly related to the As^{3+}/As^{1-} ratio (governed by the redox state of the fluid), rather than absolute As and S concentrations.

Ag-Hg-barite veins, which dominantly consist of native silver and barite without arsenides occur in close spatial association with the five-element veins of the northern Odenwald. In contrast to Hg contents below 1 wt.% of native silver and Ag_2S of the five-element assemblage, the native silver of this vein type has extremely high Hg contents of up to ~30 wt.% (amalgam). Still, textural and isotopic arguments indicate that the amalgam-barite association is caused by the dissolution of Ag_2S, which is itself primarily derived by the remobilisation of primary native silver of the five-element assemblage. After initial precipitation, primary silver is dissolved, proximally transported and re-precipitated as Ag_2S at temperatures around 200°C. In a second step the Ag_2S is incongruently dissolved to native silver and barite. Due to the successive decrease of S^{2-}/SO_4^{2-} with decreasing temperature (closed system), the activity of S^{2-} is at some point sufficiently low to dissolve Ag_2S and precipitate Ag and barite (~140°C = calculated; 135°C = measured homogenization temperature). Concomitantly, this decrease of the S^{2-} activity leads to the enrichment of Hg, since its solubility drastically decreases as the Hg bisulphide-complexes are increasingly destabilised (Krupp, 1988; Barnes and Seward, 1997).

In conclusion, five-element veins seem to form when methane (often cryptic in the ore fluid) is introduced into active hydrothermal Pb-Zn-Cu-sulphide systems. Isolated methane in the sedimentary aquifer is mobilised during active tectonic episodes, and

has to be transported along migration pathways to mix with ascending basement brines. As a consequence, the system is shifted from a rock-buffered to a methane-buffered system, which is associated with drastic changes of the fO_2 and the pH. As soon as the methane is consumed, the system evolves back to a rock-buffered system, in which sulphides are predominant.

The applied genetic model includes and agrees with all textural, mineralogical and chemical aspects of five-element veins, and therefore improved the scientific understanding of this mineralogical fascinating hydrothermal vein-type deposit significantly.

4. SUMMARY AND CONCLUSIONS

The executed experiments yield new and important insights into the evolution and modification of continental basement brines by fluid-rock, fluid-fluid and fluid-gas interaction. Particularly, the source and fractionation of halogens during fluid-rock and fluid-fluid interaction and its implication for the Cl/Br ratio as a "conservative" reservoir tracer have been discussed extensively. The presented results and conclusions contribute to the general understanding of halogen systematics in hydrothermal environments.

Lead, Zn, Cu and W are released by alteration of felsic minerals, while biotite alteration releases Ni, As and additional Zn and Cu. Although biotite contains higher Zn concentrations, the majority of Pb and Zn is mobilised by feldspar alteration. This clearly demonstrates that the absolute concentration of an element in the source mineral is less important than its affinity of being released to the fluid (mobility). Consequently, even minerals with relatively low metal concentrations, such as feldspar can serve as metal source if these are efficiently released to the fluid during mineral alteration. Among all tested parameters that have a significant influence on the fluid composition, grain-size seems to have the strongest impact on the experimental leachates. Therefore, it is most likely that naturally occurring cataclastic zones have not only a major impact on the permeability on the host rock (fluid pathway), but also on the fluid composition of basement brines. This hypothesis is furthermore strengthened by temporal variations in fluid compositions of individual fluid inclusions from the Jurassic Brandenberg vein, which can be attributed to fluid-rock interaction at cataclastic zones below the hydrothermal vein (root zone). Time resolved trace element, Rb/Cs and Cl/Br variations

of vein-hosted fluid inclusions are suitable to monitor alteration processes that occur in these cataclastic root zones. By combining these parameters with empirical Rb/Cs data, it was possible to model repetitive hydro-chemical cycles, which are directly related to the generation of fresh reactive rock in the root zone during tectonically active episodes.
On the other hand, the influence of active tectonics (post-Cretaceous veins) and paleo-topography (Jurassic veins) on the composition of the sedimentary fluid involved in ore formation was studied in detail. It could be demonstrated that the sedimentary aquifers are inhomogeneous with respect to their composition on the scale of the Schwarzwald due to tectonic displacement (post-Cretaceous veins) and differing conditions during deposition (Jurassic veins). These compositional differences of the yet eroded sedimentary cover can be deduces from archived fluid inclusions of hydrothermal veins.
The combined study of the regional geology, basement brines, sedimentary brines and the ore fluids (mixture) of different vein-types and ages enabled a profound reconstruction of the evolution of involved fluids during the last 300 million years.
An entirely new genetic model for five-element veins has been proposed, which seems to be universally valid for the majority of five-element veins and therefore might potentially decipher a longstanding enigma in the scientific field of ore petrology. This model includes the tectonic liberation of hydrocarbons, their transportation and their significant impact on the condition of the ore fluid. It is capable of explaining all textural and chemical features that are typical of five-element veins. To testify this model, it was successively applied to the five-element veins of the Odenwald, which formed due to mixing of a metal-rich basement fluid, a sulphur-rich sedimentary/basinal fluid and methane or a methane-bearing fluid.
The presented studies include innovative and profound insights into fluid-rock, fluid-fluid and fluid-gas interaction, which are generally relevant for hydrothermal processes in the upper crust. The findings are generally valid and readily applicable to other systems/deposits on a global scale. Consequently, this thesis contributes significantly and fundamentally to the scientific understanding of hydrothermal systems.

5. REFERENCES

Ahmed, A.H., Arai, S., Ikenne, M., 2009. Mineralogy and Paragenesis of the Co-Ni Arsenide Ores of Bou Azzer, Anti-Atlas, Morocco. Economic Geology, 104(2): 249-266.

Andrews, A., Owsiacki, L., Kerrich, R., Strong, D., 1986. The silver deposits at Cobalt and Gowganda, Ontario. I: Geology, petrography, and whole-rock geochemistry. Canadian Journal of Earth Sciences, 23(10): 1480-1506.

Appold, M.S., Garven, G., 1999. The hydrology of ore formation in the Southeast Missouri District; numerical models of topography-driven fluid flow during the Ouachita Orogeny. Economic Geology, 94(6): 913-935.

Aquilina, L., Pauwels, H., Genter, A., Fouillac, C., 1997. Water-rock interaction processes in the Triassic sandstone and the granitic basement of the Rhine Graben: Geochemical investigation of a geothermal reservoir. Geochimica et cosmochimica acta, 61(20): 4281-4295.

Baatartsogt, B., Schwinn, G., Wagner, T., Taubald, H., Beitter, T., Markl, G., 2007. Contrasting paleofluid systems in the continental basement: a fluid inclusion and stable isotope study of hydrothermal vein mineralization, Schwarzwald district, Germany. Geofluids, 7(2): 123-147.

Barnes, H., Seward, T., 1997. Geothermal systems and mercury deposits. Geochemistry of hydrothermal ore deposits, 3: 699-736.

Behr, H.-J., Gerler, J., 1987. Inclusions of sedimentary brines in post-Variscan mineralizations in the Federal Republic of Germany—a study by neutron activation analysis. Chemical geology, 61(1): 65-77.

Boiron, M.C., Cathelineau, M., Richard, A., 2010. Fluid flows and metal deposition near basement/cover unconformity: lessons and analogies from Pb–Zn–F–Ba systems for the understanding of Proterozoic U deposits. Geofluids, 10(1‐2): 270-292.

Bons, P.D., Fusswinkel, T., Gomez-Rivas, E., Markl, G., Wagner, T., Walter, B., 2014. Fluid mixing from below in unconformity-related hydrothermal ore deposits. Geology, 42(12): 1035-1038.

Brander, T., 2000. U/He-chronologische Fallstudien an Eisen-und Manganerzen, Heidelberg, 225 pp.

Bucher, K., Stober, I., 2002. Water-rock reaction experiments with Black Forest gneiss and granite, Water-Rock Interaction. Springer, pp. 61-95.

Bugge, A., 1931. Gammel og ny geologi ved Kongsberg sölvverk. Norsk Geologisk Tidsskrift, 12: 123.

Changkakoti, A., Morton, R., Gray, J., Yonge, C., 1986. Oxygen, hydrogen, and carbon isotopic studies of the Great Bear Lake silver deposits, Northwest Territories. Canadian Journal of Earth Sciences, 23(10): 1463-1469.

Cheilletz, A., Levresse, G., Gasquet, D., Azizi-Samir, M., Zyadi, R., Archibald, D.A., Farrar, E., 2002. The giant Imiter silver deposit: Neoproterozoic epithermal mineralization in the Anti-Atlas, Morocco. Mineralium Deposita, 37(8): 772-781.

Chi, G., Savard, M.M., 1997. Sources of basinal and Mississippi Valley-type mineralizing brines: mixing of evaporated seawater and halite-dissolution brine. Chemical Geology, 143(3): 121-125.

Franklin, J., Kissin, S., Smyk, M., Scott, S., 1986. Silver deposits associated with the Proterozoic rocks of the Thunder Bay District, Ontario. Canadian Journal of Earth Sciences, 23(10): 1576-1591.

Frape, S., Blyth, A., Blomqvist, R., McNutt, R., Gascoyne, M., 2003. Deep fluids in the continents: II. Crystalline rocks. Treatise on geochemistry, 5: 541-580.

Frape, S., Fritz, P., McNutt, R.t., 1984. Water-rock interaction and chemistry of groundwaters from the Canadian Shield. Geochimica et Cosmochimica Acta, 48(8): 1617-1627.

Frenzel, M., Hirsch, T., Gutzmer, J., 2016. Gallium, germanium, indium, and other trace and minor elements in sphalerite as a function of deposit type—A meta-analysis. Ore Geology Reviews, 76: 52-78.

Fußwinkel, T., Wagner, T., Wälle, M., Wenzel, T., Heinrich, C.A., Markl, G., 2013a. Fluid mixing forms basement-hosted Pb-Zn deposits: Insight from metal and halogen geochemistry of individual fluid inclusions. Geology, 41(6): 679-682.

Fußwinkel, T., Wagner, T., Wenzel, T., Wälle, M., Lorenz, J., 2013b. Evolution of unconformity-related Mn Fe As vein mineralization, Sailauf (Germany): Insight from major and trace elements in oxide and carbonate minerals. Ore Geology Reviews, 50: 28-51.

Geyer, O.F., Gwinner, M.P., Geyer, M., Nitsch, E., Simon, T., 2011. Geologie von Baden-Württemberg, 5. Auflage. Schweizerbart, 627 pp.

Gleeson, S., Turner, W., 2007. Fluid inclusion constraints on the origin of the brines responsible for Pb–Zn mineralization at Pine Point and coarse non‐saddle and saddle dolomite formation in southern Northwest Territories. Geofluids, 7(1): 51-68.

Gleeson, S.A., Wilkinson, J.J., Stuart, F.M., Banks, D.A., 2001. The origin and evolution of base metal mineralising brines and hydrothermal fluids, South Cornwall, UK. Geochimica et Cosmochimica Acta, 65(13): 2067-2079.

Göb, S., Loges, A., Nolde, N., Bau, M., Jacob, D.E., Markl, G., 2013. Major and trace element compositions (including REE) of mineral, thermal, mine and surface waters in SW Germany and implications for water–rock interaction. Applied geochemistry, 33: 127-152.

Gross, W., 1975. New ore discovery and source of silver-gold veins, Guanajuato, Mexico. Economic Geology, 70(7): 1175-1189.

Hellmann, R., Wirth, R., Daval, D., Barnes, J.-P., Penisson, J.-M., Tisserand, D., Epicier, T., Florin, B., Hervig, R.L., 2012. Unifying natural and laboratory chemical weathering with interfacial dissolution–reprecipitation: A study based on the nanometer-scale chemistry of fluid–silicate interfaces. Chemical Geology, 294: 203-216.

Holland, H.D., 1972. Granites, solutions, and base metal deposits. Economic Geology, 67(3): 281-301.

Kissin, S.A., 1992. Five-element (Ni-Co-As-Ag-Bi) veins. Geoscience Canada, 19(3).

Krupp, R., 1988. Physicochemical aspects of mercury metallogenesis. Chemical geology, 69(3): 345-356.

Leisen, M., Boiron, M.-C., Richard, A., Dubessy, J., 2012. Determination of Cl and Br concentrations in individual fluid inclusions by combining microthermometry and LA-ICPMS analysis: Implications for the origin of salinity in crustal fluids. Chemical Geology, 330–331: 197-206.

Lipp, U., Flach, S., 2003. Wismut-, Kobalt-, Nickel-und Silbererze im Nordteil des Schneeberger Lagerstättenbezirkes.

Lodemann, M., Fritz, P., Wolf, M., Ivanovich, M., Hansen, B.T., Nolte, E., 1997. On the origin of saline fluids in the KTB (continental deep drilling project of Germany). Applied geochemistry, 12(6): 831-849.

Lüders, V., Möller, P., 1992. Fluid evolution and ore deposition in the Harz Mountains (Germany). European Journal of Mineralogy, 4(5): 1053-1068.

Lüders, V., Plessen, B., di Primio, R., 2012. Stable carbon isotopic ratios of CH 4–CO 2-bearing fluid inclusions in fracture-fill mineralization from the Lower Saxony Basin (Germany)–A tool for tracing gas sources and maturity. Marine and Petroleum Geology, 30(1): 174-183.

Lüders, V., Reutel, C., Hoth, P., Banks, D.A., Mingram, B., Pettke, T., 2005. Fluid and gas migration in the North German Basin: fluid inclusion and stable isotope constraints. International Journal of Earth Sciences, 94(5-6): 990-1009.

Markl, G., 2015. Schwarzwald: Lagerstätten und Mineralien aus vier Jahrhunderten, 1. Auflage. Bode Verlag, 672 pp.

Marks, M.A., Marschall, H.R., Schühle, P., Guth, A., Wenzel, T., Jacob, D.E., Barth, M., Markl, G., 2013. Trace element systematics of tourmaline in pegmatitic and hydrothermal systems from the Variscan Schwarzwald (Germany): The importance of major element composition, sector zoning, and fluid or melt composition. Chemical Geology.

Marshall, D.D., Diamond, L.W., Skippen, G.B., 1993. Silver transport and deposition at Cobalt, Ontario, Canada; fluid inclusion evidence. Economic Geology, 88(4): 837-854.

Mitchell, J., Halliday, A., 1976. Extent of Triassic/Jurassic hydrothermal ore deposits on the North Atlantic margins. Transactions of the Institution of Mining and Metallurgy B, 85: 159-61.

Möller, P., Woith, H., Dulski, P., Lüders, V., Erzinger, J., Kämpf, H., Pekdeger, A., Hansen, B., Lodemann, M., Banks, D., 2005. Main and trace elements in KTB‐VB fluid: composition and hints to its origin. Geofluids, 5(1): 28-41.

Munz, I., Yardley, B., Banks, D., Wayne, D., 1995. Deep penetration of sedimentary fluids in basement rocks from southern Norway: Evidence from hydrocarbon and brine inclusions in quartz veins. Geochimica et Cosmochimica Acta, 59(2): 239-254.

Nickel, E., 1975. Geologische Position und Petrogenese des kristallinen Odenwaldes. Mineralien und Gesteine im Odenwald. Aufschluû Sonderbd, 27: 1-25.

Nordstrom, D.K., Lindblom, S., Donahoe, R.J., Barton, C.C., 1989. Fluid inclusions in the Stripa granite and their possible influence on the groundwater chemistry. Geochimica et Cosmochimica Acta, 53(8): 1741-1755.

O'Keeffe, W., 1986. Age and postulated source rocks for mineralization in central Ireland as indicated by lead isotopes, in Andrew, C.J., Crowe, R.W.A., Finlay, S., Pennell, W.M., and Pyne, J., eds. Geology and genesis of mineral deposits in Ireland: Dublin, Irish Association for Economic Geology: 617-624.

Ondrus, P., Veselovsky, F., Gabasova, A., Drabek, M., Dobes, P., Maly, K., Hlousek, J., Sejkora, J., 2003a. Ore-forming processes and mineral parageneses of the Jáchymov ore district. Journal of GEOsciences, 48(3-4): 157-192.

Ondrus, P., Veselovsky, F., Gabasova, A., Hlousek, J., Srein, V., 2003b. Geology and hydrothermal vein system of the Jáchymov (Joachimsthal) ore district. Journal of GEOsciences, 48(3-4): 3-18.

Ondrus, P., Veselovsky, F., Gabasova, A., Hlousek, J., Srein, V., Vavrin, I., Skala, R., Sejkora, J., Drabek, M., 2003c. Primary minerals of the Jáchymov ore district. Journal of GEOsciences, 48(3-4): 19-147.

Orville, P., 1972. Plagioclase cation exchange equilibria with aqueous chloride solution: results at 700 C and 2000 bars in the presence of quartz. TC, 1: 4.

Otto, J., 1967. Der Fluoritgang der Grube "Gottesehre" bei Urberg, Kr. Säckingen (Südschwarzwald). Jahresh Geol Landesamt Baden-Wuerttemberg, 9: 25-50.

Pfaff, K., Hildebrandt, L.H., Leach, D.L., Jacob, D.E., Markl, G., 2010. Formation of the Wiesloch Mississippi Valley-type Zn-Pb-Ag deposit in the extensional setting of the Upper Rhinegraben, SW Germany. Mineralium Deposita, 45(7): 647-666.

Ramdohr, P., 1975. Der Silberkobalterzgang mit Kupfererzen vom Wingertsberg bei Nieder-Ramstadt im Odenwald. Aufschluss, 27: 237-243.

Richard, A., Banks, D.A., Mercadier, J., Boiron, M.-C., Cuney, M., Cathelineau, M., 2011. An evaporated seawater origin for the ore-forming brines in unconformity-related uranium deposits (Athabasca Basin, Canada): Cl/Br and δ37Cl analysis of fluid inclusions. Geochimica et Cosmochimica Acta, 75(10): 2792-2810.

Richard, A., Cathelineau, M., Boiron, M.-C., Mercadier, J., Banks, D.A., Cuney, M., 2016. Metal-rich fluid inclusions provide new insights into unconformity-related U deposits (Athabasca Basin and Basement, Canada). Mineralium Deposita, 51(2): 249-270.

Savoye, S., Aranyossy, J.-F., Beaucaire, C., Cathelineau, M., Louvat, D., Michelot, J.-L., 1998. Fluid inclusions in granites and their relationships with present-day groundwater chemistry. European journal of mineralogy, 10(6): 1215-1226.

Sibson, R., Moore, J.M.M., Rankin, A., 1975. Seismic pumping—a hydrothermal fluid transport mechanism. Journal of the Geological Society, 131(6): 653-659.

Sibson, R.H., 1996. Structural permeability of fluid-driven fault-fracture meshes. Journal of Structural Geology, 18(8): 1031-1042.

Siemann, M.G., Schramm, M., 2000. Thermodynamic modelling of the Br partition between aqueous solutions and halite. Geochimica et Cosmochimica Acta, 64(10): 1681-1693.

Simon, K., 1990. Hydrothermal alteration of Variscan granites, southern Schwarzwald, Federal Republic of Germany. Contributions to Mineralogy and Petrology, 105(2): 177-196.

Staude, S., Bons, P.D., Markl, G., 2009. Hydrothermal vein formation by extension-driven dewatering of the middle crust: an example from SW Germany. Earth and Planetary Science Letters, 286(3): 387-395.

Staude, S., Göb, S., Pfaff, K., Ströbele, F., Premo, W.R., Markl, G., 2011. Deciphering fluid sources of hydrothermal systems: a combined Sr-and S-isotope study on barite (Schwarzwald, SW Germany). Chemical Geology, 286(1): 1-20.

Staude, S., Mordhorst, T., Nau, S., Pfaff, K., Brügmann, G., Jacob, D.E., Markl, G., 2012a. Hydrothermal carbonates of the Schwarzwald ore district, southwestern Germany: Carbon source and conditions of formation using δ18O, δ13C, 87Sr/86Sr, and fluid inclusions. The Canadian Mineralogist, 50(5): 1401-1434.

Staude, S., Werner, W., Mordhorst, T., Wemmer, K., Jacob, D.E., Markl, G., 2012b. Multi-stage Ag–Bi–Co–Ni–U and Cu–Bi vein mineralization at Wittichen, Schwarzwald, SW Germany: geological setting, ore mineralogy, and fluid evolution. Mineralium Deposita, 47(3): 251-276.

Stein, E., 2001. The geology of the Odenwald crystalline complex. Mineralogy and petrology, 72(1-3): 7-28.

Stober, I., Bucher, K., 1999a. Deep groundwater in the crystalline basement of the Black Forest region. Applied geochemistry, 14(2): 237-254.

Stober, I., Bucher, K., 1999b. Origin of salinity of deep groundwater in crystalline rocks. Terra Nova-Oxford, 11(4): 181-185.

Stober, I., Bucher, K., 2004. Fluid sinks within the earth's crust. Geofluids, 4(2): 143-151.

Stober, I., Bucher, K., 2005. The upper continental crust, an aquifer and its fluid: hydaulic and chemical data from 4 km depth in fractured crystalline basement rocks at the KTB test site. Geofluids, 5(1): 8-19.

Stober, I., Jodocy, M., Burisch, M., Person, R., 2013. Tiefenwässer im Oberen Muschelkalk-Aquifer des Oberrheingrabens und des Südwestdeutschen Molassebeckens. Grundwasser: 1-11.

Sverjensky, D.A., 1981. The origin of a Mississippi Valley-type deposit in the Viburnum Trend, southeast Missouri. Economic Geology, 76(7): 1848-1872.

Wagner, T., Cook, N., 2000. Late-Variscan antimony mineralisation in the Rheinisches Schiefergebirge, NW Germany: evidence for stibnite precipitation by drastic cooling of high-temperature fluid systems. Mineralium Deposita, 35(2-3): 206-222.

Wilkerson, G., Deng, Q., Llavona, R., Goodell, P.C., 1988. Batopilas mining district, Chihuahua. Economic Geology, 83(8): 1721-1736.

Wilkinson, J., Eyre, S., Boyce, A., 2005. Ore-forming processes in Irish-type carbonate-hosted Zn-Pb deposits: Evidence from mineralogy, chemistry, and isotopic composition of sulfides at the Lisheen mine. Economic Geology, 100(1): 63-86.

Wood, S., Samson, I., 1998. Solubility of ore minerals and complexation of ore metals in hydrothermal solutions. Rev. Econ. Geol, 10: 33-80.

Yardley, B.W., 2005. 100th Anniversary Special Paper: metal concentrations in crustal fluids and their relationship to ore formation. Economic Geology, 100(4): 613-632.

Zienert, A., 1957. Die Großformen des Odenwaldes. Selbstverl. d. Geograph. Inst. d. Univ.

6. APPENDIX

a. *Burisch, M., Marks, M.A.W., Nowak, M. and Markl, G. (2016): The effect of temperature and cataclastic deformation on the composition of upper crustal fluids - An experimental approach. Chemical Geology 433, 24-35.*

b. *Burisch, M. Walter, B.F., Wälle, M. and Markl, G. (2016): Tracing fluid migration pathways in the root zone below unconformity-related hydrothermal veins: Insights from trace element systematics of individual fluid inclusions. Chemical Geology 429, 44-50.*

c. *Walter, B.F., Burisch, M. and Markl, G. (2016): Long-term chemical evolution and modification of continental basement brines - a field study from the Schwarzwald, SW Germany. Geofluids*

d. *Walter, B.F., Burisch, M., Marks, M.A.W. and Markl, G. (submittet): Major element and trace metal systematic of fluid inclusions in hydrothermal veins: metal provenance and the reconstruction of eroded sedimentary units*

e. *Walter, B.F., Burisch, M., Fußwinkel, T., Marks, M.A.W., Apukhtina, O.B., Wälle, M., Heinrich, C. and Markl, G. (in prep.): Multi-reservoir fluid mixing processes in rift-related hydrothermal vein-type deposits*

f. *Markl, G., Burisch, M., Neumann, U., 2016. Natural fracking and the genesis of five-element veins. Mineralium Deposita: 51(6): 703-712.*

g. *Burisch, M., Gerdes, A., Walter, B.F., Neumann, U., Fettel, M. and Markl, G. (submitted): Methane and the origin of five-element veins: mineralogy, age, fluid inclusion chemistry and ore forming processes - a case study of the Odenwald, SW Germany*

Nr.	**Accepted for publication yes/no**	**Number of all authors**	Position of the candidate in list of authors	Scientific ideas of candidate (%)	Data generation by candidate (%)	Analysis and Interpretation by candidate (%)	Paper writing by candidate (%)
a	yes	4	1	60	80	90	70
b	yes	4	1	80	10	80	80
c	yes	3	2	30	10	40	40
d	no	4	2	30	10	30	30
e	no	8	2	30	10	40	40
f	yes	3	2	20	70	40	25
g	no	6	1	70	90	80	80

Chemical Geology 433 (2016) 24–35

Contents lists available at ScienceDirect

Chemical Geology

journal homepage: www.elsevier.com/locate/chemgeo

The effect of temperature and cataclastic deformation on the composition of upper crustal fluids — An experimental approach

Mathias Burisch *, Michael A.W. Marks, Marcus Nowak, Gregor Markl

Universität Tübingen, Fachbereich Geowissenschaften, Wilhelmstrasse 56, 72074 Tübingen, Germany

ARTICLE INFO

Article history:
Received 26 February 2016
Received in revised form 30 March 2016
Accepted 31 March 2016
Available online 11 April 2016

Keywords:
Halogen systematic
Hydrothermal ore
Metals
Brittle deformation
Cl/Br
Cataclasis
Water–rock interaction

ABSTRACT

We investigated the potential of common crystalline rocks to facilitate the geochemical evolution of continental basement brines and to serve as a metal source for hydrothermal ore deposits. We performed leaching experiments on typical crystalline basement rocks (granite and gneiss), a redbed sandstone and their mineral separates (feldspar, quartz and biotite) at variable T (25, 180, 275 and 350 °C), P (ambient pressure, 0.9, 1.4 and 1.9 kbar), grain-size fractions (<0.01 mm, 0.063–0.125 and 2–4 mm) and variable fluid/rock ratios (10 to 1.1) with ultrapure water and 25 wt.% NaCl solution as solvents.

The modification of the fluid chemistry during water–rock interaction strongly depends on grain-size: leachates (using pure H_2O) of fine-grained rock powders have lower Na/Cl and Cl/Br ratios but much higher chlorinities (by a factor of up to 40) compared to leachates from coarse-grained rock powders. The Cl/Br ratios of all leachates are lower than that of their respective whole-rocks. Smaller grain-sizes of the starting materials yield element ratios (Cl/Br and Na/Cl) similar to those found in natural fluids, emphasizing the influence of cataclastic deformation on the fluid chemistry of crustal fluids. During our leaching experiments, Pb, Zn, Cu and W are released by felsic minerals, while biotite alteration releases Ni, As and additional Zn and Cu.

Our experiments confirm that crystalline rocks may serve as metal source for hydrothermal ore deposits. Short-term water–rock interactions along cataclastic fault zones in the brittle crust may influence the geochemical evolution of upper crustal fluids. This is further suggested by low F/Cl and Cl/Br ratios in some of the leachates being very similar to halogen systematics in natural fluid samples.

1. Introduction

Fluids are of major importance during most geological transport processes related to magmatism, metamorphism or formation of ore deposits. Hence, understanding the nature and evolution of their chemistry has been the focus of many studies in the last decades (Frape et al., 1984; Vovk, 1987; Nurmi et al., 1988; Lodemann et al., 1997; Markl et al., 1998; Savoye et al., 1998; Frape et al., 2003; Gleeson et al., 2003; Stober and Bucher, 2004; Gleeson and Turner, 2007; Piribauer et al., 2011).

Fluids with high salinity (up to 26 wt.% NaCl equivalent) appear to be typical of the middle and lower parts of the upper continental crust (Lodemann et al., 1997; Stober and Bucher, 1999a; Frape et al., 2003). Such deep-seated fluids represent a large halogen reservoir and influence the redistribution of metals in the crust (e.g. Yardley, 2005). The major cations in crustal fluids are Na or Ca, the dominant anion is invariably Cl, resulting in Na/Cl ratios of around one (or lower for Ca-dominated basement fluids). Deep-seated fluids show relatively high Br concentrations, resulting in low Cl/Br mass ratios (Cl/Br is given as mass ratio in this work) below the seawater ratio of 288 (Frape et al., 1984; Stober and Bucher, 1999a).

At shallow crustal depths, however, fluids are typically Ca and HCO_3-rich (Frape et al., 2003), except for fluids being derived from evaporite-bearing (mostly halite) aquifers having high Na and Cl concentrations (Stober and Bucher, 1999a). However, halite dissolution brines typically contain significant amounts of HCO_3 and very low Br (Stober and Bucher, 1999b), since halite incorporates only minor amounts of Br (Cl/Br ~2000–10,000; Siemann and Schramm, 2000). Hence, the Cl/Br ratio is often used to discriminate between halite dissolution brines (often shallow origin) and deep fluids and/or fluids derived by seawater evaporation (Chi and Savard, 1997; Savoye et al., 1998; Stober and Bucher, 1999b; Leisen et al., 2012; Fusswinkel et al., 2013), without specifically knowing what causes low Cl/Br ratios in deep crustal fluids.

Although highly saline basement fluids have been known for decades, the processes causing their extreme chlorinities combined with low Cl/Br and Na/Cl ratios are not understood in detail: some authors propose an in-situ source for halogens (e.g., Cl and Br being leached from hydrous silicates), which increases during mineral hydration reactions (e.g. Kullerud, 1996; Markl and Bucher, 1998), or may be

* Corresponding author.
E-mail address: mathias.burisch@ifg.uni-tuebingen.de (M. Burisch).

http://dx.doi.org/10.1016/j.chemgeo.2016.03.031
0009-2541/

inherited and pre-enriched from fluid inclusion leakage (Nordstrom et al., 1989). On the contrary, others propose that the dominant source of the salinity is not within the crystalline basement itself but is related to evaporation (Bottomley et al., 1999; Boiron et al., 2010; Richard et al., 2011) or freezing of large amounts of seawater during glacial periods (Herut et al., 1990). Once halite saturation is reached, the Cl/Br ratio decreases because of the strong incompatibility of Br in halite (McCaffrey et al., 1987; Siemann and Schramm, 2000) and is thereby passively enriched in the residual brine, which migrates subsequently downwards (Spencer, 1987; Bons et al., 2014).

Basement brines are often invoked as an important source for metals such as Pb, Zn, Cu, Co, Ni, U or Ag, typically found in hydrothermal vein-type deposits (basement-, unconformity-, and basin-hosted) (Wilkinson et al., 2005; Yardley, 2005; Gleeson and Turner, 2007; Boiron et al., 2010; Richard et al., 2011; Fusswinkel et al., 2013). Whether these metal-rich continental basement brines are a ubiquitous phenomenon (Yardley, 2005) or if they reflect local exceptions, having anomalous high metal concentrations (Wilkinson et al., 2009) is poorly constrained.

Here, we report the results of leaching experiments performed with Variscan basement rocks (granite and gneiss) and Triassic sandstone of the Schwarzwald, SW Germany. Compared to previous leaching experiments on rocks from the Schwarzwald (Bucher and Stober, 2002), our experiments cover much larger time (t) and temperature (T) intervals and include experiments with 25 wt.% NaCl solution (s25) and variable fluid/rock ratios. The experiments represent an undisturbed internal geochemical signal, without an external element source and therefore show if interaction with granite and gneiss is able to explain the geochemical characteristics of basement fluids. Furthermore, we consider the modes of fluid modification during water–rock interaction of externally derived fluids, being introduced into the crystalline basement.

2. Starting materials and analytical methods

2.1. Samples

Granite, gneiss and sandstone samples used for this study were collected in the central Schwarzwald, Germany, which are taken here as a type example of a Variscan upper crustal section (as has been done in several studies before, see e.g. Bucher and Stober, 2002; Fusswinkel et al., 2013; Walter et al., 2015). Paragneiss (MB2) was collected from the Hechtsberg quarry near Hausach, granite (MB3) from the Eselsbach near Schramberg and Triassic redbed sandstone (MB5) from Kuhbach near Lahr. The paragneiss has an average grain-size of 5 mm and consists of about 42 vol.% biotite, 32 vol.% plagioclase, 14 vol.% quartz, 7 vol.% K-feldspar, 1 vol.% garnet and accessory apatite and titanite (determined by image analysis). The granite has an average grain-size of 10–15 mm and contains about 44 vol.% K-feldspar, 31 vol.% quartz, 14 vol.% plagioclase, 7 vol.% biotite, 1 vol.% muscovite and accessory apatite, ilmenite, magnetite, monazite and zircon. In both basement rocks, plagioclase is partly sericitizied (the degree of sericitization being stronger in the granite), while K-feldspar is almost unaltered. Around 10 vol.% of the granite's primary biotite is replaced by fine-grained intergrowths of hematite, orthoclase and muscovite. The sandstone has an average grain-size of 0.5–1 mm, a porosity of 3 vol.% and consists of around 90 vol.% quartz, 6 vol.% K-feldspar and minor amounts of illitisized plagioclase and apatite. The cement is of argillic type and contains clay minerals and euhedral hematite (photomicrographs and microprobe data of the rock-forming minerals are included in the electronic supplement).

2.2. Sample preparation

Alteration crusts and secondary mineral veins were carefully removed. After coarse crushing, three aliquots of each sample (around 5 kg each) were crushed, ground and sieved until the whole aliquot was entirely processed. Thereby, a fine-grained fraction FG (<10 μm), a medium-grained fraction MG (63–125 μm) and a coarse-grained fraction CG (2–4 mm) of each sample were produced. A fourth aliquot (~5 kg) of gneiss and granite was used for mineral separation, which resulted in a felsic (quartz and feldspar) and a biotite fraction. No significant loss of mass during processing of the whole-rock samples could be recognized. 0.4 kg of felsic granite and gneiss separates, 0.3 kg of gneissic biotite and 0.2 kg of granitic biotite could be derived from 5 kg starting material.

2.3. Leaching experiments

Batch experiments at 25 °C with different grain-sizes and at various P–T, as well as multi-step experiments with changing fluid/rock ratios were carried out (Table 1).

2.3.1. Batch experiments at 25 °C (I)

Whole rock powders (FG, MG, CG) (Ia and c) and mineral separates (Ib and d) of gneiss and granite (FG) were leached in ultrapure water (pw) and 25 wt.% NaCl solution (s25) for 1 (t_1), 10^3 (t_2) and 4.5×10^4 (t_3) min, using an individual beaker (pure quartz glass) for each time interval t to maintain a constant fluid/rock ratio of 10 (10 g sample) (Table 1). The beakers were manually shaken three times a day.

2.3.2. Batch experiments at elevated P and T (II)

Gold capsules of 6 cm length and 5 mm diameter were used in horizontal autoclaves with H_2O as pressure medium. To avoid fluid loss and reduce the amount of encapsulated air during welding, the filled unsealed capsules were frozen in liquid nitrogen before sealing. MG whole rock was leached with a fluid/rock ratio of 10 (between 88 and 94 mg of rock material) at 180 °C/0.9 kbar, 275 °C/1.4 kbar and 350 °C/1.9 kbar for 4.5×10^4 min (Table 1).

2.3.3. Multistep experiments at 25 °C (III)

CG of gneiss and granite were leached in pw for 4.5×10^4 min at a fluid/rock ratio of 3.33 (120 g of sample material). These leachates were separated from the slurry, transferred into new beakers and MG of the respective lithologies was added using a fluid/rock ratio of 10. This was repeated three times after 10^3 min, resulting in a subsequent decrease of the fluid/rock ratio to 1.1 (Table 1). With this setup we try to mimic a migration path of a fluid batch, which is successively modified by the reaction with fresh cataclastic material.

2.4. Analytical procedures

All analyses were carried out at the Institut für Geowissenschaften, University of Tübingen, Germany.

2.4.1. Rocks

Major and trace elements of whole-rocks (triplicates) and mineral separates were determined by X-ray fluorescence (XRF) and total reflection X-ray fluorescence (TXRF). Fluorine, Cl and Br were extracted from whole-rock powders by pyrohydrolysis and quantified by ion chromatography (IC), using a similar setup as described by (Köhler et al., 2009). The effective detection limits for whole rocks are about 5 μg/g for F and Cl and 0.1–0.15 μg/g for Br (depending on the F concentration of the sample). Based on the frequent analyses of standard solutions, the relative uncertainty is ≤7%.

All leachates were filtered with a 0.2 μm Chromafile Xtra PVDF-20/25 for cations and a Xtra RC-20/25 for anions, which were analysed with a Dionex ICS 1000 ion chromatography system (CS12-A- and AS9-HC columns). Uncertainties are about 7% with detection limits of below 10 μg/l for Na^+, K^+, Mg^{2+}, Ca^{2+}, F^-, Cl^- and NO_3^-, and 2 μg/l for Br^-, PO_4^{3-} and SO_4^{2-}. Ni, Zn, Cu, Pb, W and As were determined

Table 1
Overview of experimental setup and conditions.

Setup	Experiment	Solvent	Sample material	Grain-size	Time interval	Duration (min)	T (°C)	Fluid/rock	Rock type	Amount of samples
Ia	Bpw	H_2O	Whole rock	FG	t1	1	25	10	gr, gn, sst	3
Ia	Bpw	H_2O	Whole rock	FG	t2	1×10^3	25	10	gr, gn, sst	3
Ia	Bpw	H_2O	Whole rock	FG	t3	4.5×10^4	25	10	gr, gn, sst	3
Ia	Bpw	H_2O	Whole rock	MG	t1	1	25	10	gr, gn, sst	3
Ia	Bpw	H_2O	Whole rock	MG	t2	1×10^3	25	10	gr, gn, sst	3
Ia	Bpw	H_2O	Whole rock	MG	t3	4.5×10^4	25	10	gr, gn, sst	3
Ia	Bpw	H_2O	Whole rock	CG	t1	1	25	10	gr, gn, sst	3
Ia	Bpw	H_2O	Whole rock	CG	t2	1×10^3	25	10	gr, gn, sst	3
Ia	Bpw	H_2O	Whole rock	CG	t3	4.5×10^4	25	10	gr, gn, sst	3
										27
Ib	Bpw	H_2O	Fspar-Qtz	FG	t1	1	25	10	gr, gn	2
Ib	Bpw	H_2O	Fspar-Qtz	FG	t3	4.5×10^4	25	10	gr, gn	2
Ib	Bpw	H_2O	Biotite	FG	t1	1	25	10	gr, gn	2
Ib	Bpw	H_2O	Biotite	FG	t3	4.5×10^4	25	10	gr, gn	2
										8
Ic	Bs25	25 wt.% NaCl	Whole rock	MG	t3	4.5×10^4	25	10	gr, gn, sst	3
Ic	Bs25	25 wt.% NaCl	Whole rock	CG	t3	4.5×10^4	25	10	gr, gn, sst	3
										6
Id	Bs25	25 wt.% NaCl	Fspar-Qtz	FG	t3	4.5×10^4	25	10	gr, gn	2
Id	Bs25	25 wt.% NaCl	Biotite	FG	t3	4.5×10^4	25	10	gr, gn	2
										4
II	BpwHT	H_2O	Whole rock	MG	t3	4.5×10^4	180	10	gr, gn, sst	3
II	BpwHT	H_2O	Whole rock	MG	t3	4.5×10^4	275	10	gr, gn, sst	3
II	BpwHT	H_2O	Whole rock	MG	t3	4.5×10^4	350	10	gr, gn, sst	3
										9
III	MS	H_2O	Whole rock	MG	t3	4.5×10^4	25	3.3	gr, gn	2
III	MS	H_2O	Whole rock	FG	t2	1×10^3	25	2.5	gr, gn	2
III	MS	H_2O	Whole rock	FG	t2	1×10^3	25	1.7	gr, gn	2
III	MS	H_2O	Whole rock	FG	t2	1×10^3	25	1.1	gr, gn	2
										8

FG/MG/CG = fine-/medium-/coarse-grained.
gr = granite; gn = gneiss; sst = sandstone.
B = batch; MS = multi-step; pw = pure water; s25 = 25 wt.% salinity; HT = high temperature.

with a S2 PICOFOX (Bruker) TXRF spectrometer equipped with a Mo X-ray tube operated at 50 kV and 600 μA and a silicon drift detector (SDD), having effective detection limits better than 1 μg/l. HCO_3^- was determined by titrimetry. Electroneutrality is typically $<\pm 3\%$, and is in all analyses $<\pm 6\%$.

Table 2
Major and trace element compositions of rock samples.

Sample	MB2	MB3	MB5
Rock type	Gneiss	Granite	Sandstone
wt.%			
SiO_2	58.94	73.21	94.14
TiO_2	0.68	0.22	0.06
Al_2O_3	18.25	13.77	2.97
Fe_2O_3	6.05	1.70	0.32
MnO	0.09	0.03	0.02
MgO	3.54	0.37	0.13
CaO	2.05	0.18	0.05
Na_2O	3.53	2.64	0.14
K_2O	3.00	6.14	2.04
P_2O_5	0.17	0.11	0.06
LOI	3.26	0.97	0.37
μg/g			
Ni	74	58	<1
Cu	7	2	<1
Zn	84	32	20
As	2	20	<1
W	129	190	51
Pb	13	41	18
F	600	980	68
Cl	120	240	47
Br	0.4	1.5	0.5
Sum	99.64	99.49	100.32

3. Results

3.1. Halogens and trace elements in rock samples

Halogen contents are highest in the granite (980 μg/g F, 240 μg/g Cl and 1.5 μg/g Br), lower in the gneiss (600 μg/g F, 120 μg/g Cl and 0.4 μg/g Br) and very low in the sandstone (68 μg/g F, 47 μg/g Cl and 0.5 μg/g Br; Table 2). Zinc, Ni and Cu are highest in the gneiss (84, 74 and 7 μg/g, respectively), whereas the highest As, W and Pb concentrations occur in the granite (19, 190 and 40 μg/g, respectively; Table 2).

3.2. Trace elements in mineral separates

Feldspar contains up to 21 μg/g Zn, 150 μg/g W, 104 μg/g Pb and 3 μg/g Cu (Table 3). The trace element contents of quartz are up to 7 μg/g Zn, 10 μg/g W, 8 μg/g Pb and 2 μg/g Cu. Biotite contains up to 28 μg/g Ni, 5 μg/g Cu, 70 μg/g As, 15 W, 8 Pb and 810 μg/g Zn (Table 3).

Table 3
Trace element compositions of mineral separates.

Sample	MB2	MB2	MB2	MB3	MB3	MB3
Rock type	Gneiss	Gneiss	Gneiss	Granite	Granite	Granite
Mineral	Quartz	Fspar	Biotite	Quartz	Fspar	Biotite
Ni	<0.5	<0.5	28	<0.5	<0.5	5
Cu	2	1	5	2	3	<1
Zn	7	21	320	6	17	810
As	<0.8	<0.8	4	<0.8	2	70
W	10	150	10	2	39	15
Pb	4	19	2	8	104	8

In μg/g.

Table 4
Experimental leaching data including blank runs, ordered according to their setups I (a, b, c, d), II and III (see Table 1).

Setup	Ia	Ia	Ia	Ia	Ia	Ia	Ia	Ia	Ia	Ia	Ia
Sample	MB2	MB2	MB2	MB2	MB2	MB2	MB2	MB2	MB2	MB3	MB3
Rock type	Gneiss	Gneiss	Gneiss	Gneiss	Gneiss	Gneiss	Gneiss	Gneiss	Gneiss	Granite	Granite
Sample mat.	Whole-rock	Whole-rock	Whole-rock	Whole-rock	Whole-rock	Whole-rock	Whole-rock	Whole-rock	Whole-rock	Whole-rock	Whole-rock
Experiment	Bpw	Bpw	Bpw	Bpw	Bpw	Bpw	Bpw	Bpw	Bpw	Bpw	Bpw
Grain size	CG	CG	CG	MG	MG	MG	FG	FG	FG	CG	CG
Time (min)	1	1×10^3	4.5×10^4	1	1×10^3	4.5×10^4	1	1×10^3	4.5×10^4	1	1×10^3
Temp (°C)	24	25	23	23	25	24	24	24	24	25	24
pH	7.5	9.6	9.6	9.8	9.7	9.4	9.4	9.4	9.5	6.4	7.0
Fluid/rock	10.0	10.0	10.0	10.0	10.0	10.0	10.0	10.0	10.0	10.0	10.0
Ca (mg/l)	1.314	4.635	4.392	2.000	4.334	5.600	1.954	2.294	4.783	0.160	0.239
Mg (mg/l)	0.081	0.609	0.495	0.287	0.640	0.988	0.407	0.462	1.057	0.022	0.044
Na (mg/l)	0.138	0.808	0.884	1.522	2.557	4.458	9.844	11.909	12.790	0.109	0.497
K (mg/l)	0.461	1.875	1.353	4.285	8.442	10.075	19.905	21.388	23.745	0.175	0.519
alk. (meq/l)	0.086	0.358	0.269	0.278	0.564	0.759	0.991	1.121	1.371	0.010	0.035
SO_4 (mg/l)	0.011	0.048	2.849	0.027	0.062	0.311	0.097	0.120	0.164	0.000	0.061
Cl (mg/l)	0.099	0.099	0.104	0.650	0.802	0.945	2.208	2.234	2.399	0.290	0.295
F (mg/l)	0.002	0.030	0.028	0.040	0.154	0.325	0.182	0.526	0.748	0.002	0.016
Br (mg/l)	0.000	0.000	0.000	0.012	0.013	0.012	0.035	0.035	0.033		
NO_3 (mg/l)	0.013	0.023	0.021	0.034	0.036	0.133	0.201	0.122	0.211	0.004	0.040
PO_4 (mg/l)	0.011	0.048	0.000	0.003	0.000	0.026	0.000	0.029	0.026	0.010	0.022
Ni (µg/l)	–	–	<1	<1	<1	<1	–	–	1	–	–
Cu (µg/l)	–	–	<1	1	1	1	–	–	1	–	–
Zn (µg/l)	–	–	2	4	3	2	–	–	3	–	–
As (µg/l)	–	–	2	<1	2	6	–	–	6	–	–
W (µg/l)	–	–	<1	<1	2	5	–	–	640	–	–
Pb (µg/l)	–	–	<1	<1	<1	<1	–	–	<1	–	–
%Cl	1	1	1	5	7	8	18	19	20	1	1
%F	0.00	0.05	0.05	0.07	0.26	0.54	0.30	0.88	1.25	0.00	0.02
%Br	0	1	0	30	33	31	88	88	84	0	0

Setup	Ia	Ia	Ia	Ia	Ia	Ia	Ia	Ia	Ia	Ia	Ia
Sample	MB3	MB3	MB3	MB3	MB3	MB3	MB3	MB5	MB5	MB5	MB5
Rock type	Granite	Granite	Granite	Granite	Granite	Granite	Granite	Sandstone	Sandstone	Sandstone	Sandstone
Sample mat.	Whole-rock	Whole-rock	Whole-rock	Whole-rock	Whole-rock	Whole-rock	Whole-rock	Whole-rock	Whole-rock	Whole-rock	Whole-rock
Experiment	Bpw	Bpw	Bpw	Bpw	Bpw	Bpw	Bpw	Bpw	Bpw	Bpw	Bpw
Grain size	CG	MG	MG	MG	FG	FG	FG	CG	CG	CG	MG
Time (min)	4.5×10^4	1	1×10^3	4.5×10^4	1	1×10^3	4.5×10^4	1	1×10^3	4.5×10^4	1
Temp (°C)	23	24	24	24	24	24	24	24	24	24	24
pH	7.0	7.1	7.8	7.9	8.9	9.0	8.9	6.0	6.4	6.7	6.4
Fluid/rock	10.0	10.0	10.0	10.0	10.0	10.0	10.0	10.0	10.0	10.0	10.0
Ca (mg/l)	0.175	0.451	0.788	1.055	0.124	0.188	0.090	0.553	0.281	0.463	0.307
Mg (mg/l)	0.040	0.079	0.150	0.234	0.025	0.024	0.016	0.079	0.041	0.071	0.067
Na (mg/l)	0.630	2.490	3.115	3.669	7.345	9.435	11.939	0.100	0.231	0.305	0.599
K (mg/l)	0.523	2.716	3.759	4.397	7.744	8.668	9.733	0.120	0.226	0.366	2.074
alk. (meq/l)	0.040	0.061	0.119	0.164	0.105	0.168	0.247	0.037	0.018	0.031	0.018
SO_4 (mg/l)	0.042	0.105	0.189	0.230	0.365	0.557	0.530	0.032	0.187	0.232	0.141
Cl (mg/l)	0.329	4.885	5.293	5.572	13.242	13.746	13.498	0.121	0.291	0.319	2.683
F (mg/l)	0.034	0.070	0.159	0.241	0.561	1.191	1.786	0.002	0.012	0.027	0.015
Br (mg/l)		0.060	0.066	0.068	0.142	0.141	0.144	0.000	0.000	0.001	0.035
NO_3 (mg/l)	0.040	0.047	0.054	0.000	0.199	0.170	0.054	0.023	0.035	0.005	0.044
PO_4 (mg/l)	0.024	0.019	0.059	0.038	0.159	0.278	0.602	0.006	0.051	0.164	0.049
Ni (µg/l)	<1	–	–	<1	–	–	<1	–	–	7	–
Cu (µg/l)	1	–	–	2	–	–	3	–	–	2	–
Zn (µg/l)	<1	–	–	2	–	–	4	–	–	18	–
As (µg/l)	44	–	–	141	–	–	451	–	–	<1	–
W (µg/l)	1	–	–	67	–	–	1550	–	–	<1	–
Pb (µg/l)	<1	–	–	<1	–	–	<1	–	–	<1	–
%Cl	1	20	22	23	55	58	56	3	6	7	57
%F	0.03	0.07	0.16	0.25	0.57	1.21	1.82	0.03	0.18	0.39	0.21
%Br	0	40	44	46	94	94	96	0	0	2	69

Setup	Ia	Ia	Ia	Ia	Ia	Ib	Ib		Ib	Ib	Ib
Sample	MB5	MB5	MB5	MB5	MB5	MB2	MB2	MB3	MB3	MB2	MB2
Rock type	Sandstone	Sandstone	Sandstone	Sandstone	Sandstone	Gneiss	Gneiss	Granite	Granite	Gneiss	Gneiss
Sample mat.	Whole-rock	Whole-rock	Whole-rock	Whole-rock	Whole-rock	Fspar-qtz	Fspar-qtz	Fspar-qtz	Fspar-qtz	Biotite	Biotite
Experiment	Bpw	Bpw	Bpw	Bpw	Bpw	Bpw	Bpw	Bpw	Bpw	Bpw	Bpw
Grain size	MG	MG	FG	FG	FG	FG	FG	FG	FG	FG	FG
Time (min)	1×10^3	4.5×10^4	1	1×10^3	4.5×10^4	1	4.5×10^4	1	4.5×10^4	1	4.5×10^4
Temp (°C)	24	24	24	24	24	24	24	24	24	24	24
pH	6.7	7.2	7.9	8.0	7.9	8.0	8.2	6.5	6.9	8.0	8.3
Fluid/rock	10.0	10.0	10.0	10.0	10.0	10.0	10.0	10.0	10.0	10.0	10.0
Ca (mg/l)	0.848	0.755	0.140	0.185	0.233	1.951	2.403	0.130	0.322	2.158	4.241
Mg (mg/l)	0.167	0.181	0.026	0.022	0.040	0.131	0.278	0.023	0.032	0.396	1.738
Na (mg/l)	0.675	1.002	1.504	1.827	2.525	22.892	38.238	8.338	14.784	3.347	5.953

(continued on next page)

Table 4 (*continued*)

Setup	Ia	Ia	Ia	Ia	Ia	Ia	Ia	Ia	Ia	Ia	Ia
Sample	MB2	MB2	MB2	MB2	MB2	MB2	MB2	MB2	MB2	MB3	MB3
K (mg/l)	2.550	2.782	8.184	9.089	12.836	7.528	8.689	4.189	7.549	30.190	40.346
alk. (meq/l)	0.053	0.063	0.111	0.122	0.216	1.185	1.824	0.112	0.434	0.944	1.475
SO_4 (mg/l)	0.279	0.365	0.911	1.261	1.397	0.272	0.414	0.328	0.402	2.048	2.842
Cl (mg/l)	3.033	3.233	4.500	4.352	4.566	3.002	3.373	11.800	12.000	1.665	1.767
F (mg/l)	0.038	0.037	0.233	0.465	0.643	0.193	1.161	0.174	0.667	0.346	0.998
Br (mg/l)	0.036	0.039	0.052	0.053	0.052	0.046	0.046	0.132	0.135	0.012	0.009
NO_3 (mg/l)	0.038	0.036	0.196	0.079	0.000	0.310	0.363	0.262	0.232	0.452	0.601
PO_4 (mg/l)	0.097	0.037	0.331	0.804	1.331	0.000	0.000	0.269	0.765	0.000	0.000
Ni (μg/l)	–	4	–	–	6	<1	<1	0	<1	<1	<1
Cu (μg/l)	–	1	–	–	4	1	2	1	5	<1	<1
Zn (μg/l)	–	23	–	–	18	3	10	3	12	4	7
As (μg/l)	–	<1	–	–	17	<1	<1	10	15	<1	1
W (μg/l)	–	221	–	–	419	1000	6000	451	1590	5	10
Pb (μg/l)	–	<1	–	–	<1	<1	<1	0	<1	<1	<1
%Cl	65	69	96	93	97	–	–	–	–	–	–
%F	0.55	0.54	3.43	6.84	9.41	–	–	–	–	–	–
%Br	71	78	105	105	105	–	–	–	–	–	–

Setup	Ib	Ib	Ic	Ic	Ic	Ic	Ic	Ic	Id	Id	Id
Sample	MB3	MB3	MB2	MB2	MB3	MB3	MB5	MB5	MB2	MB3	MB2
Rock type	Granite	Granite	Gneiss	Gneiss	Granite	Granite	Sandstone	Sandstone	Gneiss	Granite	Gneiss
Sample mat.	Biotite	Biotite	Whole rock	Whole rock	Whole rock	Whole rock	Whole rock	Whole rock	Fspar-qtz	Fspar-qtz	Biotite
Experiment	Bpw	Bpw	Bs25	Bs25	Bs25	Bs25	Bs25	Bs25	Bs25	Bs25	Bs25
Grain size	FG	FG	CG	MG	CG	MG	CG	MG	FG	FG	FG
Time (min)	1	4.5×10^4	4.5×10^4	4.5×10^4	4.5×10^4	4.5×10^4	4.5×10^4	4.5×10^4	4.5×10^4	4.5×10^4	4.5×10^4
Temp (°C)	24	24	24	25	24	25	24	24	24	23	24
pH	6.5	6.8	9.5	9.4	7.0	7.8	6.8	7.2	8.1	6.6	8.2
Fluid/rock	10.0	10.0	10.0	10.0	10.0	10.0	10.0	10.0	10.0	10.0	10.0
Ca (mg/l)	0.116	3.621	–	–	–	–	–	–	–	–	–
Mg (mg/l)	0.024	0.408	–	–	–	–	–	–	–	–	–
Na (mg/l)	2.274	5.098	–	–	–	–	–	–	–	–	–
K (mg/l)	14.635	30.792	–	–	–	–	–	–	–	–	–
alk. (meq/l)	0.235	0.698	–	–	–	–	–	–	–	–	–
SO_4 (mg/l)	1.166	1.675	–	–	–	–	–	–	–	–	–
Cl (mg/l)	2.264	2.673	–	–	–	–	–	–	–	–	–
F (mg/l)	2.883	7.559	–	–	–	–	–	–	–	–	–
Br (mg/l)	0.012	0.008	–	–	–	–	–	–	–	–	–
NO_3 (mg/l)	0.374	0.746	–	–	–	–	–	–	–	–	–
PO_4 (mg/l)	0.000	0.058	–	–	–	–	–	–	–	–	–
Ni (μg/l)	<1	<1	<1	<1	<1	<1	<1	<1	<1	<1	<1
Cu (μg/l)	1	2	54	76	102	137	48	61	49	57	89
Zn (μg/l)	4	5	67	68	116	136	81	80	65	42	52
As (μg/l)	31	260	2	6	65	138	<1	<1	<1	25	2
W (μg/l)	2	6	<1	<1	<1	42	<1	311	6075	1641	<1
Pb (μg/l)	<1	<1	42	66	19	20	1	25	34	74	1
%Cl	–	–	–	–	–	–	–	–	–	–	–
%F	–	–	–	–	–	–	–	–	–	–	–
%Br	–	–	–	–	–	–	–	–	–	–	–

Setup	Id	II	II	II	II	II	II	II	II	II	III
Sample	MB3	MB2	MB2	MB2	MB3	MB3	MB3	MB5	MB5	MB5	MB2
Rock type	Granite	Gneiss	Gneiss	Gneiss	Granite	Granite	Granite	Sandstone	Sandstone	Sandstone	Gneiss
Sample mat.	Biotite	Whole rock	Whole rock	Whole rock	Whole rock	Whole rock	Whole rock	Whole rock	Whole rock	Whole rock	Whole rock
Experiment	Bs25	BpwHT	BpwHT	BpwHT	BpwHT	BpwHT	BpwHT	BpwHT	BpwHT	BpwHT	MS
Grain size	FG	MG	MG	MG	MG	MG	MG	MG	MG	MG	CG
Time (min)	4.5×10^4	4.5×10^4	4.5×10^4	4.5×10^4	4.5×10^4	4.5×10^4	4.5×10^4	4.5×10^4	4.5×10^4	4.5×10^4	4.5×10^4
Temp (°C)	24	180	275	350	180	275	350	180	275	350	23
pH	6.9	–	–	–	–	–	–			–	8.9
Fluid/rock	10.0	10.0	10.0	10.0	10.0	10.0	10.0	10.0	10.0	10.0	3.3
Ca (mg/l)	–	8.185	13.954	2.478	1.013	1.700	1.885	2.651	0.971	0.941	6.467
Mg (mg/l)	–	0.039	0.107	0.119	0.047	0.088	0.117	0.178	0.044	0.134	0.858
Na (mg/l)	–	31.230	65.200	97.461	33.170	53.021	75.078	5.078	8.853	16.962	2.332
K (mg/l)	–	4.959	16.810	27.429	2.620	6.577	20.114	10.743	21.780	53.722	2.490
alk. (meq/l)	–	1.768	3.726	4.880	1.260	2.157	3.209	0.499	0.712	1.818	0.544
SO_4 (mg/l)	–	0.366	0.779	0.000	0.586	0.681	0.806	0.665	2.113	3.047	0.062
Cl (mg/l)	–	1.183	2.383	2.550	5.216	5.891	6.481	3.752	3.912	4.200	0.248
F (mg/l)	–	0.650	2.540	1.992	0.600	2.997	7.427	0.180	0.422	1.353	0.096
Br (mg/l)	–	0.015	0.015	0.015	0.068	0.068	0.068	0.045	0.045	0.048	0.000
NO_3 (mg/l)	–	2.775	1.830	0.855	3.514	0.945	1.705	0.476	3.140	1.640	0.033
PO_4 (mg/l)	–	0.092	0.000	0.164	0.554	0.143	0.456	0.000	1.763	2.471	0.000
Ni (μg/l)	<1	13	34	104	8	30	78	36	9	24	1
Cu (μg/l)	104	<1	2	1	5	7	19	3	4	9	<1
Zn (μg/l)	87	12	50	117	34	50	124	39	26	63	3
As (μg/l)	255	35	157	16	1404	1789	1311	2	<1	<1	2
W (μg/l)	<1	641	910	1457	555	888	2215	1507	1604	1827	<1

Table 4 (*continued*)

Setup	Ia	Ia	Ia	Ia	Ia	Ia	Ia	Ia	Ia	Ia	Ia
Sample	MB2	MB2	MB2	MB2	MB2	MB2	MB2	MB2	MB2	MB3	MB3
Pb (μg/l)	1	2	5	5	<1	5	5	1	1	1	<1
%Cl	–	10	20	21	22	25	27	80	83	90	1
%F	–	1.08	4.24	3.32	0.61	3.05	7.57	2.65	6.21	19.90	0.05
%Br	–	36	38	38	45	45	45	90	90	96	0

Setup	III	III	III	III	III	III	III			
Sample	MB2	MB2	MB2	MB3	MB3	MB3	MB3	Blank	Blank	Blank
Rock type	Gneiss	Gneiss	Gneiss	Granite	Granite	Granite	Granite	–	–	–
Sample mat.	Whole rock	Whole rock	Whole rock	Whole rock	Whole rock	Whole rock	Whole rock	–	–	–
Experiment	MS	MS	MS	MS	MS	MS	MS	Bpw	Bs25	BpwHT
Grain size	MG	MG	MG	CG	MG	MG	MG	–	–	–
Time (min)	4.57×10^4	4.61×10^4	4.71×10^4	4.5×10^4	4.57×10^4	4.61×10^4	4.71×10^4	4.5×10^4	4.5×10^4	4.5×10^4
Temp (°C)	23	23	23	23	23	23	23	24	23	350
pH	9.4	9.1	8.9	7.0	7.4	7.7	7.9	5.7	5.8	–
Fluid/rock	2.5	1.7	1.1	3.3	2.5	1.7	1.1	–	–	–
Ca (mg/l)	6.800	7.590	10.235	0.846	1.731	4.060	7.359	0.010	–	0.300
Mg (mg/l)	1.783	1.433	1.976	0.166	0.321	0.744	1.378	<0.010	–	0.010
Na (mg/l)	4.733	8.360	13.272	1.322	4.231	9.773	17.362	0.017	–	0.300
K (mg/l)	8.929	13.290	16.380	1.102	5.101	11.122	18.221	0.014	–	0.500
alk. (meq/l)	0.871	1.082	1.432	0.099	0.210	0.405	0.689	<0.010	–	<0.010
SO_4 (mg/l)	0.116	0.177	0.310	0.153	0.334	0.711	1.221	<0.010	–	0.100
Cl (mg/l)	1.243	2.988	6.031	1.011	6.724	18.334	33.060	0.010	–	<0.002
F (mg/l)	0.255	0.544	0.915	0.088	0.211	0.458	0.746	<0.002	–	<0.002
Br (mg/l)	0.014	0.043	0.090	0.006	0.090	0.238	0.465	<0.002	–	<0.002
NO_3 (mg/l)	0.073	0.137	0.829	0.019	0.028	0.080	0.136	<0.010	–	<0.010
PO_4 (mg/l)	0.000	0.000	0.000	0.043	0.063	0.049	0.049	<0.010	–	<0.010
Ni (μg/l)	5	5	5	1	5	6	6	<1	<1	10
Cu (μg/l)	2	3	4	<1	2	2	3	<1	1	25
Zn (μg/l)	2	3	3	3	3	3	3	1	2	12
As (μg/l)	7	6	7	148	218	302	310	<1	<1	<1
W (μg/l)	1	2	7	<1	22	69	119	<1	<1	278
Pb (μg/l)	<1	<1	<1	<1	0	<1	<1	<1	<1	<1
%Cl	8	7	8	1	24	24	21	–	–	–
%F	0.43	0.45	0.51	0.03	0.13	0.13	0.10	–	–	–
%Br	35	36	39	2	52	49	50	–	–	–

3.3. Leachates

3.3.1. Blank runs

Blank runs do not exceed 2% (I, III) and 10% (II) of the lowest concentrations in the experiments (Table 4). Exceptions are W and Cu, reaching up to 20 and 100%, respectively, of the concentrations of the leachates (contaminated by the gold capsule) Consequently, Cu concentrations in HT (II) are excluded from the discussion.

3.3.2. Batch experiments with rocks

Na, K, Ca and Mg contents of leachates generally increase with time (t) and temperature (T) (Figs. 1 & 2; Table 4), while smaller grain-sizes exclusively increases Na and K in the leachates. Sodium increases from CG to FG (up to 13 mg/l in gneiss), but are highest in HT (II) (up to 97.5 mg/l in gneiss). Highest K concentrations occur in HT sandstone (up to 53.7 mg/l at 350 °C), while maximum K concentrations of type Ia experiments occur in FG gneiss leachates (23.7 mg/l). Calcium increases with T and t (except 350 °C gneiss) and is higher in the gneiss leachates (up to 14 mg/l). Consequently, the overall cation signature of leachates changes towards more Na- and K-dominant signatures with T and smaller grain-size, while t promotes Ca-dominated fluids (Fig. 3 & Table 5). Alkalinity ($HCO_3^- + CO_3^{2-}$ in meq/l) of all leachates increases with t, T and smaller grain-size (Figs. 1 & 2; Table 4) and is highest in gneiss leachates (up to 4.9 meq/l, II at 350 °C). Fluorine concentrations increase with t, T and smaller grain-sizes and are highest in granite leachates (7.4 mg/l, II at 350 °C). In contrast, Cl and Br concentrations are constant over t and T. Smaller grain-size, however, largely increases Cl, and Br, especially in granite leachates (up to 13.5 and 0.14 mg/l, respectively) (Fig. 1; Table 4). Accordingly, t and T causes a relative enrichment of alkalinity and to a lesser extent F. In contrast, smaller grain-size and short t favourably yield Cl-dominated fluid signatures (Fig. 3 & Table 5). The mass of halogens of the leachates was normalized to the respective halogen mass of whole rock (%Halogen = $C_{leachate}$ / C_{rock} × 100) (Fig. 4; Table 4), enabling estimations of the relative halogen release (%F, %Cl and %Br). Released %F after 4.5×10^4 min (at 25 °C, Ia) is generally small (2–8%), but increase significantly with T. MG of Ia (25 °C) have less than 0.7% F, while MG of II (at 350 °C) have up to 20% F. %Cl in CG leachates is <2% for the gneiss and granite and <10% for the sandstone but increases to 20% (gneiss), 60% (granite) and 100% (sandstone) in FG leachates. Similarly, released proportions of Br are highest in FG leachates: around 90% (gneiss), 95% (granite) and 100% (sandstone). Hence, in contrast to Cl and F almost all the rock's Br is released instantaneously to the fluid, if grain-size is sufficiently small (Fig. 4; Table 4).

Type Ia (pw) leachates of gneiss have 640 μg/l W and granite leachates contain 451 μg/l As and 1550 μg/l W, but other metals are very low (Fig. 5; Ni and Pb are below detection limit (b.d.l.)). Sandstone leachates contain 6 μg/l Ni, 17 μg/l As and 419 μg/l W. Arsenic and W concentrations increase from CG to FG (Fig. 5). Metal concentrations in Ic (s25) are substantially higher (Fig. 5): Highest Pb (up to 66 μg/l) occur in gneiss, highest Cu and Zn (up to 137 μg/l Cu and 136 μg/l Zn) in granite leachates. As and W are similar to Ia experiments. Leachates at elevated T (II) have up to 104 μg/l Ni, 117 μg/l Zn, 157 μg/l As and 1457 μg/l W, which is significantly higher compared to Ia/Ic, while Pb does not exceed 5 μg/l in II (Table 4).

3.3.3. Batch experiments with mineral separates at 25 °C (Ib and Id)

Felsic leachates contain more Cl and even more Br than the respective biotite leachates, resulting in lower Cl/Br of felsic compared to biotite leachates. While Cl/Br does not change with T in felsic leachates, Cl/Br of biotite leachates increase substantially with T (Fig. 6). Id

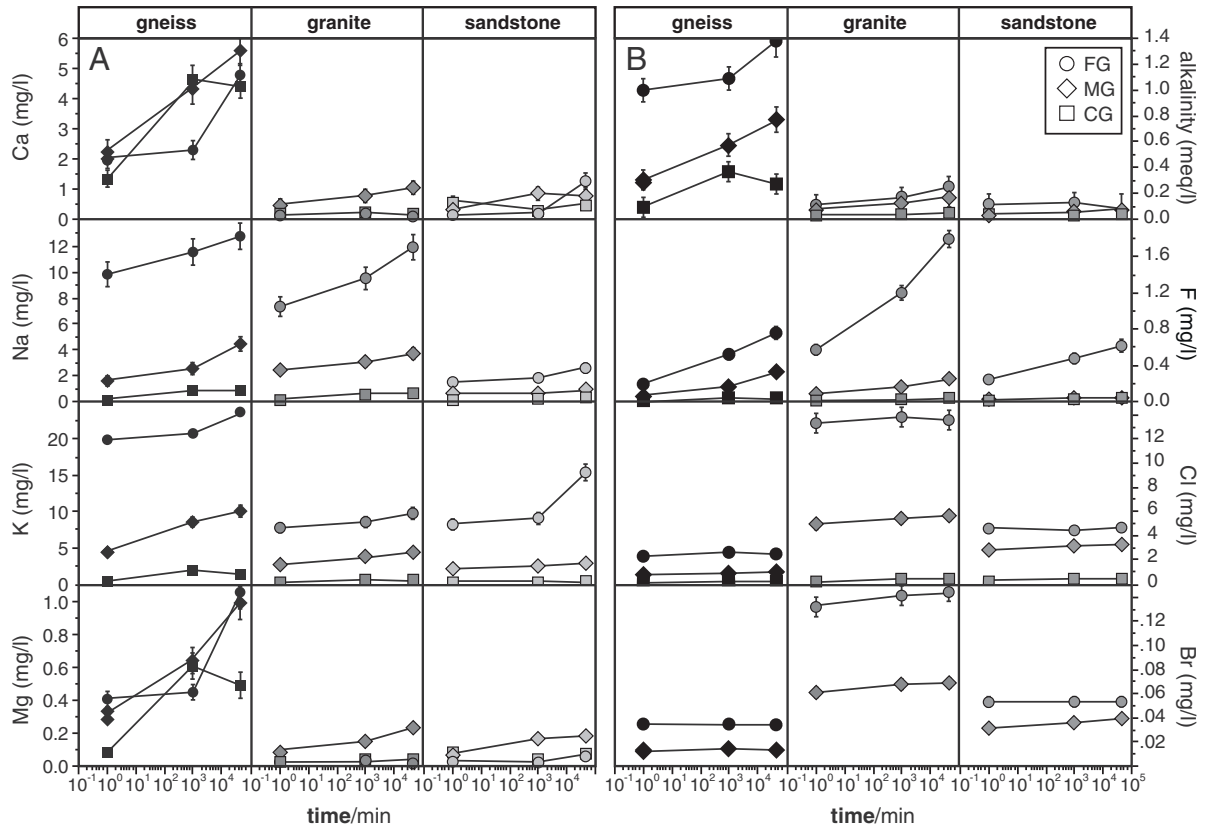

Fig. 1. Major cations (panel A) and anions (panel B) of fine- (circle), medium- (square) and coarse-grained (rectangles) leachates of gneiss, granite and sandstone at 25 °C over time (Ia). Data points of same grain-size are connected with lines.

felsic leachates contain up to 57 μg/l Cu, up to 65 μg/l Zn and up to 74 μg/l Pb while Id biotite leachates contain up to 104 μg/l Cu and up to 87 μg/l Zn (Table 4).

3.3.4. Multistep experiments with rocks at 25 °C (III)

Short reaction times and smaller fluid/rock ratios cause a relative enrichment of Na, K, Cl and Br in the leachates. The amount of F, Cl and Br per kg of rock increases from CG to MG and is on average for granite/gneiss leachates: 12/16 mg F, 560/100 mg Cl and 7.8/1.4 mg Br using MG.

4. Discussion

The origin of the chlorinity of continental brines with characteristically low Cl/Br ratios is highly debated (Lodemann et al., 1997; Bottomley et al., 1999; Stober and Bucher, 1999b; Kullerud, 2000; Gleeson et al., 2001; Möller et al., 2005; Gleeson and Smith, 2009; Nahnybida et al., 2009; Boiron et al., 2010; Richard et al., 2011). Importantly, such fluids have been increasingly invoked in ore-forming processes, since their high salinity increases the solubility of Pb, Zn and Cu (Holland, 1972; Yardley, 2005; Gleeson and Turner, 2007; Richard et al., 2011; Smith et al., 2012). The precise provenance of these ore-forming metals (Ni, Cu, Zn, Pb, U, Ag and W) and As is, however, still unknown.

Fluid/rock ratios below 1 are difficult to handle from a technical point of view, since the lower the ratio, the higher the potential that secondary halogen- or metal- bearing minerals precipitate, which is not wanted for studying element mobility. Therefore, fluid/rock ratios assumed for reactive flow in natural hydrothermal systems ($f/r \ll 1$) (Norton and Knight, 1977; Campbell et al., 1984) could unfortunately not be applied to the experiments. Grain-sizes of 0.005 mm to 2 mm make up the majority of the mass in such cataclastic zones (Gerald and Stünitz, 1993; An and Sammis, 1994; Billi, 2005). FG and MG leachates lie within this range, while CG leachates are used to draw conclusions how undeformed rocks behave during water–rock interaction (e.g. porous flow).

4.1. Halogen release during water–rock interaction

Halogens in crystalline rocks are distributed between two different reservoirs: A) Highly soluble phases (HSP) (e.g., halides), halogens adsorbed to the surface of minerals (Hellmann et al., 2012) and highly soluble phases present as fluid inclusions; B) Low soluble phases (LSP) in which halogens are structurally bound (e.g., mica, amphibole, apatite).

The halogen contents of FG leachates ($t = 1$ min) are suitable to estimate a minimum value for the proportion of each halogen present as HSP (Fig. 4). To confirm this assumption we used microprobe data to calculate the amount of structurally bound Cl and F in the whole rock, which agrees with the experimentally derived values ($C_{\text{whole-rock}} - C_{t\,=\,1\text{ min}}$). The potential release of halogens in LSP increases with reaction progress. Therefore, F/Cl and Cl/Br (Fig. 6) of leachates are suitable to discuss the behaviour of each element in the two reservoirs during water–rock interaction. Low %F in all experiments indicates that the majority (>95%) of F is restricted to LSP, particularly biotite and apatite. In contrast, Cl is to 20% (gneiss), 60% (granite) and 97% (sandstone) assigned to HSP, while Br is to 90–100% (all rock types) present as HSP. The majority of Cl and Br present as HSP are hosted by the felsic fraction (Ib). The more Cl (and Br) is present as HSP, the more %Cl can potentially be released by cataclastic deformation.

F/Cl ratios increase with t, Cl/Br of gneiss and granite leachates slightly increase with t and T (Fig. 6). In felsic leachates, F/Cl increases, while Cl/Br is constant with t. In contrast, F/Cl and Cl/Br

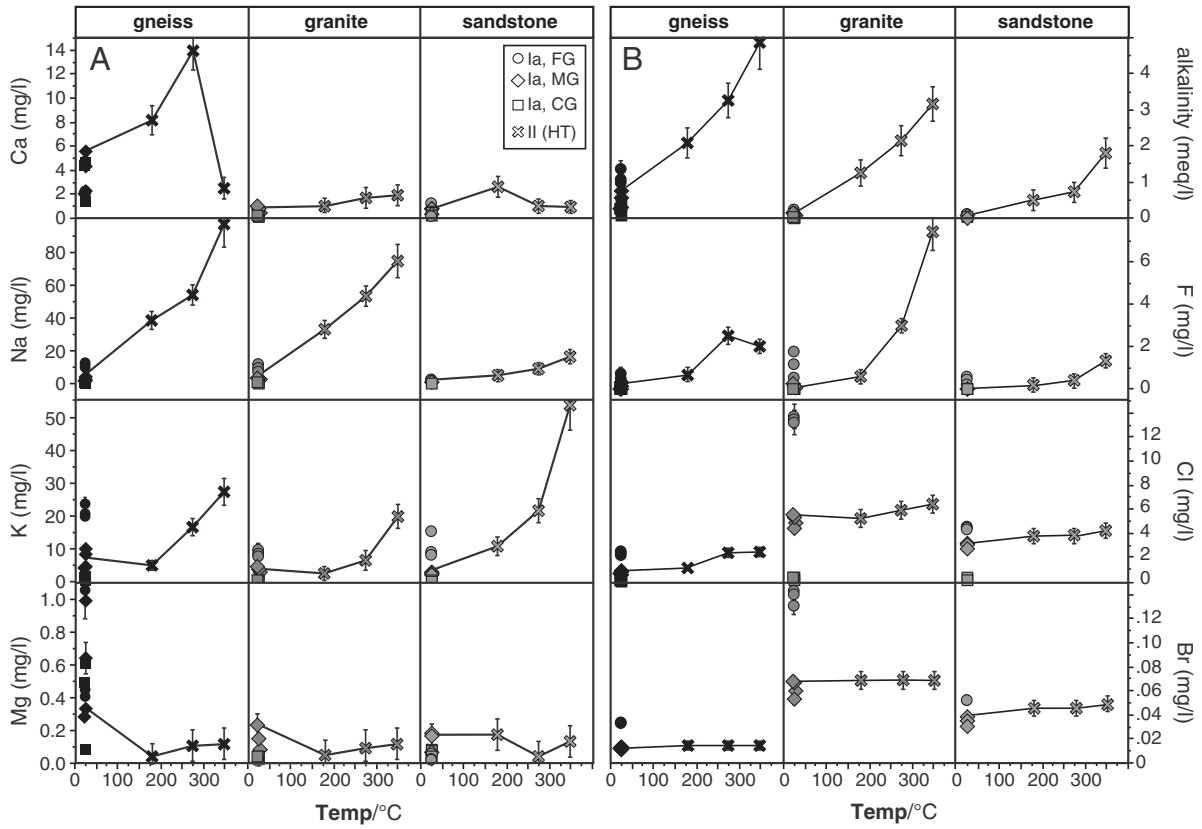

Fig. 2. Major cations (Fig. 1A) and anions (Fig. 1B) of fine- (circle), medium- (square), and coarse-grained (rectangles) leachates of gneiss, granite and sandstone after 31 days and variable temperatures. Data points of same grain-size are connected with lines.

both increase significantly with t in the biotite leachates (Fig. 6). Disproportional abundances of F, Cl and Br in HSP and LSP and the different behaviour of these reservoirs during water–rock interaction results in fractionation, yielding F/Cl and Cl/Br ratios in the leachates that are lower than their whole rock composition (Fig. 6). The degree of fractionation is highest when rock types are leached in which F, Cl and Br are very unevenly distributed in the different reservoirs (e.g. gneiss: 80% Cl and 10% Br are present as LSP). Therefore, t_1 gneiss leachates (Ia) have the smallest Cl/Br (~60) with the highest deviation from the rock (Fig. 6). Furthermore, the degree of fractionation can be enhanced by transient, short-lived water–rock reactions, in which HSP are selectively leached, while mineral alteration of halogen-bearing phases (LSP), promoted by t and T, causes a trend of F/Cl and Cl/Br of leachates towards their whole rock ratio (Fig. 6). Consequently, the halogen ratio of the fluid is essentially controlled by the proportion of each halogen present in HSP, rather than by the halogen ratio of the host rock during flow along cataclastic zones.

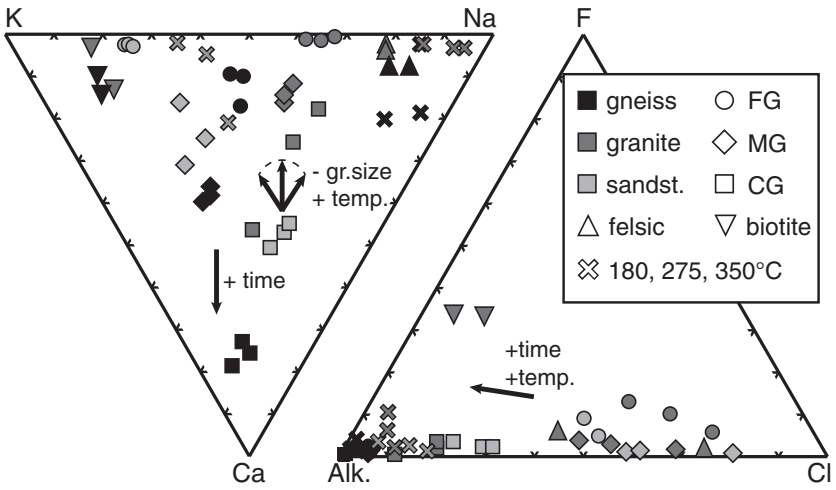

Fig. 3. Overall fluid signature of leachates in meq/l, including all investigated rock types, whole rock and mineral separates. A general trend of increasing Ca and decreasing Cl with time and temperature is indicated as black arrow.

Table 5
Overall fluid signatures of leachates.

Experiment	Gneiss	Granite	Sandstone
Ia (CG)	Ca–HCO_3	Ca–Na–HCO_3	Ca–HCO_3
Ia (MG)	Ca–K–HCO_3	Na–K–Cl–HCO_3	K–Ca–Cl–HCO_3
Ia (FG)	K–Na–HCO_3	Na–K–Cl	K–Na–Cl–HCO_3
II	Na–HCO_3	Na–HCO_3	K–HCO_3
Ib (fsp-qtz)	Na–HCO_3	Na–Cl–HCO_3	–
Ib (biotite)	K–HCO_3	K–HCO_3	–

4.2. Origin of chlorinity

Two major processes may increase the chlorinity of fluids in crystalline environments during water–rock interaction: 1.) Active leaching of Cl, which includes mineral dissolution (LSP) and liberation of elements present as HSP during cataclastic deformation. 2.) The chlorinity can be passively increased by the removal of H_2O (desiccation) due to the alteration of anhydrous minerals to hydrous, e.g. clay minerals (Kullerud, 1996; Markl and Bucher, 1998; Markl and Bucher, 1998; Stober and Bucher, 2004).

4.2.1. The effect of mineral alteration on the Na/Cl ratio

Na and Cl are fluid-mobile elements, which are typically not incorporated into secondary fracture minerals (McNutt et al., 1990; Brockamp et al., 2003; Bucher et al., 2012). However, a possible exception is volume conservative albitization (in contrast to passive removal of anorthite). In HSP Na/Cl typically ranges between 0.2 and 1 depending on the proportions of Ca, K and Na, since Cl is the major anion. HT experiments (II) indicate that alteration of the undeformed rock matrix

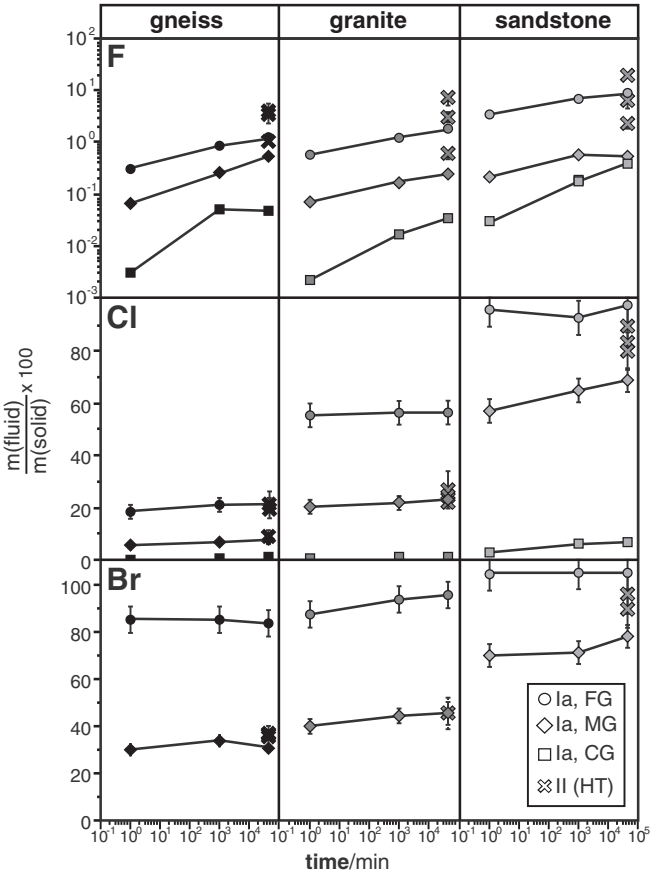

Fig. 4. Fluorine-, Cl- and Br-release in leachates of variable grain-size and temperature against time (Ia and II). The halogen mass of the leachates is normalized to the halogen mass in the whole rock of the respective sample. Lines connect same grain-size.

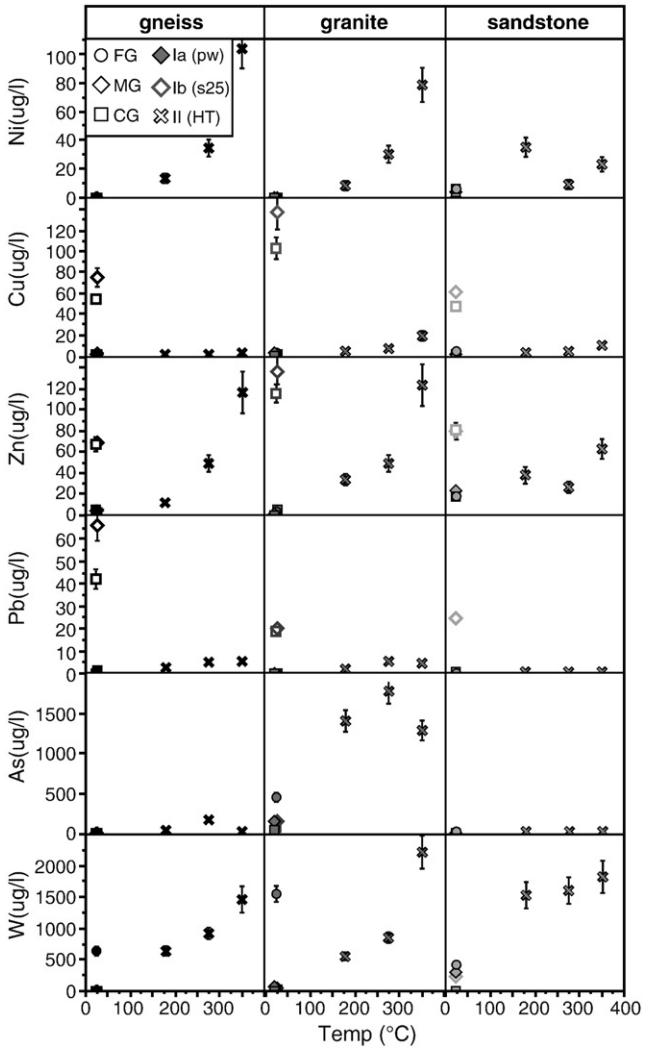

Fig. 5. Nickel, Cu, Zn, Pb, As and W concentrations of leachates, including Ia, Ib, Ic, Id and II (pw, s25 and HT) experiments of variable grain-size against temperature.

(in contrast to selective leaching) results in much higher Na/Cl ratios (Fig. 7A). On the other hand, smaller grain-size results in a general trend towards low Na/Cl (Fig. 7A). This results in two different trends: A) Chlorinity increase associated with increasing Na/Cl (liberating LSP) and B) chlorinity increase associated with decreasing Na/Cl (liberating HSP). Deep crustal fluids typically show low Na/Cl ratios (since Cl is the dominant anion), which can be experimentally attained by short-term water–rock reactions with decreasing fluid/rock ratios (Fig. 7B). Hence, desiccation seems to be a less important process compared to selective leaching of HSP in the formation of deep crustal fluids, since the alteration of feldspar and biotite (to e.g. illite or chlorite) seems to result in Na/Cl ratios much higher than those observed in deep crustal fluids. Consequently, fluid modification along cataclastic zones plays an important role for the geochemistry of crustal fluids above the brittle–ductile transition zone, where dynamic tectonics continuously produce cataclastic zones and fractures (Sibson, 1996; Gleeson et al., 2003). Not only the host rock in the proximity of such cataclastic zones is extensively altered, but also distal pervasive rock alteration (Bruhn et al., 1994; Everett et al., 1999; Just et al., 2004) further enhances fluid modification.

4.2.2. Chlorinity limits by leaching highly soluble phases

The maximum chlorinity obtainable by leaching HSP is probably limited by the salinities of the liberated fluid inclusions, which may vary largely between rock-types. The salinity of fluid inclusions in

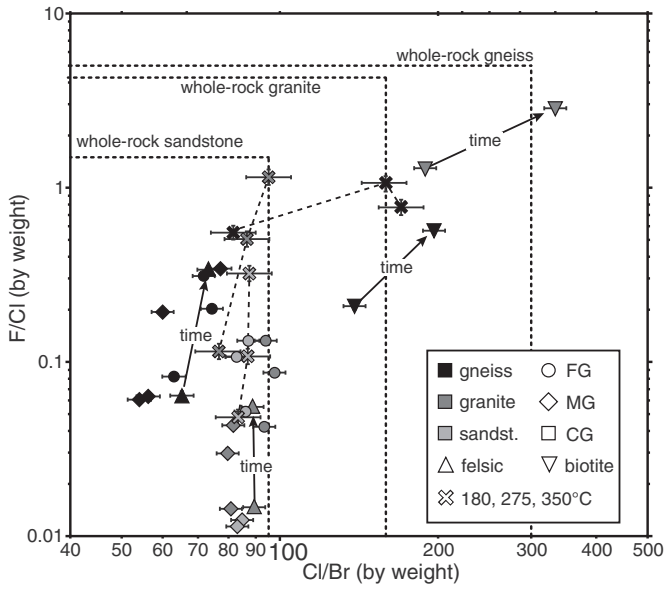

Fig. 6. F/Cl (by weight) against Cl/Br (by weight) of fine- and medium-grained leachates including UP and HT experiments, as well as leachates of felsic and mafic mineral separates. F/Cl and Cl/Br values of the whole-rock (Table 3) are indicated with lines. Increasing temperature within HT experiments is indicated as dotted lines.

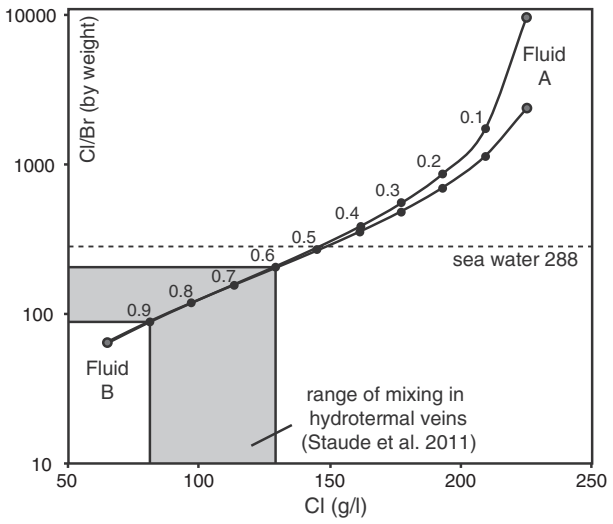

Fig. 8. Mixing model showing Cl/Br (wt.) versus Cl (mg/l) of basement brine (B) (derived by dissolution of highly soluble phases of the rock matrix) and halite dissolution brine (A). Two curves indicate different halite compositions. Mixing fractions are given above the data points. The grey area indicates the mixing ratios proposed by Staude et al., 2011, yielding low Cl/Br ratios and high chlorinities.

granites of this region do not exceed 8.5 wt.% (Simon, 1990; Burisch unpublished data). Fluid inclusion compositions in gneisses are rarely reported, but typically cover a low to intermediate salinity range (e.g. Loizenbauer et al., 2001). Additional highly soluble halogens present at e.g. grain-boundary salts can hardly be quantified, but their presence could potentially increase the limit of the salinity to a certain extent.

4.2.3. The impact of basement rock/fluid on externally derived fluids

As fluids with salinities of up to 26 wt.% have been reported from many hydrothermal vein-type deposits and from deep continental drill-holes (e.g. Frape et al., 1984; Yardley, 2005; Baatartsogt et al., 2007; Fusswinkel et al., 2013), there might be at least one additional halogen source involved in the genesis of such low Cl/Br brines. Halite dissolution brines (high Cl/Br) and bittern brines (low Cl/Br) are both extremely enriched in Cl and may serve as Cl source. A calculation assuming mixing of a halite dissolution brine (A) with a salinity of 27 wt.% NaCl and a Cl/Br of 10,000 or 2400 for Triassic and Tertiary halite (Stober and Bucher, 1999b) with a basement-derived fluid (B) constrained by 8.5 wt.% NaCl and a Cl/Br of 65 (based on leaching data and fluid inclusion salinity) was carried out to simulate the modification of an external fluid by mixing with batches of basement fluid during percolation through crystalline rocks, or during simultaneous ascent (Bons et al., 2014) (Fig. 8). Mixing minor amounts of sedimentary brine A with a basement fluid B increase the salinity significantly, while the Cl/Br ratio stays substantially below 288 (seawater). Therefore, the Cl/Br ratio should be evaluated critically and if possible

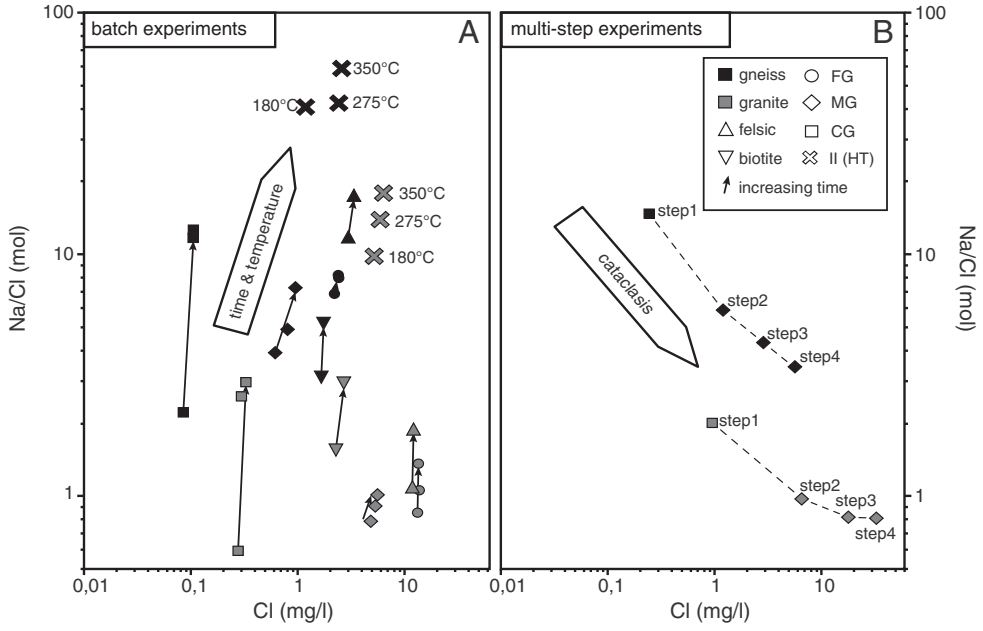

Fig. 7. Na/Cl (molar) versus Cl (mg/l) of batch experiments (UP and HT) on the left and multistep experiments on the right including leachates of gneiss and granite (and their mineral separates). On the left, the arrows indicate an increase of time from 1 to 44,600 min. Errors are smaller than symbols.

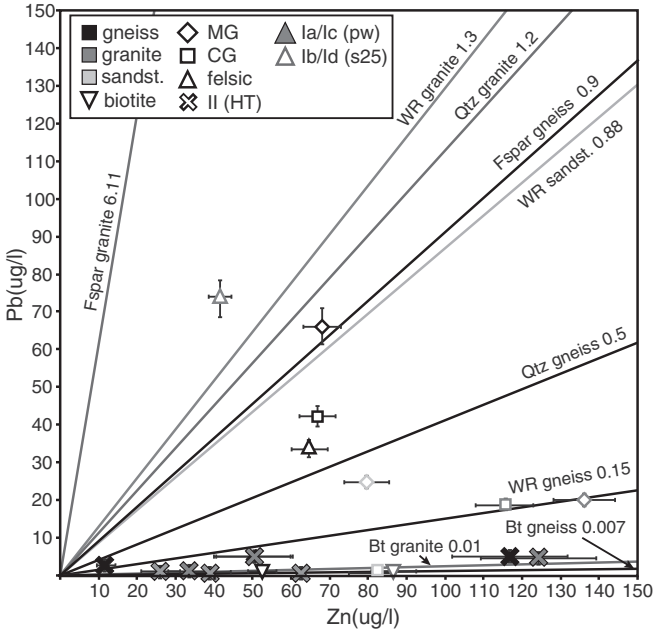

Fig. 9. Pb against Zn (in μg/l) of S25 and HT leachates of gneiss and granite and their mineral separates after 31 days. Whole rock and mineral separate compositions are indicated as lines.

combined with other chemical tracers when used as a reservoir tracer. On the other hand, the low Cl/Br ratio of externally derived bittern brines is not altered during water–rock and/or fluid–fluid interaction with basement rocks/fluids.

4.2.4. Implications for natural fluids

High and low salinity fluids may show low Cl/Br (Leisen et al., 2012 and references therein). Our data indicate, that low salinity (1–12 wt.%) fluids with low Cl/Br ratios (e.g. Miron et al., 2013) could be directly derived from leaching of crystalline rocks. Highly saline fluids (18–27 wt.%) with low Cl/Br ratios (e.g. Boiron et al., 2010; Richard et al., 2011), however, seem to require an external source for at least Cl.

4.3. Base metal mobility and implications for ore-forming fluids

Less than 5% of Ni, Pb and Zn of the whole rocks are released into the fluid during our experiments. This indicates that even more metals could possibly be leached from the host rock and supports the potential of ordinary crystalline rocks as metal sources (e.g. Wilkinson et al., 2005; Yardley, 2005; Pfaff et al., 2010; Fusswinkel et al., 2013). Nickel, As and W release rates are sensitive to temperature, while Pb mobility depends on the chlorinity and Zn is sensitive to both parameters (Fig. 9). Lead and Zn geochemically behave very similarly in aqueous solutions (Holland, 1972). Therefore, the Pb/Zn fluid ratio is probably controlled by its source (Yardley, 2005). Higher Pb/Zn of whole rock leachates compared to Pb/Zn of the respective biotite (Fig. 9), indicate that the alteration of felsic minerals predominantly governs the Pb/Zn ratio at low T and results in Pb/Zn >0.5. On the other hand, biotite alteration results in Pb/Zn of <0.15, due to its high Zn contents. Although, feldspar contains less Zn than biotite, Zn concentrations in the felsic leachates almost reach those of biotite leachates, indicating that substantial amounts of Zn can be leached from felsic minerals.

5. Conclusions

Depending on rock type, the amount of halogens present as highly soluble phases (HSP, c.f. fluid inclusions and grain boundary salts) can vary substantially. The majority of Br (>90%) resides in HSP, mainly present in felsic minerals. The proportion of Cl present as HSP depends on rock type, while the majority of F is structurally bound. As a consequence, selective leaching of HSP causes significant lower halogen ratios (Cl/Br and F/Cl) of fluids relative to the host rock. Natural settings, such as cataclastic zones create favourable conditions for halogen fractionation during water–rock interaction. Furthermore, Cl/Br and Na/Cl ratios of natural basement fluids indicate that fluid modification along cataclastic fractures seems to be an important process in the formation of basement brines, involved in vein-type hydrothermal ores. Substantial amounts of Ni, Pb, Zn, As and W can be leached from ordinary crystalline rocks. Substantial amounts of Zn (up to 65 μg/l) are present in felsic leachates (Id), although the felsic minerals have low absolute Zn contents.

Acknowledgements

We would like to thank Antonin Richard, Kurt Bucher and an anonymous reviewer for constructive comments that improved the manuscript substantially, Jeremy Fein for the editorial handling, Thomas Wenzel and Udo Neumann for supportive discussions, Benjamin Walter for discussion and the support in collecting the samples, Bernd Steinhilber and Gabriele Stoschek for their patient help in the Laboratory, Barbara Maier for constructing special sample holders for the autoclaves and Dagmar Kost, Dorothea Muehlbayer-Renner, Frederik Reinhard, Marcel Henker and Franziska Hauff for processing the whole rock fractions and mineral separates.

Appendix A. Supplementary data

Supplementary data to this article can be found online at http://dx.doi.org/10.1016/j.chemgeo.2016.03.031.

References

An, L.-J., Sammis, C.G., 1994. Particle size distribution of cataclastic fault materials from southern California: a 3-D study. Pure Appl. Geophys. 143 (1–3), 203–227.
Baatartsogt, B., et al., 2007. Contrasting paleofluid systems in the continental basement: a fluid inclusion and stable isotope study of hydrothermal vein mineralization, Schwarzwald district, Germany. Geofluids 7 (2), 123–147.
Billi, A., 2005. Grain size distribution and thickness of breccia and gouge zones from thin (<1 m) strike-slip fault cores in limestone. J. Struct. Geol. 27 (10), 1823–1837.
Boiron, M.C., Cathelineau, M., Richard, A., 2010. Fluid flows and metal deposition near basement/cover unconformity: lessons and analogies from Pb–Zn–F–Ba systems for the understanding of Proterozoic U deposits. Geofluids 10 (1–2), 270–292.
Bons, P.D., et al., 2014. Fluid mixing from below in unconformity-related hydrothermal ore deposits. Geology 42 (12), 1035–1038.
Bottomley, D., et al., 1999. The origin and evolution of Canadian Shield brines: evaporation or freezing of seawater? New lithium isotope and geochemical evidence from the Slave craton. Chem. Geol. 155 (3), 295–320.
Brockamp, O., Clauer, N., Zuther, M., 2003. Authigenic sericite record of a fossil geothermal system: the Offenburg trough, central Black Forest, Germany. Int. J. Earth Sci. 92 (6), 843–851.
Bruhn, R.L., Parry, W.T., Yonkee, W.A., Thompson, T., 1994. Fracturing and hydrothermal alteration in normal fault zones. Pure Appl. Geophys. 142 (3–4), 609–644.
Bucher, K., Stober, I., 2002. Water–rock reaction experiments with Black Forest gneiss and granite. Water–Rock Interaction. Springer, pp. 61–95.
Bucher, K., Stober, I., Seelig, U., 2012. Water deep inside the mountains: unique water samples from the Gotthard rail base tunnel, Switzerland. Chem. Geol. 334, 240–253.
Campbell, A.R., Rye, D., Petersen, U., 1984. A hydrogen and oxygen isotope study of the San Cristobal Mine, Peru; implications of the role of water to rock ratio for the genesis of wolframite deposits. Econ. Geol. 79 (8), 1818–1832.
Chi, G., Savard, M.M., 1997. Sources of basinal and Mississippi Valley-type mineralizing brines: mixing of evaporated seawater and halite-dissolution brine. Chem. Geol. 143 (3), 121–125.
Everett, C., Wilkinson, J., Rye, D., 1999. Fracture-controlled fluid flow in the Lower Palaeozoic basement rocks of Ireland: implications for the genesis of Irish-type Zn–Pb deposits. Geol. Soc. Lond., Spec. Publ. 155 (1), 247–276.
Frape, S., Fritz, P., McNutt, R.t., 1984. Water–rock interaction and chemistry of groundwaters from the Canadian Shield. Geochim. Cosmochim. Acta 48 (8), 1617–1627.
Frape, S., Blyth, A., Blomqvist, R., McNutt, R., Gascoyne, M., 2003. Deep fluids in the continents: II. Crystalline rocks. Treatise Geochem. 5, 541–580.
Fusswinkel, T., et al., 2013. Fluid mixing forms basement-hosted Pb–Zn deposits: insight from metal and halogen geochemistry of individual fluid inclusions. Geology 41 (6), 679–682.
Gerald, J.F., Stünitz, H., 1993. Deformation of granitoids at low metamorphic grade. I: reactions and grain size reduction. Tectonophysics 221 (3), 269–297.

Gleeson, S., Smith, M., 2009. The sources and evolution of mineralising fluids in iron oxide–copper–gold systems, Norrbotten, Sweden: constraints from Br/Cl ratios and stable Cl isotopes of fluid inclusion leachates. Geochim. Cosmochim. Acta 73 (19), 5658–5672.
Gleeson, S., Turner, W., 2007. Fluid inclusion constraints on the origin of the brines responsible for Pb–Zn mineralization at Pine Point and coarse non-saddle and saddle dolomite formation in southern Northwest Territories. Geofluids 7 (1), 51–68.
Gleeson, S.A., Wilkinson, J.J., Stuart, F.M., Banks, D.A., 2001. The origin and evolution of base metal mineralising brines and hydrothermal fluids, South Cornwall, UK. Geochim. Cosmochim. Acta 65 (13), 2067–2079.
Gleeson, S., Yardley, B.D., Munz, I., Boyce, A., 2003. Infiltration of basinal fluids into high-grade basement, South Norway: sources and behaviour of waters and brines. Geofluids 3 (1), 33–48.
Hellmann, R., et al., 2012. Unifying natural and laboratory chemical weathering with interfacial dissolution–reprecipitation: a study based on the nanometer-scale chemistry of fluid–silicate interfaces. Chem. Geol. 294, 203–216.
Herut, B., Starinsky, A., Katz, A., Bein, A., 1990. The role of seawater freezing in the formation of subsurface brines. Geochim. Cosmochim. Acta 54 (1), 13–21.
Holland, H.D., 1972. Granites, solutions, and base metal deposits. Econ. Geol. 67 (3), 281–301.
Just, J., Kontny, A., De Wall, H., Hirt, A.M., Martín-Hernández, F., 2004. Development of magnetic fabrics during hydrothermal alteration in the Soultz-sous-Forets granite from the EPS-1 borehole, Upper Rhine Graben. Geol. Soc. Lond., Spec. Publ. 238 (1), 509–526.
Köhler, J., Schönenberger, J., Upton, B., Markl, G., 2009. Halogen and trace-element chemistry in the Gardar Province, South Greenland: subduction-related mantle metasomatism and fluid exsolution from alkalic melts. Lithos 113 (3), 731–747.
Kullerud, K., 1996. Chlorine-rich amphiboles: interplay between amphibole composition and an evolving fluid. Eur. J. Mineral. 355–370.
Kullerud, K., 2000. Occurrence and origin of Cl-rich amphibole and biotite in the Earth's crust—implications for fluid composition and evolution. Hydrogeology of Crystalline Rocks. Springer, pp. 205–225.
Leisen, M., Boiron, M.-C., Richard, A., Dubessy, J., 2012. Determination of Cl and Br concentrations in individual fluid inclusions by combining microthermometry and LA-ICPMS analysis: implications for the origin of salinity in crustal fluids. Chem. Geol. 330–331, 197–206.
Lodemann, M., et al., 1997. On the origin of saline fluids in the KTB (continental deep drilling project of Germany). Appl. Geochem. 12 (6), 831–849.
Loizenbauer, J., et al., 2001. Structural geology, single zircon ages and fluid inclusion studies of the Meatiq metamorphic core complex: implications for Neoproterozoic tectonics in the Eastern Desert of Egypt. Precambrian Res. 110 (1), 357–383.
Markl, G., Bucher, K., 1998. Composition of fluids in the lower crust inferred from metamorphic salt in lower crustal rocks. Nature 391 (6669), 781–783.
Markl, G., Ferry, J., Bucher, e.K., 1998. Formation of saline brines and salt in the lower crust by hydration reactions in partially retrogressed granulites from the Lofoten Islands, Norway. Am. J. Sci. 298 (9), 705–757.
McCaffrey, M., Lazar, B., Holland, H., 1987. The evaporation path of seawater and the coprecipitation of Br^- and K^+ with halite. J. Sediment. Res. 57 (5), 928–937.
McNutt, R.H., Frape, S.K., Fritz, P., Jones, M.G., MacDonald, I.M., 1990. The 87Sr86Sr values of Canadian Shield brines and fracture minerals with applications to groundwater mixing, fracture history, and geochronology. Geochim. Cosmochim. Acta 54 (1), 205–215.
Miron, G.D., Wagner, T., Wälle, M., Heinrich, C.A., 2013. Major and trace-element composition and pressure–temperature evolution of rock-buffered fluids in low-grade accretionary-wedge metasediments, Central Alps. Contrib. Mineral. Petrol. 165 (5), 981–1008.
Möller, P., et al., 2005. Main and trace elements in KTB-VB fluid: composition and hints to its origin. Geofluids 5 (1), 28–41.
Nahnybida, T., Gleeson, S.A., Rusk, B.G., Wassenaar, L.I., 2009. Cl/Br ratios and stable chlorine isotope analysis of magmatic–hydrothermal fluid inclusions from Butte, Montana and Bingham Canyon, Utah. Mineral. Deposita 44 (8), 837–848.
Nordstrom, D.K., Lindblom, S., Donahoe, R.J., Barton, C.C., 1989. Fluid inclusions in the Stripa granite and their possible influence on the groundwater chemistry. Geochim. Cosmochim. Acta 53 (8), 1741–1755.
Norton, D., Knight, J., 1977. Transport phenomena in hydrothermal systems: cooling plutons. Am. J. Sci. 277 (United States).
Nurmi, P.A., Kukkonen, I.T., Lahermo, P.W., 1988. Geochemistry and origin of saline groundwaters in the Fennoscandian Shield. Appl. Geochem. 3 (2), 185–203.
Pfaff, K., Hildebrandt, L.H., Leach, D.L., Jacob, D.E., Markl, G., 2010. Formation of the Wiesloch Mississippi Valley-type Zn–Pb–Ag deposit in the extensional setting of the Upper Rhinegraben, SW Germany. Mineral. Deposita 45 (7), 647–666.
Piribauer, C.J., Meyer, F.M., Sindern, S., Vennemann, T.W., Prochaska, W., 2011. Fluid inclusions in the Outokumpu Deep Drill Core: implications for paleofluid evolution and composition of modern deep saline fluids. Geol. Surv. Finland Spec. Pap. 51, 169–180.
Richard, A., et al., 2011. An evaporated seawater origin for the ore-forming brines in unconformity-related uranium deposits (Athabasca Basin, Canada): Cl/Br and $\delta^{37}Cl$ analysis of fluid inclusions. Geochim. Cosmochim. Acta 75 (10), 2792–2810.
Savoye, S., et al., 1998. Fluid inclusions in granites and their relationships with present-day groundwater chemistry. Eur. J. Mineral. 10 (6), 1215–1226.
Sibson, R.H., 1996. Structural permeability of fluid-driven fault-fracture meshes. J. Struct. Geol. 18 (8), 1031–1042.
Siemann, M.G., Schramm, M., 2000. Thermodynamic modelling of the Br partition between aqueous solutions and halite. Geochim. Cosmochim. Acta 64 (10), 1681–1693.
Simon, K., 1990. Hydrothermal alteration of Variscan granites, southern Schwarzwald, Federal Republic of Germany. Contrib. Mineral. Petrol. 105 (2), 177–196.
Smith, M., Gleeson, S., Yardley, B., 2012. Hydrothermal fluid evolution and metal transport in the Kiruna District, Sweden: contrasting metal behaviour in aqueous and aqueous-carbonic brines. Geochim. Cosmochim. Acta.
Spencer, R.J., 1987. Origin of CaCl brines in Devonian formations, western Canada sedimentary basin. Appl. Geochem. 2 (4), 373–384.
Staude, S., Göb, S., Pfaff, K., Ströbele, F., Premo, W.R., Markl, G., 2011. Deciphering fluid sources of hydrothermal systems: a combined Sr-and S-isotope study on barite (Schwarzwald, SW Germany). Chemical Geology 286, 1–20.
Stober, I., Bucher, K., 1999a. Deep groundwater in the crystalline basement of the Black Forest region. Appl. Geochem. 14 (2), 237–254.
Stober, I., Bucher, K., 1999b. Origin of salinity of deep groundwater in crystalline rocks. Terra Nova-Oxford 11 (4), 181–185.
Stober, I., Bucher, K., 2004. Fluid sinks within the earth's crust. Geofluids 4 (2), 143–151.
Vovk, I., 1987. Radiolytic Salt Enrichment and Brines in the Crystalline Basement of the East European Platform, Saline Water and Gases in Crystalline Rocks. Ottawa, Geological Association of Canada Special Paper, pp. 197–210.
Walter, B.F., Immenhauser, A., Geske, A., Markl, G., 2015. Exploration of Hydrothermal Carbonate Magnesium Isotope Signatures as Tracers for Continental Fluid Aquifers, Schwarzwald Mining District. SW Germany, Chemical Geology.
Wilkinson, J., Eyre, S., Boyce, A., 2005. Ore-forming processes in Irish-type carbonate-hosted Zn–Pb deposits: evidence from mineralogy, chemistry, and isotopic composition of sulfides at the Lisheen mine. Econ. Geol. 100 (1), 63–86.
Wilkinson, J.J., Stoffell, B., Wilkinson, C.C., Jeffries, T.E., Appold, M.S., 2009. Anomalously metal-rich fluids form hydrothermal ore deposits. Science 323 (5915), 764–767.
Yardley, B.W., 2005. 100th Anniversary Special Paper: metal concentrations in crustal fluids and their relationship to ore formation. Econ. Geol. 100 (4), 613–632.

Chemical Geology 429 (2016) 44–50

Contents lists available at ScienceDirect

Chemical Geology

journal homepage: www.elsevier.com/locate/chemgeo

Tracing fluid migration pathways in the root zone below unconformity-related hydrothermal veins: Insights from trace element systematics of individual fluid inclusions

Mathias Burisch [a,*], Benjamin F. Walter [a], Markus Wälle [b], Gregor Markl [a]

[a] Fachbereich Geowissenschaften, Eberhard Karls University of Tübingen, Wilhelmstrasse 56, 72074 Tübingen, Germany
[b] Institute of Geochemistry and Petrology, ETH Zurich, Clausiusstrasse 25, CH-8092 Zürich, Switzerland

ARTICLE INFO

Article history:
Received 25 January 2016
Received in revised form 9 March 2016
Accepted 9 March 2016
Available online 12 March 2016

Keywords:
Ore mineralization
Fluid mixing
Rb/Cs
Clay formation
Alteration
Water–rock interaction

ABSTRACT

The temporal evolution of fracture networks below hydrothermal veins (root zones) and their impact on fluid chemistry, vein mineralogy and ore formation is insufficiently understood for unconformity-related hydrothermal veins in regions of extension, such as the common epithermal sediment-, unconformity- and basement-hosted Pb–Zn deposits. As metals and other trace elements are presumably mobilized during water–rock interaction of highly saline brines with igneous and metamorphic basement rocks, the evolution of these fracture zones seems to play a major role for hydrothermal ore formation. Laser ablation-inductively coupled plasma-mass spectrometry (LA-ICPMS) microanalysis of individual, texturally well-characterized fluid inclusions, hosted in fluorite and quartz of the Jurassic–Cretaceous Brandenberg fluorite–barite–quartz–galena–sphalerite vein near Todtnau, Schwarzwald, SW Germany, was carried out. Fluid mobile elements (Rb, Cs, Li, W, Ba, Zn, Pb, Sr), preferentially released by the alteration of primary rock-forming minerals (process tracer) were analysed as well as the Cl/Br ratio (source tracer) of fluid inclusions in genetically early fluorite and later quartz. A distinct decrease of trace elements within the fluid inclusions with time indicates successive alteration of primary minerals at the fracture wall to clay minerals with consecutive fluid pulses. A maximum concentration of trace elements in the fluid and consequent ore precipitation is associated with the initial phase of formation of a fracture root. Later fluid pulses migrate along pre-existing fractures so that the amount of fresh reactive rock material decreases with each fluid pulse. As a consequence, multiple generations of ore minerals require the formation of new fracture branches in the root zone of hydrothermal veins. Therefore, it seems that cataclastic zones below hydrothermal veins essentially control ore formation, and their tectonically induced dynamics might be one key parameter that governs the temporal interval of ore precipitation.

1. Intoduction

The nature of the feeding systems of hydrothermal unconformity-related vein-type deposits and of the detailed relation between active tectonics, fluid flow and mineral precipitation are poorly constrained. Few studies have addressed feeder systems of other hydrothermal systems: Richardson et al. (1987) and Everett et al. (1999) describe alteration and concomitant metal depletion of the wall rock in large-scale fractured root zones below volcanogenic massive sulphide and Irish-type deposits, and Seedorff et al. (2008) investigated root zones in porphyry systems and noted the important role of these zones for understanding the genesis of the associated ore systems, especially their geological lifetime and their impact on fluid flow and chemistry. If, however, this interconnected network is a new fracture system related to recent/local tectonics (which also is responsible for vein opening), or if this system has been active over a relatively long time and discontinuously feeds into reactivated mineralizations, is completely unknown, as yet, no approach has been proposed to track changes in the root zone with time. This is exactly what we try to address in the present contribution by proposing a new geochemical tool, which allows monitoring the degree of host rock alteration in the root zone of fracture systems, and therefore provides indirect evidence of the life time of such fracture meshes below the actual vein. In contrast to previous studies (e.g. Richardson et al., 1987; Everett et al., 1999; Seedorff et al., 2008), which were based on direct petrographic investigations of the root zones, this contribution focuses on chemical tracers archived in the fluid inclusions of the hydrothermal veins above the root zones. This approach renders it possible to characterize the temporal evolution of the root zone below a specific hydrothermal vein, even if the actual root zone is not exposed/accessible.

Previous work on epithermal sediment- and basement-hosted unconformity-related vein deposits mainly focused on the chemical and hydrodynamic processes that cause ore precipitation in particular,

* Corresponding author.
E-mail address: mathias.burisch@ifg.uni-tuebingen.de (M. Burisch).

http://dx.doi.org/10.1016/j.chemgeo.2016.03.004
0009-2541/

the fluid mixing (e.g. Russell et al., 1981; Sverjensky, 1981; Gleeson et al., 2001; Muchez et al., 2005; Boiron et al., 2010; Leach et al., 2010; Richard et al., 2011; Bons et al., 2014; Fußwinkel et al., 2013; Walter et al., 2015 and references therein). As shown by numerous workers (e.g. Sverjensky, 1981; Boiron et al., 2010; Gleeson and Yardley, 2002 and references therein) fluid mixing occurs between (I) hot, deep-seated fluids from the crystalline basement, and (II) cooler, sediment-derived fluids from the overburden sequence (e.g. Richard et al., 2011; Staude et al., 2009, 2012; Boiron et al., 2010; Fußwinkel et al., 2013; Walter et al., 2015; Walter et al., 2016 and references therein). Most authors suggest the basement brine to be metal-rich (Boiron et al., 2010; Bons et al., 2014; Fußwinkel et al., 2013, Wilkinson et al., 2005) in unconformity-related veins (Fig. 1C).

In contrast to the referred contributions, this study focuses on the temporal evolution of fluid migration paths, which govern the chemical composition (focusing on trace elements) of the basement fluid involved in ore-forming processes. The conceptual model is based on the following assumptions: If the fracture system below hydrothermal veins remains physically unchanged over a specific time interval of mineral precipitation, major element chemistry should not change significantly over time, while other chemical tracers (Rb/Cs, Li, W, Pb, Zn) in the fluid should show a systematic variation with time. After initial fracture opening, fresh primary host minerals like feldspar or micas become altered to secondary minerals like e.g. illite or chlorite (Stober and Bucher, 2004; Brockamp, 2005) in non-magmatic epithermal systems. Early fluids should be rich in elements released by primary, but not incorporated into secondary minerals. In contrast, adsorption effects of fluid components on secondary mineral surfaces should increase with progressing alteration of the fracture wall. These changes with time: a juvenile fracture provides a large volume of fresh, unaltered minerals, which become successively altered to secondary phases (Jébrak, 1997; Stober and Bucher, 2004; Kendrick et al., 2008; Seelig and Bucher, 2010). Later fluid pulses, migrating on the same fracture networks, will find less unaltered mineral surfaces that can potentially react.

The Rb/Cs ratio is a suitable tracer for this approach, since both elements typically substitute for K in primary rock-forming minerals, but fractionate during clay mineral formation (Göb et al., 2013 and references therein). Rb is incorporated into the structure of clay minerals, while Cs is adsorbed on clay surfaces (Göb et al., 2013 and references therein). Hence, the Rb/Cs ratio of a fluid can be modified by alteration of feldspars and biotite to clay minerals (Aquilina et al., 1997; Göb et al., 2013, and references therein). As a consequence, Rb/Cs ratios <2 are typical of fluids, which interacted with unaltered crystalline rocks (on-going host rock alteration), while Rb/Cs ratios of ~2 represent equilibrium conditions during alteration of primary minerals to clay minerals. Rb/Cs ratios >5 indicate water–rock interaction with pre-existing clay minerals (no alteration of primary phases) (Göb et al., 2013). Other elements like W, Zn and Pb are released by feldspars, Li and Zn by biotites during water–rock interaction (Burisch et al., 2015) and should therefore systematically decrease in the fluid with increasing alteration of the fracture walls.

Epithermal, unconformity-related hydrothermal veins containing Pb–Zn, Fe–Mn, Cu or also Ag ores, occur widespread in central Europe, where the Variscan basement is exposed and was subjected to extension (Boiron et al., 2010, and references therein). The characteristic mineral assemblage typically consists of fluorite, quartz, sometimes barite, with galena and sphalerite as the most common ore minerals in addition to fahlores, chalcopyrite and other, subordinate sulphides and sulf-arsenides. The majority of these veins formed during the Jurassic, when extensional stress regimes related to the opening of the northern Atlantic prevailed (Mitchell and Halliday, 1976; Boiron et al., 2010 and references therein). Mixing of two highly saline brines across the basement-cover unconformity induced mineral precipitation, including a sedimentary and a deep-seated basement fluid (Staude et al., 2009, Boiron et al., 2010; Fußwinkel et al., 2013; and references therein).

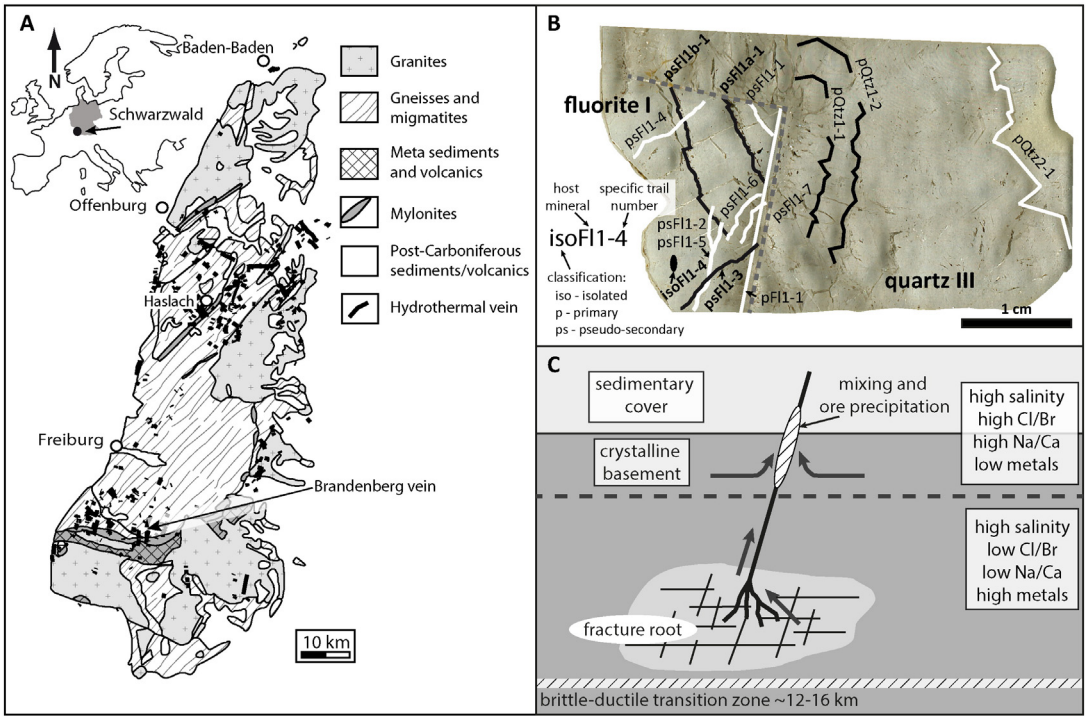

Fig. 1. A) geological overview map based on Eisbacher et al. (1989) and Wimmenauer and Stenger (1989) including the most important hydrothermal veins (Markl, 2015) and the sample location, the Brandenberg vein. B) double-polished thin section of fluorite I overgrown by quartz III. Black colours were used for FIAs, which could be analysed by LA-ICPMS, white colours were used for FIAs which could only be analysed by microthermometry. The first two letters indicate the nature of FIAs: iso — isolated, p — primary and ps — pseudo-secondary. Capital letters indicate the host mineral: Fl — fluorite and Qtz — quartz. C) Schematic illustration of the litho- and fluid-stratigraphy (based on Bucher and Stober (2010); Geyer and Gwinner (2011); Fußwinkel et al. (2013) and Walter et al. (2016) and the major processes related to vein formation: Host rock alteration in the root zone, fluid migration and mixing in the actual fracture induces ore precipitation.

Interconnected fracture systems in the crystalline basement are the major fluid pathways (e.g. Stober and Bucher, 2007) for deep-seated brines. They govern both direction and chemistry of a migrating fluid (Richardson et al., 1987; Everett et al., 1999; Boiron et al., 2010; Burisch et al., 2015) since along these connected fractures, the reaction surface of fluid and rock is significantly increased. Hence, the spatial and temporal evolution of a fracture zone has a significant impact on the fluid chemistry, and therefore on the ore-forming potential of a basement fluid (Jébrak, 1997). Due to crustal thinning associated with a significant pressure increase of isolated fluid batches (Staude et al., 2009), fault-fracture meshes might form as a consequence of rock failure (Sibson, 1996). These feed into larger fractures (the actual hydrothermal veins) at shallower crustal levels (Fig. 1C). In this contribution, the temporal evolution of fracture networks below unconformity-related hydrothermal veins is indirectly monitored based on chemical data of fluid inclusions in mineralized veins. This study, hence, provides new insight into the relationship between host rock alteration in the root zone and ore deposition at higher stratigraphic levels (Fig. 1C).

2. Regional geology and hydrothermal vein formation of the Schwarzwald mining district

2.1. Jurassic veins of the Schwarzwald and ore forming processes

The Schwarzwald is situated in south-western Germany and is an asymmetrically exhumed basement window, dominantly composed of granites and gneisses (Fig. 1A). Uplift and erosion was associated with the formation of the Tertiary Upper Rhinegraben Rift (Geyer and Gwinner, 2011 and references therein). Comparable deposits can be found in the Erzgebirge (Klemm, 1994), the Bohemian Massif (Walther, 1982; Ondrus et al., 2003), the Harz (Lüders et al., 1993), France (Boiron et al., 2010), Ireland (Wilkinson et al., 2005) and Morocco (Ahmed et al., 2009; Gasquet et al., 2005), just to name some examples.

Before opening of the Rhinegraben the basement rocks were covered by 1.5 km thick Triassic and Jurassic sediments including middle Triassic evaporites (often containing halite) (Geyer and Gwinner, 2011 and references therein). The oldest record of hydrothermal activity in the Schwarzwald goes back to 320 Ma, but one of the temporal maxima of hydrothermal vein formation in central Europe was during the Jurassic–Cretaceous period (Mitchell and Halliday, 1976; Boiron et al., 2010). In contrast to the post-Cretaceous veins, the sedimentary cover was tectonically undisturbed during the Jurassic, since the prevailing extensional stress regime did not promote the formation of large-scale tilting or rotation. Still, the Jurassic phase can be regarded as the most important hydrothermal maximum in the Schwarzwald (and in central Europe) and remained tectonically active during the entire phase of extension (Staude et al., 2009). Vein formation in the Jurassic was initiated by mixing of two chemically distinct fluids (binary mixing), including the Brandenberg hydrothermal vein near Todtnau presented in this study. Fußwinkel et al. (2013); Bons et al. (2014) and Walter et al. (2016) showed that the two fluids involved in mixing are a highly saline, metal-rich basement fluid with low Cl/Br and a highly saline sedimentary fluid with high Cl/Br (halite dissolution) (Fig. 1C). Changes in the proportion of the two fluids can be monitored by Cl/Br ratio of the single inclusions.

2.2. Ore geology of the Brandenberg vein

Based on previous studies (Staude et al., 2009, Walter et al., 2015, and references therein), the Jurassic–Cretaceous Brandenberg vein near Todtnau in the Schwarzwald mining district (latitude: N 47.841301; longitude: E 7.972786) was selected for such a study (Fig 1A and B), since this vein shows all characteristics typical of hydrothermal veins of the Jurassic–Cretaceous period in central Europe (major element composition, mode of host rock alteration, mineral assemblage and geometric orientation) (Metz et al., 1957; Behr and Gerler, 1987; Behr et al., 1987; Baatartsogt et al., 2007; Staude et al., 2009; Boiron et al., 2010; Walter et al., 2016). Furthermore, it shows clear relative age relations of gangue and ore minerals and individual primary and pseudo-secondary fluid inclusions sufficiently large for LA-ICPMS analysis of single inclusions hosted in fluorite and quartz.

The Brandenberg vein is a NNE–SSW (355–20°), steep dipping (60–85° W) mineralized vein, which extends over approximately 300 m in length. The 50 to 150 cm thick vein pinches gently out to the North and is crosscut by a younger fault in the south. The vein is hosted by fine-grained gneiss, which is weakly affected by alteration (only a few mm). The alteration type is propyllitic. The mineralization is distinctively banded due to a succession of mineral assemblages. The paragenetic sequence starts with quartz I impregnating the host rock, which is followed by very little pyrite, overgrown by small crystals of quartz II (pre-ore stage). Fluorite I is precipitated co-genetically along with galena, and chalcopyrite (ore stage). This stage is followed by quartz III, very little fluorite II, quartz IV and calcite I (post ore-stage) (Metz et al., 1957).

3. Sample characterization and analytical procedure

3.1. Fluid inclusion petrography

A sample containing early fluorite I intergrown with minor amounts of galena (Fig. 1B) and overgrown by later euhedral chevron quartz III was prepared for detailed texturally resolved fluid inclusion studies (Fig 1B). Other gangue minerals could not be analysed, since their FIs were unfortunately too small for LA-ICPMS analysis. Analysed inclusion sizes range from 20 to 120 μm. No clay minerals were observed in thin section. Both gangue minerals contain visible growth zones including several generations of petrographically unambiguous fluid inclusion assemblages (FIAs). A detailed classification scheme and an overview of relative ages of FIAs are given in Fig. 1B and 2B. Isolated fluid inclusions in fluorite (isoFl1–4) are the oldest ones and are of primary (p) character. FIA psFl1a-1 in fluorite is of pseudo-secondary (ps) character, but is crosscut and therefore clearly older than primary FIA pFl1–1. FIAs psFl1b-1 is older than psFl1–3, which can be deduced from indirect crosscutting relations with psFl1–2 and psFl1–5. Age relations between psFl1a-a and psFl1b-1 cannot be derived from crosscutting relations, but psFl1b-1 is crosscut by psFl1–6 (which is crosscut by pFl1–1) and therefore along with psFl1a-1 older than pFl1–1. The oldest FIA in quartz is pQtz1–1, followed by pQtz1–2 and pQtz-3 (Fig. 1B). Not all of these FIAs could be analysed by LA-ICPMS, but Table ES2 includes the entire microthermometric background data set.

3.2. Methods

Fluid inclusion thermometry was performed using a Linkam THMS-600 cooling–heating stage. Synthetic fluid inclusion standards were used for calibration. LA-ICPMS microanalysis of individual fluid inclusions was conducted with a Perkin Elmer Elan 6100DRC quadrupole ICPMS connected to an ETH-GeoLas 193 nm ArF excimer laser system at the ETH Zurich. An energy density of 15–20 J/cm^2 with a laser puls frequency of 10 Hz and a variable beam diameter of 5–30 μm was used. Analytical and standardization procedures are reported in Heinrich et al. (2003) and Seo et al. (2011). LA-ICPMS analyses of single fluid inclusions were performed for 27 elements (Li, B, Na, Mg, S, Cl, K, Ca, Mn, Fe, Co, Ni, Cu, Zn, As, Br, Rb, Sr, Mo, Sb, Cs, Ba, W, Tl, Pb, Bi and Si). Calcium (fluorite) and Si (quartz) were used for host mineral matrix correction. All peaks signals of the analytes were checked for temporal correlation with the Na and Cl peak signals to preclude signals potentially derived by ablation of the host mineral and to verify that the measured elements are in solution. Microthermometrically determined Na was used as internal standard, assuming a $CaCl_2$–NaCl–H_2O system (Steele-MacInnis et al., 2011). Since Na concentrations vary less than

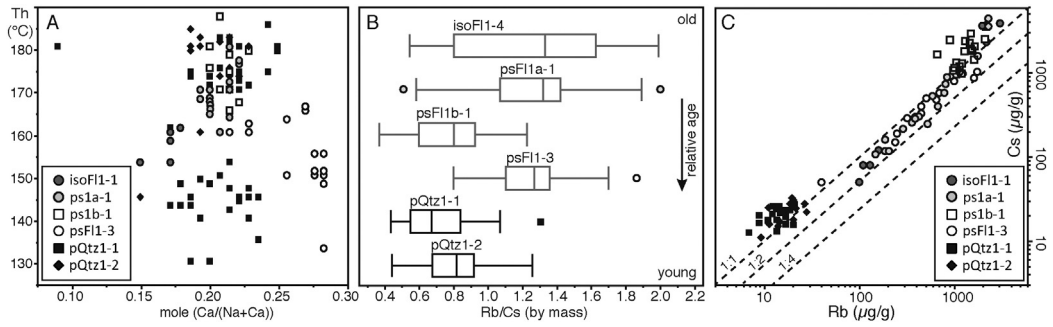

Fig 2. A) Homogenisation temperature T_h against Ca/(Ca + Na) of fluid inclusions determined by microthermometry. FIAs are ordered according to their relative age, starting with the oldest isoFl1–4 to the youngest pQtz1–2. Neither T_h nor Ca/(Ca + Na) show a systematic variation with relative age. B) Box plots, showing range, quartile and average values of Rb/Cs of different FIAs. FIAs are ordered according to their relative age, starting with the oldest isoFl1–4 at the top and ending with the youngest pQtz1–2 at the bottom. There is a distinct decrease in Rb/Cs from psFl1–3 to psFl1b-1 indicating progressing host rock alteration in the root zone of the fracture. C) Rb vs. Cs plot of analysed FIAs. The absolute concentrations of Rb and Cs are lowest in the post-ore quartz. Rb/Cs ratios of 1, 2 and 4 are indicated as dotted lines, suggested by Göb et al. (2013) as a monitor for host-rock alteration.

0.5 wt.% within one FIA, average values of Na were used for each FIA. Signal processing was carried out using the SILLS software package of Guillong et al. (2008). The complete dataset is given in the electronic supplement.

4. Results

The data set consists of 215 (of which only 107 could be analysed by LA-ICPMS) analyses of single fluid inclusions hosted in fluorite and quartz, including isolated (iso) and pseudo-secondary (ps) FIAs in fluorite and exclusively primary FIAs in the quartz sample (Fig. 1B). In contrast to distinct differences in trace element chemistry of FIAs in fluorite and quartz, microthermometric data (salinity, Ca/(Ca + Na) and T_h) of FIAs in both minerals strongly overlap and show the same (narrow) variability (see Fig. 2A). FIAs in both minerals show a narrow range of salinities (22.0–24.5 wt.%, NaCl + $CaCl_2$) and homogenization temperatures T_h (uncorrected 130–192°C) (Fig 2 A and Table ES1). There seems to be no systematic change in major fluid chemistry with relative age of the FIAs (Fig. 2A). First melting can be detected around −50°C, freezing during cooling runs happens at −70 to −100°C, which indicates a ternary NaCl–$CaCl_2$–H_2O system with a eutectic temperature of −52.0°C. Ice is the last-melting phase. The final melting temperature of ice is in the range of −21.0° to −24.5°C, that of hydrohalite between −21.7° and −25.1°C. The molar Ca/(Ca + Na) ratios range from 0.09–0.28. Within one trail, salinity and T_h are almost constant, but they show small variations between different trails within one sample (Fig 2A).

LA-ICPMS analyses could be performed on 107 fluid inclusions of FIAs isoFl1–4, psFl1a-1, psFl1b-1, psFl1–3, pQtz1–1 and pQtz1–2 (from old to young, see Fig. 2B). Fluid inclusions in fluorite (isoFl1–4, psFl1a-1, psFl1–3 and psFl1b-1), have average concentrations of 1943 µg/g Li, 957 µg/g Br, 1004 µg/g Rb, 388 µg/g Sr, 1257 µg/g Cs, 137 µg/g Ba, 436 µg/g Zn, 225 µg/g W, 237 µg/g Pb and Cl/Br ratios between 113 and 694, while average concentrations in fluid inclusions hosted by quartz (pQtz1–1 and pQtz1–2) have 346 µg/g Li, 1209 µg/g Br, 16 µg/g Rb, 402 µg/g Sr, 21 µg/g Cs, 25 µg/g Ba, 26 µg/g Zn, W is below detection limit (except for one inclusion, which has 12 µg/g), 24 µg/g Pb and Cl/Br ratios of 38–285 (Fig. 3 A, B, C, D and E). FIAs in fluorite are extremely enriched in Li, Rb, Cs, Zn, Pb and W compared to FIAs in quartz. Highest absolute Rb can be observed in isoFl1–4 (up to 3040 µg/g), while highest Cs occurs in psFl1a-1 (up to 4580 µg/g) (Fig. 2B and C). Average Rb/Cs values of FIAs in fluorite range between 1.2 and 1.4, with a relatively large spread (0.5 to 2.0). PsFl1b-1 shows relatively low average Rb/Cs values of 0.8, caused by a stronger enrichment of Cs compared to isoFl1–4, psFl1a-1 and psFl1–3. Average values of Li, Ba and Pb are highest in psFl1b-1 (2381 µg/g Li, 334 µg/g Ba and 482 µg/g Pb) and lowest in isoFl1–4 (1883 µg/g Li, 81 µg/g Ba and 185 µg/g Pb). In contrast, primary FIAs in quartz are generally depleted in trace elements (dilution factor $C_{quartz}/C_{fluorite}$ is in the range of 0.001 to 0.1) having much lower Rb (less than 28 µg/g) and Cs (less than 40 µg/g) concentrations (Fig. 2B and C). Both pQtz1–1 and pQtz1–2 have average Rb/Cs ratios of 0.7 to 0.8, with a relatively large spread (0.4 to 1.3). pQtz1–1 and pQtz1–2 do not show significant differences in their trace element budget. Average Cl/Br ratios are slightly higher in FIAs in quartz (146) compared to fluorite (298), but scatter strongly within each FIA. Average Sr concentrations do not vary significantly in all FIAs (302 to 451 µg/g).

5. Discussion and conclusions

5.1. The Cl/Br ratio as source tracer and mixing monitor

Fußwinkel et al. (2013) and Walter et al. (2016) showed that the Jurassic hydrothermal veins formed by a strictly binary mixing between a basement brine with low Cl/Br ratios (60–100, Walter et al., 2016 and references therein) and a sedimentary fluid, which has high Cl/Br ratios due to halite dissolution (Cl/Br = 10.000, Stober and Bucher, 2004) (Fig. 1C). Fast mineral precipitation led to a large scatter in Cl/Br ratios in one FIA, since during rapid mixing the proportion of each involved fluid component can vary (Fußwinkel et al., 2013).

Although the analysed fluid inclusions show a range in Cl/Br ratios from ~20 to ~700 (Fig 3A), there is no systematic variation in Cl/Br from old to young FIAs, indicating that the variation of Cl/Br is not caused by a systematic variation of the degree of mixing, but is rather an effect of (unsystematic) rapid mixing (Fußwinkel et al., 2013). Therefore, the Cl/Br ratio of analysed fluid inclusions implies, that the general mixing ratio does not significantly change from early fluorite to late quartz formation (Fig 3A), which is important for further considerations. This assumption is strengthened by the unsystematic variation of Ca/(Ca + Na) and the intense dilution (~0.001) of trace elements from isoFl1–4 to pQtz1–2, while dilution factors for mixing can be assumed to be in the range of 0.5–0.75 (Schwinn et al., 2006).

5.2. Rb/Cs and trace elements

The Rb/Cs ratio and the maximum values of Rb, Cs, Li, Pb + Zn, W and Ba concentrations decrease with time (from early fluorite, isoFl1–4 to late quartz, pQtz1–2) (Fig 3 B, D, E and F). Strontium and Cl/Br do not follow this temporal variation (Fig 3 A and C).

When fluid migration paths are established first (fracture opening), abundant fresh reactive mineral surfaces are present along the fracture walls, reacting immediately with the percolating fluid. Therefore, first generation fracture fluids are enriched in Rb, Cs and other fluid-mobile trace elements released by feldspar (W, Pb, Ba, Zn and Sr) and mica (Li, Zn and Ba). The enrichment of these elements indicates, that the basement fluid involved in fluorite precipitation was governed by

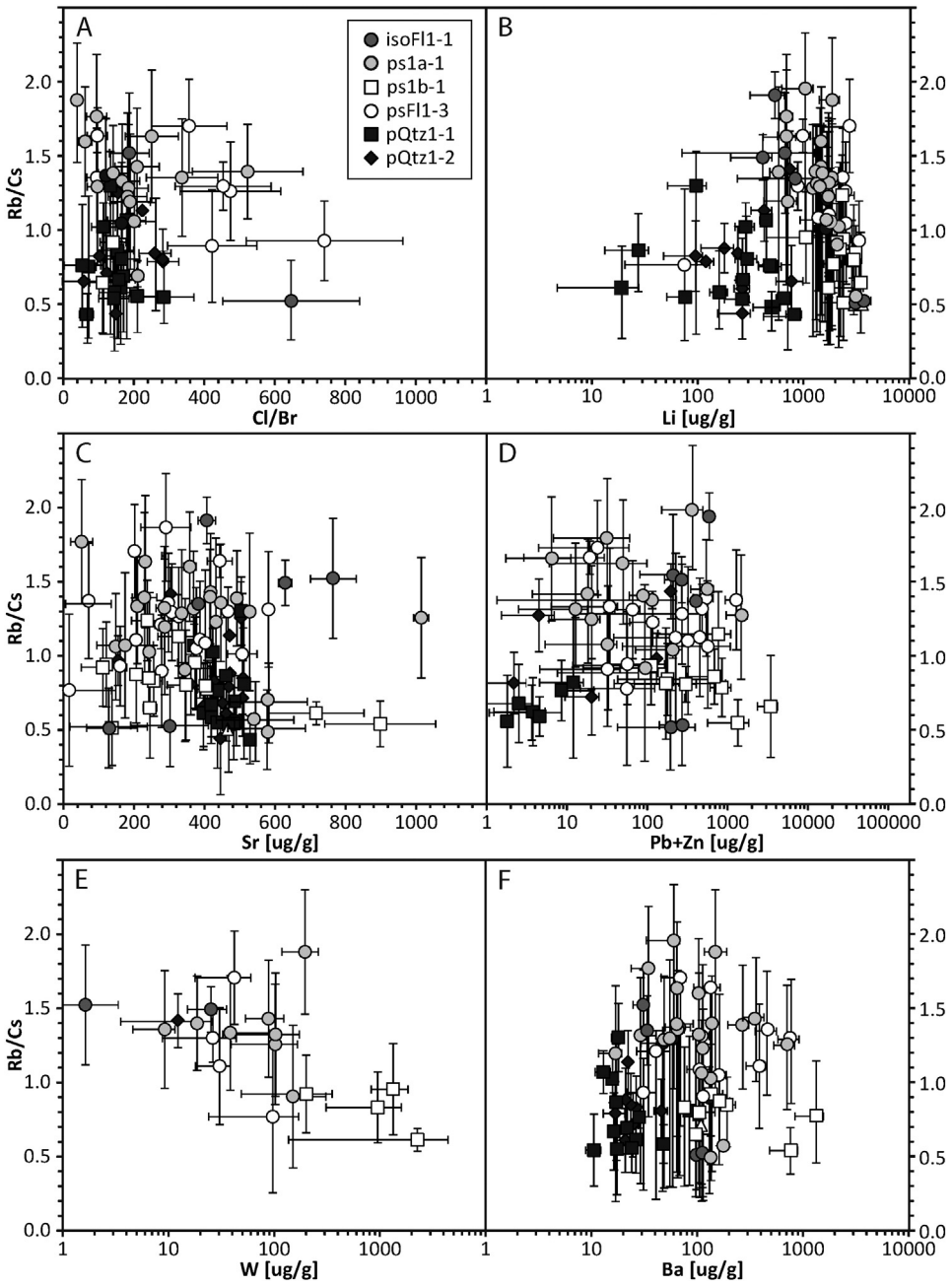

Fig. 3. Rb/Cs versus A) Cl/Br. Although fluorites show a slightly higher variability in Cl/Br ratios, no correlation between Rb/Cs and Cl/Br can be observed. B) Li concentrations are highest in Fl hosted by fluorite, which are often associated with elevated Rb/Cs ratios. C) Sr shows no clear correlation with Rb/Cs, D) Pb + Zn concentrations show a systematic decrease from fluorite I to quartz III, E) W concentrations are clearly higher in fluid inclusions in fluorite. F) Ba content is highest in FIAs in fluorite I, decreasing significantly in FIAs in quartz III.

the alteration of primary host minerals to clay minerals before it ascended and mixed with a sedimentary fluid.

The lower values of Rb, Cs, W, Pb, Zn, Li and Ba in the later quartz indicate that later fluid batches migrated along the same fracture networks, rather than establishing new fracture systems. With each fluid pulse, the abundance of fresh rock material decreases, and therefore causes a decrease in the absolute concentration of trace elements in the ascending fluid. Since Rb is structurally incorporated into clay minerals and Cs is only adsorbed onto surfaces of clay minerals and remaining mica (Göb et al., 2013 and references therein), leaching the absorbed Cs results in lower Rb/Cs ratios compared to alteration of primary rock-forming minerals. This is in agreement with the decrease of average Rb/Cs and absolute Rb and Cs from early fluorite to late quartz, caused by progressing host rock alteration in the fracture root zone. Low Rb/Cs of the quartz shows that the later fluid pulses did not dissolve clay minerals, which would result in high Rb/Cs ratios (typically above 2, Göb et al., 2013) and that the majority of adsorbed Cs has already been leached from existing clay minerals. As long as minor amounts of fresh rock material are still available along fracture-fault meshes (Sibson, 1996), the Rb/Cs ratio positively correlates with the ratio of fresh/altered rock. As a consequence of progressing alteration, ore (galena) precipitation is associated with early fluorite I, since the early generation of basement brine was substantially richer in trace elements like Pb than the following fluid pulses. This is in good agreement with the chemical modification of basement fluids along cataclastic fractures as discussed by Jébrak (1997) and Burisch et al. (2015).

Empirical data of granitic and sedimentary fluids (Göb et al., 2013) combined with data of this study were used to model an entire cycle of a hydrothermal fracture governed by the host rock alteration in the

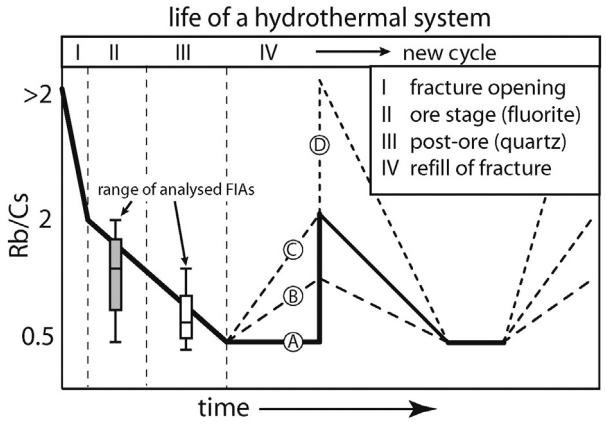

Fig. 4. Schematic model of the temporal evolution of the fluid's Rb/Cs ratio, within the root zone of a hydrothermal vein. A, B, C and D indicate four general possibilities of a transition from one cycle/fluid-pulse to the following.

root zone below (Fig. 4). Meteoric/sedimentary fluids have typically Rb/Cs above 2 (3.8 to 21.8, Göb et al., 2013). At some point, after these fluids percolated through the crystalline basement they will obtain steady-state Rb/Cs ratios of around 2 (Stage I). This is assumed, since Walter et al. (2016) showed that the basement brines contain significant amounts of a Triassic sedimentary fluid (bittern brine). This does not change, until new fracture systems open, providing vast amounts of fresh granitic rock material. This drastically decreases the Rb/Cs of the fracture fluid and increases trace metal concentrations tremendously (stage II). In stage III the amount of available fresh rock and released trace metals in the fluid is substantially decreased.

Although both Rb and Cs concentrations decrease in stage III, Cs concentrations decrease to a lesser extent and therefore, the Rb/Cs ratio further decreases until no fresh rock is available any more (end of stage III). After all fresh rock is consumed (stage IV), four general possibilities of fracture fluid evolution can be assumed. A) The Rb/Cs of the fluid instantaneously increases to a value of 2, since fluids in equilibrium with basement rocks (a granitic fluid is here taken to be representative of the crystalline basement, since empirical data for basement rocks other than granites are lacking) flood the system. B) Rb/Cs increases slowly towards a steady state of water–rock interaction with igneous and metamorphic rocks (only data for granite available), but before the fluid reaches equilibrium values of 2, new fractures open and a new cycle begins. C) Similar to B), but the fracture fluid reaches equilibrium with crystalline basement rocks before a new cycle starts. D) An externally derived sedimentary fluid (high Rb/Cs) enters the fracture (see Fig. 4).

Combining the Rb/Cs ratio with Pb, Zn, W, Li and Ba concentration, this data allows reconstructing the temporal evolution of a fracture network below a hydrothermal vein. This evolution has a major impact on fluid chemistry and therefore ore precipitation. Again, the important role of fluid modification and metal uptake along cataclastic fractures has been shown (see also Burisch et al., 2015). After the initial break-up of the fracture network, successive fluid pulses continued to migrate on the same fractures during the formation of the Brandenberg vein. Reactivation and concomitant fluid migration along pre-existing fracture zones is associated with successive alteration of the fracture walls. As a consequence, metal concentrations are highest in the earliest fluids in a specific fracture system, since large amounts of fresh wall rock are available. Accordingly, the post-ore quartz III shows much lower trace metal concentration and is therefore barren. This implies that a dynamic fracture network (or fault-fracture meshes, Sibson, 1996) in the root zone is a substantial requisite for the formation of several ore generations in one hydrothermal vein, where the formation of new migration paths in the root of the hydrothermal vein provides sufficient fresh rock material to allocate the metals to consecutive fluid pulses (Fig. 4). New fault-fracture meshes (interconnected fractures in the root zone) are generated episodically, whenever fluid pressure and/or strain cause rock failure (Sibson, 1996). On the other hand, metal and trace element concentrations in static fracture zones decrease in consecutive fluid pulses and show their maximum at the time of early fracture zone generation. These observations agree well with the observations made by Jébrak (1997), which link the stage of ore formation in hydrothermal breccia to the "wear" stage, which is the stage immediately following the initial formation of the breccia.

The conclusions of this contribution can only be applied to hydrothermal ore deposits, in which the metals and other trace elements are dominantly controlled by host rock alteration (in the fracture root zone). As a consequence, these conclusions can only be applied to magmatic systems if the amount of dissolved trace elements derived from water–rock interaction relative to those of magmatic origin can be quantitatively determined.

Acknowledgements

We would like to thank Richard Tosdal, Kåre Kullerud and an anonymous reviewer for their constructive comments, that helped to improve the manuscript significantly and S. Kaulfuß for sample preparation. This study was supported by the German Research Foundation (DFG), grant 2135/20-1.

References

Ahmed, A.H., Arai, S., Ikenne, M., 2009. Mineralogy and paragenesis of the Co–Ni arsenide ores of Bou Azzer, Anti-Atlas, Morocco. Econ. Geol. 104 (2), 249–266.
Aquilina, L., Pauwels, H., Genter, A., Fouillac, C., 1997. Water–rock interaction processes in the Triassic sandstone and the granitic basement of the Rhinegraben: geochemical investigation of a geothermal reservoir. Geochim. Cosmochim. Acta 61, 4281–4295.
Baatartsogt, B., Schwinn, G., Wagner, T., Taubald, H., Beitter, T., Markl, G., 2007. Contrasting paleofluid systems in the continental basement: a fluid inclusion and stable isotope study of hydrothermal vein mineralization, Schwarzwald district, Germany. Geofluids 7 (2), 123–147.
Behr, H.J., Gerler, J., 1987. Inclusions of sedimentary brines in post-Variscan mineralizations in the Federal Republic of Germany—a study by neutron activation analysis. Chem. Geol. 61 (1), 65–77.
Behr, H.J., Horn, E.E., Frentzel-Beyme, K., Reutel, C., 1987. Fluid inclusion characteristics of the Variscan and post-Variscan mineralizing fluids in the federal republic Of Germany. Chem. Geol. 61 (1), 273–285.
Boiron, M.C., Cathelineau, M., Richard, A., 2010. Fluid flows and metal deposition near basement/cover unconformity: lessons and analogies from Pb–Zn–F–Ba systems for the understanding of Proterozoic U deposits. Geofluids 10 (1–2), 270–292.
Bons, P.D., Fußwinkel, T., Gomez-Rivas, E., Markl, G., Wagner, T., Walter, B., 2014. Fluid mixing from below in unconformity-related hydrothermal ore deposits. Geology 42 (12), 1035–1038.
Brockamp, O.C., 2005. A km-scale illite alteration zone in sedimentary wall rocks adjacent to a hydrothermal fluorite vein deposite. Clay Miner. 40, 245–260.
Bucher, K., Stober, I., 2010. Fluids in the upper continental crust. Geofluids 10 (1–2), 241–253.
Burisch, M., Marks, M., Nowak, M., Markl, G., 2015. The Effect of Temperature and Cataclastic Deformation on Salinity, Halogen Systematics and Metal Transport Capacities of Continental Basement Brines — An Experimental Approach: SGA Abstract in: Proceedings of the 13th Biennial SGA Meeting, Nancy, France. vol. 5 (2134 p).
Eisbacher, G.H., Lüschen, E., Wickert, F., 1989. Crustal-scale thrusting and extension in the Hercynian Schwarzwald and Vosges, Central Europe. Tectonics 8 (1), 1–21.
Everett, C., Wilkinson, J., Rye, D., 1999. Fracture-controlled fluid flow in the lower Palaeozoic basement rocks of Ireland: implications for the genesis of Irish-type Zn–Pb deposits: Geological Society, London. Spec. Publ. 155 (1), 247–276.
Fußwinkel, T., Wagner, T., Wälle, M., Wenzel, T., Heinrich, C., Markl, G., 2013. Fluid mixing forms basement-hosted Pb–Zn deposits: insight from metal and halogen geochemistry of individual fluid inclusions. Geology 41, 679–682.
Gasquet, D., Levresse, G., Cheilletz, A., Azizi-Samir, M.R., Mouttaqi, A., 2005. Contribution to a geodynamic reconstruction of the Anti-Atlas (Morocco) during Pan-African times with the emphasis on inversion tectonics and metallogenic activity at the Precambrian–Cambrian transition. Precambrian Res. 140 (3), 157–182.
Geyer, O.F., Gwinner, M.P., 2011. Geologie von Baden–Württemberg. — 5. Auflage, Stuttgart, Schweizerbart'sche Verlagsbuchhandlung (Nägele u. Obermiller) (627 p.).
Gleeson, S., Yardley, B., 2002. Extensional veins and Pb–Zn mineralisation in basement rocks: the role of penetration of formation brines. Water–Rock Interaction. Springer, pp. 189–205.
Gleeson, S.A., Wilkinson, J.A., Stewart, F.M., Banks, D.A., 2001. The origin and evolution of base metal mineralising brines and hydrothermal fluids, south Cornwall. UK: Geochim. Cosmochim. Acta 65, 2067–2079.

Göb, S., Loges, A., Nolde, N., Bau, M., Jacob, D.E., Markl, G., 2013. Major and trace element compositions (including REE) of mineral, thermal, mine and surface waters in SW Germany and implications for water–rock interaction. Appl. Geochem. 33, 127–152.
Guillong, M., Meier, D., Allan, M., Heinrich, C., Yardley, B., 2008. SILLS: a MATLAB-based program for the reduction of laser ablation ICP-MS data of homogeneous materials and inclusions. Mineralogical Association of Canada Short Course vol. 40, pp. 328–333.
Heinrich, C.A., Pettke, T., Halter, W.E., Aigner-Torres, M., Audétat, A., Günther, D., Hattendorf, B., Bleiner, D., Guillong, M., Horn, I., 2003. Quantitative multi-element analysis of minerals, fluid and melt inclusions by laser-ablation inductively-coupled-plasma mass-spectrometry. Geochim. Cosmochim. Acta 67, 3473–3496.
Jébrak, M., 1997. Hydrothermal breccias in vein-type ore deposits: a review of mechanisms, morphology and size distribution. Ore Geol. Rev. 12 (3), 111–134.
Kendrick, M.A., Honda, M., Gillen, D., Baker, T., Phillips, D., 2008. New constraints on regional brecciation in the Wernecke Mountains, Canada, from He, Ne, Ar, Kr, Xe, Cl, Br and I in fluid inclusions. Chem. Geol. 255 (1–2), 33–46.
Klemm, W., 1994. Review of data on the composition of hydrothermal solutions during the Variscan and post-Variscan mineralizations in the Erzgebirge. Germany. Monogr. Series on Mineral Deposits 31, pp. 61–69.
Leach, D.L., Bradley, D.C., Huston, D., Pisarevsky, S.A., Taylor, R.D., Gardoll, S.J., 2010. Sediment-hosted lead-zinc deposits in Earth history. Econ. Geol. Bull. Soc. Econ. Geol. 105, 593–625. http://dx.doi.org/10.2113/gsecongeo.105.3.593.
Lüders, V., Gerler, J., Hein, U.F., Reutel, C.H.R., 1993. Chemical and thermal development of ore-forming solutions in the Harz Mountains: a summary of fluid inclusion studies. Monogr. Ser. Miner Depos 30, 117–132.
Markl, G., 2015. Schwarzwald: Lagerstätten und Mineralien aus vier Jahrhunderten, 1. Auflage, Bode Verlag.
Metz, R., Richter, M., Schürenberg, H., 1957. Die Blei-Zink-Erzgänge des Schwarzwaldes. Beih. Geol. Jahrb. 29, 1–277.
Mitchell, J.G., Halliday, A.N., 1976. Extent of Triassic–Jurassic hydrothermal ore deposits on the North Atlantic margins. Trans. Inst. Min. Metall. B85, 159–161.
Muchez, P., Heijlen, W., Banks, D., Blundell, D., Boni, M., Grandia, F., 2005. Extensional tectonics and the timing and formation of basin-hosted deposits in Europe. Ore Geol. Rev. 27, 241–267.
Ondrus, P., et al., 2003. Ore-forming processes and mineral parageneses of the Jáchymov ore district. J. Geosci. 48 (3–4), 157–192.
Richard, A., Banks, D.A., Mercadier, J., Boiron, M.C., Cuney, M., Cathelineau, M., 2011. An evaporated seawater origin for the ore-forming brines in unconformity-related uranium deposits (Athabasca Basin, Canada): Cl/Br and δ 37 Cl analysis of fluid inclusions. Geochim. Cosmochim. Acta 75 (10), 2792–2810.
Richardson, C., Cann, J., Richards, H., Cowan, J., 1987. Metal-depleted root zones of the Troodos ore-forming hydrothermal systems, Cyprus. Earth Planet. Sci. Lett. 84 (2), 243–253.
Russell, M.J., Solomon, M., Walshe, J.L., 1981. The genesis of sediment-hosted exhalative zinc + lead deposits. Mineral. Deposita 16, 113–127.
Schwinn, G., Wagner, T., Baatartsogt, B., Markl, G., 2006. Quantification of mixing processes in ore-forming hydrothermal systems by combination of stable isotope and fluid inclusion analyses. Geochim. Cosmochim. Acta 70 (4), 965–982.
Seedorff, E., Barton, M.D., Stavast, W.J., Maher, D.J., 2008. Root zones of porphyry systems: extending the porphyry model to depth. Econ. Geol. 103 (5), 939–956.
Seelig, U., Bucher, K., 2010. Halogens in water from the crystalline basement of the Gotthard rail base tunnel (Central Alps). Geochim. Cosmochim. Acta 74 (9), 2581–2595.
Seo, J.H., Guillong, M., Aerts, M., Zajacz, Z., Heinrich, C.A., 2011. Microanalysis of S, Cl, and Br in fluid inclusions by LA–ICP-MS. Chem. Geol. 284 (1), 35–44.
Sibson, R.H., 1996. Structural permeability of fluid-driven fault-fracture meshes. J. Struct. Geol. 18 (8), 1031–1042.
Staude, S., Bons, P.D., Markl, G., 2009. Hydrothermal vein formation by extension-driven dewatering of the middle crust: an example from SW Germany. Earth Planet. Sci. Lett. 286, 387–395.
Steele-MacInnis, M., Bodnar, R., Naden, J., 2011. Numerical model to determine the composition of H_2O–NaCl–$CaCl_2$ fluid inclusions based on microthermometric and microanalytical data. Geochim. Cosmochim. Acta 75 (1), 21–40.
Stober, I., Bucher, K., 2004. Fluids sinks within the earth's crust. Geofluids 4, 143–151.
Stober, I., Bucher, K., 2007. Hydraulic properties of the crystalline basement. Hydrogeol. J. 15, 213–224.
Sverjensky, D.A., 1981. The origin of a Mississippi Valley-type deposit in the viburnum trend, southeast Missouri. Econ. Geol. 76 (7), 1848–1872.
Walter, B.F., Immenhauser, A., Geske, A., Markl, G., 2015. Exploration of hydrothermal carbonate magnesium isotope signatures as tracers for continental fluid aquifers, Schwarzwald mining district, SW Germany. Chem. Geol.
Walter, B.F., Burisch, M., Markl, G., 2016. The Long-Term Chemical Evolution and Modification of Continental Basement Brines — A Field Study from the Schwarzwald, SW Germany. Geofluids Accepted. http://dx.doi.org/10.1111/gfl.12167.
Walther, H.W., 1982. Zur Bildung von Erz-und Minerallagerstätten in der Trias von Mitteleuropa. Geol. Rundsch. 71 (3), 835–855.
Wilkinson, J., Eyre, S., Boyce, A., 2005. Ore-forming processes in Irish-type carbonate-hosted Zn–Pb deposits: evidence from mineralogy, chemistry, and isotopic composition of sulfides at the Lisheen Mine. Econ. Geol. 100 (1), 63–86.
Wimmenauer, W., Stenger, R., 1989. Acid and intermediate HP metamorphic rocks in the Schwarzwald (Federal Republic of Germany). Tectonophysics 157 (1), 109–116.

GEOFLUIDS

Geofluids (2016) doi: 10.1111/gfl.12167

REVIEW

Long-term chemical evolution and modification of continental basement brines – a field study from the Schwarzwald, SW Germany

B. F. WALTER, M. BURISCH AND G. MARKL

Department of Geosciences, Eberhard Karls University Tübingen, Tübingen, Germany

ABSTRACT

Highly saline, deep-seated basement brines are of major importance for ore-forming processes, but their genesis is controversial. Based on studies of fluid inclusions from hydrothermal veins of various ages, we reconstruct the temporal evolution of continental basement fluids from the Variscan Schwarzwald (Germany). During the Carboniferous (vein type i), quartz–tourmaline veins precipitated from low-salinity (<4.5wt% NaCl + $CaCl_2$), high-temperature (≤390°C) H_2O-NaCl-(CO_2-CH_4) fluids with Cl/Br mass ratios = 50–146. In the Permian (vein type ii), cooling of H_2O-NaCl-(KCl-$CaCl_2$) metamorphic fluids (T ≤ 310°C, 2–4.5wt% NaCl + $CaCl_2$, Cl/Br mass ratios = 90) leads to the precipitation of quartz-Sb-Au veins. Around the Triassic–Jurassic boundary (vein type iii), quartz–haematite veins formed from two distinct fluids: a low-salinity fluid (similar to (ii)) and a high-salinity fluid (T = 100–320°C, >20wt% NaCl + $CaCl_2$, Cl/Br mass ratios = 60–110). Both fluids types were present during vein formation but did not mix with each other (because of hydrogeological reasons). Jurassic–Cretaceous veins (vein type iv) record fluid mixing between an older bittern brine (Cl/Br mass ratios ~80) and a younger halite dissolution brine (Cl/Br mass ratios >1000) of similar salinity, resulting in a mixed H_2O-NaCl-$CaCl_2$ brine (50–140°C, 23–26wt% NaCl + $CaCl_2$, Cl/Br mass ratios = 80–520). During post-Cretaceous times (vein type v), the opening of the Upper Rhine Graben and the concomitant juxtaposition of various aquifers, which enabled mixing of high- and low-salinity fluids and resulted in vein formation (multicomponent fluid H_2O-NaCl-$CaCl_2$-(SO_4-HCO_3), 70–190°C, 5–25wt% NaCl-$CaCl_2$ and Cl/Br mass ratios = 2–140). The first occurrence of highly saline brines is recorded in veins that formed shortly after deposition of halite in the Muschelkalk Ocean above the basement, suggesting an external source of the brine's salinity. Hence, today's brines in the European basement probably developed from inherited evaporitic bittern brines. These were afterwards extensively modified by fluid–rock interaction on their migration paths through the crystalline basement and later by mixing with younger meteoric fluids and halite dissolution brines.

Key words: fluid inclusion, fluid mixing, fluid modification, hydrothermal ore, mineralization

Received 17 June 2015; accepted 16 January 2016

Corresponding author: Benjamin F. Walter, Department of Geosciences, Eberhard Karls University Tübingen, Wilhelmstrasse 56, 72074 Tübingen, Germany. Email: benjamin.walter@uni-tuebingen.de. Tel: +49 7071 29 73155. Fax: +49 7071 29 3060.

Geofluids (2016)

INTRODUCTION

During the last decades, highly saline, rock-buffered basement brines with >20wt% salinity have been recognized as a common phenomenon worldwide, mainly based on data from deep drilling projects which recovered fluid samples from up to 12 km depth (Frape & Fritz 1987; Pauwels *et al.* 1993; Stober & Bucher 2004; Möller *et al.* 2005; Shouakar-Stash *et al.* 2007). The recognition of these brines stored in basement rocks changed the ideas about fluid flow, water–rock interaction and hydrothermal mineralization in the upper brittle continental crust. Many of these brines are of basinal origin and discharge into the basement (Bons *et al.* 2014 and references therein). Understanding the brines' chemical and physical properties

is of scientific and economic interest (e.g. Yardley 2005; Agemar *et al.* 2013).

During formation of epithermal, unconformity-related, hydrothermal ore deposits (Pb, Zn, Cu, Ni, Ag), most authors see deep-seated brines as the provenance of metals. Tectonic processes (e.g. Banks *et al.* 2000; Gleeson *et al.* 2001; Boiron *et al.* 2002; Staude *et al.* 2009) mobilize these brines and form ore deposits due to a change in physiochemical parameters caused by mixing, with other fluids derived from different aquifers (e.g. sedimentary cover) (Fußwinkel *et al.* 2013; Bons *et al.* 2014), cooling (e.g. Wagner & Cook 2000 and references therein) or boiling (e.g. Banks *et al.* 1991 and references therein). Today, there is general consensus about the important influence of highly saline basement brines for ore formation in epithermal, unconformity-related, hydrothermal ore deposits, but the source, formation, mobilization and chemical modification of such fluids are still under debate (e.g. Fritz & Frape 1982; Stober & Bucher 2004; Yardley 2005).

Two different models of basement brine evolution have been proposed: according to the first model, low-salinity fluids are modified by fluid–rock interaction accompanied by desiccation processes (Fritz & Frape 1982; Markl & Bucher 1998; Stober & Bucher 2004). During hydrothermal alteration, feldspars and micas are altered to clay minerals. Therefore, the interstitial water is passively enriched in solutes ('internal source'). In contrast, an alternative model proposes that the high salinity of basement brines was derived from external sources, such as evaporites in the sedimentary cover (e.g. Bottomley *et al.* 1994; Gleeson & Yardley 2002; Bejaoui *et al.* 2014 and references therein). According to this model, the precipitation of halite in shallow marine basins produces near-surface residual brines (bittern brine), which are migrating downwards into the basement ('external source') (e.g. Bons *et al.* 2014 and references therein). This model is supported by mass-balance calculations, which imply that fluid–rock reactions and fluid inclusion leakage alone cannot explain the high salinity in many locations (Savoye *et al.* 1998). Also, experiments by Burisch *et al.* (2015) indicate that fluid–rock interaction alone is not sufficient to produce brines with up to 28wt% with low Cl/Br ratios. For such highly saline fluids with low Cl/Br ratios, an external fluid source seems to be required. Regardless of their source, brines resident in crystalline basement rocks, which we refer to as 'basement brines', represent fluids that have evolved significantly altered by water–rock interaction with their host rocks.

Understanding low-grade metamorphic or hydrothermal processes in the upper brittle crust critically depends on determining the chemical evolution of such basement brines. In this study, we try to reconstruct the chemical history of a basement brine over geologic timescales. This attempt is based on detailed fluid inclusion investigations in minerals from hydrothermal vein-type deposits of different ages in a well-defined area, combined with crush-leach analyses and published analyses of waters from deep drillings. We investigated carefully chosen and well-characterized samples of hydrothermal veins from the Schwarzwald mining district in SW Germany (Staude *et al.* 2009 and references therein). The more or less continuous hydrothermal mineralization over the past 320 million years (Pfaff *et al.* 2009 and references therein) permits construction of a detailed fluid history which can be used to evaluate the controls on basement brine origins and evolution.

GEOTECTONIC SETTING AND MAIN CHARACTERISTICS OF SCHWARZWALD MINERALIZATION

Geotectonic setting

The Schwarzwald comprises exhumed Variscan basement gneisses and granites overlain by Lower Permian to Upper Jurassic sedimentary units (Fig. 1). The paragneiss units are deformed and metamorphosed to dominantly to upper amphibolite grade during Variscan (Carboniferous) collisional processes (Geyer & Gwinner 2011 and references therein). Postcollisional S-type granites, which today form about 50% of the exposed Schwarzwald basement, intruded into the gneisses at 335–315 Ma (Hann *et al.* 2003; Geyer & Gwinner 2011 and references therein). After erosion, during Rotliegend (Permian) times, small sediment traps were filled by proximal red beds (arkoses, conglomerates) (Geyer & Gwinner 2011). During the Lower Triassic, quartzitic Buntsandstein units were deposited, followed by Middle Triassic Muschelkalk limestones, shales and evaporites (gypsum and/or halite). Late Triassic (Keuper) sediments are dominated by clastic sediments and evaporitic units (mainly gypsum) (Geyer & Gwinner 2011). Clastic sediments and carbonates were deposited on the shallow continental Tethys shelf during Jurassic times, but no sediments formed during the Cretaceous.

The initial break-up of the Upper Rhine Graben during the Paleogene resulted in the deposition of clastic, chemical and evaporitic sediments in the rift valley (Geyer & Gwinner 2011). Simultaneous with rifting, the uplift of the rift shoulders resulted in extensive erosion of the sedimentary overburden formed the erosional window of the basement rocks exposed today.

Hydrothermal vein-type mineralization in the Schwarzwald

Hydrothermal veins formed more or less continuously in basement rocks and their sedimentary cover in SW Ger-

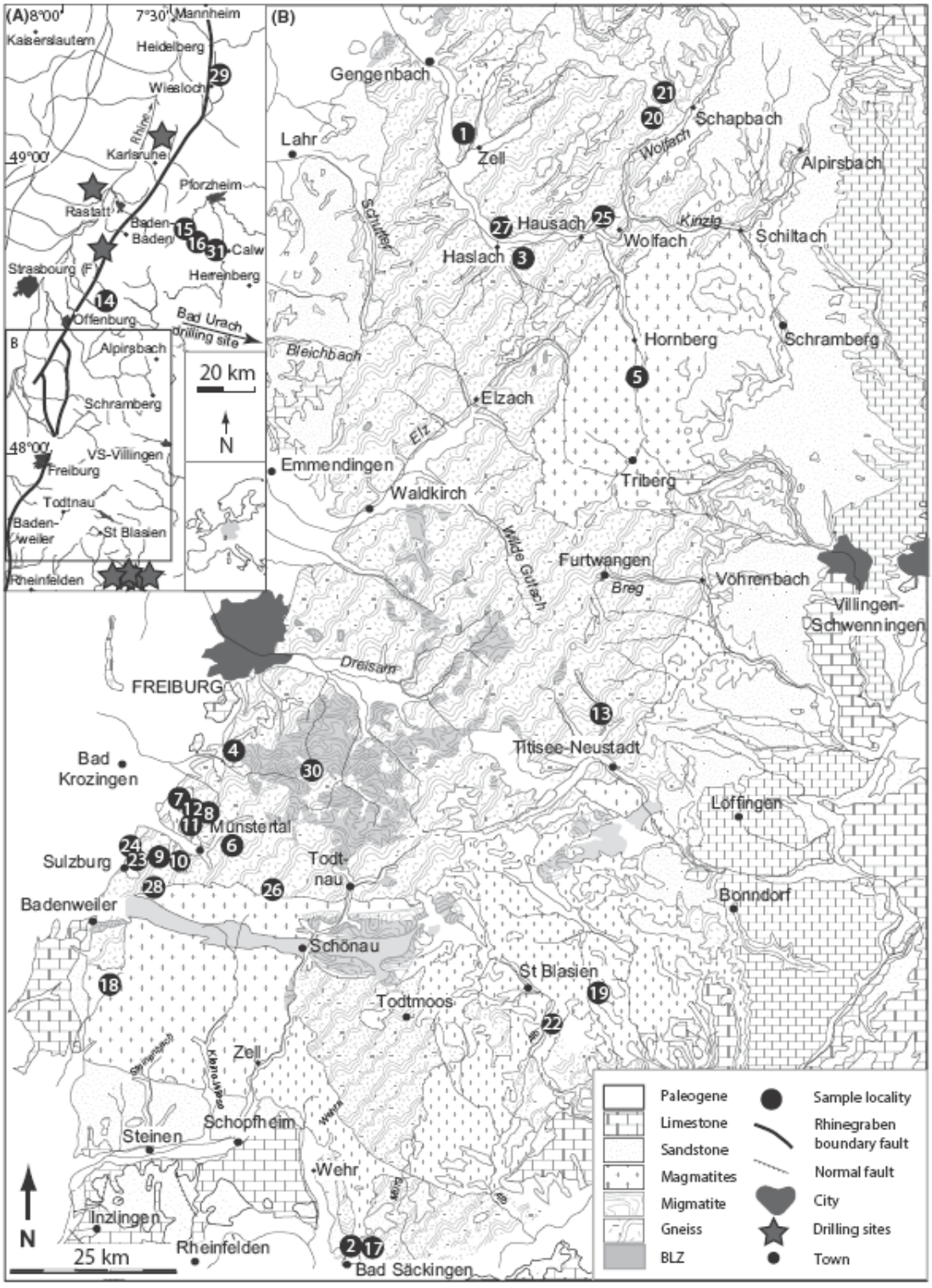

Fig. 1. Geological overview of the Schwarzwald mining district in SW Germany with sample locations. (A) Overview map. (B) Close-up of the Schwarzwald mining district modified after Pfaff *et al.* (2011). Sample localities 1–31 (for more information refer to Table S1 in the electronic supplement).

many from about 320 Ma until the present day (Pfaff *et al.* 2009 and references therein; Staude *et al.* 2009; Loges *et al.* 2012). An extensive data set on many different aspects of fluid flow and hydrothermal vein formation exists. This data set includes studies on microthermometry (e.g. Behr & Gerler 1987, Behr *et al.* 1987, Staude *et al.* 2009, 2012a; Fußwinkel *et al.* 2013; Walter *et al.* 2015), trace element distribution in fahlore and sphalerite (Staude *et al.* 2010; Pfaff *et al.* 2011), stable and radiogenic isotopes of O, C, H, S, Sr, Pb, Cu, Fe, Mg (Staude *et al.* 2011, 2012b; Walter *et al.* 2015 and references therein), REE distribution in fluorites (Schwinn & Markl 2005), palaeo-fluid models (Pfaff *et al.* 2010; Staude *et al.* 2011; Fußwinkel *et al.* 2013; Bons *et al.* 2014; Walter *et al.* 2015), geochemistry of modern thermal and mineral waters (Stober & Bucher 1999; Loges *et al.* 2012; Göb *et al.* 2013), leaching experiments on basement and cover rocks (Bucher & Stober 2002; Burisch *et al.* 2015), modern fluid flow models and hydraulic aquifer properties (Stober & Bucher 2005; Bucher & Stober 2010) and the regional geology (Geyer & Gwinner 2011 and references therein). This information is an important prerequisite for the challenging task of deciphering the chemical evolution of a basement fluid.

Following the work of Behr & Gerler (1987); Behr *et al.* (1987); Staude *et al.* (2009); Pfaff *et al.* (2009, 2010); and Walter *et al.* (2015), the hydrothermal veins are subdivided into five formation stages based on structural, mineralogical and microthermometrical arguments (Table 1): (i) Carboniferous, (ii) Permian, (iii) Triassic–Jurassic boundary, (iv) Jurassic–Cretaceous and (v) post-Cretaceous. The general age constraints, chemical and physical characteristics of the different veins and mineralizing fluids are summarized in Table 1.

The Carboniferous veins (i) are quartz–tourmaline veins with trace wolframite, scheelite and cassiterite (Marks *et al.* 2013). These veins occur in close proximity to granitic intrusions and are therefore most likely related to Variscan magmatic activity (Leutwein & Sonet 1974; Marks *et al.* 2013). Oxygen isotope pairs of tourmaline and quartz in those veins indicate temperatures of up to 550°C. Fluid chemistry and temperatures indicate a distinct magmatic fluid component (Marks *et al.* 2013).

The Permian group (ii) comprises mainly very low-grade Sb±Ag±Au-bearing quartz veins. Their precipitation is interpreted to have resulted from cooling of a low-salinity, high-temperature late Variscan metamorphic basement fluid (Staude *et al.* 2009 and references therein; Wagner & Cook 2000).

Veins from the Triassic–Jurassic boundary (iii) are quartz–chalcedony–haematite veins with only minor amounts of barite (Brander 2000). With the exception of rarely occurring pyrite, they contain no ores. The 'Permian veins' of Staude *et al.* (2009) comprise our types (ii) and (iii).

The majority of the hydrothermal veins of the Schwarzwald belong to the Jurassic–Cretaceous group (iv) which comprises variable modal amounts of fluorite, barite, quartz and carbonates with large amounts of either Ag-Bi-Co-Ni-U, Fe-Mn or Pb-Zn-Cu ores (e.g. Mertz *et al.* 1986; Wernicke & Lippolt 1993, 1997; Meyer *et al.* 2000; Werner *et al.* 2002; Pfaff *et al.* 2009; Staude *et al.* 2009, 2011, 2012a,b; Werner 2011; Walter *et al.* 2015). In contrast to the earlier veins, their formation involved a deep-seated highly saline brine (20–28wt% salinity), which was mobilized and mixed with colder formation waters in extensional basin-related fault systems (Staude *et al.* 2009, 2010, 2011, 2012b; ; Fußwinkel *et al.* 2013; Walter *et al.* 2015). In this vein type, no indications of significant fluid cooling and boiling processes were found. This hydrothermal activity was probably related to the opening of the North Atlantic (e.g. Wetzel *et al.* 2003; Pfaff *et al.* 2009; Staude *et al.* 2009).

During Paleogene rifting, Upper Rhine Graben-parallel NE-SW to NNE-SSW-striking fault systems were generated or reactivated. Group (v) mineralization formed in these fault zones (Pfaff *et al.* 2009 and references therein; Staude *et al.* 2012b and references therein) and includes barite, quartz fluorite and/or various carbonates, which precipitated together with Pb and less commonly, As, Zn, Cu, Bi and Ni ores (Staude *et al.* 2009). The variability in mineralogy and fluid chemistry (salinity 1–23wt% NaCl + $CaCl_2$) of these post-Cretaceous veins is interpreted as a consequence of multicomponent, multi-aquifer fluid mixing processes caused by a juxtaposition of different aquifers during opening of the Upper Rhine Graben rift (Walter *et al.* 2015).

Sample material

Samples of fluorite, barite, quartz and carbonates from various Schwarzwald veins were selected based on the following criteria: (1) every mineralization event (i) to (v) is represented; (2) the age of formation of the sampled vein is known based on radiogenic isotope dating or a combination of structural, mineralogical and fluid inclusion criteria; (3) the veins contain sufficient amounts of gangue minerals in up to centimetre-sized crystals, which show growth zonation. This is important because the fluid inclusions on the growth zones (former crystal surfaces) can be directly related to the fluids present during vein formation; (4) sample locations are distributed over the whole mining district to include mineralization from various depths. The sample numbers are reported in Table S2 in the supplement.

The samples from (i) Carboniferous veins consist of massive, fluid inclusion-rich, milky quartz with brownish tourmaline crystals up to 5 cm (Fig. 2A). The samples from (ii) Permian mineralization show massive, fine-grained grey quartz (coloured by tiny Sb-bearing sulphides) alternating with milky, coarser grained quartz, subhedral to euhedral

Table 1 Types of veins and fluid signatures of the Schwarzwald ore district.

Group	Age	Mineralogy	Mineralization	Structural position	Age constraints	Fluid type	Salinity in wt % ($NaCl + CaCl_2$)	T_h in °C	Na/K mass ratio	Cl/Br mass ratio
i	Carboniferous	Quartz-tourmaline[1]	W-Sn	Spatially associated and genetically related to specific granites	U-Pb age of host granite[2]	H_2O-NaCl±(CO_2±CH_4)†	–*; 0–4†	–*; 130–390°C†	–*; 3.2–5.6†	–*; 48–146†
ii	Permian	Quartz	Sb±Ag±Au	Only in basement rocks (granite and gneiss)	High fluid temperatures >250°C never reached again after Permian times by the SW German basement at shallow depths; comparison with very similar veins from the Taunus[3]	H_2O-NaCl-KCl*,†	<5*; 2–4.5†	150–300°C*; 99–280°C†	–*; 4.2†	–*; 94†
iii	Triassic-Jurassic	Quartz-haematite	Fe	Only in basement rocks (granite and gneiss)	(U-Th)/He age[4]	H_2O-NaCl-KCl† & H_2O-NaCl-$CaCl_2$†	–*; 0.7–3.3 & 23.3–25.8†	–*; 121–224°C†	–*; 0.3–5.5†	–*; 60–112†
iv	Jurassic-Cretaceous	Fluorite-quartz-barite barite–quartz	Pb-Zn-Cu-Ag & U-Bi-Co-Ni-Ag & Fe-Mn	From >2000 m below the basement/cover unconformity up to the boundary between Lower and Middle Triassic sediments[5]	Rb-Sr and U-Pb age-dating[6]	H_2O-NaCl-$CaCl_2$*,†[5,6,7,8]	20–28*[5,6,7,8] 23–26†	50–180°C*[5,6,7,8] 50–143°C†	–*; 0.8–10.4†	49–824*[8]; 62–522†
v	Post-Cretaceous	Quartz-barite-fluorite	Pb-Zn-Cu-Ag & Cu-Ni-Bi-Ag	Spatially closely associated with Upper Rhine Graben faults or tributary fault systems	Structural position on Rhine Graben-related faults[6]	H_2O-NaCl-$CaCl_2$± (SO_4±CO_2±HCO_3)*,†[5,6,7,9,10]	0–25*[5,7,9]; 5–25†	50–150°C*[5,6,7, 9]; 66–194°C†	–*; 1.7–8.7†	–*; 2–144†

*Literature data. †This study. References: 1 Marks *et al.* (2013); and references therein; 2 Leutwein & Sonet (1974); 3 Wagner & Cook (2000); 4 Brander (2000); 5 Staude *et al.* (2009); 6 Pfaff *et al.* (2009); and references therein; 7 Walter *et al.* (2015); 8 Fußwinkel *et al.* (2013); 9 Pfaff *et al.* (2010); 10 Pfaff *et al.* (2011).

crystallized in vugs (Fig. 2B). The mineralization of group (iii) are quartz–haematite veins with alternating red, yellow or grey chalcedony and transparent, euhedral quartz generations (Fig. 2C). Breccias are common. Every mineralization sequence starts with a ferriferous chalcedony, which is overgrown by milky and coarse-grained, sometimes euhedral quartz. The younger quartz generations differ in grain size, colour and brecciation style. The youngest quartz generation (Fig. 2C) forms always clear, very coarse-grained, euhedral crystals with many sealed cracks. Late-stage euhedral haematite crystals occur locally in quartz vugs. Group (iv) samples contain coarse-grained quartz, fluorite, barite and in some cases minor amounts of carbonates with Pb-Zn-Cu ores (Fig. 2D). Their mineralogy is highly variable: some veins consist of exclusively fluorite (e.g. BW255 fl) or quartz (e.g. HM24a); others contain complex sequences of all gangue minerals and ores. Post-Cretaceous veins of group (v) show in many cases textures similar to the Jurassic–Cretaceous ones. Again, pure quartz or fluorite veins as well as complex sequences of alternating gangue minerals can be observed. Many group (iv) and (v) veins show huge crystal sizes (up to many dm, commonly zoned) and the pseudomorphic replacement of barite and rarely fluorite by quartz (Fig. 2E).

Analytical procedure

Microthermometry

For the microthermometric study, samples were cut perpendicular to the longitudinal orientation of the respective

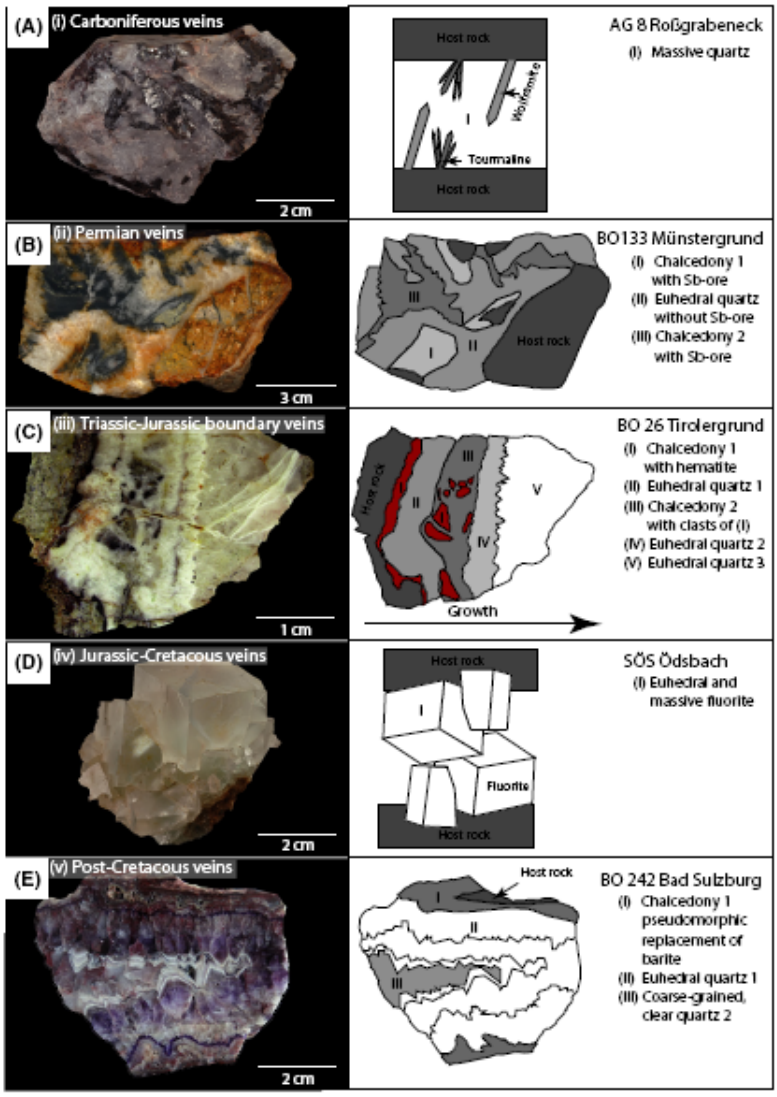

Fig. 2. Photographs and sketches illustrating the various vein types. (A) Carboniferous quartz–tourmaline vein from the Roßgrabeneck near Nordrach; (B) Permian quartz vein with Sb-mineralization from the Münstergrund vein near Staufen; (C) Triassic–Jurassic quartz–haematite vein from the Lattfelsen near Staufen; (D) Jurassic fluorite from the Ödsbach mine near Oberkirch; (E) post-Cretaceous agate–barite vein from the Speichel, Bad Sulzburg.

vein. Each sample was oriented from early precipitates nucleating on the host rock (rim), to late-stage precipitates facing the commonly open vein centre (vug). The samples were prepared as double-polished thick sections (200–400 μm).

Relative chronological sequences of fluid inclusions (fluid inclusion assemblages (FIA) after Goldstein & Reynolds 1994) were then investigated by optical microscopy. Clearly identified primary (p), pseudo-secondary (ps) and secondary (s) inclusions were identified in addition to isolated inclusions (iso) and clusters of inclusions (c) with no relation to former crystal surfaces or fractures. The 'iso' and 'c' type inclusions provide no clear chronological or genetic information. A detailed explanation is given in Fig. 4 of Walter *et al.* (2015).

Microthermometric investigations were performed using a Linkam (model THMS 600) fluid inclusion stage on a Leica DMLP microscope at Tübingen University. For each inclusion, we measured the ice melting temperature ($T_{m,ice}$), the hydrohalite melting temperature ($T_{m,hh}$) and the homogenization temperature (T_h). For calibration, synthetic H_2O, H_2O-NaCl and H_2O-CO_2 standards were used and only results with a maximum variation of the final melting temperatures of less than 0.1°C were accepted for interpretation; for homogenization temperatures, a variation of up to 1°C was accepted due to poor visibility in some samples. Single measurements with strong deviation in salinity and homogenization temperature within a homogeneous trail are neglected as are data of fluid inclusions in which post-entrapment modification cannot strictly be ruled out.

For the calculation of salinity in the ternary NaCl-$CaCl_2$-H_2O system, the Microsoft Excel-based calculation sheet of Steele-MacInnes *et al.* (2011) was used. The degree of fill was estimated optically based on filling degree tables (Shepherd *et al.* 1985). Pressure correction was done using the formula of Bodnar & Vityk (1994) in combination with estimates on basement and sedimentary overburden based on Geyer & Gwinner (2011). All T_h are presented as uncorrected values, because for most of the presented veins hydrostatic conditions can be assumed. As the effect of pressure on the homogenization temperature is highly dependent on the salinity, the correction does not affect the majority of the discussed fluid inclusions. Exceptions are the Carboniferous and the Permian veins, which have lower salinities and are formed under higher pressures. Consequently, the pressure-related effects on T_h are discussed in detail in the discussion chapter. The uncertainties of this approach are discussed in Walter *et al.* (2015).

Crush-leach ion chromatography

After careful microthermometric analysis and characterization of the fluid inclusions, samples with only one fluid signature (identical fluid characteristics in p, s, ps and c inclusions) were carefully hand-picked to remove visible impurities. The samples dominantly show primary inclusions, but secondary inclusions cannot be entirely excluded. Samples were only analysed if primary and secondary inclusions showed identical microthermometric behaviour. Two grams per sample (fluorite, quartz, calcite or barite) was separated, heated in a beaker at 60–70°C for 3 hours in concentrated HNO_3 on a sand bath and then washed with ultrapure water twice a day for 7 days. After 2 hours of drying, they were crushed to fine powder and 11 ml of acidulated ultrapure water (pH ~2) was added to suppress the adsorption of Ca^{2+} and other highly charged cations onto surfaces (Köhler *et al.* 2009).

This solution was injected into a Dionex ICS 1000 ion chromatography system at the University of Tübingen (IonPac AS 9-HC 2 mm column for anions; IonPac CS 12-A column for cations). For anions (F, Cl, Br, NO_3, PO_4 and SO_4), the disposable syringe filter CROMAFILE® Xtra RC-20/25 was used; for cations (Li, Na, K, Mg, Ca, Ba, Sr), the disposable syringe filter CROMAFILE® Xtra PVDF-(20/25) was chosen. Blank runs were performed to check for possible contamination. Reference materials were used to monitor the reproducibility and precision of the measurements. The total error was below 20% relative (1 sigma level). Note that the detected NO_3 is related to the acidification of the samples with HNO_3. Absolute elemental fluid concentrations were calculated by normalizing the Cl concentration derived from crush-leach analysis to the Cl concentration derived from microthermometry.

RESULTS

The results reported in Tables 1, 2 and S1 in the electronic supplement clearly show that the five fluid types distinguished in section Hydrothermal vein-type mineralization in the Schwarzwald have distinct chemical compositions.

Dominantly late magmatic Carboniferous veins of group (i): fluid type (A)

Carboniferous veins contain only one fluid signature (fluid (A)). Type A fluids have homogenization temperatures between 130°C and 389°C. Two maxima at about 250°C and 350°C can be recognized in T_h. Final ice melting temperatures between 0°C and −3.3°C result in a calculated salinity of 0–4wt% ($NaCl_{eq}$) (one outlier at 9wt%). First melting of ice can be recognized at about −11°C. A $CaCl_2$-poor or $CaCl_2$-free system is indicated by hydrohalite melting at the binary H_2O-NaCl eutectic temperature of −21.2°C; the freezing temperature is above the ternary H_2O-NaCl-$CaCl_2$ eutectic temperature of −52°C. In addition, CO_2 can be optically recognized by a double bubble. Further volatile phases detected by Micro-Raman

Table 2 overview of microthermometric results ordered according to fluid petrography (p, s and ps).

Vein type	Fluid type	T first melt in °C	Tm ice in °C	Tm hydrohalite in °C	Salinity (wt % NaCl + $CaCl_2$)	Th °C	Ca/(Na + Ca) in mole
I Carboniferous	A	P ~−21°C	P 0 to −3.3°C	P −21.2°C	P 0 to 5.5	P 148 to 343	P no Ca
		S ~−21°C	S 0 to −3.3°C	S −21.2°C	S 0 to 5.5	S 113 to 389	S no Ca
		Ps not observed	Ps not observed	Ps −21.2°C	Ps not observed	Ps not observed	Ps no Ca
II Permian	B	P ~−21°C	P −0.5 to −3.2	P −21.2°C	P 0.8 to 5.4	P 99 to 264	P no Ca
		S ~−21°C	S −0.2 to −5.1	S −21.2°C	S 0 to 8.2	S 127 to 313	S no Ca
		Ps not observed	Ps not observed	Ps −21.2°C	Ps not observed	Ps not observed	Ps no Ca
III Triassic–Jurassic	B & C	P ~−21°C & ~−50°C	P −0.4 to −24.7	P −21.2 to −25.9	P 0.6 to 25.2	P 98 to 320	P no Ca
		S ~−21°C & ~−50°C	S −0.4 to −22.8	S −21.2 to −25.0	S 0.9 to 23.9	S 125 to 216	S no Ca
		Ps ~−21°C & ~−50°C	Ps −0.4 to −25.0	Ps −21.2 to −25.9	Ps 0.4 to 25.4	Ps 111 to 190	Ps no Ca
IV Jurassic–Cretaceous	CD	P ~−50°C	P −21.2 to −28.5	P −10.4 −26.4	P 22.7 to 27.1	P 50 to 156	P 0.2 to 0.4
		S ~−50°C	S −19.2 to −28.1	S −10.4 −26.5	S 21.2 to 27.1	S 77 to 129	S 0.2 to 0.4
		Ps ~−50°C	Ps −21.8 to −25.2	Ps −19.0 to −24.1	Ps 22.9 to 26.8	ps 115 to 124	Ps 0.2 to 0.4
V post-Cretaceous	CD &	P ~−21°C & ~−50°C	P −2.5 to −25	P −21. to −26.6	P 4.5 to 25.2	P 67 to 1805 110	P no Ca to 0.4
	DE	S ~−21°C & ~−50°C	S −0.7 to −26.3	S −21.2 to −26.4	S 1.0 to 25.1	to 165	S no Ca to 0.4
		Ps ~−21°C & ~−50°C	Ps −23.5 to −25.0	Ps −21.2 to −25.0	Ps 23.7 to 24.5	Ps 71 to 131	Ps no Ca to 0.4

are CH_4 and N_2. The degree of fill depends on the volatile content: The liquid-rich volatile-poor inclusions show a degree of fill above 0.8. The volatile-rich inclusions have ratios of 0.5–0.8. Hence, in Carboniferous veins an H_2O-NaCl-CO_2-CH_4 fluid was present. Br was only detected in five samples which resulted in a Cl/Br mass ratio of 48 and 146. Na/K mass ratios are 3.2–5.6.

Permian quartz veins of group (ii): fluid type (B)

Permian quartz veins contain inclusions of a distinct fluid type (B). The fluid inclusions of type B freeze in the range −30 to −45°C. First melting can be observed above −20°C which implies a binary NaCl-H_2O or NaCl-KCl-H_2O system. Ice is the last melting phase in the range of −0.3 to −5.1°C, which results in a calculated salinity of 2–4.5wt% $NaCl_{eq}$. Homogenization temperatures range from 99 to 310°C. Within FIA, the salinity and T_h are constant, but these parameters can vary between different trails. The filling degree ranges from 0.8 to 0.95. The crush-leach analyses confirm a NaCl-H_2O fluid with Cl/Br mass ratios of 94 and Na/K mass ratios of 4.2.

Triassic–Jurassic veins of group (iii): alternating type B and C type fluids

Veins of group (iii) contain primary fluid inclusions of type B and a different fluid type (type C), which alternate between different quartz layers in some samples (Fig. 3A). Fluid inclusions containing fluid type C freeze between −70 and −100°C. Homogenization temperatures vary between 121 and 224°C (Fig. 3E). Within each fluid inclusion assemblage, the temperature variation is small. The first melt can be observed around −50°C. Final melting temperatures of ice show variations between −20.2°C and −24.7°C. Final dissolution temperatures of hydrohalite range from −19.7°C to −25.9°C, showing filling degrees between 0.9 and 0.95. Calculated salinities vary between 23.3 and 25.8wt% (NaCl + $CaCl_2$) assuming a NaCl-$CaCl_2$-H_2O system.

Petrographic observations (Fig. 3A) (alternating low- and high-salinity fluid signatures) indicate that, while both fluids were present at the time of sample formation, there is no evidence of mixing to form fluids intermediate in composition between types B and C. Instead, fluid inclusions of this age contain either B or C in alternating layers within a sample. Because crush-leach analyses of these samples cannot resolve the microscopic interlayering of FIA containing type B and type C fluids, they represent mixtures of both fluid types. The two mixed analyses show Na/K mass ratios of 0.3 and 5.5 with Cl/Br mass ratios of 60 and 112 (Fig. 3F). Thus, their element budget is dominated by the high-salinity, high total dissolved solids (TDS) fluids of type C.

Jurassic–Cretaceous veins of group (iv): mixed fluid type CD

This vein type shows exclusively high-salinity fluids (Fig. 3B,D–F). The inclusions freeze between −70 to −100°C. First melting can be detected above −50°C implying a ternary NaCl-$CaCl_2$-H_2O system with a eutectic temperature at −52.0°C. Ice and hydrohalite are last melting phases. The final melting temperature of ice is in the range of −19.1° to −27.1°C, of hydrohalite between −10.4° to −26.4°C, which records a salinity of 23–26wt% (NaCl + $CaCl_2$). Homogenization temperatures vary from 50 to 143°C. Within single trail, salinity and T_h are almost constant, but they vary between different trails within one sample. The degree of fill is constant at 0.95.

Crush-leach analyses confirm a NaCl-$CaCl_2$-H_2O fluid. Important element mass ratios for later discussions, regarding, for example, fluid mixing and fluid source, are Na/K between 0.8 and 10.4 and Cl/Br mass ratios between 62 and 522. The high Cl/Br mass ratios in this vein type are notable. Most inclusions of fluid type CD are similar in salinity and temperature to type C but vary in Cl/Br mass ratios and show a stronger scatter in salinity, which requires the definition of a mixed fluid type CD, including an additional, high Cl/Br mass ratio reservoir D (Fig. 3F).

Post-Cretaceous veins of group (v): fluid type CD and DE

Micro-Raman analysis shows that H_2O is the dominant Raman-active species in the fluid in all trails. In some samples, sulphate can be detected. Based on charge balance calculations, it seems very likely that HCO_3 appears to be present. Individual FIA may show freezing temperatures between −70 to −100°C and/or −30 to −45°C, respectively. Inclusions with low freezing points have eutectic temperatures of −52°C, the others of −21.2°C corresponding to a NaCl-$CaCl_2$-H_2O and a NaCl-H_2O fluid, respectively. All measurements from individual FIA form a cloud rather than a point in the NaCl-$CaCl_2$-H_2O ternary phase diagram of Steele-MacInnes *et al.* (2011), a feature that testifies to Ca/Na variations of single inclusions in individual FIA.

The last species to dissolve is invariably ice. The final melting temperature of ice is in the range of 0 to −27.0°C and for hydrohalite between −21.2 and −26.4°C, which implies a salinity of 5–25wt% (NaCl + $CaCl_2$). Homogenization temperatures are in the range from 66 to 194°C. Within single trails, the salinity and T_h are constant, but they may vary between different trails.

Crush-leach analyses and laser Raman spectroscopy confirm the NaCl-($CaCl_2$)-H_2O fluid with different amounts of SO_4 and HCO_3. Na/K mass ratios vary between 1.7 and 8.7 and Cl/Br mass ratios between 2 and 144. Veins of group (v) contain fluids with a large variation in salinity (Fig. 3E), involving both the CD fluid signature and a mixture of fluid end-member D with a low TDS end-member E.

DISCUSSION

Fluid types in the context of geological setting and time

In the following, the temporal chemical evolution of deep-seated basement brines is placed in a well-defined geological context and the processes that govern this development are discussed. Hydrothermal veins are well suited to this because they contain zoned minerals with large primary inclusions. In contrast, fluid inclusions in basement host rocks (granites and gneisses), which could also record changes in fluid chemistry, cannot be reliably related to a specific event in time.

Reservoir A, fluid type A – from veins of group (i): late magmatic fluids are expelled to the middle and upper crust

The oldest fluids detected in the Schwarzwald basement are those of fluid type A. These fluids with a significant magmatic component (granite age 322 ± 20 Ma; Leutwein & Sonet 1974) are high-temperature, low-salinity NaCl-H_2O or H_2O-CO_2-CH_4 fluids with Na/K mass ratios of 3.2–5.6 and Cl/Br mass ratios around 100. The low Cl/Br ratio in this low-salinity fluid type is most likely of magmatic origin (Irwin & Roedder 1995) or could be derived from water–rock interaction with the surrounding gneisses (Burisch *et al.* 2015). The large range in homogenization temperatures indicates continuous fluid cooling, as the fluid chemistry remains constant with decreasing T_h. Evidence for a change in other parameters is lacking. These 'Variscan fluids' have also been reported by Behr & Gerler (1987) and Behr *et al.* (1987). Veins of group (i) can be exclusively observed in the direct vicinity of magmatic intrusions. Highly differentiated granitic melts like the Variscan intrusions in the Schwarzwald or the Erzgebirge typically crystallize at shallow depths (Romer *et al.* 2012). As a consequence, we assume a crystallization depth of 1–3 km. The vein geometry can be described as pockets rather than discrete veins. Taking this into account, lithostatic conditions during vein formation can be assumed. Pressure corrections for a lithostatic pressure of 1 kbar (around 3 km depth) increase the uncorrected temperatures in average by 90°C. This indicates a fluid close to thermal equilibrium with two feldspars (Giggenbach 1988), that is with the basement rocks (Fig. 4). As about 50% of the present outcrops in the Schwarzwald consist of granites, we assume that fluid type A (Fig. 5A) was the typical fluid in the middle and upper crust during late Variscan, Carboniferous times.

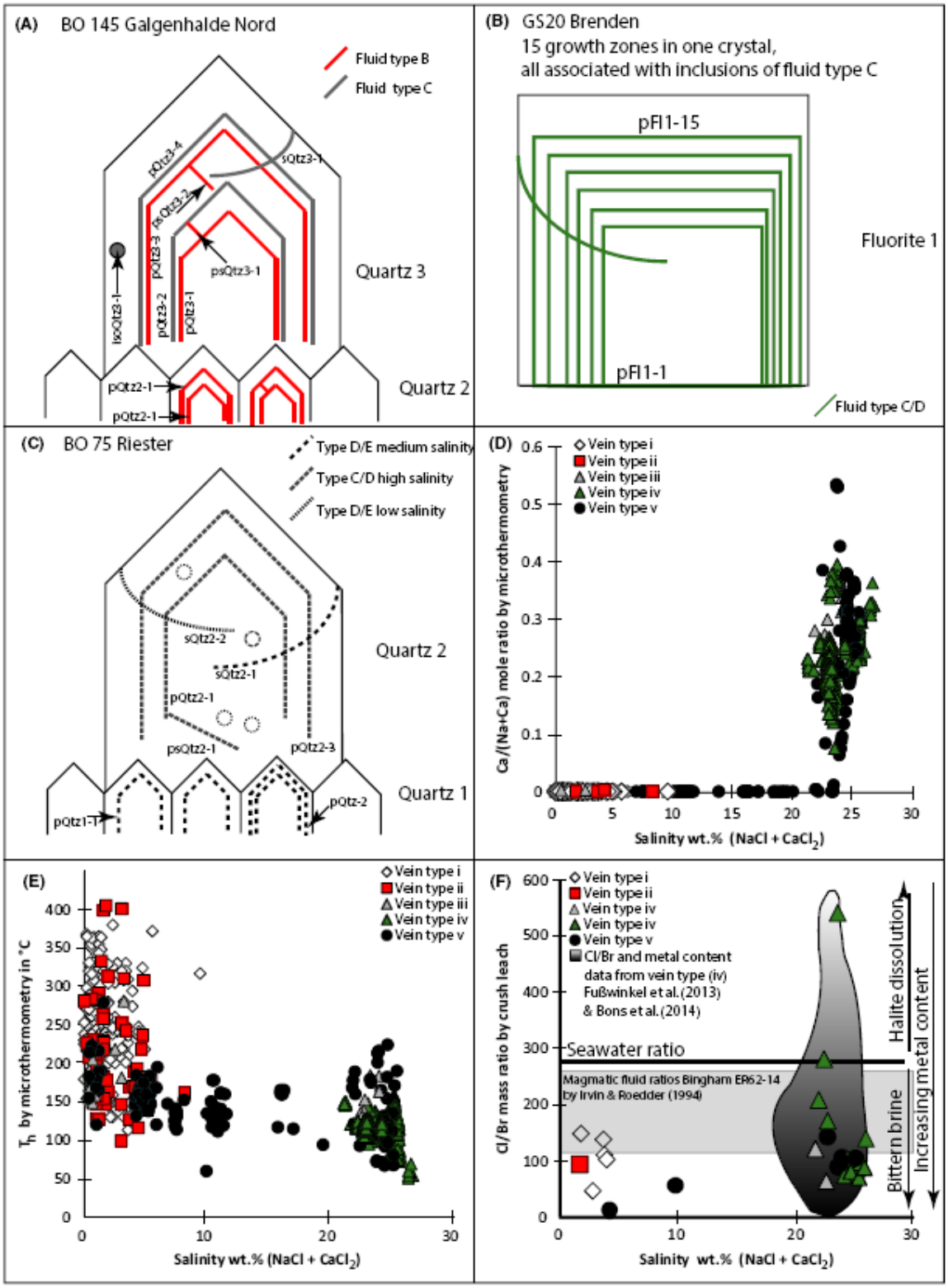

Fig. 3. Schematic presentation of the petrological results of fluid inclusion assemblages. (A) Sample BO145 from the Triassic–Jurassic Galgenhalde Nord vein. Note alternating high- and low-salinity fluids on growth zones. (B) Sample GS20 from the Jurassic–Cretaceous Brenden vein; only high-salinity fluids are present. (C) Sample BO75 from the post-Cretaceous Riester vein with alternating, high-salinity, moderate and low-salinity fluids. Some assemblages contain sulphate and/or CO_2; (D) Ca/(Na + Ca) molar ratio (from microthermometry) versus salinity; (E) homogenization temperatures (uncorrected) versus salinity; (F) Cl/Br mass ratio versus salinity. High Cl/Br is typically associated with halite dissolution. Cl/Br mass ratios can be internally derived by WRI with basement rocks or externally by a descending bittern brine.

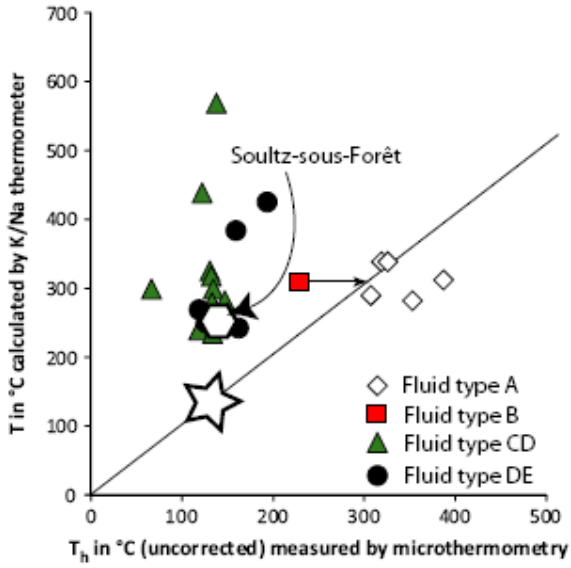

Fig. 4. Temperatures, calculated by the K/Na thermometer of Giggenbach (1988) versus homogenization temperature measured by microthermometry. Fluid samples from the Bad Urach bore-hole (big star), which is situated 80 km, east of the Upper Rhine Graben lies on a 1:1 line. A pressure correction for the type B fluid results in +30°, which shift the uncorrected data point towards the 1:1 line. The Jurassic–Cretaceous and post-Cretaceous veins were not pressure corrected.

Reservoir B, fluid type B – from veins of group (ii): the typical late metamorphic basement fluid, when almost no cover rocks are present

Type B fluids are high-temperature, low-salinity H_2O-NaCl-KCl-($CaCl_2$) or H_2O-KCl-NaCl-($CaCl_2$) fluids (Fig. 5B) with a Na/K mass ratio of 0.7–4.2 (Fig. 4), a Cl/Br mass ratio of 70–90 (Fig. 3F) and high homogenization temperatures up to 280°C (Fig. 3E). Such fluids are typical of late metamorphic fluids in cooling orogenies, for example the Rheinisches Schiefergebirge (Germany), the Western Carpathians (Romania) and the Massif Central (France) (Wagner & Cook 2000; Bellot *et al.* 2003). It should be noted that in the Permian, the sedimentary cover consisted of a maximum of some tens of metres of red beds in the whole area (Geyer & Gwinner 2011). Even the deepest Permian veins (2 km below basement/cover unconformity) do not show higher salinity fluid inclusions. The K/Na thermometer of Giggenbach (1988) for sample ML10 records temperatures up to 320°C in good agreement with the measured, uncorrected fluid inclusion homogenization temperatures up to 280°C. Veins from group (ii) can only be recognized within the crystalline basement situated closely below the Permian surface. Breccia geometry indicates hydraulic fracturing (Jébrak 1997). Therefore, pressures between lithostatic and hydrostatic conditions can be assumed. The possible range includes hydrostatic conditions at 1 km (0.1 kbar) up to lithostatic conditions at 2 km depth (0.6 kbar). Pressure corrections for 0.6 kbar for these low-salinity inclusions increase the measured homogenization temperatures in average by 40°C. Hence, the typical basement fluid was of low salinity in the Permian. This also would explain why the Permian veins do not contain metals like Pb and Zn, which are typically mobilized as Cl complexes from the basement (Yardley 2005 and references therein, Burisch *et al.* 2015).

Hydrothermal activity at the Triassic–Jurassic boundary: the switch from low to high salinity (reservoir B and C, alternating fluid types B and C)

The first high-salinity fluid inclusions (unmixed fluid type C) in the study area occur in quartz–haematite veins formed at the Triassic–Jurassic boundary, in which euhedral haematite in vugs was age-dated by U-Th/He to 180–200, 202 ± 2 and 235 ± 20 Ma by Brander (2000). The oldest quartz layer in these samples contains type B, the next younger quartz layer containing type C fluid inclusions. Here, fortuitous and unique samples record the transition from an earlier low-salinity regime to a later high-salinity fluid regime (Fig. 5C). The fact that type B fluids can be recognized in younger veins indicates a persistent fluid reservoir in the basement. Hence, fluid type B persisted from the Permian to at least the late Triassic. The low Cl/Br mass ratios of 60 and 112 (Fig. 3F) and high salinities (Burisch *et al.* 2015) indicate a bittern brine origin for the type C inclusions.

Reservoir C and D, fluid type CD: mixed, highly saline fluids in a sediment-covered basement

In the Jurassic, large, north–south striking faults through the brittle part of the central European crust opened as a far-field consequence of the opening of the North Atlantic (e.g. Wetzel *et al.* 2003; Pfaff *et al.* 2009; Staude *et al.* 2009 and references therein). At that time and until the upper Cretaceous, mineralization in the Schwarzwald records fluid inclusions of one type: fluid type CD. These

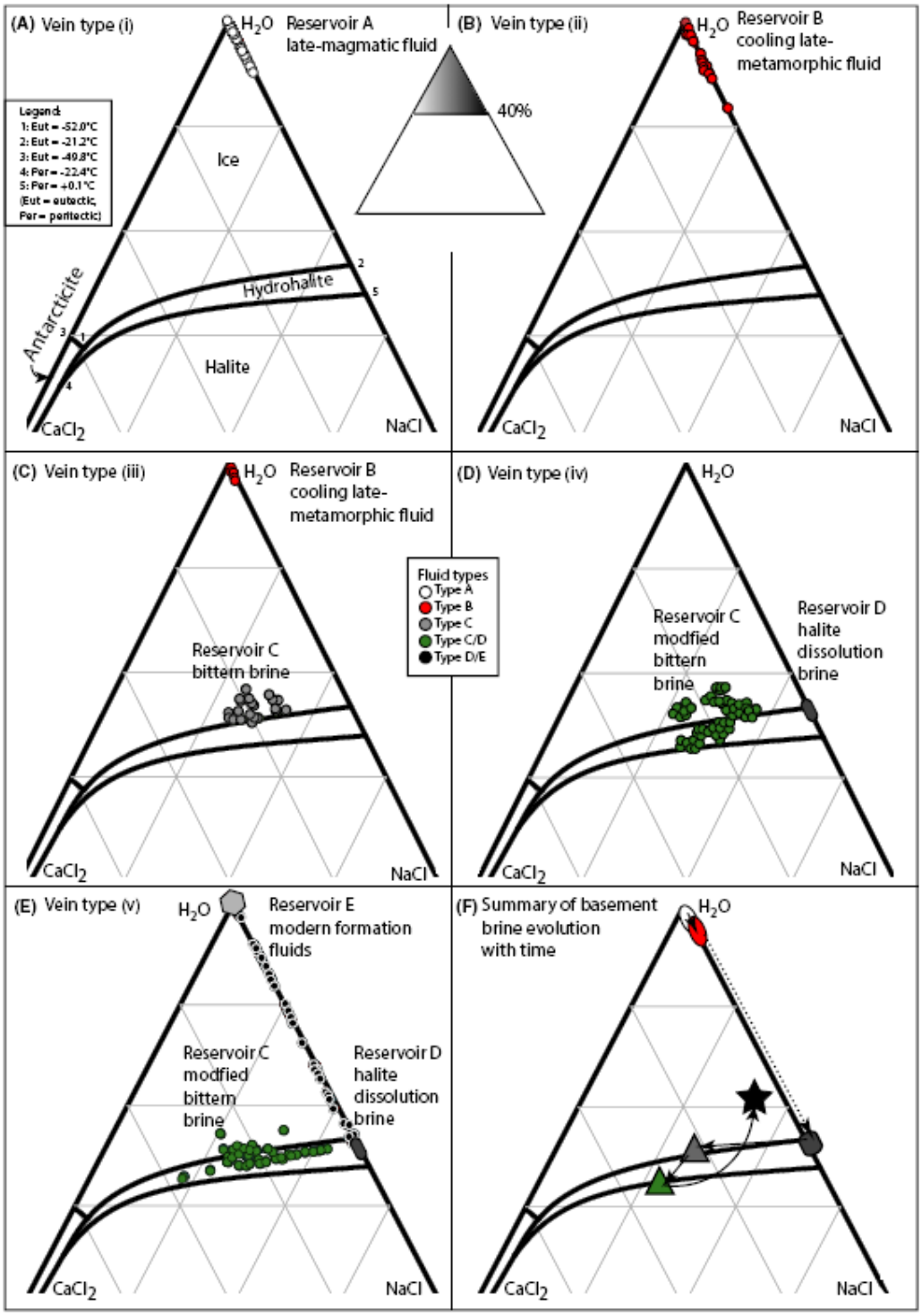

Fig. 5. Phase diagrams of the ternary H_2O-NaCl-$CaCl_2$ fluid system. Note that (F) is a summary of (A) to (E). The colours of the symbols in (F) refer to the different fluid types. Figure (F) summarizes the development from low-salinity fluids in Carboniferous and Permian times to a highly saline, modified bittern brine (basement brine), which formed by descending surficial bittern brines (in middle Triassic), that were modified (Ca increase and metal uptake) by WRI (water rock interactions) with crystalline rocks. The black star illustrates the modern basement brine in the Upper Rhine Graben, showing a distinct dilution by low TDS meteoric/formation fluids.

contain fluids of very high salinity (Figs 3E and 5D) and intermediate temperature which are interpreted as mixtures of two highly saline brines: one basement-derived with low Cl/Br mass ratios (fluid type C) and one cover-derived fluid with high Cl/Br mass ratio (fluid type D) (Staude *et al.* 2009, 2011, 2012a,b; Fußwinkel *et al.* 2013; Walter *et al.* 2015). Fußwinkel *et al.* (2013) demonstrated that the deep basement brine (reservoir C) with Cl/Br mass ratio of ~80 (inherited from the bittern brine) contained high amounts of dissolved metals, which originated by water–rock interaction with crystalline rocks (specifically, Pb and Zn) (see literature data in Fig. 3F). The second, metal-poor end-member (reservoir D) was proposed to be a Triassic Muschelkalk (limestone) formation fluid with very high Cl/Br mass ratios of >1000 (see literature data in Fig. 3F). The mixed 'ore fluid' (fluid type CD) consequently shows Cl/Br mass ratios between 60 and 820 (Fußwinkel *et al.* 2013 and this study).

The basement brine end-member of fluid type CD is a NaCl-dominated highly saline (21–26wt% NaCl + $CaCl_2$) fluid with a Na/K mass ratio of 0.8–10.4 (Fig. 4). Interestingly, the K/Na thermometer results in temperatures up to 560°C, which are not plausible for the geothermal regime and much higher than T_h (pressure corrected) from microthermometry. This indicates that the mixed CD type fluids are not in chemical equilibrium with their host rocks. This might suggest fast mixing processes during vein formation and fluid inclusion entrapment (see also Bons *et al.* 2014).

Reservoir C, D and E, fluid type CD and DE – from veins of group (v): the influence of the Rhine Graben opening

Vein group (v) occurs either as discrete veins on Rhine Graben-related faults or as younger generations of gangue and ore minerals in the centre of older veins, which are reopened by Neogene strike-slip tectonics. In both cases, fluid inclusions show no clear systematics in Na/K and Cl/Br mass ratios. This is interpreted as a result of mixing during the precipitation processes (Staude *et al.* 2009; Walter *et al.* 2015); in addition to type CD fluids, mixing obviously involved more than two end-members including a low-salinity reservoir E (Fig. 5E). This appears reasonable, as many of the group (v) veins are situated on deep faults where different lithologies of the Mesozoic sedimentary overburden are juxtaposed to the crystalline basement (Walter *et al.* 2015). Figure 3C illustrates the complex sequence of fluid inclusions recording various mixing processes within one crystal.

Most fluid inclusions contain fluid type DE with variable salinities between 0 and 25wt%; rarely the fluid type CD (highly saline) is also present in this vein type. Similar fluids were reported by, for example, Smith *et al.* (1998). Hence, a highly saline end-member exists, which is assigned to the highly saline basement brine, already present as type CD fluids. In most cases, however, only the reservoir D mixed and was diluted by lower salinity fluids from reservoir E. Comparing the fluid inclusion records of vein types (iv) and (v) implies that the reservoirs of fluid type CD were still available in Paleogene times. The fact that ternary C-D-E mixtures are lacking (Fig. 5E) is potentially an effect of fluid stratification. Similar to CD fluids, the K/Na thermometer for type DE yields geologically implausible temperatures of up to 430°C, indicating disequilibrium between rock and fluid, most likely caused by rapid mixing processes.

Modern fluids: The stratification of modern mineral and thermal waters and the modern basement brine

One of the reasons to choose the Schwarzwald as a model region for characterizing the evolution of basement brines is the large amount of data available from numerous deep bore-holes and many thermal and mineral wells in the study area (Fig. 1). More than ten deep drillings and tens of thermal and mineral water wells provide an insight into the recent fluid situation in the Upper Rhine Graben (Soultz-sous-Forêt, NAGRA drillings, Bruchsal, and Bühl; Pearson *et al.* 1989; Pauwels *et al.* 1993) and in the distal undisturbed basement and cover sequence (Urach, KTB, NAGRA drillings: Pearson *et al.* 1989; Stober & Bucher 2004; Möller *et al.* 2005). These data show that present-day fluids in the study area are stratified. Shallow ground waters are weakly mineralized Ca-Na-HCO_3 fluids, chemically controlled by weathering reactions in the subsurface (Bucher & Stober 2010). The sulphate content increases with depth by oxidation of host rock sulphides (Bucher & Stober 2010). The TDS increases further with depth and a high-salinity Na-Ca-Cl fluid is present below about 3 km (Bucher & Stober 2010). The carbonate and chloride fluids apparently do not mix (Bucher & Stober 2010).

The K/Na thermometer applied to fluids from Bad Urach or KTB records a close agreement between calculated and measured temperatures (Stober & Bucher 2004; Möller *et al.* 2005), which implies equilibrium between fluid and rock (Fig. 4). Also the modern Cl/Br mass ratios of 80–100 (Pearson *et al.* 1989; Stober & Bucher 2004; Möller *et al.* 2005) show no significant admixture of any sedimentary formation fluid which would be expected to result in higher ratios. In contrast, the chloridic fluids derived from the crystalline part of the Soultz-sous-Forêt drill hole record Na-K-temperatures more than 100°C (Fig. 4) above the measured ones (Pauwels *et al.* 1993); their Cl/Br mass ratios up to 255 support an influx of meteoric or formation fluids (Pauwels *et al.* 1993). Hence, in the vicinity of the Rhine Graben, mixing processes affecting the chlorine rich fluids still go on today and lead to a fluid mixture which is not in equilibrium with the

crystalline basement. These mixing processes may be driven by topographic fluid flow (Agemar *et al.* 2013).

History and development of the basement brine

Veins of groups (i) and (ii) record low-salinity fluids with significant magmatic or late metamorphic components in thermal equilibrium with the basement rocks (Figs 4 and 5A,B). Around the Triassic–Jurassic boundary, the first highly saline fluids were recorded in group (iii) veins (Fig. 5C). It is important to notable that in the middle Triassic, the study area was, for the first time after the Variscan orogeny, covered by a shallow ocean, in which the evaporate sequence reached halite saturation. This coincided with the occurrence of a high-salinity basement brine (reservoir C) shortly after formation of the evaporates (Fig. 5C,D).

Halite precipitation leads to a decrease in Cl/Br mass ratios in the residual fluid below the seawater ratio of 288 (see seawater evaporation line by McCaffrey *et al.* (1987) in Fig. 6). Hence, the low Cl/Br values of about 80 (mass ratios) and the highly saline basement brine end-member (reservoir C) of mixed type CD fluids may record downward migration of such residual bittern brines (fluid type C, reservoir C) (Fig. 5C and arrow 1 in Fig. 6) into the basement during the Triassic (see Bons *et al.* 2014). The large-scale albitization phenomena (Brockamp *et al.* 2003; Schlegel *et al.* 2007) in the crystalline basement of the central Schwarzwald are very likely related to the influx of such NaCl-rich fluids. Plagioclase dissolution and conversion to albite enriched the originally Ca-poor bittern brine in Ca and in base metals. Rough phase equilibrium calculations show that plagioclase with an X_{An} of 0.3 can shift the fluid to a Ca/(Ca + Na) of up to ~0.7 in the temperature range 30–220°C. Hence, the observed Ca/(Ca + Na) ratios of 0.2–0.3 in the high-salinity type C fluids could easily be explained by such albitization reactions. Furthermore, the formation of secondary minerals (e.g. chlorite, illite, smectite) as a consequence of biotite breakdown causes a modification of the bittern brine towards higher K and lower Mg concentrations (see arrow 1 in Fig. 6) (Brockamp *et al.* 2003, 2011).

Hence, it seems very plausible that the Jurassic–Cretaceous high-metal, low Cl/Br mass ratios of 'basement brine' reported by Fußwinkel *et al.* (2013) (our type C) is a modified middle Triassic bittern brine (Fig. 6). During the Jurassic and Cretaceous, it was mixed with a halite dissolution brine (NaCl-dominated and high Cl/Br mass ratios, end-member of line 2 in Fig. 6) derived by interaction of meteoric waters with the Muschelkalk evaporites

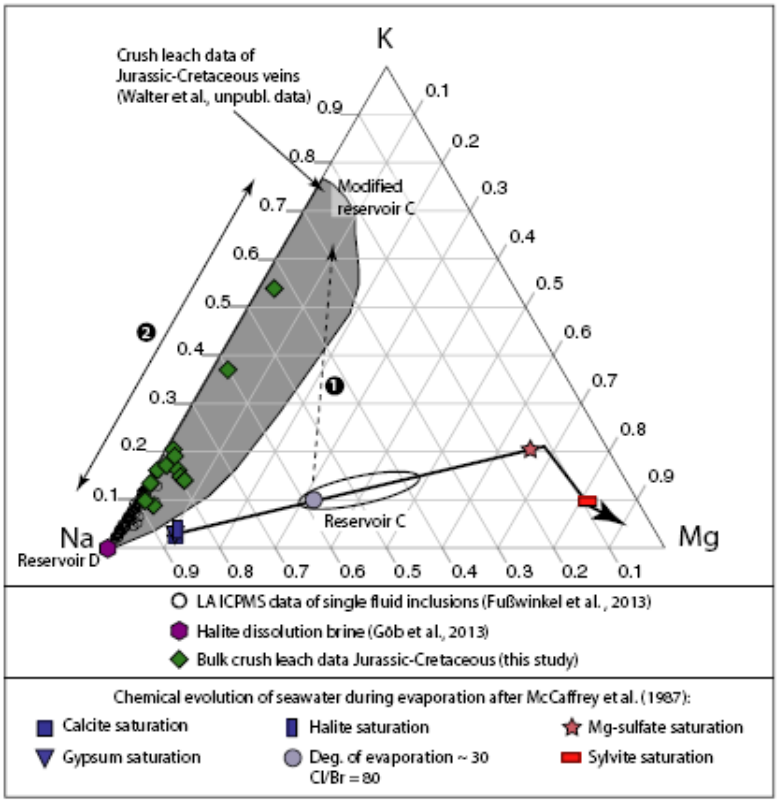

Fig. 6. Ternary diagram showing Na, Mg and K. The dotted arrow (1) indicates the modification of a bittern brine by water–rock interaction, shifting its composition, away from the seawater evaporation line towards higher K and lower Mg. During this process, the breakdown of rock-forming minerals during water–rock interaction modifies the fluid signature and concomitantly leads to increasing metal contents in the fluid. Fluid mixing (2) of a modified bittern brine (low Cl/Br mass ratio, high metal content) and a halite dissolution brine (high Cl/Br mass ratio, low metal content) yields the mixed two-component fluid signature CD.

(mixed fluid CD, see Fig. 3F and line 2 in Fig. 6). Early diagenetic dissolution textures in the middle Triassic host rocks reported by Geyer & Gwinner (2011) confirm that such processes indeed took place.

Alteration of feldspars (mainly plagioclase) and micas to clay minerals consumes water and leads to a desiccation process which both increase the salinity and the metal content in a fluid. The basement brine end-member (reservoir C) in type CD fluids would then have formed by a combination of inherited salinity from the middle Triassic Muschelkalk Ocean (Fig. 5D) and a long reaction time with the granitic/gneissic basement. Furthermore, the desiccation process consumes water within the basement, which causes a hydraulic gradient that enables downward migration of the younger (Middle–Upper Triassic) halite dissolution brine (fluid type D) with higher Cl/Br mass ratios (Stober & Bucher 2004; Bons *et al.* 2014). As the topography during the Jurassic and Cretaceous was too flat to drive topographic fluid flow, and as gravitational downward movement of the surface brine is unlikely due to the similar density of the bittern (reservoir C = basement) and the halite dissolution (reservoir D = surface) brines, this 'desiccation suck' (downward migration of brines caused by water consumption at depth; Stober & Bucher 2004; Bons *et al.* 2014) appears the only viable mechanism to bring large amounts of surface water to depth.

The Triassic–Jurassic boundary marks the first occurrence of highly saline basement brines. The group (iii) samples show that two fluids of different salinity were present during the first occurrence of a high-salinity brine (reservoir C, fluid type C), at the Triassic–Jurassic boundary (Fig. 3A and 5C). The low Cl/Br mass ratios are in agreement with a bittern brine origin. The lack of fluids of intermediate salinity shows that no fluid mixing occurred between type B and C fluids, although based on our FIA textural observations (Fig. 3), they intermittently coexisted on scales ranging from regional to individual fractures. This resembles the modern situation, in which NaCl- and Ca-HCO_3 fluids coexist in horizontally stratified reservoirs in SW Germany without any sign of mixing (Bucher & Stober 2010). Later on, this may have changed and type B fluid signature might be modified, by mixing or replacement with the much more saline type C (Fig. 7), so that it can no longer be recognized. Type B fluids were not observed in any younger sample (Figs 5 and 7). Interestingly, no deep-seated low-salinity fluids were found in the deep boreholes of KTB and Kola. If any type B fluid is present today, it would be expected to be just above the brittle/ductile transition zone (~12–15 km), deep below the depth of the drill holes (<8 km).

Since the break-up of the Upper Rhine Graben, various types of meteoric and formation waters (low TDS; Fig. 5E) entered the basement by topographic fluid flow (Agemar *et al.* 2013). The multisource fluids found in Paleogene veins still show a minor component of the highly saline basement brine, which is potential evidence that the fluid stratification in the continental central European basement still prevails until today (Pauwels *et al.* 1993; Bucher & Stober 2010). Diluting the high-salinity NaCl-$CaCl_2$ basement fluids by meteoric and/or formation fluids with low TDS (Pauwels *et al.* 1993) could explain the shift in average salinity from ~23wt% during the

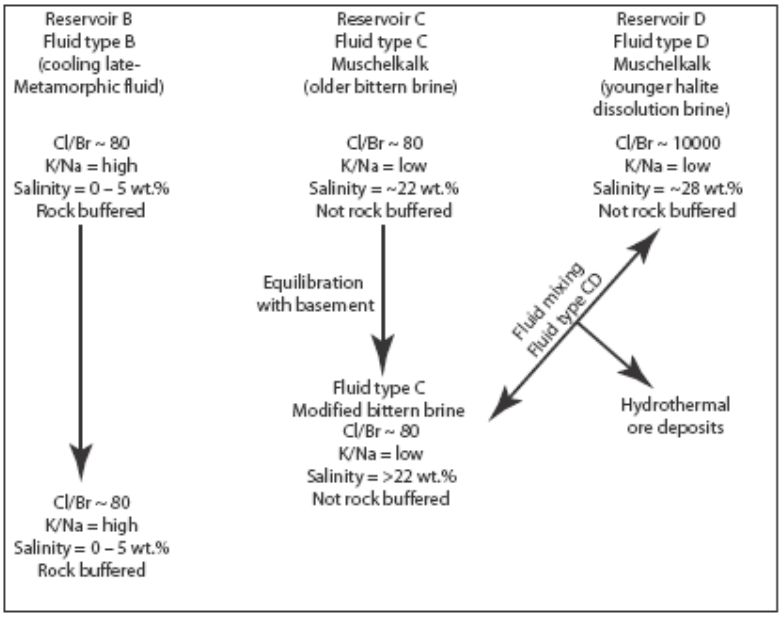

Fig. 7. Summary of fluid reservoirs B, C and D and their influence on hydrothermal ore deposition.

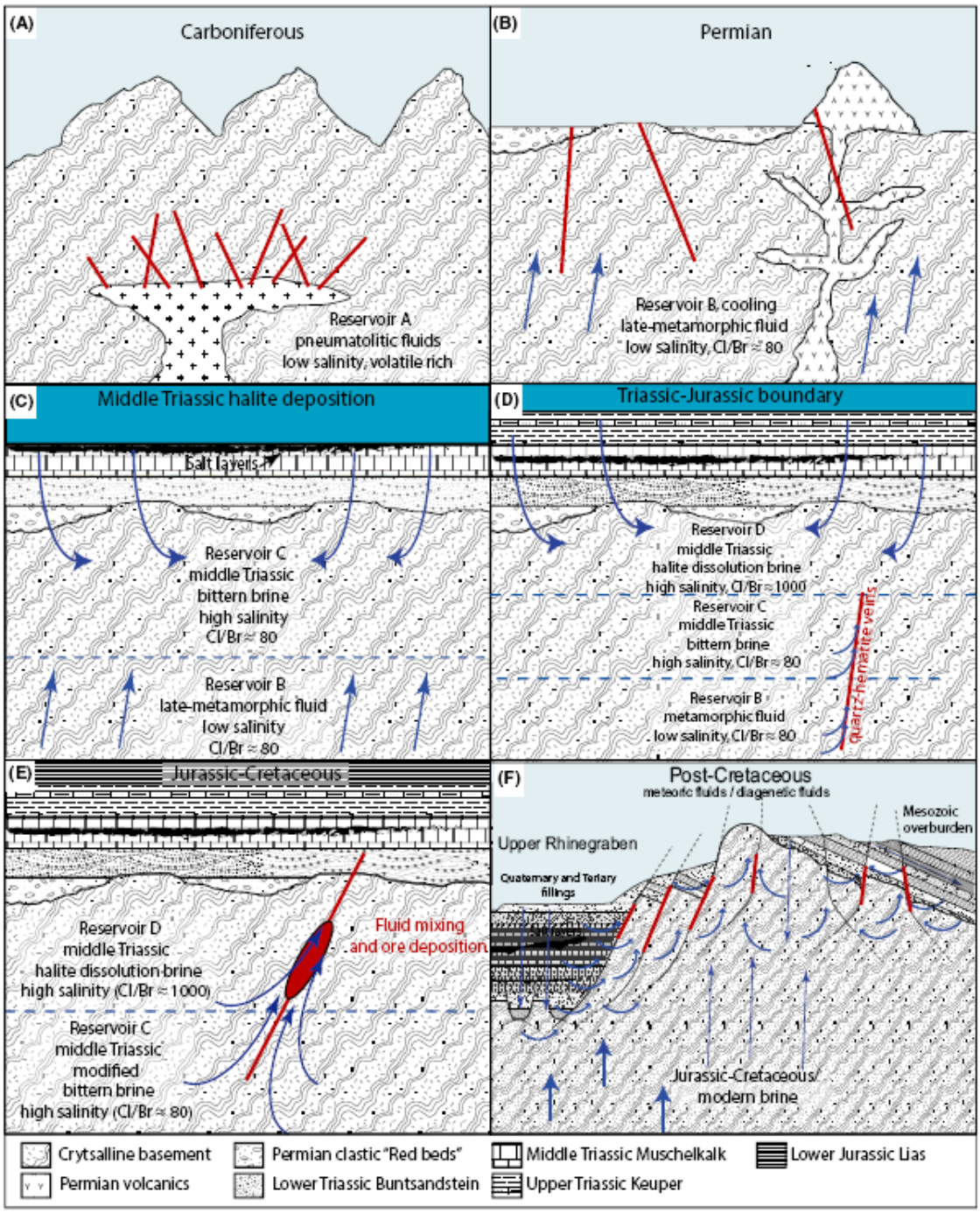

Fig. 8. Schematic crustal sections showing the evolution of the central European basement brine from (A) Carboniferous to (F) post-Cretaceous time. (A) Carboniferous fluids showing exclusively low salinity, volatile rich, high temperature in quartz–tourmaline veins, (B) Permian fluids showing only low salinity, high temperature in quartz veins with Sb-Au mineralization. (C) First deposition of halite in a shallow ocean in the Triassic and subsequently sinking of a bittern brine into the basement. (D) At the Triassic–Jurassic boundary, first dissolution of the halite and formation of a halite dissolution brine that sinks downwards (Bons *et al.* 2014). Furthermore, formation of the Triassic–Jurassic quartz–haematite veins with alternating fluid signatures. (E) Opening of fracture networks as a far-field consequence of the North Atlantic opening and formation of the Jurassic–Cretaceous veins by binary fluid mixing. (F) Multi-component fluid mixing and vein formation in the complex geological environment of the Upper Rhine Graben rift.

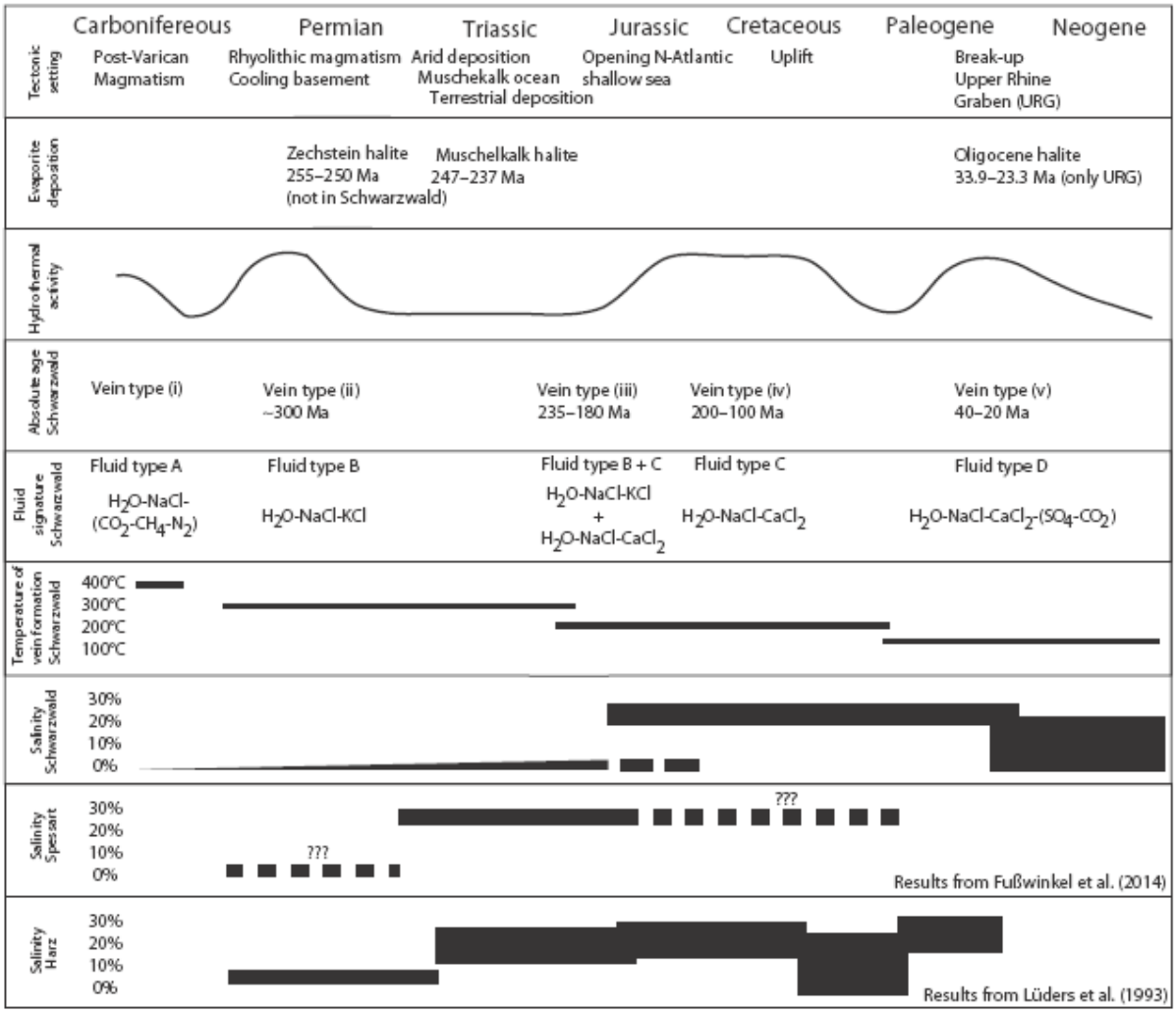

Fig. 9. Temporal comparison of ore precipitation in the Schwarzwald, Harz and Spessart mining districts. Data from Lüders *et al.* (1993) and Fußwinkel *et al.* (2014). Note that the first recognition of a high-salinity basement brine is invariably linked to the formation of halite-bearing evaporites at the surface.

Jurassic to ~17wt% today. This modification is also visible in the higher Cl/Br mass ratios of 255 in the modern brine of Soultz-sous-Forêt (Fig. 1) in contrast to the fluids of the Bad Urach and KTB drill holes, which are not proximal to the rift (Fig. 1), showing depleted Cl/Br mass ratios of 80–105.

The history of the basement brine in the context of large-scale ore mineralization

An interesting additional aspect of this study is the relation of brine development and Pb-Zn-Cu-Ag ore deposition in the study area. Before large-scale mixing occurred (Fig. 7), only very low amounts of ore were precipitated in vein types (i), (ii) and (iii), which precipitated from low-salinity fluids A and B and high-salinity type C (pure end-member fluids). However, as soon as mixing between fluid type C and D occurred, during Jurassic to Paleogene times, massive ore precipitation can be recognized (Fig. 7). The occurrence of high metal concentrations in the mixed CD fluid correlates with the timing of the first percolation of the bittern brine into the crystalline basement. Hence, our data imply in accordance with Fußwinkel *et al.* (2013) that the high-salinity type C bittern brine (modified by fluid–rock reactions in the crystalline basement) was the major carrier of metals. Thus, in the Schwarzwald, the mobilization of metals and the formation of ore deposits are directly linked to and crucially dependent on the formation of evaporites at the surface.

CONCLUSIONS

Upper and middle crustal fluids from SW Germany were investigated by crush-leach analyses of primary fluid inclusions from well-characterized hydrothermal veins of known age. This approach allows the reconstruction of chemical changes and modifications of these fluids over the last 300 Ma (Figs 8 and 9). During the Carboniferous, Permian and Triassic, only dominantly magmatic or metamorphic, high-temperature/low-salinity fluids (probably in equilibrium with their host rock) are recorded. With the beginning of the Jurassic, however, highly saline brines emerge and a subsequent two-component mixing process between basement brine and cover fluid appears to be responsible for their composition during the Jurassic and Cretaceous. Finally, a multicomponent mixing process (basement with various types of cover fluid reservoirs) is necessary to explain the observed variation in fluid compositions related to the onset of Rhine Graben rifting in the Paleogene.

The most striking feature of the reconstruction of the fluid history is the shift from low-salinity to high-salinity fluids around the Triassic–Jurassic boundary (Fig. 9) and its temporal relation to the evaporites at the surface. A comparison of our study area with two other well-studied mineralized regions in central Europe, the Spessart and the Harz mountains (Lüders *et al.* 1993; Fußwinkel *et al.* 2014) indicates that this link between evaporates and high-salinity ore fluids may be also true for other ore districts (of similar type) in central Europe. In contrast to the Schwarzwald, the Spessart and the Harz mountains were covered much earlier by halite-bearing evaporitic sediments during the late Permian. Interestingly, the first high-salinity basement brines in these regions appear in early Triassic veins already. Hence, high-salinity basement fluids emerged in all three regions shortly after the deposition of marine evaporitic halite at the surface. In the Schwarzwald, this happens during the end of the Triassic, in the Spessart and Harz mountains, at the beginning of the Triassic (Fig. 9). Consequently, this suggests that the high salinity in basement brines develops by a combination of external (evaporitic fluids) and internal (desiccation) processes.

ACKNOWLEDGEMENTS

We would like to thank C. Manning and two anonymous reviewers, who helped to improve the manuscript substantially as well as M. Marks and T. Wenzel who helped with many hints and discussions. Furthermore, we would like to thank G. Stoschek and B. Steinhilber for their help with crush-leach analyses and technical support and P. Jeiseke and S. Kaulfuß for sample preparation. This study was supported by the Alfried-Krupp Prize for Young University Teachers of the Krupp Foundation to Gregor Markl and the German Research Foundation (DFG), grant 2135/20-1.

REFERENCES

Agemar T, Brunken J, Jodocy M, Schellschmidt R, Schulz R, Stober I (2013) Untergrundtemperaturen in Baden-Wurttemberg. *Zeitschrift der Deutschen Gesellschaft für Geowissenschaften*, 164, 49–62.

Banks DA, Davies GR, Yardley BWD, McCaig AM, Grant NT (1991) The chemistry of brines from an Alpine thrust system in the Central Pyrenees: an application of fluid inclusion analysis to the study of fluid behaviour in orogenesis. *Geochimica et Cosmochimica Acta*, 55, 1021–30.

Banks DA, Giulliani G, Yardley BWD, Cheilletz A (2000) Emerald mineralisation in Columbia: fluid chemistry and the role of brine mixing. *Mineralium Deposita*, 35, 699–713.

Behr HJ, Gerler J (1987) Inclusions of sedimentary brines in post-Variscan mineralizations in the Federal Republic of Germany—a study by neutron activation analysis. *Chemical Geology*, 61, 65–77.

Behr HJ, Horn EE, Frentzel-Beyme K, Reutel C (1987) Fluid inclusion characteristics of the Variscan and post-Variscan mineralizing fluids in the Federal Republic of Germany. *Chemical Geology*, 61, 273–85.

Bejaoui J, Bouhlel S, Sellami A, Braham A (2014) Geology, mineralogy and fluid inclusion study of Oued Jebs Pb–Zn–Sr deposit; comparison with the Bou Grine deposit (diapirs zone, Tunisian atlas). *Arabian Journal of Geosciences*, 7, 2483–97.

Bellot J-P, Lerouge C, Bailly L, Bouchot V (2003) The Biards Sb-Au–bearing shear zone (Massif Central, France): an indicator of crustal-scale transcurrent tectonics guiding Late Variscan Collapse. *Economic Geology*, 98, 1427–47.

Bodnar RJ, Vityk MO (1994) Interpretation of microthermometric data for H_2O -NaCl fluid inclusions. In: *Fluid Inclusions in Minerals: Methods and Applications. Short Course IMA* (eds de Vivo B, Frezzotti ML), pp. 117–30. Virginia Polytechnic Institute, Pontignano-Siena.

Boiron MC, Cathelineau M, Banks DA, Buschaert S, Fourcade S, Coulibaly Y, Michelot JL, Boyce A (2002) Fluid transfer at a basement/cover interface. Part II. Large-scale introduction of chlorine into the basement by Mesozoic basinal brines. *Chemical Geology*, 192, 121–40.

Bons PD, Fusswinkel T, Gomez-Rivas E, Markl G, Wagner T, Walter BF (2014) Fluid mixing from below in unconformity-related hydrothermal ore deposits. *Geology*, 42, 1035–8.

Bottomley DJ, Conrad Gregoire D, Raven KG (1994) Saline ground waters and brines in the Canadian Shield: geochemical and isotopic evidence for a residual evaporite brine component. *Geochimica et Cosmochimica Acta*, 58, 1483–98.

Brander T (2000) U/HE-chronologische Fallstudien an Eisen- und Manganerzen. Dissertation. Ruprecht-Karls Universität Heidelberg, Heidelberg.

Brockamp O, Clauer N, Zuther M (2003) Authigenic sericite record of a fossil geothermal system: the Offenburg trough, central Black Forest, Germany. *International Journal of Earth Sciences*, 92, 843–51.

Brockamp O, Schlegel A, Clauer N (2011) Mesozoic hydrothermal impact on Rotliegende and Bunter immature sandstones of the High Rhine trough and its adjacent eastern area (southern Black Forest, Germany). *Sedimentary Geology*, 234, 76–88.

Bucher K, Stober I (2002) Water–rock reaction experiments with Black Forest gneiss and granite. In: *Water–Rock Interaction,*

Water Science and Technology Library (eds Stober I, Bucher K), pp. 61–96. Kluwer Academic Publishers, Dordrecht.

Bucher K, Stober I (2010) Fluids in the upper continental crust. *Geofluids*, 10, 241–53.

Burisch M, Marks M, Nowak M, Markl G (2015) The Effect of temperature and cataclastic deformation on salinity, halogen systematics and metal transport capacities of continental basement brines – an experimental approach: SGA abstract. In: *Proceedings of the 13th Biennial SGA Meeting*, vol. 5, pp. 2134. SGA proceedings, Nancy, France.

Frape S, Fritz P (1987) Geochemical trends for groundwaters from the Canadian Shield. *Geological Association of Canada Special Papers*, 33, 19–38.

Fritz P, Frape ST (1982) Saline groundwaters in the Canadian Shield—a first overview. *Chemical Geology*, 36, 179–90.

Fußwinkel T, Wagner T, Wälle M, Wenzel T, Heinrich C, Markl G (2013) Fluid mixing forms basement-hosted Pb-Zn deposits: Insight from metal and halogen geochemistry of individual fluid inclusions. *Geology*, 41, 679–82.

Fußwinkel T, Wagner T, Wenzel T, Wälle M, Lorenz J (2014) Red bed and basement sourced fluids recorded in hydrothermal Mn–Fe–As veins, Sailauf (Germany): a LA-ICPMS fluid inclusion study. *Chemical Geology*, 363, 22–39.

Geyer OF, Gwinner MP (2011) Geologie von Baden - Württemberg. – 5., völlig neu bearbeitete Auflage, Stuttgart, Schweizerbart'sche Verlagsbuchhandlung (Nägele u. Obermiller), 627.

Giggenbach WF (1988) Geothermal solute equilibria. Derivation of Na-K-Mg-Ca geoindicators. *Geochimica et Cosmochimica Acta*, 52, 2749–65.

Gleeson SA, Yardley BWD (2002) Extensional veins and PbZn mineralisation in basement rocks: the role of pentration of formation brines. In: *Water-Rock Interaction*, (eds Stober I, Bucher K), pp. 189–205. Kluwer Academic Publishing, Germany.

Gleeson SA, Wilkinson JJ, Stuart FM, Banks DA (2001) The origin and evolution of base metal mineralising brines and hydrothermal fluids, South Cornwall, UK. *Geochimica et Cosmochimica Acta*, 65, 2067–79.

Göb S, Loges A, Nolde N, Bau M, Jacob DE, Markl G (2013) Major and trace element compositions (including REE) of mineral, thermal, mine and surface waters in SW Germany and implications for water–rock interaction. *Applied Geochemistry*, 33, 127–52.

Goldstein RH, Reynolds TJ (1994) Systematics of fluid inclusions in diagenetic minerals. *SEPM Short Course Notes*, 31, 199.

Hann HP, Chen F, Zedler H, Frisch W, Loeschke J (2003) The Rand Granite in the southern Schwarzwald and its geodynamic significance in the Variscan belt of SW Germany. *International Journal of Earth Science*, 92, 821–42.

Irwin J, Roedder E (1995) Diverse origins of fluid in magmatic inclusions at Bingham (Utah, USA), Butte (Montana, USA), St. Austell (Cornwall, UK), and Ascension Island (mid-Atlantic, UK), indicated by laser microprobe analysis of Cl, K, Br, I, Ba + Te, U, Ar, Kr, and Xe. *Geochimica et Cosmochimica Acta*, 59, 295–312.

Jébrak M (1997) Hydrothermal breccias in vein-type ore deposits: a review of mechanisms, morphology and size distribution. *Ore Geology Reviews*, 12, 111–34.

Köhler J, Schönenberger J, Upton B, Markl G (2009) Halogen and trace-element chemistry in the Gardar Province, South Greenland: subduction-related mantle metasomatism and fluid exsolution from alkalic melts. *Lithos*, 113, 731–47.

Leutwein F, Sonet J (1974) Geochronologische Untersuchungen im Südschwarzwald. *Neues Jahrbuch für Mineralogie – Abhandlungen*, 121, 252–71.

Loges A, Wagner T, Kirnbauer T, Göb S, Bau M, Berner Z, Markl G (2012) Source and origin of active and fossil thermal spring systems, northern Upper Rhine Graben, Germany. *Applied Geochemistry*, 27, 1153–69.

Lüders V, Gerler J, Hein U, Reutel C (1993) Chemical and thermal development of ore-forming solutions in the Harz Mountains: a summary of fluid inclusion studies. *Monograph Series on Mineral Deposits*, 30, 117–32.

Markl G, Bucher K (1998) Composition of fluids in the lower crust inferred from metamorphic salt in lower crustal rocks. *Nature*, 391, 781–3.

Marks MA, Marschall HR, Schühle P, Guth A, Wenzel T, Jacob DE, Barth M, Markl G (2013) Trace element systematics of tourmaline in pegmatitic and hydrothermal systems from the Variscan Schwarzwald (Germany): the importance of major element composition, sector zoning, and fluid or melt composition. *Chemical Geology*, 344, 73–90.

McCaffrey M, Lazar B, Holland H (1987) The evaporation path of seawater and the coprecipitation of Br^- and K^+ with halite. *Journal of Sedimentary Research*, 57, 928–37.

Mertz DF, Lippolt HJ, Huck KH (1986) K/Ar, Ar-40/Ar-39, and Rb/Sr investigations on the genesis of the Clara vein deposit, Central Black Forest. Jahrestagung Dtsch. *Geophysikalischen Ges. e.V.*, 46, 235.

Meyer M, Brockhamp O, Clauer N, Renk A, Zuther M (2000) Further evidence for a Jurassic mineralizing event in central Europe: K-Ar dating of hydrothermal alteration and fluid inclusion systematics in wall rocks of the Käfersteige fluorite vein deposit in the northern Black Forest, Germany. *Mineralium Deposita*, 35, 754–61.

Möller P, Woith H, Dulski P, Lüders V, Erzinger J, Kämpf H, Pekdeger A, Hansen B, Lodemann M, Banks DA (2005) Main and trace elements in KTB-VB fluid: composition and hints to its origin. *Geofluids*, 5, 28–41.

Pauwels H, Fouillac C, Fouillac A-M (1993) Chemistry and isotopes of deep geothermal saline fluids in the Upper Rhine Graben: origin of compounds and water–rock interactions. *Geochimica et Cosmochimica Acta*, 57, 2737–49.

Pearson JFJ, Lolcama JL, Scholtis A (1989) Chemistry of waters in the Böttstein, Weiach, Riniken, Schafisheim, Kaisten and Leuggern boreholes: a hydrochemically consistent data set. *NAGRA Technical Report*, 86–19, 153.

Pfaff K, Romer RL, Markl G (2009) U-Pb ages of ferberite, chalcedony, agate, "U-mica" and pitchblende: constraints on the mineralization history of the Schwarzwald ore district. *European Journal of Mineralogy*, 21, 817–36.

Pfaff K, Hildebrandt LH, Leach DL, Jacob DE, Markl G (2010) Formation of the Wiesloch Mississippi Valley-type Zn-Pb-Ag deposit in the extensional setting of the Upper Rhinegraben, SW Germany. *Mineralium Deposita*, 45, 647–66.

Pfaff K, Koenig MA, Wenzel T, Ridley I, Hildebrandt LH, Leach DL, Markl G (2011) Trace and minor element variations and sulfur isotopes in crystalline and colloform ZnS: incorporation mechanisms and implications for their genesis. *Chemical Geology*, 286, 118–34.

Romer RL, Förster H-J, Kroner U, Müller A, Rötzler J, Seltmann R, Wenzel T (2012) *Granites of the Erzgebirge – Relation of Magmatism to Metamorphic and Tectonic Evolution of the Varsican Orogen*. Scientific Technical Report 12/15, GFZ German Research Centre for Geosciences.

Savoye S, Aranyossy J-F, Beaucaire C, Cathelineau M, Louvat D, Michelot J-L (1998) Fluid inclusions in granites and their relationships with present-day groundwater chemistry. *European Journal of Mineralogy*, 10, 1215–26.

Schlegel A, Brockamp O, Clauer N (2007) Response of clastic sediments to episodic hydrothermal fluid flows in intramontane troughs: a case study from Black Forest, Germany. *European Journal of Mineralogy*, 19, 833–48.

Schwinn G, Markl G (2005) REE systematics in hydrothermal fluorite. *Chemical Geology*, 216, 225–48.

Shepherd TJ, Rankin AH, Alderton DHM (1985) *A Practical Guide to Fluid Inclusion Studies*, p. 239. Blackie, Glasgow.

Shouakar-Stash O, Alexeev S, Frape S, Alexeeva L, Drimmie R (2007) Geochemistry and stable isotopic signatures, including chlorine and bromine isotopes, of the deep groundwaters of the Siberian Platform, Russia. *Applied Geochemistry*, 22, 589–605.

Smith MP, Savary V, Yardley BWD, Valley JW, Royer JJ, Dubois M (1998) The evolution of the deep flow regime at Soultz-sous-Forêts, Rhine Graben, eastern France: evidence from a composite quartz vein. *Journal of Geophysical Research*, 103, 27223–37.

Staude S, Bons PD, Markl G (2009) Hydrothermal vein formation by extension-driven dewatering of the middle crust: an example from SW Germany. *Earth and Planetary Science Letters*, 286, 387–95.

Staude S, Dorn A, Pfaff K, Markl G (2010a) Assemblages of Ag-Bi sulfosalts and conditions of their formation: the type locality of schapbachite ($Ag_{0.4}Pb_{0.2}Bi_{0.4}S$) and neighboring mines in the Schwarzwald ore district, southern Germany. *Canadian Mineralogist*, 48, 441–66.

Staude S, Mordhorst T, Neumann R, Prebeck W, Markl G (2010b) Compositional variation of the tennantite–tetrahedrite solid-solution series in the Schwarzwald ore district (SW Germany): The role of mineralization processes and fluid source. *Mineralogical Magazine*, 74, 309–39.

Staude S, Göb S, Pfaff K, Ströbele F, Premo WR, Markl G (2011) Deciphering fluid sources of hydrothermal systems: a combined Sr- and S-isotope study on barite (Schwarzwald, SW Germany). *Chemical Geology*, 286, 1–20.

Staude S, Mordhorst T, Nau S, Pfaff K, Brügmann G, Jacob DE, Markl G (2012a) Hydrothermal Carbonates of the Schwarzwald ore district, southwestern Germany: carbon source and conditions of formation using $\delta^{18}O$, $\delta^{13}C$, $^{87}Sr/^{86}Sr$, and fluid inclusions. *The Canadian Mineralogist*, 50, 1401–34.

Staude S, Werner W, Mordhorst T, Wemmer K, Jacob DE, Markl G (2012b) Multi-stage Ag–Bi–Co–Ni–U and Cu–Bi vein mineralization at Wittichen, Schwarzwald, SW Germany: geological setting, ore mineralogy, and fluid evolution. *Mineralium Deposita*, 47, 251–76.

Steele-MacInnes M, Bodnar RJ, Naden J (2011) Numerical model to determine the composition of H_2O-NaCl-$CaCl_2$ fluid inclusions based on microthermometric and microanalytical data. *Geochimica et Cosmochimica Acta*, 75, 21–40.

Stober I, Bucher K (1999) Deep groundwater in the crystalline basement of the Black Forest region. *Applied Geochemistry*, 14, 237–54.

Stober I, Bucher K (2004) Fluids sinks within the earth's crust. *Geofluids*, 4, 143–51.

Stober I, Bucher K (2005) The upper continental crust, an aquifer and its fluid: hydraulic and chemical data from 4 km depth in fractured crystalline basement rocks at the KTB test site. *Geofluids*, 5, 8–19.

Wagner T, Cook NJ (2000) Late-Variscan antimony mineralisation in the Rheinisches Schiefergebirge, NW Germany: evidence for stibnite precipitation by drastic cooling of high-temperature fluid systems. *Mineralium Deposita*, 35, 206–22.

Walter BF, Immenhauser A, Geske A, Markl G (2015) Exploration of hydrothermal carbonate magnesium isotope signatures as tracers for continental fluid aquifers, Schwarzwald mining district, SW Germany. *Chemical Geology*, 400, 87–105.

Werner W (2011) Mineralische Rohstoffe. In: (eds Hann P, Zedler H) *Erläuterungen zum Blatt 8113 Todtnau*. pp. 98–115, 3 Abb.; Freiburg i. Br. (LGRB, Hrsg.).

Werner W, Franzke HJ, Wirsing G, Jochum J, Lüders V, Wittenbrink J (2002) mit einem Beitrag von B. Steiber: Die Erzlagerstätte Schauinsland bei Freiburg im Breisgau. Bergbau, Geologie, Hydrogeologie, Mineralogie, Geochemie, Tektonik und Lagerstättenentstehung. Ber. Naturforsch. Ges. Freiburg, 92: 110 S., 26 Abb., 9 Tab., 16 Taf.; Freiburg i. Br.

Wernicke RS, Lippolt HJ (1993) Botryoidal hematite from the Schwarzwald (Germany): heterogeneous uranium distributions and their bearing on the helium dating method. *Earth and Planetary Science Letters*, 114, 287–300.

Wernicke RS, Lippolt HJ (1997) (U + Th)–He evidence of Jurassic continuous hydrothermal activity in the Schwarzwald basement, Germany. *Chemical Geology*, 138, 273–85.

Wetzel A, Allenbach R, Allia V (2003) Reactivated basement structures affecting the sedimentary facies in a tectonically "quiescent" epicontinental basin: an example from NW Switzerland. *Sedimentary Geology*, 157, 153–72.

Yardley BWD (2005) Metal concentrations in crustal fluids and their relationship to ore formation. *Economic Geology*, 100, 613–32.

SUPPORTING INFORMATION

Additional Supporting Information may be found in the online version of this article:

Table S1. Results of the microthermometry.

Table S2. Results crush leach and age constrains for the individual samples.

Appendix S1. Supplement analytical uncertainties.

Mineralium Deposita

Major element and trace metal composition of fluid inclusions from unconformity related, hydrothermal vein-type deposits with base metal mineralization: the reconstruction of eroded sedimentary units

--Manuscript Draft--

Manuscript Number:	MIDE-D-16-00103
Full Title:	Major element and trace metal composition of fluid inclusions from unconformity related, hydrothermal vein-type deposits with base metal mineralization: the reconstruction of eroded sedimentary units
Article Type:	Regular Articles
Corresponding Author:	Benjamin Florian Walter, Dr. Eberhard Karls Universitat Tubingen Tübingen, GERMANY
Corresponding Author Secondary Information:	
Corresponding Author's Institution:	Eberhard Karls Universitat Tubingen
Corresponding Author's Secondary Institution:	
First Author:	Benjamin Florian Walter, Dr.
First Author Secondary Information:	
Order of Authors:	Benjamin Florian Walter, Dr.
	Mathias Burisch, MSc
	Michael Marks, PD. Dr.
	Gregor Markl, Prof. Dr.
Order of Authors Secondary Information:	
Funding Information:	German Research Foundation (DFG) (Ma2135/20-1) — Dr. Benjamin Florian Walter
Abstract:	Mixing of sedimentary formation fluids with basement-derived brines is an important mechanism for the formation of hydrothermal veins. We focus on the sources and metal contents of the sediment-derived fluid component in ore-forming processes and present a comprehensive fluid inclusion study on 84 Jurassic hydrothermal veins from the Schwarzwald mining district (SW Germany). Our data derive from about 2300 fluid inclusions and reveal differences in the average fluid composition between the northern, central and southern Schwarzwald: Fluids from the northern and southern Schwarzwald are characterized by high salinities (18-26 wt.% NaCl+CaCl2), low Ca/(Ca+Na)-ratios (0.1-0.4) and variable Cl/Br-ratios (30-1140). In contrast, fluids from the central Schwarzwald show even higher salinities (23-27 wt.% NaCl+CaCl2), higher Ca/(Ca+Na)-ratios (0.2-0.9) and less variable Cl/Br-ratios (40-130). These fluid compositions correlate with the nature and thickness of the now eroded sedimentary cover rocks. Compared to the northern and the southern Schwarzwald, where halite precipitation occurred during the middle Triassic, the sedimentary basin in the central Schwarzwald was relatively shallow at this time and no halite was precipitated. Accordingly, Cl/Br-ratios of fluids from the central Schwarzwald provide no evidence for the reaction of a sedimentary brine with halite, whereas those from the northern and southern Schwarzwald do. Instead, elevated Ca/(Ca+Na), high SO4 contents and relatively low Cl/Br imply the presence of a gypsum dissolution brine during vein formation in the central Schwarzwald which agrees with the reconstructed regional Triassic geology. Hence, the information archived in fluid inclusions from hydrothermal veins in the crystalline basement have the potential for reconstructing sedimentary rocks in the former overburden.
Suggested Reviewers:	Kåre Kullerud

	kare.kullerud@uit.no knowledgeable experts in the field of water-rock interaction
	Matthew Steele-MacInnis steelemacinnis@email.arizona.edu knowledgeable expert in the field of fluid inclusion analysis
	Sarah Gleeson sarah.gleeson@gfz-potsdam.de knowledgeable expert in the field of water-rock interaction
	Michael Bau m.bau@jacobs-university.de knowledgeable expert in the field of water-rock interaction
	Antonin Richard antonin.richard@univ-lorraine.fr knowledgeable expert in the field of water-rock interaction
	David Dolejs david.dolejs@minpet.uni-freiburg.de knowledgeable expert in the field of water-rock interaction

EBERHARD KARLS
UNIVERSITÄT
TÜBINGEN

Fachbereich Geowissenschaften
Geologie und Geodynamik

Benjamin Walter

Telefon +49 7071 29-73155

Universität Tübingen ·Wilhelmstr. 56, 72074 Tübingen, Germany

Benjamin.walter@uni-tuebingen.de

Editorial Office
Mineralium Deposita

Tübingen, 30th May 2016

Dear Editors,

please consider the manuscript 'Major element and trace metal composition of fluid inclusions from unconformity related, hydrothermal vein-type deposits with base metal mineralization: the reconstruction of eroded sedimentary units' for possible publication in Mineralium Deposita. The presented conclusions are general and applicable to other hydrothermal systems. Therefore, our findings might be of great interest for a broad audience (e.g. petrologists, economic geologists, geochemists, hydrogeologists)

We are looking forward to reviews of our manuscript and suggest knowledgeable experts in the field of water-rock interaction:

- Kåre Kullerud (University of Tromso, Finland), kare.kullerud@uit.no
- Matthew Steele-MacInnis (University of Arizona), steelemacinnis@email.arizona.edu
- Sarah Gleeson (GFZ, Germany), sarah.gleeson@gfz-potsdam.de
- Michael Bau (University of Bremen), m.bau@jacobs-university.de
- Antonin Richard, (Université de Lorraine, France) antonin.richard@univ-lorraine.fr
- David Dolejs, (University of Freiburg), david.dolejs@minpet.uni-freiburg.de

Please do not choose Bruce Yardley, David Banks or Jamie Wilkinson as reviewers, since there seem to exist competing interests or personal things involved, judging from former reviews on other manuscripts by them.

We confirm that all four authors approve the publication of this article and that none of the material has been previously published (including the internet) or submitted elsewhere.

On behalf of all authors, yours sincerely,
Benjamin Walter

Major element and trace metal composition of fluid inclusions from unconformity related, hydrothermal vein-type deposits with base metal mineralization: the reconstruction of eroded sedimentary units

Benjamin F. Walter*, Mathias Burisch, Michael A.W. Marks, Gregor Markl

Department of Geosciences, University of Tübingen, Wilhelmstrasse 56, 72074 Tübingen, Germany

*Corresponding author: benjamin.walter@uni-tuebingen.de, Tel: 004972072/2973155

Keywords: hydrothermal ore; base metals; Cl/Br systematics, fluid mixing, basement brine

Abstract:

Mixing of sedimentary formation fluids with basement-derived brines is an important mechanism for the formation of hydrothermal veins. We focus on the sources and metal contents of the sediment-derived fluid component in ore-forming processes and present a comprehensive fluid inclusion study on 84 Jurassic hydrothermal veins from the Schwarzwald mining district (SW Germany). Our data derive from about 2300 fluid inclusions and reveal differences in the average fluid composition between the northern, central and southern Schwarzwald: Fluids from the northern and southern Schwarzwald are characterized by high salinities (18-26 wt.% $NaCl+CaCl_2$), low Ca/(Ca+Na)-ratios (0.1-0.4) and variable Cl/Br-ratios (30-1140). In contrast, fluids from the central Schwarzwald show even higher salinities (23-27 wt.% $NaCl+CaCl_2$), higher Ca/(Ca+Na)-ratios (0.2-0.9) and less variable Cl/Br-ratios (40-130).

These fluid compositions correlate with the nature and thickness of the now eroded sedimentary cover rocks. Compared to the northern and the southern Schwarzwald, where halite precipitation occurred during the middle Triassic, the sedimentary basin in the central Schwarzwald was relatively shallow at

this time and no halite was precipitated. Accordingly, Cl/Br-ratios of fluids from the central Schwarzwald provide no evidence for the reaction of a sedimentary brine with halite, whereas those from the northern and southern Schwarzwald do. Instead, elevated Ca/(Ca+Na), high SO_4 contents and relatively low Cl/Br imply the presence of a gypsum dissolution brine during vein formation in the central Schwarzwald which agrees with the reconstructed regional Triassic geology. Hence, the information archived in fluid inclusions from hydrothermal veins in the crystalline basement have the potential for reconstructing sedimentary rocks in the former overburden.

1. Introduction:

Fluid mixing is proposed as a major ore-precipitating process for many hydrothermal ore systems (e.g. Duane and De Wit, 1988; Tornos et al., 1991; McCaig et al., 2000; Klemm et al., 2004; Fußwinkel et al., 2013; Bons et al., 2014; Fußwinkel, 2014). Previous studies on hydrothermal ore deposits include combinations of microthermometry, stable and radiogenic isotopes (O-C-H-Sr-Cl-Br-Pb-Zn-Mg), trace element studies on fluids and gangue minerals, and paleo-hydrological modelling (e.g., Kessen et al., 1981; Garven et al., 1999; Bau et al., 2003; Wilkinson et al., 2005b; Shouakar-Stash et al., 2007; Wilkinson, 2010; Pfaff et al., 2011; Staude et al., 2011; Fußwinkel et al., 2013; Walter et al., 2015). In many well-studied mining districts (such as the Alaskan Brooke Range, the south East Basin and the Massif Central in France, the Irish Midlands ,the Maestrat basin and the Catalan Coastal Ranges in Spain and Upper Silesia in Poland) mixing of hotter, deep-seated fluids from the crystalline basement with cooler, sediment-derived fluids from the overburden has been suggested to be the major process causing hydrothermal mineral precipitation (e.g., Banks et al., 2002; Leach et al., 2004, Boiron et al., 2010; Aquilina et al., 2011; Richard et al., 2015). In general, the basement-derived fluids are assumed to represent the dominant metal source, whereas the sedimentary fluids are typically metal-poor (Banks et al., 2000a, 2002; Boiron et al., 2002; Fußwinkel et al., 2013; Bons et al., 2014). Most previous studies focused on the metal-rich basement fluids, although the importance of a sedimentary fluid component was noticed and attention was drawn to the “fluid from above” (Yardley, 2005; Boiron et al., 2010; Bons et al., 2014; Fusswinkel et al., 2014). However, studying these sedimentary fluids in more detail is difficult, if the former sedimentary aquifers overlying the basement rocks are

57 presently missing, because they were partly or completely eroded (e.g. Schwarzwald (Geyer and
58 Gwinner, 2011), Spessart (Wagner et al., 2010), Harz (Lüders and Möller, 1992), Irish Midlands
59 (O`Keeffe 1986; Wilkinson, 2010)) and the sedimentary overburden may be heterogeneous with
60 respect to thickness and composition on the scale of a mining district.
61 The present study, which focuses on the fluids from "above", derives information on the today eroded
62 sedimentary strata archived in fluid inclusions of hydrothermal vein-type deposits that are dominantly
63 situated in the crystalline basement close to or below the basement-cover unconformity. For our study
64 we chose the Schwarzwald mining district in SW Germany, because it is an exceptionally well-
65 investigated area. Previous studies include detailed mineralogical, microthermometric and isotopic
66 investigations on specific ore deposits (e.g. Baatartsogt, 2006, 2007; Fußwinkel et al., 2013; Markl et
67 al., 2006; Pfaff et al., 2010; Schwinn et al., 2006; Staude et al., 2007, 2009, 2010a, 2011a, 2012a, b;
68 Ströbele et al., 2012; Walter et al., 2015, 2016), stable isotope data (Staude et al., 2011a, 2012a,
69 2012b; Walter et al., 2015), trace element data for common ore minerals of the district, such as fahlore
70 and sphalerite (Staude et al., 2010b; Pfaff et al., 2011), age-dating (Pfaff et al., 2009), paleo-
71 hydrological modelling (Pfaff et al., 2010; Staude et al., 2011a; Walter et al., 2015,2016), studies on
72 the composition of modern thermal, mineral and formation waters (Stober & Bucher 1999, 2010;
73 Möller et al. 1997; Loges et al., 2012; Göb et al., 2013), hydraulic data (Stober & Bucher 2004),
74 detailed studies on the regional geology (Ziegler, 1990, Geyer and Gwinner, 2011) and experimental
75 leaching studies (Bucher and Stober, 2002; Burisch et al., 2016a).
76 The modern water column in the Schwarzwald shows a compositional stratification with HCO_3^- being
77 the dominant anion at shallow crustal levels (<2 km), while SO_4^{2-} is dominant at intermediate depths
78 and Cl^- at depths >2-3 km (Bucher & Stober, 2010). The processes responsible for this stratification
79 are, however, unclear (Stober and Bucher, 1999; Frape et al., 2003).
80 The Cl/Br-ratio of fluids is often used as a reservoir tracer (Stober & Bucher, 1999; Boiron et al.,
81 2010; Wilkinson, 2010; Fußwinkel et al., 2013). Deep crustal brines are known to have Cl/Br-ratios
82 <100, while halite dissolution brines show Cl/Br-ratios higher than that of sea water (288). Halite
83 precipitation in evaporites results in the formation of residual bittern brines, which show successively
84 decreasing Cl/Br-ratios (288-34) with increasing degree of evaporation (Frape and Fritz, 1987;

McCaffrey et al., 1987; Edmunds and Savage, 1991; Banks et al., 2000b; Stober and Bucher, 2004a; Stober and Bucher, 2004b; Möller et al., 2005; Yardley, 2005). We focus here on the qualitative source information provided by Cl/Br-systematics of fluids, in contrast to other contributions, which focus on the formation of low-Cl/Br-ratios and the development of high salinities in basement brines (Burisch et al., 2016a; Walter et al., 2016). Although water-rock interaction with crystalline rocks can result in low Cl/Br ratios (Bucher and Stober, 2002), Burisch et al. (2016a) showed that fluids with salinities above 20 wt.% and low Cl/Br-ratios can only be formed involving an externally derived bittern brine.

2. Regional geology

2.1. Geological setting

The Schwarzwald (Fig. 1) mainly consists of metasedimentary gneisses, migmatites and granites, representing a deeply eroded basement window. Gneisses are mostly paragneisses with local occurrences of orthogneisses and amphibolites that were metamorphosed during Variscan (Carboniferous) collisional processes (Geyer and Gwinner, 2011). These metamorphic rocks were intruded between 335 and 315 Ma by post-collisional granites, which today form about 50% of the exposed Schwarzwald basement (Todt, 1976; Altherr et al., 2000; Hann, 2003). These crystalline basement rocks are covered by a Paleozoic and Mesozoic sedimentary sequence (Geyer and Gwinner, 2011; and references therein).

During the Permian (Rotliegend), local sedimentary basins (thickness ≤500m) were filled by redbeds (arkoses, conglomerates; Jenkner, 1986; Nitsch and Zedler, 2009; Geyer and Gwinner, 2011) and local rhyolithic volcanism produced lavaflows and volcanoclastic sediments with a thickness of ≤250m (Geyer and Gwinner, 2011). Early Triassic, quartzitic Buntsandstein units reach a thickness of ≤400m in the northern and <50 m in the southern Schwarzwald. The Buntsandstein is an important aquifer and is locally separated from the Middle Triassic by the Rötton aquitard. Middle Triassic (Muschelkalk) units, including limestones, shales and evaporites (the latter only being present in the Middle Muschelkalk) reach thicknesses from 160 to 220m (Stober & Bucher, 2014) in the area of interest. In paleo-depressions, these units contain a halite-bearing horizon, which will be important for

113 the discussion below. This halite-bearing unit reaches its maximum thickness of about 100m in the
114 centres of these depressions whereas in shallower areas its thickness successively decreases. At paleo-
115 topographic heights transitions from halite-dominated to sulphate-dominated horizons occur. In
116 contrast, Late Triassic (Keuper) units are dominantly composed of clastic sediments and evaporitic
117 gypsum. The thickness of this unit varies between about 300m in the north to <100m in the south.
118 During the Jurassic an approximately 1000m thick unit of mostly marine carbonates were deposited
119 (Geyer and Gwinner, 2011).
120 Exhumation of the area since late Cretaceous was strongly asymmetric: In the south, rocks that were
121 situated about 2000m below the basement-cover unconformity are exposed, while in the north, the
122 exposed stratigraphic depth is about 100 m above the unconformity (Rupf and Nitsch, 2008; Geyer
123 and Gwinner, 2011; Fig. 2). A large displacement fault exists in the Elztal area, which is responsible
124 for the observation, that hydrothermal veins exposed at the surface now vary in their formation depth
125 from several 100 meters in the northern to more than 2.5 km in the southern Schwarzwald (Staude et
126 al., 2010; 2011; 2012; Walter et al., 2015a). Therefore, hydrothermal veins that formed at the same
127 time but at different stratigraphic depth are presently exposed in the Schwarzwald, which makes this
128 region particularly suited for studying fluid composition changes with depth. Associated with the late
129 Upper Rhinegraben rifting, Paleogene sediments of up to 4000 m thickness occur in the Upper
130 Rhinegraben, including Oligocene halite-bearing evaporites (Stober & Bucher, 2014).
131
132 *2.2. Previous studies of ore-forming processes in the Schwarzwald*
133 More than 1000 mineralized hydrothermal veins are documented in the Schwarzwald mining district
134 (Metz et al., 1957; Bliedner & Martin, 1986; Staude et al., 2009; Markl 2015). They consist
135 dominantly of barite, fluorite, quartz and carbonates besides base and precious metal oxides, sulfides
136 and arsenides (Fe-Mn, Cu-Pb-Zn and Ag-Bi-Co-Ni-U). Five maxima of hydrothermal vein formation
137 are known, comprising late-Carboniferous quartz-tourmaline veins, Permian quartz veins with rare Sb
138 mineralizations, Triassic-Jurassic quartz-hematite veins, Jurassic-Cretaceous fluorite-barite-quartz-
139 carbonate veins with Pb-Zn-Cu, Fe-Mn and rare Ag-Bi-Co-Ni-U ores, and post-Cretaceous quartz-
140 barite-fluorite or carbonate veins with Pb-Zn-Cu-(As) ores (Staude et al., 2012; Pfaff et al., 2009,

141 Walter et al., 2016).

142 Abundant ore formation occurred over the Jurassic-Cretaceous period in an extensional setting related
143 to the break-up of the North Atlantic (Staude et al., 2009). During this time, the sedimentary stack was
144 mostly undisturbed (in contrast to the geological situation during the Paleogene related to the Upper
145 Rhine Graben rifting). Numerous previous studies provide evidence that the observed fluid inclusion
146 composition found in these veins can be explained by mixing of a metal-rich basement brine and a
147 metal-poor halite dissolution brine (Staude et al., 2009, 2010, 2011, 2012a, 2012b, Ströbele et al.,
148 2012, Pfaff et al., 2011; Walter et al., 2015, 2016). The asymmetric exhumation of the crystalline
149 basement (see above) enables a direct comparison of Jurassic-Cretaceous hydrothermal veins from
150 different crustal levels. Although the large-scale Jurassic topography is assumed to have been flat,
151 exact depth estimations are not possible because the topography probably varied locally, as did the
152 absolute amount of exhumation. Therefore, the difference in stratigraphic depth of formation we are
153 referring to is only of a qualitative to semi-quantitative nature.

154 For many ore districts, hydrogeological models contradict geochemical models (e.g. Boiron et al.,
155 2010; Kendrick et al., 2011), since the emplacement of a meteoric fluid to great depths followed by
156 mixing with a second fluid on its ascent is difficult to explain from a hydrogeological point of view
157 (e.g. to bring down fluids with similar high salinity or density is not possible by gravity-driven
158 infiltration, Bons et al., 2014 and references therein). The major driving force for vertical fluid flow is
159 assumed to be the consumption of water at depth due to alteration of primary minerals (Stober &
160 Bucher 2004).

161 For the Jurassic-Cretaceous hydrothermal veins of the Schwarzwald district, however, a
162 hydrogeological mixing model, which is in agreement with geochemical (e.g. Cl/Br-mass ratios,
163 salinity, formation temperature) and hydrogeological observations (e.g. hydraulic fracturing) is
164 available (Stober & Bucher, 2004; Bons et al., 2014; Walter et al., 2016). Compositional and isotope
165 data for Jurassic-Cretaceous fluid inclusions confirm binary mixing between a basement brine and a
166 sedimentary formation fluid (Pfaff et al., 2010, 2011; Staude et al., 2009; 2010a, 2010b, 2011, 2012a,
167 Ströbele et al., 2012; Fußwinkel et al., 2013; Walter et al., 2015, Walter et al., 2016). The basement
168 brine is typically highly saline (22±2 wt% $NaCl+CaCl_2$) and metal-rich (Zn, Pb) with a Cl/Br below

150 (Fußwinkel et al., 2013, Walter et al., 2016). The sedimentary fluid is equally saline but less metal-rich and partly exhibits high Cl/Br-ratios (up to 10.000), indicating the dissolution of halite (Stober and Bucher, 1999; 2014; Stober 2014, Walter et al., 2016). The only possibility for developing such high Cl/Br-fluids during the Jurassic was interaction with Triassic evaporites, since at that time the southern margin of the marine evaporate-bearing Zechstein facies ended in the very northern part of the Schwarzwald (Geyer & Gwinner, 2011 and references therein).

3. Sample material

Samples with centimetre-sized euhedral crystals of fluorite, barite, quartz and carbonates were selected based on the following criteria: (1) veins that formed unambiguously during the Jurassic-Cretaceous (based on structural, chemical and age-dating arguments, see details in Pfaff et al., 2011 and Walter et al., 2016), (2) abundant gangue minerals with homogeneous fluid inclusions of high salinity (22-28 wt.% $NaCl+CaCl_2$) with a maximal variance of ±2 wt.% salinity ($NaCl+CaCl_2$) within a given sample and (3) no detectable overprint by post-Cretaceous low- to high-salinity fluids (see Staude et al., 2009, 2010, 2011, 2012a, b, Walter et al., 2015, 2016). Samples, which did not meet criterion (3) were excluded, since an overprint by post-Cretaceous fluids, which interacted with Oligocene halite in the Upper Rhinegraben, possibly would have distorted the Jurassic Cl/Br-signature (see Stober & Bucher, 1999, Walter et al., 2015, 2016). Samples from the Paleogene MVT deposit at Wiesloch are an exception, since they are younger than the Jurassic veins, but they are still older than the Oligocene salt deposits related to the Rhinegraben rift (Pfaff et al., 2010; Geyer and Gwinner, 2011). Therefore, they formed under undisturbed hydrogeological conditions and show Cl/Br systematics almost similar to the Jurassic veins.

Only gangue minerals (crystals up to 4cm) without visible impurities were analysed to minimize potential contamination. For Jurassic hydrothermal veins, which consist of more than one gangue mineral, several co-genetic gangue minerals (quartz, barite, fluorite or calcite) of the same vein were analysed whenever possible.

In most of the veins, silicification of the host rock pre-dates the formation of hydrothermal veins. On the top of these silicified selvages, coarse-grained fluorite and/or barite precipitated. In many veins,

this stage was followed by the formation of clear, euhedral, coarse-grained quartz. There are significant differences in vein mineralogy correlating with the geographic and stratigraphic position of the respective veins. Veins from the northern Schwarzwald are either barite-quartz or fluorite-barite veins with Cu-Bi mineralization, veins from the central Schwarzwald are fluorite±barite-(carbonate-quartz) veins with Pb-Zn, Fe-Mn or U-Bi-Co-Ni mineralizations, and veins from the southern Schwarzwald are fluorite-quartz-barite veins with Pb-Zn ores.

4. Analytical procedure

Samples from 51 veins from the northern, central and southern Schwarzwald (Fig. 1) were analysed by microthermometry (in fluorite, quartz and carbonate) and 84 samples (fluorite, quartz, carbonate and barite) were crushed and leached and subsequently analysed by a combination of ion chromatography (IC) and total reflection X-ray fluorescence (TXRF). When possible, several samples of one vein were analysed in order to avoid possible nugget effects and to check the reproducibility of the results. In total of 188 crush-leach analyses were performed. For most samples, new heating-freezing experiments were done to characterize the fluid inclusions, but the dataset also includes 20 samples, for which microthermometric and crush-leach data already existed from former studies (Staude et al., 2012; Walter et al., 2015, 2016). The complete dataset is given in the electronic supplement.

4.1 Microthermometry

Cross sections through each hydrothermal vein (perpendicular to the longitudinal extent of the veins) with up to three double polished thick sections (200 to 400µm) were produced and the chronological sequence of fluid inclusions (fluid inclusion assemblages, FIA, Goldstein and Reynolds, 1994) was determined by optical microscopy. Fluid inclusions were classified as primary (p), pseudo-secondary (ps), secondary (s), isolated inclusions (iso) and clusters of inclusions with no geometrical relation to former crystal surfaces or fractures (c). Microthermometric investigations were performed using a Linkam stage (model THMS 600). Each fluid inclusion was analysed three times for its final melting temperature of ice ($T_{m,ice}$) and hydrohalite ($T_{m,hh}$) and its homogenization temperature (T_h). Synthetic H_2O, H_2O-NaCl and H_2O-CO_2 standards were used for calibration and only fluid inclusions for which

225 triple analyses differ less than 0.1°C for $T_{m,ice}$ and $T_{m,hh}$ and 1°C for T_h were used for interpretation.
226 Fluid inclusion trails with strong deviation in salinity (> ±2wt.% NaCl + $CaCl_2$) and homogenization
227 temperature (> ±10°C) within a homogeneous trail were neglected, since this indicates fluid inclusion
228 alteration by post-entrapment processes. The salinity in the ternary NaCl-$CaCl_2$-H_2O system was
229 calculated according to Steele-MacInnes et al. (2011). For each fluid inclusion the degree of filling
230 was estimated based on filling degree tables (Shepherd et al., 1985; Bakker and Diamond, 2006). A
231 pressure correction (Bodnar and Vityk, 1994) was applied assuming hydrostatic conditions with a
232 depth of the water column inferred from the paleo-depth estimated by (Geyer and Gwinner, 2011).
233 Uncertainties of this approach are discussed in Walter et al. (2015). Since the salinity for the Jurassic-
234 Cretaceous fluid inclusions of the Schwarzwald is invariably high, pressure corrections have only
235 minor effects on the homogenization temperature. As microthermometry of fluid inclusions in barite is
236 difficult because fluid inclusions are often destroyed during freezing, data obtained from fluid
237 inclusion in barite were only used for calculating salinities in cases where the data agreed with data
238 from quartz, fluorite or calcite of the same or a related vein and were excluded from Ca/(Ca+Na)-
239 calculations.
240
241 *4.2 Major, minor and trace element composition of fluid inclusions*
242 From 188 samples that contained only one fluid type (as determined by microthermometry prior to
243 crush-leach analysis), about 2g of fluorite, quartz, calcite or barite (grain size of 0.5 to 1 mm) were
244 handpicked to avoid visible impurities. These separates were first washed for 3 hours in HNO_3 at 60-
245 70°C (the carbonates were washed in Milli-Q water only) and subsequently washed for one week with
246 ultrapure water, changing the water twice a day. These samples were then dried and crushed in an
247 agate mortar. Subsequently, 10 ml ultrapure water was added, which was acidified with suprapure
248 HNO_3 to suppress adsorption of doubly-charged cations (especially Ca^{2+}; Köhler et al., 2009). The
249 loaded solutions were injected into a Dionex ICS 1000 ion chromatography systems, equipped with an
250 IonPac AS 9-HC 2mm column for quantification of anions (F, Cl, Br, NO_3, PO_4 and SO_4) and an
251 IonPac CS 12-A column for cations (Li, Na, K, Mg, Ca, Ba, Sr). For injection of the solutions, we
252 used disposable syringe filters CROMAFILE® Xtra RC-20/25 and CROMAFILE® Xtra PVDF-20/25

253 for anions and cations, respectively (Ladenburger 2012, and Ladenburger et al., 2012). Blank runs
254 were carried out before and after each analysis and defined standard solutions were regularly analyses
255 to monitor the reproducibility and precision of the measurements. Uncertainties were usually smaller
256 than 15% and effective detection limits were generally <10 mg/l. Absolute concentrations were
257 calculated based on the salinity determined by microthermometry using Cl as internal standard.
258 The concentrations of several trace metals (Mn, Fe, Co, Ni, Cu, Zn, As, Se, Rb, Y, W, Tl, Pb, Bi, Th
259 and U were determined by TXRF using a S2 PICOFOX (Bruker AXS Microanalysis) equipped with a
260 Mo-tube operated with a 50 kV and 600µA. Each 1 ml of the crush-leach solutions (see above) were
261 centrifuged and filtered. Subsequently, each 190 µl of the solutions were mixed with 10 µl Ga solution
262 with a Ga concentration of 5 mg/l. Three aliquots (10µl) were pipetted onto polished quartz-glass disks
263 and dried at 70°C. The dried sample cakes were then analysed for 1000 s. The effective detection
264 limits for trace metals in the recalculated fluid are in the order of 10-50 mg/l, depending on the
265 dilution factor of the analysed solution. Absolute metal concentrations were obtained by normalizing
266 the measured values to the Cl concentrations determined by microthermometry.
267
268 *4.3 Analytical uncertainties*
269 Quartz, barite, calcite and fluorite were used for crush-leach analyses. A contamination of the
270 leachates by dissolution of host minerals is potentially relevant for fluorite (Ca, F), calcite (Ca, Mg)
271 and barite (Ba, Sr, SO_4). The complete dataset in the electronic supplement includes these elements,
272 but their concentrations in the respective inclusions were excluded from interpretation. Many of our
273 crush-leach solutions contain dissolved carbonate from fluid inclusions (as indicated by the presence
274 of CO_2 based on Raman spectroscopy) and we assume that the positive deviations from electrical
275 neutrality can be ascribed to carbonate species, as has been done before (e.g. Bottrell et al., 1988;
276 Channer and Spooner, 1991; Banks et al., 2000; Dolnischek et al. 2014). This has, however, no impact
277 on the reliability of Cl and Br data in the crush-leach analyses and especially not on the Cl/Br mass-
278 ratios, nor on the quality of the microthermometric data (Ca-Na variations, salinity or homogenization
279 temperatures).
280 Crush-leach solutions were carefully filtered and centrifuged before analysis to exclude potential

281 contamination because of suspended particles of ore minerals. Some analyses revealed very high metal
282 contents (up to about 55000 mg/l Pb and 52000 mg/l Cu). To evaluate the validity of these analyses
283 we performed calculations using Geochemists Workbench Version 10.0.2. Using the compositions of
284 BW163 and STD2 (table 2 of the electronic supplement), at neutral pH, fO_2 of sulfide stability and
285 150°C the model shows that these high Pb and Cu concentrations are still well below the saturation of
286 Pb and Cu minerals in these particular solutions (0.7 mol/l Pb (~145 g/l) and 10 mol/l Cu (~635 g/l).
287
288 **5. Results**
289 We focus our presentation here on the microthermometric data and important element ratios (molar
290 Ca/(Na+Ca)-; Cl/Br- and Pb/Zn-mass ratios). The recalculated fluid compositions are given in tables 1
291 and 2, the complete dataset is available as electronic supplement. All investigated fluid inclusions
292 exhibit high salinities (18-28 wt.% $NaCl+CaCl_2$) with homogenization temperatures (T_h) between 50
293 and 192°C (Fig. 3A-C; Table 2 of the electronic supplement). Freezing temperatures vary between -70
294 and -100°C. First melting occurs above -50°C implying a ternary $NaCl-CaCl_2-H_2O$ system with a
295 eutectic temperature at -52.0°C, and ice and hydrohalite as last-melting phases. The final melting
296 temperature of ice is in the range of -9.4° to -36.9°C, of hydrohalite between -2.3° to -50.9°C. The
297 molar Ca/(Ca+Na)-ratios were calculated according to Steele-MacInnis et al. (2011) and range from
298 0.1 to 0.9 (Fig. 3A, D, E, F & G). In a given fluid inclusion trail, salinity and T_h do not significantly
299 vary between individual fluid inclusions, but can vary between different trails within one sample. In
300 the following, we present our data sorted by geographical and stratigraphic position in the basement,
301 starting with the lowermost veins of the southern Schwarzwald.
302
303 *5.1 Southern Schwarzwald (veins up to 2km below the basement-cover unconformity)*
304 The Jurassic-Cretaceous veins of the southern Schwarzwald show salinities of 18-26 wt.%
305 ($NaCl+CaCl_2$). The Cl/Br-ratios are variable (33±7 to 1139±228) and molar Ca/(Na+Ca)-ratios range
306 between 0.09 and 0.4. Homogenization temperatures range from 77 to 198°C (weighted average of
307 140°C), (Pb + Zn) contents reach 56.000 mg/l (Fig. 4) .
308

309 *5.2 Central Schwarzwald (veins close to the basement-cover unconformity)*

310 The Jurassic-Cretaceous veins of the central Schwarzwald show higher salinities than those of the
311 southern Schwarzwald of 23-27 wt.% ($NaCl+CaCl_2$). The Cl/Br ratios show relatively small variations
312 (37±7 to 133±27) with a weighted average around 90. The Ca/(Na+Ca)-ratios range between 0.21 and
313 0.89, in average higher than those from southern Schwarzwald fluids (Fig. 3A, B C and F).
314 Homogenization temperatures range from 59-159°C (weighted average of 120°C), maximum (Pb +Zn)
315 contents reach 20.000 mg/l (Fig. 4) .

316

317 *5.3 Northern Schwarzwald and Wiesloch MVT deposit (veins above the basement-cover unconformity)*

318 Two fluid types are observed in the northern Schwarzwald (Fig. 3A, C & F): the first one shows the
319 highest salinities (up to 27 wt.% $NaCl+CaCl_2$) with Ca/(Na+Ca)-ratios of 0.24-0.43, Cl/Br-mass-ratios
320 of 56±11 to 89±18, very similar to fluids observed in central Schwarzwald veins (see above). The fluid
321 inclusions show homogenization temperatures of 50 to 148°C. The second fluid type exhibits lower
322 salinities (20-24 wt.%. $NaCl+CaCl_2$), variable Cl/Br-ratios (125±25 to 340±68, Pfaff et al., 2010) and
323 lower Ca/(Na+Ca)-ratios (0.08-0.21), similar to the fluid observed in southern Schwarzwald veins.
324 Homogenization temperatures range from 60-136°C (weighted average of 110°C), maximum (Pb +
325 Zn) contents reach 6.800 mg/l.

326

327 **6. Discussion**

328 *6.1. Ca-Na and Cl-Br variations*

329 Although the fluid chemistry of Jurassic-Cretaceous hydrothermal veins (Fig. 3A-H) shows large
330 overlaps, it correlates with geographic/stratigraphic position and can be divided into three groups:
331 Hydrothermal veins in the northern and central Schwarzwald, which are at present exposed at the
332 surface, occur in sedimentary and basement rocks few hundred meters above and below the basement-
333 cover unconformity, while in the southern Schwarzwald they are hosted exclusively by crystalline
334 basement rocks far below (>2000 m) the unconformity. Hence, the classification into the three groups
335 (southern, central and northern Schwarzwald) is analogous to deep, intermediate and shallow
336 formation depth (Fig. 2). However, because of uncertainties in absolute overburden thickness, the

337 division into the three groups is of qualitative rather than quantitative character and no absolute
338 overburden values can be derived.
339 Mixing models based on microthermometry, LA-ICPMS analyses of single fluid inclusions, stable and
340 radiogenic isotopes and trace element contents of fahlore and sphalerite (Pfaff et al., 2011; Staude et
341 al., 2012; Fusswinkel et al. 2013) imply that the fraction of sedimentary fluid involved in the
342 formation of a specific mineralization is higher in the central and northern Schwarzwald (where the
343 veins are in proximity to the evaporite-bearing Muschelkalk aquifer) than in the south (where the veins
344 are >2 km below the Muschelkalk aquifer; Pfaff et al., 2011; Staude et al., 2009; 2010b; 2011a; 2012a;
345 2012b; Ströbele et al. 2012; Walter et al. 2015). However, the distribution of Cl/Br-ratios implies that
346 other factors than the stratigraphic depth of formation control the Cl/Br ratio. While high Cl/Br-ratios
347 (Figs. 3G & H) above the sea water ratio (288) occur in the northern Schwarzwald (including the post-
348 Cretaceous Wiesloch MVT deposit), veins from the central Schwarzwald have Cl/Br-ratios of 90 ± 30,
349 typical of basement fluids that did not dissolve halite (Frape and Fritz, 1987; Banks et al., 2000b;
350 Stober and Bucher, 2004; Yardley, 2005). On the other hand, veins from the deepest stratigraphic
351 levels in the southern Schwarzwald show again variable Cl/Br-ratios above the sea water ratio (up to
352 1140), possibly indicating the influence of a halite-bearing aquifer in the sedimentary cover (Fig. 3H).
353 The observed Cl/Br-variations can be explained using paleo-topography models for the Permian and
354 Triassic when a topographic high existed in the central Schwarzwald area and halite-bearing
355 evaporites were deposited north, south and east of it. Evaporites in the central Schwarzwald, however,
356 did not significantly exceed the anhydrite stage (Fig. 5; Ziegler, 1990; Hansch & Simon, 2003; Rupf
357 and Nitsch, 2008; Geyer and Gwinner, 2011). Thus, in contrast to the north and the south, the
358 sedimentary fluid in the central Schwarzwald appears to have never interacted with a halite-bearing
359 aquifer. This is in good agreement with elevated slightly higher mole Ca/(Ca+Na)-ratios and
360 invariably low Cl/Br-mass-ratios for fluids in the central Schwarzwald fluid inclusions (Figs. 3A, D,
361 E, F, G & 5). In contrast, the sedimentary fluids in the north and south interacted with halite and as a
362 consequence, fluid inclusions exhibit variable Cl/Br (33 to 1139) and relatively lower Ca/(Ca+Na)-
363 mole ratios of 0.1-0.4 (Figs. 3A, D, E, F, G & 6). In addition to the high Ca/(Ca+Na)- and low Cl/Br-
364 ratios, hydrothermal fluid inclusion data from the central Schwarzwald show elevated SO_4 contents for

numerous samples (Fig. 7A & B), for those data an analytical bias can be excluded. We suggest that this is because the sedimentary fluid involved in hydrothermal vein formation interacted with anhydrite/gypsum-bearing sediments (Fig. 7C). Sulphide oxidation can be excluded as a dominant source for the observed SO_4^{2-} concentration, since these sulphate-rich fluid inclusions are restricted to the central Schwarzwald: sulphide oxidation would have affected also fluids in the northern and southern Schwarzwald, since sulphides are present everywhere in the crystalline basement rocks

As a consequence, it can be assumed that the emanation of the bittern brines (in early Triassic times) was restricted to the north and the south (where halite precipitated). There, the basin was apparently deeper (Fig. 6), since bittern brines only form as a result of halite precipitation (see seawater evaporation line in Fig. 6 in Walter et al., 2016). Therefore, the bittern brine with the inherited low Cl/Br-ratio had to percolate a significantly longer distance (vertically and laterally) through the crystalline basement to the central Schwarzwald, compared to the north and south.

We assume that the downward migrating fluid (bittern brine or sedimentary fluid) did not significantly mix with other fluids at shallow crustal levels, since the high fracture density and the occurrence of large scale fracture zones enables a fast downward movement in the uppermost part of the crust. Reaching deeper crustal levels, fast vertical fluid movement is promoted by fracture orientation, which is preferably vertical (Brown and Hoek, 1978). With increasing depth, the abundance of well-developed fracture networks decreases, favouring lateral dissemination of fluids, which benefits a stratification of fluid in deeper parts of the brittle crust (Fig. 6A). The general driving force for large scale vertical fluid movements are most likely desiccation processes caused by the consumption of H_2O during mineral alteration at depth as described by Stober and Bucher 2004 and Bons et al. 2014.

Using the hydraulic conductivity given by Stober and Bucher (2007), average flow velocities around 10^{-6} and 10^{-8} m/s (in granite and gneiss, respectively) can be assumed in 4 km depth. A rough estimate of the time that bittern brines need to travel from the surface (north and south) to a depth of 10 km (depth slightly above of brittle-ductile transition) in the central Schwarzwald results in 1000 – 100.000 years. Taking into account that the hydraulic conductivity further decreases at depths below 4 km, using an extremely low average fluid velocity of 10^{-10} m/s over the entire rock column, the travel time still does not exceed 9 Ma. This calculation shows that there was sufficient time between the

393 formation and downward migration of bittern brines during evaporite formation in the Triassic and the
394 first occurrence of basement brines with low Cl/Br involved in Jurassic vein formation (Walter et al.,
395 2016).
396
397 *6.2 Salinity variations*
398 In addition to variations in their major element composition, the fluid salinities of the northern, central
399 and southern Schwarzwald veins are quite variable including large overlaps (Figs. 3A, B, C & F).
400 Based on the observation that the amount of sedimentary fluid involved in vein formation decreases
401 from north to south, one could expect a gradual increase in the salinity (due to the higher proportion of
402 highly saline basement fluid). This is, however, not the case, since the hydrothermal veins in the
403 southern Schwarzwald show lower salinities (Fig. 3C) than those observed in the northern and central
404 Schwarzwald. According to Bons et al. (2014) and Walter et al. (2016), a layer of a late-metamorphic,
405 low-salinity fluid with low Cl/Br (initially formed during the Permian) was situated below the highly
406 saline basement brine, since this fluid migrated into the basement before the late Triassic bittern brine
407 arrived. This fluid did not mix substantially with the modified bittern brine and therefore the former
408 fluid stratification was preserved (Bons et al., 2014). Since the hydrothermal veins in the southern
409 Schwarzwald formed at greater stratigraphic depths, it is likely that these hydrothermal veins
410 incorporated fluid batches of basement fluids, which include relatively small amounts of late-
411 metamorphic fluids situated below the Jurassic basement brine (Bons et al. 2014). The involvement of
412 small amounts of low-salinity metamorphic fluid batches in hydrothermal vein formation might
413 explain the slightly lower salinity in fluid inclusions from the southern Schwarzwald. This “mixing
414 from below” (Bons et al., 2014) dilutes the deep-seated brine’s salinity (Fig. 6), while the halogen
415 signature (low Cl/Br) remains unchanged.
416
417 *6.3 Minor and trace element variations*
418 Independent from the fluid information from “above”, certain trace elements (especially Pb and Zn) in
419 the mixed fluid show some mentionable features, which can be compared to results of previous studies
420 (e.g. Yardley, 2005; Wilkinson et al., 2005a, b, 2009, 2010; Richard et al., 2016, Burisch et al., 2016a,

421 b; Walter et al., 2016). Most of the authors furnish evidence for a major metal source in the crystalline
422 basement (e.g. Banks et al., 2000a, 2002; Boiron et al., 2002; Fußwinkel et al., 2013; Bons et al.,
423 2014).
424 The overall trace element concentrations of fluid inclusions of each district show large variations
425 including significant overlaps (table 2, ES I, Fig. 4). Reasons for the large spread in their absolute
426 concentrations are diverse and include local hydrogeological anomalies, precipitation of ore minerals
427 in deeper parts of the same vein and/or local anomalies of the mixing ratio during ore precipitation.
428 Trace metals are much more affected by these processes than e.g. Cl and Br, which results in complex
429 chemical variations. Hence, the large scatter in the most solutes is not surprising. Nevertheless, based
430 on the maximum and average concentrations of Pb, Zn, (Fig. 4A, B & C) two major features are
431 recognized: (I) A difference in maximum concentrations of Pb and Zn in the deep basement (southern
432 Schwarzwald) to much lower maximum values, around the basement-cover unconformity (central
433 Schwarzwald) (Figs. 4A-C) and (II) variation in the Pb/Zn-ratio with increasing depth of formation
434 (Fig. 4C).
435 Field observations (vein and ore mineralogy) confirm a decrease of Pb + Zn mineralization, with
436 decreasing formation depth (Fig. 4B), advancing the unconformity in the mineralization outcrops.
437 Breakdown of feldspar and biotite due to interaction between the basement fluid and its surrounding
438 rock increases the Pb + Zn (Fig. 4A, B & C) in the basement fluid (Wilkinson et al., 2005a, Yardley
439 2005, Burisch et al., 2016a, b, Walter et al., 2016). Therefore, the maximum (Pb + Zn) content
440 increases with stratigraphic depth due to advanced reaction times between fluid and rock. Since Pb and
441 Zn behave geochemically similar (Burisch et al., 2016a), a variation in the Pb/Zn-ratio cannot simply
442 be explained by water-rock interaction or fractionation processes (see Fig. 4C). If galena precipitated
443 preferably in deeper veins compared to sphalerite, a fractionation of Pb and Zn would be the
444 consequence, but no observation supports such a mechanism (Metz et al., 1957). Therefore, we
445 suggest an additional source of Zn within the sedimentary cover (Fig. 4A). The prime candidate would
446 be the Muschelkalk, which is one of the Zn-richest lithologies in SW Germany and Zn can easily be
447 leached out of the carbonate rock (Martin, 2009). Therefore, the decrease in the Pb/Zn-ratio (Fig. 4C)
448 is most likely an effect of the basement brine's mixing with an additional Zn-rich, Pb-depleted

sedimentary fluid. This is in agreement with the model of Bons et al. (2014) and further supports its validity, because the fluids derived from the Muschelkalk limestone aquifer in the southern Schwarzwald (because the Permian is missing and the Buntsandstein pinches out towards the south) should be the main constituent of the fluid layer right above the "basement brine" in the stratified fluid section during the Jurassic-Cretaceous in the Schwarzwald.

Conclusion

The combination of literature data with a large set of fluid inclusion compositions from discontinuity-related hydrothermal veins of different formation depth allowed us to design a model that explains large-scale lateral and vertical chemical variations. Ore-forming fluids record information about the sedimentary rocks/aquifers from which they originated. Based on detailed regional geology, systematic fluid inclusion analyses of hydrothermal veins can in some cases be used to reconstruct eroded sedimentary units, if there was a recognizable difference in paleo-aquifer chemistry at the time of formation. Careful investigation of base metal contents in such fluids may allow the identification of specific fluid sources and a qualitative estimate of mixing ratios can be deduced from such data. Therefore, base metal variations may have the potential to serve as reservoir tracer in hydrothermal systems. Trace element differences provide evidence for metal variations governed by the host aquifers of the fluids involved in mixing processes. The sedimentary fluids are in most cases not the dominant source of Pb and Zn, but limestone-derived fluids may introduce additional Zn, which has a significant impact on the Pb/Zn-ratio, but not so much on absolute concentrations in ore-forming fluids.

Acknowledgments

We would like to thank Ingrid Stober, her comments improved this manuscript substantially. Edgar Nitsch (LGRB) is gratefully acknowledged for invaluably hints of the paleo-topography of the sedimentary cover in SW-Germany. We thank Gabi Stoschek and Bernd Steinhilber for their help with crush-leach analyses. Furthermore we thank S. Kaulfuß and P. Jeiseke for sample preparation. This study was supported by the Alfried-Krupp Prize for Young University Teachers of the Krupp

Foundation to Gregor Markl and the German Research Foundation (DFG), grant Ma2135/20-1.

References cited:

Altherr R, Holl A, Hegner E, Langer C, Kreuzer H (2000) High-potassium, calc-alkaline I-type plutonism in the European Variscides: northern Vosges (France) and northern Schwarzwald (Germany), Lithos 50, 51-73.

Aquilina L, Boulvais P, Mossmann J-R (2011) Fluid migration at the basement/sediment interface along the margin of the southeast basin (France): implications for Pb–Zn ore formation. Mineralium Deposita, 46, 959-979.

Baatartsogt B, Wagner T, Taubald H, Mierdel K, Markl G (2006) Hydrogen isotope determination of fluid inclusion water from hydrothermal fluorite: The results depend on the extraction technique. Chemical Geology, 1-21.

Baatartsogt B, Schwinn T, Wagner T, Taubald H, Beitter T, Markl G (2007) Contrasting paleofluid systems in the continental basement: a fluid inclusion and stable isotope study of hydrothermal vein mineralizations, Schwarzwald district, Germany. Geofluids, 7, 1-25.

Bakker RJ, Diamond LW (2006) Estimation of volume fractions of liquid and vapor phases in fluid inclusions, and definition of inclusion shapes. American Mineralogist, 91, 635-657.

Banks D, Boyce A, Samson I (2002) Constraints on the origins of fluids forming Irish Zn-Pb-Ba deposits: Evidence from the composition of fluid inclusions. Economic Geology, 97, 471-480.

Banks D, Green R, Cliff R, Yardley B (2000) Chlorine isotopes in fluid inclusions: determination of the origins of salinity in magmatic fluids. Geochimica et Cosmochimica Acta, 64, 1785-1789.

Bau M, Romer RL, Lüders V, Dulski P (2003) Tracing element sources of hydrothermal mineral deposits: REE and Y distribution and Sr-Nd-Pb isotopes in fluorite from MVT deposits in the Pennine Orefield, England. Mineralium Deposita, 38, 992-1008.

Behr HJ, Gerler J (1987) Inclusions of sedimentary brines in post-Variscan mineralizations in the Federal Republic of Germany—a study by neutron activation analysis. Chemical Geology, 61, 65-77.

Behr HJ, Horn EE, Frentzel-Beyme K, Reutel C (1987) Fluid inclusion characteristics of the Variscan and post-Variscan mineralizing fluids in the Federal Republic of Germany. Chemical Geology, 61, 273-285.

Bliedtner M, Martin M (1986) Erz- und Minerallagerstätten des Mittleren Schwarzwaldes. LGRB, Freiburg. 786 pp

Bodnar RJ, Vityk MO (1994) Interpretation of microthermometric data for H_2O-NaCl fluid inclusions. In: De Vivo B, Frezzotti ML (eds) Fluid inclusions in minerals, methods and applications. Virginia Tech, Blacksburg,. 117-130.

Boiron M-C, Cathelineau M, Banks DA, Fourcade S, Vallance J (2003) Mixing of metamorphic and surficial fluids during the uplift of the Hercynian upper crust: consequences for gold deposition. Chemical Geology 194, 119-141.

Boiron M-C, Cathelineau M, Banks DA, Buschaert S, Fourcade S, Coulibaly Y,

523 Michelot JL, Boyce A (2002) Fluid transfer at a basement/cover interface. Part II.
524 Large-scale introduction of chlorine into the basement by Mesozoic basinal brines.
525 Chemical Geology 192, 121-140.
526 Boiron MC, Cathelineau M, Richard A (2010) Fluid flows and metal deposition near
527 basement/cover unconformity: lessons and analogies from Pb-Zn-F-Ba systems for the
528 understanding of Proterozoic U deposits. Geofluids, 10, 270-292.
529 Bons PD, Fusswinkel T, Gomez-Rivas E, Markl G, Wagner T, Walter B (2014) Fluid
530 mixing from below in unconformity-related hydrothermal ore deposits. Geology,
531 42(12), 1035-1038.
532 Bottrell SH, Yardley BWD, Buckley F (1988). A modified crush-leach method for
533 the analysis of fuid inclusion electrolytes. Bulletin de Mineralogie, 111, 279-290.
534 Brown E, Hoek E (1978) Trends in relationships between measured in-situ stresses and
535 depth, International Journal of Rock Mechanics and Mining Sciences &
536 Geomechanics Abstracts. Elsevier, 211-215.
537 Bucher K, Stober I (2002) Water-rock reaction experiments with Black Forest gneiss and
538 granite. Water Science and Technology Library, 40, 61-95.
539 Bucher K, Stober I (2010) Fluids in the upper continental crust. Geofluids, 10(1-2), 241-253.
540 Burisch M, Marks M, Novak M, Markl G (2016a). The importance of temperature and
541 cataclastic deformation for halogen (F, Cl, Br) systematics and metal transport
542 capacities of continental basement brines – an experimental approach. Chemical
543 Geology, doi:10.1016/j.chemgeo.2016.03.031
544 Burisch M, Walter BF, Wälle M, Markl G. (2016b) Tracing fluid migration pathways in the
545 root zone below unconformity-related hydrothermal veins: Insights from trace element
546 systematics of individual fluid inclusions. *Chemical Geology*, *429*, 44-50.
547 Duane M, De Wit M (1988) Pb-Zn ore deposits of the northern Caledonides: Products
548 of continental-scale fluid mixing and tectonic expulsion during continental collision.
549 Geology, 16, 999-1002.
550 DeR Channer DM, Spooner ETC (1992) Analysis of fluid inclusion leachates from
551 quartz by ion chromatography. Geochimica et Cosmochimica Acta, 56(1), 249-259.
552 Dolníček Z, René M, Hermannová S, Prochaska W (2014) Origin of the Okrouhlá
553 Radouň episyenite-hosted uranium deposit, Bohemian Massif, Czech Republic: fluid
554 inclusion and stable isotope constraints. Mineralium Deposita, 49(4), 409-425.
555 Edmunds WM, Savage D (1991) Geochemical characteristics of groundwater in granites
556 and related crystalline rocks. Applied Groundwater Hydrology, a British Perspective
557 (eds DowningRA, WilkinsonWB), 199-216.
558 Frape S, Blyth A, Blomqvist R, McNutt R, Gascoyne M (2003) Deep fluids in the
559 continents: II. Crystalline rocks. Treatise on geochemistry 5, 541-580.
560 Frape S, Fritz P (1987) Geochemical trends for groundwaters from the Canadian Shield.
561 Geological Association of Canada Special Papers, 33, 19-38.
562 Fußwinkel T, Wagner T, Wälle M, Wenzel T, Heinrich C, Markl G (2013) Fluid
563 mixing forms basement-hosted Pb-Zn deposits: Insight from metal and halogen
564 geochemistry of individual fluid inclusions. Geology, 41, 679-682.
565 Fusswinkel T, Wagner T, Wenzel T, Wälle M, Lorenz J (2014) Red bed and basement
566 sourced fluids recorded in hydrothermal Mn–Fe–As veins, Sailauf (Germany): A LA-
567 ICPMS fluid inclusion study. Chemical Geology, 363, 22-39.
568 Garven G, Appold MS, Toptygina VI, Hazlett TJ (1999) Hydrogeologic modeling of
569 the genesis of carbonate-hosted lead-zinc ores. Hydrogeology Journal 7, 108-126.
570 Geyer OF, Gwinner MP (2011) Geologie von Baden -Württemberg. – 5., völlig neu
571 bearbeitete Auflage. Schweizerbart`sche Verlagsbuchhandlung (Nägele u.
572 Obermiller), Stuttgart, 627pp
573 Göb S, Loges A, Nolde N, Bau M, Jacob DE, Markl G (2013) Major and trace

element compositions (including REE) of mineral, thermal, mine and surface waters in SW Germany and implications for water-rock interaction. Applied Geochemistry, 33, 127-152

Goldstein RH, Reynolds TJ (1994) Systematics of fluid inclusions in diagenetic minerals: SEPM Short Course 31. Society for Sedimentary Geology, 199.

Hann HP,Chen F, Zedler H, Frisch W, Loeschke J (2003) The rand granite in the southern Schwarzwald and its geodynamic significance in the variscan belt of SW Germany. International Journal of Earth Sciences, 92, 821-842.

Hansch W, Simon T (2003) Das Steinsalz aus dem Mittleren Muschelkalk Südwest-deutschlands. - museo, 20, 152-159

Jenkner B (1986) Ein Vorschlag zur Neugliederung des sedimentären Oberrotliegenden in der Baden-Badener Senke und ihrer nordöstlichen Fortsetzung (Nordschwarzwald). Jahrbuch des Geologischen Landesamtes Baden-Württemberg, 28, 49-159.

Kendrick M, Honda M, Oliver N, Phillips D (2011) The noble gas systematics of late-orogenic H_2O–CO_2 fluids, Mt Isa, Australia. Geochimica et Cosmochimica Acta 75, 1428-1450.

Kessen K, Woodruff M, Grant N (1981) Gangue mineral 87 Sr/86 Sr ratios and the origin of Mississippi Valley-type mineralization. Economic Geology, 76, 913-920.

Klemm L, Pettke T, Graeser S, Mullis J, Kouzmanov K (2004) Fluid mixing as the cause of sulphide precipitation at Albrunpass, Binn Valley, Central Alps. Schweizer Mineralogische und Petrologische Mitteilungen, 84, 189-212.

Köhler J, Schönenberger J, Upton B, Markl G (2009) Halogen and trace-element chemistry in the Gardar Province, south Greenland: subduction-related mantle metasomatism and fluid exsolution from alkalic melts. Lithos, 113(3), 731-747.

Ladenburger S (2012) Crush-Leach Analysen an Flüssigkeitseinschlüssen von hydrothermalen Erzlagerstätten des Schwarzwaldes. Unpublished BSc Thesis, Tübingen, 134p.

Ladenburger S, Marks M, Markl G (2012) Analysis of crush leach solutions from hydrothermal ore deposits by combining ion chromatography (IC) and total reflection X-ray fluorescence spectroscopy (TXRF).

Leach DL, Marsh E, Emsbo P, Rombach CS, Kelley KD, Anthony M (2004) Nature of Hydrothermal Fluids at the Shale-Hosted red Dog Zn-Pb-Ag Deposit, Brooks Range, Alaska. Economic Geology, 99, 1449-1480.

Loges A, Wagner T, Kirnbauer T, Göb S, Bau M, Berner Z, Markl G (2012) Source and origin of active and fossil thermal spring systems, northern Upper Rhine Graben, Germany. Applied Geochemistry 27, 1153-1169.

Lüders V, Möller P (1992) Fluid evolution and ore deposition in the Harz Mountains (Germany). European Journal of Mineralogy, 4, 1053-1068.

Markl G, Lahaye Y, Schwinn G (2006) Copper isotopes as monitors of redox processes in hydrothermal mineralization. Geochimica et Cosmochimica Acta, 70, 4215-4228.

Markl G (2015) Schwarzwald - Lagerstätten und Mineralien aus vier Jahrhunderten. Bode Verlag, Salzhemmendorf. Volume I, 672 p

Martin M (2009) Geogene Grundgehalte (Hintergrundwerte) in den petrogeochemischen Einheiten von Baden-Württemberg. LGRB-Informationen, 24, 98.

Matter A, Peters TJ, Bläsi H-R, Meyer J, Ischni H, Meyer C (1988a) Sondierungsbohrung Weiach Nagra Techn. Ber. 86-01. Nagra, Wettingen, 438pp.

Matter A, Peters TJ, Bläsi H-R, Schenker F, Weiss H-P (1988b) Sondierungsbohrung Schafisheim. Nagra Techn. Ber. 86-03. Nagra, Baden, 321pp.

McCaffrey M, Lazar B, Holland H (1987) The evaporation path of seawater and the coprecipitation of Br^- and K^+ with halite. Journal of Sedimentary Research 57, 928-937.

McCaig AM, Tritlla J, Banks DA (2000) Fluid mixing and receycling during Pyrenean thrusting: Evidence from fluid inclusion halogen ratios. Geochimica et Cosmochimica Acta, 64, 3395-3412.

Metz R, Richter M, Schürenberg H (1957) Die Blei-Zink-Erzgänge des Schwarzwaldes. Beiheft Geologisches Jahrbuch, 29, 277.

Möller P, Stober I, Dulski P (1997) Seltenerdelement-, Yttrium-Gehalte und Bleiisotope in Thermal- und Mineralwässern des Schwarzwaldes. Grundwasser, 2(3), 118-132.

Möller P, Woith H, Dulski P, Lüders V, Erzinger J, Kämpf H, Pekdeger A, Hansen B, Lodemann M, Banks DA (2005) Main and trace elements in KTB-VB fluid: composition and hints to its origin. Geofluids 5, 28-41.

Nitsch E, Zedler H (2009) Oberkarbon und Perm in Baden-Württemberg. . LGRB-Information 22, 7-102.

O'Keeffe W (1986) Age and postulated source rocks for mineralization in central Ireland as indicated by lead isotopes, in Andrew, C.J., Crowe, R.W.A., Finlay, S., Pennell, W.M., and Pyne, J., eds. Geology and genesis of mineral deposits in Ireland: Dublin, Irish Association for Economic Geology, 617-624.

Pfaff K, Hildebrandt LH, Leach DL, Jacob DE, Markl G (2010) Formation of the Wiesloch Mississippi Valley-type Zn-Pb-Ag deposit in the extensional setting of the Upper Rhinegraben, SW Germany. Mineralium Deposita, 45, 647-666.

Pfaff K, Koenig MA, Wenzel T, Ridley I, Hildebrandt LH, Leach D., Markl G (2011) Trace and minor element variations and sulfur isotopes in crystalline and colloform ZnS: Incorporation mechanisms and implications for their genesis. Chemical Geology, 286, 118-134.

Pfaff K, Romer RL, Markl G (2009) U-Pb ages of ferberite, chalcedony, agate, "U-mica" and pitchblende: constraints on the mineralization history of the Schwarzwald ore district. European Journal of Mineralogy, 21, 817-836.

Richard A, Cathelineau M, Boiron MC, Mercadier J, Banks DA, Cuney M (2015) Metal-rich fluid inclusions provide new insights into unconformity-related U deposits (Athabasca Basin and Basement, Canada). *Mineralium Deposita*, 1-22.

Rupf I, Nitsch E (2008) Das Geologische Landesmodell von Baden-Württemberg: Datengrundlagen, technische Umsetzung und erste geologische Ergebnisse.Landesamt für Geologie, Rohstoffe und Bergbau Baden-Württemberg. LGRB-Information, 21.

Schwinn G, Wagner T, Baatartsogt B, Markl G (2006) Quantification of mixing processes in ore-forming hydrothermal systems by combination of stable isotope and fluid inclusion analyses. Geochimica et Cosmochimica Acta, 70, 965-982.

Shepherd TJ, Rankin AH, Alderton DH (1985) A practical guide to fluid inclusion studies. Blackie Glasgow, p. 239

Shouakar-Stash O, Alexeev S, Frape S, Alexeeva L, Drimmie R (2007) Geochemistry and stable isotopic signatures, including chlorine and bromine isotopes, of the deep groundwaters of the Siberian Platform, Russia. Applied Geochemistry, 22, 589-605.

Staude S, Bons PD, Markl G (2009) Hydrothermal vein formation by extension-driven dewatering of the middle crust: An example from SW Germany. Earth and Planetary Science Letters, 286, 387-395.

Staude S, Dorn A, Pfaff K, Markl G (2010a). Assemblages of Ag-Bi sulfosalts and conditions of their formation: the type locality of schapbachite ($Ag_{0.4}Pb_{0.2}Bi_{0.4}S$) and neighboring mines in the Schwarzwald ore district, southern Germany. Canadian Mineralogist, 48, 441-466.

Staude S, Göb S, Pfaff K, Ströbele F, Premo WR, Markl G (2011) Deciphering fluid sources of hydrothermal systems: A combined Sr- and S-isotope study on barite (Schwarzwald, SW Germany). Chemical Geology, 286, 1-20.

Staude S, Mordhorst T, Nau S, Pfaff K, Brügmann G, Jacob DE, Markl G (2012a)

hydrothermal carbonates of the Schwarzwald ore district, southwestern Germany: carbon source and conditions of formation using δ18O, δ13C, 87Sr/86Sr, and fluid inclusions. The Canadian Mineralogist, 50, 1401-1434.

Staude S, Mordhorst T, Neumann R, Prebeck W, Markl G (2010b) Compositional variation of the tennantite-tetrahedrite solid-solution series in the Schwarzwald ore district (SW Germany): The role of mineralization processes and fluid source. Mineralogical Magazine, 74, 309-339.

Staude S, Wagner T, Markl G (2007) Mineralogy, mineral chemistry and fluid evolution of the hydrothermal Wenzel deposit, southern Germany: implications for the formation of Kongsberg-type silver deposits. Canadian Mineralogist, 45, 1147-1176.

Staude S, Werner W, Mordhorst T, Wemmer K, Jacob D, Markl G (2012b) Multi-stage Ag–Bi–Co–Ni–U and Cu–Bi vein mineralization at Wittichen, Schwarzwald, SW Germany: geological setting, ore mineralogy, and fluid evolution. Mineralium Deposita, 47, 251-276.

Steele-MacInnes M, Bodnar RJ, Naden J (2011) Numerical model to determine the composition of H_2O-NaCl-$CaCl_2$ fluid inclusions based on microthermometric and microanalytical data. Geochimica et Cosmochimica Acta, 75, 21-40.

Stober I (1995) Die Wasserführung des kristallinen Grundgebirges. Ferdinand Enke Verlag.Stober, I., Bucher, K., 1999. Deep groundwater in the crystalline basement of the Black Forest region. Applied Geochemistry, 14, 237-254.

Stober I, Bucher K (1999) Origin of salinity of deep groundwater in crystalline rocks. Terra Nova, 11(4), 181-185.

Stober I, Bucher K (2004) Fluid sinks within the earth's crust. Geofluids 4, 143-151.

Stober I, Bucher K (2007) Hydraulic properties of the crystalline basement. Hydrogeology Journal 15, 213-224.

Stober I, Bucher K (2014) Hydraulic and hydrochemical properties of deep sedimentary reservoirs of the Upper Rhine Graben, Europe. Geofluids. DOI: 10.1111/gfl.12122

Stober I (2014) Hydrochemical properties of deep carbonate aquifers in the SW German Molasse basin. Geothermal Energy, 2(1), 1-20.

Ströbele F, Staude S, Pfaff K, Premo WR, Hildebrandt LH, Baumann A, Pernicka E, Markl G (2012) Pb isotope constraints on fluid flow and mineralization processes in SW Germany Neues Jahrbuch für Mineralogie-Abhandlungen: Journal of Mineralogy and Geochemistry 189, 287-309.

Todt W (1976) Zirkon U/Pb-Alter des Malsburg-Granits vom Südschwarzwald. Neues Jahrb Mineral Monatsh 12, 532-544.

Tornos F, Casquet C, Locutura J, Collado R (1991) Fluid inclusion and geochemical evidence for fluid mixing in the genesis of Ba-F (Pb-Zn) lodes of the Spanish central System. Min. Magazine, 55, 225-234.

Wagner T, Okrusch M, Weyer S, Lorenz J, Lahaye Y, Taubald H, Schmitt RT (2010) The role of the Kupferschiefer in the formation of hydrothermal base metal mineralization in the Spessart ore district, Germany: insight from detailed sulfur isotope studies. Mineralium Deposita, 45, 217-239.

Walter BF, Immenhauser A, Geske A, Markl G (2015) Exploration of hydrothermal carbonate magnesium isotope signatures as tracers for continental fluid aquifers, Schwarzwald mining district, SW Germany. Chemical Geology, 400, 87-105

Walter BF, Burisch M Markl G (2016) The long-term chemical evolution of continental basement brines – a field study from the Schwarzwald, SW Germany. Geofluids, DOI: 10.1111/gfl.12167

Wilkinson JJ, Stoffell B, Wilkinson CC, Jeffries TE, Appold MS (2009). Anomalously metal-rich fluids form hydrothermal ore deposits. *Science*, *323*(5915), 764-767.

Wilkinson J (2010) A review of fluid inclusion constraints on mineralization in the Irish ore

727 field and implications for the genesis of sediment-hosted Zn-Pb deposits. Economic
728 Geology, 105, 417-442.
729 Wilkinson JJ, Eyre SL, Boyce AJ (2005a) Ore-forming processes in Irish-type carbonate-
730 hosted Zn-Pb deposits: Evidence from mineralogy, chemistry, and isotopic
731 composition of sulfides at the Lisheen mine. Economic Geology, 100(1), 63-86.
732 Wilkinson J, Weiss D, Mason T, Coles B (2005b) Zinc isotope variation in hydrothermal
733 systems: preliminary evidence from the Irish Midlands ore field. Economic Geology
734 100, 583-590.
735 Yardley BWD (2005) Metal concentrations in crustal fluids and their relationship to ore
736 formation. Economic Geology, 100, 613-632.
737 Ziegler PA (1990) Geological Atlas of Western and Central Europe, Shell Internationale
738 Petroleum Maatschappij BV/Geological Society of London.
739

740 **Figure captions**
741
742 **Fig. 1.** Geological map of the Schwarzwald mining district (Southwest Germany) with sample
743 locations. The sample localities 1 to 84 refer to Table 2 in the electronic supplement. Map modified
744 after Pfaff et al. (2011)
745
746 **Fig. 2.** Schematic profile from northern to southern Schwarzwald illustrating today`s outcrop situation
747 for the hydrothermal veins. Note that asymmetric exhumation of the Schwarzwald caused today vein
748 outcrops over a stratigraphy of more than 2km. The colour-coding red (northern Schwarzwald), blue
749 (central Schwarzwald) and green (southern Schwarzwlad) is used in all following figures.
750
751 **Fig. 3.** General Characteristics of the Schwarzwald fluids. (A) Variations in molar Ca/(Na+Ca)-ratio
752 and salinity based on single fluid inclusions. Weighted average is used to compensate heterogeneous
753 numbers of fluid inclusions measured in individual samples. (B) Salinity versus uncorrected
754 homogenization temperatures. Pressure correction for these high salinity fluids is negligible. Note that
755 southern Schwarzwald fluids show lowest salinities but highest formation temperatures. In contrast,
756 fluids from the northern Schwarzwald have highest salinities and lowest average temperatures. (C)
757 Variations in salinities illustrated as boxplots, which show systematic variations (including large
758 overlaps) with formation depth. (D) Mole Ca versus mole Na content of the fluid. Variations in Ca
759 contents of the fluids based on microthermometry of individual inclusions. (E) Variation in mole Ca
760 contents based single fluid inclusion measurements. (F) Mole Ca/(Na+Ca)-ratio of the fluid versus
761 salinity.. (G) Cl/Br (crush leach) versus Ca content (microthermometry) of the fluid. Note correlation
762 of the southern and northern Schwarzwald in Cl/Br. (H) log Cl versus log Br plot. Note analyses of the
763 southern and northern Schwarzwald fall on a mixing line between a bittern brine and a halite
764 dissolution brine.
765
766 Fig. 4. (A) Distribution of Pb and Zn contents in context of the geographic position and stratigraphic
767 depth. The combination of Pb and Zn in the right diagram illustrates their similar behaviour in the
768 hydrothermal fluid. (B) Pb +Zn (assumed to be derived from crystalline basement rocks) as boxplots.

Note variation with formation depth. Southern Schwarzwald shows the highest Pb + Zn content in the fluid. (C) Pb/Zn-mass-ratio as boxplot. Highest Pb/Zn-mass-ratio can be recognized in the southern Schwarzwald.

Fig. 5. Paleo-distribution of Middle-Triassic halite sequence above the today eroded basement complex of the Schwarzwald (Map is based on Hansch & Simon (2003) and Geyer and Gwinner (2011, and references therein). Isopaches are lines of the same thickness. Furthermore the map shows the paleo-topographic features. Development of the paleo heights and depressions can be recognized since Carboniferous and Permian times. Note correlation of veins with Cl/Br ratios (black dots) with the paleo-occurrence of halite. Furthermore the veins below the paleo heights of the Muschelkalk where no halite was deposited show depleted Cl/Br ratios around 90.

Fig. 6. Formation model for the Jurassic-Cretaceous veins adopted from Walter et al. (2016) (A) during Middle Triassic halite deposition in the depressions a bittern brine migrate downwards in the basement and formed a fluid stratified section with the older metamorphic fluid. (B) In depressions (with halite sequences) of the Middle-Late Triassic a halite dissolution brine descends by a hydraulic head (Bons et al., 2014) that is triggered by desiccation processes in the crystalline basement. On topographic heights of the central Schwarzwald sulfate/carbonate dissolution brines migrate downwards. These younger late Triassic fluids formed a fluid stratified section with the older bittern brine and the deeper-seated late metamorphic fluid. (C) During Jurassic-Cretaceous pathways were opened and the fluids of the fluid stratified section ascend and mix in hydrofractures and the hydrothermal veins (red ore body) were precipitated.

Fig. 7. (A) Cl/Br versus SO_4 (crush leach data). Note high Cl/Br in the southern and northern Schwarzwald and high SO_4 in the central Schwarzwald for some of the samples. (B) SO_4 content of the plaeofluids illustrated as boxplots. Only calcite, quartz and fluorite samples are used. (C) plot illustrates three component mixing in the fluid inclusions. References noted: [1] Fußwinkel et al., 2013, [2] Göb et al., 2013

Figure 1

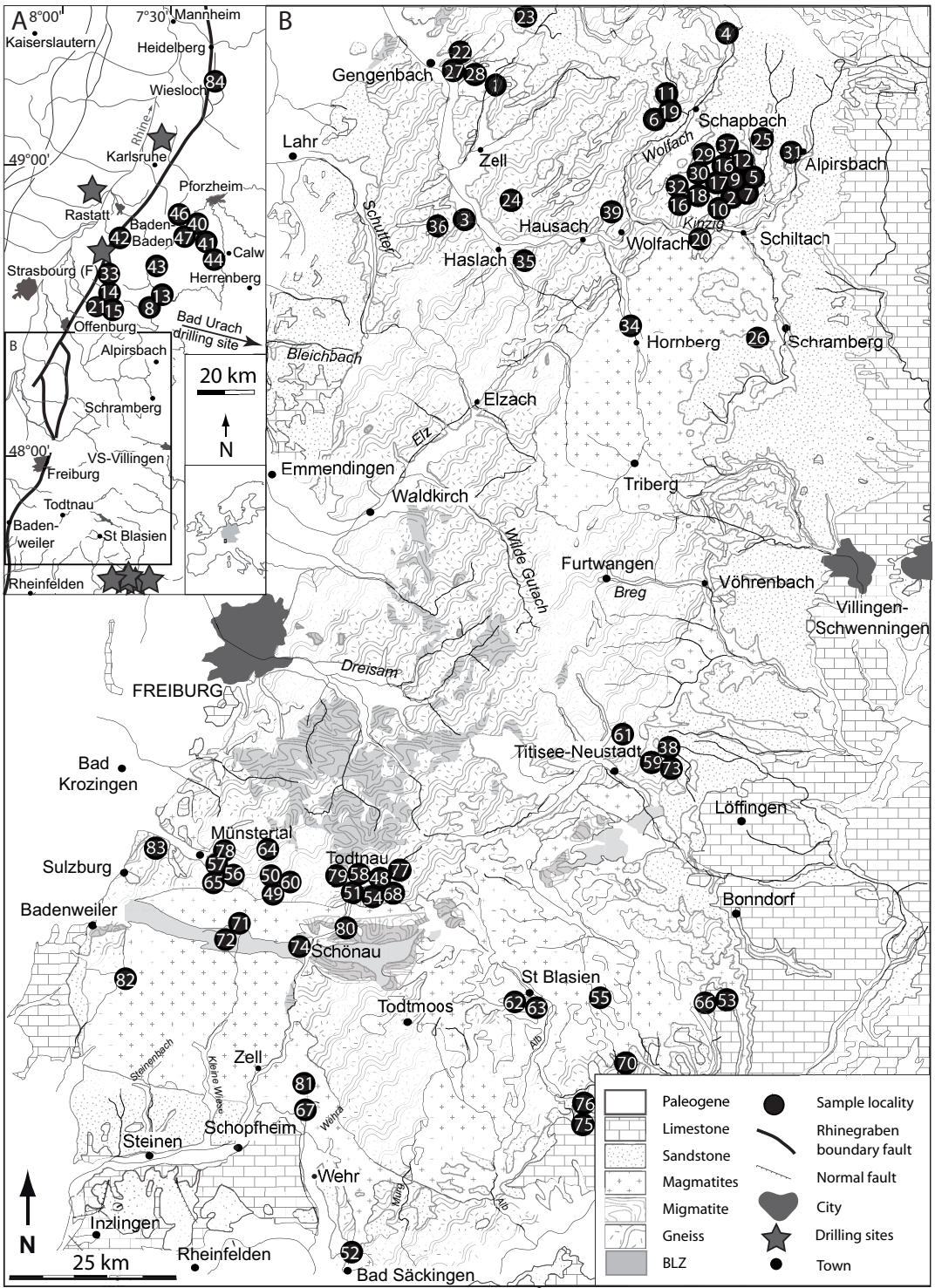
A
B
8°00'
7°30'
Mannheim
Kaiserslautern
Heidelberg
Wiesloch
Rhine
Karlsruhe
49°00'
Pforzheim
Rastatt
Baden-Baden
Calw
Strasbourg (F)
Herrenberg
Offenburg
Bad Urach drilling site
Alpirsbach
Schramberg
48°00'
VS-Villingen
Freiburg
Todtnau
Baden-weiler
St Blasien
Rheinfelden
20 km
N
Gengenbach
Lahr
Zell
Schapbach
Wolfach
Alpirsbach
Hausach
Haslach
Schiltach
Hornberg
Schramberg
Bleichbach
Elzach
Elz
Emmendingen
Waldkirch
Triberg
Furtwangen
Breg
Wilde Gutach
Vöhrenbach
Villingen-Schwenningen
Dreisam
FREIBURG
Titisee-Neustadt
Bad Krozingen
Löffingen
Münstertal
Sulzburg
Todtnau
Bonndorf
Badenweiler
Schönau
St Blasien
Todtmoos
Zell
Steinen
Schopfheim
Wehra
Wehr
Inzlingen
Rheinfelden
Bad Säckingen
25 km
Paleogene
Limestone
Sandstone
Magmatites
Migmatite
Gneiss
BLZ
Sample locality
Rhinegraben boundary fault
Normal fault
City
Drilling sites
Town

Figure 2

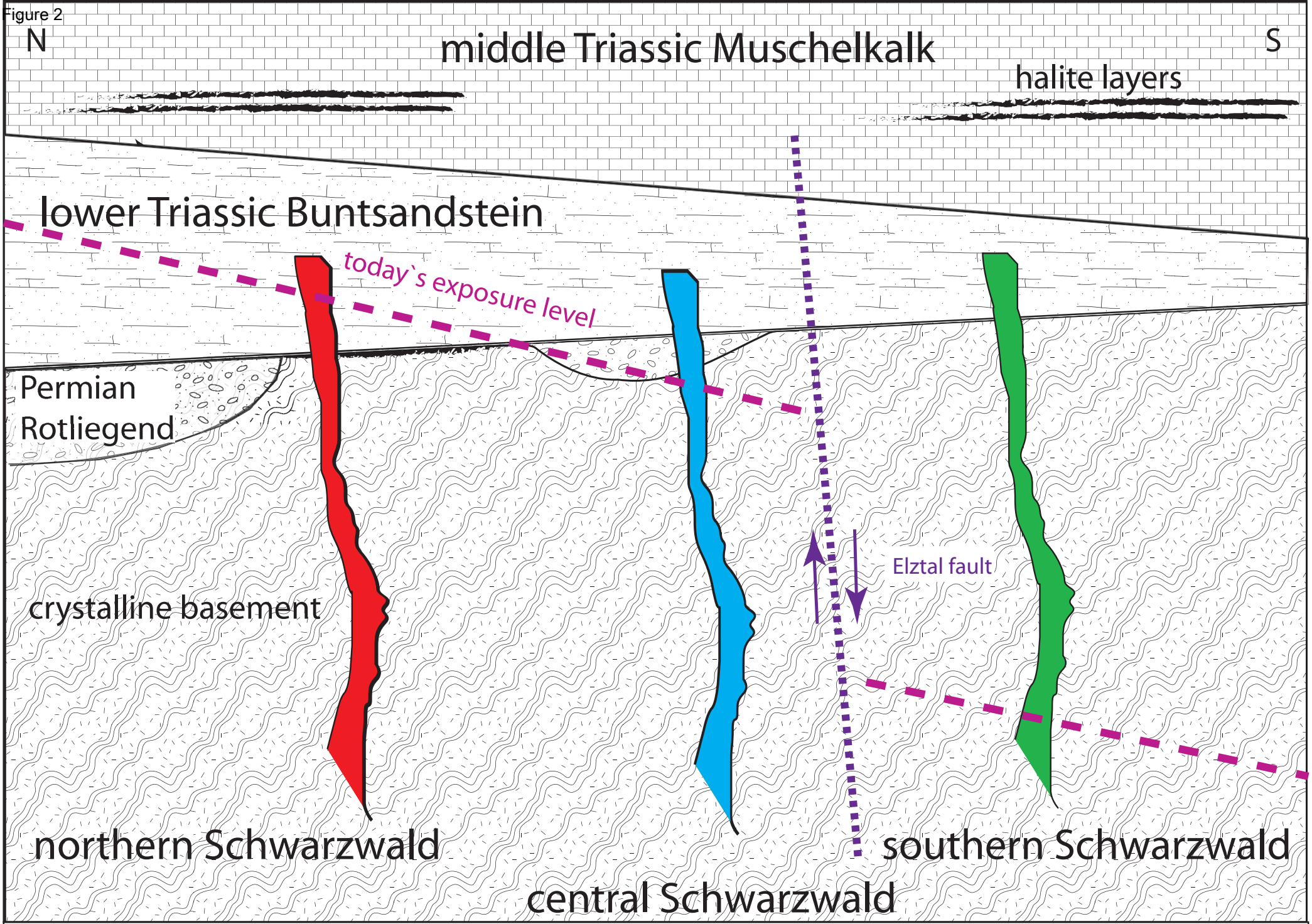
N
middle Triassic Muschelkalk
S
halite layers
lower Triassic Buntsandstein
today`s exposure level
Permian
Rotliegend
crystalline basement
Elztal fault
northern Schwarzwald
central Schwarzwald
southern Schwarzwald
granite and gneisses
clastic sediments
sandstones
limestones

Figure 3

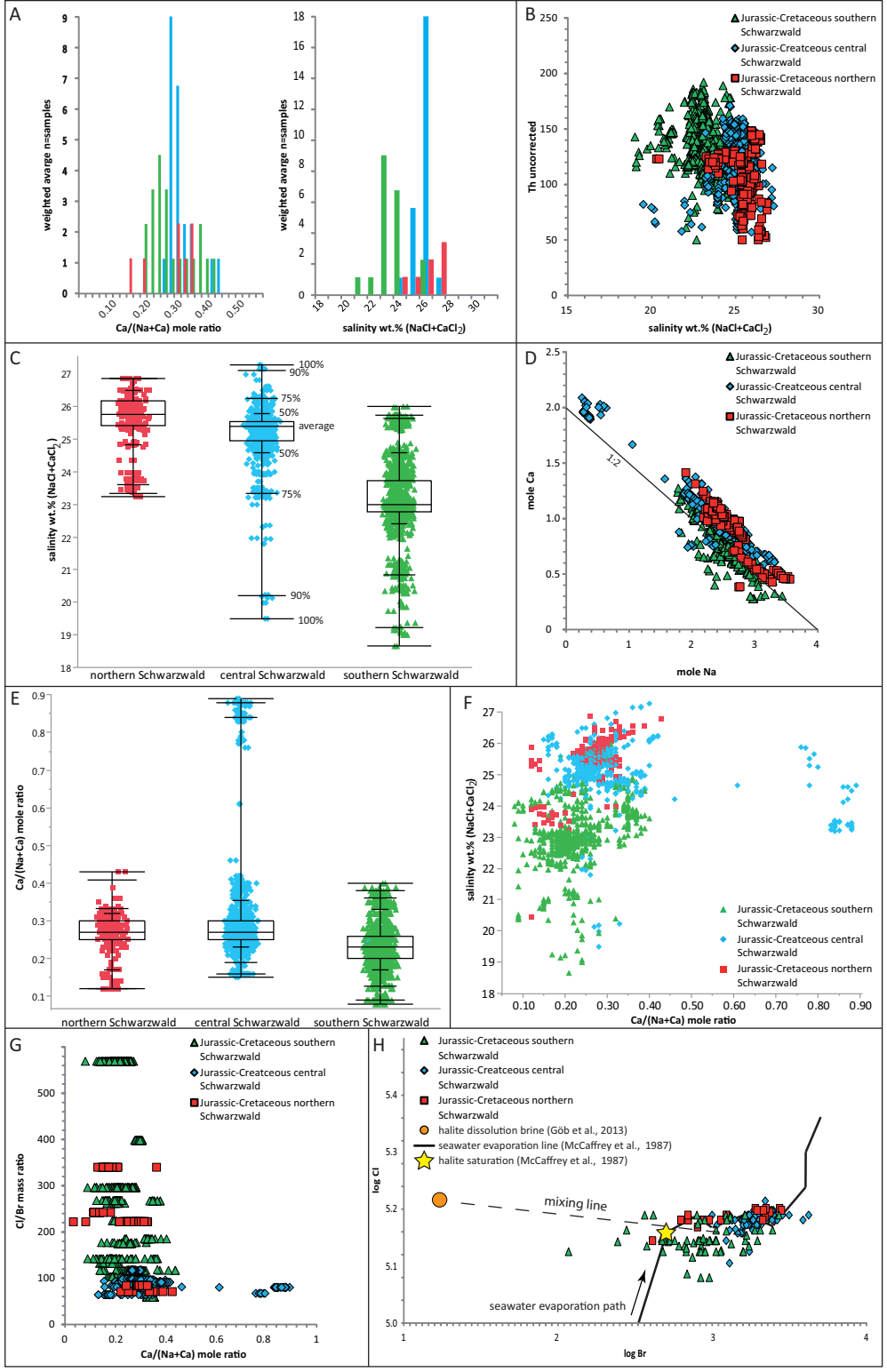
A
weighted avarge n=samples
Ca/(Na+Ca) mole ratio
salinity wt.% (NaCl+CaCl2)
B
Th uncorrected
salinity wt.% (NaCl+CaCl2)
Jurassic-Cretaceous southern Schwarzwald
Jurassic-Creatceous central Schwarzwald
Jurassic-Cretaceous northern Schwarzwald
C
salinity wt.% (NaCl+CaCl2)
100%
90%
75%
50%
average
50%
75%
90%
100%
northern Schwarzwald
central Schwarzwald
southern Schwarzwald
D
mole Ca
mole Na
1:2
E
Ca/(Na+Ca) mole ratio
northern Schwarzwald
central Schwarzwald
southern Schwarzwald
F
salinity wt.% (NaCl+CaCl2)
Ca/(Na+Ca) mole ratio
G
Cl/Br mass ratio
Ca/(Na+Ca) mole ratio
H
log Cl
log Br
halite dissolution brine (Göb et al., 2013)
seawater evaporation line (McCaffrey et al., 1987)
halite saturation (McCaffrey et al., 1987)
mixing line
seawater evaporation path

Figure 4

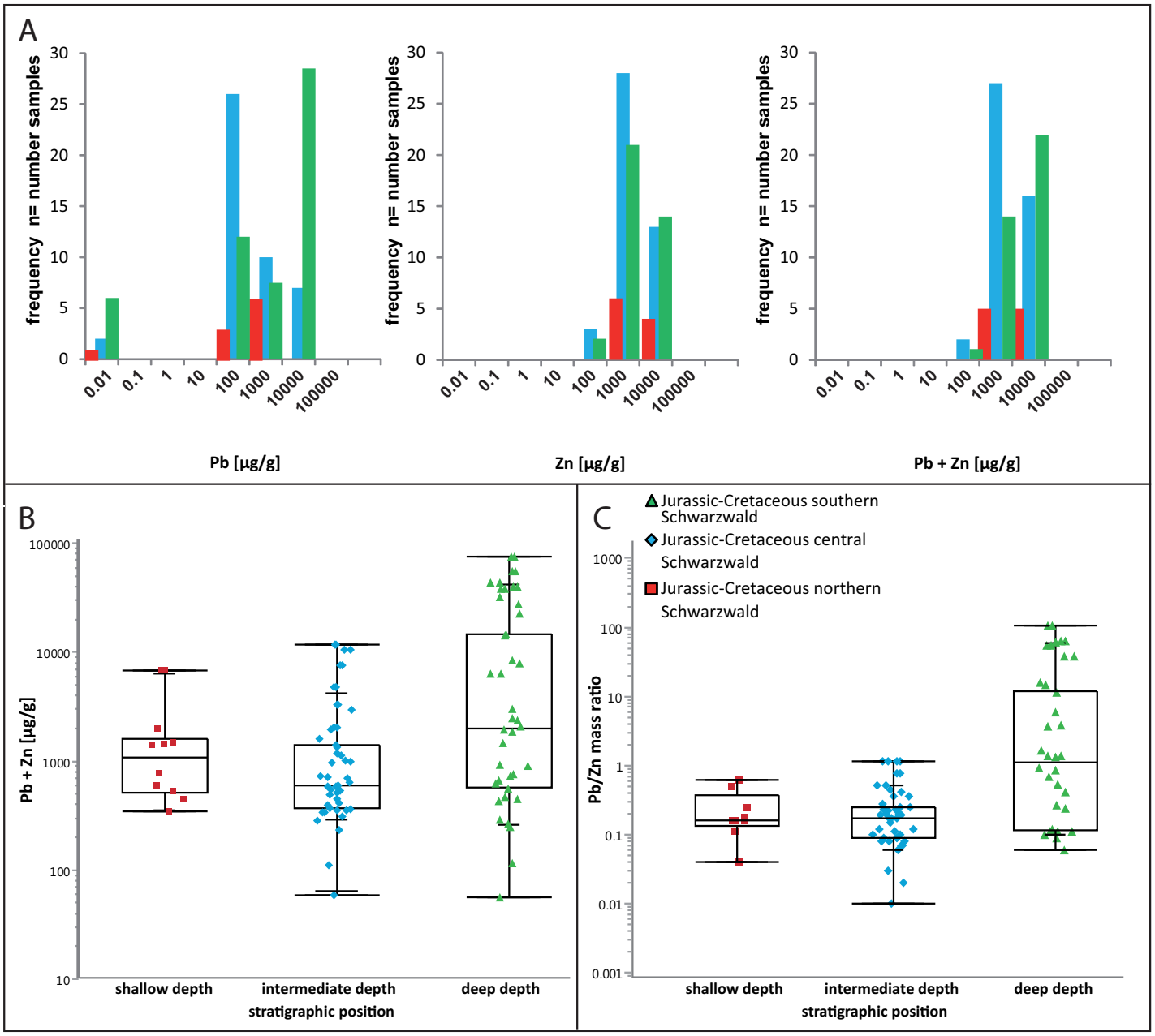
A
frequency n= number samples
30
25
20
15
10
5
0
0.01
0.1
1
10
100
1000
10000
100000
Pb [µg/g]
Zn [µg/g]
Pb + Zn [µg/g]
B
Pb + Zn [µg/g]
100000
10000
1000
100
10
shallow depth
intermediate depth
deep depth
stratigraphic position
C
Jurassic-Cretaceous southern Schwarzwald
Jurassic-Cretaceous central Schwarzwald
Jurassic-Cretaceous northern Schwarzwald
Pb/Zn mass ratio
1000
100
10
1
0.1
0.01
0.001
shallow depth
intermediate depth
deep depth
stratigraphic position

Figure 5

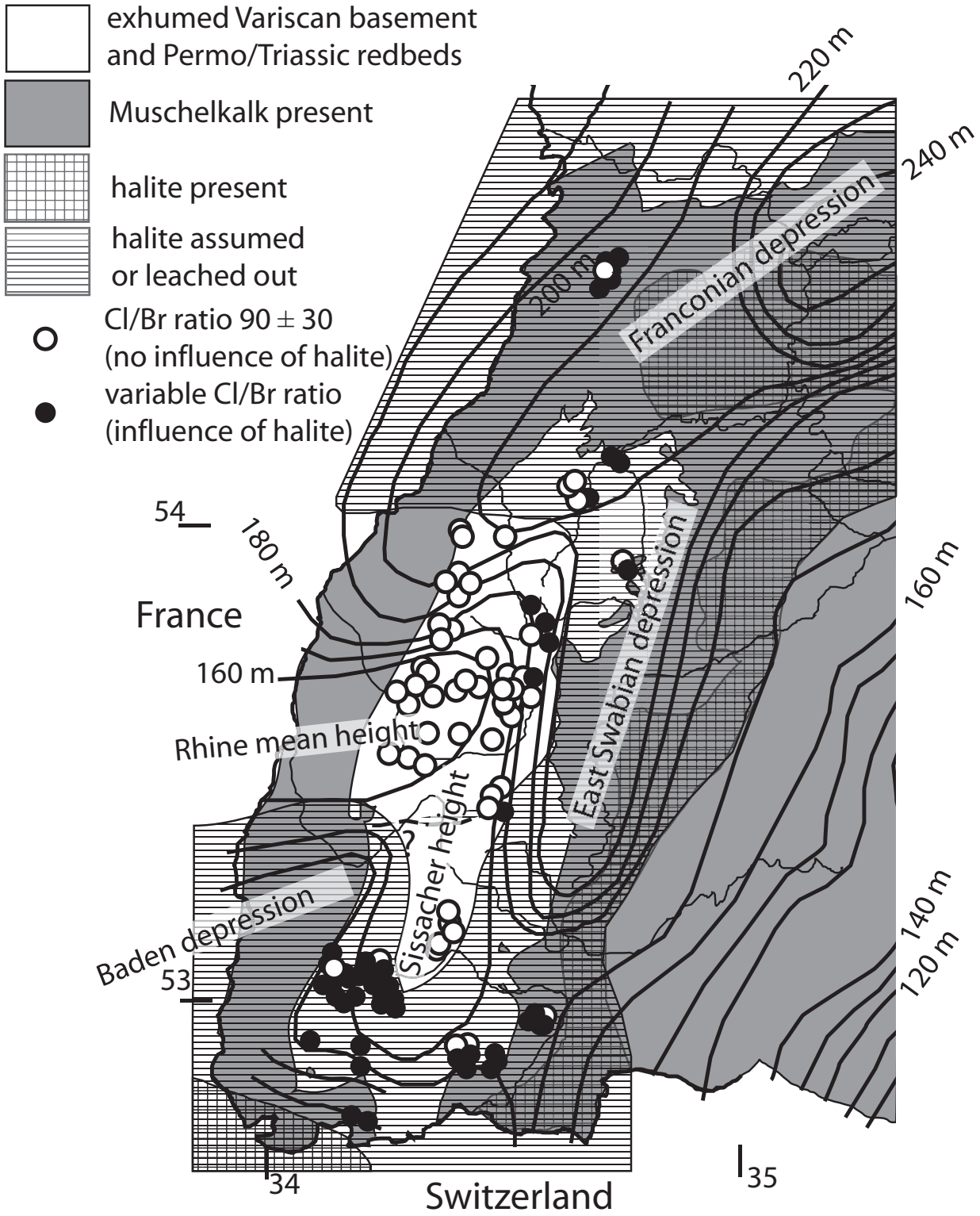
exhumed Variscan basement
and Permo/Triassic redbeds
Muschelkalk present
halite present
halite assumed
or leached out
Cl/Br ratio 90 ± 30
(no influence of halite)
variable Cl/Br ratio
(influence of halite)
220 m
240 m
200 m
Franconian depression
54
180 m
France
160 m
160 m
Rhine mean height
East Swabian depression
Sissacher height
140 m
120 m
Baden depression
53
34
35
Switzerland

Figure 6

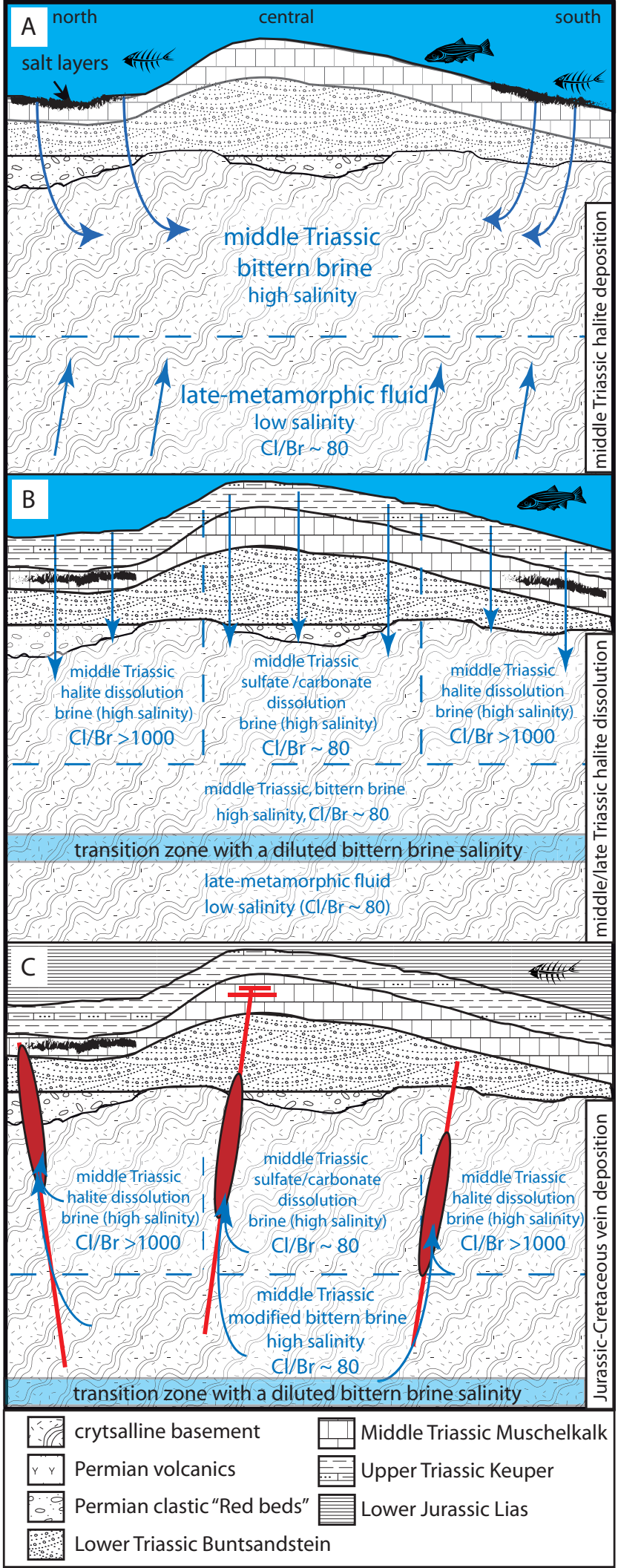
A
north
central
south
salt layers
middle Triassic
bittern brine
high salinity
late-metamorphic fluid
low salinity
Cl/Br ~ 80
middle Triassic halite deposition
B
middle Triassic
halite dissolution
brine (high salinity)
Cl/Br >1000
middle Triassic
sulfate /carbonate
dissolution
brine (high salinity)
Cl/Br ~ 80
middle Triassic
halite dissolution
brine (high salinity)
Cl/Br >1000
middle Triassic, bittern brine
high salinity, Cl/Br ~ 80
transition zone with a diluted bittern brine salinity
late-metamorphic fluid
low salinity (Cl/Br ~ 80)
middle/late Triassic halite dissolution
C
middle Triassic
halite dissolution
brine (high salinity)
Cl/Br >1000
middle Triassic
sulfate/carbonate
dissolution
brine (high salinity)
Cl/Br ~ 80
middle Triassic
halite dissolution
brine (high salinity)
Cl/Br >1000
middle Triassic
modified bittern brine
high salinity
Cl/Br ~ 80
transition zone with a diluted bittern brine salinity
Jurassic-Cretaceous vein deposition
crytsalline basement
Permian volcanics
Permian clastic "Red beds"
Lower Triassic Buntsandstein
Middle Triassic Muschelkalk
Upper Triassic Keuper
Lower Jurassic Lias

Figure 7

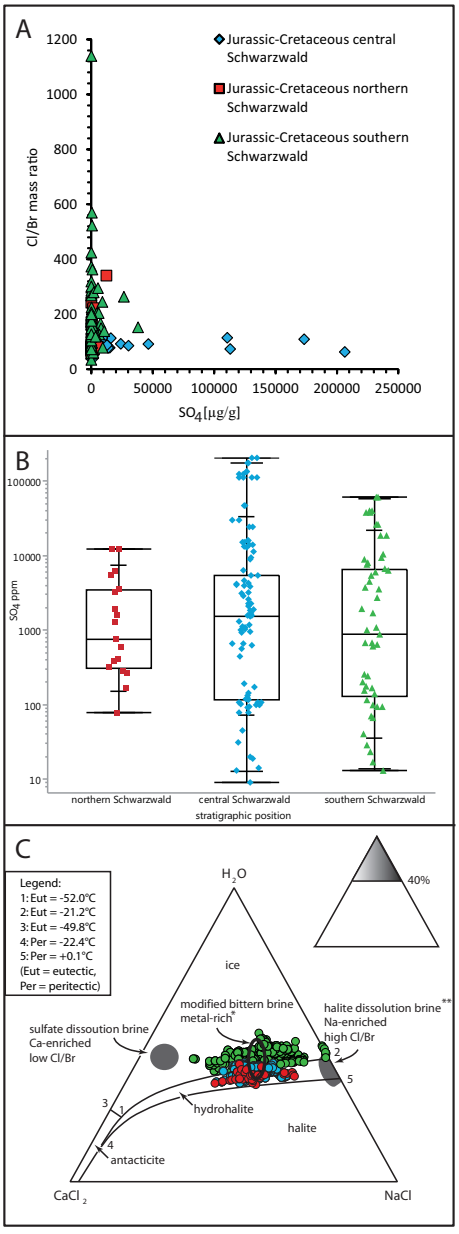
A
Jurassic-Cretaceous central Schwarzwald
Jurassic-Cretaceous northern Schwarzwald
Jurassic-Cretaceous southern Schwarzwald
Cl/Br mass ratio
1200
1000
800
600
400
200
0
0
50000
100000
150000
200000
250000
SO4 [µg/g]
B
SO4 ppm
100000
10000
1000
100
10
northern Schwarzwald
central Schwarzwald
southern Schwarzwald
stratigraphic position
C
Legend:
1: Eut = -52.0°C
2: Eut = -21.2°C
3: Eut = -49.8°C
4: Per = -22.4°C
5: Per = +0.1°C
(Eut = eutectic,
Per = peritectic)
H2O
40%
ice
modified bittern brine
metal-rich*
halite dissolution brine**
Na-enriched
high Cl/Br
sulfate dissoution brine
Ca-enriched
low Cl/Br
2
5
3
1
hydrohalite
halite
4
antacticite
CaCl2
NaCl

Table 1

Table 1 major element concentrations, recalculated paleo-fluid chemistry

map No.	location	sample	mineral	salinity wt% ($NaCl+CaCl_2$)	Cl/Br	Li ppm	Na ppm	K ppm	Mg ppm	Ca ppm	Sr ppm	Ba ppm	F ppm	Cl ppm	Br ppm	SO4 ppm
1	Amalie Nordrach	SAM3qtz	quartz	25.0	113	577	52810	59460	2996	282500		29700	3296	151660	1342	627
2	Anton Heubach	SHB12brt	barite	25.5	77	88	64120	5865	3047	36390			151	151650	1976	
3	Artenberg quarry	BW204	quartz	24.5	76	163	63700	9665	616	65140	2650	341	3973	154680	2037	569
3	Artenberg quarry	BW124	calcite	24.5	73	250	44520	3973	1672			1854	3647	154690	2124	3099
3	Artenberg quarry	BW125	calcite	25.0	67	247	44380	2875	886				175	154670	2312	951
3	Artenberg quarry	BW186fl	fluorite	25.0	57	582	87230	9063	1686			1338		151650	2640	20
4	Bad Rippoldsau Prosper	BW114	quartz	24.5	79	174	59030	7331	942	42990		1783	4238	145580	1833	922
4	Bad Rippoldsau Prosper	BW114	quartz	24.5	74	205	56340	14950	2279	66290			4794	145590	1956	2908
5	Bleibersgrund	SW153-1	fluorite	23.0	90	164	60190	3894	3092			2630		151650	1681	106
5	Bleibersgrund	SW153-2	fluorite	25.0	94	217	58610	4292	1682			515		145590	1556	79
5	Bleibersgrund	SW153-3	fluorite	25.0	88	187	61920	4113	2229			148		151650	1727	91
5	Bleibersgrund	SN153-4	fluorite	25.0	99	251	65150	6328	1209			530		151650	1539	79
5	Bleibersgrund	SN153-1	fluorite	25.0	70	270	73660	6460	4768			2552		151650	2171	19
5	Bleibersgrund	SN153-2	fluorite	25.0	66	476	76700	7145	2642			1129		157720	2402	14
5	Bleibersgrund	SN153-4	fluorite	25.0	74	365	74460	16920	2011			84760		163780	2210	118
6	Clara Barytgang	ML39	quartz	25.8	83	189	59150	7800	2546	29970	2193	638	4988	154680	1867	1188
6	Clara Barytgang	ML39	quartz	25.8	81	196	59700	13880	1682	29000	1657		1454	154680	1907	665
6	Clara Barytgang	SK18brt	barite	25.5	66	282	73490	11570	2698	91550			14015	151650	2305	
6	Clara Sohle 6	BW21	fluorite	25.5	94	512	79680	61670	6454			4103		151650	1619	1858
6	Clara. Barytgang[1]	ad5	quartz	25.3	98	287	61360	10580	4751	31510			1304	151650	1547	6264
7	Daniel im Gallenbach	BW205	fluorite	25.0	83	342	59970	6636	1613			4243		154680	1873	13
7	Daniel im Gallenbach Wittichen	BW239brt	barite	25.0	67	123	79100	7979	3242	46640			14010	157720	2351	
7	Daniel. o.	SW163	fluorite	26.2	96	216	58710	4432	1264			53910		151650	1579	1567
8	Dorothea	QDC52	barite	26.2	85	79	35590	13390	1831	119790			493	157720	1859	
8	Dorothea	L76	fluorite	26.0	84	0	59220	8903	1396			23770		155900	1861	2075
9	Emanuel	SRZ17	fluorite	26.2	93	265	60100	5940	949			2370		150440	1619	98
9	Emanuel	WN5 fl	fluorite	26.0	90	248	61860	7083	1297			84100		154680	1725	5476
9	Emanuel	SRZ17	fluorite	26.0	75	278	63350	10060	1110			537		154680	2073	1083
9	Emanuel	SRZ18	fluorite	22.5	70	316	61460	9396	1268					154680	2197	3851
9	Emanuel Rainerzau	SRZ17	fluorite	22.5	70	515	70170	8461	1459			20342		154680	2202	122
9	Emanuel Rainerzau	SRZ18	fluorite	22.5	77	407	67200	17320	2124		23820	137290		154680	2010	15017

map No.	location	sample	mineral	salinity in wt% (NaCl+CaCl2)	Cl/Br	Li ppm	Na ppm	K ppm	Mg ppm	Ca ppm	Sr ppm	Ba ppm	F ppm	Cl ppm	Br ppm	SO4 ppm (absolute)
10	Ferdinant im Tiefenbach	STFB1brt	barite	22.8	61	93	73140	4355	8195	57334			150	154680	2533	
11	Fl Grube Wildschapbach	BW15	quartz	25.5	82	107	94140	25050	3769	86629		2103	28519	154680	1879	4583
11	Friedrich Christian[1]	TF46	quartz	25.5	82	115	48210	8611	3259	54189		811	14821	154680	1895	3934
11	Friedrich Christian	TM112	quartz	25.5	75	319	36260	8096	1583	62702		711	7373	154680	2058	1296
11	Friedrich Christian	TM113	calcite	25.5	73	280	60850	8665	2185		37220	63660	21633	154680	2130	113067
11	Friedrich Christian[1]	BW92	calcite	26.0	76	351	48760	9468	2760				829	154680	2036	11371
11	Friedrich Christian	TM113	calcite	23.0	91	303	51110	43850	9302				32958	148620	1642	46483
11	Friedrich Christian	ad 18	quartz	23.0	112	154	61240	22680	1661	57558		332	1791	145590	1300	15964
11	Friedrich Christian	gs135qtz1	quartz	23.0	112	385	84180	7450	1432	64496	30	3017	1001	151650	1355	1108
11	Friedrich Christian	gs137 qtz	quartz	24.0	112	204	94110	12280	1330	101011	730		1754	151650	1349	8999
11	Friedrich Christian	SFC 174 qtz	quartz	22.5	113	1334	54940	6516	498	154451		113		139520	1233	110697
11	Friedrich Christian	BW14brt	barite	22.0	119	513	121720	17210	8000	358440			81875	139520	1170	
12	Frisch Glück im Sulzbächel	BW191	calcite	23.0	54	791	95280	6155	2740			30	108	154680	2864	2294
12	Frisch Glück im Sulzbächel	BW193	fluorite	22.9	37	163	119940	10380	3399		4280	1683		154680	4225	102
13	Hallwangen Himmlisch Heer	BW240brt	barite	23.0	67	221	65670	11190	3954	277679			72741	151650	2269	
14	Hennenloch Oberkirch	SK5brt	barite	23.0	77	418	57750	10350	10100	43361			1052	154680	2005	
15	Hesselbach	BW183	fluorite	22.9	75	548	71880	30300	3667					154680	2060	1913
15	Hesselbach	BW183	fluorite	22.0	91	405	94750	18590	2052			9542		154680	1698	
15	Hesselbach	BW259brt	barite	22.0	79	250	96650	11000	2401			16070	4390	154680	1960	
16	Hohberg	BW182	Fluorit	23.0	72	207	48300	14320	3215					154680	2154	446
16	Ilse	SW145-1	fluorite	24.0	93	206	58330	5137	1451			1083		151650	1629	98
16	Ilse	SW145-2	fluorite	25.5	91	255	60140	5104	1658			15600		151650	1671	132
16	Ilse	SW145-3	fluorite	25.5	96	85	71770	5556	2267			1175		151650	1581	106
17	Johann am Burgfelsen	SW162	quartz	25.0	91	64	67600	9345	1098	50806	29	221	126	143760	1581	24042
17	Johann am Burgfelsen	SW162	quartz	25.0	93	55	67340	8866	1100	47260	5	412	151	143760	1541	9525
17	Johann am Burgfelsen	SW162	quartz	25.0	98	242	56990	7988	844	32280	60	222	318	143760	1462	4272

map No.	location	sample	mineral	salinity in wt% (NaCl+CaCl2)	Cl/Br	Li ppm	Na ppm	K ppm	Mg ppm	Ca ppm	Sr ppm	Ba ppm	F ppm	Cl ppm	Br ppm	SO4 ppm (absolute)
17	Johann am Burgfelsen	SW137	fluorite	22.0	93	338	60000	4648	1160			243		152860	1638	101
17	Johann am Burgfelsen	SW147	calcite	22.0	94	395	150500	18990	16540			23860	13600	151650	1610	13330
17	Johann am Burgfelsen	SW137-1	fluorite	23.0	70	297	63180	5741	1671			9261		155290	2219	45
17	Johann am Burgfelsen	BW64	fluorite	23.0	80	307	46680	6593	1391			42		154680	1931	144
17	Johann am Burgfelsen	SW137	fluorite	22.1	90	86	57660	8063	1108					154680	1721	
18	Josefstreu im Tiefenbach	OJ75brt	barite	19.8	65	370	48270	5357	3166			37580	6973	154680	2382	
19	Katharina im Wildschappbach	BW48	fluorite	19.8	83	112	50590	13810	1307			462		154680	1874	115
19	Katharina im Wildschappbach	PKT3brt	barite	23.0	66	116	73290	5807	3160			13520	80	154680	2334	
20	Mooswald Lehengericht	SLG2brt	barite	23.0	66	730	82180	11020	3566			65890	19510	154680	2342	
21	Ödsbach[1]	SÖS	fluorite	23.0	62	448	98850	10600	1731			4649		154680	2498	9
21	Ödsbach	SÖ1	fluorite	23.0	76	301	57010	7527	985			985		154680	2029	173
22	Ohlsbach	CM9	calcite	23.0	72	448	66130	15340	1877		37230	102750	311	148620	2074	12350
22	Ohlsbach	CM6	fluorite	24.6	91	473	73000	16240	955					148620	1641	1015
23	Ottenhöfen	TF51	quartz	23.2	63	750	44360	9525	1993	55240		397	14930	157720	2492	2586
23	Ottenhöfen	BW82	quartz	23.2	64	348	54890	25690	1372	56000		326	2449	157720	2449	1036
24	Otto bei den Schottenhöfen	Ottobrt	quartz	23.0	103	392	63000	14820	1400	31630			589	146190	1417	
24	Otto bei den Schottenhöfen	Ottobrt	barite	22.0	49	375	118220	14320	20117			3772	159	154680	3154	
25	Rainerzau Alte Gabe Gottes	SRZ15	barite	22.0	72	81	58460	7153	1463			24540	44080	154680	2137	
25	Rainerzau Silbersee quarry	SRZ10	barite	23.0	66	410	91640	19210	14310			224230	45630	154680	2330	
26	Rammstein quarry Tennenbronn	Stb2-2	fluorite	25.5	79	66	61940	5529	1679			3996		151650	1914	
26	Rammstein quarry Tennenbronn	BW237	barite	24.0	93	359	126360	13010	3606			13080	3057	151650	1626	

map No.	location	sample	mineral	salinity in wt% (NaCl+CaCl2)	Cl/Br	Li ppm	Na ppm	K ppm	Mg ppm	Ca ppm	Sr ppm	Ba ppm	F ppm	Cl ppm	Br ppm	SO4 ppm (absolute)
26	Rammstein quarry Tennenbronn	STB2-2	fluorite	23.5	82	281	70300	6137	1709			32750		151650	1843	108
26	Rammstein quarry Tennenbronn	STB2-1	fluorite	23.5	98	426	52080	4527	1286		189	5622		127390	1295	95
26	Rammstein quarry Tennenbronn	STB2-1	fluorite	24.0	77	397	67470	7870	1875			20680		133450	1744	31
27	Silberbrünnele Haigerach	BW20	quartz	23.0	39	247	15680	11700	2407	86580	4457	245	14420	151650	3883	1517
28	Silberbrünnele Haigerach	SK3qtz	quartz	22.0	84	273	44860	34990	2752	78330		1531	127	154680	1831	30250
29	Simson	SW144	fluorite	25.0	78	174	76640	19730	1912			19240		154680	1973	
30	Sophia	SW51	calcite	22.0	97	292	63310	6113	1820			4991	200	151650	1565	13300
30	Sophia	SW78	fluorite	23.0	84	258	63610	10800	1741					154680	1831	191
31	St. Georgstollen Glaswald Alpirsbach	SAB32	barite	23.0	81	263	103450	8904	3834	52910			13800	153770	1887	
32	St. Roman Hoberg	BW235	barite	24.0	89	538	86220	5325	2820	41820			3970	154680	1744	
33	Silbergründle	ML4	quartz	18.0	75	304	99570	32290	3902	134700			11970	151650	2018	3229
34	Tunnelbau Hornberg	TM92	calcite	22.0	108	28	228070	115150	135560				11840	151650	1404	17340
35	Urenkopf	XSU19	calcite	22.0	75	18	34960	4451	4805			6193	551	148620	1986	4155
35	Urenkopf	XSU19b	calcite	20.1	76	37	30570	3140	3274				12090	148620	1945	13870
35	Urenkopf	XSU19b	calcite	22.5	85	502	44510	9812	5789				3177	148620	1752	4060
36	Ursula Welchensteinach	BW260qtz	quartz	22.5	62	395	100080	59640	73260	40330		11950	5811	151650	2448	20650
37	Vogelsang Wittichen	BW189	fluorite	22.0	155	236	84140	11510	525			4695		154680	999	
38	Wachtbühl[1]	BW87	quartz	22.3	86	430	71290	87600	4685	50120		1721	7692	148620	1721	12850
38	Wachtbühl	BW87b	quartz	23.9	138	192	95510	22870	5407	60570	4714	7540	10790	148620	1074	2281
39	Wenzel	BW91	calcite	25.0	91	135	49690	3912	746			217	511	151650	1658	664
39	Wenzel	BW91	calcite	25.5	82	138	53320	6499	5069			274	1503	151650	1845	5370
39	Wenzel	BW91	calcite	24.5	94	151	51950	4751	2426				9467	148620	1585	1592
39	Wenzel	BW91	calcite	24.5	89	609	51640	5231	1691				841	148620	1668	1697
40	Calmbach Klosterberggang	BW179	quartz	25.0	340	495	126800	11630	11572	103820		4780	14560	139520	410	12260

map No.	location	sample	mineral	salinity in wt% (NaCl+CaCl2)	Cl/Br	Li ppm	Na ppm	K ppm	Mg ppm	Ca ppm	Sr ppm	Ba ppm	F ppm	Cl ppm	Br ppm	SO4 ppm (absolute)
41	Käfersteige (fl1)	BW174	fluorite	25.0	134	353	129180	13740	1178			19990		151650	1136	593
41	Käfersteige (fl1)	BW174	fluorite	24.5	163	289	88400	10000	810			36950		151650	928	268
41	Käfersteige (fl1)	BW174	fluorite	24.5	158	272	72370	8240	726			4116		151650	958	408
41	Käfersteige (fl1)	BW174	fluorite	23.0	172	291	69600	12760	1286			8995		151650	880	326
41	Käfersteige (fl2)	BW175	fluorite	25.0	242	260	98300	17300	1246			47810		151650	627	79
41	Käfersteige (fl2)	BW175	fluorite	25.0	217	260	81350	19650	2853			989		151650	700	1263
42	Kälbelberg Baden-Baden	BW199	barite	25.0	66	132	80830	13330	3787	54570			2903	156500	2369	
42	Kälbelberg Baden-Baden	BW199	barite	25.0	71	290	44120	9430	2577	33840			1215	156500	2205	
43	Königswart	BW104	quartz	25.0	222	254	101690	9410	772	44750	62	835	8470	154680	698	1557
43	Königswart	Königswartqtz	quartz	25.0	125	184	45240	43310	2285	43240	3111	5103	82	154680	1235	3541
44	Neubulach	ML2	quartz	25.8	70	242	58460	18120	1324	103330		1048	55930	153470	2199	3304
44	Neubulach	ML2	quartz	25.8	89	442	62280	18320	1505	35400	2311	168	4682	151650	1705	6156
44	Neubulach[1]	Hm24a	quartz	25.5	71	323	54330	33100	2609	55730	152	1912	26270	151650	2129	1961
45	Reutbach bei Heilgenwald	BW173	fluorite	25.5	84	416	55180	11180	2344			965		158930	1902	386
46	Reutbach bei Heilgenwald	BW173b	fluorite	25.3	58	427	71790	29950	1332			9197		158930	2737	743
46	Reutbach bei Heilgenwald	BW173c	fluorite	25.0	56	338	83300	28810	1913			26420		157720	2816	
46	Reutbach bei Heilgenwald	BW173b	fluorite	25.0	71	478	49940	12310	919		218771	6611		158930	2234	285
47	Rittwald bei Grunbach	BW172a	fluorite	26.2	73	332	72830	11530	555			1265		157720	2150	168
47	Rittwald bei Grunbach	BW172	fluorite	26.2	81	371	52900	10850	1335			511		157720	1954	5469
48	Anna bei Fahl[1]	BW117a	quartz+Fl	26.0	161	496	76990	12040	626			3370	108040	136490	847	29
48	Anna bei Fahl	BW117	quartz+Fl	26.2	224	389	85360	2636	23695				927690	136490	609	253
48	Anna bei Fahl	JST11	quartz	26.0	203	251	81640	12490	1936	40470			21280	136490	673	4527
49	Anna Wieden	BW188	fluorite	26.0	182	319	55800	16180	1201		19351	1766		138310	759	199
50	Anton Wieden	BW73b	fluorite	22.5	126	214	70180	17930	1304					154680	1229	678
50	Anton Wieden	BW73	fluorite	22.5	95	383	48580	6605	895					154680	1622	179
50	Anton Wieden	BW73	fluorite	22.5	95	224	81130	9259	1230			4521		154680	1634	641

map No.	location	sample	mineral	salinity in wt% (NaCl+CaCl2)	Cl/Br	Li ppm	Na ppm	K ppm	Mg ppm	Ca ppm	Sr ppm	Ba ppm	F ppm	Cl ppm	Br ppm	SO4 ppm (absolute)
50	Anton Wieden	SHB13	barite	22.8	57	692	97100	60240	12201	90840			144900	154680	2714	
50	Anton Wieden	TM158	barite	25.5	33	981	54845	39580	28184				139860	157720	4789	
51	Baumhalde Todtnau	STD2	barite	25.5	52	349	42490	27400	41940				50350	139520	2688	
51	Baumhalde Todtnau	BW103	quartz	25.5	144	277	66380	9580	414	25900		421	47510	139520	971	
51	Baumhalde Todtnau	BW213	quartz	25.5	166	434	83610	65360	4541	74310		1776	31230	139520	841	7563
52	Bergsee Bad Säckingen[1]	BW255fl	fluorite	26.0	522	384	106560	26930	2010			269150		145580	279	682
53	Birkendorf Sägehalde	BW55	fluorite	23.0	79	160	47020	7235	732		2691	1335		136490	1731	98
54	Brandenberg	Jst21	quartz	23.0	197	231	70230	11160	1371	168760		829	105390	133450	678	606
54	Brandenberg	GS111F	fluorite	23.0	133	306	67240	15190	273					139520	1050	
54	Brandenberg	GS111Q	quartz	24.0	151	230	105560	27130	4488	250330		12630	64660	138910	918	38150
54	Brandenberg	GS111	fluorite	22.5	131	307	64190	14070	292					139520	1065	
54	Brandenberg	GS83	fluorite	22.0	296	240	77890	11740	377					139520	472	
55	Brenden[1]	GS20	fluorite	23.0	268	561	64580	15870	1696					138910	518	
56	Teufelsgrund	BW190	quartz	22.9	148	457	77890	24250	6640	189200			4969	133450	900	8040
57	Erzfall Schindler	BW39	quartz	23.0	162	152	65230	9172	1206	193740			55330	133450	826	1098
58	Fahl Todtnau	TM161	dolomite	23.0	318	283	128750	13780	70854			65300	47470	139520	439	60360
59	Fahlenbach bei Hammereisenbach	BW241brt	barite	22.9	71	192	78190	8400	1684	48090			2824	145590	2054	
60	Finstergrund	BW178	fluorite	22.0	372	211	85370	18100	1327			3290		154680	416	
60	Finstergrund	BW178	fluorite	22.0	423	319	88150	14340	1603			526		154680	366	
60	Finstergrund	BW178	fluorite	23.0	170	485	64290	19970	1127					151650	892	240
60	Finstergrund	BW178	fluorite	24.0	182	100	91960	12190	707			5019		151650	834	40
60	Finstergrund	TM153	dolomite	25.5	103	353	67980	4390	448050			38280	7826	151650	1471	6761
61	Friedenweiler	FFW22	fluorite	25.5	84	321	65920	12500	1963			126090		133450	1583	166
61	Friedenweiler	FFW22	fluorite	25.0	84	328	54890	12750	1890			5942		133450	1594	23
62	Neue Hoffnung Gottes St. Balsien	BW23	quartz	25.0		342	67180	28360	6547	128070		16640	106720	139520		39640
62	Neue Hoffnung Gottes St. Balsien	BW111	fluorite	25.0	173	323	72260	9230	352			904		139520	808	13

map No.	location	sample	mineral	salinity in wt% (NaCl+CaCl2)	Cl/Br	Li ppm	Na ppm	K ppm	Mg ppm	Ca ppm	Sr ppm	Ba ppm	F ppm	Cl ppm	Br ppm	SO4 ppm (absolute)
62	Neue Hoffnung Gottes St. Balsien	BW9	fluorite	22.0	117	234	58700	8730	273					134060	1143	95
63	Gottesehre Urberg	ML42	calcite	22.0	125	263	49229	6290	439			177	49170	120110	959	6416
63	Gottesehre Urberg	ML42	calcite	23.0	142	228	50050	8620	579				20120	120110	844	2713
64	Grube Tannenboden	ML38	fluorite	23.0	277	278	67750	8760	711			4867		139520	503	156
64	Grube Tannenboden	ML38	fluorite	22.1	285	223	70270	10690	590			1413		139520	490	0
64	Grube Tannenboden	ML38	quartz	19.8	203	258	74600	7898	771	21390			2490	139520	687	6092
64	Grube Tannenboden	STW1-2	barite	19.8	85	421	63250	5790	24927	314540			41130	139520	1643	
64	Grube Tannenboden	ML38	quartz	23.0	170	773	92740	12210	584	284760		2655	39770	139520	823	17
65	Herrenwald im Münstertal	SK18	quartz	23.0	185	281	99220	24430	3182	286860		4717		149230	807	
66	Igelschlatt[1]	BW32	fluorite	23.0	161	285	55450	10387	401			134		140730	875	93
66	Igelschlatt	BW32	fluorite	23.0	267	431	79330	68320	1081			13460		140730	526	
67	Kirchfelsen Wheratal	BW252	fluorite	23.0	146	524	93670	13330	1581			16460		13952	958	67
68	Lisbühl West	STD1	barite	24.6	283	347	174900	10600	17798	80110			295580	133450	471	
68	Lisbühl West	BW228qtz	quartz	23.2	278	491	79620	13600	935	32780	2191	828	2661	133450	479	1941
69	Mauswald Todtnau	BW207	quartz	23.2	294	335	80440	16200	2220	156570		2748	91285	139520	474	5383
70	Neuschurf Witznau	BW254brt	barite	23.0	194	305	89930	13210	613	387170			107080	154680	796	
71	Nonnenmattweiher	FP19	fluorite	22.0	59	315	59530	28380	3298					145590	2463	1723
72	Nonnenmattweiher	FP19	barite	22.0	97	325	106040	32560	4161	51900			60680	142550	1465	
72	Nonnenmattweiher	FP19	quartz	23.0	85	671	68050	25600	8466	59390		832		142550	1673	
72	Nonnenmattweiher	TF11	quartz	25.5	77	187	91310	19390	5897	62190		2884	59300	145590	1892	9350
73	Rappenloch	FRL30brt	barite	24.0	71	489	54920	8170	1695	41750			6011	139520	1966	
74	Schönenberg bei Schönau i.W.	BW256brt	barite	23.5	1139	401	128200	20030	1482	678330			140350	133450	117	
75	Sengalenbachfl	Sengalenbachfl	fluorite	23.5	122	328	74940	8197	379			37450		151650	1246	3758
76	Silberberg Todtnau vein 2	BW212	fluorite	24.0	158	274	77350	13500	942			155230		133450	844	997
77	Silberberg Todtnau	BW109	quartz	23.0	262	218	72270	28620	1325	17310		46670	102920	139520	532	26560

map No.	location	sample	mineral	salinity in wt% (NaCl+CaCl2)	Cl/Br	Li ppm	Na ppm	K ppm	Mg ppm	Ca ppm	Sr ppm	Ba ppm	F ppm	Cl ppm	Br ppm	SO4 ppm (absolute)
77	Silberberg Todtnau	BW109	quartz	22.0	244	302	84140	12420	1077	29760	3812	23840	16900	139520	572	8986
77	Silberberg Todtnau	Jst32	quartz	25.0	137	1253	77580	29150	5387	156430			88020	145590	1060	10590
78	Teufelsgrund	STG1	barite	22.0		418	56645	27730	31645	39243			96700	109190		
78	Teufelsgrund	BO132brt	barite	23.0	148	246	94230	47690	3666	437550			84960	133450	902	
78	Teufelsgrund Fl1	BW163	fluorite	23.0	118	218	45490	6877	861			606		133450	1133	116
79	Waldschweine Todtnau	BW56	fluorite	24.0	177	1418	48930	8908	946			1421		121930	688	140
80	Waldweg südwestlich Präg	BW26	fluorite	18.0	362	384	80420	22440	1821			37860		136490	377	879
80	Waldweg südwestlich Präg	BW26	fluorite	22.0	207	672	85490	17880	1184			4006		136490	661	
81	WehratalstollenCC	WehratalstollenCC	calcite	22.0	126	324	151860	10600	18670			17510	523	133450	1061	18860
82	Wies bei Malsburg[1]	BW211	fluorite	20.1	199	219	73810	11210	678		24	19280		135270	680	70
83	Wonnen Nord	BO90	quartz	22.5	117	577	56850	10300	1744	34440			1101	144980	1238	3557

Reference 1: Walter et al., 2016

Table 2 recalculated trace element concentrations of the paleo-fluids in ppm

map No.	location	sample	Mn	Fe	Co	Ni	Cu	Zn	As	Se	Rb	Y	W	Tl	Pb	Bi	Th	U
1	Amalie Nordrach	SAM3qtz	5755	11390	1659	859	29300	2234	10300	0	441	8386	0	77	2518	1630	722	5101
2	Anton Heubach	SHB12brt	1324	21860	0	388	21	287	628	0	53	0	0	0	24	0	11	54
3	Artenberg quarry	BW186fl	357	234	0	0	4	242	12	0	90	0	0	8	41	0	0	10
4	Bad Rippoldsau Prosper	BW114	1579	5729	0	282	18440	1845	342	0	217	278	0	0	1426	0	0	49
5	Bleibersgrund	SN153-4	220	48	0	0	18	472	0	0	24	0	0	18	43	0	0	0
5	Bleibersgrund	SN153-1	2452	11	0	0	18	323	285	0	33	12	0	8	37	0	4	10
5	Bleibersgrund	SN153-2	462	123	0	0	11	497	121	0	56	7	0	5	99	0	4	6
5	Bleibersgrund	SN153-4	482	105	0	0	40	1036	0	0	53	0	0	40	95	0	0	0
6	Clara Barytgang	ML39	1127	4963	11	15	266	574	155	0	70	0	0	0	159	0	0	0
6	Clara Barytgang	SK18brt	11410	36570	0	0	13390	916	804	0	164	21	0	11	83	0	63	244
7	Daniel im Gallenbach	BW205	515	2278	0	0	93	337	39	0	33	15	0	8	76	0	0	0
7	Daniel im Gallenbach Wittichen	BW239brt	407	733	58	50	2493	671	720	0	292	165	0	56	340	2716	184	920
8	Dorothea	L76	334	403	0	15	64	530	10	0	54	0	0	0	61	0	0	0
9	Emanuel Rainerzau	SRZ17	367	259	4	0	9	375	33	0	58	84	0	9	72	0	0	8
9	Emanuel Rainerzau	SRZ18	616	7449	0	0	43	435	317	0	252	158	0	32	54	0	0	189
10	Ferdinant im Tiefenbach	STFB1brt	1220	3687	23	30	12250	1913	30580	49	53	0	0	0	24	10	0	406
11	Friedrich Christian	TF46	1109	5543	0	45	923	9910	135	0	37	0	0	0	1878	0	0	0
13	Hallwangen Himmlisch Heer	BW240brt	688	2980	0	0	70	635	68	0	127	0	0	0	0	0	0	242
14	Hennenloch Oberkirch	SK5brt	163460	7961	78	37	526	2917	0	0	187	263	0	23	47	18	119	853
15	Hesselbach	BW183	40790	204360	0	0	11280	7648	4849	0	2227	200	0	0	0	0	0	155
17	Johann am Burgfelsen	SW147	660	892	0	0	21	627	125	0	177	0	0	25	93	12	66	244

map No.	location	sample	Mn	Fe	Co	Ni	Cu	Zn	As	Se	Rb	Y	W	Tl	Pb	Bi	Th	U
17	Johann am Burgfelsen	SW137	175	813	0	0	777	253	24	0	35	10	0	7	104	0	5	9
19	Katharina im Wildschappbach	BW48	725	989	16	16	45330	916	5629	20	111	22	0	14	60	1442	73	305
19	Katharina im Wildschappbach	PKT3brt	869	3006	0	0	950	546	10	0	101	0	0	0	34	241	27	161
20	Mooswald Lehengericht	SLG2brt	595	1374	0	48	10920	1044	6400	0	340	156	0	74	371	42	275	1093
22	Ohlsbach	CM6	1080	2791	0	0	149	580	140	0	116	0	0	0	116	0	5	4
24	Otto bei den Schottenhöfen	Ottobrt	227	1896	0	98	723	1232	516	0	45	0	0	0	127	0	0	0
24	Otto bei den Schottenhöfen	Ottobrt	584	765	0	0	76	519	176	0	121	0	55	9	18	0	12	47
25	Rainerzau Alte Gabe Gottes	SRZ15	1054	1373	0	0	1690	313	720	4	86	16	0	0	25	314	20	169
25	Rainerzau Silbersee quarry	SRZ10	433	4573	148	0	7365	1644	6589	0	399	214	0	0	413	0	282	3190
26	Rammstein quarry Tennenbronn	Stb2-2	288	55	0	0	11	285	15	0	47	0	0	9	72	0	0	0
26	Rammstein quarry Tennenbronn	STB2-1	235	969	0	0	54	273	158	0	166	98	0	0	98	0	69	957
26	Rammstein quarry Tennenbronn	STB2-1	272	103	0	0	8	290	60	0	53	8	0	9	49	0	0	15
27	Silberbrünnele Haigerach	BW20	189	132	0	37	795	1085	98	0	53	0	0	0	90	0	0	0
30	Sophia	SW51	860	8545	0	74	2470	946	97	0	181	393	0	0	1079	0	17	32
30	Sophia	SW78	39	154	0	0	27	59	0	0	0	0	0	0	0	0	0	0
31	St. Georgstollen Glaswald Alpirsbach	SAB32	4479	1917	0	0	23	486	0	0	176	70	0	63	108	0	118	395
35	Urenkopf	XSU19b	657	973	0	0	307	509	17	0	85	39	0	25	35	0	27	192
35	Urenkopf	XSU19b	48	355	0	0	33	276	0	0	0	42	0	33	121	0	0	0
36	Ursula Welchensteinach	BW260qtz	9451	50075	0	6120	19130		16630	0	2114	565	0	148	10460	0	0	141

map No.	location	sample	Mn	Fe	Co	Ni	Cu	Zn	As	Se	Rb	Y	W	Tl	Pb	Bi	Th	U
38	Wachtbühl	BW87	123	55	0	0	10	96	7	0	103	0	0	0	16	0	0	0
39	Wenzel	BW91	187	1550	0	139	1046	1299	28	0	61	5	10	0	299	0	0	0
41	Käfersteige (fl1)	BW174	34	116	0	0	80	214	0	0	22	0	0	0	22	0	0	0
41	Käfersteige (fl1)	BW174	716	21140	0	0	1559	465	686	0	262	20	0	10	76	0	0	0
41	Käfersteige (fl2)	BW175	7823	92180	0	0	10020	654	1209	0	300	43	0	0	119	0	0	0
42	Kälbelberg Baden-Baden	BW199	5709	36490	0	63	185	922	297	0	233	64	0	0	564	0	0	52
42	Kälbelberg Baden-Baden	BW199	1482	2086	0	0	98	1427	54	0	367	135	0	31	0	25	185	618
43	Königswart	BW104	118	474	0	106	621	305	13	0	55	27	0	0	148	0	0	0
43	Königswart	Königswartqtz	507	4236	0	82	1888	535	419	1583	158	0	0	23	61	842	0	90
44	Neubulach	ML2	166	1148	0	26	307	298	86	0	61	0	0	0	48	0	0	0
44	Neubulach	Hm24a	538	3855	0	606	3639	1704	349	0	151	0	0	0	275	0	0	0
47	Rittwald bei Grunbach	BW172a	1442	3567	0	28	349	6536	10	0	23	0	0	0	291	0	0	15
47	Rittwald bei Grunbach	BW172	1135	1491	0	0	49	1130	59	0	236	0	0	0	279	0	0	0
48	Anna bei Fahl	BW117a	95	82	0	0	26	405	0	0	73	0	0	28	43	0	0	0
48	Anna bei Fahl	BW117	579	10733	0	1040	5877	2673	358	0	199	512	0	0	3667	0	97	224
50	Anton Wieden	BW73	0	475	0	161	934	2094	0	0	0	0	0	0	0	0	0	0
50	Anton Wieden	BW73	164	135	0	0	5	141	47	0	83	27	0	0	2251	0	10	13
50	Anton Wieden	TM158	5675	14539	1184	705	1714	2486	1787	0	479	0	0	0	0	776	285	6279
51	Baumhalde Todtnau	STD2	31400	65850	0	2920	52130	61300	34320	0	2770	7786	0	0	14450	0	2555	16641
51	Baumhalde Todtnau	BW213	106	67	0	24	106	125	60	0	77	13	0	0	1818	0	0	9
53	Birkendorf Sägehalde	BW55	138	18250	0	0	135	147	374	0	331	62	0	74	103	0	115	240
54	Brandenberg	GS111F	77	320	0	164	801	783	189	0	36	0	0	0	42970	0	0	0
58	Fahl Todtnau	TM161	0	808	0	0	112	565	0	0	0	6276	0	0	0	0	0	0
60	Finstergrund	BW178	1462	918	0	0	12	699	106	0	173	25	0	19	71	7	45	187
60	Finstergrund	TM153	3745	1708	53	45	383	633	317	0	106	22	0	0	2412	0	0	0

map No.	location	sample	Mn	Fe	Co	Ni	Cu	Zn	As	Se	Rb	Y	W	Tl	Pb	Bi	Th	U
61	Friedenweiler	FFW22	743	1805	0	52	375	1326	984	0	195	0	0	0	141	0	0	58
62	Neue Hoffnung Gottes St. Balsien	BW23	506	1867	0	0	19	191	800	0	140	28	0	0	77	0	0	0
62	Neue Hoffnung Gottes St. Balsien	BW111	228	93	0	0	29	137	198	0	82	0	0	0	8285	0	0	17
63	Gottesehre Urberg	ML42	803	166	0	0	16	61	141	0	160	19	0	0	6301	0	0	12
64	Grube Tannenboden	ML38	488	473	0	8	39	125	9	0	55	55	0	0	165	0	7	5
64	Grube Tannenboden	ML38	180	2208	0	24	384	624	10	0	31	0	0	0	0	0	0	0
64	Grube Tannenboden	STW1-2	18190	167270	0	0	14	349	0	0	74	35	0	20	321	0	27	163
67	Kirchfelsen Wheratal	BW252	84	110	0	0	132	106	5	0	85	24	0	10	11	0	0	8
68	Lisbühl West	STD1	8048	85480	0	0	3111	25830	2082	0	1984	1616	0	0	1604	0	1172	3887
68	Lisbühl West	BW228qtz	5478	6207	241	313	1878	1206	1303	7198	78	76	0	0	13570	819	0	0
69	Mauswald Todtnau	BW207	0	2181	0	433	2373	4229	0	0	0	376	0	0	3690	0	0	0
72	Nonnenmattweiher	FP19	687	3453	0	0	85	840	97	0	174	0	0	0	80	0	37	215
72	Nonnenmattweiher	TF11	203	375	0	0	250	899	0	0	0	0	0	0	0	0	0	0
73	Rappenloch	FRL30brt	839	395	0	0	12	426	44	0	125	0	13	15	46	10	65	167
74	Schönenberg bei Schönau i.W.	BW256brt	914	35510	0	0	12070	3276	65540	0	212	0	0	43	19560	0	78	898
75	Sengalenbach	Sengalenbach	322	59240	0	0	6920	427	3043	44	41	0	35	74		193	0	131
77	Silberberg Todtnau	BW109	195	23900	0	0	1076	496	592	0	65	72	0	0	31380	0	0	0
77	Silberberg Todtnau	BW109	215	3119	0	265	1507	710	0	0	70	0	0	0	1172	0	0	0
77	Silberberg Todtnau	Jst32	0	3083	0	223	1712	6024	0	0	0	163	0	0	8260	0	0	0

map No.	location	sample	Mn	Fe	Co	Ni	Cu	Zn	As	Se	Rb	Y	W	Tl	Pb	Bi	Th	U
78	Teufelsgrund	STG1	17180	24470	0	864	22210	30080	7689	0	2912	1256	0	1290	8062	0	1696	0
78	Teufelsgrund	BO132brt	768	92070	0	0	5098	8672	7581	85	234	245	0	25	31800	23	0	
79	Waldschweine Todtnau	BW56	4872	25060	0	0	32	1437	512	0	245	103	0	0	54670	34	0	16
80	Waldweg südwestlich Präg	BW26	97	20480	0	69	5523	646	159	0	107	0	0	0	80	0	0	135
81	Wehratalstollen	Wehratalstollen	1335	65	24	54	8	36	0	0	123	37	0	0	20	14	17	

Multi-reservoir fluid mixing processes in rift-related hydrothermal vein-type deposits

Benjamin F. Walter, Mathias Burisch, Tobias Fusswinkel, Michael A.W. Marks, Markus Wälle, Christoph Heinrich, Olga B. Apukhtina, Gregor Markl

Abstract

Fluid mixing is an important process during the formation of many hydrothermal vein-type deposits. In this contribution, we present evidence for hydrothermal fluid systems and associated mineralization, in which mineral precipitation is initiated by fluid mixing of more than two fluids. A well investigated natural laboratory, the Schwarzwald mining district (situated at the eastern shoulder of the post-Cretaceous Rhinegraben failed rift in SW Germany), has been chosen to investigate such mixing processes on the scale of a large mining district, a single location and a single growth zone within one sample. Based on our observations, we relate the observed diversity of the hydrothermal veins in terms of mineralogy and fluid inclusion chemistry to the disturbed geological environment during ongoing rifting. Literature data on the regional geology, current groundwater reservoirs, formation processes and hydraulic features are augmented by new fluid inclusion analyses from post-Cretaceous, hydrothermal vein minerals including microthermometry, crush leach (IC and TXRF), Microraman and LA-ICPMS data of single fluid inclusions.

Fluid petrography and microthermometry show complex sequences of alternating fluid signatures on different growth zones of one crystal. High (20-26 wt. % $NaCl+CaCl_2$), moderate (5-20 wt. % $NaCl+CaCl_2$) and low salinity (<5 wt. % $NaCl+CaCl_2$), sulfate-bearing and CO_2-bearing primary fluids inclusions may alternate on various growth zones of one single crystal. Such variations are observed abundantly in minerals from different localities. Bulk crush leach analyses show significant variations in major element composition of the trapped fluids, which can generally be described in the $Na-K-Ca-Cl-SO_4-HCO_3$-system. These variations are caused by mixing of fluids from different aquifers and in various proportions. Ancient fluids show chemical similarities to modern groundwater aquifers such as granitic basement, Lower Triassic Buntsandstein sandstones or Middle Triassic

Muschelkalk limestones, which can be directly sampled in today's wells. Single fluid inclusion investigations by LA-ICPMS support this interpretation and show multi-component fluid mixing processes on the scale of single localities and even on the scale of single crystal growth zones. The latter can be used to calculate a maximum duration of mineral growth (before the fluid is homogenized), which implies very short-lived fluid events on the order of seconds to hours.

By defining end member reservoirs, mixing of different fluid signatures in various ratios was calculated; these hydro-chemical calculations show that almost all mixed fluid compositions are saturated with respect to barite. In contrast, fluorite-saturated fluids can only be modelled by mixing of a basement brine with fluids from Triassic sandstone. All fluid mixtures are strongly undersaturated with respect to galena, chalcopyrite and sphalerite, the most commonly observed ore minerals in the hydrothermal veins. As the calculated fluid mixtures are typically relatively oxidized and contain high sulfate/sufide ratios, precipitation of sulfides was most probably related to short-lived reduction events caused by an influx of hydrocarbons or by reactions with graphitic wall rocks.

Structurally, multi-aquifer fluid mixing processes involving aquifers of different chemical and physical constitution are triggered by a major "short-circuit" such as a tectonic rifting event. The Rhinegraben obviously was able to act as such a trigger and thereby initiated the formation of a large number of mineralogically diverse hydrothermal ore deposits.

1. Introduction

The chemical and hydraulic properties of fluids causing the formation of unconformity-related hydrothermal vein-type (specifically base-metal) ore deposits are key parameters to understand the genesis of these systems. Most studies related to this are based on a combination of microthermometry (Wilkinson, 2010), stable and radiogenic isotopes (Bau et al., 2003; Kessen et al., 1981; Shouakar-Stash et al., 2007; Staude et al., 2011b; Wilkinson et al., 2005), trace element studies of fluids and gangue (Fusswinkel et al., 2013; Pfaff et al., 2011) or paleo-hydrological modelling (Garven et al., 1999). Examples include the Alaskan Brooke Range (Leach et al., 2004), the South East Basin in France (Aquilina et al., 2011), the Irish Midlands (Banks et al., 2002), the Massif Central in France, the Maestrat basin and the Catalan Coastal Ranges in Spain and Upper Silesia in Poland (Boiron et al.,

2010), the St. Lawrence rift in Canada (Carignan et al., 1997) and the Otavi Mountainland in Namibia (Deane, 1995). Numerous workers concluded, that fluid mixing typically takes place between hot, deep-seated fluids from the crystalline basement, and cooler, sediment-derived fluids from the overburden sequence (e.g. Staude et al., 2009, 2012, Wilkinson, 2010, Fusswinkel et al., 2013, 2014a, Bons et al., 2014, Walter et al., 2015). Most authors agree that dominantly metals are transported by basement brines or deep-seated basinal fluids (Fusswinkel et al., 2013; Boiron et al., 2010) and it is this mid-crustal metal-rich fluid most contributions focus on. However, the simplified model of a two-component mixing system can only be applied to geological environments where the two reservoirs are spatially separated, which is often an oversimplified assumption not able to explain the diversity of fluid compositions and mineral assemblages in hydrothermal veins related to rift systems or large scale lineaments (e.g. Yukon Territory, Rio Grande Rift, Illinois, Nova Scotia, Newfoundland, Sardinia (Van Alstine, 1976)). All these examples share the similarity that more than two aquifers with different chemical properties were involved during vein formation. It is typical of such districts, that veins of different gangue and ore mineral associations are observed within a relatively small area (e.g. Bjørlykke et al., 1990; Van Alstine, 1976).

The same holds true for the Schwarzwald mining district (SW Germany) bordered by the post-Cretaceous Rhinegraben rift, where mineralogically diverse hydrothermal veins occur along and in the vicinity (up to 50 km) of the graben boundary fault (e.g. Metz et al., 1957, Bliedner & Martin, 1986; Baatartsogt et al., 2007; Staude et al., 2009). These veins occur in various types of sedimentary and basement host rocks brought into contact with each other during rifting. This work focuses on the following aspects:

- An integrated study on ore-forming fluids using microthermometry, crush-leach, TXRF and LA-ICPMS analyses on various types of post-Cretaceous mineralizations across the entire mining district.
- The geochemical characterization of possible source aquifers and their connection to modern formation fluids.
- The links between the various fluid sources/aquifers and the different types of mineralizations.

- The details of mixing on the scale of a mining district, a single locality and a single crystal.

The samples for this study were carefully chosen based on a large dataset on hundreds of samples from the Schwarzwald mining district investigated over the last ten years. These data include microthermometry, major, minor and trace element compositions of gangue, ore and supergene minerals, age-dating, stable isotope data, paleo-hydrological modelling and studies on modern thermal and mineral waters (e.g., Baatartsogt et al., 2006; 2007; Bons et al., 2014; Fusswinkel et al., 2013; Göb et al., 2011; 2013; Loges et al., 2012; Markl et al., 2006; Pfaff et al., 2009; 2010; 2011; Schwinn and Markl, 2006; Schwinn et al., 2006; Staude et al., 2007; 2009; 2010a, b; 2011; 2012a + b; Ströbele et al., 2012). The well-known geology of the region (Geyer and Gwinner, 2011; Ziegler, 1990) and numerous studies on modern water chemistry and hydraulic properties of the different aquifers (Stober and Bucher, 1999a, 1999b, 1999c, 2000, 2004, 2005a, 2005b, 2007; Stober et al., 1999, He et al., 1999, Bucher et al., 2009; Bucher and Stober, 2000, 2002, 2010, Ludwig et al., 2011, Stober 2011) make this region an ideal one for the present study. It is important to note that the Upper Rhinegraben rift is still tectonically active and >20 thermal and mineral wells occur along the boundary faults and in their vicinity (Göb et al., 2013).

The sedimentary rocks present on top of the partially eroded basement and along the graben shoulders are the same as during the onset of rifting in the Paleogene. Hence, it appears reasonable to assume that today's groundwater compositions have at least some similarities to those which formed the hydrothermal veins since the onset of rifting during the Paleogene. For some of the aquifers (basement, Muschelkalk limestones), this similarity in terms of salinity, Cl/Br ratios and major and minor element composition has been shown in Walter et al. (in press, submitted Jura). This approach thus enables to draw conclusions on ore-forming processes based on the comparison with active water data.

1.1 Regional geology

The Schwarzwald consists of exhumed Variscan basement gneisses and granites covered by Permian to Upper Jurassic sedimentary units (Fig. 1). The paragneiss unit locally contains orthogneisses and

amphibolites, all of which being intruded by post-collisional S-type granites between 335 and 315 Ma (Altherr et al., 2000; Hann et al.,, 2003; Kalt et al., 2000; Todt, 1976). During the Rotliegend (Permian), local basins were filled by redbed arkoses and conglomerates (Geyer and Gwinner, 2011; Jenkner, 1986; Nitsch and Zedler, 2009). In the early Triassic, quartzitic Buntsandstein units (up to 400 m in the northern and <50 m in the southern Schwarzwald) were deposited, while middle Triassic (Muschelkalk) limestones and evaporites (halite or gypsum in some facies) reached a thickness of 160-220 m. The Late Triassic (Keuper) is dominated by clastic sediments and evaporitic units (mainly gypsum), with a thickness decreasing from about 300 m in the north to <100 m in the south (Geyer and Gwinner, 2011). About 1000 m of clastic sediments and carbonates were deposited on the shallow continental Tethys shelf during Jurassic times, including organic-rich shales during the lower Jurassic (Lias ε). No sediments were deposited during the Cretaceous.

During the Paleogene, the commencing rifting of the Upper Rhinegraben resulted in the deposition of about 400 m of clastic sediments and evaporites (gypsum, anhydrite, dolomite, Na-K-Mg halides) in the rift valley (Geyer and Gwinner, 2011; Rupf and Nitsch, 2008). The rifting was accompanied by the uplift of the rift shoulders, associated with erosional exhumation of the crystalline basement. Uplift and erosion was stronger in the southern relative to the middle and northern Schwarzwald; while in the middle and northern Schwarzwald, the basement-cover unconformity is preserved to the present day, the southern Schwarzwald is eroded to a depth of about 1.5-2 km below the former unconformity (Rupf and Nitsch, 2008).

1.2 Hydrothermal veins in SW Germany

Hydrothermal veins in the Schwarzwald formed in basement rocks and their Permian and Triassic sedimentary cover since about 300 Ma (Loges et al., 2012; Pfaff et al., 2009; Staude et al., 2009).

Based on structural, mineralogical and microthermometric arguments five formation stages for the hydrothermal veins are distinguished (Table 1; Walter et al., 2015; 2016: (i) Carboniferous, (ii) Permian, (ii) Triassic-Jurassic; (iv) Jurassic-Cretaceous and (v) post-Cretaceous veins. This study deals with the latter group (v) only. These veins formed during Paleogene rifting along Upper Rhinegraben-parallel NE-SW to NNE-SSW-striking fault systems. They consist of barite-quartz,

various carbonates with or without barite and quartz or barite-quartz-fluorite assemblages mostly with Pb ores; less commonly, As, Zn, Cu, Bi and Ni ores are present (Staude et al., 2009; Ströbele et al., 2012; Werner, 1994). The formation of the Wiesloch MVT-deposit at 23 Ma in the paleo-karst of the Muschelkalk limestones (Pfaff et al., 2010; Ströbele et al., 2012) also belongs to this group of mineralizations (Tables 1 and 2).

1.3 Modern reservoirs and associated fluids

1.3.1 *Basement*

Data from numerous drill holes and wells indicate that a vertical fluid stratification in the Schwarzwald basement exists today (Bucher & Stober, 2010): Shallow wells (<1 km depth) produce weakly mineralized Ca-Na-HCO_3 fluids with total chlorinity increasing with depth (<5 wt.%). At about 3 to 4 km, the fluids change into CO_2-bearing Ca-Na-HCO_3-SO_4-fluids, probably due to host rock sulfide oxidation. In the transition zone from oxidized to reduced conditions, the sulfate and CO_2 content decreases with increasing chlorinity. The deepest fluids probed today (down to about 8 km depth) are high-salinity Na-Ca-Cl fluids (~20 wt.%) typical of basement brines worldwide. They have, for example, a Cl/Br mass ratio of ~ 90 and are enriched in P and As (Bucher and Stober, 2010; Edmunds and Savage, 1991; Emmermann et al., 1995; Frape and Fritz, 1987; Frape et al., 1984; Köhler, 1992; Kozlovsky, 1984; Sanjuan et al., 2010). This fluid stratification is believed to result from successive infiltration of surface waters into the crust over time (Agemar et al., 2013; Bons et al., 2014; Walter et al., 2016 and references therein).

1.3.2 Sedimentary cover (Permian-Jurassic)

The different compositions and permeabilities of the various sedimentary cover rocks result in variable fluid compositions. The aquifer properties are variable: in the crystalline basement (see above), fluid in the aquifer is migrating over fluid filled fractures, in the Buntsandstein sandstones of matrix porosity and the Muschelkalk limestone is a karst aquifer (Geyer and Gwinner 2011 and references therein; Ufrecht 2006).

Fluids from Permian redbeds are typically Na-Ca-(K)-Cl fluids with a maximum TDS (total dissolved solids) of 124 g/L (Pauwels et al., 1993) with occasional enrichments of Ni, Cd and U (Köhler, 1992).

Lower Triassic (Buntsandstein) formation waters are Na-Ca-HCO_3-Cl-(SO_4) fluids with a maximum TDS of 207 g/L and Cl/Br ratios of 165-327 (Pauwels et al., 1993, Ludwig et al., 2011). Elevated Rb and Cs contents have been reported in fluids of the Buntsandstein formation at Soultz-sous-Forêt, probably related to the dissolution of mica (Aquilina et al. 1997a; Pauwels et al., 1993).

Fluids in the middle Triassic (Muschelkalk) limestone-gypsum-halite formation are quite variable, depending of the specific sedimentary facies. Those which interacted with the halite formation are Na-(Ca)-Cl fluids with a TDS up to 246 g/L (Göb et al., 2013; He et al., 1999) and show high chlorinity and high Cl/Br ratios up to 9900 (Stober and Bucher, 1999). In contrast, those from the dolomite and gypsum/anhydrite lithologies are Na-Ca-(Mg)-Cl-HCO_3-SO_4 and Ca-Mg-Na-HCO_3-SO_4-Cl fluids of low to moderate salinity (6 g/L) and a Cl/Br ratio of 25-725 (He et al., 1999; Göb et al., 2013).

Fluids in the upper Triassic (Keuper) clay-, sand- and marlstones are of the Ca-Na-HCO_3-SO_4-Cl type with TDS (≤2.5 g/L), Cl/Br ratios of 405-533 and local enrichments of B and P (Köhler et al., 1992; Göb et al., 2013). The Keuper rocks are of minor importance as aquifers (Stober and Bucher, 2014).

The Lower Jurassic (Lias) clay formation is an aquitard rather than an aquifer, but pore fluids show a Na-Mg-Ca-Cl-SO_4 composition (Pearson et al., 2003). The organic-rich Posidonia formation (Lias ε) is internationally recognized as a petroleum source rock (Geyer and Gwinner 2011, and references therein) and hence, fluids from this stratum may contain abundant methane and higher hydrocarbons.

In and along the Rhinegraben valley, the Middle Jurassic (Dogger, Hauptrogenstein Fe-rich limestones) contains an important karst aquifer with two different types of fluids: a Na-Ca-Cl and a Ca-Mg-HCO_3-SO_4 water (He et al., 1999). Upper Jurassic strata are very rare in the vicinity of the Rhinegraben and are therefore not considered further here.

1.3.3 Paleogene and Quarternary Sediments in the Upper Rhinegraben

The Tertiary filling of the Upper Rhinegraben mainly consists of limestones and evaporite sequences, with locally occurring organic-rich shales. Quarternary sediments are mainly gravel. At depth, the Upper Rhinegraben is underlain by the strata of the former sedimentary cover discussed above (Fig. 2). Hydrothermal sulfates (dominantly anhydrite and gypsum, more rarely barite) derived from more than 400 m thick sulfate-bearing strata in the rift are common in fractures (Lorenz, 2002) and formed

198 from Ca-SO_4-rich fluids partially related to gypsum dehydration. Fluids that have interacted with
199 Oligocene halite are Na-dominated, have a high salinity and high Cl/Br ratios up to 2400 (Stober and
200 Bucher, 1999). Additionally, fluids which interacted with the 600m thick Oligocene gypsum-
201 anhydrite-halite-sylvite formation in the graben are expected to have a $CaSO_4$-NaCl-KCl signature
202 (Borchert, 1959).
203 In addition, Ca-Mg-HCO_3-(SO_4) fluids are known from the psephitic graben filling sediments (Geyer
204 and Gwinner, 2011; Köhler, 1992) and oil field brines are known from the organic-rich shales of the
205 Pechelbronn formation (Otto and Tòth, 1988).
206 Lorenz (2002) showed complex interactions between formation waters, highly mineralized basement
207 fluids and meteoric waters. Sanjuan et al. (2010) and Lorenz (2002) described a convection system
208 with a downward flow in the centre and an upward flow at the boundaries of the Rhinegraben. The
209 major upward fluid flow occurs from the deepest point in the centre of the rift towards the west, which
210 follows the asymmetric geometry of the rift (Fig. 2; Agemar et al., 2013).
211

212 ## *2. Sample material*

213 ### *2.1 Samples used for microthermometry, Raman spectroscopy and crush leach analyses*

214 For this study we analysed all representative (mineralogy, volume, fluid chemistry and structural
215 position) and accessible post-Cretaceous, Upper Rhinegraben-related veins in the Schwarzwald
216 mining district (Fig. 3). Their diverse mineralogy (Fig. 4, Table 2) makes it necessary to analyse fluid
217 inclusions in quartz, carbonates, fluorite and barite. If available, euhedral and clear crystals of
218 centimeter size and with visible growth zoning were chosen. Samples with macroscopically visible
219 intergrowths of different gangue and ore minerals were strictly excluded for crush leach analyses.
220

221 ### *2.2 Samples used for LA-ICPMS analyses on individual fluid inclusions*

222 To investigate the processes relevant for ore formation on the scale of one deposit, six locations have
223 been investigated in detail. These six veins are situated in fractures of the Upper Rhinegraben fault
224 system (SSW-NNE trending). The selected centimetre-sized quartz samples contain primary fluid
225 inclusions on macroscopically visible growth zones. In four of the six localities these quartz crystals

represent the youngest precipitates of the paragenetic sequence of the respective deposit, only the Badenweiler and Böschlisgrund samples contain fluid inclusions in the ore-stage quartz.

Sample TF35 derives from the Hausbaden mine near Badenweiler ("Quarzriff"), which is a typical quartz-barite vein with galena and sphalerite located directly on the Rhinegraben boundary fault. Here, crystalline basement rocks are in direct contact with tilted blocks of Buntsandstein sandstones, Muschelkalk limestones, and gypsum-bearing Keuper shales.

Two sample of the barren barite-quartz veins from the Tirolergrund and Wurmbach (BO26 and BO92) were collected about 500m east of the Rhinegraben boundary fault east of Staufen and Ballrechten, respectively, within a paragneiss basement unit. These veins probably formed around the Triassic-Jurassic boundary, but show clear evidence for a post-Cretaceous overprint (Walter et al., 2016)

The Karl-August quartz vein (sample BO66) occurs near Kropbach/Münstertal 2 km east of the Rhinegraben boundary fault. It follows a granitic dyke in the paragneiss unit and contains massive sphalerite overgrown by large euhedral quartz crystals.

The Riggenbach and Böschlisgrund veins (samples BO29 and BO98) consist of an early quartz-galena-sphalerite stage followed by later siderite stage with Cu-Ni ores. Young euhedral large quartz crystals overgrow this paragenetic sequence. The Riggenbach mine is situated in the Münstertal, about 4 km East of the Rhinegraben boundary fault, while the Böschlisgrund vein crops out northeast of the town of Sulzburg about 5 km east of the Rhinegraben boundary fault.

3. Methods

3.1 Microthermometry

Microthermometric investigations were performed using a Linkam stage (model THMS 600) at the Universität Tübingen. Up to three double polished thick sections (200 to 400µm) were produced from a cross-section through each vein to determine the chronological sequence of fluid inclusion assemblages (FIA, Goldstein and Reynolds, 1994) by optical microscopy. The observed fluid inclusions were classified as primary (p), pseudo-secondary (ps), secondary (s), isolated inclusions (iso) and clusters of inclusions with no geometrical relation to former crystal surfaces or fractures (c). Each fluid inclusion was analysed three times with respect to the final melting temperature of ice

($T_{m,ice}$) and hydrohalite ($T_{m,hh}$) and the homogenization temperature (T_h). The data include only fluid inclusions, for which triple analyses differ less than 0.1°C for $T_{m,ice}$ and $T_{m,hh}$ and less than 1°C for T_h. Synthetic H_2O, H_2O-NaCl and H_2O-CO_2 standards were used for calibration.

Fluid inclusions strongly deviating in salinity and homogenization temperature from a close-by homogeneous trail were neglected, since this may indicate fluid inclusion alteration by post-entrapment processes. The salinity in the ternary SO_4-free NaCl-$CaCl_2$-H_2O system was calculated according to Steele-MacInnes et al. (2011). The volume proportion for each fluid inclusion was estimated based on filling degree tables and reported in the volume proportion notation (Shepherd et al., 1985; Bakker and Diamond, 2006). A pressure correction according to Bodnar and Vityk (1994) was applied, assuming hydrostatic conditions with a depth of the water column inferred from the paleo-depth estimated by Geyer and Gwinner (2011). Uncertainties of this approach are discussed in Walter et al. (2015). Since hydrostatic conditions can be assumed and overburden is negligible for the post-Cretaceous veins of interest, the pressure correction has only minor effects on the homogenization temperature.

Microthermometry of fluid inclusions in barite is difficult, since they are easily destroyed during freezing or heating (decrepitation, leakage, necking-down). Consequently, microthermometric data obtained from fluid inclusions in barite were only used for calculating salinities, if the data agreed with data of quartz, fluorite or calcite from the same or a closely related vein, and they were principally excluded from Ca/(Ca+Na) calculations.

3.2 Crush leach analyses

About 2g of fluorite, quartz, calcite or barite with a grain size of 0.5 to 1 mm were handpicked from 155 selected samples for which microthermometric investigations assured that only one fluid type was present in the respective crystals. Visible impurities were removed and the separates were further cleaned for 3 hours in HNO_3 at 60-70°C (the carbonate samples being cleaned in MilliQ water only). Subsequently, the samples were washed for one week with MilliQ water, changing the water twice a day. These pre-treated samples were dried, crushed to fine powder in an agate mortar and 10 ml MilliQ water were added. To suppress the adsorption of doubly-charged cations (especially Ca^{2+}),

crush leach solutions were acidified with 10 µl suprapure HNO_3 (Köhler et al., 2009). The loaded solution was injected into a Dionex ICS 1000 ion chromatography systems, equipped with an IonPac AS 9-HC and CS 12-A 2mm column for quantification of anions (F, Cl, Br, NO_3, PO_4 and SO_4) and cations (Li, Na, K, Mg, Ca, Ba, Sr), respectively. For injection of the solutions, we used disposable syringe filters CROMAFILE© Xtra RC-20/25 and CROMAFILE© Xtra PVDF-20/25 for anions and cations, respectively. Blank runs were carried out before and after each analysis and defined standard solutions were regularly analysed to monitor the reproducibility and precision of the measurements. Uncertainties were usually smaller than 15% and effective detection limits were generally <10 mg/l.

The concentrations of several trace metals (Cu, Ni, Co, Pb, Zn, Bi) were determined by Total Reflection X-Ray Fluorescence Spectroscopy (TXRF) using an S2 PICOFOX (Bruker AXS Microanalysis) equipped with a Mo-tube operated with 50 kV and 600µA. For these analyses, each 1 ml of the crush leach solutions (see above) were centrifuged and filtered. Subsequently, 190 µl of the solutions were mixed with 10 µl Ga solution with a Ga concentration of 5 mg/l. Three aliquots (10µl) were pipetted onto polished quartz-glass disks and dried at 70°C. The dried sample cakes were then analyzed for 1000 s. Effective detection limits for these metals vary with the degree of dilution (based on the crush-leach procedure, see above) and were generally <50 mg/l for Cu, Ni, Pb and Zn and <100 mg/l for Co and Bi.

Quartz, barite, calcite and fluorite were used for crush leach analyses (IC and TXRF). A contamination of the leachates by the dissolution of these host minerals is potentially relevant for fluorite (Ca, F), calcite (Ca) and barite (Ba, Sr, S). The complete dataset in the electronic supplement includes these elements, but their concentrations are excluded from interpretation. Many of our crush-leach solutions contain dissolved carbonate from fluid inclusions (as indicated by the presence of CO_2 based on Raman spectroscopy) and we assume that the positive deviations from electroneutrality can be ascribed to carbonate species, as has been done before (e.g. Bottrell et al., 1988; Channer and Spooner, 1991; Banks et al., 2000; Dolnischek et al. 2014). This assumption has no impact on the quality of Cl and Br data in the crush-leach analyses and especially not on the Cl/Br ratios, nor on the quality of microthermometric data (Ca-Na systematics, salinity or homogenization temperatures). The leaching solutions were filtered and centrifuged before analysis, to exclude contamination by suspended

particles of e.g. ore minerals. Several analyses revealed high metal contents of up to 48200 mg/l Pb and 51900 mg/l Cu. To evaluate the validity of these analyses we carried out calculations with Geochemist Workbench Version 10.0.2. Using the compositions and salinities of BO65 and ML40 (table 2 of the electronic supplement) at neutral pH, an fO_2 in the sulfide stability field and a temperature of 150°C, the calculations show that the Pb and Cu concentrations of all crush-leach analyses are well below the saturation of galena (0.7 mol/l or ~145 g/l Pb) and chalcopyrite (10 mol/l or ~635 g/l Cu).

3.3 LA-ICPMS microanalyses of single fluid inclusions

LA-ICPMS microanalysis of individual fluid inclusions was conducted at the ETH Zürich using a Perkin Elmer Elan 6100DRC quadrupole ICPMS connected to an ETH-GeoLas 193 nm ArF excimer laser system. An energy density of 15-20 J/cm^2 with a laser pulse frequency of 10 Hz, with a variable beam size was used. Analytical and standardization procedures are reported in (Heinrich et al., 2003) and (Seo et al., 2011). The following 27 isotopes were analyzed: ^{7}Li, ^{11}B, ^{23}Na, ^{24}Mg, ^{32}S, ^{35}Cl, ^{39}K, ^{44}Ca (not quantified in fluorite but used for matrix correction), ^{55}Mn, ^{57}Fe, ^{59}Co, ^{60}Ni, ^{63}Cu, ^{66}Zn, ^{75}As, ^{79}Br, ^{85}Rb, ^{88}Sr, ^{95}Mo, ^{107}Ag, ^{121}Sb, ^{133}Cs, ^{137}Ba, ^{182}W, ^{205}Tl, ^{208}Pb, ^{209}Bi and ^{28}Si (for the quartz host correction). The peaks of the analysed elements strictly follow the Na and Cl peaks in the time-resolved LA-ICPMS signals, which demonstrates that these element peaks are derived from the solutions and not from the host mineral. For absolute concentrations, the measured concentrations were related to the NaCl salinity determined by microthermometry in the $CaCl_2$-NaCl-H_2O system (Steele-MacInnes et al., 2011). Data reduction was done using the SILLS software package (Guillong et al., 2008). The complete dataset is presented in the electronic supplement.

3.4 Microraman spectroscopy

Microraman measurements were performed with a confocal Raman spectrometer Renishaw InVia Reflex at Universität Tübingen to detect and identify volatile phases in representative fluid inclusion assemblages,. All measurements were carried out with a laser wavelength of 532nm (green) using a laser output of 50%. The use of a 50% objective results in a numerical aperture of 0.55 with an

opening angle of 66.7°. The slit diaphragm was regulated and corrected automatically. The focus diameter was approximately 2µm, the measurement time was 30 seconds with a three-rate accumulation. To correct any influence from the matrix, measurements in the host mineral were performed under identical conditions and orientation. As far as possible (depending on inclusion size), separate measurements focussing on liquid and on vapour were done. For qualitative evaluation, the Raman database for fluid inclusions of Frezzotti et al. (2012) was used.

3.5 Cathodoluminescence (CL) microscopy

Cathodoluminescence (CL) microscopy studies of different hydrothermal phases were performed to obtain additional qualitative information on the fluid petrography of fluid inclusion assemblages. Furthermore, replacement textures of barite and anhydrite were studied. We used a 'hot cathode' CL microscope (type HC1-LM) at Universität Tübingen with an acceleration voltage of the electron beam of typically ~14 kV and a beam current density of ~9 µA mm^{-2} on the sample surface.

4. Results

4.1. Classification of fluid signatures

Detailed petrography (optical microscopy and microthermometry) of fluid inclusion assemblages (FIAs) enables their classification according to their relative age (Fig. 5). Major differences between primary and secondary fluid inclusions can be summarized as follows: Primary inclusions along crystal growth zones are typically smaller (<5-15 µm) than secondary inclusions and pseudosecondary assemblages (<5-80 µm), which mostly occur along (partly) sealed fractures and crosscut the primary structures often exhibiting angular shapes. Fluid inclusion data of all genetic characters (p, s, ps, iso) are brought into a relative temporal sequence.

In general, veins situated directly on the Rhinegraben boundary fault or on conjugated faults show complex, alternating fluid signatures (low, medium and high salinity fluid inclusion assemblages of variable temperatures, table 3) within neighbouring FIA. Veins situated on fault far away of the Rhinegraben boundary fault typically do not show such complex sequences.

366

367 *Signature A: low salinity, medium to low temperature*

368 Fluid inclusions of type A (table 3) occur in p, s, ps, iso and c FIAs. They freeze in the range -30 to -
369 45°C and first melting occurs above -20°C, implying a binary NaCl-H_2O system with a eutectic
370 temperature of -21.2°C. The final melting temperature of ice is in the range of 0°C to -5°C, resulting in
371 calculated salinities of 0 - 5wt.% (NaCl+$CaCl_2$). Homogenization temperatures (Th) range from 50 to
372 354°C with a conspicuously high abundance of fluid inclusions with Th around 180°C. Within a given
373 trail, salinity and T_h are constant, but may vary between different trails. Fluid inclusions with LV10 to
374 LV1 and sizes of 4 to 40µm can be observed. In most cases, the inclusions are irregularly shaped and
375 occur on (not very well) healed cracks. Microraman analyses show only H_2O, HCO_3^- or CO_3^{2-}, but no
376 SO_4^{2-} in the fluid.

377

378 *Signature B: high salinity, low to moderate temperature*

379 Type B inclusions (table 3) occur in p, s, ps, iso and c assemblages with freezing temperatures
380 between -70 and -100°C and first melting above -50°C, implying a ternary NaCl-$CaCl_2$-H_2O system
381 with an eutectic temperature at -52.0°C. Ice and hydrohalite are observed as last dissolving phases.
382 The final melting temperature of ice is in the range of -29.0 to -18.5°C, of hydrohalite between -28.5
383 and -17.5°C, indicating salinitites of 20 - 26 wt.% (NaCl+$CaCl_2$). Homogenization temperatures range
384 from 70 to 230°C with a Gaussian mean at 130°C. The molar Ca/(Na+Ca) ratio varies between 0.02-
385 0.53. Within one trail, salinity and T_h are constant, but may vary between different trails. Inclusions
386 have sizes of <5 to 100µm. Most inclusions are irregularly shaped and occur on primary growth zones
387 and nicely healed fractures. Microraman analyses show H_2O as the only Raman-active species in all
388 FIA

389

390 *Signature C: variable salinity, low to moderate temperature*

391 Fluid type C (table 3) occurs as p, s, ps and iso FIAs. Inclusions with freezing point depressions
392 between -70 to -100°C and -30-45°C are observed in numerous samples. In contrast to the previously
393 described groups, two different FIAs occur: one with a eutectic temperature of -21.2 and another with

a eutectic temperature of -52°C. Although the Ca/(Na+Ca) molar ratios of these FIA vary, all fluids of intermediate salinity (i.e., between 0.9 and 20 wt.% $NaCl+CaCl_2$) are compiled in fluid group C. Additionally, the Ca/(Na+Ca) molar ratio may vary within one FIA. In all analysed FIAs, ice is the last dissolving species. The final ice melting temperature is in the range of -2.6 to -18°C, hydrohalite melts between -20.9 and -25.8°C, which results in a calculated salinity of 5 to 20 wt.% ($NaCl+CaCl_2$). Homogenization temperatures vary between 59 and 202°C with a Gaussian peak at 140°C. Molar Ca/(Na+Ca) ratios vary between 0 and 0.3. Within one trail, salinity and T_h are constant, but they may vary between different trails. Inclusions have sizes of <5 to 100µm and LV15 to LV1. Most inclusions are round and occur on primary growth zones and nicely healed fractures. Microraman analyses show in all trails only H_2O as Raman-active species.

Signature D: H_2O-CO_2-(NaCl)

In contrast to the previously described fluid types, type D fluids (table 3) are relatively rare. Only primary and secondary inclusions have been found. The CO_2 phase transition occurs in all inclusions at -56.8°C. Homogenization of the carbonic liquid into vapour (transition $L_{car}L_{aq}V$ to $L_{aq}V$) occurs between +21 and 31°C. For the larger inclusions clathrate dissolutionhas been detected at +4.9 to +5.9°C. The first melting of ice happens at about -18°C. Final dissolution of ice occurs at -4.7 to -7.6°C does not support a pure H_2O-CO_2 fluid. Thus, an additional NaCl component seems likely, as Microraman analyses show only CO_2 and H_2O bands. T_h varies between 134 and 219°C and occurs into the vapour phase with L(LV)10 to L(LV)20. Based on the software package "CLATHRATES" (Bakker, 1997) a salinity of maximum 5 wt. % $NaCl_{eq}$ is calculated. The carbonic liquid has a rather low density because it homogenizes into the vapour and total homogenization occurs at low T, too. This points towards very little CO_2 in the bulk inclusion, X_{CO2} of 0.02-0.05.

Signature E: Multi-component system with unknown salinity without CO_2 at moderate temperatures

Secondary and isolated assemblages of this fluid type (table 3) were found in few samples only. First melting occurs above -45°C, freezing point depressions range from -70 to -100°C, final ice melting was detected between -10.9 and -15°C, final dissolution of a cubic dark green solid phase (probably

sylvite) was reached at +20 to +24°C and a lime green long prismatic solid phase (probably anhydrite) dissolved at +43° to +63°C (Fig. 6A-D). During repeated heating-freezing cycles, each phase transition could be reproduced in every single run. Microraman analyses verified the presence of dissolved sulfate in these fluid inclusions. Based on the microthermometric and Microraman results, this type of fluid obviously has a composition in the NaCl-KCl-$CaSO_4$-H_2O-system. The homogenisation temperature is constant within one trail, but ranges from 98°C to 220°C, with a mean of 130°C. Inclusion sizes vary from <5µm to >100µm with LV10 to LV5.

Signature F: Multi-component system with unknown salinity with CO_2 at moderate temperatures

Type F fluid inclusions (table 3) are of primary and secondary origin. Their most important attribute is a clearly visible double-bubble, which is characteristic of CO_2- or CH_4-bearing fluids. The CO_2 phase transition occurs between -56.4 and -56.8°C. The homogenization of CO_2 liquid into vapour ($L_{car}L_{aq}V$ to $L_{aq}V$) is reached between +21.3 and +31°C.

Two types of inclusions are found: One (F1) shows a freezing point depression between -40 and -60°C, final melting of ice from -9.7 to -17.4°C. In many inclusions, a cubic dark green solid phase dissolves between +22.5 and +24.5°C (probably sylvite). Sometimes, a long prismatic lime green solid phase is observed (xxxx?s.o.), melting between +60 and +75.2°C. Hydrohalite nucleation disappears close to the binary eutectic of -21.2°C. Microraman data show CO_2 and sulfate bands. Based on the microthermometric and microraman results, this is an H_2O-CO_2-SO_4-NaCl-KCl fluid. Uncorrected homogenization temperatures vary between 210°C and 307°C with L(LV)10 to L(LV)20.

A second fluid type (F2) shows a freezing point depression below -80° and first melting between -40 and -50°C. Final dissolution of hydrohalite occurs between -23.0°C and -26.0°C and the final ice melting occurs in the range of -0.1°C and -0.8°C. An unknown columnar lime green phase shows a phase transition into liquid at +24 to +27.1°C. The total homogenisation of all vapor species is in the range 140 to 180°C. Clathrates may be observed in some FIAs, finally melting at +5.1°C to +6.3°C. Similar to signature D, a salinity of about 5-25 wt. % $NaCl_{eq}$ can be calculated. Microraman data show sulfate and CO_2 bands. The carbonic liquid has also a low density based on the homogenization into the vapour phase, with a total homogenization at low T. A small X_{CO2} of 0.02-0.05 in the bulk

inclusion can be assumed. Type F2 inclusions probably contain Na-Ca-K-H_2O-SO_4-CO_2 fluids with L(LV)10 to L(LV)20.

Finally, in addition to A, B, C, D, E and F type fluids, most samples contain young FIAs characterized by water-rich, mono-phase liquid inclusions.

4.2 Crush leach analyses

In total, 155 crush leach analyses of 96 veins were performed. The complete dataset is presented in the electronic supplement (HCO_3 is derived by charge balance). Bulk trace element systematics show Cu (b.d.l.-51.920ppm), Zn (b.d.l.-45.130ppm), As (b.d.l.-52.980ppm), Pb (b.d.l.-43.800ppm), U (b.d.l.-12.250ppm), Ni (b.d.l.-8790ppm), Y (b.d.l.-8880ppm), Rb (b.d.l.-7400ppm), Co (b.d.l.-3280ppm), Th (b.d.l.-2250ppm), Tl (b.d.l.-1470ppm), W (b.d.l.-1070ppm) and Bi (b.d.l.-510ppm). Highest Th and U concentrations are found in fluids hosted especially in barite and sometimes in calcite. In general, there is no systematic dependence of the fluid composition on the proximal host rocks, salinity, homogenization temperatures, vein type or trace element distribution. Cl/Br mass ratios range unsystematically from low to high values, even between adjacent veins, the only exception being the veins of the Badenweiler system: these veins exclusively show high Cl/Br ratios.

4.3 LA-ICP-MS of single fluid inclusions

LA-ICPMS analyses were performed on 110 fluid inclusions from six samples. The results are presented in figure 6, table 4 and in table ES3 of the supplementary material. Within one FIA, salinity and Ca/(Na+Ca) molar ratio are almost constant, but trace metal concentrations vary. Trace element systematics of single fluid inclusions show Li (b.d.l.-17480ppb), B (b.d.l.-2160ppb), Mg (b.d.l.-36420ppb), S (b.d.l.-91620ppb), Mn (b.d.l.-3890ppb), Fe (b.d.l.-12830ppb), Co (b.d.l.-400ppb), Ni (b.d.l.-16390ppb), Cu (b.d.l.-3990ppb), Zn (b.d.l.-10900ppb), As (b.d.l.-3370ppb) Rb (b.d.l.-1910ppb), Sr (b.d.l.-3090), Mo (b.d.l.-3620ppb), Sb (b.d.l.-3860ppb), Cs (b.d.l.-8270ppb), Ba (b.d.l.-3980ppb), W (b.d.l.-3750ppb), Tl (b.d.l.-2380ppb), Pb (b.d.l.-17750ppb) and Bi (b.d.l.-394ppb).Most data of all analysed veins plot into a cloud that forms a triangle.

5. Discussion

The crush-leach and LA-ICP-MS results show a large diversity in fluid composition, but surprisingly, no clear correlation between fluid composition and vein mineralogy exists. Both methods render consistent results in terms of Cl/Br ratios (Fig. 7): the bulk Cl/Br ratios derived from crush leach analyses are perfectly within the range of LA-ICP-MS data and are interpreted to summarize over small-scale variabilities, thus providing an average composition of the mixed fluid. In the following sections, we discuss the possible relationship of the observed fluid mixtures in fluid inclusions to the sedimentary aquifers and their formation fluids introduced above. This is done to constrain the fluid sources and the source aquifers involved in vein formation.

5.1 Effects of formation temperature and salinity on vein mineralogy

While there is no recognizable correlation between formation temperature and vein mineralogy (Fig. 8), fluid salinity appears to have a certain impact on vein mineralogy, particularly on the presence of ore minerals. Metals like Pb and Zn are typically transported as Cl-complexes under the conditions of formation of the Schwarzwald mining district (Yardley, 2005; Burisch et al. 2016a), and hence, it is no surprise that veins with medium to high salinity (chlorinity) fluid inclusions often show significant amounts of galena, sphalerite and fahlore. The large variation in homogenization temperature of the individual fluid signatures is probably an effect of inhomogeneous penetration depth of the sedimentary fluid into the basement (e.g. the Buntsandstein is exhumed on the shoulders but is also situated more than 2km below today surface in the Rhinegraben).

5.2 Processes of vein formation: Multi-component mixing and the importance of tectonic juxtaposition of diverse lithologies for the aquifers properties

As shown above, the vein mineralogy shows no strict correlation to the fluid inclusion chemistry. Still, fluid mixing has to be the dominant formation process, which is shown by numerous authors, as fluid cooling alone is not a sufficiently efficient mechanism in this setting to cause the observed amount of hydrothermal mineralization, the diversity of vein mineralogy, the mineral textures and fluid chemistry (Fußwinkel et al., 2013; Bons et al., 2014; Walter et al., 2015, 2016, Jura).

In contrast to the spatially unsystematic variability of fluid chemistry in post-Cretaceous veins, fluid compositions in Jurassic-Cretaceous veins show clear systematics depending on their depth of formation and the type of sedimentary overburden (Walter et al., 2016, Jura). This difference is consistently described by a two-component mixing in a tectonically undisturbed environment, which prevailed during the Jurassic and Cretaceous. Juxtaposition of various types of aquifers (at least three, possibly more) due to tectonic processes in the Cenozoic (see above), however, requires the consideration of more than two fluid components involved in mixing (see e. g. Fig 6C, 8F in Walter et al., 2015, in press brine). Our multi-aquifer mixing model is capable of explaining the unsystematic variation in major, minor and trace element composition, salinity, formation temperatures and isotopic variations (not further discussed here; see Walter et al., 2015).

Fluid ascent may have been triggered by topographic fluid flow or by tectonic opening of confined aquifers in the tectonically disturbed environment of the rift shoulders (Agemar et al., 2013). During earthquakes, pathways opened or were reactivated and the confined aquifers released their fluids. Fluid mixing of two or more aquifers occurred, minerals precipitated in the pathways (partially sealing them) and hence, the ancient pathways are now the mineralized veins.

5.3 Aquifers involved in vein formation

5.3.1 Fluid signature A

The low salinity fluids of group A are interpreted as weakly mineralized meteoric fluids (see Fig. 9, reservoir 1). Some of the samples containing type A fluid inclusions have K-Ca-Na-Cl-HCO_3 and Na-K-Ca-Cl-HCO_3 signatures in the crush leach analyses, which have to the best of our knowledge no modern analogy. Without exception, this fluid type occurs in veins very close to Permian rhyolites. We suggest that the extensive alteration of K-feldspar under relatively acidic conditions to gibbsite, pyrophyllite and/or kaolinite, which can be observed in these rhyolites, results in substantial K release to the fluid at the time of alteration which is interpreted also as the time of mineralisation (Brockamp et al., 2003, 2011).

534 *5.3.2 Fluid signature B and C Na-Ca-Cl*

535 The medium to highly saline Na-Ca-Cl and Ca-Na-Cl fluid types B and C mainly occur in quartz-
536 barite veins with a Pb-Zn mineralization (Table 2). A possible source of these fluids is a mixture of
537 formation waters from the Muschelkalk halite facies (Fig.9, reservoir 2) and highly mineralized
538 basement fluids (Fig. 9, reservoir 3). This is supported by variable Cl/Br mass ratios and high metal
539 contents. Differences in the Na/Ca ratios are probably related to variable mixing ratios (see Walter et
540 al., Jura). The variation from medium to high salinity can be explained by mixing fluid type A as a
541 third component to types B and C, which dilutes the other two components. Increasing amounts of
542 fluid A result in a salinity decrease of the final fluid.

543

544 *5.3.3 Fluid signature D: Ca-(Na)-HCO_3 and Ca-(Na)-SO_4*

545 Fluid signature D shows the largest variation of salinities from 1-26 wt.% ($NaCl+CaCl_2$). Since these
546 fluids have bicarbonate and sulfate as dominant anions, the calculated salinity is imprecise, as these
547 components cannot be accounted for in the salinity calculations (Steele-MacInnes et al., 2011).
548 However, this wide range of salinities reflects a mixing continuum of two or more endmembers. Based
549 on modern fluid stratigraphy in the Schwarzwald basement, one fluid type could be a low salinity,
550 surface- or subsurface-derived fluid residing for some time in the basement, which results in a weak
551 basement brine-like signature. The Ca dominance may be a product of plagioclase alteration which has
552 been invoked as explanation for the low chlorinity fluids with high Ca and bicarbonate content
553 (Bucher & Stober, 2010). The high salinity endmember, bicarbonate-dominated fluids are probably
554 released from a limestone aquifer like the Muschelkalk (Fig. 9, reservoir 2) or the Jurassic
555 Hauptrogenstein (Fig. 9, reservoir 4) where such fluids are present today (He et al., 1999).
556 Fluids with a Ca-(Na)-SO_4 signature occur in sample BW144 where microtextures clearly indicate the
557 former presence of gypsum or anhydrite (Fig. 10) today replaced by quartz. The investigated fluid
558 inclusions are exclusively hosted in young quartz replacing the sulfate. The same fluid signature could
559 be observed at Schlossberg West and at Calmbach; in both veins, barite is completely pseudomorphed
560 by quartz and sulfides are lacking. Thus, this fluid signature is interpreted as a local phenomenon at or
561 around dissolving sulfates, providing no general source information.

562

563 *5.3.4 Fluid signature E and F: Na-K-Ca-Cl-(SO_4)-(HCO_3), Ca-Na-K-Cl-SO_4-(HCO_3) and Na-Ca-K-*
564 *Cl-SO_4-(HCO_3)*

565 The chemical variability of fluid types E and F makes it difficult to dedicate these fluids to a specific
566 source. These fluid signatures are not sufficiently unique and resemble fluids present in almost all
567 modern sedimentary aquifers (Göb et al., 2013 and references therein). Veins of different mineralogy
568 comprise these signatures, most of them being situated in the crystalline basement. Low Cl/Br ratios
569 indicate no significant influence of the middle Triassic evaporites. As sulfate occurs in higher
570 concentrations than bicarbonate (if this is present at all), it is most likely that these fluids are derived
571 from intermediate depths of the crystalline basement (Fig. 9, reservoir 5), Triassic Buntsandstein
572 (reservoir 6) and/or the lower or upper Muschelkalk (Fig 9, reservoir 7). High Na/Ca, low Cl/Br ratios
573 and the variation of low to high salinity suggest a strong basement component in the mixed fluid of
574 some of the veins.

575

576 *In all,* it seems plausible that most of the fluorite and quartz veins precipitated from a chloride-rich
577 brine mixed with a bicarbonate-dominated low salinity fluid (Fig. 11A). A small group of quartz veins
578 (unsystematically distributed in the mining district) precipitated from a Cl-SO_4-HCO_3 fluid.
579 Furthermore, Fig. 11B shows that some quartz and barite precipitated from a Ca-Na fluid with variable
580 Ca/Na ratios. The combination of Figs. 11A, B and F implies that for most veins, the Cl-rich brine
581 endmember is a basement brine, just those with high Cl/Br and high Ca/Na ratios probably involved
582 the halite facies aquifer of the Middle Triassic Muschelkalk.

583

584 **5.4 Metal provenance**

585 The fluids responsible for formation of mineralized and barren veins are chemically similar (figure 8).
586 Therefore, the presence or absence of metal enrichment in the veins is unlikely to have been metal
587 solubility controlled, but rather points towards fluid source rocks and aquifers having exerted a first
588 order control on the fluids' metal budgets. Based on earlier work (Walter et al. (Jura) and Burisch et al.
589 (2016a, b)), fluids derived from crystalline basement rocks are the dominant source for Pb and Zn in

590 geologically undisturbed environments (e. g., SW Germany during the Jurassic and Cretaceous).
591 Fluids derived from redbeds (Buntsandstein and Rotliegend) are considered as the major source for
592 Cu, Co and Bi (e.g. Koziy et al., 2009; Hendrickson et al., 2015 and references therein). In the case of
593 the present study, however, the juxtaposition of different aquifers during graben formation may have
594 enabled the participation of several fluid sources.
595 Fluids from most samples show that their chemistry are enriched in Cu and Zn and depleted in Ni (Fig.
596 11C). Walter et al. (Jura) explained the same systematic feature in Jurassic veins with depth-depending
597 variations in the fluid mixing ratios. However, these variations with depth cannot be recognized in
598 post-Cretaceous veins. At many localities at the Rhinegraben boundary fault, Buntsandstein units lie
599 next to crystalline basement, and mixing between these two aquifers was easily possible. Hence, also
600 in post-Cretaceous times, the sources of Zn and Cu were identical to the Cu and Zn sources for
601 Jurassic-Cretaceous veins (Walter et al., Jura). Data for single fluid inclusions show that highest
602 Pb+Zn, As, W and Sb contents correlate low Cl/Br mass ratios (also with high salinities) (Fig. 12B-E).
603 We suggest that this indicates that these elements are derived from basement brines.
604 Fluids trapped in barites of different vein types are in cases enriched in U in contrast to quartz and
605 fluorite gangue generations from the identical veins (Fig. 11E). Possibly, this observation is related to
606 the oxidation state of the fluid and implies, that the barite-forming fluids were more oxidized (and
607 therefore, enriched in fluid-mobile U^{6+}) than the quartz- and fluorite-forming fluids. A possible source
608 for the U is the crystalline basement. Oxidized fluids that penetrates the basement rocks are able to
609 receive U for the primary minerals of the granites and gneisses of the crystalline basement.
610
611 *5.3.7 Ore fluid and metal precipitation*
612 The LA-ICPMS data of fluid inclusions show a Gaussian distribution for Pb+Zn with a statistical
613 maximum between 100 and 1000ppb for the Karl August, Riggenbach and Tirolergrund veins. All
614 investigated fluid inclusions are hosted in young quartz crystals, which are not in equilibrium with
615 sphalerite (sphalerite is older and probably belongs to a separate fluid event). The Gaussian mean
616 values indicate that these values are average values of a mixed ore fluid from which sphalerite could
617 potentially, but has not yet precipitated, as a consequence of relative or absolute low sulfide activities.

618 The Badenweiler and the Böschlisgrund veins, in contrast, show much lower Pb+Zn contents which
619 can be explained by prior precipitation of sulfides: in both veins, the analysed fluid inclusions are
620 hosted in galena-, sphalerite- and chalcopyrite-rich quartz. The same interpretation is suggested for the
621 Ni+Cu, W and for the Sb systematics. As none of these veins contain any Sb- or W-bearing phases, it
622 is plausible that these fluid inclusions show the unchanged, average Sb and W content of the mixed
623 ore fluid, derived from the diluted basement brine.
624
625 **5.5 Fluid mixing recorded in various growth zones of single quartz crystals**
626 Some veins show heterogeneous FIAs, i. e. variations of salinity, Ca/Na and homogenization
627 temperatures between adjacent FIA (e. g., Riggenbach, Fig. 13). Specifically, some of the Münstertal
628 and Sulzburg veins (Katzental, Himmelsehre, Krebsgrund, Karl August; Fig. 5) show complicated
629 sequences of different fluids on different growth zones in one quartz crystal.
630 Data for a sample from the Karl August mine are discussed in detail (Fig. 14). In this sample, the fluid
631 composition in terms of salinity, sulfate and CO_2 content varies strongly from one growth zone to
632 another. The variability of the fluid inclusion chemistry on a small scale requires a multi-component
633 fluid mixing, since these variations cannot simply originate from mixing of only two fluids with
634 variable mixing ratios. General aspects of these complex mixtures are: Cl/Br ratios above 150, high
635 salinities and Ca/(Na+Ca) molar ratios of 0.3-0.5 record the involvement of a saline Muschelkalk
636 fluid, while low Cl/Br, high salinities and Ca/(Na+Ca) of 0.1 to 0.3 are typical of deep seated
637 basement brines. Sulfate and CO_2 have, hence, to be derived from at least a third fluid component.
638 These complex multi-component mixtures only occur in close proximity (within few kilometres) to the
639 Rhinegraben boundary fault and it is most plausible, that short-lived tectonic movements established
640 and destroyed various aquifer systems or fluid migration paths, which can be recorded on single
641 growth zones of discontinuously growing quartz.
642
643 **5.5 Complex fluid behaviour recorded by FIAs on single growth zones**
644 A primary growth zone in e.g. a euhedral quartz crystal was an exposed surface during its formation
645 and different fluid inclusions on one growth zone should consequently record the same fluid event

(Van den Kerkhof, & Hein 2001, and references therein).

Figure 14 illustrates LA-ICPMS results for the Karl-August mine near Kropbach. The heterogeneity of these fluid inclusions in terms of their minor and trace element concentrations within one event of crystal growth can be clearly seen (also taking the analytical error into account). During trapping, the fluids are not completely homogenized and therefore show variable mixing ratios on small scales (e.g., Fusswinkel et al., 2013; Bons et al., 2014) The FIAs in the Karl-August mine near Kropbach record ternary mixing ratios (reservoirs 2/3/1) between (81/19/0), (1/5/94) and (2/75/23) on one primary growth zone (fig. 14A). These observations imply that the crystallisation of the host quartz is more rapid than the diffusional or turbulent flow equilibration of the fluid components.

The calculation of the time required to homogenize the mixed fluid batches assuming only diffusion as the driving force, consequently yields a minimum growth rate for the host mineral. For a rough assessment of the growth rates of one quartz growth zone, two contiguous fluid inclusions (Ø = ~20 µm) of the FIA pQtz3-5 with a distance of 50µm were selected. One inclusion has a sulfate content of 4000ppm, a Cl content of 81.600ppm, a Cl/Br mass ratio of 100, a salinity of 24wt% and shows a homogenization temperature of 191°C, while the other inclusion has a sulfate content of 15.400ppm, a Cl content of 30.300ppm, a Cl/Br mass ratio of 300, the identical salinity and a homogenization temperature of 131°C.

After fracture formation, fluids from different aquifers enter the fracture and do not completely homogenize for a specific (short) time interval. Two different types of equilibria are considered: thermal equilibration with $DT \approx 10^{-6}$ m^2/s and chemical equilibration $Dm \approx 10^{-9}$ m^2/s. Using these diffusion coefficients in the equation $\langle X \rangle^2 = D\Delta T$ yields durations of ~2.5s for chemical equilibration and a time for 0.005s for thermal equilibration of the 50 µm distance. Compared to experimental growth rates (e.g. 2 µm/h Okamoto & Sekine, 2011, and references therein), the time intervals based on thermal and chemical diffusion are much smaller. However, the experiments of Okamoto & Sekine (2011) do not consider mixing processes and far-from-equilibrium conditions, which possibly yield much higher growth rates. Alternatively, the observed temperature difference in adjacent fluid inclusions would require a time gap between their trapping or post-entrapment modifications, which both do not seem very plausible considering the textural observations.

674

675

676 *5.6 The Rb/Cs ratio and its bearing on the fluid pathways*

677 The Rb/Cs ratio is a suitable tracer for fluid pathways because Rb and Cs can be adsorbed to and
678 incorporated into clay minerals that are present along such pathways: Burisch et al. (2016a and
679 references therein) and Göb et al. (2013) showed that a fluid Rb/Cs ratio <2 is typical of fluids which
680 interacted with unaltered crystalline rocks, while Rb/Cs ratios of ~2 represent equilibrium conditions
681 during alteration of primary minerals to clay minerals. Rb/Cs ratios >5 indicate water-rock interaction
682 with pre-existing clay minerals (no alteration of primary phases). Most of the measured Rb/Cs ratios
683 (Fig. 16) are below 2 which indicates that new pathways were opened during post-Cretaceous fluid
684 activity, rather than reactivating older fractures. Higher Rb/Cs ratios are present in young FIAs in the
685 Karl August vein. These young growth zones obviously record a reactivation and fluid migration
686 along previous established pathways, while the older quartz generations and growth zones in the same
687 vein show low Rb/Cs ratios.

688

689 **5.7 Temporal and chemical evolution of the aquifers**

690 In contrast to the tectonically undisturbed aquifers during the Jurassic and Cretaceous, post-Cretaceous
691 rocks and their aquifers influence each other by fluid migration from one to another aquifer. For
692 example, Muschelkalk fluids are modified by migrating into the Buntsandstein aquifer, which is
693 indicated by elevated Ca/(Na+Ca) mole ratios and high Cl/Br mass ratios in todays Buntsandstein
694 aquifer fluids (dissolution of halite). Mixing or large scale fluid migration prior to mineralization
695 makes it impossible to distinguish between defined reservoir signatures in the post-Cretaceous veins
696 with the following two exceptions:

697 - Fluid signatures with high Cl/Br and high Ca/(Na+Ca) molar ratios can be related to fluids
698 dissolving halite of the Muschelkalk formation (which are, most plausibly, middle
699 Muschelkalk aquifer fluids).
700 - High salinity and low Cl/Br mass ratios with high metal contents are typical of basement
701 brines.

Unfortunately, a more detailed distinction of reservoir signatures from Buntsandstein, Keuper, Jurassic or Tertiary sediments is not possible based on our analyses of mixed fluids in fluid inclusions of the post-Cretaceous veins. However, it is still possible to model different mixing processes and compare them to field observations.

5.8 Sources and aquifers: prediction and modelling

To evaluate the influence of the different fluid sources on the formation of the mineral veins, we performed various fluid mixing calculations (Fig., 17; Table 5) with the GEOCHEMIST WORKBENCH (Version 10.0.2) software, using fluid data representative of the most important aquifers (Göb et al., 2013; Pauwels et al., 1993; Pearson et al., 1989; Stober and Bucher, 2004). These calculations indicate the following:

1. Fluorite-saturated fluids are only produced by mixing of the basement brine and fluids derived from the Buntsandstein (Fig. 17, table 5). Post-Cretaceous fluorite veins are all situated in areas that were once covered by the Buntsandstein formation.
2. Barite may precipitate from most mixed fluids (Fig. 17, table 5). This is in agreement with field observations: barite-dominated veins are the most common in the post-Cretaceous vein group independent of the host rock (in contrast to the Jurassic veins; (Metz et al., 1957; Staude et al., 2009; Walter et al., 2015; 2016).
3. Many mixed fluid compositions are saturated with respect to gypsum and especially anhydrite (Fig. 17, table 5). Although gypsum and/or anhydrite are extremely rare in the post-Cretaceous veins of the Schwarzwald, pseudomorphic replacement textures of quartz after anhydrite or gypsum can be recognized at some localities (e. g., Badenweiler, Laitschenbach, Laisacker, Lampisweg). We suggest that most of the precipitated gypsum/anhydrite was dissolved by later fluid batches or during cooling which explains the discrepancy of the predicted anhydrite/gypsum mineralization (based on this model) and their apparent absence in many veins.
4. Fluid mixtures of basement brine and Buntsandstein brine are close to saturation with respect to quartz and chalcedony (Fig. 17, table 5) which explains the observation that all veins hosted by

730 Buntsandstein in the northern Schwarzwald are quartz- or chalcedony-dominated. Also the "Quarzriff"
731 near Badenweiler occurs, where Buntsandstein is in contact with the basement directly along the
732 Rhinegraben boundary fault. Furthermore, some sedimentary aquifers are saturated with respect to
733 chalcedony. These result is also in agreement with field observations where often chalcedony rims
734 around detrital grains can be observed.
735
736 *5.8.2 Saturation indices and formation of metal ore minerals*
737 Textures of the mineralized barite veins often show nests of galena that are co-genetic with barite or
738 galena–barite alternations. Based on our calculations (see table 5), it is unlikely that barite and
739 galena/sphalerite precipitated synchronically during simple mixing, since the log saturation indices for
740 galena and sphalerite are between -120 and -50. This undersaturation may be a consequence of high
741 sulfate/sulfide ratios close to 1.
742 To sum these arguments up: (A) sulfides are typically formed during fluid mixing. (B) The metal
743 source is a deep-seated basement brine (Fusswinkel et al., 2013; Walter et al., brine, Jura). (C) The
744 solubility of sphalerite and galena is very low in the presence of sulfide in fluids. (D) Basement brines
745 are not saturated with respect to galena and sphalerite, due to the low absolute sulphur concentrations
746 in these fluids.
747 Based on these arguments it is unlikely that the metals and the sulfide ions are transported in the same
748 fluid batch. Accordingly, the sulfide (and not dominantly sulfate) is transported in the sedimentary
749 fluid component, galena and sphalerite precipitated upon mixing, or reduction due to methane influx e.
750 g. from shale gas or gas-bearing fluids caused sulfide precipitation (Werner et al., 2002; Markl et al.,
751 submitted).
752 The model shows that barite is produced during mixing of two oxidized fluids, which is in agreement
753 with the fluids recognized in the modern hydrology. An influx of methane (or CH_4- and/or H_2S-
754 bearing fluids (Sverjensky, 1984, 1987; Carpenter et al., 1974)) during mixing and concomitant
755 oxidation of CH_4 to CO_2 may strongly reduce the fluid, resulting in a substantial decrease of the
756 sulfate/sulfide ratio and subsequent sulfide precipitation. Oilfield brines are strongly reduced and
757 enriched in H_2S and CH_4 and such fluids are locally present in the Paleogene Pechelbronn formation

(Otto & Tòth, 1988) and widespread in the Lower Jurassic Lias ε shales (Geyer & Gwinner, 2011). Simple mass balance calculations imply that only very small amounts of methane have to be added to one liter of a fluid contianing 2 ppm Pb or Zn to precipitate galena or sphalerite: ~0.01 mmol and ~0.03 mmol, respectively.

5.9 The relation of post-Cretaceous mineralization fluids to modern thermal wells

The following section focuses on the comparison of the post-Cretaceous fluids/aquifers with modern fluids/aquifers. Modern thermal wells like Baden-Baden show temperatures up to 66°C (Göb et al., 2013) and low TDS up to 4.2 g/L. In contrast to the paleo-fluid systems, fluid mixing is not important in modern wells (Bucher and Stober, 2010). The fluids are released by open fractures and show no seasonal variations in temperature or chemistry. The hydrothermal calcite precipitated from such wells produces sinters with growth-rates of several cm/year (e. g., in Baden-Baden). An artesian upwelling of saline (TDS = 0.2 g/L) thermal waters can be recognized at Ohlsbach, where a saline NaCl-rich brine from depth (>3 km with a TDS 16 g/L) ascends into a gravel aquifer and becomes strongly diluted (Stober et al., 1999).

In contrast, the hydrothermal veins discussed in this work show strong evidence of fluid mixing. Our rough calculation of growth rates suggests ephemeral events of fracture opening, fluid release into the fracture from different crustal levels and aquifers, fluid mixing and vein mineralization that triggers crystal growth and concomittant fracture sealing. S-Isotope data by Schwinn et al. (2006) indicate an equilibration of the metal-rich high-salinity basement brine at 350°C which can be compared to a depth of >5 km. This basement component (which would be necessary for modern ore mineralization to form) is not seen in modern thermal wells. Based on this argumentation it appears that there were (and are?) two different hydrothermal systems present in the Schwarzwald: (i) a relatively shallow system persistent over a long time in open fractures producing constant hydrothermal fluid without a basement brine component and (ii) various short–lived hydrothermal systems in quickly sealed fractures, involving deep basement brines and producing hydrothermal mineralizations by fluid mixing. The latter system does not appear to be active today, at least not close to the surface, despite of the ongoing seismic activity in SW Germany.

786

787 **5.10 Analogy of post-Cretaceous veins in the Schwarzwald and the Vosges**

788 There are many similar types of mineralizations east and west of the Rhinegraben, in the Schwarzwald
789 and Vosges mountains (Agard et al., 1975; Hohl 2007). If the rift was perfectly symmetrical and the
790 lithologies east and west of it were identical, one would expect identical fluid types and
791 mineralizations. However, there are differences. In order to show such differences, the mineralization
792 of Hausbaden/Badenweiler (Schwarzwald) and Schlezbourg-Donnerloch/Steinbach (Vosges) were
793 investigated in detail as an example (Gutierrez Lanz, 1985, and references therein). Both veins occur
794 on the respective Rhinegraben boundary faults, both are therefore of post-Cretaceous age, both have
795 macroscopically and microscopically very similar mineral textures, show a dominant massive white
796 quartz phase with minor fluorite and contain galena and some chalcopyrite as main ores. Both veins
797 show multiple episodes of brecciation. Figure 18 A-D illustrates the difference of microthermometric
798 results between Vosges (Steinbach vein) and Schwarzwald (whole database). The fluid inclusions
799 from Steinbach show a distinct range in Fig. 18 and have much higher homogenization temperatures
800 than those of any Schwarzwald vein in the same (low to medium) salinity range.
801 These significantly higher temperatures in Steinbach cannot be simply explained by a higher
802 geothermal gradient, as Agemar et al. (2013) did not observe significant variations in underground
803 temperature at 2500m b.s.l. (measured in geothermal drillings in the Rhinegraben). However, the
804 Upper Rhinegraben has an asymmetric tilt. The basement-cover uniformity is significantly deeper on
805 the French side of the graben (Beccaletto et al., 2010). Still, today's 150°C isotherm is situated deep
806 below the unconformity and to reach the measured temperatures of 230-250°C, the Steinbach fluid has
807 to be released from a depth deeper than 5km from a crystalline basement reservoir. This reservoir
808 assumption is supported by low Cl/Br ratios and elevated metal concentrations at Steinbach, because
809 the shallower reservoirs show Cl/Br mass ratios of 200 and higher (Pauwels et al., 1993). Furthermore,
810 Pauwels et al. (1993) and Aquilina et al. (1997) calculated reservoir temperatures at 4.5-5km in
811 Soultz-sous-Forêt (French side of the Rhinegraben, close to the Vosges mountains) in the crystalline
812 basement of 220-260°C, which is in good agreement with the measured temperatures in Steinbach. In
813 summary, the asymmety of the Rhinegraben appears to release hotter fluids in the west, which,

814 however, produce very similar types of mineralizations.

815

816 ***6. Summary and conclusions***

817 The diverse mineralogy of the post-Cretaceous hydrothermal veins in the vicinity of the Rhinegraben
818 in central Europe is the consequence of multi-component fluid mixing processes (Fig. 19) related to
819 the tectonic activity of the post-Cretaceous Rhinegraben rift. These short-lived (in the range of
820 seconds to hours) mixing processes involve numerous different kinds of aquifers including crystalline
821 basement and various sedimentary cover rocks. The interaction of different aquifers is observed on the
822 scales of a district, a location and a single crystal. The most important aquifers involved in mixing are
823 the crystalline basement and the Muschelkalk aquifers. Fluids from the Buntsandstein, Keuper and the
824 various Jurassic aquifers are of minor importance, but may (if involved) locally govern the vein
825 mineralogy. Temperature and salinity variations cannot explain the observed differences in vein
826 mineralogy, although salinity variations are important for metal transport and therefore for the amount
827 of base metal precipitation during fluid mixing.

828 The chemical composition of the various basement and sedimentary aquifers evolves and changes with
829 time (Walter et al., 2016), which increases the complexity of fingerprinting the fluid sources. Our
830 results imply that the modern thermal wells are fed by a stable, long-living fluid system without much
831 fluid mixing. This system is discontinuously augmented by short-lived fluid mixing events involving a
832 deep-seated brine (which is not normally seen today, with the one exception of the Ohlsbach plume
833 (Stober et al., 1999)) and hydrothermal vein formation, probably caused by tectonics.

834 A comparative study on a hydrothermal vein from the western, French side of the Rhinegraben rift
835 shows much higher temperatures which are assumed to be an effect of the asymmetric tilt of the
836 Rhinegraben: on the latitude of the southern Schwarzwald the rift is much deeper on the French side
837 (Vosges). Hence it seems plausible that fluid migration by topographic fluid flow reaches higher
838 depths on the French than on the German side of the rift.

839 Mixing calculations show that all combinations of modern basement and sediment aquifer fluids result
840 in fluids oversaturated with respect to barite. This is in good agreement with the observation that most

of the investigated veins contain abundant barite. Furthermore, all calculated mixed fluids are strongly undersaturated with respect to sulfides. We suggest that the hydrothermal sulfides precipitated during short-lived injections of methane or hydrocarbon-bearing fluids into the hydrothermal fluid system.

7. Acknowledgements

We would like to thank to S. Schafflick for sample preparation in Tübingen. We are grateful to Udo Neumann and T. Wenzel who helped with many hints and discussions. Furthermore, we gratefully acknowledge the help of G. Stoschek and B. Steinhilber with crush leach analyses and technical support. This study was supported by the German Research Foundation (DFG), grant MA2135/20-1.

9. References

Altherr, R., Holl, A., Hegner, E., Langer, C., and Kreuzer, H., 2000, High-potassium, calc-alkaline I-type plutonism in the European Variscides: northern Vosges (France) and northern Schwarzwald (Germany). Lithos, v. 50, p. 51-73.

Agard, J., Fluck, P., Weil, R., Wimmenauer, W., 1975. Geologie des gites minéraux des Vosges et des regions limitrophes. *Mém BRGM*, *87*, 1-189.

Agemar, T., Brunken, J., Jodocy, M., Schellschmidt, R., Schulz, R and Stober, I., 2013. Untergrundtemperaturen in Baden-Württemberg. Zeitschrift der Deutschen Gesellschaft für Geowissenschaften, 164, 49–62.

Aquilina, L., Boulvais, P., and Mossmann, J.-R., 2011, Fluid migration at the basement/sediment interface along the margin of the Southeast basin (France): implications for Pb–Zn ore formation: Mineralium Deposita, v. 46, no. 8, p. 959-979.

Aquilina, L., Pauwels, H., Genter, A., and Fouillac, C., 1997a, Water-rock interaction processes in the Triassic sandstone and the granitic basement of the Rhine Graben: Geochemical investigation of a geothermal reservoir: Geochimica et cosmochimica acta, v. 61, no. 20, p. 4281-4295.

Aquilina, L., Pauwels, H., Genter, A., and Fouillac, C., 1997b, Water-rock interaction processes in the Triassic sandstone and the granitic basement of the Rhinegraben: Geochemical investigation of a geothermal reservoir.: Geochimica et Cosmochimica Acta, v. 61, p. 4281-4295.

Baatartsogt, B., Wagner, T., Taubald, H., Mierdel, K. and Markl, G., 2006. Hydrogen isotope determination of fluid inclusion water from hydrothermal fluorite: The results depend on the extraction technique. Chemical Geology, 1-21.

Baatartsogt, B., Schwinn, G., Wagner, T., Taubald, H., Beitter, T., and Markl, G., 2007, Contrasting paleofluid systems in the continental basement: a fluid inclusion and stable isotope study of hydrothermal vein mineralization, Schwarzwald district, Germany.: Geofluids, v. 7, p. 123-147.

879 Bakker, R.J. 1997, Clathrates: Computer programs to calculate fluid inclusion V-X properties
880 using clathrate melting temperatures. Computers & Geosciences, v. 23, 1-18.
881 Banks, D. A., Boyce, A. J., and Samson, I. M. 2002. Constraints on the origins of fluids
882 forming Irish Zn-Pb-Ba deposits: Evidence from the composition of fluid inclusions.
883 *Economic Geology*, *97*(3), 471-480.
884 Bau, M., Romer, R. L., Lüders, V., and Dulski, P., 2003, Tracing element sources of
885 hydrothermal mineral deposits: REE and Y distribution and Sr-Nd-Pb isotopes in
886 fluorite from MVT deposits in the Pennine Orefield, England: Mineralium Deposita,
887 v. 38, no. 8, p. 992-1008.
888 Beccaletto, L., Capar, L., Cruz-Mermy, D., Rupf, I., Nitsch E., Oliviero, G., Elsass, P., Perrin,
889 A., and Stephane, M., 2010, The GeORG project – Geological Potential of the Upper
890 Rhine Graben - Situation, goals and first scientific results. – Abstr., 23ème Réunion
891 des Sciences de la Terre (RST2010), Bordeaux
892 Bjørlykke, A., Ihlen, P. M., Olerud, S., 1990. Metallogeny and lead isotope data from the
893 Oslo Paleorift. *Tectonophysics*, *178*(1), 109-126.
894 Bliedtner, M., and Martin, M., 1986. *Erz- und Minerallagerstätten des Mittleren*
895 *Schwarzwaldes: eine bergbaugeschichtliche und lagerstättenkundliche Darstellung*.
896 Geologisches Landesamt Baden-WürttembergBoiron, M. C., Cathelineau, M., and
897 Richard, A., 2010, Fluid flows and metal deposition near basement/cover
898 unconformity: lessons and analogies from Pb-Zn-F-Ba systems for the understanding
899 of Proterozoic U deposits.: Geofluids, v. 10, p. 270-292.
900 Bons, P. D., Fusswinkel, T., Gomez-Rivas, E., Markl, G., Wagner, T., and Walter, B.F. ,
901 2014, Fluid mixing from below in unconformity-related hydrothermal ore deposits:
902 Geology, p. G35708. 35701.
903 Borchert, H., 1959, Ozeane Salzlagerstätten: Grundzüge der Entstehung und Metamorphose
904 ozeaner Salzlagerstätten sowie des Gebirgsverhaltens von Salzgesteinsmassen, Gebr.
905 Borntraeger.
906 Brockamp, O., Clauer, N., Zuther, M., 2003. Authigenic sericite record of a fossil geothermal
907 system: the Offenburg trough, central Black Forest, Germany. International Journal of
908 Earth Sciences, 92, 843–51.
909 Brockamp, O., Schlegel, A., Clauer, N., 2011. Mesozoic hydrothermal impact on Rotliegende
910 and Bunter immature sandstones of the High Rhine trough and its adjacent eastern
911 area (southern Black Forest, Germany). Sedimentary Geology, 234, 76–88.
912 Bucher, K., and Stober, I., 2000. The composition of groundwater in the continental
913 crystalline crust. In *Hydrogeology of crystalline rocks* (pp. 141-175). Springer
914 Netherlands.
915 Bucher, K., and Stober, I., 2002. Water-rock reaction experiments with Black Forest gneiss
916 and granite. In *Water-Rock Interaction* (pp. 61-95). Springer Netherlands.
917 Bucher, K., and Stober, I., 2010, Fluids in the upper continental crust: Geofluids, v. 10, no. 1-
918 2, p. 241-253.
919 Bucher, K., Zhu, Y., and Stober, I., 2009a. Groundwater in fractured crystalline rocks, the
920 Clara mine, Black Forest (Germany). *International Journal of Earth Sciences*, *98*(7),
921 1727-1739.
922 Bucher, K., Zhu, Y., and Stober, I., 2009b. Groundwater in fractured crystalline rocks, the
923 Clara mine, Black Forest (Germany). *International Journal of Earth Sciences*, *98*(7),
924 1727-1739.
925 Burisch, M., Marks, M., Novak, M. and Markl, G., (2016a). The importance of temperature
926 and cataclastic deformation for halogen (F, Cl, Br) systematics and metal transport
927 capacities of continental basement brines – an experimental approach. Chemical
928 Geology, 433, 24-35.
929 Burisch, M., Walter, B.F., Wälle, M., & Markl, G. (2016b) Tracing fluid migration pathways

930 in the root zone below unconformity-related hydrothermal veins: insights from trace
931 element systematics of individual fluid inclusions. Chemical Geology, 429, 44-50.
932 Carignan, J., Gariépy, C., and Hillaire-Marcel, C., 1997, Hydrothermal fluids during
933 Mesozoic reactivation of the St. Lawrence rift system, Canada: C, O, Sr and Pb
934 isotopic characterization: Chemical Geology, v. 137, no. 1, p. 1-21.
935 Carpenter, A.B., Trout, M.L. and Pickett, E.E., 1974. Preliminary report on the origin and
936 chemical evolution of lead-and zinc-rich oil field brines in central Mississippi.
937 Economic Geology, 69(8): 1191-1206.
938 Chaussidon, M., and Jambon, A., 1994. Boron content and isotopic composition of oceanic
939 basalts: geochemical and cosmochemical implications Earth Planet. Sci. Lett., 121, pp.
940 277–291
941 Davies, G.R., and Smith, L.B., 2006. Structurally controlled hydrothermal dolomite reservoir
942 facies: An overview: AAPG Bulletin, v. 90, p. 1641–1690,
943 Deane, J., 1995, The structural evolution of the Kombat deposits, Otavi Mountainland,
944 Namibia: Communications of the Geological Survey of Namibia, v. 10, p. 99-107.
945 Edmunds, W. M., and Savage, D., 1991, Geochemical characteristics of groundwater in
946 granites and related crystalline rocks: Applied Groundwater Hydrology, a British
947 Perspective (eds DowningRA, WilkinsonWB), p. 199-216.
948 Emmermann, R., Althaus, E., Giese, P., and Stöckhert, B., 1995, KTB Hauptbohrung results
949 of geoscientific investigation in the KTB field laboratory, final report: 0-9101 m: KTB
950 Report, v. 95-2, p. E.
951 Frape, S., and Fritz, P., 1987, Geochemical trends for groundwaters from the Canadian
952 Shield: Geological Association of Canada Special Papers, v. 33, p. 19-38.
953 Frape, S., Fritz, P., and McNutt, R. t., 1984, Water-rock interaction and chemistry of
954 groundwaters from the Canadian Shield: Geochimica et Cosmochimica Acta, v. 48,
955 no. 8, p. 1617-1627.
956 Frezzotti, M. L., Tecce, F., and Casagli, A., 2012, Raman spectroscopy for fluid inclusion
957 analysis: Journal of Geochemical Exploration, v. 112, p. 1-20.
958 Fusswinkel, T., Wagner, T., Wälle, M., Wenzel, T., Heinrich, C., and Markl, G., 2013, Fluid
959 mixing forms basement-hosted Pb-Zn deposits: Insight from metal and halogen
960 geochemistry of individual fluid inclusions: Geology, v. 41, p. 679-682.
961 Garven, G., Appold, M. S., Toptygina, V. I., and Hazlett, T. J., 1999, Hydrogeologic
962 modeling of the genesis of carbonate-hosted lead-zinc ores: Hydrogeology Journal, v.
963 7, p. 108-126.
964 Genter, A., Evans, K., Cuenot, N., Fritsch, D., and Sanjuan, B., 2010, Contribution of the
965 exploration of deep crystalline fractured reservoir of Soultz to the knowledge of
966 enhanced geothermal systems (EGS): Comptes Rendus Geoscience, v. 342, no. 7, p.
967 502-516.
968 Geyer, O. F., and Gwinner, M. P., 2011, Geologie von Baden -Württemberg. – 5., völlig neu
969 bearbeitete Auflage, Stuttgart, Schweizerbart`sche Verlagsbuchhandlung (Nägele u.
970 Obermiller), 627 p.:
971 Göb, S., Loges, A., Nolde, N., Bau, M., Jacob, D. E., and Markl, G., 2013, Major and trace
972 element compositions (including REE) of mineral, thermal, mine and surface waters in
973 SW Germany and implications for water-rock interaction: Applied Geochemistry.
974 Göb, S., Wenzel, T., Bau, M., Jacob, D. E., Loges, A., and Markl, G., 2011, The redistribution
975 of rare-earth elements in secondary minerals of hydrothermal veins, Schwarzwald,
976 southwestern Germany: The Canadian Mineralogist, v. 49, no. 5, p. 1305-1333.
977 Guillong, M., Meier, D., Allan, M., Heinrich, C., and Yardley, B., 2008, SILLS: a MATLAB-
978 based program for the reduction of laser ablation ICP-MS data of homogeneous
979 materials and inclusions: Mineralogical Association of Canada Short Course, v. 40, p.
980 328-333.

Gutierrez Lanz, J.R. (1985): Etude des filons a Pb-Zn-Cu comportant une gangue sulfatee siliciferee de la region de Thann-Watwiller (Vosges sud), Doktorarbeit , Institute National Polytechnique De Lorraine. 321 p.

Hann, H. P. e. A., 2003, The rand granite in the southern Schwarzwald and its geodynamic significance in the variscan belt of SW Germany: International Journal of Earth Sciences, v. 92, p. 821-842.

He, K., Stober, I., and Bucher, K., 1999, Chemical evolution of thermal waters from limestone aquifers of the Southern Upper Rhine Valley: Applied geochemistry, v. 14, no. 2, p. 223-235.

Heinrich, C. A., Pettke, T., Halter, W. E., Aigner-Torres, M., Audétat, A., Günther, D., Hattendorf, B., Bleiner, D., Guillong, M., and Horn, I., 2003, Quantitative multi-element analysis of minerals, fluid and melt inclusions by laser-ablation inductively-coupled-plasma mass-spectrometry.: Geochimica et Cosmochimica Acta, v. 67, p. 3473-3496.

Hendrickson, M. D., Hitzman, M. W., Wood, D., Humphrey, J. D., & Wendlandt, R. F. 2015. Geology of the Fishtie deposit, Central Province, Zambia: iron oxide and copper mineralization in Nguba Group metasedimentary rocks. *Mineralium Deposita*, *50*(6), 717-737.

Hohl, J.-L. (2007): Le grand livre des minéraux d'alsace, La nuée Bleue/DANN, Strasbourg, 237 p.

Jenkner, B., 1986, Ein Vorschlag zur Neugliederung des sedimentären Oberrotliegenden in der Baden-Badener Senke und ihrer nordöstlichen Fortsetzung (Nordschwarzwald): Jahrbuch des Geologischen Landesamtes Baden-Württemberg, v. 28, p. 49-159.

Kalt, A., Altherr, R., and Hanel, M., 2000, The Variscan basement of the Schwarzwald.: Eur. J. Mineral., Beih., v. 12, p. 1-43.

Kessen, K., Woodruff, M., and Grant, N., 1981, Gangue mineral 87 Sr/86 Sr ratios and the origin of Mississippi Valley-type mineralization: Economic Geology, v. 76, no. 4, p. 913-920.

Köhler, W. R., 1992, Beschaffenheit ausgewählter, nicht direkt anthropogen beeinflußter oberflächennaher und tiefer Grundwasservorkommen in Baden-Würtemberg: Tübinger Geowissenschaftliche Arbeiten, v. 10, p. 144.

Kolchugin A.N., Immenhauser, A., Walter, B.F. and Morozov, V.P., (submitted to Marine and Petroleum Geology) Diagenesis of the palaeo-oil-water transition zone in a Lower Pennsylvanian carbonate reservoir: constraints from cathodoluminescence microscopy and isotope geochemistry.

Koziy, L., Bull, S., Large, R., and Selley, D., 2009, Salt as a fl uid driver, and basement as a metal source, for stratiform sediment-hosted copper deposits: Geology, v. 37, p. 1107–1110, doi:10.1130/G30380A.1

Kozlovsky, Y., 1984, The world's deepest well: Scientific American, v. 251, p. 106-112.

Leach, D. L., Marsh, E., Emsbo, P., Rombach, C. S., Kelley, K. D., and Anthony, M., 2004, Nature of Hydrothermal Fluids at the Shale-Hosted red Dog Zn-Pb-Ag Deposit, Brooks Range, Alaska.: Economic Geology, v. 99, p. 1449-1480.

Loges, A., Wagner, T., Kirnbauer, T., Göb, S., Bau, M., Berner, Z., and Markl, G., 2012, Source and origin of active and fossil thermal spring systems, northern Upper Rhine Graben, Germany: Applied Geochemistry, v. 27, no. 6, p. 1153-1169.

Lorenz, G. D., 2002, Diagenese der känozoischen Sedimente des Oberrheingrabens als Hinweis der tertiären Fluidentwicklung.

Lüders, V., Plessen, B., Romer, R. L., Weise, S. M., Banks, D. A., Hoth, P., Dulski, P., and Schettler, G., 2010, Chemistry and isotopic composition of Rotliegend and Upper Carboniferous formation waters from the North German Basin.: Chemical Geology, v.

276, p. 198-208.
Ludwig, F., Stober, I., and Bucher, K. (2011). Hydrochemical groundwater evolution in the bunter sandstone sequence of the Odenwald mountain range, Germany: a laboratory and field study. *Aquatic geochemistry*, *17*(2), 165-193.
Markl, G., Lahaye, Y., and Schwinn, G., 2006, Copper isotopes as monitors of redox processes in hydrothermal mineralization.: Geochimica et Cosmochimica Acta, v. 70, p. 4215-4228.
Markl, G., Burisch, M. and Neumann, U. (2016)
Martin, M., 2009, Geogene Grundgehalte (Hintergrundwerte) in den petrogeochemischen Einheiten von Baden-Württemberg: LGRB-Informationen, v. 24, p. 98.
Metz, R., Richter, M., and Schürenberg, H., 1957, Die Blei-Zink-Erzgänge des Schwarzwaldes: Beiheft Geologisches Jahrbuch, v. 29, p. 277.
Nitsch, E., and Zedler, H., 2009, Oberkarbon und Perm in Baden-Württemberg. : LGRB-Information, v. 22, p. 7-102.
Otto, C. J., and Toth, J., 1988. Hydrogeological controls and indicators for oil deposits in rift grabens-An example from the Upper Rhine graben, France. *AAPG Bulletin (American Association of Petroleum Geologists);(USA)*, *72*(CONF-8809346--).
Pauwels, H., C., F., and A.C., F., 1993, Chemistry and isotopes of deep geothermal saline fluids in the Upper Rhine Graben: Origin of compounds and water-rock interactions: Geochimica et Cosmochimica Acta, v. 57, no. 12, p. 2737-2749.
Pearson, F. J., Lolcama, J. L., and Scholtis, A., 1989, Chemistry of waters in the Böttstein, Weiach, Riniken, Schafisheim, Kaisten and Leuggern boreholes: a hydrochemically consistent data set: NAGRA Technical Report, v. 86-19, p. 153.
Pearson, F.J., Arcos, D., Bath, A., Boisson, J.-Y., Fernández, A.M., Gäbler, H.-E., Gaucher, E., Gautschi, A., Griffault, L., Hernán, P., and Waber, H.N., 2003. Mont Terri Project - Geochemistry of water in the Opalinus Caly Formation at the Mont 'Terri Rock Laboratory. Berichte des BWG, Serie Geologie, Bern.
Pfaff, K., Hildebrandt, L. H., Leach, D. L., Jacob, D. E., and Markl, G., 2010, Formation of the Wiesloch Mississippi Valley-type Zn-Pb-Ag deposit in the extensional setting of the Upper Rhinegraben, SW Germany: Mineralium Deposita, v. 45, no. 7, p. 647-666.
Pfaff, K., Koenig, M. A., Wenzel, T., Ridley, I., Hildebrandt, L. H., Leach, D. L., and Markl, G., 2011, Trace and minor element variations and sulfur isotopes in crystalline and colloform ZnS: Incorporation mechanisms and implications for their genesis: Chemical Geology, v. 286, no. 3-4, p. 118-134.
Pfaff, K., Romer, R. L., and Markl, G., 2009, U-Pb ages of ferberite, chalcedony, agate, "U-mica" and pitchblende: constraints on the mineralization history of the Schwarzwald ore district.: Eur. J. Mineral., v. 21, p. 817-836.
Rupf, I., and Nitsch, E., 2008, Das Geologische Landesmodell von Baden-Württemberg: Datengrundlagen, technische Umsetzung und erste geologische Ergebnisse.: LGRB-Information, v. 21.
Sanjuan, B., Millot, R., Dezayes, C., and Brach, M., 2010, Main characteristics of the deep geothermal brine (5km) at Soultz-sous-Forêts (France) determined using geochemical and tracer test data: Comptes Rendus Geoscience, v. 342, no. 7, p. 546-559.
Schwarz, M., and Henk, A., 2005, Evolution and structure of the Upper Rhine Graben: insights from three-dimensional thermomechanical modelling.: International Journal of Earth Science, v. 94, p. 732-750.
Schwinn, G., and Markl, G., 2005, REE systematics in hydrothermal fluorite.: Chemical Geology, v. 216, p. 225-248.
Schwinn, G., Wagner, T., Baatartsogt, B., and Markl, G., 2006, Quantification of mixing processes in ore-forming hydrothermal systems by combination of stable isotope and fluid inclusion analyses.: Geochimica et Cosmochimica Acta, v. 70, p. 965-982.

1082 Seo, J. H., Guillong, M., Aerts, M., Zajacz, Z., and Heinrich, C. A., 2011, Microanalysis of S,
1083 Cl, and Br in fluid inclusions by LA–ICP-MS: Chemical Geology, v. 284, no. 1, p. 35-
1084 44.
1085 Sverjensky, D.A., 1984. Oil field brines as ore-forming solutions. Economic Geology, 79(1):
1086 23-37.
1087 Sverjensky, D.A., 1987. The role of migrating oil field brines in the formation of sediment-
1088 hosted Cu-rich deposits. Economic Geology, 82(5): 1130-1141.
1089 Shouakar-Stash, O., Alexeev, S., Frape, S., Alexeeva, L., and Drimmie, R., 2007,
1090 Geochemistry and stable isotopic signatures, including chlorine and bromine isotopes,
1091 of the deep groundwaters of the Siberian Platform, Russia: Applied geochemistry, v.
1092 22, no. 3, p. 589-605.
1093 Staude, S., Bons, P. D., and Markl, G., 2009, Hydrothermal vein formation by extension-
1094 driven dewatering of the middle crust: An example from SW Germany.: Earth and
1095 Planetary Science Letters, v. 286, p. 387-395.
1096 Staude, S., Dorn, A., Pfaff, K., and Markl, G., 2010a, Assemblages of Ag-Bi sulfosalts and
1097 conditions of their formation: the type locality of schapbachite ($Ag_{0.4}Pb_{0.2}Bi_{0.4}S$) and
1098 neighboring mines in the Schwarzwald ore district, southern Germany.: Canadian
1099 Mineralogist, v. 48, p. 441-466.
1100 Staude, S., Göb, S., Pfaff, K., Ströbele, F., Premo, W. R., and Markl, G., 2011a, Deciphering
1101 fluid sources of hydrothermal systems: A combined Sr- and S-isotope study on barite
1102 (Schwarzwald, SW Germany): Chemical Geology, v. 286, no. 1-2, p. 1-20.
1103 Staude, S., Göb, S., Pfaff, K., Ströbele, F., Premo, W. R., and Markl, G., 2011b, Deciphering
1104 fluid sources of hydrothermal systems: a combined Sr-and S-isotope study on barite
1105 (Schwarzwald, SW Germany): Chemical Geology, v. 286, no. 1, p. 1-20.
1106 Staude, S., Mordhorst, T., Nau, S., Pfaff, K., Brügmann, G., Jacob, D.E., and Markl, G., 2012
1107 . Hydrothermal carbonates of the Schwarzwald ore district, southwestern Germany:
1108 Carbon source and conditions of formation using $\delta^{18}O$, $\delta^{13}C$, $^{87}Sr/^{86}Sr$, and fluid
1109 inclusions. The Canadian Mineralogist, 50(5), 1401-1434.
1110 Staude, S., Mordhorst, T., Neumann, R., Prebeck, W., and Markl, G., 2010b, Compositional
1111 variation of the tennantite-tetrahedrite solid-solution series in the Schwarzwald ore
1112 district (SW Germany): The role of mineralization processes and fluid source.:
1113 Mineralogical Magazine, v. 74, p. 309-339.
1114 Staude, S., Wagner, T., and Markl, G., 2007, Mineralogy, mineral chemistry and fluid
1115 evolution of the hydrothermal Wenzel deposit, southern Germany: implications for the
1116 formation of Kongsberg-type silver deposits.: Canadian Mineralogist, v. 45, p. 1147-
1117 1176.
1118 Staude, S., Werner, W., Mordhorst, T., Wemmer, K., Jacob, D., and Markl, G., 2012b, Multi-
1119 stage Ag–Bi–Co–Ni–U and Cu–Bi vein mineralization at Wittichen, Schwarzwald,
1120 SW Germany: geological setting, ore mineralogy, and fluid evolution: Mineralium
1121 Deposita, v. 47, no. 3, p. 251-276.
1122 Steele-MacInnes, M., Bodnar, R. J., and Naden, J., 2011, Numerical model to determine the
1123 composition of H2O-NaCl-CaCl2 fluid inclusions based on microthermometric and
1124 microanalytical data.: Geochimica et Cosmochimica Acta, v. 75, p. 21-40.
1125 Stober, I., and Bucher, K., 1999a, Deep groundwater in the crystalline basement of the Black
1126 Forest region: Applied Geochemistry, v. 14, p. 237-254.
1127 Stober, I., and Bucher, K., 1999b. Origin of salinity of deep groundwater in crystalline rocks.
1128 *Terra Nova-Oxford*, *11*(4), 181-185.
1129 Stober, I., Richter, A., Brost, E., and Bucher, K., 1999c. The Ohlsbach Plume–Discharge of
1130 deep saline water from the crystalline basement of the Black Forest, Germany.
1131 *Hydrogeology Journal*, *7*(3), 273-283.
1132 Stober, I., and Bucher, K.,, 2004, Fluid sinks within the earth's crust: Geofluids, v. 4, p. 143-

151.
Stober, I., and Bucher, K., 2005a. The upper continental crust, an aquifer and its fluid: hydaulic and chemical data from 4 km depth in fractured crystalline basement rocks at the KTB test site. *Geofluids*, *5*(1), 8-19.
Stober, I., and Bucher, K., 2005b. Deep-fluids: Neptune meets Pluto. *Hydrogeology Journal*, *13*(1), 112-115.
Stober, I., and Bucher, K., 2007. Hydraulic properties of the crystalline basement. *Hydrogeology Journal*, *15*(2), 213-224.
Stober, I., and Bucher, K., 2014. Permeability and Fluid Flow in the Upper Continental Crust. In *2014 GSA Annual Meeting in Vancouver, British Columbia*.
Stober, I., and Bucher, K., 2015a. Hydraulic conductivity of fractured upper crust: insights from hydraulic tests in boreholes and fluid-rock interaction in crystalline basement rocks. *Geofluids*, *15*(1-2), 161-178
Stober, I., and Bucher, K., 2015b. Significance of Hydraulic Conductivity as Precondition to Fluid Flow in Fractured and Faulted Crystalline Basement and its Impact on Fluid-Rock Interaction Processes. *Significance*, *19*, 25.
Stober, I., 2011. Depth-and pressure-dependent permeability in the upper continental crust: data from the Urach 3 geothermal borehole, southwest Germany. *Hydrogeology Journal*, *19*(3), 685-699.
Stober, I., 2013. Geothermal fluid and reservoir properties in the Upper Rhine Graben, Europe. In *Second EAGE Sustainable Earth Sciences (SES) Conference and Exhibition*.
Ströbele, F., Staude, S., Pfaff, K., Premo, W. R., Hildebrandt, L. H., Baumann, A., Pernicka, E., and Markl, G., 2012, Pb isotope constraints on fluid flow and mineralization processes in SW Germany Neues Jahrbuch für Mineralogie-Abhandlungen: Journal of Mineralogy and Geochemistry, v. 189, no. 3, p. 287-309.
Todt, W., 1976, Zirkon U/Pb-Alter des Malsburg-Granits vom Südschwarzwald: Neues Jahrb Mineral Monatsh, v. 12, p. 532-544.
Ufrecht, W., 2006, Zur Hydrogeologie der Aquifersysteme Buntsandstein und Muschelkalk zwischen Neckar und Donau.: Schriftenreihe des Amtes für Umweltschutz, p. 19-48.
Van Alstine, R., 1976, Continental rifts and lineaments associated with major fluorspar districts: Economic Geology, v. 71, no. 6, p. 977-987.
Van den Kerkhof, A. M., & Hein, U. F. 2001. Fluid inclusion petrography. *Lithos*, *55*(1), 27-47.
Walter, B.F., Immenhauser, A., Geske, A. and Markl, G., 2015. Exploration of hydrothermal carbonate magnesium isotope signatures as tracers for continental fluid aquifers, Schwarzwald mining district, SW Germany. Chemical Geology, 400, 87-105..
Walter B.F., Burisch, M. and Markl, G., submitted to Geofluids.Long-term chemical evolution and modification of continental basement brines – a field study from the Schwarzwald, SW Germany
Walter, B.F., Burisch, M., Marks, M.A.W. and Markl, G., submitted to Chemical Geology. Major element and trace metal systematics of fluid inclusions in hydrothermal veins: metal provenance and the reconstruction of eroded sedimentary units
Werner, W. F., Hans Joachim, 1994, Tektonik und Mineralisation der Hydrothermalgänge am Schwarzwaldrand im Bergbaurevier Freiamt-Sexau: Abh. geol. Landesamt Baden-Württemberg, v. 14, p. 27-98.
Werner, W., Franzke, H.J., Wirsing, G., Jochum, J., Lüders, V., Wittenbrink, 2002. mit einem Beitrag von B. Steiber: Die Erzlagerst€atte Schauinsland bei Freiburg im Breisgau. Bergbau, Geologie, Hydrogeologie, Mineralogie, Geochemie, Tektonik und Lagerstättenentstehung. Ber. Naturforsch. Ges. Freiburg, 92: 110 S., 26 Abb., 9 Tab., 16 Taf.; Freiburg i. Br.

Wetzel, A., Allenbach, R., and Allia, V., 2003, Reactivated basement structures affecting the sedimentary facies in a tectonically "quiescent" epicontinental basin: an example from NW Switzerland.: Sedimentary Geology, v. 157, p. 153-172.
Wilkinson, J., 2010, A review of fluid inclusion constraints on mineralization in the Irish ore field and implications for the genesis of sediment-hosted Zn-Pb deposits: Economic Geology, v. 105, no. 2, p. 417-442.
Wilkinson, J., Weiss, D., Mason, T., and Coles, B., 2005, Zinc isotope variation in hydrothermal systems: preliminary evidence from the Irish Midlands ore field: Economic Geology, v. 100, no. 3, p. 583-590.
Yardley, B.W., 2005. 100th anniversary special paper: metal concentrations in crustal fluids and their relationship to ore formation. *Economic Geology*, *100*(4), 613-632.
Ziegler, P. A., 1990, Geological Atlas of Western and Central Europe., Shell Internationale Petroleum Maatschappij B.V.

Figure captions

Fig. 1. Geological map of the rift shoulders and the hydrothermal veins of group (v). GeoRG data after Beccaletto et al. (2010) was used.

Fig. 2. Structural positions of the different aquifers within the Upper Rhinegraben, from surface to 5 km b.s.m. The map is based on GeoRG data after Beccaletto et al. (2010). Note the asymmetric tilt of the rift.

Fig. 3. Geological overview of the Schwarzwald mining district in SW Germany with sample locations. (**A**) Overview map. (**B**) Close-up of the Schwarzwald mining district modified after Pfaff et al. (2011). Sample localities sorted after mineralization type (for more information refer to Table 1 in the electronic supplement).

Fig. 4. Examples of post-Cretaceous hydrothermal veins including different mineral assemblages. (**A**) Segen Gottes fluorite-barite vein near Schnellingen; (**B**) barite-quartz vein with sphalerite, Schauinsland mine near Freiburg; (**C**) Siderite-chalocopyrite vein, Riggenbach near Staufen; (**D**) barren barite vein, Freudenstadt.

Fig 5. Schematic petrography of fluid inclusion assemblages. Note alternating, high salinity, moderate and low salinity fluids. Some assemblages contain sulfate and/or CO_2.

Fig. 6. Trace element systematics of different post-Cretaceous veins. Data from the Jurassic-Cretaceous Brandenberg vein are taken from Burisch et al. (2016b). Outliers are excluded from the boxplots.

Fig. 7. Diagram is illustrating that Cl/Br of crush leach results are a bulk of all single fluid inclusions by LA-ICPMS analyses.

Fig 8. Homogenization temperature versus salinity (microthermometrical data) sorted according to vein mineralogy. There seems to be no correlation between the microthermometric data and vein mineralogy.

Fig 9. Ternary phase diagram of the NaCl-CaCl2-H2O system. Included data is restricted to signatures A-C. The black boxes indicate the reservoir fluid compositions, their numbering is consistent with the numbering used in the text.

Fig 10. Cathodolumenscense and microphotographs (AxPol) of pseudomorphic replacement of quartz after anhydrite.

Fig. 11. Crush leach results (A) SO_4-Cl-HCO_3 system. Note, fluids from fluorite only scatter between Cl and HCO_3. (B) Na-Ca-K system. Most of the data points of barite and quartz showing Na and Ca as dominant cation. All the K rich fluids are of low salinity. (C) Metal distribution in the Ni-Cu-Zn system. All FIAs hosted by fluorite, barite and quartz are Ni poor. In contrast, there is an isolated group of Ni-rich carbonates. (D) illustrates the fluid

1245 signatures in the As-Pb-Zn system. Interestingly, almost all barites are Pb-poor. (E)
1246 dominantly fluids from barite are enriched in U. (F) Cl/Br versus Cl content.
1247
1248 **Fig. 12.** LA-ICPMS results of single fluid inclusions from six veins. (A) Cl/Br versus Cu +Ni
1249 content. (B) Cl/Br versus Pb + Zn. (C) Cl/Br versus As content. (D) Cl/Br versus W content.
1250 (E) Cl/Br versus Sb content. (F) Cl/Br versus B content. For all plots note triangle shape of
1251 the data cloud.
1252
1253 **Fig. 13.** Temporal evolution of fluid mixing. Data of the Riggenbach siderite-quartz-
1254 chalocpyrite vein are illustrated. Na/Ca, salinity and T_H vary with time.
1255
1256 **Fig. 14.** LA-ICPMS results of the Karl August vein near Kropbach. (A) S content versus Cl
1257 content. (B) Cl/Br mass ratio versus Pb + Zn content. (C) Cl/Br mass ratio versus Cu +Ni
1258 content. Ternary mixing and variation in mixing ratio with time (represented by FIAs) can be
1259 observed.
1260
1261 **Fig. 15.** Schematic illustration of the fluid trapping involving heterogeneous co-existing fluid
1262 batches (schlieren).
1263
1264 **Fig. 16.** Rb vs Cs content. Most of the data points are plotting below a Rb/Cs ratio of <2.
1265
1266 **Fig. 17.** Mixing model results log SI versus wt.% basementbrine. (A) basement versus
1267 Buntsandstein. (B) basement brine versus Muschelkalk (halite facies). (C) basement brine
1268 versus Muschelkalk (sulfate facies). (D) basement brine versus Keuper. (E) basement brine
1269 versus Hauptrogenstein. (F) basement brine versus crystalline intermediate depth. (G)
1270 basement brine versus crystalline shallow depth.

Fig. 18. Microthermometrical results arranged after Schwarzwald (blue) and Steinbach in the Vosges (red). (A) homogenization temperatures versus salinity. (B) Ca/(Na+Ca) mole ratio versus salinity. (C) Ca/(Na+Ca) mole ratio versus homogenization temperatures. (D) mole Ca versus mole Na.

Fig. 19. Schematic crustal sections showing multi-component fluid mixing and vein formation in the complex geological environment of the Upper Rhinegraben rift.

Table 1 Types of veins and fluid signatures of the Schwarzwald ore district modified after Walter et al. (2016, and references therein).

Table 2 Overview of mineralization types in the post-Cretaceous period with some representative localities.

Table 3 fluid characteristica

Table 4 maxium values LA-ICPMS data of single inclusions of six veins

Table 4 Aquiferdata (representative for the most important aquifers) of Göb et al. (2013); Pauwels et al. (1993); (Pearson et al. 1989); Stober and Bucher (2004) were used and combined as input parameter for modelling.

Fig 1

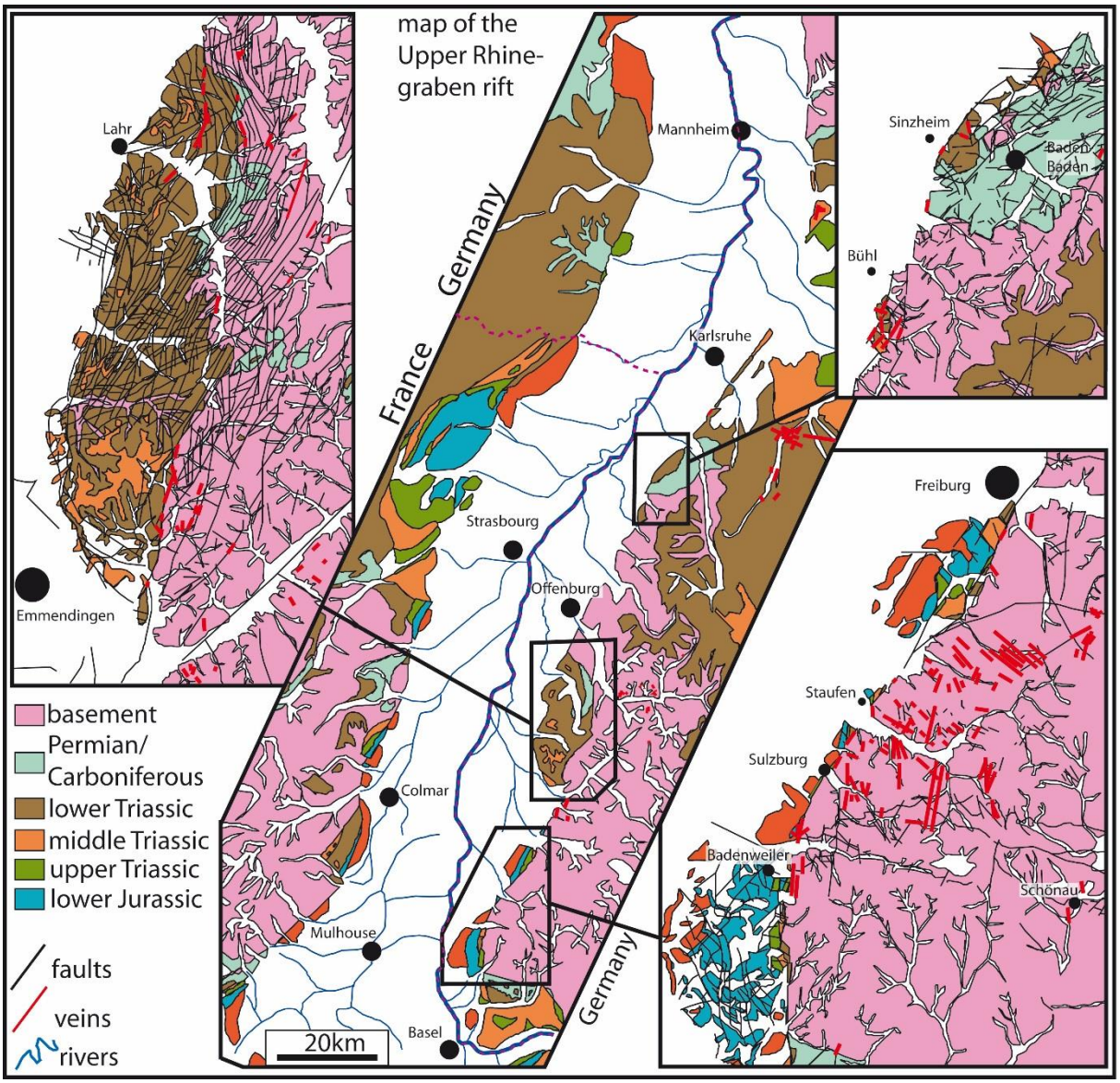
map of the
Upper Rhine-
graben rift
Lahr
Mannheim
Sinzheim
Baden-
Baden
Bühl
Karlsruhe
France
Germany
Freiburg
Strasbourg
Offenburg
Emmendingen
Staufen
Sulzburg
Colmar
Badenweiler
Schönau
Mulhouse
Basel
Germany
20km
basement
Permian/
Carboniferous
lower Triassic
middle Triassic
upper Triassic
lower Jurassic
faults
veins
rivers

fig 2

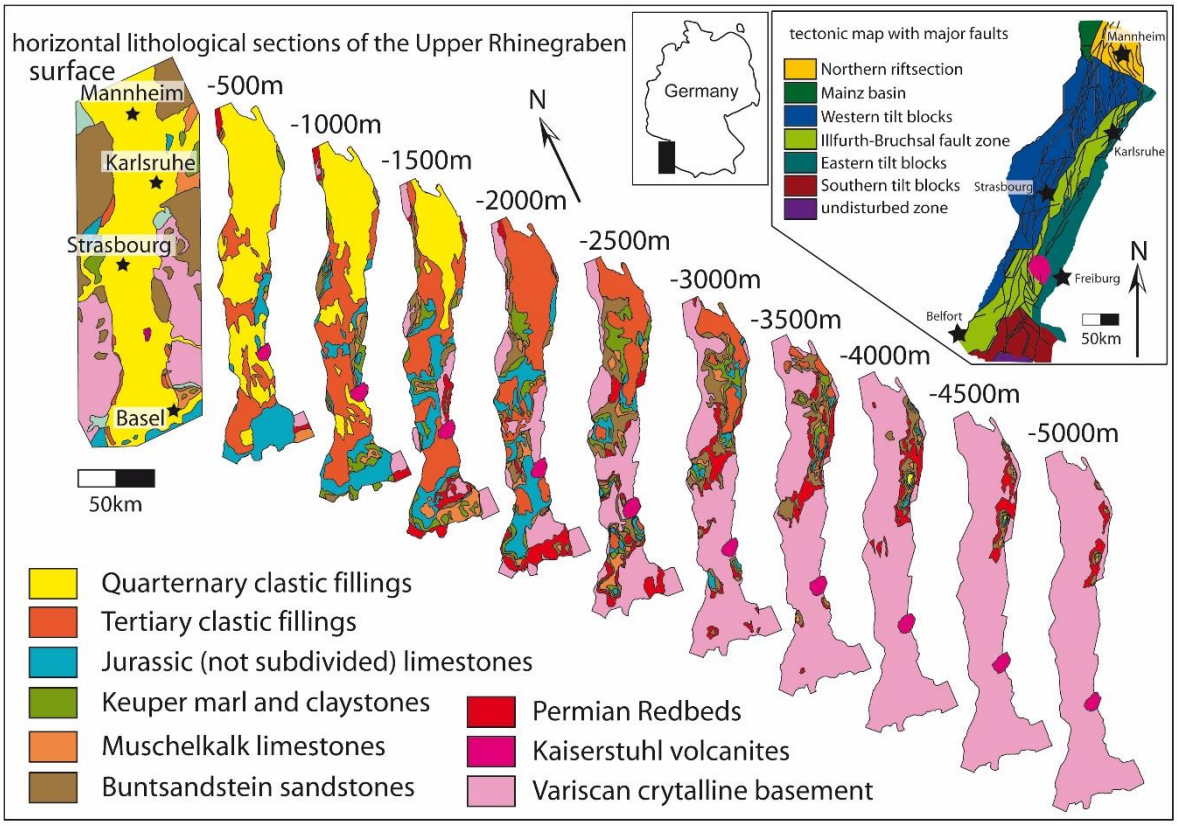
horizontal lithological sections of the Upper Rhinegraben
surface
-500m
-1000m
-1500m
-2000m
-2500m
-3000m
-3500m
-4000m
-4500m
-5000m
Mannheim
Karlsruhe
Strasbourg
Basel
50km
N
Germany
tectonic map with major faults
Northern riftsection
Mainz basin
Western tilt blocks
Illfurth-Bruchsal fault zone
Eastern tilt blocks
Southern tilt blocks
undisturbed zone
Mannheim
Karlsruhe
Strasbourg
Freiburg
Belfort
N
50km
Quarternary clastic fillings
Tertiary clastic fillings
Jurassic (not subdivided) limestones
Keuper marl and claystones
Muschelkalk limestones
Buntsandstein sandstones
Permian Redbeds
Kaiserstuhl volcanites
Variscan crytalline basement

fig 3

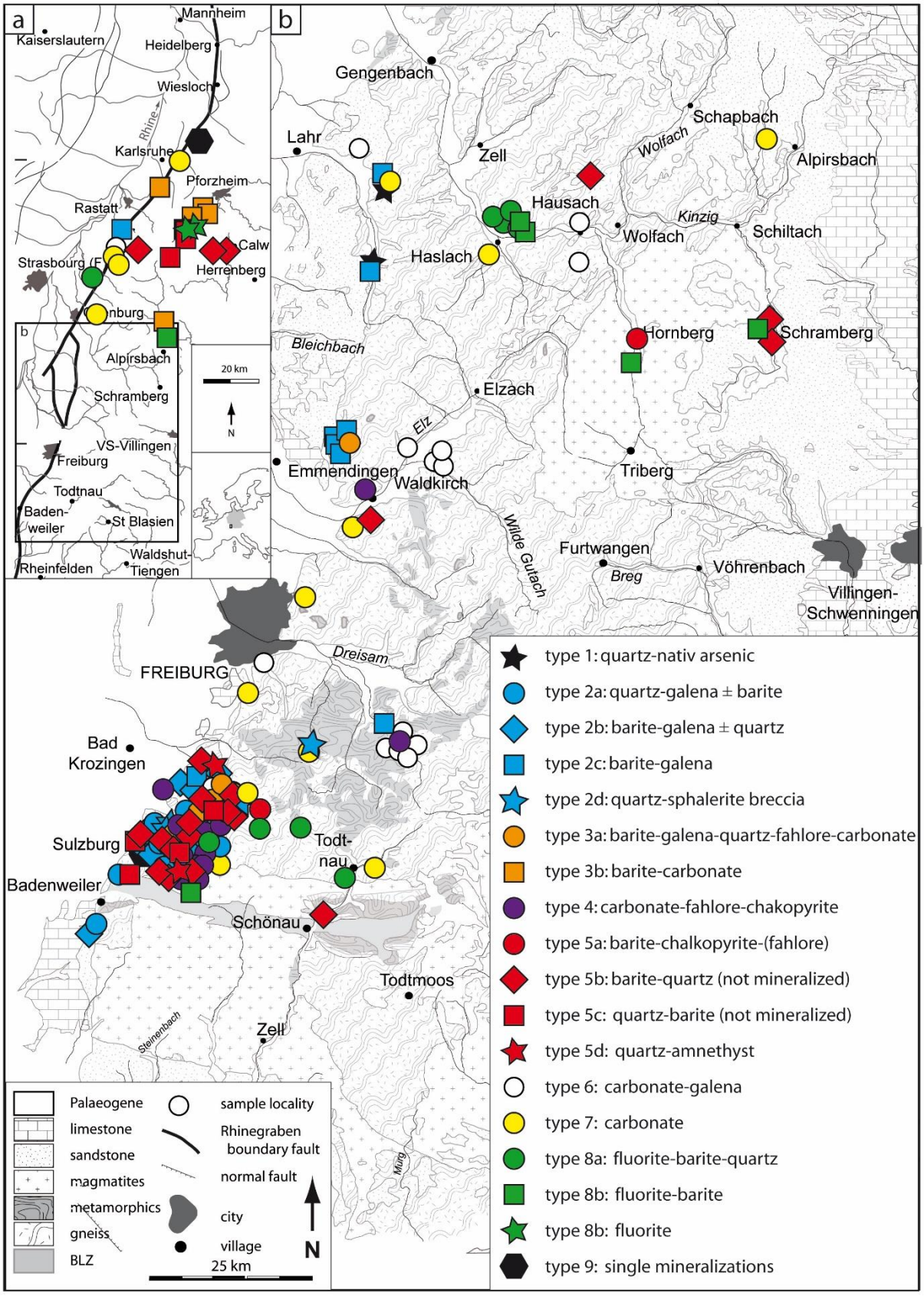
a
b
Mannheim
Kaiserslautern
Heidelberg
Wiesloch
Rhine
Karlsruhe
Pforzheim
Rastatt
Calw
Strasbourg (F)
Herrenberg
Freiburg
Alpirsbach
Schramberg
VS-Villingen
Todtnau
Baden-weiler
St Blasien
Waldshut-Tiengen
Rheinfelden
20 km
N
Gengenbach
Lahr
Zell
Schapbach
Wolfach
Alpirsbach
Hausach
Kinzig
Wolfach
Schiltach
Haslach
Hornberg
Schramberg
Bleichbach
Elzach
Elz
Emmendingen
Waldkirch
Triberg
Wilde Gutach
Furtwangen
Breg
Vöhrenbach
Villingen-Schwenningen
Dreisam
FREIBURG
Bad Krozingen
Sulzburg
Badenweiler
Todt-nau
Schönau
Todtmoos
Zell
Steinenbach
Murg
Palaeogene
limestone
sandstone
magmatites
metamorphics
gneiss
BLZ
sample locality
Rhinegraben boundary fault
normal fault
city
village
25 km
N
type 1: quartz-nativ arsenic
type 2a: quartz-galena ± barite
type 2b: barite-galena ± quartz
type 2c: barite-galena
type 2d: quartz-sphalerite breccia
type 3a: barite-galena-quartz-fahlore-carbonate
type 3b: barite-carbonate
type 4: carbonate-fahlore-chakopyrite
type 5a: barite-chalkopyrite-(fahlore)
type 5b: barite-quartz (not mineralized)
type 5c: quartz-barite (not mineralized)
type 5d: quartz-amnethyst
type 6: carbonate-galena
type 7: carbonate
type 8a: fluorite-barite-quartz
type 8b: fluorite-barite
type 8b: fluorite
type 9: single mineralizations

fig 4.

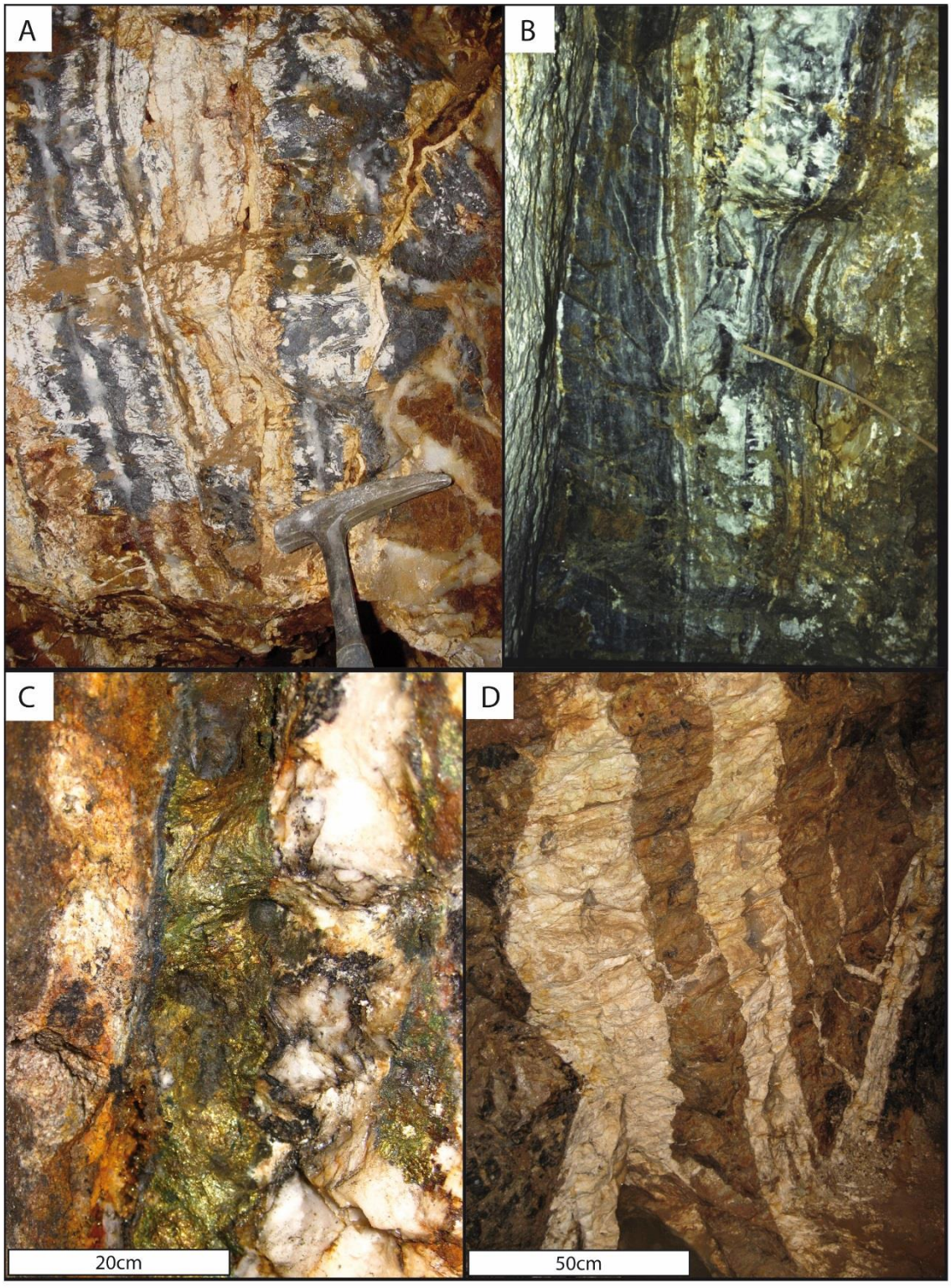

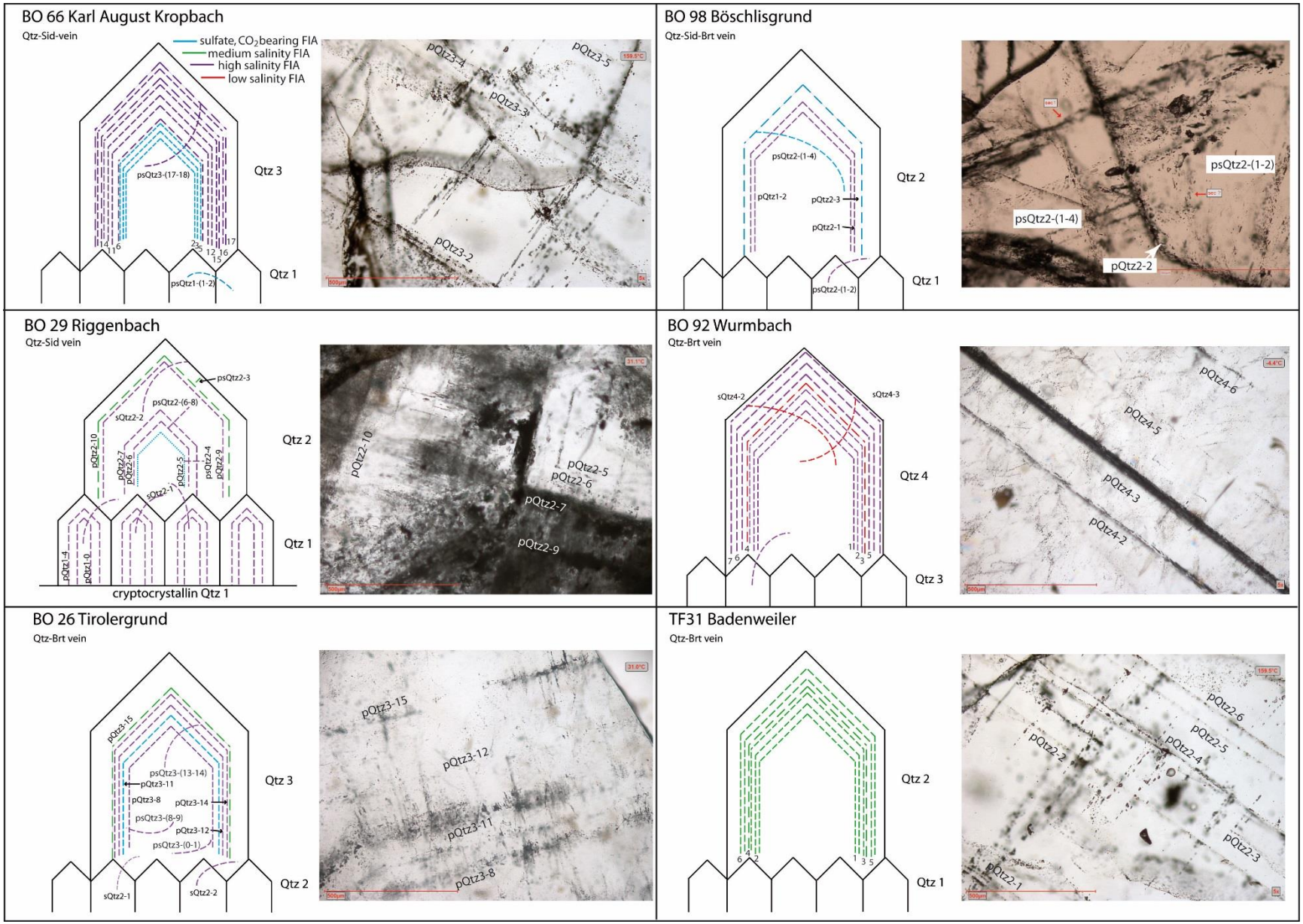
BO 66 Karl August Kropbach
Qtz-Sid-vein
sulfate, CO2bearing FIA
medium salinity FIA
high salinity FIA
low salinity FIA
psQtz3-(17-18)
Qtz 3
Qtz 1
psQtz1-(1-2)
pQtz3-4
pQtz3-5
pQtz3-3
pQtz3-2
BO 98 Böschlisgrund
Qtz-Sid-Brt vein
psQtz2-(1-4)
pQtz1-2
pQtz2-3
pQtz2-1
Qtz 2
Qtz 1
psQtz2-(1-2)
psQtz2-(1-2)
psQtz2-(1-4)
pQtz2-2
BO 29 Riggenbach
Qtz-Sid vein
psQtz2-3
psQtz2-(6-8)
sQtz2-2
pQtz2-10
pQtz2-7
pQtz2-6
pQtz2-5
psQtz2-4
pQtz2-9
sQtz2-1
pQtz1-4
pQtz1-0
Qtz 2
Qtz 1
cryptocrystallin Qtz 1
pQtz2-10
pQtz2-5
pQtz2-6
pQtz2-7
pQtz2-9
BO 92 Wurmbach
Qtz-Brt vein
sQtz4-2
sQtz4-3
Qtz 4
Qtz 3
pQtz4-6
pQtz4-5
pQtz4-3
pQtz4-2
BO 26 Tirolergrund
Qtz-Brt vein
pQtz3-15
psQtz3-(13-14)
pQtz3-11
pQtz3-8
pQtz3-14
psQtz3-(8-9)
pQtz3-12
psQtz3-(0-1)
sQtz2-1
sQtz2-2
Qtz 3
Qtz 2
pQtz3-15
pQtz3-12
pQtz3-11
pQtz3-8
TF31 Badenweiler
Qtz-Brt vein
Qtz 2
Qtz 1
pQtz2-6
pQtz2-5
pQtz2-4
pQtz2-2
pQtz2-3
pQtz2-1

fig 5.

fig 6.

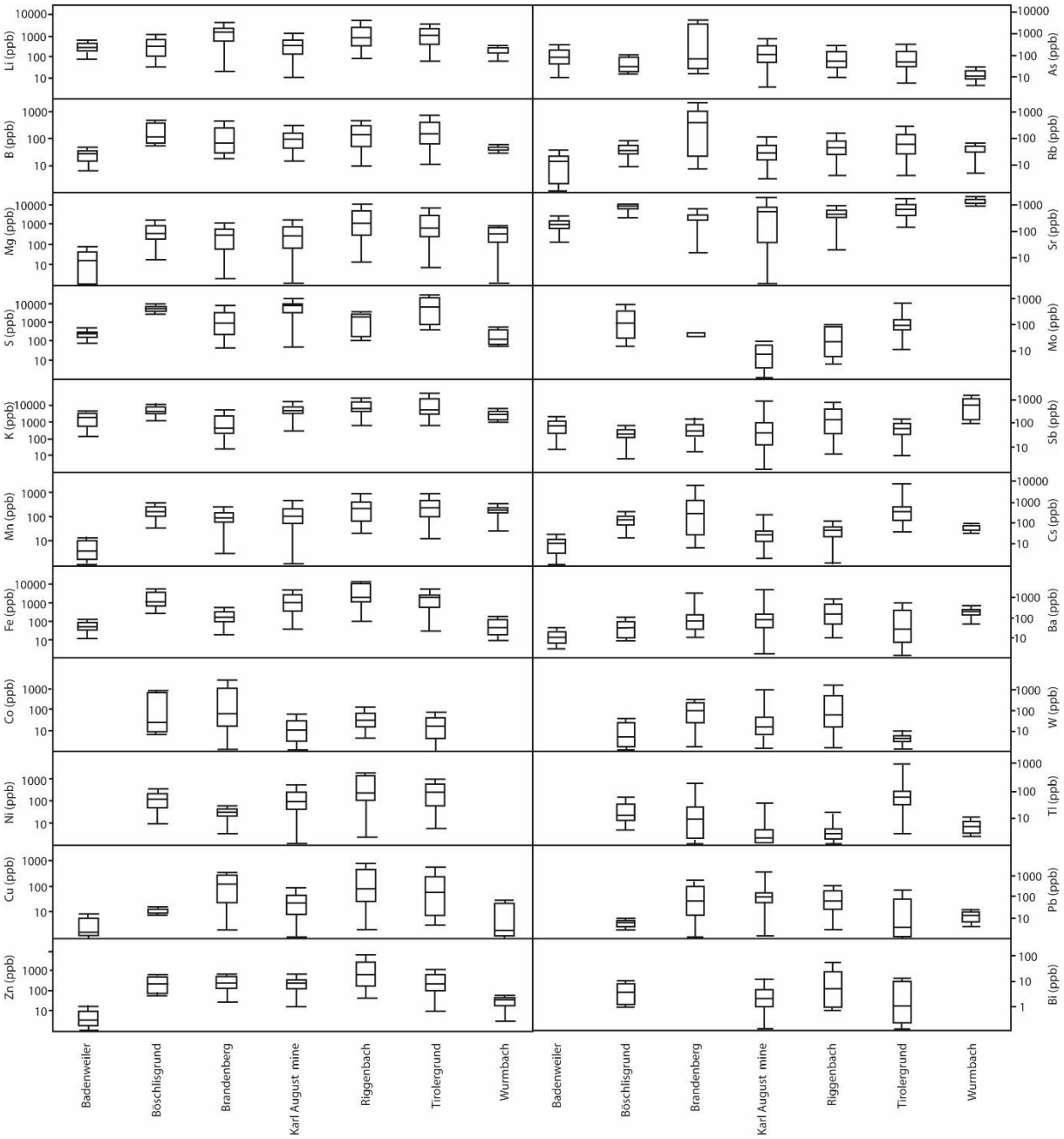
Li (ppb)
As (ppb)
B (ppb)
Rb (ppb)
Mg (ppb)
Sr (ppb)
S (ppb)
Mo (ppb)
K (ppb)
Sb (ppb)
Mn (ppb)
Cs (ppb)
Fe (ppb)
Ba (ppb)
Co (ppb)
W (ppb)
Ni (ppb)
Tl (ppb)
Cu (ppb)
Pb (ppb)
Zn (ppb)
Bi (ppb)
Badenweiler
Böschlisgrund
Brandenberg
Karl August mine
Riggenbach
Tirolergrund
Wurmbach

fig 7.

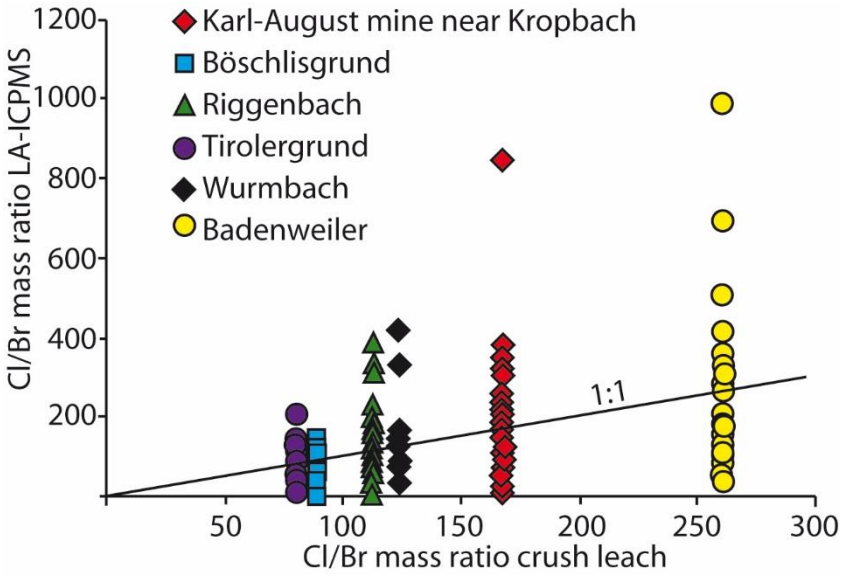
Karl-August mine near Kropbach
Böschlisgrund
Riggenbach
Tirolergrund
Wurmbach
Badenweiler
1:1
Cl/Br mass ratio LA-ICPMS
Cl/Br mass ratio crush leach
1200
1000
800
600
400
200
50
100
150
200
250
300

fig 8.

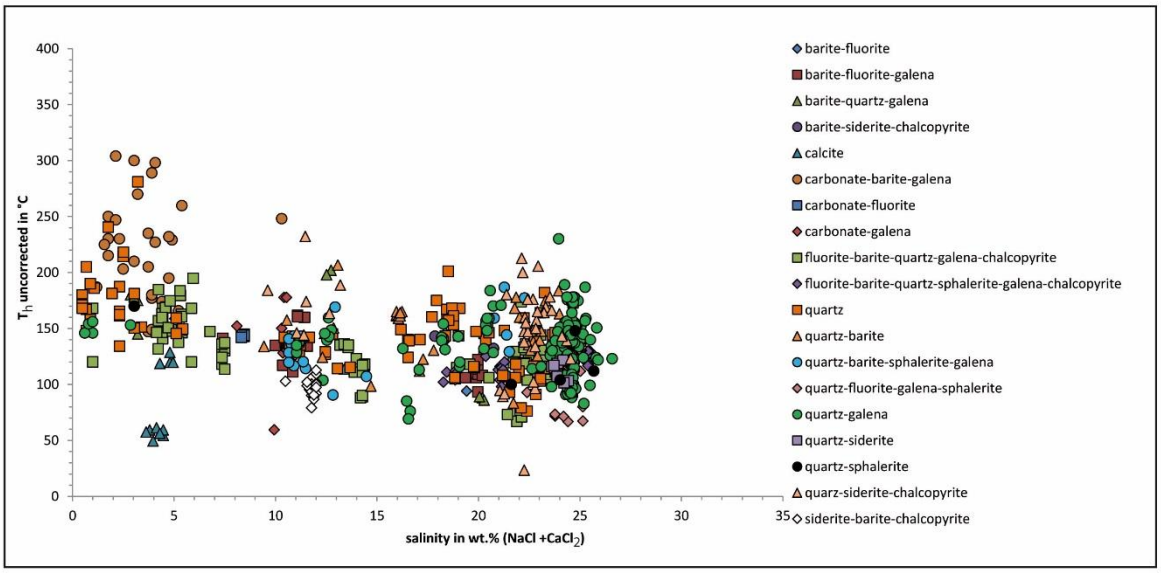
400
350
300
250
200
150
100
50
0
T_h uncorrected in °C
0
5
10
15
20
25
30
35
salinity in wt.% (NaCl +$CaCl_2$)
barite-fluorite
barite-fluorite-galena
barite-quartz-galena
barite-siderite-chalcopyrite
calcite
carbonate-barite-galena
carbonate-fluorite
carbonate-galena
fluorite-barite-quartz-galena-chalcopyrite
fluorite-barite-quartz-sphalerite-galena-chalcopyrite
quartz
quartz-barite
quartz-barite-sphalerite-galena
quartz-fluorite-galena-sphalerite
quartz-galena
quartz-siderite
quartz-sphalerite
quarz-siderite-chalcopyrite
siderite-barite-chalcopyrite

fig 9.

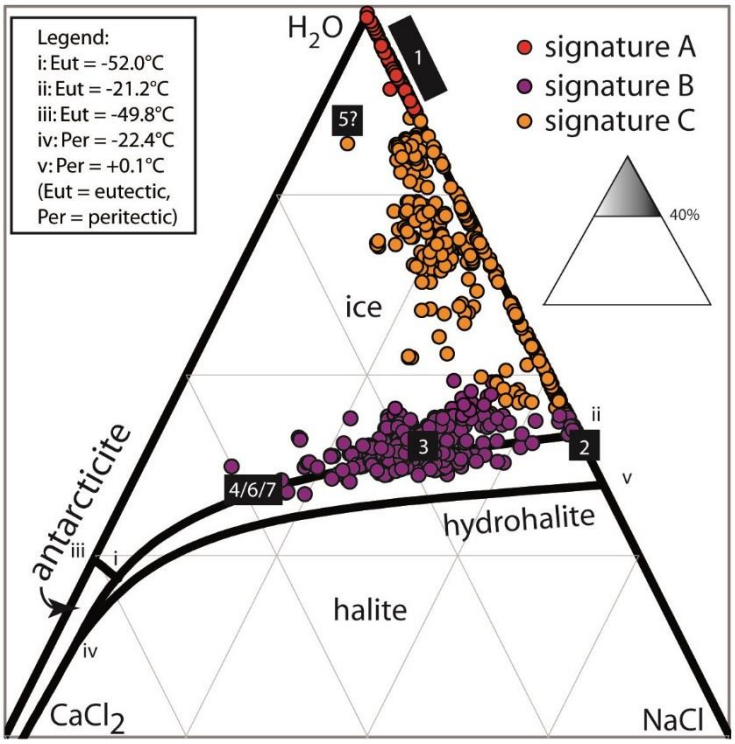
Legend:
i: Eut = -52.0°C
ii: Eut = -21.2°C
iii: Eut = -49.8°C
iv: Per = -22.4°C
v: Per = +0.1°C
(Eut = eutectic,
Per = peritectic)
H2O
signature A
signature B
signature C
40%
1
5?
ice
ii
2
3
4/6/7
v
hydrohalite
antarcticite
iii
i
halite
iv
CaCl2
NaCl

fig 10.

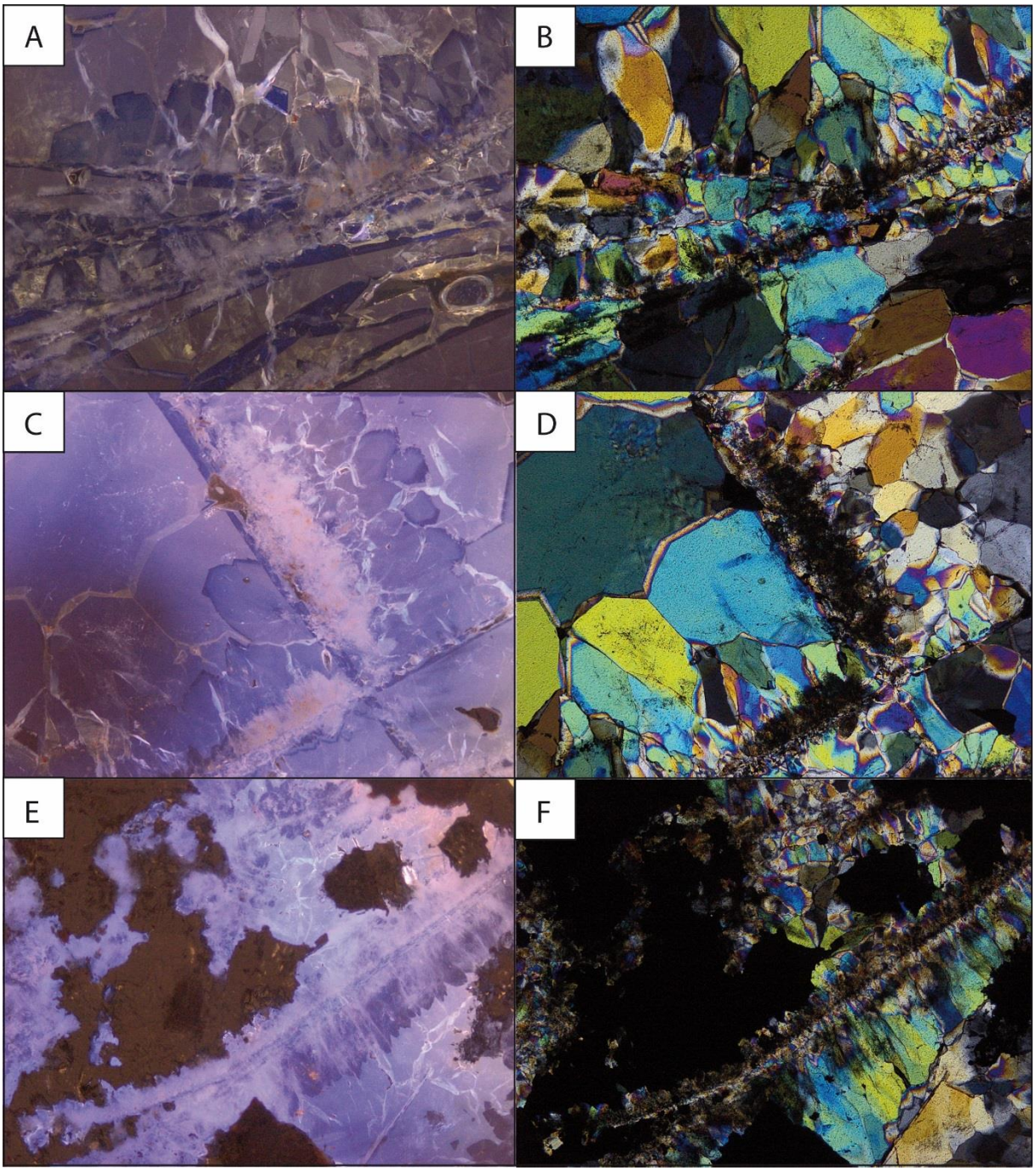

fig 11.

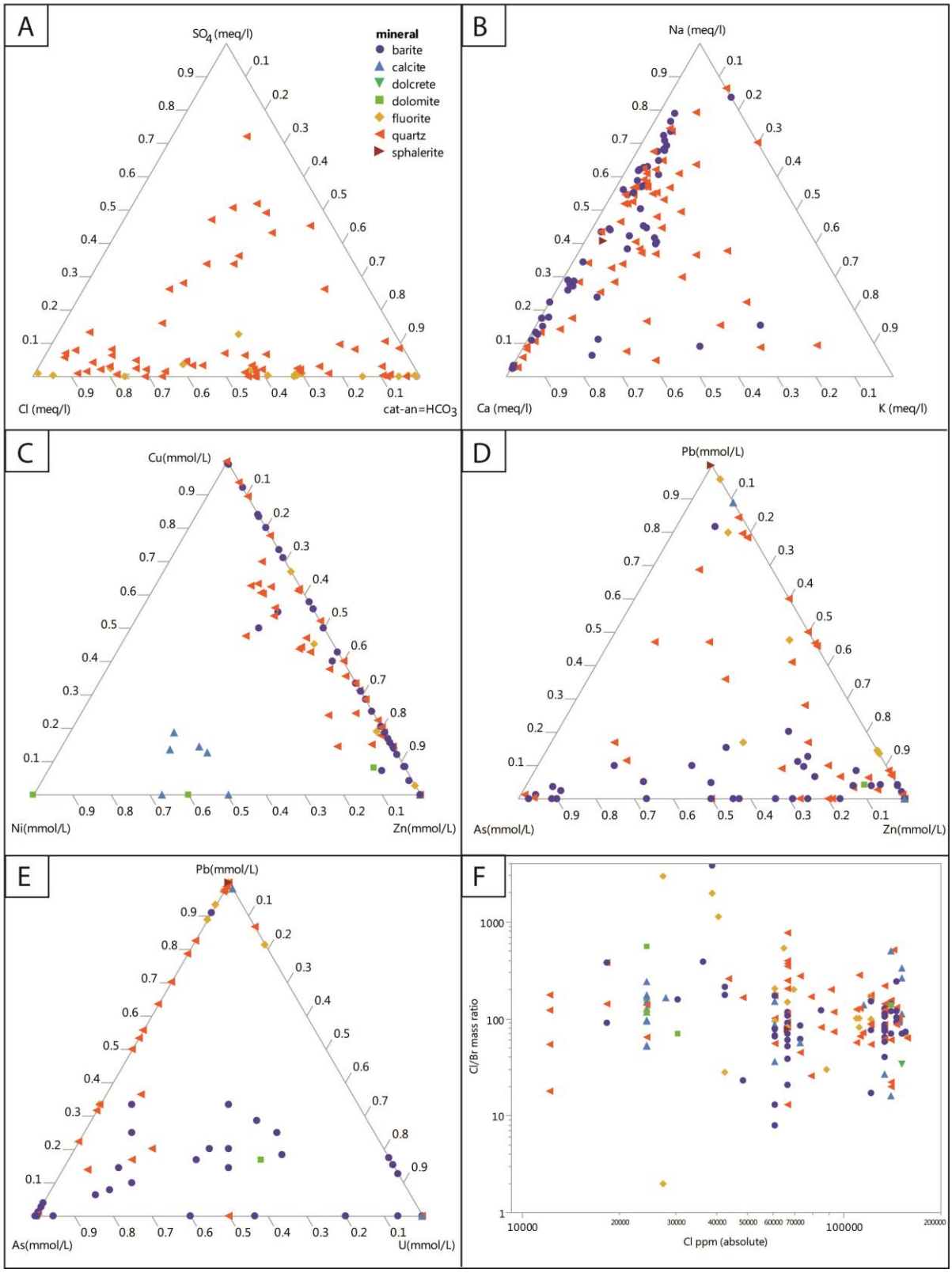
A
SO4 (meq/l)
mineral
barite
calcite
dolcrete
dolomite
fluorite
quartz
sphalerite
Cl (meq/l)
cat-an=HCO3
B
Na (meq/l)
Ca (meq/l)
K (meq/l)
C
Cu(mmol/L)
Ni(mmol/L)
Zn(mmol/L)
D
Pb(mmol/L)
As(mmol/L)
Zn(mmol/L)
E
Pb(mmol/L)
As(mmol/L)
U(mmol/L)
F
Cl/Br mass ratio
Cl ppm (absolute)

fig 12.

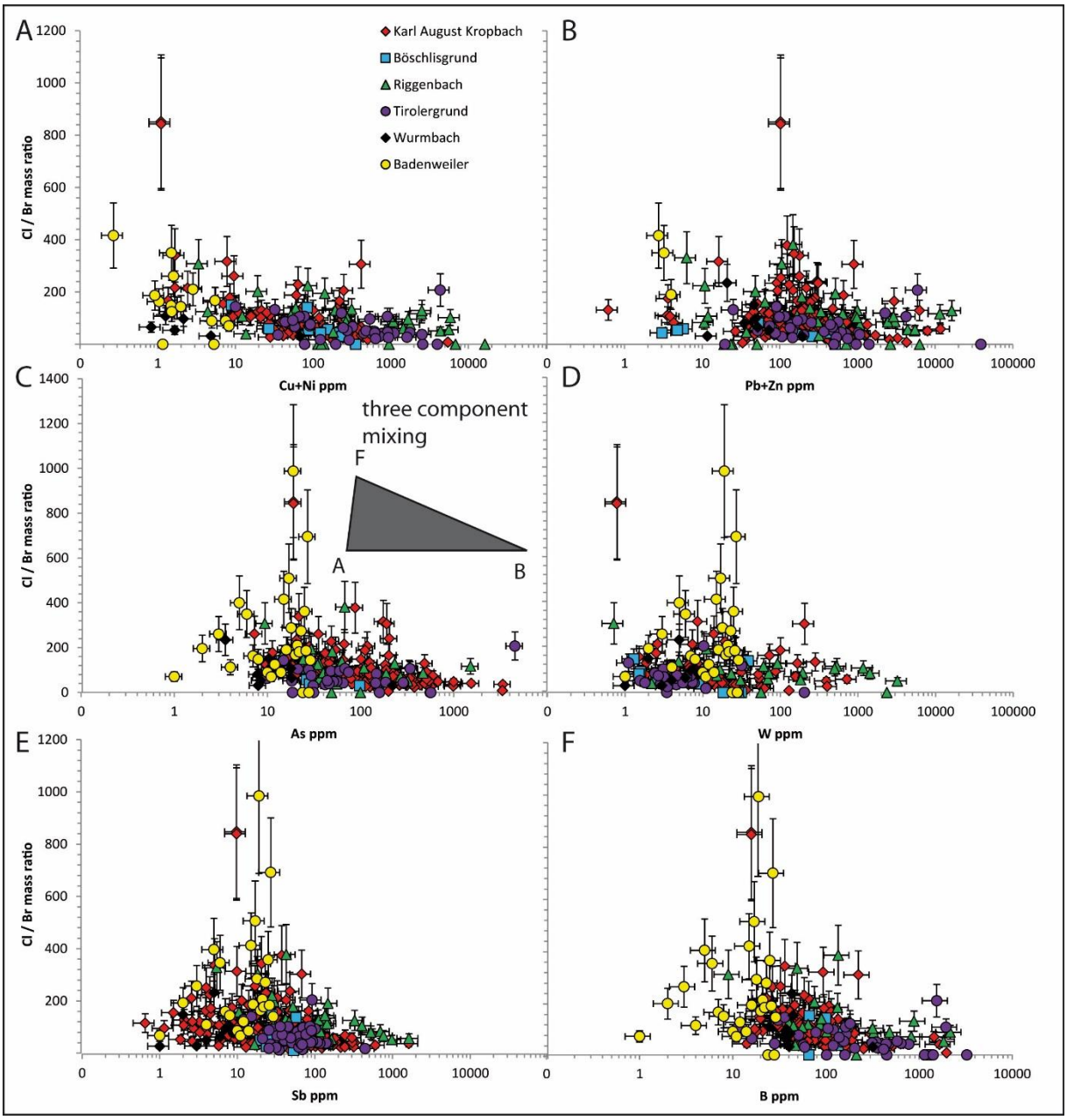
A
B
C
D
E
F
Karl August Kropbach
Böschlisgrund
Riggenbach
Tirolergrund
Wurmbach
Badenweiler
Cl / Br mass ratio
Cu+Ni ppm
Pb+Zn ppm
As ppm
W ppm
Sb ppm
B ppm
three component mixing
F
A
B

fFig 13.

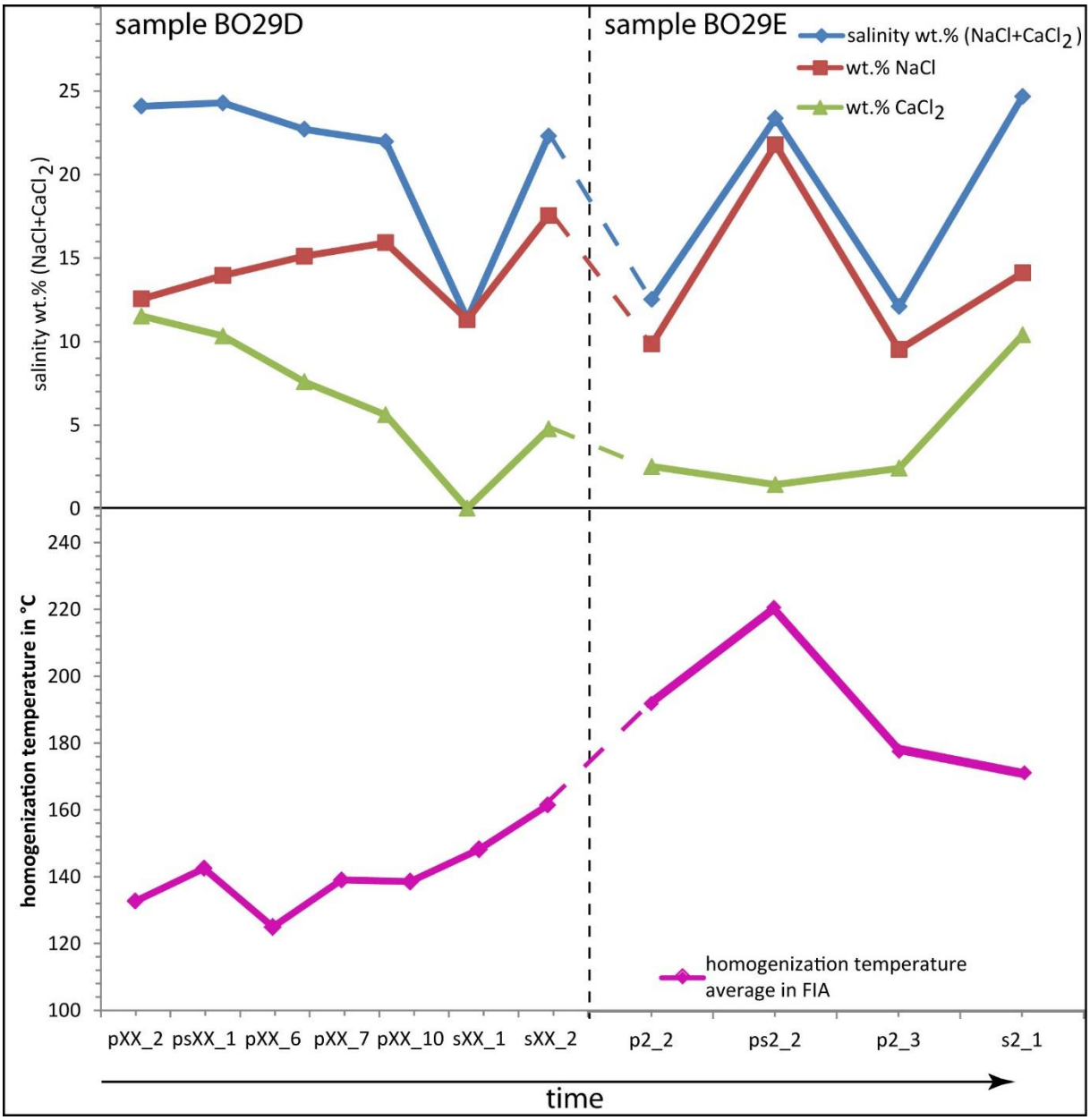
sample BO29D
sample BO29E
salinity wt.% (NaCl+CaCl2)
wt.% NaCl
wt.% CaCl2
salinity wt.% (NaCl+CaCl2)
25
20
15
10
5
0
homogenization temperature in °C
240
220
200
180
160
140
120
100
homogenization temperature average in FIA
pXX_2
psXX_1
pXX_6
pXX_7
pXX_10
sXX_1
sXX_2
p2_2
ps2_2
p2_3
s2_1
time

fig 14.

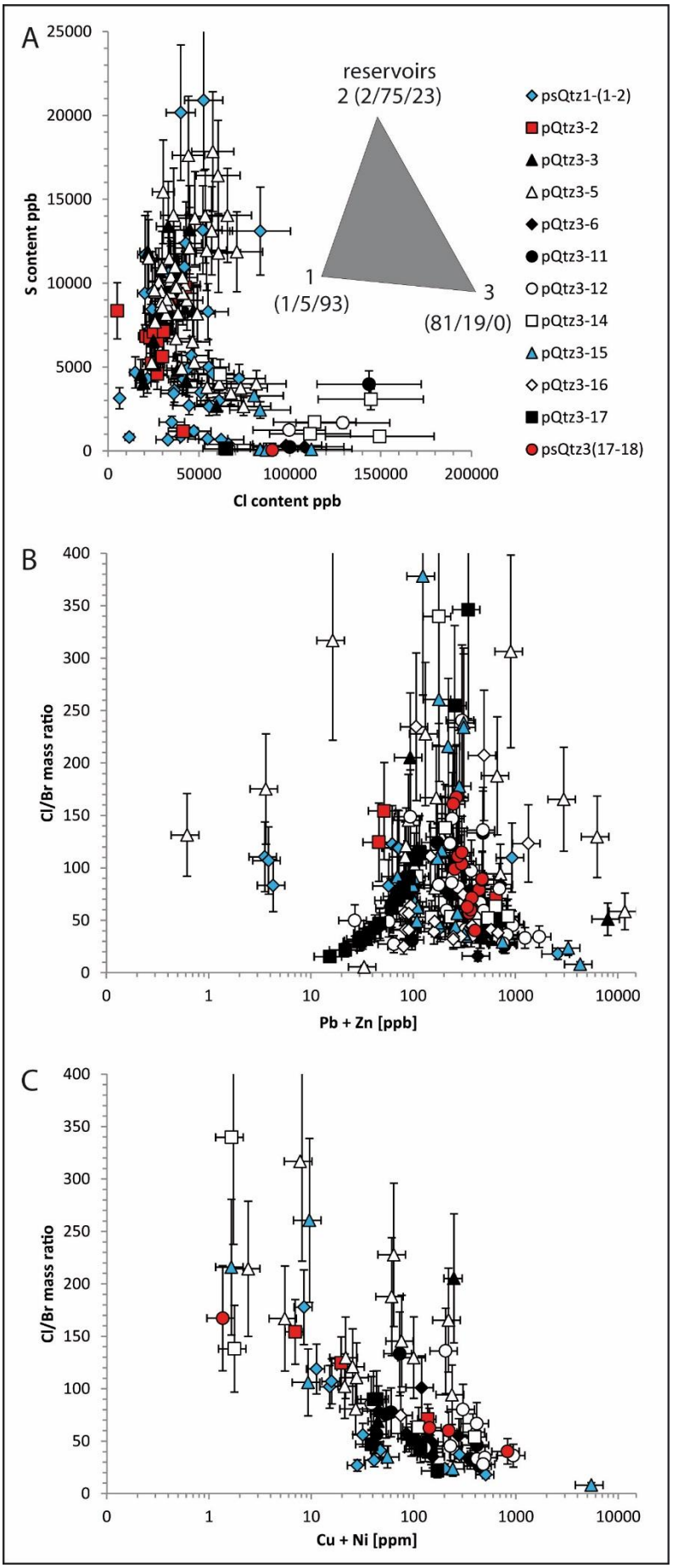
A
S content ppb
Cl content ppb
reservoirs
2 (2/75/23)
1
(1/5/93)
3
(81/19/0)
psQtz1-(1-2)
pQtz3-2
pQtz3-3
pQtz3-5
pQtz3-6
pQtz3-11
pQtz3-12
pQtz3-14
pQtz3-15
pQtz3-16
pQtz3-17
psQtz3(17-18)
B
Cl/Br mass ratio
Pb + Zn [ppb]
C
Cl/Br mass ratio
Cu + Ni [ppm]

fig 15.

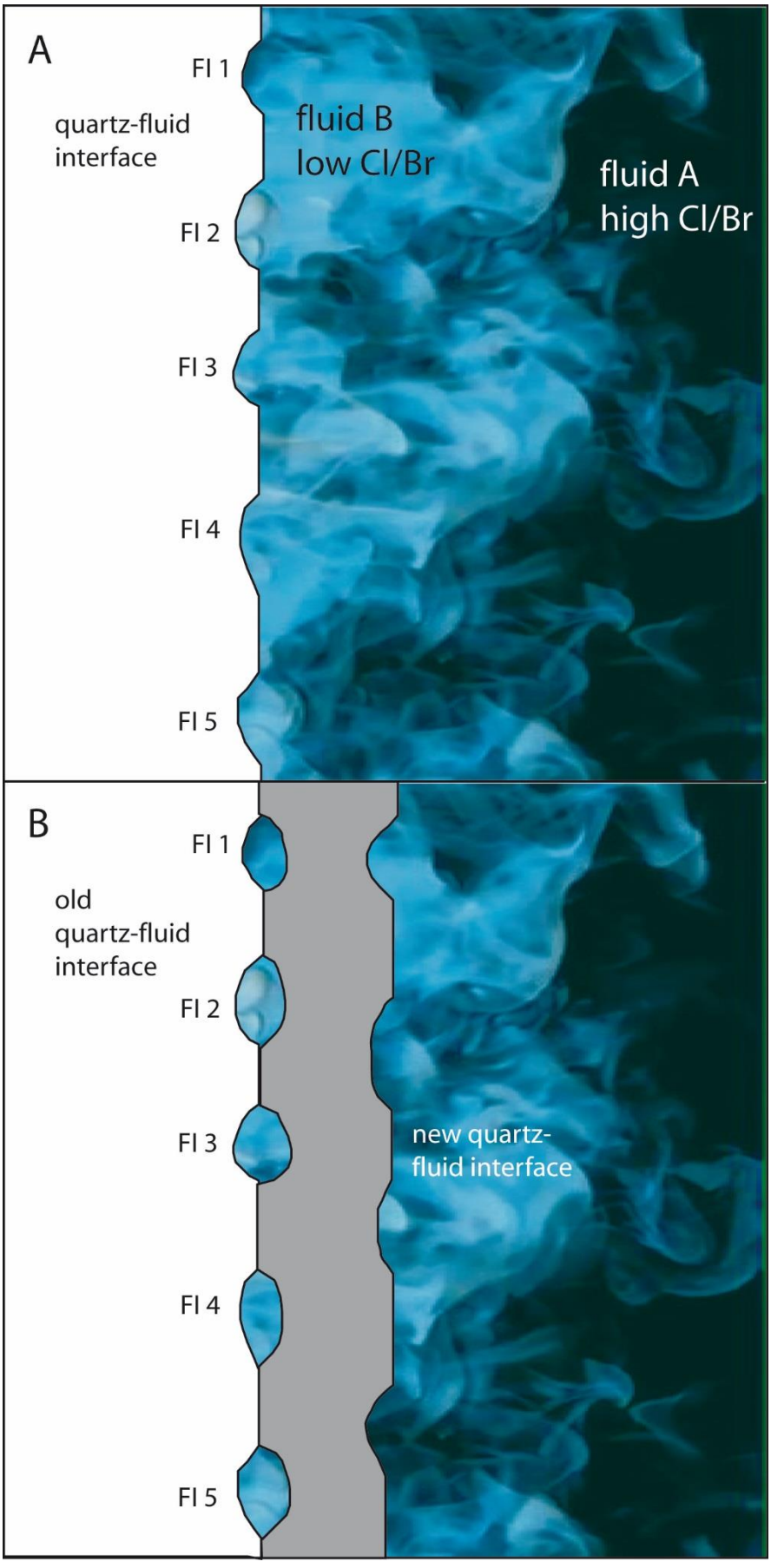
A
FI 1
quartz-fluid
interface
fluid B
low Cl/Br
fluid A
high Cl/Br
FI 2
FI 3
FI 4
FI 5
B
FI 1
old
quartz-fluid
interface
FI 2
FI 3
new quartz-
fluid interface
FI 4
FI 5

fig 16

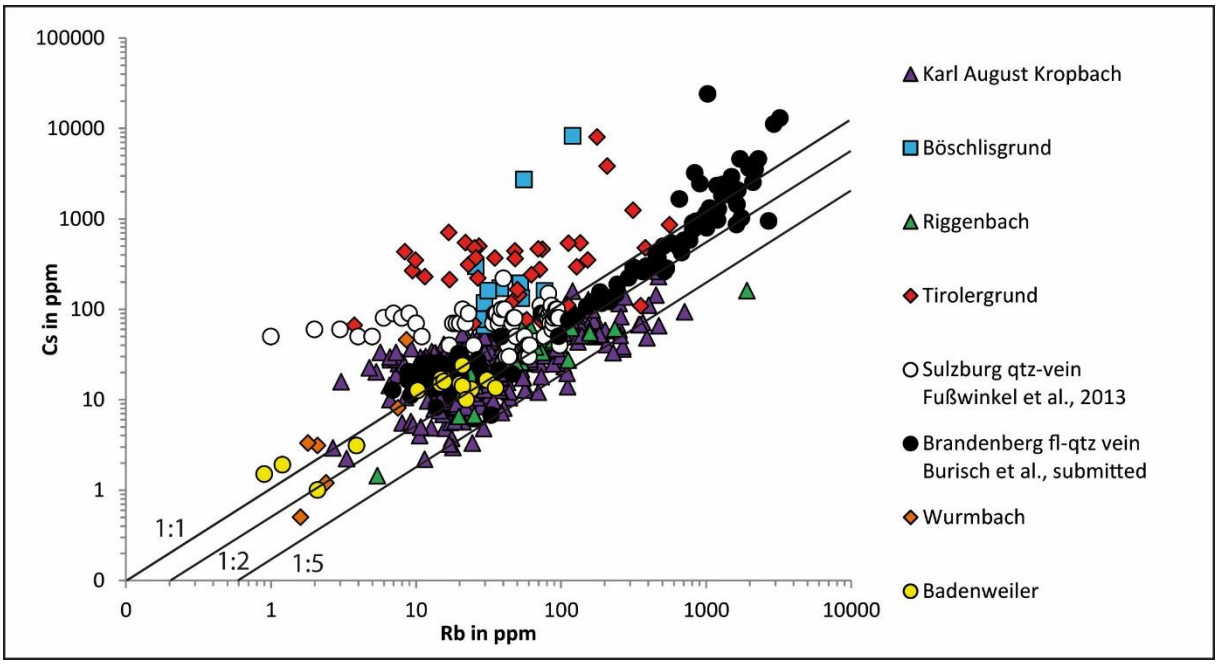
100000
10000
1000
100
10
1
0
Cs in ppm
0
1
10
100
1000
10000
Rb in ppm
1:1
1:2
1:5
Karl August Kropbach
Böschlisgrund
Riggenbach
Tirolergrund
Sulzburg qtz-vein
Fußwinkel et al., 2013
Brandenberg fl-qtz vein
Burisch et al., submitted
Wurmbach
Badenweiler

fig 17.

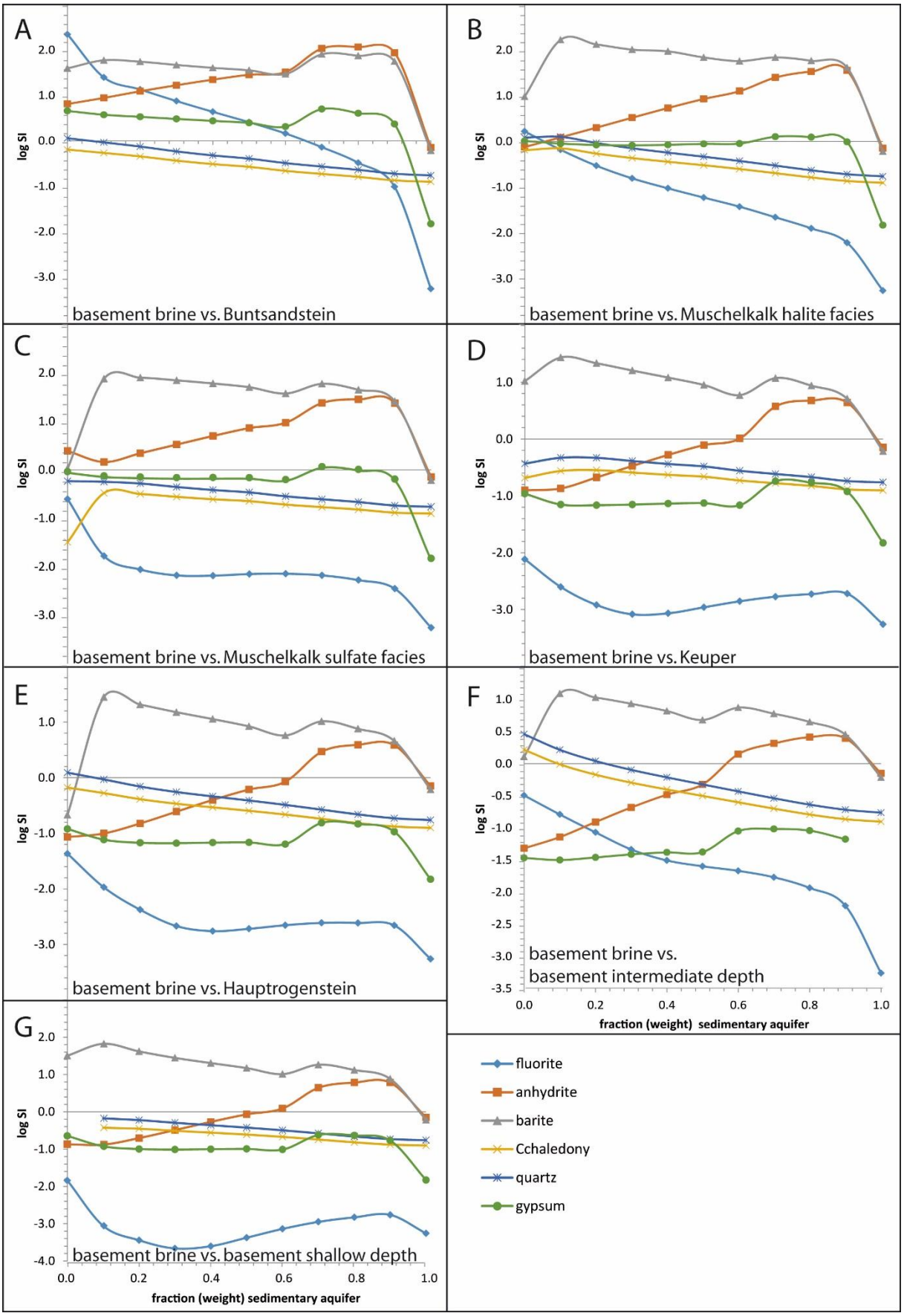
A
log SI
basement brine vs. Buntsandstein
B
basement brine vs. Muschelkalk halite facies
C
basement brine vs. Muschelkalk sulfate facies
D
basement brine vs. Keuper
E
basement brine vs. Hauptrogenstein
F
basement brine vs.
basement intermediate depth
fraction (weight) sedimentary aquifer
G
basement brine vs. basement shallow depth
fraction (weight) sedimentary aquifer
fluorite
anhydrite
barite
Cchaledony
quartz
gypsum

fig 18.

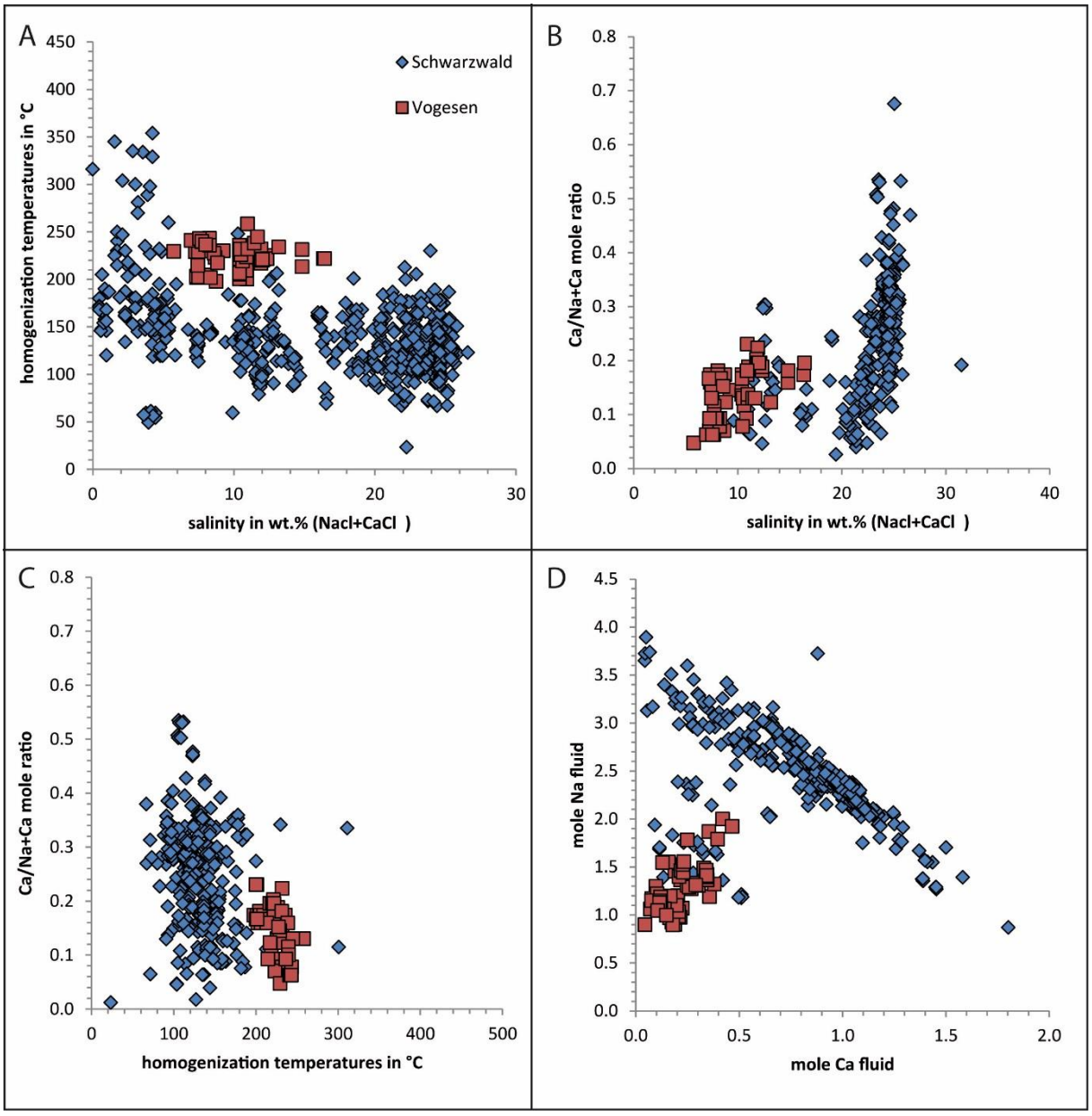
A
Schwarzwald
Vogesen
homogenization temperatures in °C
salinity in wt.% (Nacl+CaCl)
B
Ca/Na+Ca mole ratio
salinity in wt.% (Nacl+CaCl)
C
Ca/Na+Ca mole ratio
homogenization temperatures in °C
D
mole Na fluid
mole Ca fluid

fig 19.

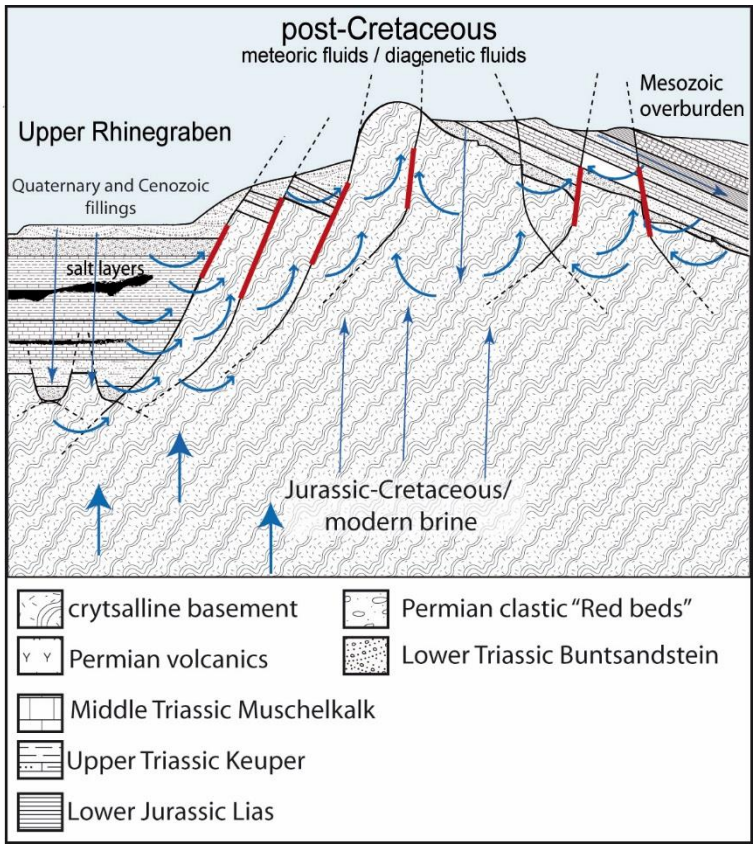
post-Cretaceous
meteoric fluids / diagenetic fluids
Mesozoic overburden
Upper Rhinegraben
Quaternary and Cenozoic fillings
salt layers
Jurassic-Cretaceous/ modern brine
crytsalline basement
Permian volcanics
Middle Triassic Muschelkalk
Upper Triassic Keuper
Lower Jurassic Lias
Permian clastic "Red beds"
Lower Triassic Buntsandstein

Miner Deposita
DOI 10.1007/s00126-016-0662-z

LETTER

Natural fracking and the genesis of five-element veins

Gregor Markl[1] · **Mathias Burisch**[1] · **Udo Neumann**[1]

Received: 27 April 2016 / Accepted: 9 May 2016

Abstract Hydrothermal Ag-Co-Ni-Bi-As (five-element vein type) ore deposits show very conspicuous textures of the native elements silver, bismuth, and arsenic indicating formation from a rapid, far-from-equilibrium process. Such textures include up to dm-large tree- and wire-like aggregates overgrown by Co-Ni-Fe arsenides and mostly carbonates. Despite the historical and contemporary importance of five-element vein type deposits as sources of silver, bismuth, and cobalt, and despite of spectacular museum specimens, their process of formation is not yet understood and has been a matter of debate since centuries. We propose, based on observations from a number of classical European five-element vein deposits and carbon isotope analyses, that "natural fracking," i.e., liberation of hydrocarbons or hydrocarbon-bearing fluids during break up of rocks in the vicinity of an active hydrothermal system and mixing between these hydrocarbons (e.g., methane and/or methane-bearing fluids) and a metal-rich hydrothermal fluid is responsible for ore precipitation and the formation of the unusual ore textures and assemblages. Thermodynamic and isotope mixing calculations show that the textural, chemical, and isotopic features of the investigated deposits can entirely be explained by this mechanism.

Editorial handling: B. Lehmann

✉ Gregor Markl
markl@uni-tuebingen.de

[1] Fachbereich Geowissenschaften, Universität Tübingen, Wilhelmstr. 56, 72074 Tübingen, Germany

Introduction

Hydrothermal ore deposits are important economic sources for many metals and have been so since ancient times. A particularly high-grade and interesting deposit type is here considered: the five-element vein type (Bi-Co-Ni-Ag-As) containing various combinations of Co-Ni-Fe arsenides (mainly safflorite, skutterudite, loellingite, rammelsbergite, and niccolite) with or without native silver, arsenic, antimony, and bismuth in mostly carbonate gangue (Kissin 1992). Because of the extraordinary enrichment especially of native silver and bismuth (ore shoots of some tens of meters size with hundreds of kilograms to tonnes of metals in almost monomineralic aggregates have been observed), the five-element vein deposits have been the economic foundations of some regions during the medieval, modern, and present times. The quality of their mineral specimens has additionally attracted interest by collectors and museums since the fifteenth century. Some of the world's most famous ore deposits such as Schneeberg/Germany, Jachymov/Czech Republic, Kongsberg/Norway, Cobalt/Ontario, Batopilas/Mexico, or Bou Azzer/Morocco belong to this type of deposit and have been or are a major source of especially silver and cobalt.

The observations

Most workers have tried to explain the formation of these deposits based on fluid inclusion or electrochemical arguments involving iron oxidation (Ondrus et al. 2003), fluid mixing (Marshall et al. 1993; Staude et al. 2012), boiling, and cooling, or a combination of these parameters (Kissin 1992). Earlier studies, however, imply that neither temperature or pressure during formation nor host rock type or alteration style, age, or fluid composition provided any clue to a

Published online: 20 May 2016

common mechanism of formation, as none of these parameters is typical of all deposits of this type, and Kissin (1992) proposed up to seven different genetic hypotheses.

Our line of arguments is based on textures observed during the macroscopic and microscopic inspection of hundreds of specimens from European five-element deposits, such as Wittichen and Wenzel (Staude et al. 2007, 2012), Mackenheim and Nieder-Beerbach (Fettel 1978; Ramdohr 1975), Schneeberg (Keil 1933; Lipp 2003) and Bieber (Wagner and Lorenz 2002) in Germany, Turtmanntal in Switzerland (Meisser 2003), and a large literature compilation on worldwide deposits (see Kissin 1992, and references therein; Ahmed et al. 2009; Bastin 1950; Clavel 1963; Gammon 1966; Keil 1933; Lietz 1939; Marshall 2008; Ondrus et al. 2003; Petruk 1968; Wilkerson et al. 1988) (Table 1). The following typical features are recognized:

1. In all deposits investigated, a low-grade, sub-economic "ordinary" sulfide-dominated hydrothermal assemblage involving pyrite, chalcopyrite, tennantite-tetrahedrite solid solutions, sphalerite, or galena is followed first by native elements ± arsenides/antimonides, then by arsenides/antimonides alone, then by sulfarsenides and sulfides, and finally by gangue minerals (mostly carbonates like calcite or siderite, more rarely by barite, fluorite, or quartz).
2. Native metals and some arsenides typically form skeletal, dendritic, wire-, or fern-shaped aggregates of unusual size (up to decimeters) (Fig. 1c, d).
3. Native silver and native bismuth are typically not intergrown with each other, but occur as separate "clumps"; arsenides (if not overgrowing the native elements) are also present as separate "clumps." Both native elements and some of the arsenide aggregates appear as "floaters" in gangue, with no or only very limited contact to the host rock.
4. The element arsenic may occur both as native arsenic (As^0), as arsenides (As^{1-}), and as sulfarsenites (As^{3+}; fahlore, proustite, pearceite) hence in three different oxidation states, in one deposit. Native arsenic may be older, contemporaneous, or younger, and the sulfarsenides are typically younger than the native metals.
5. The arsenide-sulfide associations show a typical succession of early Co-Ni-rich di- and triarsenides, followed by Fe-diarsenides, then sulfarsenides, and finally sulfides. In some cases, monoarsenides may be followed by di- and triarsenides. Nickel-rich arsenides preferably grow directly around aggregates of native silver, and Co-rich arsenides around aggregates of native bismuth. Around native silver, the dominant cation changes from Ni to Co and later Fe in the zoned arsenide aggregates (Fig. 1d–f).
6. The native elements are partly dissolved during or after the growth of the arsenides and sulfarsenides/antimonides, leaving behind empty holes rimmed by the arsenide minerals (Fig. 1a). These holes are in some cases filled by later gangue calcite (Fig. 1b) and rarely, sulfides.
7. Rich ore shoots in the pinch and swell structure veins typically occur at the site of intersecting structures.
8. Host rocks typically include carbonaceous shales, graphite-rich gneisses, or lithologies very rich in iron oxides and/or iron sulfides.

The above observations lead to the following conclusions:

1. Each of these hydrothermal systems contains sulfides before and after arsenide and native metal precipitation.
2. The growth of the native metals and arsenides occurs far from equilibrium, as indicated by their unusual habit/shape.
3. Redox is an important and variable parameter during precipitation, as, e.g., shown by the occurrence of arsenic in three and sulfur in two different oxidation states, respectively.
4. Fluid conditions, fluid speciation, and specifically the arsenide/sulfide ratio change during arsenide and native metal growth, as indicated by the succession of arsenide minerals.
5. The massive occurrence of carbonates as "sealing" gangue in all deposits indicates that carbon plays a major role.

The model

All observations fit a model, in which an ordinary sulfide-dominated hydrothermal system is modified abruptly by the influx of a strongly reducing gas or fluid phase. Kerrich et al. (1986; Cobalt/Canada) and Burisch (unpublished results from Odenwald localities, Germany) recognized the occurrence of methane, propane, and ethane in fluid inclusions of gangue calcite that formed co-genetically with the arsenides. Accordingly, methane or other hydrocarbons can be assumed to serve as the necessary reducing agent. They are ubiquitous, extremely mobile, and highly reactive (Schoell 1988; Etiope and Sherwood Lollar 2013). Hydrocarbon influx is then followed by step-by-step re-oxidation due to precipitation reactions (Fig. 2), such as the following:

$$8BiCl_4^- + 6H_2O + 3CH_4 = 8Bi + 32Cl^- + 24H^+ + 3CO_2 \quad (1)$$

or

$$8AgCl_2^- + 2H_2O + CH_4 = 8Ag + 16Cl^- + 8H^+ + CO_2. \quad (2)$$

Table 1 Worldwide localities of five-element veins with their characteristic ore and gangue minerals, textures, carbon isotope compositions (where known), and references

Locality	Host rock	Characteristic elements in ore	Native elements	Special textures of native elements	Gangue in association with main ore	δ13C of carbonates (PDB)	Reference(s)	Formation temperature, fluid salinity
Wittichen, Schwarzwald, Germany	Altered leucogranite and graphite-bearing paragneiss	Ag, Bi, As, Co, Ni, U	Bismuth, silver, arsenic	Dendritic silver, skeletal bismuth	Carbonates, barite, fluorite, quartz	−6.6 to −11.2	Staude et al. (2012)	50–150 °C; ~25 wt% (NaCl + CaCl2); pH: alkaline
Wenzel, Schwarzwald, Germany	Graphite-bearing paragneiss	Ag, Sb, As, Co, Ni	Silver, Ag-Sb alloys	Dendritic Ag-Sb alloys	Calcite	−11.4 to −13	Staude et al. (2007)	80–150 °C; ~25 % (NaCl + CaCl2)
Nieder-Beerbach, Odenwald, Germany	Gabbro	Ag, Hg, As, Ni, Co, Cu, Zn	Hg-rich silver, arsenic	Skeletal silver, moss-like silver in arsenic	Calcite, barite, chlorite, quartz	−5.8 to −9.6	Fettel (1978), Ramdohr (1975)	Unknown
Mackenheim, Odenwald, Germany	Amphibolite	Bi, As, Co, Ni	Bismuth, arsenic	Dendritic bismuth	Calcite, rare quartz	−6.1 to −7.7	Fettel (1978)	Unknown
St. Andreasberg, Harz, Germany	Metasediments, lamprophyre	Ag, As, Sb, Co, Ni, Pb, Zn, Cu	Silver, antimony, arsenic	Dendrites of safflorite and silver	Calcite	Unknown	Wilke (1952)	Unknown
Bieber, Spessart, Germany	Kupferschiefer and bituminous dolomites over cristalline basement	Bi, As, Co, Ni, Cu	Bismuth	Dendritic bismuth, hopper-skutterudite	Siderite, barite	Unknown	Wagner and Lorenz (2002)	100–300 °C
Schneeberg, Erzgebirge, Germany	Phyllites, shists, meta-diabase, granite, bitumen-rich shists	Ag, Bi, As, Co, Ni, U, Zn, Cu, Pb	Bismuth, silver, arsenic	Moss-like or dendritic silver in arsenic, skeletal and dendritic silver (partly replaced) in carbonates, skeletal and dendritic bismuth	Dolomite-ankerite, siderite, calcite, quartz, barite	Unknown	Lipp (2003)	70–140 °C
Jachymov, Krusne hory (Erzgebirge), Czech Republic	Sulfide- and graphite-rich mica shists, amphibolite, rhyolite	Ag, Bi, As, Co, Ni, U, Zn, Pb, Cu	Silver, bismuth. arsenic	Dendritic silver, skeletal bismuth	Dolomite	Unknown	Ondrus et al. (2003)	Flincs in dolomite of the arsenide phase: 100–145 °C, 22–24 wt% (CaCl2-NaCl)
Turtmanntal, Switzerland	Various chlorite-mica shists with amphibolite layers and sulfid-rich fahlbands	Bi, As, Co, As, Cu	Bismuth	Original shape is not preserved due to deformation	Siderite, dolomite	Unknown	Meisser (2003)	Unknown
Chalanches, Allemont, Isere, France	Basic volcanics with fahlbands, gabbro, biotite gneiss	Ag, Bi, Hg, As, Co, Ni, Cu	Silver, amalgam, bismuth, antimony	Fern-like silver	Carbonates	Unknown	Clavel (1963)	Unknown
Kongsberg, Oslo Region, Norway	Sulfide-rich fahlbands, diabase sills, gneiss	Ag, Hg, As, Co, Ni, Au, Cu, Pb, Zn	Hg-rich silver, arsenic	Wires and dendrites of silver	Calcite, fluorite	−26 to −1	Lietz (1939), Gammon (1966), Kissin (1992)	"NaCl saturated"
Bou Azzer, Morocco	Serpentinite, diorite	Ag, Bi, As, Co, Ni, Cu, Hg, Sb, Zn, Au, U	Silver, bismuth, (gold)	Wires, dendritic, curl-like silver	Carbonates		En-Naciri et al. (1997), Ahmed et al. (2009)	150–350 °C; 16–24 % NaCl + 21–23 % CaCl2 (arsenide stage); 5–22 % NaCl + 13–18 % CaCl2 (Ag-Hg stage)

Table 1 (continued)

Locality	Host rock	Characteristic elements in ore	Native elements	Special textures of native elements	Gangue in association with main ore	δ13C of carbonates (PDB)	Reference(s)	Formation temperature, fluid salinity
Cobalt-Gowganda, Ontario, Canada	Diabase sills, metasediments, volcanics, tholeiitic basalt, granite, lamprophyr	Ag, Bi, Sb, As, Co, Ni, Hg, Cu, Pb, Zn	Silver, amalgam, bismuth, Ag-Sb-alloys	Dendritic and fern-like habit of silver	Calcite	−5.3 to −3.1	Marshall et al. (1993), Keil (1933), Bastin (1950), Misra and Fleet (1975), Kerrich et al. (1986), Andrews et al. (1986)	140–300 °C, 0–25 % NaCl eq, boiling, high pH, and low fO_2
Batopilas, Chihuahua, Mexico	Dacite, granodiorite, serpentinized basalts	Ag, As, Ni, Co, Pb, Zn, Au	Silver, bismuth	Dendritic, fern-shaped silver	Calcite	Unknown	Wilkerson et al. (1988)	137–157 °C, 7–13 % NaCl eq

The redox change is abrupt, so precipitation is kinetically controlled and spatially restricted to early crystal seeds, which are unevenly distributed. This explains the skeletal shape of the precipitating aggregates (these shapes are typical of rapid growth) and the occurrence of typically monomineralic clumps in ore shoots. These shoots form where two chemically contrasting fluids come into contact, i.e., at the intersections of fluid-bearing structures, where the reduced fluid (methane-bearing) mixes with a more oxidized fluid (brine). These intersections form while the original hydrothermal fluid in the main structure is already present and precipitates low amounts of ordinary sulfidic assemblages.

Enhancement of rock permeability due to the formation of fault-fracture meshes as a consequence of active tectonics (Sibson 1996) is a process of "natural fracking." This process potentially releases previously isolated hydrocarbons. Most likely, these hydrocarbons are carried along with migrating crustal fluids (e.g., sedimentary, basinal, or meteoric fluids), similar to the highly debated "anthropogenic fracking" (e.g., Holzman 2011). Precipitation from a given fluid volume is geologically very rapid, probably on the order of hours to days, as the system is "catapulted" far away from equilibrium, but the process of mixing can—once started—go on for long times, as long as the fluid systems remain stable. The junction of the fault systems is the location of an extremely efficient geochemical trap, where Co, Ni, Ag, or Bi is almost quantitatively precipitated in an ore shoot (see Fig. 3a). The observed distribution of ore shoots in well-investigated ore systems supports this idea (Fig. 3b). Whether native metals or arsenides form as main ores depends on the specific pH during fluid-fluid and/or fluid-gas interaction (see Fig. 2) which explains why some veins in a specific district are, e.g., native silver-dominated, while others are dominated by arsenides or native arsenic. Ore precipitation continues as long as this mixing prevails. Afterwards, the pH-fO_2-path of Fig. 2a is followed, arsenides overgrow native metals, native metals partially dissolve, and, finally, precipitation of carbonates follows when their solubility product is exceeded (Fig. 2b) in response to methane oxidation and the concomitant increase of CO_2/HCO_3^- in the fluid.

Apparently, a key role in the process is played by arsenic. In typical hydrothermal solutions related to many of these deposits (H_2O-NaCl-$CaCl_2$, 200 °C, 500 bar, high salinity of 25 wt% NaCl eq.), arsenic is present as H_3AsO_3 or AsO_3^{3-}, but various oxidation states can be present upon reduction (As^0, As^{1-}, As^{2-}, Fig. 2c). Sulfide ions are present during the investigated process, but the arsenide/sulfide ratio changes dramatically upon reduction, from almost 0 to high values (which cannot be quantified). Hence, sulfides precipitate before the

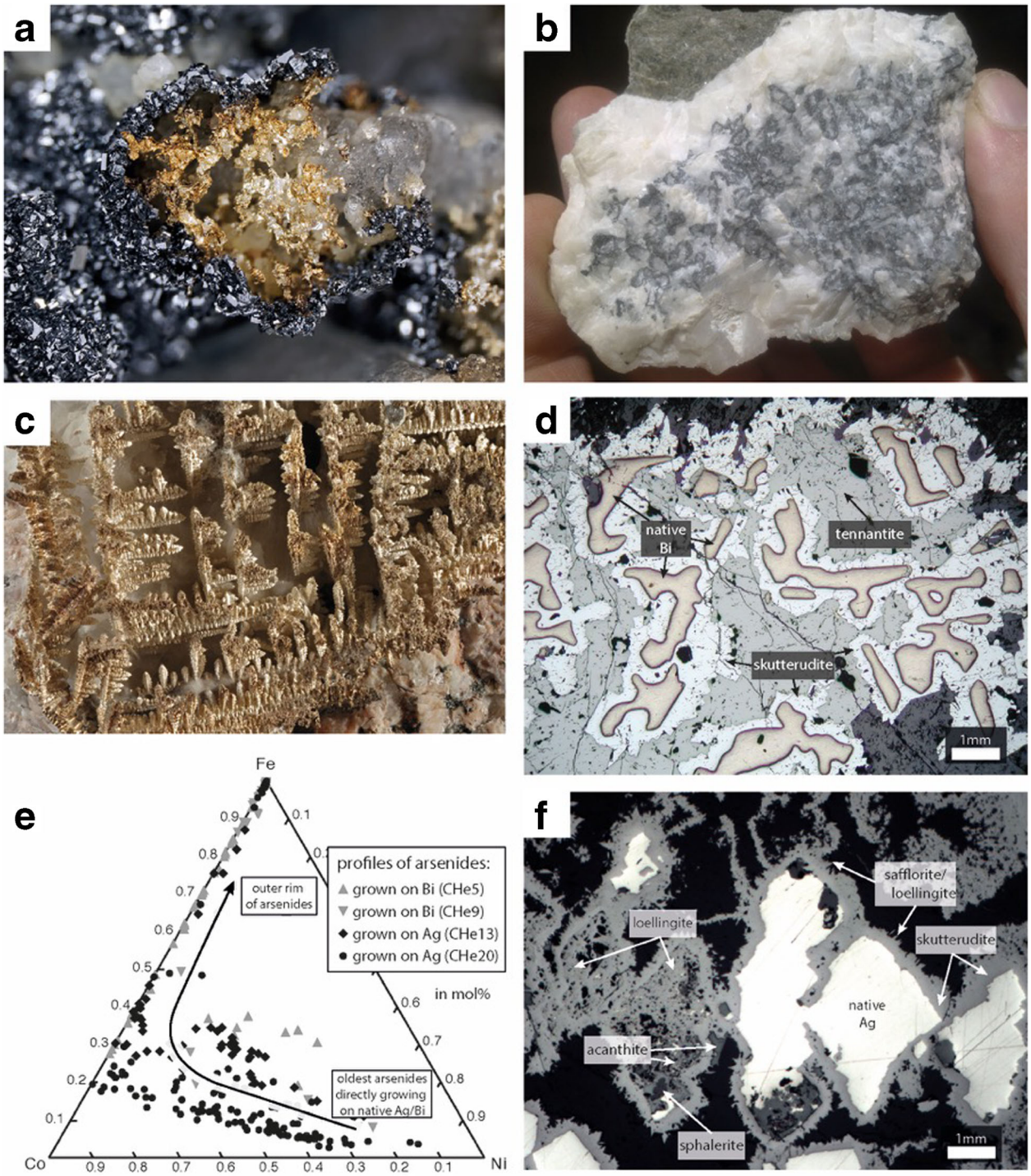

Fig. 1 Ore textures (**a**–**d**, **f**) and mineral compositions (**e**) from the five-element veins from Wittichen (**a**, **c**), the Wenzel mine (**b**), and the Odenwald (Mackenheim, **d**; Niederbeerbach, **f**; compositional data from both localities in **e**), Germany. **a** Native silver in the core of a crust of skutterudite crystals is partially dissolved. Width about 2 mm. **b** Remnants of arsenide crusts around former allargentum (which is now dissolved away and the holes are filled by calcite). Width about 6 cm. **c** Skeletal growth of native silver, etched out of calcite. Width about 4 cm. **d** Skeletal grains of native bismuth rimmed and partially replaced by skutterudite and safflorite. Youngest mineral is tennantite. Reflected light, field of view 3 mm. **e** Compositions of Fe-Co-Ni arsenides from the two Odenwald localities, analyzed by electron microprobe. **f** Dendrites of native silver overgrown by the sequence of skutterudite -> safflorite -> loellingite and by later acanthite. The silver is partially dissolved, and empty holes are partially filled by sphalerite and loellingite. Reflected light, field of view 2 mm

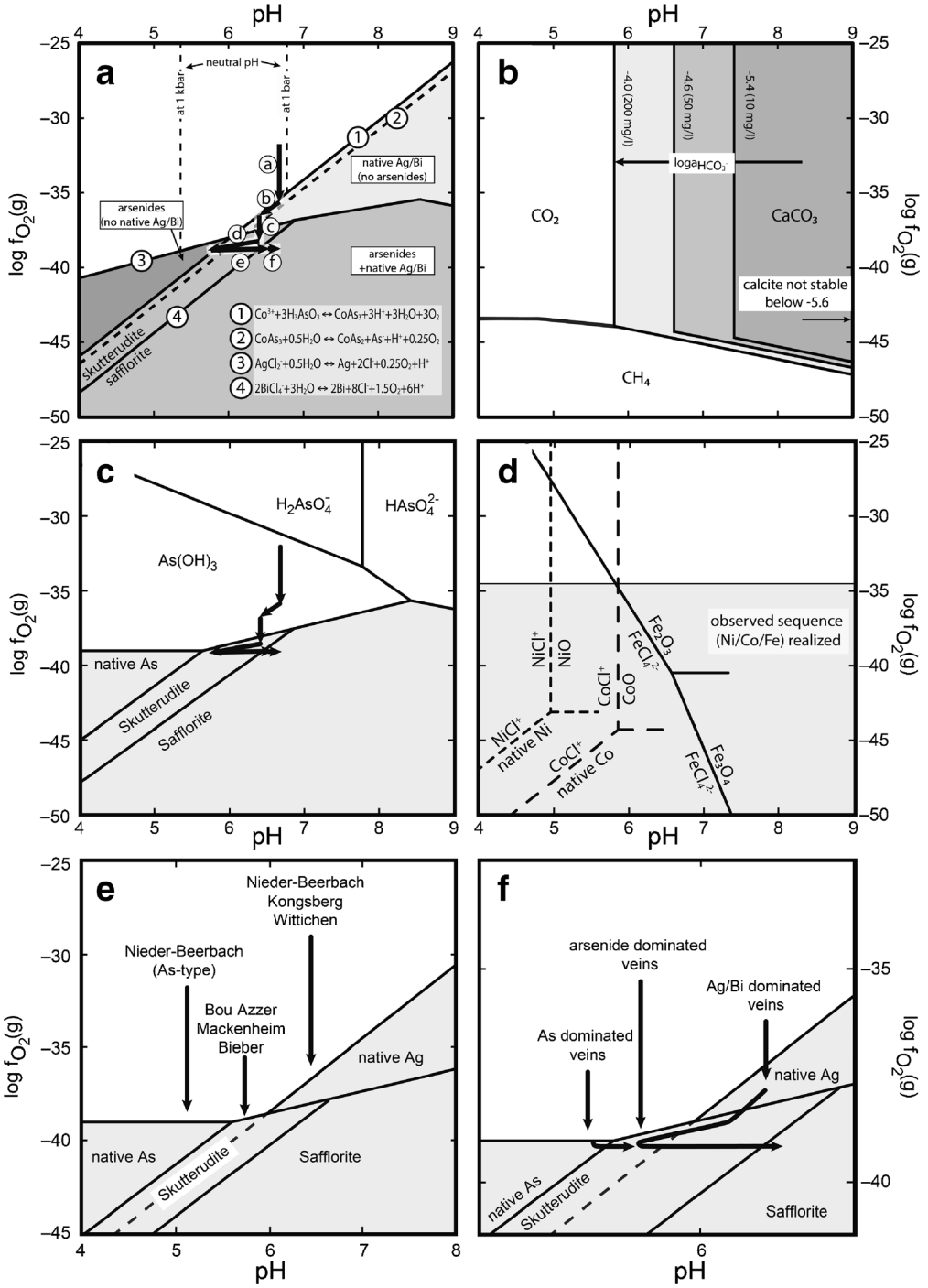

Fig. 2 pH-logfO_2 diagrams showing predominance and solubility fields, calculated at 200 °C and 50 MPa. An overview of the used input parameters is given in Table 2. **a** Pre-dominance fields of native Ag, native Bi, skutterudite, and safflorite. *Different gray scales* indicate three combinations of mineral assemblages: native metal without arsenides (*light gray*), native metals with arsenides (*medium gray*), and arsenides without or with dissolving native metals (*dark gray*). The *bold arrows* indicate the reaction path after methane influx and concomitant mineral precipitation. **b** Stability fields of CO_2, CH_4, and $CaCO_3$. *Different gray scales* indicate calcite stability dependent on three different HCO_3^- concentrations in the fluid. **c** Pre-dominance fields in the Co-As-O-H system. The *bold black arrows* indicate the same reaction path as in **a. d** Solubility of Ni-, Co-, and Fe-oxides (no thermodynamic data exist for arsenides). At logfO_2 values below about −35 (*gray shaded area*), the observed sequence of arsenides around native elements (Ni/Co/Fe) is realized. **e** Slightly different pH values (within half a log unit) during start of the fluid mixing process lead to different mineral accumulations and explain the observation that some veins in the same district or locality are dominated by, e.g., native silver, others by Co-Ni arsenides, or native arsenic. **f** Enlargement of **e**, showing the complete fluid evolution path after cessation of the reduction step

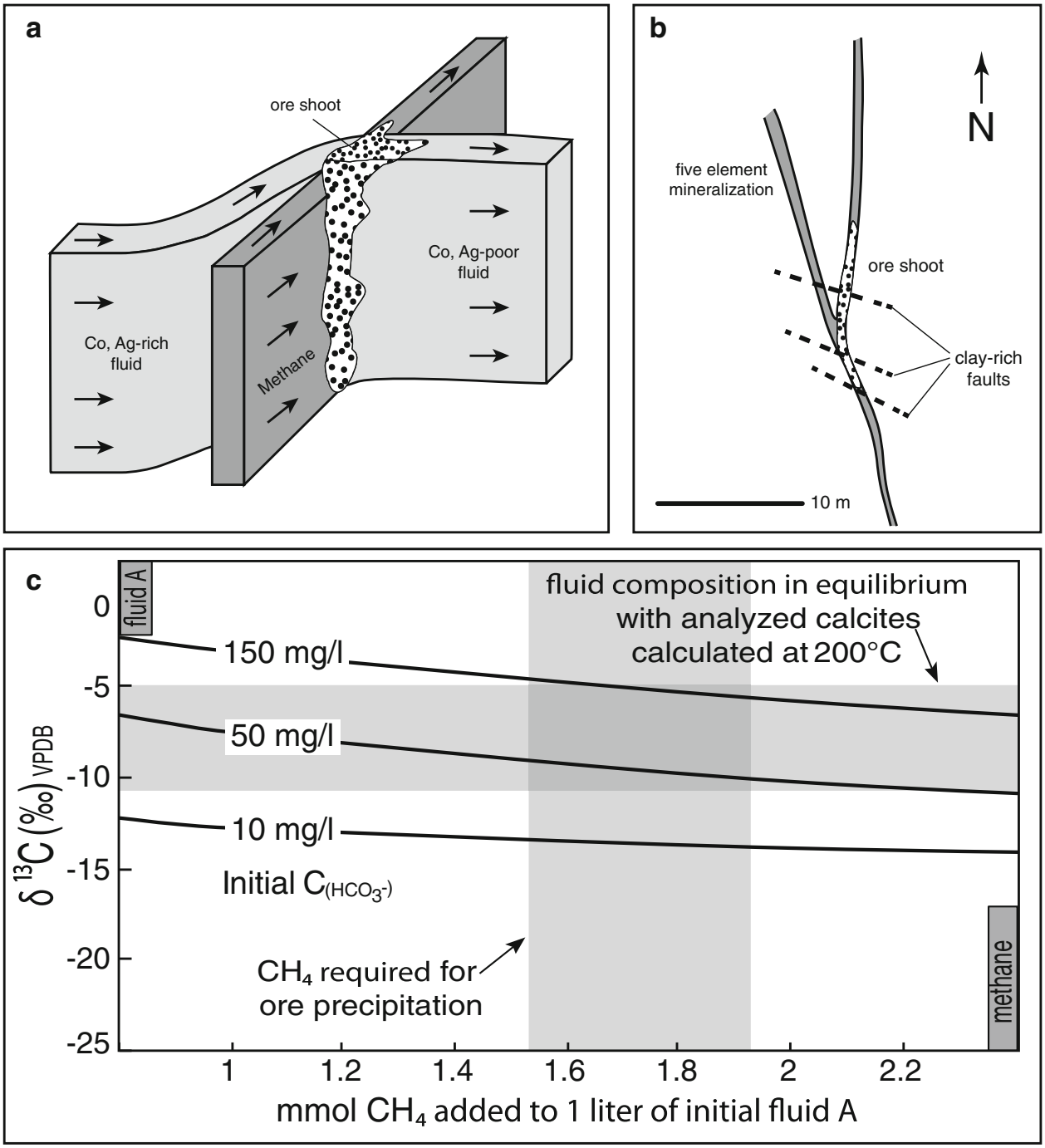

Fig. 3 **a** Schematic sketch of the model of fluid mixing at fault intersections. The ore shoot marks the former mixing zone (geochemical trap). **b** At Schneeberg/Germany, Co-Ni-Bi ore shoots occur at the intersection of two fault systems (after Lipp 2003). **c** Carbon isotope fluid compositions at 200 °C, calculated for mixing a HCO_3^--bearing fluid with methane. The *gray shaded areas* indicate the fluid composition in equilibrium with the analyzed calcite samples at 200 °C and the required amount of CH_4 to maintain sufficiently low fO_2 during ore precipitation. The *black lines* show three different HCO_3^- concentrations (10, 50, and 150 mg/l) in the initial fluid A. Initial fluids with HCO_3^- concentrations of 50 to 150 mg/l agree with the observed fluid composition after mixing with the required amount of CH_4

influx, followed by arsenides with high As/metal ratios. Sulfarsenites and sulfides as later phases show the exhaustion and/or the re-oxidation of the arsenide species in the fluid.

As mentioned above, arsenides occur in two different textures: as large clumps without and as crusts around native metals. The former may form due to

$$2AsO_3^{3-} + 4H^+ + 5CH_4 = 2As^{-} + 4H_2O + CO_2, \quad (3)$$

while the latter precipitate after re-oxidation around native metals due to

$$AsO_3^{3-} + 6H^+ + 4Ag = As^- + 4Ag^+ + 3H_2O. \quad (4)$$

This reaction, interestingly, leads directly to the dissolution of the native metals previously formed and thus explains the partial dissolution textures, which can be subsequently filled by younger calcite.

All these redox reactions have a profound influence on the pH of the solution. During native element precipitation (reactions 1 and 2), pH becomes more acidic. Although the carbonate activity due to methane oxidation reactions increases, the decreasing pH precludes carbonate precipitation in this early stage of the process. When the di- and triarsenide (i.e., arsenides with high arsenide/metal ratios) and native metal precipitation slows down and finally stops (since the introduced batch of reducing agent has entirely reacted), the system evolves back to higher pH, due to water-rock interaction, as typical crustal rocks like gneisses, granites, or amphibolites buffer fluids around neutral to slightly alkaline pH values (e.g., Möller et al. 2005). The reaction path involves partial dissolution of earlier formed native metals and successive formation of diarsenides and finally carbonates or (more rarely) sulfates. The pH variations of the given reaction path also explain the succession of Ni, Co, and Fe dominance in the diarsenides (Fig. 2d), because their chloride complexes have different stabilities. Furthermore, the observed paragenetic differences around native silver and bismuth can be explained by the fact that pH is different in both cases due to the different reaction stoichiometry involving Ag^+ vs. Bi^{3+} (reactions 1 and 2).

Carbon isotope and fluid inclusion evidence and the origin of the hydrocarbons

Evidence for the proposed process can in principle be provided by carbon stable isotope and fluid inclusion studies. Although gangue minerals appear after the native metal ore stage, we still found methane in some fluid inclusions in calcite paragenetically associated with arsenides at the Odenwald/Germany localities we investigated by Raman spectroscopy (Burisch, unpublished results), while the majority of analyzed fluid inclusions there and at other localities is methane-free and records the ordinary hydrothermal system after re-attainment of equilibrium (Staude et al. 2007, 2012; Kerrich et al. 1986; Marshall et al. 1993; Wilde et al. 2001). Alternatively, the introduced methane could also have been entirely oxidized to HCO_3^- before fluid trapping. In Kongsberg, Norway, the former presence of hydrocarbons is proven by "coal blend" (a solid C-H-O phase) intergrown with calcite (Neumann 1944).

Mass balance calculations using carbon isotope values from two representative localities (Odenwald and Wittichen/Germany) range between −5 and −10 ‰ VPDB (Table 1). As Fig. 3c shows, mixing of a hydrothermal fluid containing moderate amounts of bicarbonate (HCO_3^-; 50–150 mg/l) with the amount of methane (or methane-bearing fluid) required to maintain an fO_2 suitably low to support ore precipitation renders numbers in agreement with the analyzed carbon isotope composition of the carbonates from the arsenide-native metal associations (Table 1), supporting our model. Later, ore-free calcite generations from the same deposits show less negative carbon isotope compositions, and earlier (pre-ore) carbonate generations do not exist.

The amount of methane required to precipitate the observed amounts of ores is relatively small, on the order of 30 mg/l (Table 2). It may originate from biogenic or abiotic sources (Apps 1985; Schoell 1988; Lüders et al. 2012; Welhan 1988), the latter being, e.g., graphitic schists or H_2- or CO_2-bearing fluids reduced by catalytic contact with ferrous iron (Apps 1985), by carbonate methanation, or via Fischer-Tropsch type reactions (Etiope and Sherwood Lollar 2013). Such carbon- or sulfide-rich host lithologies are typically present close to five-element veins (Kissin 1992 and references therein; Staude et al. 2012). Hence, methane should be easily available for the process proposed, especially, as mass balance calculations show that the required quantities are small.

Table 2 Model input and output used for the construction of Fig. 3c. Input data are for the typical five-element Sophia vein, Wittichen, Germany

Parameter	Input	Output
Temperature (°C)	200	
Pressure (MPa)	50	
Salinity (wt.% NaCl eq.)	25	
Na/Ca (molar)	1	
Ag in fluid (ppm)	1	
Co in fluid (ppm)	105	
As in fluid (ppm)	270	
Mass native silver precipitated (t)	5	
Mass arsenides precipitated (t)	2000	
Volume of fluid required for observed ore mass (l)		5.0E+09
CH_4 required for ore precipitation (mmol/l)		1.78

Application to other types of ore deposits

Although our detailed study focuses on five-element type deposits, we state that the same mechanism (fracking and influx of hydrocarbons or hydrocarbon-bearing fluids into an aqueous hydrothermal system) may also be relevant for some other types of hydrothermal deposits of redox-sensitive elements (e.g., Au and U). For orogenic gold deposits, this was already suggested by Naden and Shepherd (1989), Wilde et al. (2001), and Cox et al. (1991). Textural similarities between some types of hydrothermal gold and five-element vein deposits include the skeletal to fern-like textures of the native gold, its occurrence in rich masses related to structural intersections separated by barren gangue, the association with carbonates and sulfides (Goldfarb et al. 2005), and evidence for methane in fluid inclusions of gangue minerals (Kerrich et al. 1986; Wilde et al. 2001). Note that the abundant presence of loellingite/arsenopyrite records the abundance of arsenide in the fluid indicating low fO_2 of the ore fluid. The reason for the lack of other arsenides may be low contents of Co and Ni in these fluids, since natural arsenides of Pb and Zn are unknown, and Cu arsenides (like domeykite, paxite) are very rare and, hence, crystallographically unstable under natural conditions. The conspicuous occurrence of rare Au-Ag-tellurides in some of these deposits may be due to reduction of tellurite to telluride ions upon the influx of mobile hydrocarbons.

Conclusion

We conclude that the influx of mobile hydrocarbons such as methane into active hydrothermal systems can lead to precious metal precipitation and that this mechanism explains all observed textural, mineralogical, chemical, and isotopic features of the so-called five-element veins and of at least some hydrothermal vein-type gold deposits. This influx must be sudden, possibly like a fault-valve mechanism of cyclic seismic events ("seismic pumping") and leads to far-from-equilibrium precipitation of ore minerals. In nature, such natural fracking episodes presumably last only short time spans, maybe only hours to weeks (e.g., rupturing during earthquakes), but may be followed by long periods of mixing of the two fluid systems, representing an extremely effective geochemical trap for redox-sensitive elements (Ag, As, Au, Bi, Te, U). When one of the fluids exhausts or the hydrocarbon supply ceases, the remaining hydrothermal system re-approaches equilibrium by reactions with its local host rocks and precipitates the gangue minerals and base metal sulfides in the more classical situation of physicochemical gradients.

Acknowledgments We are grateful to Peter Kolesar and Bernd Lehmann for their insightful discussions on this subject, to Michael Fettel for samples from the Odenwald deposits, to Michael Marks for help with the graphics, to Wolfgang Gerber and Matthias Reinhardt for the mineral photographs, and to Daniel Kontak and an anonymous reviewer of an earlier draft of this manuscript.

References

Ahmed AH, Arai S, Ikenne M (2009) Mineralogy and paragenesis of the Co-Ni arsenide ores of Bou Azzer, Anti-Atlas, Morocco. Econ Geol 104:249–266

Andrews AJ, Owsiacki L, Kerrich R, Strong DF (1986) The silver deposits at Cobalt and Gowganda, Ontario. I: geology, petrography, and whole-rock geochemistry. Can J Earth Sci 23:1480–1506

Apps JA (1985) Methane formation during hydrolysis by mafic rocks. Lawrence Berkeley Lab Univ Calif Berkeley Ann Rep 1984:13–17

Bastin ES (1950) Significant replacement textures at Cobalt and South Lorraine, Ontario, Canada. Econ Geol 45:808–817

Clavel M (1963) Contribution à l'étude métallogénique de la région d'Allemont, Massif de Belledonne-Isère. Thesis, Université de Nancy, 187 p

Cox SF, Wall VJ, Etheridge MA, Potter TF (1991) Deformational and metamorphic processes in the formation of mesothermal vein-hosted gold deposits—examples from the Lachlan Fold Belt in central Victoria, Australia. Ore Geol Rev 6:391–423

En-Naciri A, Barbanson L, Touray J (1997) Brine inclusions from the Co-As(Au) Bou Azzer district, Anti-Atlas Mountains, Morocco. Econ Geol 92:360–367

Etiope G, Sherwood Lollar B (2013) Abiotic methane on Earth. Rev Geophys 51:276–299

Fettel M (1978) Über die Wismut-Kobalt-Nickel-Silber-Uran-Formation im kristallinen Odenwald. Aufschluss 29:307–320

Gammon JB (1966) Fahlbands in the Precambrian of Southern Norway. Econ Geol 61:174–185

Goldfarb RJ, Baker T, Dubé B, Groves DI, Hart CJR, Gosselin P (2005) Distribution, character, and genesis of gold deposits in metamorphic terranes. Econ Geol 100th Anniv 407–450

Holzman DC (2011) Methane found in well water near fracking sites. Environ Health Perspect 119(7):a289

Keil K (1933) Über die Ursachen der charakteristischen Paragenesenbildung von gediegen Silber und gediegen Wismut mit den Kobalt-Nickel-Eisen-Arseniden auf den Gängen der Kobalt-Nickel-Wismut-Silber-Erzformation im sächsisch-böhmischen Erzgebirge und dem Cobalt-District. N Jb Min Geol Paläont 66: 407–424

Kerrich R, Strong D, Andrews A, Owsiacki L (1986) The silver deposits at Cobalt and Gowganda, Ontario. III: hydrothermal regimes and source reservoirs—evidence from H, O, C, and Sr isotopes and fluid inclusions. Can J Earth Sci 23:1519–1550

Kissin SA (1992) Five-element (Ni-Co-As-Ag-Bi) veins. In: Sheahan PA, Cherry ME (eds) Ore deposit models. Geosci Can 19:113–124

Lietz J (1939) Mikroskopische und chemische Untersuchungen an Kongsberger Silbererzen. Z Angew Mineral 2:65–113

Lipp U (2003) Wismut-, Kobalt-, Nickel- und Silbererze im Nordteil des Schneeberger Lagerstättenbezirkes. Bergbau in Sachsen 10:1–210

Lüders V, Plessen B, di Primio R (2012) Stable carbon isotopic ratios of CH_4–CO_2-bearing fluid inclusions in fracture-fill mineralization from the Lower Saxony Basin, Germany—a tool for tracing gas sources and maturity. Mar Pet Geol 30:174–183

Marshall D (2008) Economic geology models 2. Melt inclusions of native silver and native bismuth: a re-examination of possible mechanisms for metal enrichment in five-element deposits. Geosci Can 35:137–145

Marshall DD, Diamond LW, Skippen GB (1993) Silver transport and deposition at Cobalt, Ontario, Canada; fluid inclusion evidence. Econ Geol 88:837–854

Meisser N (2003) Le district cobalto-nickélifère d'Anniviers - Tourtemagne, Valais, Suisse. Min Helv 23b:57–64

Misra KC, Fleet ME (1975) Textural and compositional variations in a Ni-Co-As assemblage. Can Min 13:8–14

Möller P, Woith H, Dulski P, Lüders V, Erzinger J, Kämpf H, Pekdeger A, Hansen B, Lodemann M, Banks D (2005) Main and trace elements in KTB-VB fluid: composition and hints to its origin. Geofluids 5: 28–41

Naden J, Shepherd TJ (1989) Role of methane and carbon dioxide in gold deposition. Nature 342:793–795

Neumann H (1944) Silver deposits at Kongsberg. Nor Geol Unders 162: 1–133

Ondrus P, Veselovsky F, Gabasová A, Drábek M, Dobes P, Maly K, Hlousek J, Sejkora J (2003) Ore-forming processes and mineral parageneses of the Jáchymov ore district. J Czech Geol Soc 48: 157–192

Petruk W (1968) Mineralogy and origin of the Silverfields silver deposit in the Cobalt area, Ontario. Econ Geol 63:512–531

Ramdohr P (1975) Der Silberkobalterzgang mit Kupfererzen vom Wingertsberg bei Nieder-Ramstadt im Odenwald. Aufschluss Sb 27:237–243

Schoell M (1988) Multiple origins of methane in the Earth. Chem Geol 71:1–10

Sibson RH (1996) Structural permeability of fluid-driven fault-fracture meshes. J Struct Geol 18:1031–1042

Staude S, Wagner T, Markl G (2007) Mineralogy, mineral compositions and fluid evolution at the Wenzel hydrothermal deposit, Southern Germany: implications for the formation of Kongsberg-type silver deposits. Can Min 45:1147–1176

Staude S, Werner W, Mordhorst T, Wemmer K, Jacob DE, Markl G (2012) Multi-stage Ag–Bi–Co–Ni–U and Cu–Bi vein mineralization at Wittichen, Schwarzwald, SW Germany: geological setting, ore mineralogy, and fluid evolution. Mineral Deposita 47:251–276

Wagner T, Lorenz J (2002) Mineralogy of complex Co–Ni–Bi vein mineralization, Bieber deposit, Spessart, Germany. Min Mag 66:385–407

Welhan JA (1988) Origins of methane in hydrothermal systems. Chem Geol 71:183–198

Wilde A, Layer P, Mernagh T, Foster J (2001) The giant Muruntau gold deposit: geologic, geochronologic, and fluid inclusion constraints on ore genesis. Econ Geol 96:633–644

Wilke A (1952) Die Erzgänge von St. Andreasberg im Rahmen des Mittelharz-Ganggebietes. Geol Jb 147

Wilkerson G, Deng QP, Llavona R, Goodell P (1988) The Batopilas mining district, Chihuahua, Mexico. Econ Geol 83:1721–1736

Methane and the origin of five-element veins: mineralogy, age, fluid inclusion chemistry and ore forming processes in the Odenwald, SW Germany

Mathias Burisch[*a], Axel Gerdes[b], Benjamin F. Walter[a], Udo Neumann[a], Michael Fettel[a] and Gregor Markl[a]

*corresponding author: mathias.burisch@ifg.uni-tuebingen.de

[a] Institut für Geowissenschaften, Universität Tübingen, Wilhelmstrasse 56, 72074 Tübingen, Germany

[b] Institut für Geowissenschaften, Universität Frankfurt, Altenhöferallee 1, 60438 Frankfurt am Main

Keywords: hydrothermal ore; hydrocarbon; fluid mixing; U-Pb age dating; native metal; arsenide

ABSTRACT

Five-element veins (Ag, Bi, Co, Ni, As) have been valuable mineral deposits since medieval times. The characteristic occurrence of large aggregates of native metals (up to several dm) surrounded by a succession of arsenides makes this vein-type attractive for mining industry, natural history museums and private mineral collectors. Nevertheless, the exact formation process of these specific vein types has not been understood until recently (Markl et al., [Min. Dep. 20, p. 527-532, (2016)]). This is the first case study applying the new model to two typical examples of such mineralisations. We analysed all mineralogical varieties (Ag-, As- and Bi-dominated) of the five-element veins in the

Odenwald (SW Germany) in terms of ore textures, mineral chemistry, fluid inclusion compositions (microthermometry and Raman spectroscopy), stable isotopes (C, O and S) and radiogenic isotope compositions (U-Pb).

A variety of Ag-, Bi- and As-dominated native metal-arsenide-calcite veins, sulphide-calcite veins and arsenide-free Ag-Hg-barite veins occurs in the Odenwald and has been examined in this study. All arsenide veins have in common that up to dm-sized, often dendritic native metals are overgrown by a succession of arsenides, followed by carbonate and finally sulphides. Arsenide composition shows a distinct chemical trend from Ni- to Co and finally Fe-dominated. In contrast, spatially closely related Ag-Hg-barite veins consist of almost mono-mineralic amalgam inter-grown with barite.

U-Pb age dating of calcite and prehnite was applied for the first time to constrain the age of hydrothermal mineralization. The results imply that the five-element veins formed at 170-180 Ma from Na-Ca-Cl fluids at 290°C, salinities of ~27 wt.% and Ca/(Ca+Na) of 0.30 to 0.35 in the presence of methane. The age data clearly relate the relevant fluid migration to extension and crustal thinning caused by the opening of the North Atlantic. Ternary mixing of a deep-seated metal-rich basement brine, a sulfide-bearing (H_2S and HS^-) basinal/sedimentary brine and methane-dominated fluid/gas induced ore formation. Mixing of such chemically contrasting fluids results in a strong chemical disequilibrium of the mixed fluid, which potentially leads to rapid precipitation of native metals and arsenides with these specific ore textures. In contrast, sulphide-bearing calcite veins formed under similar P-T-conditions due to mixing of fluid A and B, while fluid C was absent. Additionally, U-Pb analyses of post-ore calcite yields ages of ~60 Ma, which indicates that this calcite formation event is associated with the onset of the Upper Rhine Graben rifting.

Veins with amalgam and barite form as a consequence of post-ore oxidation of Ag_2S at ~135°C. Conspicuously, this secondary silver II has Hg contents of up to ~30 wt.%, in contrast to Hg contents below 1 wt.% of primary silver I and Ag_2S. The formation of amalgam was most likely related to decrease of the S^{2-}/SO_4^{2-} ratio due to cooling of the late hydrothermal fluid resulting in the destabilisation of Hg-bisulfide complexes in this fluid.

GRAPHICAL ABSTRACT

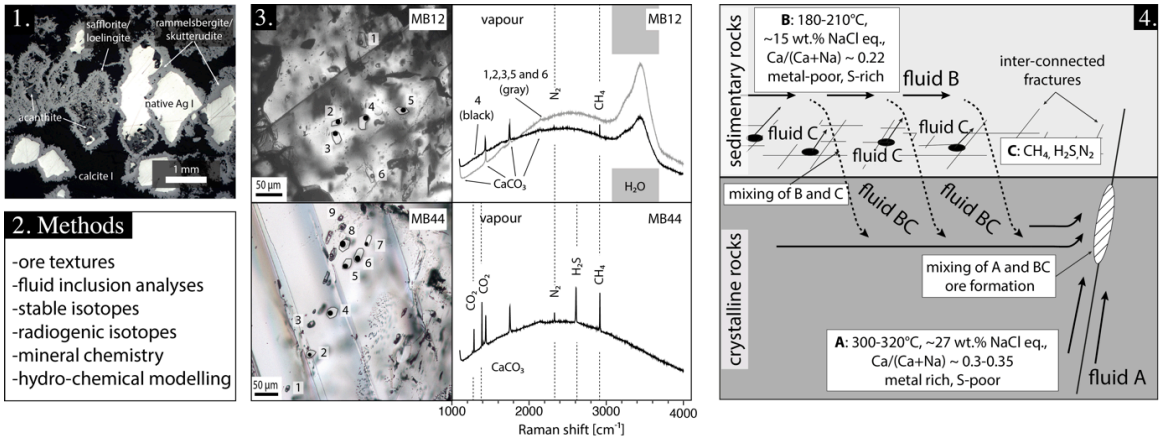

INTRODUCTION

Hydrothermal vein deposits with native Ag, As or Bi overgrown by a succession of Ni-, Co- and Fe-arsenides and typically floating in carbonate gangue minerals are called five-element veins, based on the elements Ag, As, Co, Ni and Bi (Kissin, 1992). Although this nomenclature does not correctly describe all subtypes of this mineralisation type, since some elements do not occur at some localities and/or elements like Sb and U may additionally occur in assemblages at others, it is nevertheless used in this contribution, since it is established in the literature (Bastin, 1939; Kissin, 1992).

Five-element deposits are typically of relatively low tonnage, but very high grade, and therefore have been of great economic importance as Ag, Co and U ores since medieval

67 times. The most widely known and the best investigated deposits are probably
68 Schneeberg/Germany (Lipp and Flach, 2003), Jachymov/Czech Republic (Ondrus et al.,
69 2003a; Ondrus et al., 2003b; Ondrus et al., 2003c), Kongsberg-Modum/Norway (Bugge,
70 1931), Cobalt-Gowganda/Canada (Andrews et al., 1986), Thunder Bay/Canada (Franklin
71 et al., 1986), Batopilas/Mexico (Wilkerson et al., 1988), Imiter/Morocco (Cheilletz et al.,
72 2002) and Bou Azzer/Morocco (Ahmed et al., 2009).
73 Hydrothermal five-element veins can be sediment-, unconformity- and/or basement-
74 hosted and the host rock composition is very variable and includes igneous,
75 metamorphic and sedimentary rocks. Reported formation temperatures range from
76 ~150 to 450°C, and hence, the mode of host rock alteration is also variable (Kissin,
77 1992; Staude et al., 2012). Although the mineral assemblages and the ore textures are
78 very similar implying that all of theses deposits have similarities in their general genetic
79 process, formation temperature, fluid salinity, host rock and alteration type strongly
80 vary for each locality (Kissin, 1992; Staude et al., 2012). Kissin (1988) suggested that the
81 formation of five-element veins is caused by the circulation of connate brines in
82 environments of continental rifting. Marshall et al. (1993) proposed that silver
83 deposition is caused by a decrease of chlorine activity due to mixing of silver-rich highly
84 saline with (paleo-) meteoric fluids. However, these models could not explain the
85 textural details, which are included in the refined genetic model proposed by Markl et al.
86 (2016). This model links the formation of five element veins to the influx of methane
87 and/or hydrocarbon-bearing fluids into pre-existing hydrothermal systems. Oxidation of
88 CH_4 to CO_2 subsequently results in very reducing conditions of the mixed ore fluid,
89 which facilitates the precipitation of the native metals and arsenides. The progressive
90 oxidation of methane leads to precipitation of calcite at the end of the ore succession as

a consequence of the dissolution of CO_2 and concomitant increase in HCO_3^- activity (Markl et al., 2016).

The majority of the existing work on five-element veins is relatively old and therefore does often not contain modern analytical data of e. g. fluid inclusions using Raman spectroscopy (see compilations in (Bastin, 1939; Kissin, 1992); Staude et al. (2012) and Markl et al. (2016)). The few exceptions include Marshall et al. (1993), Ahmed et al. (2009), Ondrus et al. (2003b) and Staude et al. (2012). Hence, to our knowledge, apart from textural observations and indirect isotopic evidence, only two samples of five-element veins from the Cobalt-Gowganda deposit (Kerrich et al., 1986) have been described to contain methane, propane and ethane which would support the model of Markl et al. (2016). Here, the present contribution can add important data.

The five-element veins at Nieder-Beerbach and Mackenheim in the Odenwald of SW Germany were first briefly described by Ramdohr (1923 and 1975), and later in more detail by Fettel (1978 and 1982), but have never been investigated in detail, using modern analytical techniques. Fluid chemistry, formation conditions and timing of ore precipitation were, hence, insufficiently understood. The investigated localities are sub-economic, but their relatively small dimensions and the excellent outcrop and sample situation since about 1970 enabled comprehensive sampling of all kinds of mineralogical variations with locality, time and depth of exposure. This opened up a unique opportunity to investigate the complex connections of a "big picture" on a spatially small scale.

Investigation of ore textures, mineral chemistry, fluid inclusions (including microthermometry and Ramam spectroscopy), stable isotope (C, O and S) analysis of gangue and sulfide minerals and radiometric U-Pb age dating of arsenides and gangue minerals (calcite and prehnite) were used to constrain the conditions and processes

during formation of the Odenwald veins and to compare them to the new general genetic model of Markl et al. (2016).

GEOLOGICAL SETTING

Regional Geology

The crystalline complex of the Odenwald is a deeply eroded basement window of a former subduction-related volcanic arc, situated at the northern margin of the Saxothuringikum also known as the mid-German Crystalline High (Stein, 2001). The subduction was related to the convergent plate tectonics of the Variscan orogeny, 380 to 300 Ma ago (Oncken et al., 1999). The Odenwald crystalline window is bordered to the west by the Cenozoic Upper Rhine Graben, to the north by the Saar-Selke Trough and to the south and east by the Permo-Triassic sedimentary cover (Nickel, 1975). The crystalline Odenwald consists of two units: the larger, western Bergsträsser Odenwald and the eastern Böllstein Anticline, which are separated by the sinistral strike-slip Otzberg fault (Fig. 1).

The Böllstein Anticline consists of amphibolite facies orthogneisses (410±10Ma, S-type protolith), paragneisses and schists (375±5Ma)(Stein, 2001), while the Bergsträsser Odenwald consits dominantly of calc-alkaline (I-type) magmatic rocks (90 vol.%), which can be subdivided into 4 individual diapiric intrusions (from north to south: Frankeinstein complex, Weschnitz pluton, Tromm and Heidelberg granite) and the strongly deformed NNE-SSW trending Flasergranitoid zone, a complex mixture of dominantly meta-granitoid rocks, which are interrupted by four metamorphic units ("Schieferzüge"). In general, the composition of the magmatic rocks (excluding the complex Flasergranitoid zone) of the Bergsträsser Odenwald shows a trend towards

more acidic rocks from north (gabbros and diorites) to south (mostly granites) (Stein, 2001).

The investigated Ag-dominated hydrothermal veins at Nieder-Beerbach are hosted by igneous rocks of the Frankenstein pluton in the north (Fig. 1B), which is the oldest intrusive complex of the Bergstrasser Odenwald (365 Ma) and consists of medium- to coarse-grained pyroxene-hornblende and olivine gabbros. Diorites occur at the northern and southern margins of the complex, while granodioritic and granitic dykes exclusively occur in the north (Stein, 2001).

Four metamorphic units form narrow zones, which interrupt the magmatic intrusions, of which the most important ones are the Eberstadt-Rossdorf, the Auerbach-Grossbieberau, the Heppenheim and the Weinheim-Waldmichelbach Schieferzug (Fig. 1A and C). The last one hosts the investigated Bi-dominated five-element veins of the southern Odenwald (Mackenheim, Fig. 1 C). These units consist of a variety of amphibolite facies (sometimes retrograded to greenschist facies) rocks, where meta-greywackes and amphibolites are predominant, specifically fine-grained biotite-plagioclase gneisses, muscovite gneisses and schists, biotite-muscovite gneisses and hornblende gneisses and quartzites (Stein, 2001).

Prior to erosion, the crystalline basement was covered by organic-rich upper Carboniferous and Permo-Triassic silicio-clastic and chemical sediments with estimated thicknesses of at least 600 m (Nickel, 1975). Carbonate-dominated sediments of the Jurassic and Cretaceous were present (Faupl, 2000), but their precise local thicknesses are poorly documented. Formation and migration of methane in Upper Cretaceous organic-rich sediments due to the thermal decomposition of organic matter during basin subsidence is documented in fluid inclusions of fracture minerals in the Northern German Basin (Lüders et al., 2005).

Ore geology

Numerous five-element veins occur in the northern, middle and southern Odenwald (Tab. 1), always accompanied by sulphide-bearing and to lesser extent by U-bearing veins. Although the difference in stratigraphic depth of formation between the northern and the southern hydrothermal veins is very small (100 m), the mineral assemblages show distinctly different compositions. Silver-dominated gabbro-hosted veins occur only in the north, while in the middle and southern Odenwald, five-element veins are Bi-dominated and hosted by marble and gneiss, respectively.

The northern-most Ag-Ni-Co-Fe-As-calcite veins are accompanied by arsenide-free Pb-Zn-Cu-calcite and Ni-U-Cu-calcite±baryte±chalcedony veins and are exposed at the Wingertsberg quarry (Ramdohr, 1975). Only 3.5 km further south, Ag-Ni-Co-Fe-As-calcite and As-Ag-Fe-calcite veins occur with predominant Pb-Zn-Cu-sulphide-calcite veins at all three quarries (Fig. 1B). Uranium-bearing veins are absent, but several arsenide-free Ag-Hg-barite-calcite veins have been observed. There is only one known occurrence of a single Bi-Ni-Co-Fe-As-calcite vein in the central Odenwald at Hochstädten, Bangertshöhe (Kühne, 1932), but further south, near Schriesheim and especially at the quarry "Viadukt" near Mackenheim (Fig. 1 C), Bi-rich veins occur. There, these are accompanied by abundant Pb-Zn-Cu-(Fe)-sulphide-calcite and U-Pb-Zn-sulphide-calcite veins.

Northern Odenwald: Ag-suites of the Waschenbach, Glasberg and Wingertsberg quarries

All three quaries are situated around 5 km southeast of Darmstadt (Fig. 1B). The quarry Wingertsberg (now flooded) is directly located in the centre of Nieder-Ramstadt (49°49'52.9"N 8°41'50.9"E), while Glasberg and Waschenbach are located directly adjacent to each other 3.5 km further to the south (49°47'51.7"N 8°41'37.4"E and 49°47'45.2"N 8°42'12.4"E) close to the village of Nieder-Beerbach (Fig 1B).

All quarries mined dominantly gabbroitic rocks of the Frankenstein pluton, which includes several lenses of picritic or dioritic composition as well as aplitic dykes. The deepest levels of these quarries are around 90-100 m b.g.s. (below ground surface). Numerous hydrothermal veins with either Ag-Ni-Co-Fe-As or As-Ag-Fe ores (Ag-arsenide veins) cut these plutonic rocks (Tab.1), typically as NW-SE trending (120-160°) almost vertical (> 80°) discontinuous pinch-and-swell structures with variable thicknesses of 1 to 30 cm (Ramdohr, 1923; Fettel, 1978; Fettel, 1982). These veins are also present at the deepest level of the quarries ~ 90 m b.g.s, while they invariably pinch out at the top, around 10-15 m b.g.s.. Propylitic host rock alteration is not pronounced and affects the host rock only within millimetres. Only in the northern Wingertsberg quarry a system of thin (< 5cm) very discontinuous pinnate joints with a U-Ni-Cu mineralisation occurs in depths greater than ~80 m b.g.s. in the Wingertsberg, which is absent at the Waschenbach and Glasberg quarry (Ramdohr, 1975; Fettel, 1978; Meisl and Pöschl, 1982).

Another type of hydrothermal veins contains Pb-Zn-Cu-S minerals and accompanies the Ag-arsenide veins at all localities investigated. These veins are steep (70-85°), NW-SE and W-E trending (100-170°) (Leyk, 1990) and, hence, similar to the Ag-arsenide veins. They are often discontinuous, only 1 to 10 cm thin and do not intersect the Ag-arsenide veins. Arsenide-free Ag veins occur also as vertical (>85°), NE-SW (30-80°) discontinuous pinch-and-swell structures with thicknesses of 1 to 25 cm (Fettel, 1982). The occurrence of these arsenide-free Ag-Hg-barite-calcite veins is restricted to the upper 30 to 45 m below the topographic surface (Fettel, 1985) of the quarries. Several other, barren barite-calcite veins occur with similar orientation and thickness (Leyk, 1990). Weak argillic host rock alteration can be recognized around all barite-calcite veins.

Southern Odenwald: Bi-suite of the Mackenheim quarry

The quarry "Viadukt" is located 18 km northeast of Heidelberg, around 1 km west of the village of Mackenheim (49°34'2.19"N 8°46'51.78") (Fig. 1C). The host rocks are dominantly amphibolite-facies meta-sediments including some amphibolite lenses. Along the metamorphic foliation, abundant quartz lenses (several cm in size) occur, which often contain small amounts of bismuthinite, molybdenite, scheelite, pyrite, titanite and native gold. Five Bi-Ni-Co-Fe-As lenses are known in the Mackenheim quarry (Tab. 1). These mineralizations are discrete NW-SE trending, almost vertical, discontinuous lense-shaped ore bodies (up to 30 x 30 m) with a maximum thickness of 60 cm. Propylitic host rock alteration is weak and penetrates the host rock typically not more than several mm.

Additionally, 20-50 cm thick, ±N-S (also NW-SE) trending Cu-Pb-Zn-sulphide-calcite veins (sometimes lense-shaped) occur unsystematically distributed in the Mackenheim quarry. The age relationship between these veins and the Bi-arsenide veins is not clear, since they do not intersect. Furthermore, spatially separated, NE-SW trending U-bearing veins occur ((Fettel, 1978; Meisl and Pöschl, 1982)). Based on (Meisl and Pöschl, 1982), they are interpreted to be younger than the arsenide-bearing veins. Barren and Bi-Co-Cu-Pb-sulphide-calcite and barite-calcite±quartz veins (both arsenide-free) typically strike in NNE-SSW orientations, being younger than the Bi-arsenide veins.

Petrographic description

The detailed description of the vein mineralogy and ore textures of this study focuses on the Ag-Ni-Co-Fe-As, As-Ag-Fe, Ag-Hg-barite, Bi-Ni-Co-Fe-As and Pb-Zn-Cu-sulphide-calcite veins. According to petrographic observations (also including those made by

Ramdohr (1923; 1975) all Ag-/As-/Bi-arsenide veins can be classified into four successive ore stages:

1. stage: sulphides older than native metals and arsenides

2. stage: native metals

3. stage: arsenides growing on native metals

4. stage: sulphides younger than native metals and arsenides

In general, three different arsenide-bearing vein types: Bi-Ni-Co-Fe-As, Ag-Ni-Co-Fe-As and As-Ag-Fe (Fig. 2 A, B, C, D, E and F) occur.

Rarely, relic sulphides can be observed encapsulated by native metals and arsenides (Ramdohr, 1975), indicating the existence of sulphides in the same veins (ore stage 1) prior to the native metal stage (ore stage 2). Although the type of native element is variable, the arsenide veins have in common that their paragenetic sequence of the five-element assemblage (ore stage 2) typically starts with dendritic or fern-like aggregates of native metals (Bi, Ag and Ag+As) (Fig. 2 A, B, C, D, E, F & Fig. 3). The native metals are followed by a sequence of euhedral arsenides (ore stage 3), which typically starts with rammelsbergite ($NiAs_2$) followed by skutterudite ($CoAs_3$), safflorite ($CoAs_2$) and loellingite ($FeAs_2$) (old to young). Replacement of native metals by safflorite and/or loellingite indicates the dissolution of native metals directly after the formation of rammelsbergite/skutterudite. The arsenide stage (ore stage 3) is invariably followed by sulphides like galena, chalocpyrite, sphalerite, acanthite, proustite, pearceite, bismuthinite, aikinite, fahlore and pyrite (ore stage 4) (see Fig. 3).

Ag-Ni-Co-Fe-As (Nieder-Beerbach and Nieder-Ramstadt)

Small, euhedral crystals of galena I (ore stage 1) occur rarely in native Ag and skutterudite at the Wingertsberg quarry (Ramdohr, 1923 and 1975), which are the

oldest documented ore minerals of the Ag-Ni-Co-Fe-As assemblage. An early, greenish-white generation of barren prehnite I and chlorite (pre-ore stage and/or ore stage 1) in the host rock and at the fracture rims are followed by dendritic, fern-like aggregates of native Ag I of up to cm-size (ore stage 2). These aggregates of native Ag I are entirely covered by small aggregates of rammelsbergite (0.2 to 2 mm), a thicker layer of euhedral skutterudite (1-4 mm) and finally up to cm-thick loellingite (all of ore stage 3, see Fig 2 A and B). The succession of arsenides is followed by brownish prehnite II and transparent, colourless, mostly euhedral calcite I. Late loellingite, prehnite II and calcite I overlap paragenetically and therefore can still be related to ore stage 3. Loellingite, prehnite II and calcite I often replace native Ag I. The degree of replacement varies strongly from small dissolution cavities to the entire dissolution of a complete aggregate (Fig. 2 A and B). Prehnite II and calcite I are followed by sulphide minerals, dominantly acanthite, sphalerite, galena II and rarely pearceite, chalcopyrite and fahlore. Acanthite often forms pseudomorphs after argentite and shows irregular transformation twinning, while other acanthite crystals appear to have formed monoclinic and transformation twins cannot be recognized. The amount of native Ag I replaced by acanthite is very variable. The abundance of Ag-sulfides may vary from accessory to major constituents (see also Ramdohr (1975)). Additionally, numerous rare minerals (like e.g fettelite or lautite) are known to occur locally in very small abundances (Fettel, 1985), but since they are not present in the investigated samples and do not belong to the primary mineral assemblage, these minerals are not considered further in this contribution.

As-Ag-Fe (Nieder-Beerbach)

Framboidal-shaped masses of native As (1-7 cm thick), containing aggregates of native Ag I (0.01 to several mm), are rimmed by a thin crust of euhedral leollingite (0.1 to 1 cm), which is followed by transparent, colourless calcite I (Fig. 2 C and D). The amount

of native Ag I is very variable and ranges from a few µm small individual, randomly distributed grains to spherical, branchy aggregates of up to 5 mm in size (ore stage 2). Native elements are replaced mostly at the rim of the vein by loellingite and calcite I (ore stage 3) and subsequently by proustite, pearceite, chalcopyrite and rarely galena (ore stage 4). The degree of replacement of the native As varies strongly. Both the weak replacement at the rims and the complete dissolution leave behind the hollow arsenide and sulphide rims.

Ag-Hg-barite-calcite (Nieder-Beerbach)

Irregularly shaped, often moss- or brush-like native Ag II intergrown with euhedral tabular-shaped barite, euhedral calcite IIa or fine masses of montmorillonite and very fine-grained quartz without arsenides are typical for this mineralization type (Fig 2 G). The native Ag II is concentrated in the centre of the vein and is often associated with minor amounts of chlorargyrite at the rims of the small Ag grains. The Ag grains frequently contain very small (2 to 20 µm) rounded grains of galena and acanthite (Fig. 2 H), while acanthite also occurs as irregularly shaped, corroded remnants, which are not encapsulated by native Ag. Brecciated pieces of older calcite I occur commonly in these veins.

Pb-Cu-Zn-S veins (Nieder-Beerbach)

Up to cm-sized grains of co-genetic galena and rarely bornite and chalcopyrite (ore stage 1) are followed by up to cm large white to colourless crystals of calcite I (ore stage 3).

Bi-Ni-Co-Fe-As-veins (Mackenheim)

Native bismuth occurs as dendritic, often fern-like aggregates of up to 5 mm in size, without contact to the host rock (Fig 2 E and F). Typically, bismuth (ore stage 2) is overgrown by euhedral layer of skutterudite (0.1 to 1 cm), but in some cases crystals of rammelsbergite occur directly on top of the native metal (Fig. 2 E), which is overgrown by massive skutterudite. Very small, euhedral quartz crystals grow directly on the host rock. Both, quartz and skutterudite are overgrown by euhedral safflorite (ore stage 3). Bismuth, rammelsbergite, skutterudite and safflorite altogether typically forming spherical aggregates or clumps. Rarely, safflorite replaces bismuth, where it was dissolved prior to or during safflorite precipitation. White to rose calcite I (up to cm in size) encapsulates the clumps of ore minerals entirely. The oldest rims of calcite I contain small safflorite crystals (ore stage 3), followed by barren calcite, while the last precipitated calcite I (ore stage 4) includes thin needles of aikinite, bismuthinite, fahlore, chalcopyrite, pyrite (As-rich) and sphalerite are often present as mostly anhedral aggregates or crusts (ore stage 4). Hydrothermal graphite is present in one single sample, where it occurs co-genetic with calcite I (ore stage 3) but without ore minerals. Transparent, greenish calcite IIb overgrowths calcite I and fills void space and cavities (post-ore stage).

METHODS

U-Pb age dating

Uranium-Pb ages were acquired *in situ* in polished thin section of calcite, prehnite and safflorite from five different samples by laser ablation- inductively coupled plasma-mass spectrometry (LA-ICP-MS) at the Goethe University Frankfurt (GUF), using a slightly modified method as previously described in (Gerdes and Zeh, 2006 and 2009). A

ThermoScientific Element 2 sector field ICP-MS was coupled to a Resolution S-155 (Resonetics) 193 nm ArF Excimer laser (CompexPro 102, Coherent) equipped with a two-volume ablation cell (Laurin Technic, Australia). Samples were ablated in a helium atmosphere (0.6 l/min) and mixed in the ablation funnel with 0.7 l/min argon and 0.04 l/min nitrogen. A squid (Laurin Technic, Australia) was used as homogeniser for the ablated material for smoothing of the signal, which resulted in a relative standard error for U of about 1% on SRM-NIST 612 for line ablation (e.g., 60µm, 3 µm/s, 5 Hz, 1 J/cm^2). Signal strength at the ICP-MS was tuned for maximum sensitivity while keeping oxide formation below 0.3 % (UO/U). Static ablation used a spot size of 80, 143 and 213 µm (depending on absolute U and Pb concentrations of the sample) and a fluence of < 1 J cm^{-2} at 5 Hz. This yielded a depth penetration of about 0.6 µm s^{-1} for SRM-NIST 614 and an average sensitivity of 420000 cps/µg g^{-1} for ^{238}U. Resulting detection limits for ^{206}Pb and ^{238}U are ~ 0.1 and 0.04 ppb, respectively. Each measurement consist of 3 s pre-ablation (removal of surface contamination), 20 s background acquisition, 20 s sample ablation and 20 s washout. Soda-lime glasses SRM-NIST 614 and 612 were used as a reference glass together with 2 carbonate standards.

Raw data were corrected offline using an in-house MS Excel© spread sheet program (Gerdes and Zeh, 2006 and 2009). The ^{207}Pb/^{206}Pb ratio was corrected for mass bias (0.3%) and the ^{206}Pb/^{238}U ratio for inter-element fraction (ca. 9%), including drift over the 12 hours of sequence time, using SRM-NIST 614. Additional matrix correction of 9% has been applied on the ^{206}Pb/^{238}U for calcite and prehnite samples, which was determined at the beginning of each day using WC-1 carbonate reference material dated by TIMS (251±2 Ma; E.T. Rasbury, pers. comm. 2014). Based on the soda-lime glasses and the common Pb corrected WC-1 data the ^{206}Pb/^{238}U fraction during 20s depth profiling of the laser was below 3%. Thus no correction has been applied for this. After

correcting for drift, mass bias, inter-element fraction and 9% matrix-offset, the WC-1 (n= 24) common Pb corrected $^{206}Pb/^{238}U$ reproduce over the three consecutive days to 250.9±0.82 Ma (MSWD = 0.74; 2SD = 1.7%). A common Pb correction has been applied only when Pb is mostly radiogenic; formed from the decay of U in the crystal. So unlike most carbonates, the WC-1 has very high percentages of radiogenic Pb. The common Pb content was determined using the ^{208}Pb signal after subtraction the radiogenic ^{208}Pb (Millonig et al., 2012). The latter is typically low in most carbonates due to low Th contents. Repeated analyses (n=35) of a Zechstein dolomite (Gypsum pit, Tettenborn, Germany) used as secondary (in-house) standard for quality control yielded an lower intercept age of 255.6 ± 3.0 Ma (MSWD: 1.4). According to the analysed standard materials accuracy and repeatability of the method can be assumed to be less than 2%. Ages were calculated using Isoplot 3.71 Ludwig (2007). All uncertainties are reported at the 2sigma level.

Microthermometry

Double polished thick sections (100-200 µm) were used to characterize fluid inclusion assemblages (FIAs) under the microscope according to the following code: primary (p), pseudo-secondary (ps), secondary (s), isolated inclusions (iso) and clusters (c) of inclusions. Microthermometry was performed using a Linkam stage (model THMS 600). Each individual fluid inclusion was analysed three times, resulting in triplets of final melting temperature of ice ($T_{m,ice}$), hydrohalite ($T_{m,hh}$) and the homogenization temperature (T_h). The results are given as average of each triplet, including only triplets with deviations of each measurement less than 0.1/1°C ($T_{m,ice}/T_h$). Synthetic H_2O, H_2O-NaCl and H_2O-CO_2 standards were analysed before and after each measurement campaign. Fluid inclusions showing signs of meta-stability and/or post-entrapment processes (e.g. necking, absence of hydro-halite) were strictly excluded. The salinity in

384 the ternary NaCl-$CaCl_2$-H_2O system was calculated according to (Steele-MacInnis et al.,
385 2011). A pressure correction according to (Bodnar and Vityk, 1994) was applied,
386 assuming hydrostatic conditions with a depth of the water column inferred from the
387 estimated paleo-depth (see discussion), resulting in only minor (< 5°C) deviations
388 between corrected and uncorrected Th. Therefore, Th is given as uncorrected values.

389 ## Micro Raman spectroscopy

390 A confocal Renishaw InVia Reflex Raman spectrometer was used to detect volatile
391 phases in the fluid inclusions. All measurements were carried out with a laser
392 wavelength of 532 nm and 20-25 mW laser power. The usage of a 50x objective results
393 in a numerical aperture of 0.55 with an opening angle of 66.7°. The focus diameter is
394 approximately 2 µm. Measurement time is 30 seconds with a three-rate accumulation.
395 This accumulation results in unreal quantitative intensities, but reduces the background
396 signal significantly. Each FI measurement consists of three individual analyses including
397 the gas phase, the liquid and the host mineral using the same sample orientation and
398 measurement settings. For qualitative evaluation, resulting Raman shifts were
399 compared with the Raman data base provided by (Frezzotti et al., 2012).

400 ## Crush-leach analysis

401 Two grams of samples MB12 and MB39 of pure calcite I (Ag- and Bi-suite) were
402 handpicked without having visible impurities. The samples were rinsed for one week
403 with ultrapure water, changing the water twice a day, then dried and powdered in an
404 agate mortar. To suppress the adsorption effects, crush leach solutions were acidified
405 with suprapure HNO_3. The loaded solution was injected into a Dionex ICS 1000 ion
406 chromatography systems, equipped with an IonPac AS 9-HC 2mm column for
407 quantification of anions (F, Cl, Br, PO_4 and SO_4) and an IonPac CS 12-A column for
408 cations (Li, Na, K, Mg, Ca, Ba, Sr). Disposable syringe filters (RC-20/25 and PVDF-20/25)

409 were used during injection. Blank runs were carried out before and after each analysis
410 and defined standard solutions were regularly analysed to monitor the reproducibility
411 and precision of the measurements. Uncertainties were smaller than 10 % and effective
412 detection limits generally < 15 µg/l.
413 Following trace metals: Mn, Fe, Co, Ni, Cu, Zn, As, Rb, W and Pb were determined by
414 Total Reflection X-Ray Fluorescence Spectroscopy (TXRF) using a S2 PICOFOX (Bruker
415 AXS Microanalysis) equipped with a Mo-tube operated with a 50 kV and 600µA. Gallium
416 was used as an internal standard. Effective detection limits for the given elements are
417 around 1 µg/l. Absolute concentrations were calculated based on the salinity
418 determined by micro thermometry using Cl as internal standard. Consequently, the
419 detection limit of the extrapolated (recalculated) fluid composition is much higher and
420 depends on the dilution factor between crush-leach solution and extrapolated fluid
421 composition (4.5 - 20 mg/l).
422

423 **Stable Isotopes**

424 Carbon and oxygen isotopes were analysed with a Gasbench II directly attached to a
425 Finnigan Mat 252 mass spectrometre. Measurements were calibrated with NBS18 ($\delta^{13}C$
426 = -5.00‰, $\delta^{18}O$ = -22.96‰, relative to VPDB) and NBS19 ($\delta^{13}C$ = 1.95, $\delta^{18}O$ = -2.20‰,
427 relative to VPDB). External reproducibility is better than ± 0.1‰ for $\delta^{13}C$ and $\delta^{18}O$.
428 The S-isotopic composition was measured with a NC 2500 connected to a Thermo Quest
429 Delta+XL mass spectrometer. NBS 123 ($\delta^{34}S$ = 17.10 ‰, relative to CDT), NBS 127 ($\delta^{34}S$
430 = 20.31 ‰, relativ to CDT), IAEA-S-1 ($\delta^{34}S$ = -0.30 ‰, relative to CDT) and IAEA-S-3
431 ($\delta^{34}S$ = 21.70 ‰, relative to CDT) were used for calibration. The reproducibility is ± 0.3
432 ‰.

Electron microprobe

Mineral compositions were determined with a JEOL Superprobe JXA-8900RL using 25 kV, 20 nA and a focused beam for all analyses except for acanthite, pearceite and proustite, which were (due to their rapid decomposition under the electron beam) analysed with a defocused beam (10 μm) at 25 kV and 5 nA. Overlap corrections for S and Co were applied.

RESULTS

U-Pb data

Loellingite of the Ag-suite has 0.6 and 20.2 mg/kg U and between 78.9 and 216 mg/kg Pb. $^{207}Pb/^{206}Pb$ and $^{238}U/^{206}Pb$ show a spread from 0.717 to 0.821 and 0.06 to 206, respectively. In the Tera-Wasserburg diagram this results in a lower intercept (LI) age of 3.6±1.6 Ma and an initial $^{207}Pb/^{206}Pb$ ($^{207}Pb/^{206}Pb_i$) of 0.801 (Tab. ES 1). Safflorite of the Bi-suite has up to 2 mg/kg U and up to 1.9 mg/kg Pb. $^{207}Pb/^{206}Pb$ and $^{238}U/^{206}Pb$ show a relatively small spread of 0.811-0.840 and 0.09-3.83, respectively, which results in a LI age of 55±19 Ma and $^{207}Pb/^{206}Pb_i$ of 0.835.

Uranium content of calcite I and prehnite II range from 0.3 to 85.1 mg/kg in Ag-Ni-Co-Fe-As- (MB31 and MB14) and from 0.2 to 24.7 mg/kg in As-Ag-Fe-veins (MB27). Lead concentration varies between 0.3 and 13.3 mg/kg in Ag-Ni-Co-Fe-As-veins and between 0.3 and 21.4 mg/kg in As-Ag-Fe veins. $^{207}Pb/^{206}Pb$ in Ag-Ni-Co-Fe-As-veins range from 0.171 to 0.815, while $^{238}U/^{206}Pb$ vary between 1.17 and 30.86. $^{207}Pb/^{206}Pb$ in As-Ag-Fe-veins range from 0.205 to 0.836 and $^{238}U/^{206}Pb$ vary between 0.05 and 29.00 (Fig 4A, B and C All three samples of the Ag-suite lie on distinct discordant lines, rendering LI ages of 172.6±4.2 Ma (calcite I and prehnite II) with $^{207}Pb/^{206}Pb_i$ of 0.825, 178±2.9 Ma with $^{207}Pb/^{206}Pb_i$ of 0.812 and 177.6±2.8 with $^{207}Pb/^{206}Pb_i$ of 0.825 for MB31, MB14 and

MB27, respectively (Fig. 4A,B and C). Corresponding calcite I from MB39 and MB55 of the Bi-Ni-Co-Fe-As vein-type have between 0.1 and 22.2 mg/kg U and 0.14 to 1.49 mg/kg Pb. $^{207}Pb/^{206}Pb$ ranges from 0.186 to 0.799 and $^{238}U/^{206}Pb$ from 1.62 to 41.45 (Fig. 4D and F). Calcite I in MB39 forms a broad array with a LI age of 172.6±8.7 Ma and $^{207}Pb/^{206}Pb_i$ of 0.820, while analyses of calcite I from MB55 form a discrete line yielding a similar LI age of 172.6±6.9 Ma with $^{207}Pb/^{206}Pb_i$ of 0.740 (Fig. 4D).

Calcite II of MB39 and MB55 have up to 361 mg/kg U, up to 3.47 mg/kg Pb, $^{207}Pb/^{206}Pb$ from 0.045 to 0.827 and $^{238}U/^{206}Pb$ from 0.82 to 161 (Fig. 4D, E and F). The data of calcite IIb of MB39 define two distinct arrays. One yields a LI age of 59.1±3.4 Ma with $^{207}Pb/^{206}Pb_i$ of 0.737, while the other yields a LI age of 13±5 Ma with $^{207}Pb/^{206}Pb_i$ of 0.824. Calcite IIb of MB55 renders a LI age of 60.3±1.8 Ma with $^{207}Pb/^{206}Pb_i$ of 0.709. Additionally, 11 data points lie when corrected for common Pb directly on the Concordia yielding an age of 61.59±0.47 Ma (Fig. 4E).

Fluid inclusions

Microthermometry

In total, 225 fluid inclusions in calcite and barite were analysed, including primary (p), clustered (c), isolated (iso), pseudo-secondary (ps) and secondary (s) fluid inclusion assemblages (FIAs) in all presented vein types. The filling degree of fluid inclusions of one FIA shows no variation and is in the range of LV12 to LV8 (Liquid-vapour volume proportion) for p, i, c and ps FIAs, while secondary FIAs have significantly smaller vapour contents of LV5 to LV2. The size of the analysed fluid inclusions ranges between 5 and 30 µm. Freezing during cooling occurs at temperatures below -68° and first melting occurs at ~ -52°C for all analysed FIAs.

Oldest primary, isolated and clustered FIAs in calcite I of Ag-Ni-Co-Fe-As, As-Ag-Fe-, Ag-Hg-barite and sulphide-veins have T_h between 265 and 292°C (Fig. 5C and D), salinities around 26.7 wt.% and Ca/(Ca+Na) between 0.3 and 0.35 (Fig. 5A and B). Pseudo-secondary and secondary FIA in calcite I of Ag-Ni-Co-Fe-As- and As-Ag-Fe-veins show Th from 220 to 106°C, within the same range of Ca/(Ca+Na) and salinity as the primary FIAs (Fig. 5 A and C).

Primary fluid inclusions in barite I and calcite IIa of Ag-Hg-barite veins have T_h between 124 and 136°C. Tm_{ice} and Tm_{HH} could not be determined in primary FIAs of barite I due to absence of hydrohalite. Primary fluid inclusions in co-genetic calcite IIa have salinities of 26.2 wt.% and Ca/(Ca+Na) ratios around 0.29 (Fig 5. B and D). Secondary FIAs in calcite IIa trend towards lower salinities (25 wt.%) and Ca/(Ca+Na) ratios (0.23) with decreasing T_h (109°C) (Fig. 5 B and D).

MB44p1 is texturally the oldest FIA in Bi-Ni-Co-Fe-As-veins and has homogeneous Th of 207°C, a constant salinity of 14.9 wt.% and a Ca/(Ca+Na) (molar) ratio of 0.22 (Fig. 5A and C). MB50p1 and MB48ps1 represents the outermost growth zone of calcite I and shows similar fluid characteristics as MB50iso1 having Th in the range of 181 to 190°C, salinities between 26.6 and 26.8 wt.% and Ca/(Ca+Na) between 0.28 and 0.32. MB50s1 and MB102iso1 have Th between 145 and 172°C, salinities of around 26.7 wt.% and Ca/(Ca+Na) ranging from 0.29 to 0.34 (Fig. 5A and D).

Micro Raman spectroscopy

Many fluid inclusions could not be analysed, since calcite often causes very high spectral intensities resulting in too high intensities in the vicinity to the bands of interest (1000 to 4000 cm^{-1}). This can unfortunately not be resolved by using lower laser energies, since low laser energies are insufficient to excite the low concentrations of gas and

505 aqueous phases of interest. However, at least 27 of 57 analysed fluid inclusions yielded
506 robust results.
507 All analysed fluid inclusions of MB44p1 (Bi-Ni-Co-Fe-As vein, Fig. 6E) contain CH_4, CO_2
508 and H_2S in the gas phase (Fig. 6F), while the coexisting fluid phase contains exclusively
509 HS^-/S^{2-}, but no CH_4 nor CO_2 (see Fig. 6G). MB50p1 and MB102iso1 could not be analysed
510 due to the effects described above. FIAs in calcite I of Pb-Zn-Cu_S-, Ag-Ni-Co-Fe-As- and
511 As-Ag-Fe-veins (MB61, MB97, MB12) do generally not contain any detectable gaseous or
512 aqueous species neither in the gas nor in the liquid phase. The only exceptions can be
513 recognized in MB12p1 hosting one fluid inclusion, which contains CH_4 (no other gaseous
514 or aqueous species) in the vapour phase (Fig. 6B). Interestingly, the fluid inclusions in
515 the vicinity of this methane-bearing fluid inclusion of the same FIA do not contain
516 detectable amounts of any Raman-active gaseous or aqueous species (except H_2O).
517 Strong matrix effects occurred in measurements of fluid inclusions of Ag-Hg-barite-veins
518 (MB59) but two measurements of fluid inclusions in barite show no detectable amounts
519 of any gaseous or aqueous species. Although sulphate can be expected to be present in
520 these inclusions, it is almost impossible to distinguish dissolved sulphate in the fluid
521 inclusion and sulphate of matrix barite.

522 *Crush-leach*
523 Bulk fluid inclusion analyses of calcite I of Bi- (MB39) and Ag-suite (MB12) show no
524 significant difference in major element composition. Both samples have high As and S
525 concentrations of up to 5486 mg/l and 734 mg/l, respectively (Tab. 2). Manganese, Co
526 and U are higher in MB39 (470 mg/l, 85 mg/l and 43 mg/l, respectively), while Ni, Fe, Zn
527 and Th are higher in MB12 (164 mg/l, 133 mg/l, 44 mg/l and 43 mg/l, respectively).
528

Stable Isotopes

Oxygen and carbon isotope compositions of 51 calcites were determined (including graphically presented data from Markl et al. (2016)). Calcite I of all vein-types (Ag-Ni-Co-Fe-As-, As-Ag-Fe-, Ag-Hg-barite- and Bi-Ni-Co-Fe-As-veins) has $\delta^{13}C$-values (VPDB) between -8.4‰ and -5.7‰ and$\delta^{18}O$-values (SMOV) between 14.3‰ and 16.8‰ (Tab. 3 and Fig. 7). Calcite IIb of Bi-Ni-Co-Fe-As veins, has a large variation of $\delta^{13}C$ from -8.1‰ to +2.4‰, while all of these calcites have relatively high $\delta^{18}O$-values of 20.4‰ to 23.1‰ (Fig. 7).

Sulphur isotope compositions of seven barite samples from Ag-Hg-barite-veins show a range of $\delta^{34}S$ -values (CDT) between 5.6‰ and 10.7‰, while six analysed samples of Ag-(As)-sulphides and galena from Ag-Ni-Co-Fe-As-, Bi-Ni-Co-Fe-As- and As-Ag-Fe-veins show very negative $\delta^{34}S$ -values between -60.5‰ and -19.7‰ (Tab. 4 and Fig. 8).

Mineral Chemistry

The following mineral phases were analysed by electron microprobe: native silver, native arsenic, native bismuth, rammelsbergite, safflorite, loellingite, skutterudite, acanthite, billingsleyite, proustite, pearceite and tennantite. Presented data include analyses from Heimig (2015) and Markl et al. (2016).

Native metals

Arsenic contains only minor amounts of impurities, on average 0.3 wt.% Se, 0.7 wt.% Sb and 0.09 wt.% Cu (Tab. 5). Silver I of Ag-Ni-Co-Fe-As-veins contains on average 1.34 wt.% As, 1.2 wt.% Hg, 0.42 wt.% Sb, 0.27 wt.% Te and 0.3 wt.% Ni+Co+Cu, but As and Hg reach up to 2.74 wt.% and 2.56 wt.%, respectively. Silver II (amalgam) of Ag-Hg-barite-veins contains high, randomly distributed Hg concentrations ranging between 11.4 and 29.5 wt.%. Besides Hg, Silver II (amalgam) is very poor in impurities (Tab. 5). Bismuth is

554 relatively pure (99.43 wt.% Bi on average), but may contain up to 2.79 wt.% As, 0.89
555 wt.% Fe and 0.37 wt.% Co. There is no systematic variation of native metal compositions
556 with depth of the exposed veins.

557 *Arsenides*

558 Skutterudite of Bi-Ni-Co-Fe-As-veins has an X_{As} (=As/(As+S+Sb+Se); molar) of 0.96 to
559 0.99. The major cation is highly variable, which results in Ni-, Co- or Fe-dominated
560 skutterudite, which furthermore may contain up to 2 wt.% Cu. X_{Fe} (Fe/(Fe+Co+Ni);
561 molar) ranges from 0.24 to 0.46, X_{Co} from 0.16 to 0.58 and X_{Ni} from 0.01 to 0.48 (Fig. 9
562 and Tab. 6). Highest X_{Ni} occur in skutterudite, which is grown directly on top of the
563 native metals, while highest X_{Fe} occur at the rims of the skutterudite aggregates.
564 Skutterudite of Ag-Ni-Co-Fe-As-veins shows generally higher X_{Ni} (0.17 to 0.68) at the
565 expense of Fe (X_{Fe} ranges between 0.09 to 0.25) (Fig. 9) than skutterudite from the Bi-
566 Ni-Co-Fe-As veins.

567 Diarsenides of Bi-Ni-Co-Fe-As-veins have X_{As} of 0.86 to 1.0 (As/(As+S+Sb)), due to
568 substitutions of As by S (Tab. 6). Nickel, Co and Fe are very variable resulting in
569 rammelsbergite, safflorite and loellingite compositions. Again, highest X_{Ni} (up to 0.7)
570 coincide with the youngest generation of rammelsbergite, directly growing on the native
571 metals, highest X_{Co} (up to 0.76) occur in safflorite, which directly grow on skutterudite,
572 while highest X_{Fe} (up to 1) can be observed at the youngest rims of the diarsenide
573 aggregates (see Fig. 9). Diarsenides of Ag-Ni-Co-Fe-As-veins tend to be Ni-richer (X_{Ni} up
574 to 0.82) compared to the diarsenides of the Bi-Ni-Co-Fe-As veins. At both localities
575 diarsenides may contain up to 3 wt.% Cu (on average 0.56 wt.% for Bi-Ni-Co-Fe-As-
576 veins and 1.28 wt.% for Ag-Ni-Co-Fe-As-veins). Highest Cu contents seem to be
577 associated with loellingite compositions. Besides the fact, that rammelsbergite
578 compositions are slightly Ni-richer in Ag-Ni-Co-Fe-As compared to Bi-Ni-Co-Fe-As veins,

no other distinct compositional variation of arsenides with depth or vein type can be observed.

Sulphides

Analyses of acanthite, proustite, billingsleyite, pearceite and tennantite are given in Table 7 of the electronic supplement. In general sulphides are poor in Hg, Co and Ni. Ag-sulphides (acanthite, proustite, billingsleyite and pearceite) do not contain any considerable minor or trace elements and show no relevant chemical variations or zonation. Tennantite occurring in Bi-Ni-Co-Fe-As-veins is in general richer in Bi and Sb, but poorer in As compared to tennantite in Ag-Ni-Co-Fe-As-veins. In both vein types tennantite is very Ag-poor (0.1 to 0.6 wt.%).

DISCUSSION

Age of ore and gangue minerals

In-situ age dating of nominally U-free minerals is increasingly used to determine sedimentary, metamorphic, igneous and tectonic processes (Gerdes and Zeh, 2009; Rasbury and Cole, 2009; Millonig et al., 2012; Coogan et al., 2016; Ring and Gerdes, 2016). This innovative approach has not yet been applied to hydrothermal ore deposits before (at least to our knowledge), Although it allows significantly improved constraints on the history of hydrothermal veins, which previously often could only be passively be constrained based on structural arguments.

Arsenides

Apparent ages of arsenides of MB55 and MB31 are much younger than calcite I, which is in conflict with textural observations, clearly showing that the ore minerals precipitate prior to calcite I. Lead-loss results in increasing $^{238}U/^{206}Pb$ at constant $^{207}Pb/^{206}Pb$ (since

both Pb isotopes are equally mobilized). The absolute amount of removed Pb, therefore dictates the resulting shift to higher $^{238}U/^{206}Pb$ from the original isochrone. Hence, lead-loss is expected to cause random shifts, depending on the degree of mineral alteration, which systematically decreases from the core of the mineral to its rim. Since, arsenide data form a distinct discordant line (within the analytical error) it can be assumed that the apparent ages of the arsenides reflect isotopic re-equilibration with fluids of younger events rather than lead-loss. The fact that only young events are isotopically preserved in the arsenides indicates, that arsenides are generally very prone to isotopic exchange reactions and consequently seem to be not suitable for age determination.

Calcite and Prehnite

Calcite I and prehnite II of five independent samples yield consistent and very robust ages of 172.6±8.7 to 178±2.9 Ma (mean value: 174.7 Ma) (Fig. 4). Textural observations indicate that the arsenides precipitate co-genetically with calcite I at the end of ore stage 3, and therefore these calcite ages also constrain the timing of ore stage 3. According to these ages, the ore stages II, III and most likely also stage I happened during the middle Jurassic, and fluid movement is hence related to the opening of the North Atlantic (Mitchell and Halliday, 1976; Boiron et al., 2010). Isotopic compositions of calcite I in MB39 span an array towards younger ages (Fig. 4). The youngest ages (~60 Ma) coincide with the oldest age of calcite IIb, and therefore most likely reflect domains within calcite I that are replaced by calcite IIb (cracks and crusts). Calcite IIb of MB39 and MB55 yield consistent concordant and LI ages of 59.1±3.4 to 60.3±1.8 Ma. These ages coincide with the oldest volcanic activity related to the rifting of the Upper Rhine Graben (e.g. Katzenbuckel, ~60-70 Ma (Lippolt et al., 1963; Schmitt et al., 2007), indicating that calcite IIb is related to fluid movement that occurred on pre-existing and new fault structures which can directly be related to the onset of the Upper Rhine

Graben rifting. Additionally to this consistent and robust age information, isotopic compositions of calcite IIb of MB39 indicate a third calcite formation event happening at 13.0±5.0 Ma (Fig. 4).

Conditions and ore forming processes of Ag-, As-, Bi-arsenide veins

P-T-conditions of ore stages 1-4

It is very reasonable to assume almost hydrostatic conditions during ore formation, since it happened in a relatively shallow, discrete, open and interconnected fracture network. Zienert (1957) showed that the rock units nowadays exposed at Mackenheim (Bi-suite) were originally situated approximately 100±50 m below the basement-cover unconformity, while the rock units at Nieder-Beerbach (Ag-suite) were situated about 100 m deeper. In the middle Jurassic, the crystalline basement was covered by about 600 m of Carboniferous and lower Permo-Triassic sediments (Nickel, 1975), although admittedly, the precise thickness of the upper Triassic and the lower and middle Jurassic units covering the crystalline Odenwald is poorly constrained. According to the thicknesses documented in the neighbouring Schwarzwald (a mountain range about 50 km south of the Odenwald), an additional thickness of up to 800 m of lower and middle Jurassic sediments can be assumed (Geyer et al., 2011). Consequently, formation depths of about 1.5 km (0.2 kbar hydrostatic) appear plausible. In any case, the deviation between uncorrected and corrected T_h is less than 5°C, due to the high salinity of the fluids. Therefore, uncorrected T_h are used in the following discussion.

The lower temperature boundary of ore stage 2 can directly be deduced from maximum T_h of calcite I, which is in the range of 272 to 286°C for all vein types except for the Bi-Ni-Co-Fe-As-type (Fig. 5C and D). However, this seems to be an effect of the poor quality and low abundance of fluid inclusions in all samples of the Bi-suite. Taking into account that both deposits show similar fluid characteristics, host rock alteration, age and almost

similar stratigraphic depths, it is reasonable to assume that they formed under very similar conditions. The presence of euhedral native bismuth indicates, that the formation temperatures of ore stage 2 have not significantly exceeded 271°C, which is the melting temperature of native Bi at ambient pressures (Nathans and Leider, 1962). Inferred from textural evidence (Markl et al., 2016) a fast continuous precipitation process of ore stage 1, 2 and 3 can be assumed, which indicates that the expected temperatures of ore stage 1 and 2 were not significantly higher than those of ore stage 3. Importantly, this implies that cooling is not a relevant factor controlling ore formation.

Primary fluid inclusions in the outermost rims of calcite I show that calcite I precipitated down to ~180°C, constraining the upper temperature limit of ore stage 4 (Fig. 5 C). The onset of ore stage 4 at ~180°C is furthermore supported by the rare occurrence of transformation twinning in Ag_2S, indicating that Ag_2S precipitated closely above and below 178±2°C (transition temperature acanthite/argentite according to Roy et al. (1959)).

Fluid characteristics

From the small, but distinct variation in Ca/(Ca+Na) ratios of primary and secondary fluid inclusions at similar temperatures and from the correlation between Ca/(Ca+Na and salinity it can be deduced that the analysed ore fluids reflect mixture of at least two fluids (A and B)(Fig. 5). An additional fluid/gas C can be recognized in FIAs of arsenide veins, while FIAs of arsenide-free sulphide veins do not contain this fluid C (Fig. 6). Consequently, the ore fluid from which the native metals and arsenides precipitated can be considered as a mixtures of three components (fluid ABC), while only two components were active in arsenide-free sulphide veins (fluid AB).

Analysed ore fluids (fluid ABC) indicate that fluid A is a Na-Ca-Cl brine, which is at least slightly higher in Ca/(Ca+Na) ratio, temperature (above 290°C) and salinity (above 27.5

677 wt.%) than the analysed FIAs of the ore fluid (ABC or AB) (Fig. 5). Fluid B can be
678 constrained from FIA MB44p1 (qualitatively), which is slightly cooler, significantly Na-
679 and sulphate/sulphide-richer and has lower salinities (~15 wt.%) than fluid A (Fig. 5). It
680 is not clear if FIA MB44p1 really reflects the end member composition of fluid B or if it
681 as well a mixture of both fluids containing only minor amounts of fluid A. Nevertheless,
682 fluid B often contains significant amounts of fluid/gas C, which consists of various
683 volatile phases (CH_4, CO_2 and H_2S). The absence of ore phases in MB44 in spite of the
684 presence of H_2S and HS^- in fluid BC implies that metal concentrations in these fluids are
685 very low.

686 *The formation process of native metals and arsenides (ore stage 2 and 3)*

687 Ore textures of ore stage 2 and 3, as well as weak host rock alteration indicate a fast
688 precipitation mechanism, presumably caused by far-from-equilibrium conditions (Markl
689 et al., 2016). Furthermore, mineral textures indicate that ore stage 1, ore stage 2 and the
690 precipitation of early calcite I (ore stage 3) happened successively and continuously
691 without a temporal hiatus during the ore sequence. Markl et al. (2016) proposed the
692 influx of methane or methane-bearing fluids into an active hydrothermal system to
693 obtain suitable conditions for the observed ore assemblage:

694 $$8AgCl_2^- + 3H_2O + CH_4 = 8Ag + 16Cl^- + 9H^+ + HCO_3^- \quad (1)$$

695 Hydro-chemical modelling shows that methane influx and its influence on the physio-
696 chemical properties of the ore fluid support a reaction path that even includes the
697 observed dissolution of native Ag after skutterudite precipitation. The presented Raman
698 data strongly supports the mechanism proposed in Markl et al. (2016), and shows that
699 ore precipitation is initiated by mixing small amounts of a very reducing, metal-poor and
700 CH_4-rich fluid (fluid BC) with a highly saline, metal-rich fluid (fluid A) (Fig. 10). Typically
701 all methane is consumed, oxidized to CO_2, immediately converted to dissolved HCO_3^- and

finally precipitated as calcite I, which is most likely the major reason that methane has only once been reported in other five-element veins (Kerrich et al., 1986; Kissin, 1992; Marshall et al., 1993; Staude et al., 2012; Markl et al., 2016) and references therein). Fortunately, due to fast trapping processes, little CH_4 was incorporated into FIA MB12 p1 before it could react to CO_2. And furthermore, CH_4 was archived in MB44p1, which reflect a fluid composition strongly dominated by fluid BC (Fig. 5 and 6). The presence of methane in ore fluids of five-element veins clearly indicates that sudden changes in the fluids' redox state causes a strong disequilibrium of the ore fluid, resulting in fast ore precipitation, while other parameters like temperature, alteration type and host rock may vary. Importantly, it could be shown that even when methane is not present in fluid inclusions it can still play an important role for ore precipitation in hydrothermal systems, since the amount of required methane is very small (Markl et al 2016) and therefore is potentially consumed instantaneously as CO_2/HCO_3^- (Eq. 1 and 4). Relatively negative isotopic compositions of calcite I (Fig. 7), indicate that significant amounts of C in those calcites is derived by isotopic lighter methane (refer to Markl et al. (2016) for more details). In contrast, calcites IIb have a large range in $\delta^{13}C$ (-6 to +2‰), but invariable high $\delta^{18}O$-compositions (~+21 to +23‰), while calcite I has invariably lower $\delta^{18}O$-compositions (around +16‰) (Fig. 7). This indicates that the $\delta^{13}C$ composition of some of the secondary calcite IIb is inherited from remobilization of calcite I, while other calcite IIb crystals seem to have incorporated HCO_3^- derived from meteoric fluids (Fig. 7).

Ni-Co-Fe succession during ore stage 3

A distinct spatial and temporal element systematic within the composition of di- and tri-arsenides of ore stage 3 can be observed (Fig. 9). Nickel-rich compositions occur always in the beginning of ore stage 3, whether as rammelsbergite and/or as Ni-rich

727 skutterudite, followed by Co-rich skutterudite and safflorite and finally loellingite. This
728 succession seems not to be related to changes in fO_2, since in all of these arsenides As
729 has an oxidation state of -I (Nickel, 1970). At low fO_2 Ni-chloro-complexes destabilize at
730 the lowest pH, followed by Co-chloro-complexes and finally Fe-chloro-complexes .
731 Consequently, a reaction path of increasing pH (due to the consumption of H^+ by
732 arsenides) at low fO_2 (maintained by oxidation of methane) results in the observed
733 element fractionation of Ni, Co and Fe (Markl et al. 2016).
734

735 ## Origin of involved fluids, solutes and gases

736 *Fluid signature of the basement brine (fluid A)*
737 Relatively high formation temperatures (~290°C), considering the estimated formation
738 depth (< 2.5 km) implies a fast almost adiabatic ascent of highly saline (Na-Ca-Cl), metal-
739 rich fluid A from deeper crustal levels. It can be assumed that the Ca/(Ca+Na) ratio is
740 controlled by host-rock albitisation of plagioclase (very An-rich in this case) in the
741 ascending fluid, inherited from deeper parts of the crystalline basement (before mixing)
742 (Burisch et al., 2016b). Middle to upper greenshist-facies conditions, are typical of
743 crustal levels above the brittle-ductile transition zone, which can be assumed to be the
744 source region of fluid A.

745 $$CaAl_2Si_2O_8 + 2Na^+ + 4SiO_{2(aq)} = 2NaAlSi_3O_8 + Ca^{2+} \quad (2)$$

746 Taking into account that fluid A might be slightly richer in Ca than the analysed FIAs
747 (fluid AB and ABC), temperatures of 300 to 320°C (Fig. 5) can be inferred from equation
748 2 using the numerical code SUBCRT92 (Johnson et al., 1992). According to the fluid
749 temperatures, these fluids ascended from greater depth. Consequently a fluid pressure
750 of 1 kbar is assumed, but pressure has only a minor influence, since no gases are
751 involved in the reaction (Eq. 2). The Jurassic ages of the mineralisation imply that

752 upward migration of fluid A is related to the opening of the North Atlantic (Mitchell and
753 Halliday, 1976; Boiron et al., 2010). Associated crustal thinning and fluid mobilization
754 due to fluid over-pressurization seems to have caused a rapid ascent of deep-seated
755 fluids (Staude et al., 2009). Prior and simultaneously to their rapid ascent, metals were
756 enriched in the fluid due to host-rock alteration (O'Keeffe, 1986; Burisch et al., 2016a;
757 Walter et al., 2016) in deeper crustal levels below the actual hydrothermal vein (Burisch
758 et al., 2016b). Closely below the basement-cover unconformity, these deep, metal-rich
759 fluids (not in thermal equilibrium with their country rocks) mixed with fluids of type B
760 and/or BC (Fig. 10), which instantaneously led to ore precipitation e.g. (Boiron et al.,
761 2010; Fußwinkel et al., 2013).

762 *Fluid signature of the sedimentary/basinal brine (fluid B)*
763 Fluid B is a Na-, S- and Cl-rich sedimentary or basinal brine, which migrated at least a
764 few hundred meters into the basement prior to mixing. The fluid originates presumably
765 from Upper Carboniferous and Permo-Triassic silicio-clastic aquifers. Most importantly,
766 dissolution of evaporites in the sedimentary aquifer, particularly halite and anhydrite,
767 cause low Ca/(Ca+Na) ratios, since halite has a much higher solubility than anhydrite.
768 The latter, however, may serve as sulphate (and, upon reduction, as sulphide) source.
769 Additionally, dissolution of sedimentary pyrite may have been relevant to a minor
770 extent.

771 *Methane (fluid C)*
772 Since fluid B occurs with and without prominent methane component, the fluid/gas
773 phase highly enriched in methane is classified and characterized separately as fluid C.
774 Although abiotic methane generation may be relevant for other systems, fluid inclusion
775 compositions imply, that the methane (fluid C) is exclusively transported along with
776 fluid B, indicating a sedimentary provenance of the analysed methane. Numerous

777 organic-rich sedimentary units occur in the Permian and Triassic basin (Geyer et al.,
778 2011), which potentially serve as source for methane (Fig. 10). Furthermore, methane
779 generation since the early Triassic associated with basin subsidence is well documented
780 in fluid inclusions of fracture minerals in the Central and Northern German Basin
781 (Lüders et al., 2005; Lüders et al., 2012). Methane was most likely derived from the
782 thermic decomposition of organic matter, while the provenance of N_2 seems to be
783 related to water-rock interaction of highly saline fluids with shale (Lüders et al., 2012).
784 The amount of CH_4-N_2 present strongly varies (Lüders et al., 2012). Reported T_h of
785 fracture minerals (carbonates and quartz) at the margin of the Northern German Basin
786 range between 160 and 250°C, while the majority lies between 160 and 210°C, which is
787 in very good agreement to the maximum temperature (~210°C) recognized in FIA
788 MB44p1. Similar to the paleo-methane generation, modern methane-rich fluids still
789 occur in the sedimentary aquifers of the Upper Rhine Graben (Sanjuan et al., 2016), in
790 close vicinity west and southwest of the Odenwald. Mobilisation of fluid C is strongly
791 dependent on the generation of fracture meshes, which drastically enhance the host
792 rock's permeability during episodes of active tectonics ("natural fracking", see Markl et
793 al. (2016)). Consequently, mixing of fluid C with fluid B is spatially and temporarily
794 restricted to zones of cataclastic deformation (Fig. 10).

795 *Sulphur*

796 The origin of H_2S and HS- in fluid B is most likely related to the dissolution of
797 sedimentary anhydrite/gypsum under reducing conditions. The break down of
798 sedimentary anhydrite/gypsum is strongly enhanced in the presence of methane at
799 temperatures above 140°C (Worden et al., 1995).

800 $$CaSO_4 + CH_4 = CaCO_3 + H_2S + H_2O \quad (3)$$

Dissolution of sedimentary sulphides (e.g. pyrite) present in the source aquifer (from e.g. shale) of fluid B might be an additional sulphur source.

Metals

Ag, Bi, Ni, Co, (U), Pb, Cu, Zn and Fe are most likely derived by water-rock interaction of fluid A with crystalline basement rocks (O'Keeffe, 1986; Ahmed et al., 2009; Fußwinkel et al., 2013; Burisch et al., 2016b), consisting of dominantly mafic to ultramafic metamorphic and igneous lithologies. In the presence of aqueous sulphide species the metal concentration is governed by low solubility sulphides (e.g. galena, sphalerite and chalcopyrite). Accordingly, it can be inferred that sulphide is very low in Fluid A and therefore is introduced by fluid B. Still, small amounts of additional Co and Ni might have been leached from placers of heavy minerals, which are potentially present in the clastic Permo-Triassic sedimentary aquifer. Crush-leach analysis of post-arsenide calcite I containing up to ~5000 mg/l As show that high As concentrations are still present in the mixed ore fluid (ABC) shortly after arsenide precipitation. Consequently, significantly higher As concentrations can be assumed to occur in fluid A. Arsenic is easily leached from ordinary basement rocks, and its mobility in crustal fluids is strongly enhanced by increasing temperature (Burisch et al., 2016a). Arsenic is favourably derived from both igneous and metamorphic rocks, while highest As concentrations are recognized in magmatic fluids or other fluids that interacted with igneous rocks (Williams et al., 2001; Yardley, 2005; Burisch et al., 2016a). Similar, modern basement brines from the granite hosted geothermal well of Soultz-sous-Forêt are strongly enriched in As. The observed late-stage Hg enrichment, finally, requires active transport of Hg in the hydrothermal solution, which is potentially mobilized by fluid-rock interaction with volcanic and anoxic, often organic-rich sediments (Krupp, 1988; Smith et al., 2008). Since Hg is favourably transported as bisulfide-complex, it can be assumed

826 that Hg is introduced to the system by fluid B and BC (since fluid A appears to be
827 sulphur-free) and was derived from fluid-rock interaction with organic-rich
828 sedimentary rocks.
829

830 ## Origin of the primary arsenide association

831 Native metals and arsenides occur within a distinct temporal interval in five-element
832 association. Although, within this temporal window sulphides are typically absent,
833 sulphides occur before and after the "arsenide window". From investigated fluid
834 compositions we can assume that the absolute concentrations of S and As are not the
835 key parameter, which control the formation of arsenides, since arsenic is also present
836 after ore stage 3. Consequently, the following discussion focuses on the specification of
837 As and its influence on the As^{-}/S^{2-} ratio.

838 *The arsenide/sulphide ratio as the controlling factor for the "arsenide window"*
839 The occurrence of sulphides before (ore stage 1) and after (ore stage 4) formation of
840 native metals (ore stage 2) is very typical of five element veins and has also been
841 documented from other deposits (Cheilletz et al., 2002; Ondrus et al., 2003a).
842 Furthermore, arsenide-free, sulphide-bearing veins (galena, chalcopyrite, bismuthinite,
843 acanthite, sphalerite and bornite) occur in close spatial and temporal connection to the
844 arsenide veins. Since it can be assumed that arsenic is abundantly present in fluid A and
845 is evidently still present in high concentrations in the fluid ABC of post-ore calcite I after
846 arsenide precipitation, we propose that the ratio of As^{-}/S^{2-}, rather than the absolute
847 arsenide or sulfide concentration, is the important key parameter governing whether
848 sulphides or arsenides precipitate (see also Markl et al. 2016). High As concentrations
849 (up to 590 mg/l) in ore fluids of arsenide-free Pb-Zn-(Cu) veins from other localities and
850 deposit types are reported by (Fußwinkel et al., 2013) and in modern fluids (up to 11.6

mg/l) from geothermal wells (Sanjuan et al., 2016). These data furthermore support the notion that the prevalent arsenic species and the arsenide/sulfide ratio are more important than the absolute concentrations. Arsenic is favourably present as oxidized As^{3+} in strongly to moderately oxidized hydrothermal solutions (Wood and Samson, 1998) and needs to be reduced to initiate arsenide precipitation.

$$2H_3AsO_3^0 + CH_4 = 2As^- + 3H_2O + HCO_3^- + 3H^+ \quad (4)$$

Consequently, arsenide-free sulphide veins occurring at Mackenheim and Nieder-Beerbach, can be considered as the "ordinary" background hydrothermal system, without the introduction of methane-bearing fluid C (Fig. 10). Since all other fluid parameters are identical to those of the arsenide veins, it can be assumed that these sulphide veins precipitated due to mixing of fluid A and fluid B without the participation of fluid C. Temporal and spatial variation of the composition and the occurrence of fluid C are related to tectonically active episodes that induce extensive fracture meshes, which enhance the rock permeability sufficiently to mobilize the hydrocarbons (Markl et al., 2016). Accordingly, it seems most likely that the involved basement fluid A reflects an "ordinary" fluid, rather than being anomalously enriched in Ag, As, Bi, Co, or Ni. The occurrence of native metals in such systems hence is dependent on the presence of an effective reducing agent (in this case methane), while the composition of the metal-transporting fluid plays a subordinate role.

Formation of Ag-Hg-barite-veins

At Nieder-Beerbach arsenide-free Ag-Hg-barite veins occur in close vicinity to the arsenide-bearing veins. Theses veins preferably occur in the upper 40 m b.g.s. and are clearly younger than the arsenide veins, which can be deduced from brecciated calcite I

875 overgrown by barite, silver II and calcite IIa (Fig. 2G and H). Their primary FIAs show
876 significantly lower Th compared to the FIAs in the arsenide-bearing veins (Fig. 5D).

877 *Secondary silver*

878 Deduced from the T_h of primary inclusions (130°C, MB59c1) in co-genetic calcite IIa, the
879 formation of the Ag-Hg-barite-veins can be related to the cooling of the hydrothermal
880 system, since the major element chemistry does not differ significantly from primary
881 FIAs in calcite I. Unfortunately, precise age data could not be acquired, as the vein
882 minerals (barite and only little calcite II) are not suitable for U-Pb age dating. The
883 presence of brecciated calcite I indicates a reactivation of pre-existing arsenide, sulphide
884 or barren veins. Increasing dilution by meteoric fluids or higher proportions of fluid B
885 during the mixing process could cause the observed shift of secondary fluid inclusion
886 compositions towards lower Ca/(Ca+Na) ratios and lower salinities with decreasing T_h
887 (< 130°C) in younger FIAs after the formation of native Ag II, calcite IIa and barite I.
888 However, primary FIA MB59c1 in calcite IIa texturally related to the formation of Ag II
889 and barite I, clearly shows similar major element compositions and salinities like the ore
890 fluids of ore stage 3 (fig 5). This argues against infiltration of meteoric fluids and/or
891 changes in the mixing ratio causing the formation of native Ag II. It seems that only
892 temperature is the major difference in the physio-chemical conditions between the
893 fluids, which were present during the formation of native Ag I and II (Fig. 11).

894 Ramdohr (1975) proposed that the irregularly shaped, sometimes moss-like textures of
895 native Ag II are typical of residual Ag derived by dissolution of Ag_2S. This assumption
896 can be strengthened by the observation of rare, small inclusions of corroded Ag_2S and
897 galena enclosed by native Ag II (Fig. 2H). Accordingly, during ore stage 4 Ag in solution
898 is proximately (cm to several tens of metres) precipitated as Ag_2S, which is occasionally
899 still present as small, corroded solid inclusions in native Ag II.

900 $2AgCl_2^- + S^{2-} = Ag_2S + 4Cl^-$ (5)

901 In a second step, Ag_2S is dissolved and synchronically forms native Ag II and barite
902 according to the following equations:

903 $Ag_2S + 2O_2 + Ba^{2+} = 2Ag + BaSO_4 + 2H^+$ (6)

904 Furthermore, $\delta^{34}S$ of barite show relatively low sulphur isotopic compositions of around
905 +5‰ compared to marine sulphate of the Permian/Triassic having values between 20
906 and 25‰ (Kampschulte and Strauss, 2004), archived as sedimentary sulphates in the
907 cover units (Fig. 8). Unusually low sulphur isotope compositions indicate that a relevant
908 sulphur source of the barites is inherited sulphur of oxidized, pre-existing sulphides
909 (Fig. 8). Mass balance calculations imply that ~50% of the sulphate in the analysed
910 barites is inherited from sulphide minerals (acanthite, proustite, pearceite and galena),
911 assuming that the other 50% are derived from dissolved marine sulphates (Fig. 8).
912 The reaction of Ag_2S to silver and barite requires a decrease of S^{2-}/SO_4^{2-} (Fig. 11), which
913 is realised by the introduction of oxidizing fluids (open system) or simply by a decrease
914 in temperature and a concomitant decrease of S^{2-}/SO_4^{2-} due to a change in sulphur
915 specification (closed system). Decomposition of anhydrite to dissolved S^{2-} preferably
916 occurs above 140°C (Worden et al., 1995). Cooling of the sedimentary basin to
917 temperatures below 140°C, results in a transition from HS^-/S^{2-}- to SO_4^{2-}-dominated
918 fluids, while other fluid parameters do not change. Both under open or closed system
919 conditions, temperature can be considered as the most relevant controlling factor. These
920 arguments are consistent with calculated stability, solubility and pre-dominance of the
921 observed mineral phases and sulphur-species summarized in Fig. 11. According to
922 textural and field observations major mobilisation of Ag happened dominantly during
923 step 1 (ores stage 3), while the dissolution of Ag_2S and proximal precipitation of native
924 Ag II (step 2) did not cause a significant transport of Ag.

Mercury enrichment associated with secondary Ag

Native Ag II is strongly enriched in Hg (up to ~30 wt.%). Considering the low Hg contents of primary Ag I and Ag_2S, this enrichment cannot be derived passively during oxidation of Ag I and/or Ag_2S, since Ag I has only low Hg (mostly around 1 wt.%) and Ag_2S is nominally Hg-free. Mercury is transported as bisulfide-complexes in hydrothermal solutions (Krupp, 1988; Barnes and Seward, 1997). The decrease in S^{2-}/SO_4^{2-} that is causing the dissolution/oxidation (most likely cooling) of sulphides is accompanied by a destabilisation of Hg-bisulfide complexes and consequently results in deposition of Hg along with Ag II, as the system cools down successively. A comparable Ag mobilization during sulphide stage (ore stage 4) and very late stage Hg enrichment can be recognized at Imiter/Morocco (Cheilletz et al., 2002).

SUMMARY AND CONCLUSIONS

Various Ag-, As and Bi- dominated five-element assemblages occur in the Odenwald, which represent a typical example of five-element veins with respect to ore mineralogy, geological setting, formation conditions and fluid chemistry. These veins formed at temperatures of around 290°C and pressures below 0.2 kbar. Although, the dominant native-element varies, major element chemistry of the associated ore fluids show invariable salinities of 26 to 27 wt.% and Ca/(Ca+Na) ratios between 0.30 and 0.35. Methane and H_2S could be detected in the vapour phase of several FIAs. The Odenwald five-element veins investigated here are formed along with e.g. Bieber/Germany (Wagner and Lorenz, 2002), Cobalt-Gowganda/Canada (Marshall et al., 1993), Bou Azzer/Morocco (Ahmed et al., 2009) and Imiter/Morocco (Cheilletz et al., 2002) at mesothermal (to hypothermal) conditions, in contrast to other (epithermal) five-element deposits like Wittichen/Germany (Staude et al., 2012) and Great Bear

949 Lake/Canada (Changkakoti et al., 1986). Consequently, formation temperature (which
950 can vary a lot among five element deposits) seems to have no effect on the mineralogy
951 (Kissin, 1992; Staude et al., 2012; Markl et al., 2016). While mafic to ultramafic igneous,
952 volcanic or metamorphic lithologies seems to be the metal source in the majority of five-
953 element veins (Kissin, 1992; Ahmed et al., 2009), the process initiating ore precipitation
954 was long poorly constrained.
955 From microthermometric data, Raman-spectroscopy and thermodynamic modelling it
956 can be concluded that ascending metal-rich deep-seated basement fluids (A) were mixed
957 closely below the basemen-cover unconformity with basinal/sedimentary fluids (B) and
958 initiated the formation of mesothermal Pb-Zn-Cu-sulphide minerals. Only if the
959 basinal/sedimentary fluids (B) include sufficient amounts of methane (C) (spatially and
960 temporarily variable) subsequent oxidation of methane results in very reducing fluid
961 conditions required for the formation of native metals and arsenide. It has been shown
962 that neither CH_4 nor CO_2 is compulsory archived in fluid inclusions although there is
963 clear evidence for the presence of methane during ore-formation. Depending on the
964 amount of involved methane, stable isotopic compositions of calcite I (ore stage 3),
965 showing relatively low average C- and O-isotope archive the participation of isotopic
966 lighter hydrocarbons. As an extremely effective reducing agent, methane influx might at
967 least in some cases play an important role in ore formation of other redox sensitive
968 elements such as U and Au.
969 Hydrocarbon-bearing basinal fluids potentially migrate several hundreds of metres from
970 their source into the crystalline basement (Munz et al., 1995), and therefore the
971 occurrence of five element veins is not compulsory restricted to crustal levels proximal
972 to unconformities. Notwithstanding, several deposits have in fact formation depth close
973 to the basement-cover unconformity, like for example those of the Odenwald (this

974 study), Wittichen (Staude et al., 2012) Cobalt-Gowganda (Andrews et al., 1986), Thunder
975 Bay (Franklin et al., 1986) and Kongsberg-Modum (Bugge, 1931).
976 High As concentrations (up to 5500 mg/kg) in the post-ore fluid (ABC) in fluid
977 inclusions of late calcite I, which precipitated after the native metals and arsenides and
978 the occurrence of sulphides temporarily before and after the native metals and
979 arsenides, indicates that the oxidation state of the As species is the controlling factor for
980 the "arsenide window", rather than absolute As concentrations in the fluid.
981 U-Pb-dating of low U-minerals such as calcite, prehnite at small scales is a new and
982 promising method. We successfully applied this method for the first time to
983 hydrothermal vein-type deposits. Hydrothermal ore deposition in the Odenwald, SW
984 Germany, occurred in the middle Jurassic, (170-180 Ma ago) and can directly be linked
985 to the opening of the North Atlantic. Continental rifting and crustal thinning induced by
986 extension enhanced upward fluid movement of deep-seated basement fluids and
987 subsequent mixing with shallower basinal/sedimentary brines. Post-ore calcite
988 formation at ~60 Ma before present can be directly related to the onset of the Upper
989 Rhine Graben rifting.
990 Secondary enrichment of Ag and Hg associated with barite and quartz do not necessarily
991 require open-system removal or oxidation of older sulphides. It is shown that cooling
992 (closed-system) of the system and a concomitant decrease in the sulphide/sulphate
993 ratio effectively results in remobilization of older sulphides (Ag_2S in this study) resulting
994 in substantial element enrichment of Ag and Hg.
995

996 **Acknowledgements**
997 We gratefully thank Thomas Wenzel, Bernd Steinhilber, Linda Marko, Gabriele Stoschek
998 and Melanie Keuper for support with analytical issues.

REFERENCES

Ahmed, A.H., Arai, S., Ikenne, M., 2009. Mineralogy and Paragenesis of the Co-Ni Arsenide Ores of Bou Azzer, Anti-Atlas, Morocco. Economic Geology, 104(2): 249-266.

Andrews, A., Owsiacki, L., Kerrich, R., Strong, D., 1986. The silver deposits at Cobalt and Gowganda, Ontario. I: Geology, petrography, and whole-rock geochemistry. Canadian Journal of Earth Sciences, 23(10): 1480-1506.

Barnes, H., Seward, T., 1997. Geothermal systems and mercury deposits. Geochemistry of hydrothermal ore deposits, 3: 699-736.

Bastin, E.S., 1939. The nickel-cobalt-native silver ore type. Economic Geology, 34(1): 1-40.

Bodnar, R., Vityk, M.O., 1994. Interpretation of microthermometric data for H2O–NaCl fluid inclusions. In: De Vivo, B., Frezzotti, M.L. (Eds.), Fluid Inclusions in Minerals, Methods and Applications. Virginia Tech, Blacksburg. 117-130.

Boiron, M.C., Cathelineau, M., Richard, A., 2010. Fluid flows and metal deposition near basement/cover unconformity: lessons and analogies from Pb–Zn–F–Ba systems for the understanding of Proterozoic U deposits. Geofluids, 10(1‐2): 270-292.

Bugge, A., 1931. Gammel og ny geologi ved Kongsberg sölvverk. Norsk Geologisk Tidsskrift, 12: 123.

Burisch, M., Marks, M.A., Nowak, M., Markl, G., 2016a. The effect of temperature and cataclastic deformation on the composition of upper crustal fluids—An experimental approach. Chemical Geology.

Burisch, M., Walter, B.F., Wälle, M., Markl, G., 2016b. Tracing fluid migration pathways in the root zone below unconformity-related hydrothermal veins: Insights from trace element systematics of individual fluid inclusions. Chemical Geology, 429: 44-50.

Changkakoti, A., Morton, R., Gray, J., Yonge, C., 1986. Oxygen, hydrogen, and carbon isotopic studies of the Great Bear Lake silver deposits, Northwest Territories. Canadian Journal of Earth Sciences, 23(10): 1463-1469.

Cheilletz, A., Levresse, G., Gasquet, D., Azizi-Samir, M., Zyadi, R., Archibald, D.A., Farrar, E., 2002. The giant Imiter silver deposit: Neoproterozoic epithermal mineralization in the Anti-Atlas, Morocco. Mineralium Deposita, 37(8): 772-781.

Coogan, L.A., Parrish, R.R., Roberts, N.M., 2016. Early hydrothermal carbon uptake by the upper oceanic crust: Insight from in situ U-Pb dating. Geology, 44(2): 147-150.

Faupl, P., 2000. Historische Geologie. Facultas Wien.

Fettel, M., 1978. Über die Wismut-Kobalt-Nickel-Silber-Uran-Formation im Kristallinen Odenwald. Aufschluss, 29: 307-320.

Fettel, M., 1982. Silver and Associated Minerals in the Northwestern Odenwald, Germany, Ore Genesis. Springer, pp. 573-581.

Fettel, M., 1985. Silber, Arsen und Lautit aus dem Odenwald. Lapis, 10(2): 35-39.

Franklin, J., Kissin, S., Smyk, M., Scott, S., 1986. Silver deposits associated with the Proterozoic rocks of the Thunder Bay District, Ontario. Canadian Journal of Earth Sciences, 23(10): 1576-1591.

Frezzotti, M.L., Tecce, F., Casagli, A., 2012. Raman spectroscopy for fluid inclusion analysis. Journal of Geochemical Exploration, 112: 1-20.

1045 Fußwinkel, T., Wagner, T., Wälle, M., Wenzel, T., Heinrich, C.A., Markl, G., 2013. Fluid
1046 mixing forms basement-hosted Pb-Zn deposits: Insight from metal and halogen
1047 geochemistry of individual fluid inclusions. Geology, 41(6): 679-682.
1048 Gerdes, A., Zeh, A., 2006. Combined U–Pb and Hf isotope LA-(MC-) ICP-MS analyses of
1049 detrital zircons: comparison with SHRIMP and new constraints for the
1050 provenance and age of an Armorican metasediment in Central Germany. Earth
1051 and Planetary Science Letters, 249(1): 47-61.
1052 Gerdes, A., Zeh, A., 2009. Zircon formation versus zircon alteration—new insights from
1053 combined U–Pb and Lu–Hf in-situ LA-ICP-MS analyses, and consequences for the
1054 interpretation of Archean zircon from the Central Zone of the Limpopo Belt.
1055 Chemical Geology, 261(3): 230-243.
1056 Geyer, O.F., Gwinner, M.P., Geyer, M., Nitsch, E., Simon, T., 2011. Geologie von Baden-
1057 Württemberg.
1058 Heimig, C., 2015. Ni-Co-As-Ag-Bi-Mineralisationen aus dem Odenwald
1059 . Unpublished M.sc. Thesis, Universität Tübingen, 119 pp.
1060 Johnson, J.W., Oelkers, E.H., Helgeson, H.C., 1992. SUPCRT92: A software package for
1061 calculating the standard molal thermodynamic properties of minerals, gases,
1062 aqueous species, and reactions from 1 to 5000 bar and 0 to 1000 C. Computers &
1063 Geosciences, 18(7): 899-947.
1064 Kampschulte, A., Strauss, H., 2004. The sulfur isotopic evolution of Phanerozoic seawater
1065 based on the analysis of structurally substituted sulfate in carbonates. Chemical
1066 Geology, 204(3): 255-286.
1067 Kerrich, R., Strong, D., Andrews, A., Owsiacki, L., 1986. The silver deposits at Cobalt and
1068 Gowganda, Ontario. III: Hydrothermal regimes and source reservoirs-evidence
1069 from H, O, C, and Sr isotopes and fluid inclusions. Canadian Journal of Earth
1070 Sciences, 23(10): 1519-1550.
1071 Kissin, S., 1988. Nickel-cobalt-native silver (five-element) veins: A riftrelated ore type.
1072 North American ConL on Tectonic Control of Ore Deposits and the Vertical and
1073 Horizontal Extent of Ore Systems. Univ. Missouri Press, Rolla: 268-279.
1074 Kissin, S.A., 1992. Five-element (Ni-Co-As-Ag-Bi) veins. Geoscience Canada, 19(3).
1075 Krupp, R., 1988. Physicochemical aspects of mercury metallogenesis. Chemical geology,
1076 69(3): 345-356.
1077 Kühne, R., 1932. Die Erzführung des Auerbacher Marmors. Chemie der Erde, 7: 503-539.
1078 Leyk, H.-J., 1990. Petrographie, Tektonik und Mineralisation im Bereich des
1079 Gabbrosteinbruchs Nieder-Beerbach der Odenwälder Hartstein Industrie / NW-
1080 Odenwald. Diploma thesis - Universität Heidelberg.
1081 Lipp, U., Flach, S., 2003. Wismut-, Kobalt-, Nickel-und Silbererze im Nordteil des
1082 Schneeberger Lagerstättenbezirkes.
1083 Lippolt, H., Gentner, W., Wimmenauer, W., 1963. Altersbestimmungen nach der Kalium-
1084 Argon-Methode an tertiären Eruptivgesteinen Südwestdeutschlands. Jahresheft
1085 des Geologischen Landesamtes in Baden-Württemberg, 6: 507-538.
1086 Lüders, V., Plessen, B., di Primio, R., 2012. Stable carbon isotopic ratios of CH 4–CO 2-
1087 bearing fluid inclusions in fracture-fill mineralization from the Lower Saxony
1088 Basin (Germany)–A tool for tracing gas sources and maturity. Marine and
1089 Petroleum Geology, 30(1): 174-183.
1090 Lüders, V., Reutel, C., Hoth, P., Banks, D.A., Mingram, B., Pettke, T., 2005. Fluid and gas
1091 migration in the North German Basin: fluid inclusion and stable isotope
1092 constraints. International Journal of Earth Sciences, 94(5-6): 990-1009.
1093 Ludwig, K., 2007. Isoplot 3.62. Berkeley Geochronology Center Special Publication, 4: 70.

1094 Markl, G., Burisch, M., Neumann, U., 2016. Natural fracking and the genesis of five-
1095 element veins. Mineralium Deposita: 1-10.
1096 Marshall, D.D., Diamond, L.W., Skippen, G.B., 1993. Silver transport and deposition at
1097 Cobalt, Ontario, Canada; fluid inclusion evidence. Economic Geology, 88(4): 837-
1098 854.
1099 Meisl, S., Pöschl, W., 1982. Radioactive Disequilibrium Studies in Uranium Occurrences
1100 of the Odenwald, West Germany, Ore Genesis. Springer, pp. 590-597.
1101 Millonig, L.J., Gerdes, A., Groat, L.A., 2012. U–Th–Pb geochronology of meta-carbonatites
1102 and meta-alkaline rocks in the southern Canadian Cordillera: a geodynamic
1103 perspective. Lithos, 152: 202-217.
1104 Mitchell, J., Halliday, A., 1976. Extent of Triassic/Jurassic hydrothermal ore deposits on
1105 the North Atlantic margins. Transactions of the Institution of Mining and
1106 Metallurgy B, 85: 159-61.
1107 Munz, I., Yardley, B., Banks, D., Wayne, D., 1995. Deep penetration of sedimentary fluids
1108 in basement rocks from southern Norway: Evidence from hydrocarbon and brine
1109 inclusions in quartz veins. Geochimica et Cosmochimica Acta, 59(2): 239-254.
1110 Nathans, M.W., Leider, M., 1962. Sudies on bismuth alloys. I. Liquidus curve of the
1111 bismuth—copper, bismuth—siver and bismuth—gold systems. The Journal of
1112 Physical Chemistry, 66(10): 2012-2015.
1113 Nickel, E., 1970. The application of ligand-field concepts to an understanding of the
1114 structural stabilities and solid-solution limits of sulphides and related minerals.
1115 Chemical Geology, 5(4): 233-241.
1116 Nickel, E., 1975. Geologische Position und Petrogenese des kristallinen Odenwaldes.
1117 Mineralien und Gesteine im Odenwald. Aufschluû Sonderbd, 27: 1-25.
1118 O'Keeffe, W., 1986. Age and postulated source rocks for mineralization in central Ireland
1119 as indicated by lead isotopes, in Andrew, C.J., Crowe, R.W.A., Finlay, S., Pennell,
1120 W.M., and Pyne, J., eds. Geology and genesis of mineral deposits in Ireland: Dublin,
1121 Irish Association for Economic Geology: 617-624.
1122 Ohmoto, H., Goldhaber, M., 1997. Sulfur and carbon isotopes. Geochemistry of
1123 hydrothermal ore deposits, 3: 517-611.
1124 Oncken, O., Winterfeld, C.v., Dittmar, U., 1999. Accretion of a rifted passive margin: the
1125 Late Paleozoic Rhenohercynian fold and thrust belt (Middle European
1126 Variscides). Tectonics, 18(1): 75-91.
1127 Ondrus, P., Veselovsky, F., Gabasova, A., Drabek, M., Dobes, P., Maly, K., Hlousek, J.,
1128 Sejkora, J., 2003a. Ore-forming processes and mineral parageneses of the
1129 Jáchymov ore district. Journal of GEOsciences, 48(3-4): 157-192.
1130 Ondrus, P., Veselovsky, F., Gabasova, A., Hlousek, J., Srein, V., 2003b. Geology and
1131 hydrothermal vein system of the Jáchymov (Joachimsthal) ore district. Journal of
1132 GEOsciences, 48(3-4): 3-18.
1133 Ondrus, P., Veselovsky, F., Gabasova, A., Hlousek, J., Srein, V., Vavrin, I., Skala, R., Sejkora,
1134 J., Drabek, M., 2003c. Primary minerals of the Jáchymov ore district. Journal of
1135 GEOsciences, 48(3-4): 19-147.
1136 Ramdohr, P., 1923. Der Silberkobalterzgang mit Kupfererzen von Nieder-Ramstadt bei
1137 Darmstadt. Notizbl Ver Erdkd, 5: 164-192.
1138 Ramdohr, P., 1975. Der Silberkobalterzgang mit Kupfererzen vom Wingertsberg bei
1139 Nieder-Ramstadt im Odenwald. Aufschluss, 27: 237-243.
1140 Rasbury, E.T., Cole, J.M., 2009. Directly dating geologic events: U‐Pb dating of
1141 carbonates. Reviews of Geophysics, 47(3).

Ring, U., Gerdes, A., 2016. Kinematics of the Alpenrhein–Bodensee graben system in the Central Alps: Oligocene/Miocene transtension due to formation of the Western Alps arc. Tectonics.
Roy, R., Majumdar, A.J., Hulbe, C., 1959. The Ag2S and Ag2Se transitions as geologic thermometers. Economic Geology, 54(7): 1278-1280.
Sanjuan, B., Millot, R., Innocent, C., Dezayes, C., Scheiber, J., Brach, M., 2016. Major geochemical characteristics of geothermal brines from the Upper Rhine Graben granitic basement with constraints on temperature and circulation. Chemical Geology, 428: 27-47.
Schmitt, A.K., Marks, M.A., Nesbor, H.D., Markl, G., 2007. The onset and origin of differentiated Rhine Graben volcanism based on U-Pb ages and oxygen isotopic composition of zircon. European Journal of Mineralogy, 19(6): 849-857.
Smith, C.N., Kesler, S.E., Blum, J.D., Rytuba, J.J., 2008. Isotope geochemistry of mercury in source rocks, mineral deposits and spring deposits of the California Coast Ranges, USA. Earth and Planetary Science Letters, 269(3): 399-407.
Staude, S., Bons, P.D., Markl, G., 2009. Hydrothermal vein formation by extension-driven dewatering of the middle crust: an example from SW Germany. Earth and Planetary Science Letters, 286(3): 387-395.
Staude, S., Werner, W., Mordhorst, T., Wemmer, K., Jacob, D.E., Markl, G., 2012. Multi-stage Ag–Bi–Co–Ni–U and Cu–Bi vein mineralization at Wittichen, Schwarzwald, SW Germany: geological setting, ore mineralogy, and fluid evolution. Mineralium Deposita, 47(3): 251-276.
Steele-MacInnis, M., Bodnar, R., Naden, J., 2011. Numerical model to determine the composition of H 2 O–NaCl–CaCl 2 fluid inclusions based on microthermometric and microanalytical data. Geochimica et Cosmochimica Acta, 75(1): 21-40.
Stein, E., 2001. The geology of the Odenwald crystalline complex. Mineralogy and petrology, 72(1-3): 7-28.
Thews, J.-D., 1996. Erläuterungen zur geologischen Übersichtskarte von Hessen 1: 300 000 (GÜK 300 Hessen).: Kristallin, Ordoviz, Silur, Devon, Karbon, 96. Hessisches Landesamt für Bodenforschung.
Wagner, T., Lorenz, J., 2002. Mineralogy of complex Co-Ni-Bi vein mineralization, Bieber deposit, Spessart, Germany. Mineralogical Magazine, 66(3): 385-407.
Walter, B.F., Burisch, M., Markl, G., 2016. Long‐term chemical evolution and modification of continental basement brines–a field study from the Schwarzwald, SW Germany. Geofluids.
Wilkerson, G., Deng, Q., Llavona, R., Goodell, P.C., 1988. Batopilas mining district, Chihuahua. Economic Geology, 83(8): 1721-1736.
Williams, P.J., Dong, G., Ryan, C.G., Pollard, P.J., Rotherham, J.F., Mernagh, T.P., Chapman, L.H., 2001. Geochemistry of hypersaline fluid inclusions from the Starra (Fe oxide)-Au-Cu deposit, Cloncurry District, Queensland. Economic Geology, 96(4): 875-883.
Wood, S., Samson, I., 1998. Solubility of ore minerals and complexation of ore metals in hydrothermal solutions. Rev. Econ. Geol, 10: 33-80.
Worden, R.H., Smalley, P.C., Oxtoby, N.H., 1995. Gas souring by thermochemical sulfate reduction at 140 C. AAPG Bulletin, 79(6): 854-863.
Yardley, B.W., 2005. 100th Anniversary Special Paper: metal concentrations in crustal fluids and their relationship to ore formation. Economic Geology, 100(4): 613-632.
Zienert, A., 1957. Die Großformen des Odenwaldes. Selbstverl. d. Geograph. Inst. d. Univ.

Figure captions

Figure 1: A) Geological map of the crystalline Odenwald and its Permo-Triassic cover modified after Stein (2001). B) Enlarged area of the Northern Odenwald modified after Thews (1996) including the locations (white stars) of the quarries at Nieder-Ramstadt (Wingertsberg), Nieder-Beerbach (Glasberg) and Waschenbach (Waschenbach), where Ag- and As- dominated ore assemblages occur. C). Enlarged area of the Southern Odenwald modified after Thews (1996) including the quarry "Viadukt" at Mackenheim, where Bi-dominated five-element assemblages occur.

Figure 2: A) Reflected light (RL) image of skeletal native silver I (Ag) overgrown by rammelsbergite (Rmb), skutterudite (Skt), safflorite (Sfl), loellingite (Loel) and calcite (Cal I). In the left area the native Ag I is mostly dissolved and replaced by loellingite, acanthite (Ac), galena (Gn), sphalerite (Sph) and calcite (Cal I). The white rectangle indicates the enlarged area which is displayed in Fig. 2B. B) The succession of rammelsbergite, skutterudite and loellingite, which formerly rimmed the native Ag, indicate the original shape of the native Ag, which is almost entirely replaced by loellingite, acanthite, galena, sphalerite and calcite (RL). C) BSE image of very porous irregularly shaped aggregates of native Ag replaced by proustite (Prou) surrounded by native As (As). At the outer rims and at the former interface between As and Ag, native metals are strongly dissolved and replaced by a crust of loellingite and calcite. Besides the irregularly shaped Ag aggregates, small grains of Ag occur randomly distributed inside of the mass of native As. D) RL image of native arsenic replaced/overgrown by euhedral loellinigte and calcite. Void space within the loellingite is subsequently filled with anhedral proustite and sphalerite. E) Rl image of native Bi (Bi) encapsulated by

rammelsbergite and skutterudite. F) RL image of skeletal native Bi overgrown by skutterudite and later calcite. G) BSE image of the second generation of native silver II (Ag II, amalgam), which is inter-grown with co-genetic barite (Ba) and calcite II (Cal II). H) RL image of irregularly shaped native Ag II including small, corroded grains of acanthite (Ac).

Figure 3: Paragenetic sequence of A) the Ag-Ni-Co-Fe-As (black), As-Ag-Fe (grey) and Ag-(Hg)-barite (meshed white) vein types. White rectangles indicate the dissolution of existing phases. B) Paragenetic sequence of the Bi-Ni-Co-Fe-As vein type. The grey shaded are indicates the temporal occurrence of the five-element assemblage.

Figure 4: Terra-Wasserburg diagrams showing $^{207}Pb/^{206}Pb$ versus $^{238}U/^{206}Pb$. Data points are indicated as 2σ error ellipsoids. Dark grey ellipsoids indicate analyses of co-genetic calcite I and prehnite II, light grey ellipsoid indicate analyses of younger calcite II. A) MB14, Ag-suite. B) MB27, As-suite. C) MB31, Ag-suite. D) MB55, Bi-suite. E) Enlarged diagram of concordant ages of MB55. F) MB39, Bi-suite.

Figure 5: Microthermometric analyses of various fluid inclusion assemblages (FIAs). A) Total salinity versus Ca/(Ca+Na) (molar) of FIAs in mesothermal Pb-Zn-Cu-S (cross), Ag-Ni-Co-Fe-As (circle), Bi-Ni-Co-Fe-As (rectangle) and As-Ag-Fe (diamond) veins. Inferred end-member reservoir compositions are indicated as white rectangles (fluid A and fluid B&BC). B) Total salinity versus Ca/(Ca+Na) (molar) in FIAs of Ag-Hg-barite (triangle) veins. C) Uncorrected homogenisation temperature versus Ca/(Ca+Na) of mesothermal arsenide and sulphide veins. Grey bars indicate the temperature intervals of ore stages 1, 2, 3, 4 and the post-ore Ag II stage. The black line indicates Ca/(Ca+Na) fluid

compositions in equilibrium with Ca-rich plagioglase (An_{90}). D) Uncorrected homogenisation temperature versus Ca/(Ca+Na) of Ag-Hg-barite veins.

Figure 6: A) Photo-micrograph of MB12p1 showing six analysed fluid inclusions. B) Representative micro-Raman analyses of MB12p1. Fluid inclusions 1, 2, 3, 5 and 6 do not contain any detectable gaseous phases (gray spectrum), while fluid inclusion 4 clearly contains methane and nitrogen (black spectrum). C) Representative spectrum of the analysed liquid phase of FIA MB12p1 showing exclusively H_2O and the signal of the matrix calcite. D) Spectrum of the matrix calcite. E) Photo-micrograph of MB44p1 showing nine analysed fluid inclusions. F) Representative spectrum of analysed vapour phase including CO_2, N2, H_2S and CH_4. . G) Representative spectrum of analysed liquid including HS^-. H) Spectrum of the matrix calcite.

Figure 7: Box plot showing $\delta^{13}C$ and $\delta\ ^{18}O$ of analysed calcites including data previously published graphically in Markl et al. (2016) of different vein types.

Figure 8: $\delta^{34}S$ of barites and sulphides of Ag-Hg-barite veins. Permo-triassic isotopic composition of marine sulphate (Kampschulte and Strauss, 2004) is indicated as black rectangle. Fractionation at 135°C between Ag_2S and SO_4^{2-} calculated according to Ohmoto and Goldhaber (1997). The isotopic mean value of analysed barites reflects a ~1/1 mixture of marine sulphate and sulphate derived from sulphide oxidation.

Figure 9: Ni-Co-Fe compositions of rammelbergite, safflorite and loellingite (diarsenides, black colour) and skutterudite (grey) of Nieder-Beerbach (circles) and

Mackenheim (triangles). A distinct trend from Ni- to Fe-rich compositions from old to young can be observed. Data includes several analyses of diarsenides from Markl et al. (2016).

Figure 10: Schematic crustal section consisting of metamorphic and igneous crystalline rocks in deeper parts discordantly covered by sedimentary rock units. A) Genetic model of Pb-Zn-Cu-S veins. Sedimentary fluid B (metal-poor, sulphur-rich) migrates into deeper stratigraphic levels (fluid stratigraphy does not compulsory coincide with rock stratigraphy) and migrates parallel to the unconformity until it is mixed with ascending fluids A (metal-rich, sulphur-poor) from deeper crustal levels. Mixing of fluid A and B initiates formation of sulphide ores. Descending fluid B does not mix with isolated methane/organic matter (fluid C). B) Genetic model of five-element veins. In contrast to Fig 10A, descending fluid B is mixed with fluid C (hydrocarbons) during downward movement, due to the liberation of fluid C as a consequence of active tectonics and the associated formation of fracture meshes. Mixing of fluid BC with fluid A finally results in the formation of native metals and arsenides.

Figure 11: Solubility of Ag_2S, native Ag, chlorargyrite and barite at 300bars, 25 wt.% NaCl and a pH of 8 in a temperature versus log fO_2 diagram. The dark grey area indicates the solubilities for a log a_{Ag}=-5, while the light grey are indicates solubilies for higher Ag concentrations of log a_{Ag}=-3. The dotted line indicates a S^{2-}/SO_4^{2-} ratio of 1. Below and above this line there is a narrow field in which sulphide and sulphides co-exist (acanthite+barite). Cooling of the system results in a decrease of the S^{2-}/SO_4^{2-} ratio, subsequently results in precipitation of barite along acanthite and finally in the dissolution of the acanthite and re-precipitation as native-Ag along with barite (at

~130°C). In some cases, further cooling/oxidation leads to the formation of additional chlorargyrite, which is rarel is present as crusts around native Ag II.

Table captions

Table 1. Overview of native metal mineral assemblages at Mackenheim and Nieder-Beerbach.

Table 2. Bulk fluid inclusion composition of calcite I.

Table 3. C- and O-isotopic compositions of calcite I and calcite II, including several analyses, which are graphically presented in Markl et al. (2016).

Table 4. S-isotopc composition of barite and sulfide minerals.

Table 5. Composition of native metals in wt.%.

Table 6. Composition of arsenides in wt.%.

Table 7. Composition of sulphides in wt.%.

Table A1 (appendix). U-Pb data of calcite I, calcite II and prehnite II.

Table A2 (appendix). Fluid inclusion data including microthermometry and Raman analyses.

Figures

Figure 1

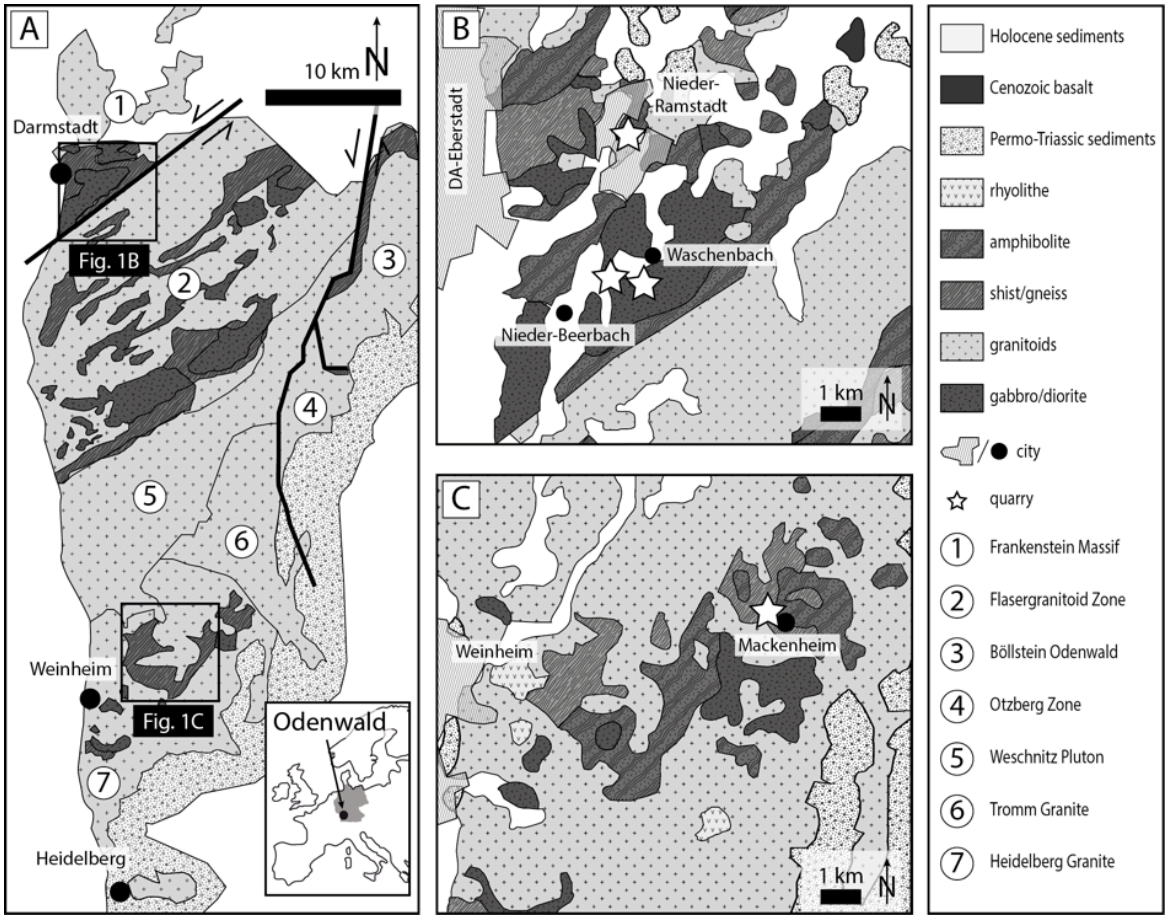

Figure 2

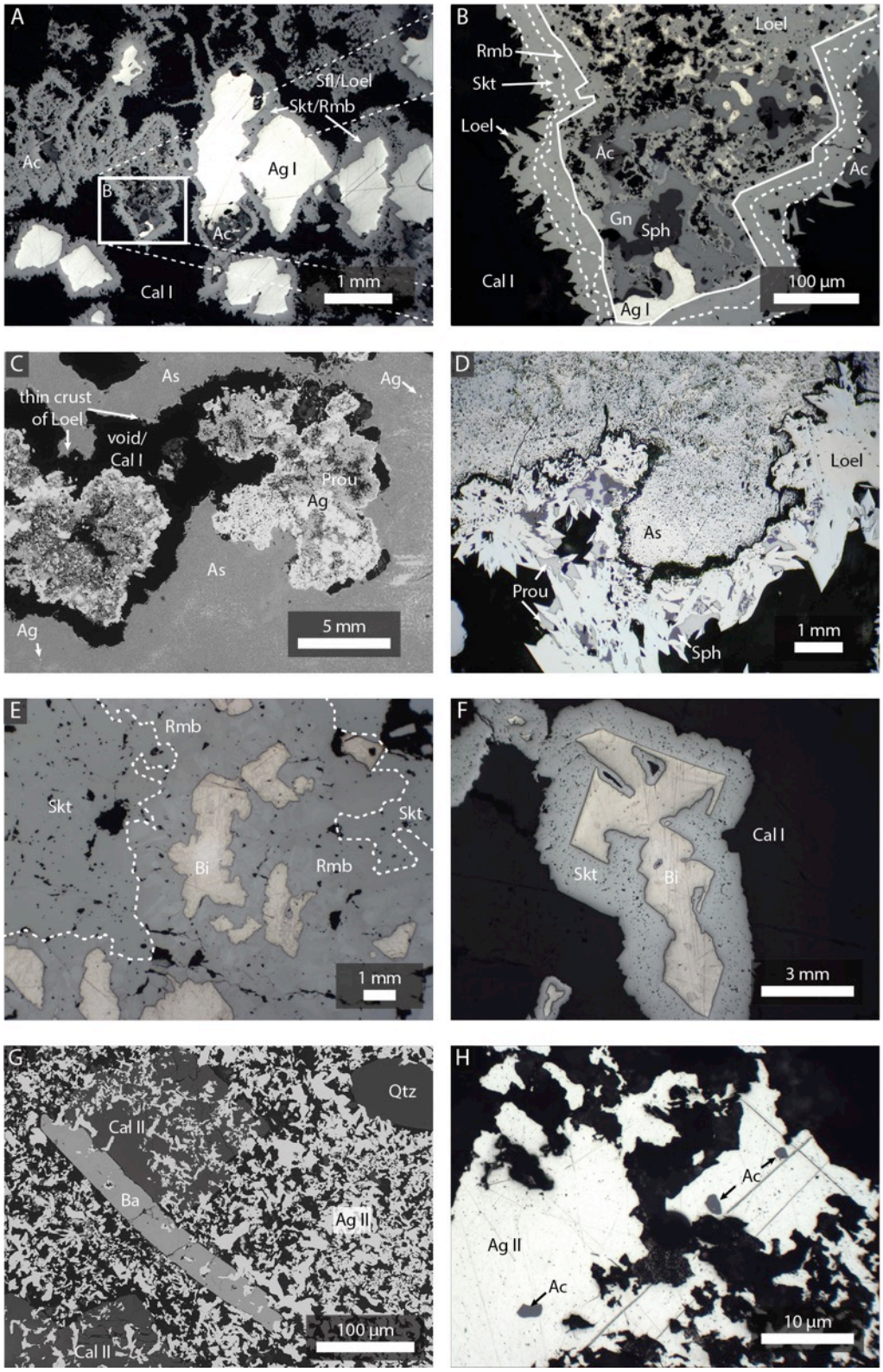
A
Sfl/Loel
Skt/Rmb
Ac
Ag I
B
Ac
Cal I
1 mm
B
Rmb
Skt
Loel
Loel
Ac
Ac
Gn
Sph
Cal I
Ag I
100 µm
C
As
Ag
thin crust
of Loel
void/
Cal I
Prou
Ag
As
Ag
5 mm
D
Loel
As
Prou
Sph
1 mm
E
Rmb
Skt
Skt
Bi
Rmb
1 mm
F
Cal I
Skt
Bi
3 mm
G
Qtz
Cal II
Ba
Ag II
100 µm
Cal II
H
Ac
Ag II
Ac
10 µm

1345

1346 Figure 3

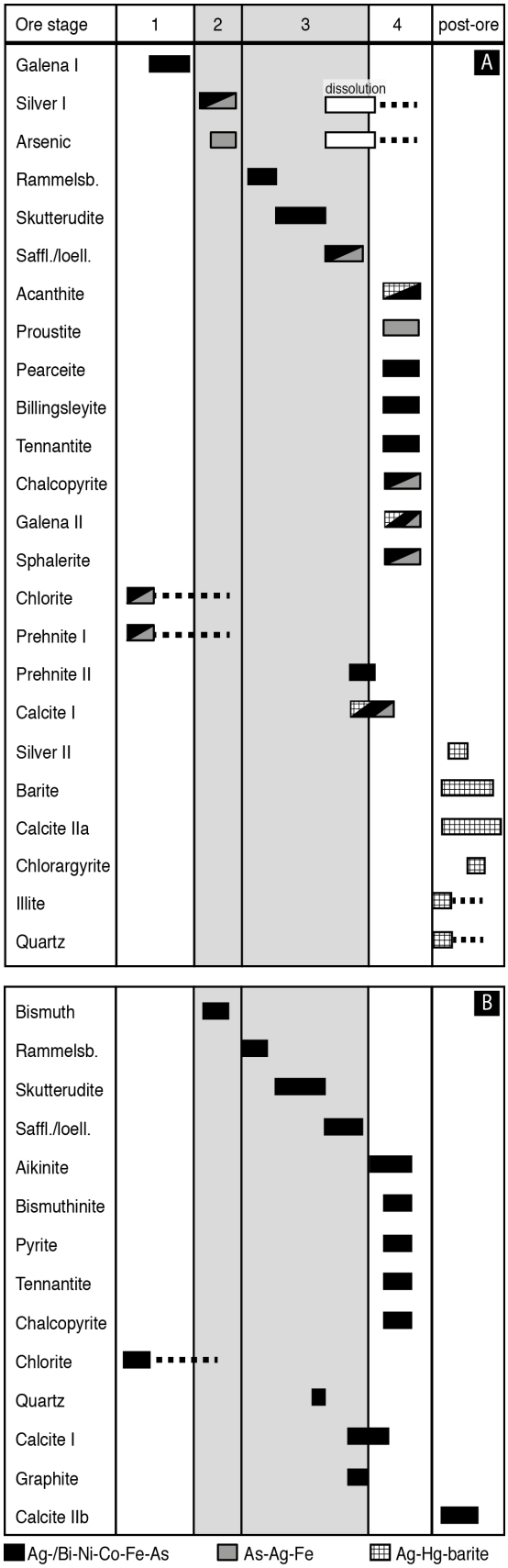

1347

Figure 4

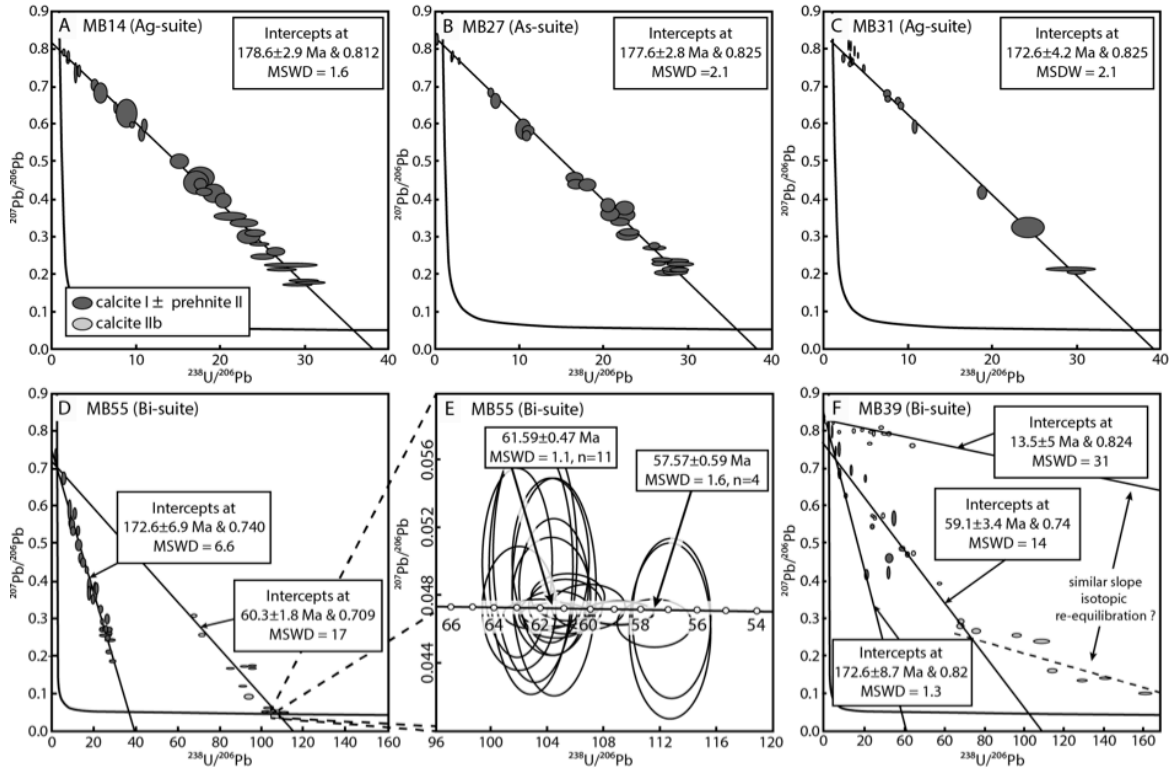
A MB14 (Ag-suite)
Intercepts at
178.6±2.9 Ma & 0.812
MSWD = 1.6
calcite I ± prehnite II
calcite IIb
B MB27 (As-suite)
Intercepts at
177.6±2.8 Ma & 0.825
MSWD =2.1
C MB31 (Ag-suite)
Intercepts at
172.6±4.2 Ma & 0.825
MSDW = 2.1
D MB55 (Bi-suite)
Intercepts at
172.6±6.9 Ma & 0.740
MSWD = 6.6
Intercepts at
60.3±1.8 Ma & 0.709
MSWD = 17
E MB55 (Bi-suite)
61.59±0.47 Ma
MSWD = 1.1, n=11
57.57±0.59 Ma
MSWD = 1.6, n=4
F MB39 (Bi-suite)
Intercepts at
13.5±5 Ma & 0.824
MSWD = 31
Intercepts at
59.1±3.4 Ma & 0.74
MSWD = 14
similar slope
isotopic
re-equilibration ?
Intercepts at
172.6±8.7 Ma & 0.82
MSWD = 1.3
207Pb/206Pb
238U/206Pb

Figure 5

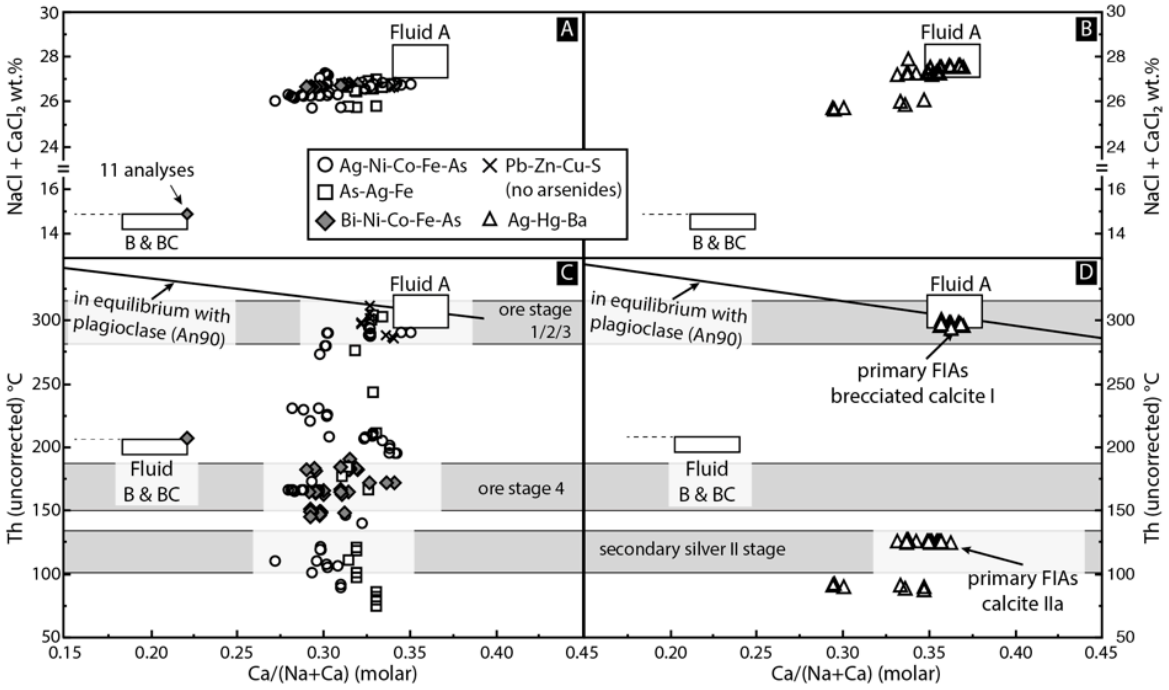
A
B
C
D
Fluid A
B & BC
11 analyses
Ag-Ni-Co-Fe-As
As-Ag-Fe
Bi-Ni-Co-Fe-As
Pb-Zn-Cu-S
(no arsenides)
Ag-Hg-Ba
NaCl + CaCl2 wt.%
Th (uncorrected) °C
Ca/(Na+Ca) (molar)
in equilibrium with
plagioclase (An90)
ore stage
1/2/3
ore stage 4
Fluid
B & BC
primary FIAs
brecciated calcite I
secondary silver II stage
primary FIAs
calcite IIa

Figure 6

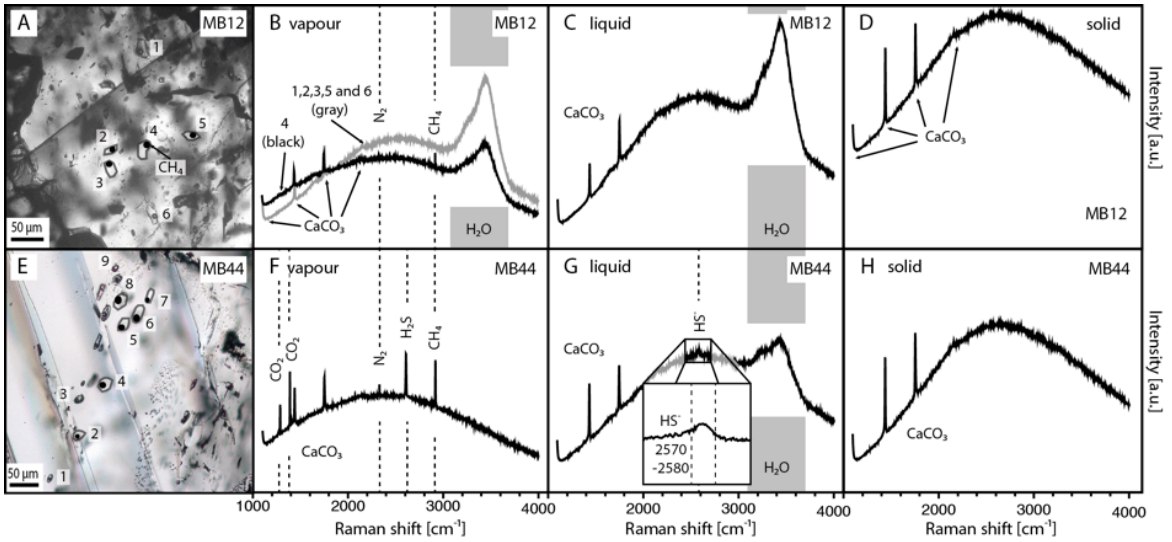
A
MB12
50 µm
CH4
B vapour
MB12
1,2,3,5 and 6
(gray)
4
(black)
N2
CH4
CaCO3
H2O
C liquid
MB12
CaCO3
H2O
D
solid
CaCO3
MB12
Intensity [a.u.]
E
MB44
50 µm
F vapour
MB44
CO2
CO2
N2
H2S
CH4
CaCO3
G liquid
MB44
HS-
CaCO3
HS-
2570
-2580
H2O
H solid
MB44
CaCO3
Intensity [a.u.]
1000
2000
3000
4000
Raman shift [cm-1]
Raman shift [cm-1]
Raman shift [cm-1]

Figure 7

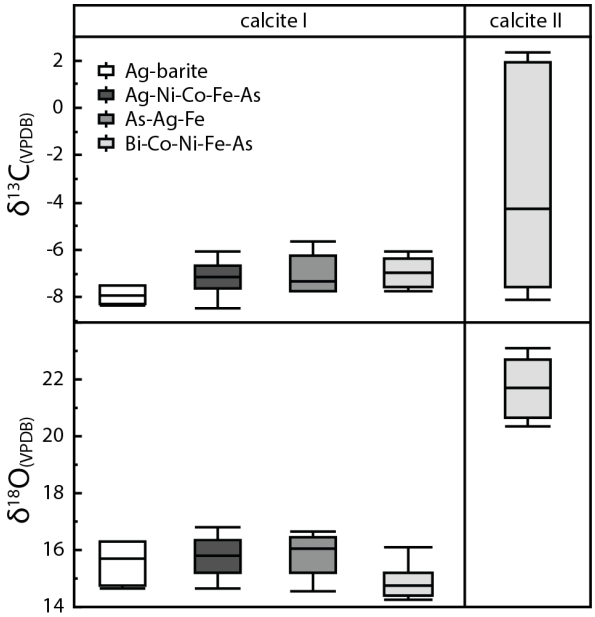
calcite I
calcite II
Ag-barite
Ag-Ni-Co-Fe-As
As-Ag-Fe
Bi-Co-Ni-Fe-As
δ13C(VPDB)
δ18O(VPDB)
2
0
-2
-4
-6
-8
22
20
18
16
14

Figure 8

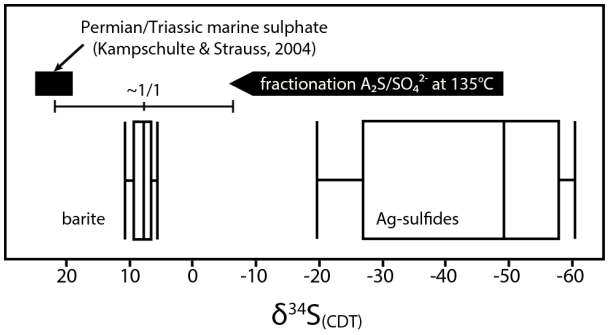
Permian/Triassic marine sulphate
(Kampschulte & Strauss, 2004)
~1/1
fractionation A_2S/SO_4^{2-} at 135°C
barite
Ag-sulfides
20
10
0
-10
-20
-30
-40
-50
-60
$\delta^{34}S_{(CDT)}$

Figure 9

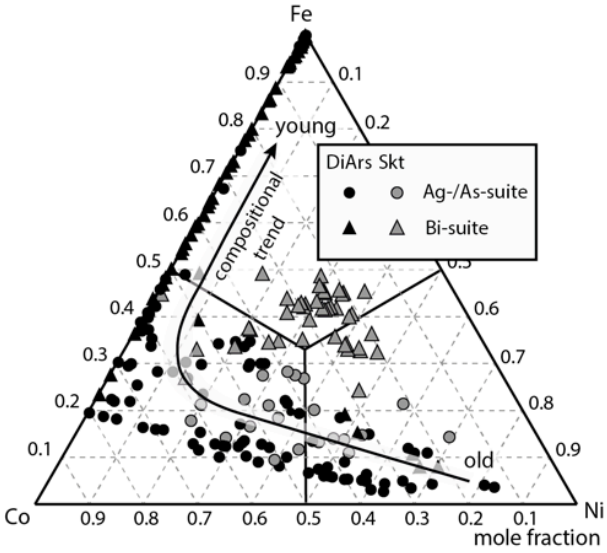
Fe
Co
Ni
mole fraction
young
old
compositional trend
DiArs Skt
Ag-/As-suite
Bi-suite
0.9
0.8
0.7
0.6
0.5
0.4
0.3
0.2
0.1

Figure 10

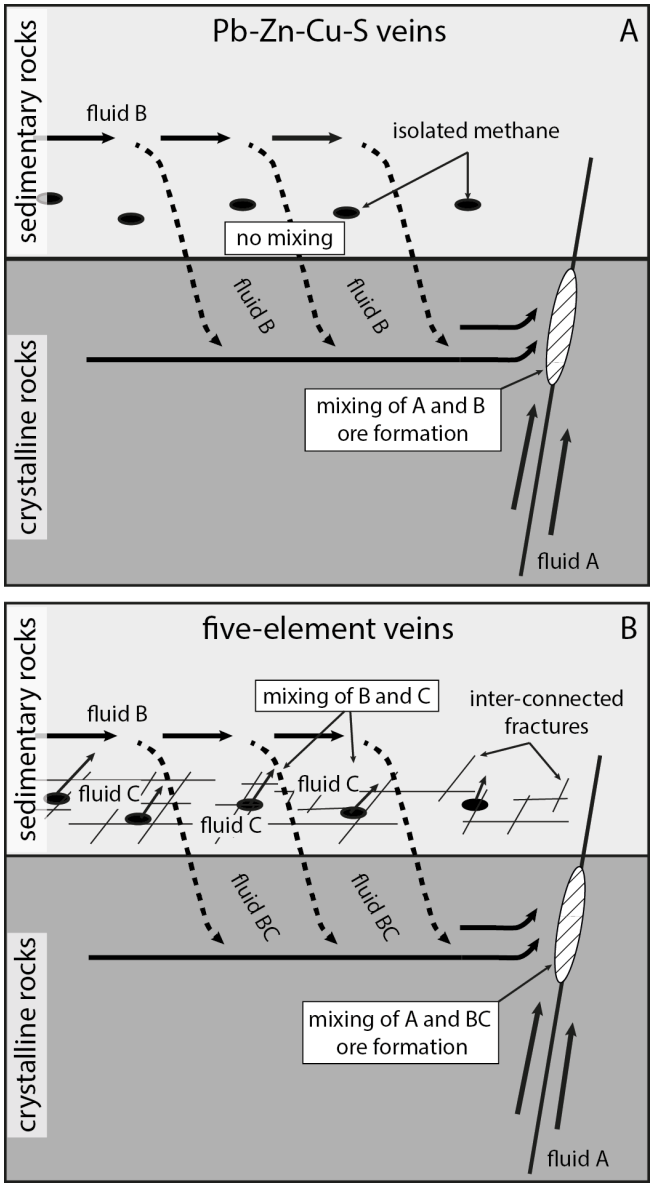
Pb-Zn-Cu-S veins
A
sedimentary rocks
fluid B
isolated methane
no mixing
fluid B
fluid B
crystalline rocks
mixing of A and B
ore formation
fluid A
five-element veins
B
sedimentary rocks
mixing of B and C
inter-connected
fractures
fluid B
fluid C
fluid C
fluid C
fluid BC
fluid BC
crystalline rocks
mixing of A and BC
ore formation
fluid A

1502 Figure 11

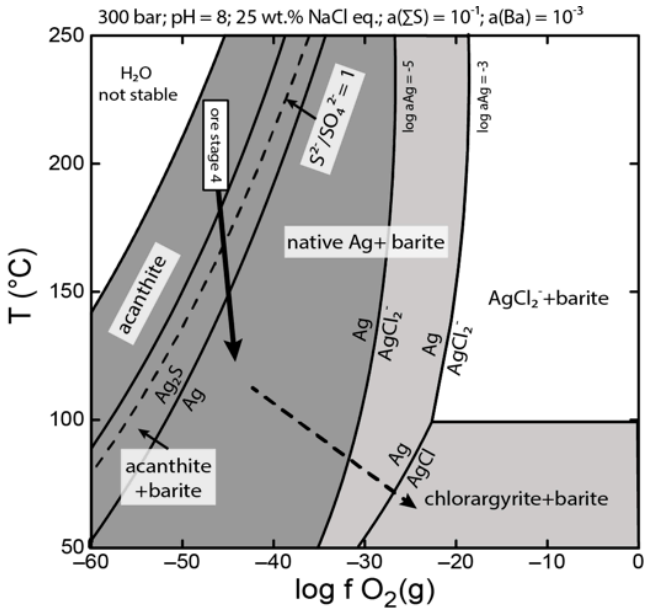

1503

Highlights

- Methane as the key parameter for the formation of five-element assemblages
- Refined genetic model of five-element veins
- Source of involved fluid components
- U-Pb age dating of calcite and prehnite applied to hydrothermal ore deposits
- Cooling related late-stage Ag-Hg enrichment

Location	Quarry	Vein type	Mineral assemblage
Nieder-Ramstadt	Wingertsberg	Ag-Ni-Co-Fe-As	native Ag, rammelsbergite, safflorite, loellingite, skutterudite, galena, chalcopyrite, sphalerite, acanthite, pearceite, tennantite, calcite, prehnite, chlorite
Nieder-Beerbach	Glasberg	Ag-Ni-Co-Fe-As	native Ag, rammelsbergite, safflorite, loellingite, skutterudite, galena, chalcopyrite, sphalerite, acanthite, pearceite, billingsleyite, tennantite, calcite, prehnite, chlorite
Nieder-Beerbach	Glasberg	As-Ag-Fe	native As, native Ag, loellingite, proustite, pearceite, galena, sphalerite, chalcopyrite
Nieder-Beerbach	Glasberg	Ag-Hg-barite	native Ag (amalgam), galena, acanthite, chlorargyrite, barite, calcite, quartz
Waschenbach	Waschenbach	Ag-Hg -barite	native Ag (amalgam), galena, acanthite, chlorargyrite, barite, calcite, quartz, clay minerals
Mackenheim	"Viadukt"	Bi-Ni-Co-Fe-As	native Bi, rammelsbergite, skutterudite, safflorite, loellingite, bismuthinite, aikinite, chalcopyrite, pyrite, (galena), quartz, calcite

Location	MH	NB
Vein type	Bi-Co-Ni-Fe-As	Ag-Ni-Co-Fe-As
Sampe	MB39	MB12
Mineral	calcite I	calcite I
Salinity (average) wt.%	26.7	26.7
Dilution factor	4337	20192
Li	89	40
Na	74571	54497
K	5077	5285
Mg	3292	3592
Ca	-	-
Ba	95	1770
F	373	783
Cl	161964	161964
Br	1668	1954
P	<43	<200
S	734	546
Mn	470	156
Fe	108	133
Co	85	64
Ni	73	164
Cu	<5	<20
Zn	11	44
As	4053	5486
Rb	26	<20
Sr	1398	4144
Pb	37	44
Bi	<5	<20
Th	14	44
U	43	<20

All elements given as mg/kg

Calcium is not given, since it is a major constituent in the host mineral

Lacation	Vein type	Sample	Mineral	$\delta^{13}C$ (VPDB)	$\delta^{18}O$ (VPDB)
MH	Bi-Ni-Co-Fe-As	MB 102	calcite I	-6.8	14.3
MH	Bi-Ni-Co-Fe-As	MB 39	calcite I	-7.5	15.1
MH	Bi-Ni-Co-Fe-As	MB 39	calcite I	-7.1	15.0
MH	Bi-Ni-Co-Fe-As	MB 41	calcite I	-7.7	15.3
MH	Bi-Ni-Co-Fe-As	MB 42	calcite I	-6.8	15.4
MH	Bi-Ni-Co-Fe-As	MB 44	calcite I	7.6	24.2
MH	Bi-Ni-Co-Fe-As	MB 45	calcite I	-7.5	14.9
MH	Bi-Ni-Co-Fe-As	MB 45	calcite I	-7.4	15.2
MH	Bi-Ni-Co-Fe-As	MB 46	calcite I	-6.2	14.3
MH	Bi-Ni-Co-Fe-As	MB 48	calcite I	-6.1	14.4
MH	Bi-Ni-Co-Fe-As	MB 49	calcite I	-6.4	14.2
MH	Bi-Ni-Co-Fe-As	MB 50	calcite I	-6.2	14.4
MH	Bi-Ni-Co-Fe-As	MB 53	calcite I	-6.3	14.2
MH	Bi-Ni-Co-Fe-As	MB 54	calcite I	-6.3	14.7
MH	Bi-Ni-Co-Fe-As	MB 55	calcite I	-7.4	14.9
MH	Bi-Ni-Co-Fe-As	MB 55	calcite I	-7.2	15.3
MH	Bi-Ni-Co-Fe-As	MB 56	calcite I	-6.3	14.5
MH	Bi-Ni-Co-Fe-As	MB 57	calcite I	-6.2	14.4
MH	Bi-Ni-Co-Fe-As	MB 77	calcite I	-7.6	14.7
MH	Bi-Ni-Co-Fe-As	MB 78	calcite I	-7.6	16.1
MH	Bi-Ni-Co-Fe-As	MB 99	calcite I	-6.4	14.9
MH	Bi-Ni-Co-Fe-As	MB 100	calcite I	-7.7	14.6
MH	Bi-Ni-Co-Fe-As	MB 101	calcite I	-6.3	15.7
MH	Bi-Ni-Co-Fe-As	MB 39	calcite II	2.4	20.7
MH	Bi-Ni-Co-Fe-As	MB 39	calcite II	1.8	20.4
MH	Bi-Ni-Co-Fe-As	MB 41	calcite II	-7.2	23.1
MH	Bi-Ni-Co-Fe-As	MB 45	calcite II	-7.4	22.6
MH	Bi-Ni-Co-Fe-As	MB 55	calcite II	-1.3	20.9
MH	Bi-Ni-Co-Fe-As	MB 77	calcite II	-8.1	22.5
NB	Ag-Hg-barite	MB 15	calcite I	-7.6	14.6
NB	Ag-Hg-barite	MB 16	calcite I	-8.2	16.3
NB	Ag-Hg-barite	MB 30	calcite I	-8.3	16.3
NB	Ag-Hg-barite	MB 59	calcite I	-7.5	15.1
NB	Ag-Ni-Co-Fe-As	MB 14	calcite I	-7.0	15.7
NB	Ag-Ni-Co-Fe-As	MB 14	calcite I	-7.0	16.8
NB	Ag-Ni-Co-Fe-As	MB 20	calcite I	-7.1	15.1
NB	Ag-Ni-Co-Fe-As	MB 24	calcite I	-6.0	15.8
NB	Ag-Ni-Co-Fe-As	MB 31	calcite I	-6.7	15.6
NB	Ag-Ni-Co-Fe-As	MB 36	calcite I	-7.5	16.4
NB	Ag-Ni-Co-Fe-As	MB 37	calcite I	-7.5	16.6
NB	Ag-Ni-Co-Fe-As	MB 58	calcite I	-6.1	15.8
NB	Ag-Ni-Co-Fe-As	MB 67	calcite I	-7.6	15.2
NB	Ag-Ni-Co-Fe-As	MB 73	calcite I	-8.4	14.6
NB	Ag-Ni-Co-Fe-As	MB 12	calcite I	-7.7	14.4
NB	Ag-Ni-Co-Fe-As	MB 12	calcite I	-7.7	14.8
NB	As-Ag-Fe	MB 26	calcite I	-7.5	16.6
NB	As-Ag-Fe	MB 27	calcite I	-6.5	16.4
NB	As-Ag-Fe	MB 27	calcite I	-7.7	15.4
NB	As-Ag-Fe	MB 61	calcite I	-5.7	15.8
NB	As-Ag-Fe	MB 74	calcite I	-7.2	16.3
NB	As-Ag-Fe	MB 86	calcite I	-7.7	14.6

Location	Mineral	Sample	Vein type	$\delta^{34}S$ (‰ CDT)
NB	barite	MB15	Ag-Hg-barite	5.5
NB	barite	MB16	Ag-Hg-barite	7.7
NB	barite	MB16	Ag-Hg-barite	10.7
NB	barite	MB22	Ag-Hg-barite	7.9
NB	barite	MB30	Ag-Hg-barite	6.9
NB	barite	MB32	Ag-Hg-barite	6.6
NB	barite	MB59	Ag-Hg-barite	9.3
MH	galena	MB64	Bi-Ni-Co-Fe-As	-41.5
NB	galena	MB12	Ag-Ni-Co-Fe-As	-44.7
NB	pearceite	MB74	Ag-Ni-Co-Fe-As	-50.0
NB	proustite	MB80	As-Ag-Fe	-48.5
NB	acanthite	MB17	Ag-Ni-Co-Fe-As	-19.7
NB	acanthite	MB82	Ag-Ni-Co-Fe-As	-60.5

Location	NB			NB			NB			MH		
Mineral	native As			native Ag I			native Ag II			native Bi		
Number of analyses	8			74			13			77		
	Min	Max	Mean	Min	Max	Mean	Min	Max	Mean	Min	Max	Mean
Se	0.17	0.42	0.31	0.00	0.00	0.00	0.00	0.00	0.00	0.00	0.06	0.02
S	0.00	0.01	0.00	0.00	0.08	0.02	0.02	0.19	0.08	0.00	0.02	0.00
Bi	0.00	0.06	0.01	0.00	0.16	0.05	0.00	0.14	0.04	97.14	100.69	99.43
Ag	0.00	0.07	0.02	95.38	97.81	96.99	69.83	89.34	83.40	0.00	0.01	0.00
As	97.68	99.16	98.46	0.27	2.74	1.34	0.00	0.08	0.02	0.00	2.79	0.58
Zn	0.00	0.01	0.00	0.00	0.02	0.00	0.00	0.00	0.00	0.00	0.02	0.00
Sb	0.14	2.25	0.71	0.11	0.60	0.42	0.00	0.00	0.00	0.00	0.05	0.00
Hg	0.00	0.00	0.00	0.98	2.56	1.21	11.40	29.50	16.37	0.00	0.07	0.01
Co	0.00	0.02	0.00	0.00	0.22	0.04	0.00	0.05	0.02	0.00	0.37	0.03
Cu	0.00	0.58	0.09	0.00	0.47	0.04	0.00	0.05	0.01	0.00	0.00	0.00
Fe	0.00	0.01	0.00	0.00	0.18	0.03	0.00	0.01	0.00	0.00	0.89	0.03
Ni	0.00	0.04	0.00	0.00	0.95	0.09	0.00	0.01	0.00	0.00	0.13	0.01
Te	0.00	0.00	0.00	0.22	0.30	0.27	0.00	0.00	0.00	0.00	0.01	0.00
Total	98.44	101.76	99.60	98.84	102.03	100.52	98.54	101.31	99.99	98.42	101.90	100.12

ction limit; all analyses are given as wt.%

eder-Beerbach; MH = Mackenheim

Location	MH			MH			MH			MH		
Mineral	loellingite			rammelsbergite			safflorite			skutterudite		
Number of analyses	32			8			31			41		
	Mean	Min	Max	Mean	Min	Max	Mean	Min	Max	Mean	Min	Max
Fe	25.65	22.75	27.48	2.90	2.17	4.30	16.68	5.11	26.89	7.55	4.89	9.18
Co	0.72	0.03	3.74	7.53	6.24	9.71	10.02	0.04	21.87	5.97	3.32	12.32
Ni	0.02	0.00	0.13	18.17	15.29	20.19	0.55	0.00	13.22	6.35	0.19	10.12
Cu	0.67	0.01	2.11	0.08	0.04	0.12	0.57	0.04	1.35	0.68	0.02	1.90
Zn	0.00	0.00	0.02	0.00	0.00	0.00	0.00	0.00	0.02	0.00	0.00	0.02
Hg	0.01	0.00	0.06	0.02	0.00	0.05	0.00	0.00	0.02	0.01	0.00	0.03
Ag	0.00	0.00	0.03	0.02	0.00	0.04	0.01	0.00	0.03	0.01	0.00	0.02
Bi	0.06	0.00	0.24	0.24	0.06	0.53	0.33	0.00	3.67	0.53	0.07	3.11
Te	0.00	0.00	0.01	0.01	0.00	0.02	0.00	0.00	0.01	0.00	0.00	0.02
As	71.59	70.09	73.89	64.57	62.31	66.72	70.77	67.67	73.31	78.60	77.14	80.11
Sb	0.02	0.00	0.06	0.00	0.00	0.00	0.00	0.00	0.04	0.00	0.00	0.01
S	0.46	0.05	1.63	4.52	2.65	6.61	0.57	0.09	2.70	0.52	0.27	1.42
Se	0.29	0.22	0.44	0.29	0.23	0.34	0.35	0.23	0.43	0.37	0.28	0.50
Total	99.48	98.03	101.90	98.35	98.15	98.88	99.85	98.18	102.02	100.57	98.01	101.99
X_{Fe}	0.97	0.87	1.00	0.11	0.08	0.15	0.63	0.19	1.00	0.39	0.24	0.49
X_{Co}	0.03	0.00	0.13	0.26	0.22	0.33	0.36	0.00	0.77	0.29	0.16	0.59
X_{Ni}	0.00	0.00	0.00	0.63	0.52	0.70	0.02	0.00	0.47	0.31	0.01	0.48

0 = below detection limit; all analyses are given as wt.%

NB = Nieder-Beerbach; MH = Mackenheim

Location	NB			NB			NB			NB		
Mineral	loellingite			rammelsbergite			safflorite			skutterudite		
Number of analyses	15			23			43			21		
	Mean	Min	Max	Mean	Min	Max	Mean	Min	Max	Mean	Min	Max
Fe	25.44	23.85	26.56	1.60	0.75	3.12	7.81	3.08	12.85	3.39	1.84	5.00
Co	0.26	0.00	1.71	9.52	3.60	12.76	15.25	10.45	20.74	8.30	3.37	12.33
Ni	0.02	0.00	0.18	16.30	10.86	22.17	3.54	0.02	10.59	7.79	3.59	14.22
Cu	1.48	0.44	3.20	0.47	0.20	1.15	1.80	0.78	2.83	1.62	0.21	3.50
Zn	0.00	0.00	0.02	0.02	0.00	0.14	0.00	0.00	0.04	0.00	0.00	0.07
Hg	0.01	0.00	0.04	0.00	0.00	0.04	0.01	0.00	0.06	0.02	0.00	0.23
Ag	0.05	0.00	0.57	0.03	0.00	0.26	0.03	0.00	0.20	0.04	0.00	0.25
Bi	0.03	0.00	0.14	0.11	0.00	0.27	0.08	0.00	0.19	0.05	0.00	0.15
Te	0.00	0.00	0.01	0.01	0.00	0.03	0.00	0.00	0.02	0.01	0.00	0.02
As	71.15	69.18	73.21	70.42	68.14	72.19	71.60	69.39	73.21	78.70	77.22	79.47
Sb	0.09	0.03	0.17	0.00	0.00	0.03	0.00	0.00	0.00	0.00	0.00	0.00
S	0.78	0.07	1.78	0.92	0.06	1.87	0.23	0.02	0.95	0.31	0.03	1.09
Se	0.33	0.24	0.42	0.38	0.28	0.44	0.37	0.26	0.46	0.40	0.31	0.48
Total	99.65	98.22	101.27	99.78	98.04	101.21	100.72	98.56	101.51	100.64	99.04	101.46
X_{Fe}	0.99	0.93	1.00	0.06	0.03	0.13	0.30	0.12	0.49	0.18	0.09	0.28
X_{Co}	0.01	0.00	0.06	0.34	0.13	0.46	0.56	0.42	0.76	0.42	0.16	0.62
X_{Ni}	0.00	0.00	0.01	0.59	0.44	0.83	0.13	0.00	0.39	0.39	0.20	0.69

0 = below detection limit; all analyses are given as wt.%

NB = Nieder-Beerbach; MH = Mackenheim

Location	MH			NB			NB			NB			NB			NB		
Mineral	tennantite			acanthite			billingsleyite			pearceite			proustite			tennantite		
Number of analyses	16			9			5			4			8			4		
	Mean	Min	Max	Mean	Min	Max	Mean	Min	Max	Mean	Min	Max	Mean	Min	Max	Mean	Min	Max
Se	0.04	0.00	0.11	0.01	0.00	0.05	0.03	0.00	0.06	0.00	0.00	0.00	0.06	0.00	0.13	0.06	0.05	0.13
S	26.46	25.53	27.12	13.22	12.89	13.74	17.49	17.45	17.53	15.79	15.73	15.85	19.59	19.41	19.87	29.45	29.27	29.63
Bi	5.94	1.94	9.90	0.06	0.00	0.14	0.00	0.00	0.00	0.00	0.00	0.00	0.07	0.00	0.30	0.01	0.00	5.94
Ag	0.44	0.24	0.67	84.53	83.57	86.68	70.54	69.41	71.67	74.52	74.42	74.61	65.31	64.22	66.36	0.10	0.07	66.11
As	9.69	2.92	12.69	0.67	0.04	0.99	10.41	7.78	13.04	6.89	6.85	6.93	13.60	13.02	14.53	22.47	22.30	22.63
Zn	3.04	2.54	4.29	0.00	0.00	0.01	0.01	0.01	0.01	0.00	0.00	0.00	0.01	0.00	0.04	0.32	0.21	3.04
Sb	12.11	5.82	23.67	0.01	0.00	0.04	1.54	0.21	2.87	0.00	0.00	0.00	0.45	0.10	1.13	0.36	0.27	12.11
Hg	0.03	0.00	0.06	0.04	0.00	0.09	0.01	0.00	0.01	0.00	0.00	0.01	0.05	0.00	0.13	0.03	0.03	0.13
Co	0.09	0.00	0.75	0.03	0.01	0.04	0.00	0.00	0.01	0.00	0.00	0.00	0.00	0.00	0.02	0.00	0.00	0.09
Cu	38.83	37.45	40.01	0.10	0.03	0.22	0.16	0.02	0.31	1.32	1.26	1.38	0.05	0.00	0.15	39.04	38.88	39.20
Fe	4.21	3.09	4.59	0.04	0.00	0.08	0.16	0.09	0.24	0.00	0.00	0.00	0.07	0.00	0.44	6.92	6.63	7.21
Ni	0.00	0.00	0.01	0.03	0.00	0.04	0.00	0.00	0.01	0.00	0.00	0.00	0.00	0.00	0.02	0.00	0.00	0.01
Te	0.00	0.00	0.00	0.06	0.00	0.23	0.19	0.19	0.19	0.21	0.20	0.22	0.00	0.00	0.00	0.00	0.00	0.00
Total	100.89	100.30	101.58	98.82	97.99	100.00	100.54	100.22	100.86	98.77	98.77	98.78	99.28	98.40	100.08	98.75	98.65	100.89

0 = below detection limit; all elements are given as wt.%

NB = Nieder-Beerbach; MH = Mackenheim

Table A1.1

Vein type	Sample	Mineral	Analysis	Spot size (μm)	^{206}Pb (cps)	U (mg/kg)	Pb (mg/kg)	Th/U	^{238}U/^{206}Pb	±2s (%)	^{207}Pb/^{206}Pb	±2s (%)
Ag-Ni-Co-Fe-As	MB14	calcite I	A305	213	85843	5.9	0.45	0	23.95	3.7	0.309	2
Ag-Ni-Co-Fe-As	MB14	calcite I	A306	213	183889	6	1.49	0	11	2.9	0.595	2.4
Ag-Ni-Co-Fe-As	MB14	calcite I	A307	213	119483	1.1	1.16	0	2.88	6.6	0.735	3
Ag-Ni-Co-Fe-As	MB14	calcite I	A309	213	464886	2.3	4.95	0	1.48	9.1	0.789	1.1
Ag-Ni-Co-Fe-As	MB14	calcite I	A310	213	102159	2.9	0.82	0	9.5	3.4	0.597	1.3
Ag-Ni-Co-Fe-As	MB14	calcite I	A311	213	52148	1.2	0.46	0	7.58	3.1	0.642	1.8
Ag-Ni-Co-Fe-As	MB14	calcite I	A312	213	120971	3.1	0.9	0	9.09	4.3	0.56	3.3
Ag-Ni-Co-Fe-As	MB14	calcite I	A313	213	157035	7.1	1.13	0	15.17	5.8	0.5	3.2
Ag-Ni-Co-Fe-As	MB14	calcite I	A314	213	231094	7.9	1.67	0	9.95	11	0.446	6.9
Ag-Ni-Co-Fe-As	MB14	calcite I	A315	213	168984	3.4	1.14	0	6.3	8.1	0.422	3.5
Ag-Ni-Co-Fe-As	MB14	calcite I	A316	213	103861	2.8	0.86	0	8.89	11.1	0.627	4.9
Ag-Ni-Co-Fe-As	MB14	calcite I	A317	213	140300	0.8	1.31	0	2	5.9	0.78	1.5
Ag-Ni-Co-Fe-As	MB14	calcite I	A318	213	145037	2.5	1.07	0	5.87	3.2	0.526	2.8
Ag-Ni-Co-Fe-As	MB14	calcite I	A319	213	32976	2	0.22	0	19.22	5.4	0.414	4.9
Ag-Ni-Co-Fe-As	MB14	calcite I	A320	213	104340	6.8	0.63	0	21.13	7.5	0.353	2.1
Ag-Ni-Co-Fe-As	MB14	calcite I	A321	213	869707	13.7	8.25	0	5.1	8	0.702	1.9
Ag-Ni-Co-Fe-As	MB14	calcite I	A322	213	196927	6.3	1.57	0	10.69	3	0.573	2.7
Ag-Ni-Co-Fe-As	MB14	calcite I	A323	213	239436	6.7	1.93	0	9.29	3.5	0.576	1.8
Ag-Ni-Co-Fe-As	MB14	calcite I	A324	213	271694	5.6	2.59	0	5.88	10.8	0.681	3.3
Ag-Ni-Co-Fe-As	MB14	calcite I	A325	213	229443	12.6	1.21	0	18.46	5.4	0.302	3.5
Ag-Ni-Co-Fe-As	MB14	calcite I	A326	213	94852	1.2	0.84	0	4.26	9	0.657	1.8
Ag-Ni-Co-Fe-As	MB14	calcite I	A327	213	301116	1.9	3.06	0	1.96	7.3	0.768	1
Ag-Ni-Co-Fe-As	MB14	calcite I	A333	213	34504	1.8	0.23	0	17.07	7	0.442	5.8
Ag-Ni-Co-Fe-As	MB14	calcite I	A334	213	507953	41.5	2.3	0	27.31	5.3	0.211	1.3
Ag-Ni-Co-Fe-As	MB14	calcite I	A335	213	65661	3.5	0.44	0	17.64	3.6	0.439	3.2
Ag-Ni-Co-Fe-As	MB14	calcite I	A336	213	188518	14.8	1.02	0	26.07	3.5	0.305	3.7
Ag-Ni-Co-Fe-As	MB14	calcite I	A337	213	205479	19.9	0.95	0	32.14	3.3	0.22	1.5

Table A1.2

Vein type	Sample	Mineral	Analysis	Spot size (μm)	^{206}Pb (cps)	U (mg/kg)	Pb (mg/kg)	Th/U	^{238}U/^{206}Pb	±2s (%)	^{207}Pb/^{206}Pb	±2s (%)
Ag-Ni-Co-Fe-As	MB14	calcite I	A338	213	160472	11.3	0.78	0	23.12	6.5	0.237	2
Ag-Ni-Co-Fe-As	MB14	calcite I	A339	213	629885	53.9	2.52	0	29.83	4.6	0.181	2
Ag-Ni-Co-Fe-As	MB14	calcite I	A340	213	516505	47.4	2.15	0	30.86	3.8	0.176	1.1
Ag-Ni-Co-Fe-As	MB14	calcite I	A341	213	46509	2.5	0.32	0	17.64	7.7	0.455	5.2
Ag-Ni-Co-Fe-As	MB14	calcite I	A342	213	169581	15.3	0.82	0	28.3	9	0.221	2.3
Ag-Ni-Co-Fe-As	MB14	calcite I	A343	213	219280	22.7	1.08	0	31.67	4.3	0.203	1.6
Ag-Ni-Co-Fe-As	MB14	calcite I	A344	213	149910	11.2	0.78	0	24.63	3.6	0.279	1.3
Ag-Ni-Co-Fe-As	MB14	calcite I	A345	213	227199	23.8	1.01	0	36.54	4.9	0.218	1.9
Ag-Ni-Co-Fe-As	MB14	calcite I	A346	213	31750	1.8	0.21	0	18.06	4.4	0.418	1.7
Ag-Ni-Co-Fe-As	MB14	calcite I	A347	213	30248	0.3	0.3	0	3.33	6.4	0.743	1.4
Ag-Ni-Co-Fe-As	MB14	calcite I	A348	213	153635	13.3	0.81	0	26.59	3.5	0.259	4
Ag-Ni-Co-Fe-As	MB14	calcite I	A349	213	918109	85.1	4.05	0	29.05	4.5	0.171	2.1
Ag-Ni-Co-Fe-As	MB14	calcite I	A350	213	72876	7.1	0.33	0	40.48	4.4	0.283	2.6
Ag-Ni-Co-Fe-As	MB14	calcite I	A351	213	157318	12.1	0.86	0	23.41	4.9	0.299	5.5
Ag-Ni-Co-Fe-As	MB14	calcite I	A352	213	112840	7.3	0.63	0	22.59	5	0.335	2.2
Ag-Ni-Co-Fe-As	MB14	calcite I	A353	213	321172	20.8	1.34	0	24.99	4.7	0.245	2.8
Ag-Ni-Co-Fe-As	MB14	calcite I	A354	213	68787	3.4	0.44	0	15.85	3.9	0.38	3.1
Ag-Ni-Co-Fe-As	MB14	calcite I	A355	213	58935	2.3	0.29	0	15.92	3.5	0.322	3
Ag-Ni-Co-Fe-As	MB14	calcite I	A356	213	21929	1.8	0.13	0	26.16	3	0.346	3
Ag-Ni-Co-Fe-As	MB14	calcite I	A357	213	259581	17.7	1.25	0	20.16	3.8	0.223	4.9
Ag-Ni-Co-Fe-As	MB14	calcite I	A358	213	38053	2.4	0.25	0	20.31	3.7	0.397	3.9
Ag-Ni-Co-Fe-As	MB14	calcite I	A363	143	232466	179.4	2.15	0	114.22	2.1	0.162	2.6
Ag-Ni-Co-Fe-As	MB14	calcite I	A366	143	328577	243.3	3.73	0	108.9	3.6	0.24	2
Ag-Ni-Co-Fe-As	MB14	calcite I	A367	143	247922	162.5	2.85	0	96.25	2.3	0.256	1.9
Ag-Ni-Co-Fe-As	MB14	calcite I	A369	143	135726	58.7	1.42	0	75.91	3	0.268	1.8
Ag-Ni-Co-Fe-As	MB14	calcite I	A370	213	98073	17.5	1.84	0	25.49	2.1	0.572	1.2
Ag-Ni-Co-Fe-As	MB14	calcite I	A371	213	79662	5.8	0.65	0	24.09	2.1	0.575	1.2

Table A1.3

Vein type	Sample	Mineral	Analysis	Spot size (μm)	^{206}Pb (cps)	U (mg/kg)	Pb (mg/kg)	Th/U	$^{238}U/^{206}Pb$	±2s (%)	$^{207}Pb/^{206}Pb$	±2s (%)
Ag-Ni-Co-Fe-As	MB14	calcite I	A372	213	73215	5.4	0.61	0	24.02	2.1	0.576	1
Ag-Ni-Co-Fe-As	MB14	calcite I	A373	213	109479	9.1	0.87	0	29.46	2.1	0.576	1.1
Ag-Ni-Co-Fe-As	MB14	calcite I	A374	213	84098	9.8	0.63	0	38.32	2.2	0.487	1.2
Ag-Ni-Co-Fe-As	MB14	calcite I	A375	213	127302	22.5	0.83	0	57.77	2	0.394	1
Ag-Ni-Co-Fe-As	MB14	calcite I	A376	213	90711	7.1	0.75	0	25.5	2.1	0.569	0.9
As-Ag-Fe	MB27	calcite I	A183	213	108552	6.2	0.57	0	21.92	4.5	0.346	2.4
As-Ag-Fe	MB27	calcite I	A184	213	38368	2.4	0.21	0	22.2	5.4	0.36	4.7
As-Ag-Fe	MB27	calcite I	A185	213	656259	5.1	6.15	0	2.72	4.6	0.773	0.9
As-Ag-Fe	MB27	calcite I	A186	213	75113	5	0.33	0	25.98	4.2	0.272	2.5
As-Ag-Fe	MB27	calcite I	A187	213	83424	6.4	0.35	0	28.16	4.1	0.217	1.6
As-Ag-Fe	MB27	calcite I	A188	213	46053	3.1	0.21	0	26.05	2.5	0.276	2.2
As-Ag-Fe	MB27	calcite I	A189	213	190710	5	1.31	0	10.75	4.1	0.575	2.1
As-Ag-Fe	MB27	calcite I	A191	213	104321	8.4	0.46	0	29	4.1	0.229	1.9
As-Ag-Fe	MB27	calcite I	A192	213	110114	8.8	0.49	0	28.47	4.8	0.237	2.4
As-Ag-Fe	MB27	calcite I	A193	213	277342	22	1.15	0	27.9	5.7	0.205	3.4
As-Ag-Fe	MB27	calcite I	A199	213	318091	24.1	1.23	0	28.68	3.7	0.211	4.2
As-Ag-Fe	MB27	calcite I	A200	213	246124	20.7	1.08	0	28.06	4.9	0.207	1.5
As-Ag-Fe	MB27	calcite I	A201	213	109246	7.3	0.44	0	26.53	2.8	0.23	1.6
As-Ag-Fe	MB27	calcite I	A202	213	70856	4.4	0.35	0	23.03	4	0.313	2.1
As-Ag-Fe	MB27	calcite I	A203	213	30764	1.9	0.17	0	22.45	4.6	0.372	5.1
As-Ag-Fe	MB27	calcite I	A204	213	64707	3.7	0.37	0	20.56	4.4	0.363	4
As-Ag-Fe	MB27	calcite I	A205	213	43537	1.4	0.2	0	16.61	5	0.443	2
As-Ag-Fe	MB27	calcite I	A206	213	64596	3.7	0.38	0	20.51	3.5	0.385	3.9
As-Ag-Fe	MB27	calcite I	A207	213	39623	2.5	0.2	0	22.77	4.8	0.307	3.6
As-Ag-Fe	MB27	calcite I	A208	213	54719	1.1	0.33	0	10.9	5.5	0.586	2.2
As-Ag-Fe	MB27	calcite I	A209	213	34980	1.7	0.23	0	16.42	4.7	0.459	2.6
As-Ag-Fe	MB27	calcite I	A210	213	30275	1.3	0.17	0	17.99	4.5	0.441	3

Table A1.4

Vein type	Sample	Mineral	Analysis	Spot size (μm)	^{206}Pb (cps)	U (mg/kg)	Pb (mg/kg)	Th/U	^{238}U/^{206}Pb	±2s (%)	^{207}Pb/^{206}Pb	±2s (%)
As-Ag-Fe	MB27	calcite I	A213	213	116840	2.2	1.01	0	6.49	5	0.689	1.4
As-Ag-Fe	MB27	calcite I	A221	213	44873	1.1	0.31	0	10.37	7.1	0.589	3.8
As-Ag-Fe	MB27	calcite I	A222	213	83711	5.9	0.36	0	26.86	3.6	0.241	2.4
As-Ag-Fe	MB27	calcite I	A223	213	131977	0.7	1.26	0	1.89	4.3	0.785	1.1
As-Ag-Fe	MB27	calcite I	A224	213	2064276	0.3	20.71	0	0.05	3.2	0.835	0.9
As-Ag-Fe	MB27	calcite I	A225	213	758433	4.3	7.31	0	1.98	4.2	0.79	0.8
As-Ag-Fe	MB27	calcite I	A226	213	2380731	0.8	24.68	0	0.11	11.5	0.836	0.7
As-Ag-Fe	MB27	calcite I	A227	213	48940	1	0.42	0	7.07	6.7	0.666	2.4
Ag-Ni-Co-Fe-As	MB31	calcite I	A244	213	126322	5.2	0.83	0	15.25	3.2	0.477	2.6
Ag-Ni-Co-Fe-As	MB31	calcite I	A250	213	16084	0.7	0.09	0	14.42	6.3	0.351	3.3
Ag-Ni-Co-Fe-As	MB31	calcite I	A251	213	45305	1.8	0.26	0	13.88	4.5	0.374	2.4
Ag-Ni-Co-Fe-As	MB31	calcite I	A252	213	46085	3.5	0.22	0	27.84	3.6	0.278	2.2
Ag-Ni-Co-Fe-As	MB31	calcite I	A253	213	93016	1.3	0.82	0	4.85	2.3	0.699	1.2
Ag-Ni-Co-Fe-As	MB31	calcite I	A254	213	93818	0.8	0.85	0	2.88	2.6	0.739	1.1
Ag-Ni-Co-Fe-As	MB31	calcite I	A255	213	156168	0.6	1.55	0	1.31	2.9	0.801	0.9
Ag-Ni-Co-Fe-As	MB31	calcite I	A257	213	45202	4.4	0.21	0	32.39	4.2	0.232	2.2
Ag-Ni-Co-Fe-As	MB31	calcite I	A260	213	49263	5.9	0.22	0	46.81	6.2	0.247	2.8
Ag-Ni-Co-Fe-As	MB31	calcite I	A267	213	71479	0.7	0.68	0	3.37	2.1	0.75	1
Ag-Ni-Co-Fe-As	MB31	calcite I	A270	213	2290612	3.6	17.55	0	0.69	2.7	0.793	0.8
Ag-Ni-Co-Fe-As	MB31	calcite I	A272	213	2352627	4.1	16.88	0	0.82	2.7	0.775	1
Ag-Ni-Co-Fe-As	MB31	calcite I	A273	213	3491477	3	27.22	0	0.38	3.6	0.819	0.8
Ag-Ni-Co-Fe-As	MB31	calcite I	A277	213	1195730	2.9	8.91	0	1.07	2.6	0.763	1.1
Ag-Ni-Co-Fe-As	MB31	calcite I	A279	213	2013738	4.4	15.07	0	0.97	2.6	0.762	1.3
Ag-Ni-Co-Fe-As	MB31	calcite I	A280	213	452272	1.2	3.47	0	1.11	4.5	0.748	1.4
Ag-Ni-Co-Fe-As	MB31	calcite I	A281	213	414255	1.7	2.7	0	1.99	3.9	0.687	1.6
Ag-Ni-Co-Fe-As	MB31	calcite I	A282	213	992471	8.2	5.81	0	3.76	5.2	0.567	1.2
Ag-Ni-Co-Fe-As	MB31	calcite I	A288	213	825779	2.2	6.12	0	1.17	2.1	0.75	1.1

Table A1.6

Vein type	Sample	Mineral	Analysis	Spot size (μm)	^{206}Pb (cps)	U (mg/kg)	Pb (mg/kg)	Th/U	^{238}U/^{206}Pb	±2s (%)	^{207}Pb/^{206}Pb	±2s (%)
Ag-Ni-Co-Fe-As	MB31	prehnite II	A302	213	100150	2.3	0.9	0	7.54	4.9	0.678	1.4
Ag-Ni-Co-Fe-As	MB31	prehnite II	A303	213	166867	0.7	1.71	0	1.48	2.2	0.812	0.8
Ag-Ni-Co-Fe-As	MB31	prehnite II	A304	213	203633	2.2	2.16	0	3.1	5.9	0.761	1.1
Bi-Ni-Co-Fe-As	MB39	calcite I	A091	213	17318	1.5	0.15	0	26.31	3.1	0.533	2.1
Bi-Ni-Co-Fe-As	MB39	calcite I	A101	80	613855	301.1	42.8	0	22	6	0.724	1.4
Bi-Ni-Co-Fe-As	MB39	calcite I	A380	213	108678	3.5	0.93	0.01	10.73	3.9	0.628	1.1
Bi-Ni-Co-Fe-As	MB39	calcite I	A388	213	27210	0.6	0.24	0.02	7.54	10.3	0.687	1.8
Bi-Ni-Co-Fe-As	MB39	calcite I	A389	213	12203	0.1	0.13	0.03	3.53	9.1	0.799	2.1
Bi-Ni-Co-Fe-As	MB39	calcite I	A390	213	14907	0.3	0.14	0.01	5.68	4.5	0.747	1.8
Bi-Ni-Co-Fe-As	MB39	calcite I	A394	213	37255	2.7	0.27	0	20.77	3.8	0.416	3.4
Bi-Ni-Co-Fe-As	MB39	calcite I	A455	143	48854	1.6	0.07	0.05	71.82	4.4	0.789	0.7
Bi-Ni-Co-Fe-As	MB39	calcite I	A456	143	86684	0.6	0.13	0.14	16.31	4.7	0.813	0.6
Bi-Ni-Co-Fe-As	MB39	calcite I	A457	143	167017	3.1	0.25	0.04	43.23	2.4	0.778	0.4
Bi-Ni-Co-Fe-As	MB39	calcite I	A460	143	112481	2.2	0.17	0.04	42.64	3.4	0.789	0.8
Bi-Ni-Co-Fe-As	MB39	calcite I	A471	80	125292	0.1	0.65	0.68	0.67	10.3	0.823	0.5
Bi-Ni-Co-Fe-As	MB39	calcite I	A472	80	113089	0.1	0.58	0.33	0.38	13	0.838	0.6
Bi-Ni-Co-Fe-As	MB39	calcite I	A473	80	162936	0.1	0.83	0.09	0.6	9.2	0.837	0.4
Bi-Ni-Co-Fe-As	MB39	calcite I	A476	80	173820	1.3	0.8	0.01	5.5	4.9	0.776	1
Bi-Ni-Co-Fe-As	MB39	calcite I	A477	80	128290	1	0.59	0	5.45	3	0.784	0.8
Bi-Ni-Co-Fe-As	MB39	calcite I	A478	80	116708	0.2	0.55	0.02	1.56	4.1	0.82	0.4
Bi-Ni-Co-Fe-As	MB39	calcite I	A479	213	338270	0.2	0.23	0.09	2.34	6.4	0.816	0.6
Bi-Ni-Co-Fe-As	MB39	calcite I	A481	143	223290	0.2	0.32	0.01	1.93	4.1	0.817	0.4
Bi-Ni-Co-Fe-As	MB39	calcite I	A482	143	244992	0.1	0.5	0.03	0.61	14.9	0.828	0.5
Bi-Ni-Co-Fe-As	MB39	calcite I	A486	80	117288	0.7	0.24	0	4.34	6.2	0.198	1.5
Bi-Ni-Co-Fe-As	MB39	calcite I	A488	80	932255	17.1	1.88	0	11.66	9	0.152	1.2
Bi-Ni-Co-Fe-As	MB39	calcite I	A489	80	4067058	6	9.04	0	0.77	8.3	0.112	0.4
Bi-Ni-Co-Fe-As	MB39	calcite I	A90	213	15943	1.1	0.15	0	20.52	3.1	0.604	1.9

Table A1.5

Vein type	Sample	Mineral	Analysis	Spot size (μm)	^{206}Pb (cps)	U (mg/kg)	Pb (mg/kg)	Th/U	^{238}U/^{206}Pb	±2s (%)	^{207}Pb/^{206}Pb	±2s (%)
Ag-Ni-Co-Fe-As	MB31	calcite I	A289	213	1091229	2.4	8.05	0	0.99	5.4	0.75	1.3
Ag-Ni-Co-Fe-As	MB31	calcite I	A290	213	1029302	1.7	7.81	0	0.72	2.6	0.776	1
Ag-Ni-Co-Fe-As	MB31	calcite I	A291	213	2641883	2.3	23.23	0	0.33	7	0.814	0.9
Ag-Ni-Co-Fe-As	MB31	calcite I	A292	213	1316785	1.6	9.94	0.02	0.55	2.5	0.804	0.8
Ag-Ni-Co-Fe-As	MB31	calcite I	A294	213	294237	2.3	2.62	0	2.59	2.5	0.662	0.9
Ag-Ni-Co-Fe-As	MB31	prehnite II	A244	213	181781	1.6	1.75	0	3.1	4.7	0.768	1.1
Ag-Ni-Co-Fe-As	MB31	prehnite II	A245	213	58045	1.6	0.43	0	10.78	2.5	0.591	2.6
Ag-Ni-Co-Fe-As	MB31	prehnite II	A246	213	151311	8.2	0.93	0	18.86	2.5	0.414	3.7
Ag-Ni-Co-Fe-As	MB31	prehnite II	A247	213	243791	1.3	2.38	0	1.86	3	0.79	0.8
Ag-Ni-Co-Fe-As	MB31	prehnite II	A248	213	100201	2.1	0.82	0	7.57	3.8	0.667	1.2
Ag-Ni-Co-Fe-As	MB31	prehnite II	A249	213	69822	1.8	0.59	0	8.81	2.9	0.658	1.3
Ag-Ni-Co-Fe-As	MB31	prehnite II	A256	213	60384	0.6	0.57	0	3.44	3	0.762	1.2
Ag-Ni-Co-Fe-As	MB31	prehnite II	A258	213	111045	6.9	0.36	0	30.09	3.2	0.2	2
Ag-Ni-Co-Fe-As	MB31	prehnite II	A259	213	178808	13.7	0.68	0	29.31	8.3	0.21	2.2
Ag-Ni-Co-Fe-As	MB31	prehnite II	A261	213	72792	4.4	0.34	0	24.32	6.7	0.322	7
Ag-Ni-Co-Fe-As	MB31	prehnite II	A262	213	26885	0.2	0.26	0	2.33	8	0.774	1.3
Ag-Ni-Co-Fe-As	MB31	prehnite II	A263	213	67019	5.7	0.28	0	29.94	2.8	0.199	1.5
Ag-Ni-Co-Fe-As	MB31	prehnite II	A264	213	42522	0.6	0.4	0	4.66	2.1	0.746	1.2
Ag-Ni-Co-Fe-As	MB31	prehnite II	A265	213	102248	0.7	1	0	2.3	2	0.782	0.9
Ag-Ni-Co-Fe-As	MB31	prehnite II	A266	213	77772	2.1	0.66	0	9.15	3.3	0.647	1.2
Ag-Ni-Co-Fe-As	MB31	prehnite II	A293	213	112210	1.1	1.08	0	3.28	2.2	0.759	1
Ag-Ni-Co-Fe-As	MB31	prehnite II	A295	213	188431	0.8	1.92	0	1.38	2.3	0.805	0.8
Ag-Ni-Co-Fe-As	MB31	prehnite II	A296	213	181289	0.8	1.81	0	1.45	3.9	0.805	0.9
Ag-Ni-Co-Fe-As	MB31	prehnite II	A297	213	149190	0.8	1.51	0	1.9	3	0.8	0.9
Ag-Ni-Co-Fe-As	MB31	prehnite II	A299	213	412446	1.5	13.34	0	1.2	2.7	0.808	0.8
Ag-Ni-Co-Fe-As	MB31	prehnite II	A300	213	680230	2.4	7	0	1.17	3.2	0.815	0.8
Ag-Ni-Co-Fe-As	MB31	prehnite II	A301	213	75386	0.7	0.74	0	3.08	2.1	0.774	1.1

Table A1.8

Vein type	Sample	Mineral	Analysis	Spot size (μm)	^{206}Pb (cps)	U (mg/kg)	Pb (mg/kg)	Th/U	^{238}U/^{206}Pb	±2s (%)	^{207}Pb/^{206}Pb	±2s (%)
Bi-Ni-Co-Fe-As	MB39	calcite II	A496	213	20100	0.1	0.01	0	21.16	3.9	0.422	1.3
Bi-Ni-Co-Fe-As	MB39	calcite II	A500	213	34189	0.1	0.02	0	0.48	19.8	0.57	1.1
Bi-Ni-Co-Fe-As	MB39	calcite II	A501	213	450635	0.1	0.16	0	0.35	4	0.249	0.6
Bi-Ni-Co-Fe-As	MB39	calcite II	A502	213	28104	0.1	0.01	0	1.02	8.5	0.491	1.7
Bi-Ni-Co-Fe-As	MB39	calcite II	A503	213	145099	0.1	0.06	0	0.04	12	0.236	2.5
Bi-Ni-Co-Fe-As	MB39	calcite II	A504	213	33728	0.1	0.02	0	1.93	15.2	0.51	1.9
Bi-Ni-Co-Fe-As	MB39	calcite II	A505	213	704352	0.1	0.34	0	0.06	25.8	0.198	1.8
Bi-Ni-Co-Fe-As	MB39	calcite II	A506	213	971015	0.1	0.3	0.01	0.44	5.7	0.18	0.7
Bi-Ni-Co-Fe-As	MB39	calcite II	A507	213	4573048	0.1	1.3	0	0.11	5.5	0.188	0.5
Bi-Ni-Co-Fe-As	MB39	calcite II	A65	213	80221	5.2	0.74	0	19.61	2.1	0.586	0.9
Bi-Ni-Co-Fe-As	MB39	calcite II	A66	213	68997	4.9	0.62	0	21.59	2.1	0.573	1
Bi-Ni-Co-Fe-As	MB39	calcite II	A72	213	78154	6.7	0.7	0	25.7	2.1	0.559	0.8
Bi-Ni-Co-Fe-As	MB39	calcite II	A73	213	71684	6.3	0.59	0	28.52	2.1	0.536	1
Bi-Ni-Co-Fe-As	MB39	calcite II	A74	213	78893	6.8	0.7	0	25.62	2.1	0.555	0.9
Bi-Ni-Co-Fe-As	MB39	calcite II	A75	213	81926	8.1	0.68	0	31.4	6.5	0.537	0.9
Bi-Ni-Co-Fe-As	MB39	calcite II	A76	213	79677	6.4	0.72	0	24.23	2.1	0.564	0.9
Bi-Ni-Co-Fe-As	MB39	calcite II	A77	213	93211	9.7	0.79	0	31.23	2.1	0.524	0.9
Bi-Ni-Co-Fe-As	MB39	calcite II	A78	213	113535	12.3	0.97	0.1	32.58	2.1	0.526	0.9
Bi-Ni-Co-Fe-As	MB39	calcite II	A79	213	83565	9.7	0.69	0	34.8	2.2	0.501	0.9
Bi-Ni-Co-Fe-As	MB39	calcite II	A80	213	338838	65.2	2.02	0.3	64.11	2.7	0.338	1.9
Bi-Ni-Co-Fe-As	MB39	calcite II	A81	213	319774	83.5	1.71	0.4	81.51	2.2	0.249	0.7
Bi-Ni-Co-Fe-As	MB39	calcite II	A82	143	106178	93.7	1.2	0.4	127.9	2.2	0.239	1.2
Bi-Ni-Co-Fe-As	MB39	calcite II	A83	143	886362	159	12.29	0.7	26.1	15.7	0.348	2.1
Bi-Ni-Co-Fe-As	MB39	calcite II	A84	143	204677	75.6	2.58	0.3	54.3	2.7	0.305	1.1
Bi-Ni-Co-Fe-As	MB39	calcite II	A85	143	72349	24.1	1.06	0.1	51.67	2.4	0.405	1.5
Bi-Ni-Co-Fe-As	MB39	calcite II	A86	143	43710	10.6	0.8	0	33.63	2.1	0.521	1.1
Bi-Ni-Co-Fe-As	MB39	calcite II	A87	143	30832	5.4	0.54	0	25.21	2.1	0.503	1.2

Table A1.7

Vein type	Sample	Mineral	Analysis	Spot size (μm)	^{206}Pb (cps)	U (mg/kg)	Pb (mg/kg)	Th/U	^{238}U/^{206}Pb	±2s (%)	^{207}Pb/^{206}Pb	±2s (%)
Bi-Ni-Co-Fe-As	MB39	calcite I	A92	213	24466	1.6	0.2	0	20.86	2.5	0.548	4
Bi-Ni-Co-Fe-As	MB39	calcite I	A93	213	15743	1	0.15	0	20.39	3.2	0.629	1.8
Bi-Ni-Co-Fe-As	MB39	calcite I	A94	213	24706	2.8	0.19	0	32.71	3.5	0.414	2.5
Bi-Ni-Co-Fe-As	MB39	calcite I	A95	213	12604	0.6	0.12	0	14.08	3.5	0.71	2.1
Bi-Ni-Co-Fe-As	MB39	calcite I	A96	213	10069	0.5	0.08	0	18.64	3.9	0.63	3.2
Bi-Ni-Co-Fe-As	MB39	calcite II	A359	213	509095	198.1	1.97	0	129.12	2.1	0.136	1.2
Bi-Ni-Co-Fe-As	MB39	calcite II	A362	213	348566	149.5	1.38	0	140.91	2.2	0.142	1.7
Bi-Ni-Co-Fe-As	MB39	calcite II	A368	143	188409	203.8	1.48	0	160.99	2.1	0.101	2.2
Bi-Ni-Co-Fe-As	MB39	calcite II	A439	213	164351	0.1	0.12	0.4	0.86	6.4	0.835	0.4
Bi-Ni-Co-Fe-As	MB39	calcite II	A440	213	114392	0.1	0.08	0.15	4.34	4.1	0.823	0.8
Bi-Ni-Co-Fe-As	MB39	calcite II	A442	213	44861	0.1	0.03	0.09	14.51	5.3	0.801	1
Bi-Ni-Co-Fe-As	MB39	calcite II	A443	213	115359	0.2	0.08	0.1	7.29	5.3	0.798	0.5
Bi-Ni-Co-Fe-As	MB39	calcite II	A444	213	36549	0.3	0.02	0.06	44.1	3.3	0.762	0.8
Bi-Ni-Co-Fe-As	MB39	calcite II	A445	213	383719	2.5	0.28	0.03	30.34	6.5	0.793	0.5
Bi-Ni-Co-Fe-As	MB39	calcite II	A446	213	121220	0.5	0.08	0.08	23.73	7.5	0.798	0.5
Bi-Ni-Co-Fe-As	MB39	calcite II	A447	213	70848	0.3	0.04	0.13	24.51	2.4	0.793	0.7
Bi-Ni-Co-Fe-As	MB39	calcite II	A449	213	57801	0.2	0.04	0.08	18.95	4.5	0.805	0.6
Bi-Ni-Co-Fe-As	MB39	calcite II	A459	143	101832	1.6	0.17	0.07	31.98	4.7	0.794	0.9
Bi-Ni-Co-Fe-As	MB39	calcite II	A461	143	202193	2.1	0.3	0.04	22.72	5.3	0.768	0.4
Bi-Ni-Co-Fe-As	MB39	calcite II	A463	213	462586	0.2	0.35	0.05	2.14	9.4	0.837	0.7
Bi-Ni-Co-Fe-As	MB39	calcite II	A464	213	165088	0.1	0.12	0.01	3	4.2	0.804	0.6
Bi-Ni-Co-Fe-As	MB39	calcite II	A465	213	123727	0.1	0.1	0.1	0.63	17.9	0.829	0.7
Bi-Ni-Co-Fe-As	MB39	calcite II	A466	213	142219	0.2	0.09	0.01	7.04	5.5	0.718	0.9
Bi-Ni-Co-Fe-As	MB39	calcite II	A467	213	191337	0.2	0.14	0.06	5.6	2.7	0.835	0.4
Bi-Ni-Co-Fe-As	MB39	calcite II	A468	213	233793	0.1	0.21	0.01	1.08	17.7	0.828	0.5
Bi-Ni-Co-Fe-As	MB39	calcite II	A469	213	107325	0.1	0.08	0.14	2.66	10.3	0.794	0.7
Bi-Ni-Co-Fe-As	MB39	calcite II	A492	213	47555	0.1	0.03	0	15.79	6.3	0.574	2.5

Table A1.10

Vein type	Sample	Mineral	Analysis	Spot size (μm)	^{206}Pb (cps)	U (mg/kg)	Pb (mg/kg)	Th/U	^{238}U/^{206}Pb	±2s (%)	^{207}Pb/^{206}Pb	±2s (%)
Bi-Ni-Co-Fe-As	MB55	calcite I	A47	213	127904	8.8	0.57	0	25.6	5.4	0.272	3.2
Bi-Ni-Co-Fe-As	MB55	calcite I	A48	213	111029	8.1	0.46	0	27.77	5.6	0.242	2.1
Bi-Ni-Co-Fe-As	MB55	calcite I	A50	213	301904	22.2	1.1	0	28.92	5.3	0.186	2.4
Bi-Ni-Co-Fe-As	MB55	calcite I	A51	213	106038	6.6	0.49	0	23.9	4	0.292	2.7
Bi-Ni-Co-Fe-As	MB55	calcite I	A52	213	90718	6.4	0.39	0	27.12	5.6	0.261	2.6
Bi-Ni-Co-Fe-As	MB55	calcite I	A53	213	46308	2.5	0.24	0	21.24	4.4	0.38	3.8
Bi-Ni-Co-Fe-As	MB55	calcite I	A54	213	81015	4.5	0.33	0	23.9	4.2	0.27	2.1
Bi-Ni-Co-Fe-As	MB55	calcite I	A55	213	42118	1.8	0.21	0	17.57	3.8	0.368	5
Bi-Ni-Co-Fe-As	MB55	calcite I	A56	213	52715	1.7	0.36	0	12.26	4.5	0.536	2
Bi-Ni-Co-Fe-As	MB55	calcite I	A57	213	22158	0.4	0.19	0	5.59	9.9	0.674	2.5
Bi-Ni-Co-Fe-As	MB55	calcite I	A58	213	37330	1.4	0.22	0	14.79	6.2	0.449	2.6
Bi-Ni-Co-Fe-As	MB55	calcite I	A59	213	40000	1.4	0.24	0	13.6	6	0.461	3
Bi-Ni-Co-Fe-As	MB55	calcite I	A60	213	24423	0.7	0.16	0	10.77	4.9	0.532	2.1
Bi-Ni-Co-Fe-As	MB55	calcite I	A64	213	71299	2.5	0.47	0	12.65	8.9	0.496	3.1
Bi-Ni-Co-Fe-As	MB55	calcite I	A65	213	134034	7.1	0.64	0	20.71	4.6	0.371	7
Bi-Ni-Co-Fe-As	MB55	calcite I	A66	213	93001	3.9	0.53	0	16.56	3.4	0.429	2.1
Bi-Ni-Co-Fe-As	MB55	calcite I	A72	213	288970	19.8	1.19	0	26.66	4.7	0.251	2.9
Bi-Ni-Co-Fe-As	MB55	calcite II	A15	213	92408	20.1	0.32	0	85.1	2.2	0.167	1.4
Bi-Ni-Co-Fe-As	MB55	calcite II	A16	213	81327	19.3	0.29	0	92.19	2.2	0.173	1.5
Bi-Ni-Co-Fe-As	MB55	calcite II	A17	213	97437	24	0.35	0	95.54	2.1	0.173	1.5
Bi-Ni-Co-Fe-As	MB55	calcite II	A18	213	71074	13	0.3	0	71.7	2.4	0.255	1.7
Bi-Ni-Co-Fe-As	MB55	calcite II	A19	213	68998	17.1	0.24	0	95.87	2.1	0.165	1.5
Bi-Ni-Co-Fe-As	MB55	calcite II	A20	213	111999	31.8	0.28	0	111.09	2	0.045	2.4
Bi-Ni-Co-Fe-As	MB55	calcite II	A21	213	113888	30.2	0.29	0	104.28	2	0.047	2.4
Bi-Ni-Co-Fe-As	MB55	calcite II	A22	213	109573	29.9	0.27	0	106.63	2	0.047	2.5
Bi-Ni-Co-Fe-As	MB55	calcite II	A23	213	683200	161.2	2.16	0	91.38	2.1	0.119	0.9
Bi-Ni-Co-Fe-As	MB55	calcite II	A24	213	609326	103.5	2.82	0	67.87	2.1	0.306	1

Table A1.9

Vein type	Sample	Mineral	Analysis	Spot size (μm)	^{206}Pb (cps)	U (mg/kg)	Pb (mg/kg)	Th/U	^{238}U/^{206}Pb	±2s (%)	^{207}Pb/^{206}Pb	±2s (%)
Bi-Ni-Co-Fe-As	MB39	calcite II	A88	143	39502	10.4	0.7	0	36.53	2.2	0.491	1.1
Bi-Ni-Co-Fe-As	MB55	arsenide	A08	213	146152	0.1	1.9	0	0.19	33.9	0.831	1
Bi-Ni-Co-Fe-As	MB55	arsenide	A09	213	153767	0.6	1.46	0	1.27	10	0.829	0.9
Bi-Ni-Co-Fe-As	MB55	arsenide	A11	213	98953	0.1	0.79	0	0.34	5.1	0.834	0.9
Bi-Ni-Co-Fe-As	MB55	arsenide	A12	213	148020	2	1.52	0	3.83	9.8	0.811	0.9
Bi-Ni-Co-Fe-As	MB55	arsenide	A13	213	137673	0.3	1.4	0	1.26	12.9	0.82	1.1
Bi-Ni-Co-Fe-As	MB55	calcite I	A211	213	13438	0.1	0.1	0	3.35	7.2	0.657	2.5
Bi-Ni-Co-Fe-As	MB55	calcite I	A212	213	53793	0.1	0.5	0	0.71	5.2	0.796	1.4
Bi-Ni-Co-Fe-As	MB55	calcite I	A214	213	58695	3.4	0.31	0	21.05	7.5	0.318	3.1
Bi-Ni-Co-Fe-As	MB55	calcite I	A215	213	52523	0.8	0.41	0	5.62	5.1	0.604	1.6
Bi-Ni-Co-Fe-As	MB55	calcite I	A216	213	51506	1.1	0.35	0	8.04	3.8	0.543	5
Bi-Ni-Co-Fe-As	MB55	calcite I	A217	213	262807	0.8	17.91	0	1.14	10.1	0.734	2.6
Bi-Ni-Co-Fe-As	MB55	calcite I	A218	213	20808	0.2	0.14	0	4.37	3.3	0.593	2
Bi-Ni-Co-Fe-As	MB55	calcite I	A219	213	34055	0.6	0.25	0	7.05	5.4	0.584	2.8
Bi-Ni-Co-Fe-As	MB55	calcite I	A220	213	97357	3.4	0.55	0	13.77	2.8	0.405	2.2
Bi-Ni-Co-Fe-As	MB55	calcite I	A28	213	72959	3.4	0.39	0	17.77	5.3	0.387	5.5
Bi-Ni-Co-Fe-As	MB55	calcite I	A29	213	42571	1	0.29	0	8.83	5.8	0.557	2.3
Bi-Ni-Co-Fe-As	MB55	calcite I	A30	213	67399	1.9	0.25	0	19.74	8.2	0.35	3
Bi-Ni-Co-Fe-As	MB55	calcite I	A31	213	111146	6.9	0.47	0	24.89	8.3	0.254	1.9
Bi-Ni-Co-Fe-As	MB55	calcite I	A32	213	23008	0.1	0.2	0	1.62	8.8	0.738	2.1
Bi-Ni-Co-Fe-As	MB55	calcite I	A38	213	28904	0.7	0.19	0	9.72	5.2	0.539	2.9
Bi-Ni-Co-Fe-As	MB55	calcite I	A39	213	87470	5.2	0.42	0	23.13	3.8	0.325	2.9
Bi-Ni-Co-Fe-As	MB55	calcite I	A40	213	224835	15.6	0.88	0	26.86	5.2	0.211	2.1
Bi-Ni-Co-Fe-As	MB55	calcite I	A41	213	149654	11	0.73	0	26.46	3.8	0.299	4.3
Bi-Ni-Co-Fe-As	MB55	calcite I	A42	213	26214	0.8	0.19	0	10.79	7.9	0.581	2.5
Bi-Ni-Co-Fe-As	MB55	calcite I	A43	213	341549	20.9	1.49	0	23.95	4.2	0.272	1.7
Bi-Ni-Co-Fe-As	MB55	calcite I	A45	213	110353	8	0.49	0	27.85	3.2	0.272	1.4

Table A2.1

Locality	Vein type	Sample	Mineral	FIA	Number	Vapour	T_{freeze}	$T_{1stmelst}$	T_{mice}	T_h	Tm_{HH}	Salinity	Ca/(Na+Ca)	Other components	
						vol. %	°C	°C	°C	°C	°C	wt.%	(molar)	Vapour	Liquid
MH	Bi-Ni-Co-Fe-As	MB102	calcite I	iso1	1	10	-68	-52	-26.3	183.0	-10.3	26.7	0.29	s.m.e.	s.m.e.
MH	Bi-Ni-Co-Fe-As	MB102	calcite I	iso1	2	10	-70	-52	-26.2	182.0	-10.3	26.7	0.29	s.m.e.	s.m.e.
MH	Bi-Ni-Co-Fe-As	MB102	calcite I	iso1	3	10	-68	-52	-26.3	181.0	-10.4	26.7	0.30	s.m.e.	s.m.e.
MH	Bi-Ni-Co-Fe-As	MB102	calcite I	ps1	1	8	-69	-52	-26.2	165.2	-10.9	26.6	0.29	n.a.	n.a.
MH	Bi-Ni-Co-Fe-As	MB102	calcite I	ps1	2	8	-69	-52	-26.3	164.2	-10.6	26.7	0.30	n.a.	n.a.
MH	Bi-Ni-Co-Fe-As	MB102	calcite I	ps1	3	8	-69	-52	-26.7	165.2	-10.4	26.8	0.31	n.a.	n.a.
MH	Bi-Ni-Co-Fe-As	MB102	calcite I	ps1	4	8	-69	-52	-26.6	167.1	-10.4	26.8	0.31	n.a.	n.a.
MH	Bi-Ni-Co-Fe-As	MB102	calcite I	ps1	5	8	-69	-52	-26.6	165.2	-10.4	26.8	0.31	n.a.	n.a.
MH	Bi-Ni-Co-Fe-As	MB102	calcite I	ps2	1	8	-70	-52	-26.6	163.2	-10.7	26.7	0.31	n.a.	n.a.
MH	Bi-Ni-Co-Fe-As	MB102	calcite I	ps2	2	8	-70	-52	-26.4	163.2	-10.5	26.7	0.30	n.a.	n.a.
MH	Bi-Ni-Co-Fe-As	MB102	calcite I	ps2	3	8	-70	-52	-26.4	166.2	-10.5	26.7	0.30	n.a.	n.a.
MH	Bi-Ni-Co-Fe-As	MB102	calcite I	ps2	4	8	-70	-52	-26.3	165.2	-10.4	26.7	0.30	n.a.	n.a.
MH	Bi-Ni-Co-Fe-As	MB102	calcite I	ps2	5	8	-70	-52	-26.4	166.2	-10.4	26.7	0.30	n.a.	n.a.
MH	Bi-Ni-Co-Fe-As	MB102	calcite I	ps2	6	8	-70	-52	-26.4	166.2	-10.4	26.7	0.30	n.a.	n.a.
MH	Bi-Ni-Co-Fe-As	MB44	calcite I	p1	1	10	-60	-52	-10.9	207.1	-24.4	14.9	0.22	CH_4, CO_2, H_2S, N_2	HS^-
MH	Bi-Ni-Co-Fe-As	MB44	calcite I	p1	2	10	-60	-52	-10.9	207.1	-24.4	14.9	0.22	CH_4, CO_2, H_2S, N_2	HS^-
MH	Bi-Ni-Co-Fe-As	MB44	calcite I	p1	3	10	-60	-52	-10.9	207.1	-24.4	14.9	0.22	CH_4, CO_2, H_2S, N_2	HS^-
MH	Bi-Ni-Co-Fe-As	MB44	calcite I	p1	4	10	-60	-52	-10.9	207.1	-24.4	14.9	0.22	CH_4, CO_2, H_2S, N_2	HS^-
MH	Bi-Ni-Co-Fe-As	MB44	calcite I	p1	5	10	-60	-52	-10.9	207.1	-24.4	14.9	0.22	s.m.e.	s.m.e.
MH	Bi-Ni-Co-Fe-As	MB44	calcite I	p1	6	10	-60	-52	-10.9	207.1	-24.4	14.9	0.22	CH_4, CO_2, H_2S, N_2	HS^-
MH	Bi-Ni-Co-Fe-As	MB44	calcite I	p1	7	10	-60	-52	-10.9	207.1	-24.4	14.9	0.22	CH_4, CO_2, H_2S, N_2	HS^-
MH	Bi-Ni-Co-Fe-As	MB44	calcite I	p1	8	10	-60	-52	-10.9	207.1	-24.4	14.9	0.22	s.m.e.	s.m.e.
MH	Bi-Ni-Co-Fe-As	MB44	calcite I	p1	9	10	-60	-52	-10.9	207.1	-24.4	14.9	0.22	s.m.e.	s.m.e.
MH	Bi-Ni-Co-Fe-As	MB44	calcite I	p1	10	10	-60	-52	-10.9	207.1	-24.4	14.9	0.22	CH_4, CO_2, H_2S, N_2	HS^-
MH	Bi-Ni-Co-Fe-As	MB44	calcite I	p1	11	10	-60	-52	-10.9	207.1	-24.4	14.9	0.22	CH_4, CO_2, H_2S, N_2	HS^-
MH	Bi-Ni-Co-Fe-As	MB48	calcite I	ps1	1	8	-80	-52	-26.8	172.6	-12.2	26.7	0.33	n.a.	n.a.
MH	Bi-Ni-Co-Fe-As	MB48	calcite I	ps1	2	8	-80	-52	-27.0	172.6	-12.3	26.7	0.34	n.a.	n.a.
MH	Bi-Ni-Co-Fe-As	MB48	calcite I	ps1	3	8	-80	-52	-27.0	172.6	-12.2	26.7	0.34	n.a.	n.a.
MH	Bi-Ni-Co-Fe-As	MB48	calcite I	ps1	4	8	-80	-52	-27.1	172.6	-12.2	26.7	0.34	n.a.	n.a.
MH	Bi-Ni-Co-Fe-As	MB48	calcite I	ps1	5	8	-80	-52	-27.0	172.6	-12.2	26.7	0.34	n.a.	n.a.
MH	Bi-Ni-Co-Fe-As	MB50	calcite I	iso1	3	9	-70	-52	-26.7	184.0	-10.4	26.8	0.31	n.a.	n.a.

Table A1.11

Vein type	Sample	Mineral	Analysis	Spot size (μm)	^{206}Pb (cps)	U (mg/kg)	Pb (mg/kg)	Th/U	$^{238}U/^{206}Pb$	±2s (%)	$^{207}Pb/^{206}Pb$	±2s (%)
Bi-Ni-Co-Fe-As	MB55	calcite II	A25	213	411817	98	1.16	0	94.02	2.2	0.091	7.7
Bi-Ni-Co-Fe-As	MB55	calcite II	A26	213	727770	190.8	1.86	0	102.5	2	0.051	1.4
Bi-Ni-Co-Fe-As	MB55	calcite II	A27	213	48807	1.1	0.35	0	8.43	7.9	0.59	4.2
Bi-Ni-Co-Fe-As	MB55	calcite II	A61	213	1337790	361.9	3.47	0	104.41	2	0.051	1
Bi-Ni-Co-Fe-As	MB55	calcite II	A62	213	311354	85.7	0.85	0	103.39	2	0.06	2.1
Bi-Ni-Co-Fe-As	MB55	calcite II	A63	213	892536	254	2.32	0	108.67	2	0.049	1.2

Table A2.3

Locality	Vein type	Sample	Mineral	FIA	Number	Vapour	T_{freeze}	$T_{1stmelst}$	T_{mice}	T_h	Tm_{HH}	Salinity	Ca/(Na+Ca)	Other components	
						vol. %	°C	°C	°C	°C	°C	wt.%	(molar)	Vapour	Liquid
NB	Ag-Hg-barite	MB16	calcite II	ps2	2	3	-80	-52	-25.6	106.7	-22.1	25.2	0.29	n.a.	n.a.
NB	Ag-Hg-barite	MB16	calcite II	ps2	3	3	-80	-52	-25.7	105.7	-22.0	25.3	0.29	s.m.e.	s.m.e.
NB	Ag-Hg-barite	MB16	calcite II	ps2	4	3	-80	-52	-25.6	106.7	-22.0	25.3	0.28	s.m.e.	s.m.e.
NB	Ag-Hg-barite	MB16	calcite II	ps2	5	3	-80	-52	-25.6	107.7	-22.2	25.2	0.29	s.m.e.	s.m.e.
NB	Ag-Hg-barite	MB58	barite	p1	1	5	-63	-52		129.0				s.m.e.	s.m.e.
NB	Ag-Hg-barite	MB58	barite	p1	2	5	-63	-52		129.0				none	none
NB	Ag-Hg-barite	MB58	barite	p1	3	5	-63	-52		131.0				none	none
NB	Ag-Hg-barite	MB59	barite	p2	4	5	-63	-52		131.1				s.m.e.	s.m.e.
NB	Ag-Hg-barite	MB59	barite	p2	5	4	-63	-52		131.1				n.a.	n.a.
NB	Ag-Hg-barite	MB59	calcite I	c2	1	12	-67	-52	-27.3	277.3	-12.2	26.8	0.35	n.a.	n.a.
NB	Ag-Hg-barite	MB59	calcite I	c2	2	12	-67	-52	-27.3	278.2	-11.6	26.8	0.35	n.a.	n.a.
NB	Ag-Hg-barite	MB59	calcite I	c2	3	12	-67	-52	-27.2	278.2	-11.6	26.8	0.34	n.a.	n.a.
NB	Ag-Hg-barite	MB59	calcite I	c2	4	12	-67	-52	-27.2	275.3	-11.6	26.8	0.34	n.a.	n.a.
NB	Ag-Hg-barite	MB59	calcite I	c2	5	12	-67	-52	-27.3	278.2	-11.6	26.8	0.35	n.a.	n.a.
NB	Ag-Hg-barite	MB59	calcite I	c2	6	12	-67	-52	-27.2	279.2	-11.6	26.8	0.34	n.a.	n.a.
NB	Ag-Hg-barite	MB59	calcite I	p1	1	12	-67	-52	-27.1	281.2	-11.6	26.8	0.34	n.a.	n.a.
NB	Ag-Hg-barite	MB59	calcite I	p1	2	12	-67	-52	-27.1	277.3	-11.7	26.8	0.34	s.m.e.	s.m.e.
NB	Ag-Hg-barite	MB59	calcite I	p1	3	12	-67	-52	-27.3	277.3	-11.7	26.8	0.35	s.m.e.	s.m.e.
NB	Ag-Hg-barite	MB59	calcite I	p1	4	12	-67	-52	-27.1	278.2	-11.7	26.8	0.34	s.m.e.	s.m.e.
NB	Ag-Hg-barite	MB59	calcite I	p1	5	12	-67	-52	-27.3	279.2	-11.5	26.9	0.35	s.m.e.	s.m.e.
NB	Ag-Hg-barite	MB59	calcite I	p1	6	12	-67	-52	-27.2	277.3	-11.6	26.8	0.34	n.a.	n.a.
NB	Ag-Hg-barite	MB59	calcite I	p1	7	12	-67	-52	-27.2	277.3	-11.7	26.8	0.34	n.a.	n.a.
NB	Ag-Hg-barite	MB59	calcite I	p1	8	12	-67	-52	-27.1	277.3	-11.5	26.8	0.34	n.a.	n.a.
NB	Ag-Hg-barite	MB59	calcite I	p1	9	12	-67	-52	-27.3	278.2	-11.7	26.8	0.35	n.a.	n.a.
NB	Ag-Hg-barite	MB59	calcite I	p1	10	12	-67	-52	-27.2	279.2	-11.4	26.8	0.34	n.a.	n.a.
NB	Ag-Hg-barite	MB59	calcite I	p1	11	12	-67	-52	-27.2	277.3	-11.5	26.8	0.34	n.a.	n.a.
NB	Ag-Hg-barite	MB59	calcite I	p1	12	12	-67	-52	-27.3	278.2	-11.7	26.8	0.35	n.a.	n.a.
NB	Ag-Hg-barite	MB59	calcite I	p1	13	12	-67	-52	-27.1	278.2	-11.6	26.8	0.34	n.a.	n.a.
NB	Ag-Hg-barite	MB59	calcite I	p1	14	12	-67	-52	-27.3	279.2	-11.4	26.9	0.35	n.a.	n.a.
NB	Ag-Hg-barite	MB59	calcite I	p1	15	12	-67	-52	-27.2	277.3	-11.6	26.8	0.34	n.a.	n.a.
NB	Ag-Hg-barite	MB59	calcite I	p1	16	12	-67	-52	-27.2	278.2	-11.6	26.8	0.34	n.a.	n.a.

Table A2.2

Locality	Vein type	Sample	Mineral	FIA	Number	Vapour	T_{freeze}	$T_{1stmelst}$	T_{mice}	T_h	Tm_{HH}	Salinity	Ca/(Na+Ca)	Other components	
						vol. %	°C	°C	°C	°C	°C	wt.%	(molar)	Vapour	Liquid
MH	Bi-Ni-Co-Fe-As	MB50	calcite I	iso1	4	9	-70	-52	-26.6	185.0	-10.4	26.8	0.31	n.a.	n.a.
MH	Bi-Ni-Co-Fe-As	MB50	calcite I	iso1	5	9	-70	-52	-26.6	184.0	-10.4	26.8	0.31	n.a.	n.a.
MH	Bi-Ni-Co-Fe-As	MB50	calcite I	p1	1	9	-69	-52	-26.7	183.0	-10.3	26.8	0.31	s.m.e.	s.m.e.
MH	Bi-Ni-Co-Fe-As	MB50	calcite I	p1	2	9	-69	-52	-26.8	183.0	-10.3	26.8	0.32	s.m.e.	s.m.e.
MH	Bi-Ni-Co-Fe-As	MB50	calcite I	p1	3	9	-66	-52	-26.8	182.0	-10.4	26.8	0.32	s.m.e.	s.m.e.
MH	Bi-Ni-Co-Fe-As	MB50	calcite I	p1	4	9	-66	-52	-26.7	182.0	-10.5	26.8	0.31	s.m.e.	s.m.e.
MH	Bi-Ni-Co-Fe-As	MB50	calcite I	p1	5	9	-66	-52	-26.8	183.0	-10.3	26.8	0.32	s.m.e.	s.m.e.
MH	Bi-Ni-Co-Fe-As	MB50	calcite I	p1	6	9	-66	-52	-26.7	182.0	-10.3	26.8	0.31	s.m.e.	s.m.e.
MH	Bi-Ni-Co-Fe-As	MB50	calcite I	p1	7	9	-66	-52	-26.7	182.0	-10.3	26.8	0.31	s.m.e.	s.m.e.
MH	Bi-Ni-Co-Fe-As	MB50	calcite I	p1	1	9	-70	-52	-26.7	190.9	-10.5	26.8	0.31	n.a.	n.a.
MH	Bi-Ni-Co-Fe-As	MB50	calcite I	p1	2	9	-70	-52	-26.7	183.0	-10.5	26.8	0.31	n.a.	n.a.
MH	Bi-Ni-Co-Fe-As	MB50	calcite I	s1	1	5	-66	-52	-26.3	147.3	-10.4	26.7	0.30	n.a.	n.a.
MH	Bi-Ni-Co-Fe-As	MB50	calcite I	s1	2	5	-70	-52	-26.2	148.3	-10.5	26.6	0.29	n.a.	n.a.
MH	Bi-Ni-Co-Fe-As	MB50	calcite I	s1	3	5	-70	-52	-26.3	147.3	-10.5	26.7	0.30	n.a.	n.a.
MH	Bi-Ni-Co-Fe-As	MB50	calcite I	s1	4	5	-65	-52	-26.3	146.3	-10.5	26.7	0.30	n.a.	n.a.
MH	Bi-Ni-Co-Fe-As	MB50	calcite I	s1	5	5	-70	-52	-26.2	151.3	-10.4	26.7	0.29	n.a.	n.a.
MH	Bi-Ni-Co-Fe-As	MB50	calcite I	s1	6	5	-66	-52	-26.3	149.3	-10.6	26.7	0.30	n.a.	n.a.
MH	Bi-Ni-Co-Fe-As	MB50	calcite I	s1	7	5	-66	-52	-26.6	148.3	-10.4	26.8	0.31	n.a.	n.a.
MH	Bi-Ni-Co-Fe-As	MB50	calcite I	s1	8	5	-69	-52	-26.2	145.3	-10.3	26.7	0.29	n.a.	n.a.
MH	Bi-Ni-Co-Fe-As	MB50	calcite I	s1	9	5	-69	-52	-26.2	149.3	-10.5	26.6	0.29	n.a.	n.a.
MH	Bi-Ni-Co-Fe-As	MB50	calcite I	s1	10	5	-67	-52	-26.2	148.3	-10.5	26.6	0.29	n.a.	n.a.
MH	Bi-Ni-Co-Fe-As	MB50	calcite I	s1	11	5	-67	-52	-26.3	148.3	-10.5	26.7	0.30	n.a.	n.a.
MH	Bi-Ni-Co-Fe-As	MB50	calcite I	s1	12	5	-75	-52	-26.3	148.3	-10.9	26.6	0.30	n.a.	n.a.
MH	Bi-Ni-Co-Fe-As	MB50	calcite I	s1	13	5	-67	-52	-26.3	149.3	-10.7	26.7	0.30	n.a.	n.a.
MH	Bi-Ni-Co-Fe-As	MB50	calcite I	s1	14	5	-67	-52	-26.3	149.3	-10.5	26.7	0.30	n.a.	n.a.
MH	Bi-Ni-Co-Fe-As	MB50	calcite I	s1	15	5	-67	-52	-26.2	149.3	-10.4	26.7	0.29	n.a.	n.a.
NB	Ag-Hg-barite	MB16	calcite II	ps1	1	3	-80	-52	-26.3	104.0	-22.1	25.5	0.33	s.m.e.	s.m.e.
NB	Ag-Hg-barite	MB16	calcite II	ps1	2	3	-80	-52	-26.1	104.9	-22.8	25.4	0.32	s.m.e.	s.m.e.
NB	Ag-Hg-barite	MB16	calcite II	ps1	3	3	-80	-52	-26.1	106.9	-21.9	25.5	0.32	s.m.e.	s.m.e.
NB	Ag-Hg-barite	MB16	calcite II	ps1	4	3	-80	-52	-26.3	105.9	-22.2	25.5	0.33	s.m.e.	s.m.e.
NB	Ag-Hg-barite	MB16	calcite II	ps2	1	3	-80	-52	-25.6	106.7	-22.0	25.3	0.28	n.a.	n.a.

Table A2.5

Locality	Vein type	Sample	Mineral	FIA	Number	Vapour	T_{freeze}	$T_{1stmelst}$	T_{mice}	T_h	Tm_{HH}	Salinity	Ca/(Na+Ca)	Other components	
						vol. %	°C	°C	°C	°C	°C	wt.%	(molar)	Vapour	Liquid
NB	Ag-Hg-barite	MB59	calcite II	c1	6	4	-80	-52	-26.7	134.9	-13.2	26.5	0.32	n.a.	n.a.
NB	Ag-Hg-barite	MB59	calcite II	c1	7	4	-80	-52	-26.6	135.9	-13.3	26.5	0.32	n.a.	n.a.
NB	Ag-Hg-barite	MB59	calcite II	c1	8	4	-80	-52	-26.7	136.9	-13.3	26.5	0.32	n.a.	n.a.
NB	Ag-Ni-Co-Fe-As	MB12	calcite I	c7	1	11	-70	-52	-26.6	265.1	-5.0	27.2	0.30	n.a.	n.a.
NB	Ag-Ni-Co-Fe-As	MB12	calcite I	c7	2	11	-70	-52	-26.6	265.1	-5.3	27.1	0.30	n.a.	n.a.
NB	Ag-Ni-Co-Fe-As	MB12	calcite I	c7	3	11	-70	-52	-26.6	265.1	-5.3	27.1	0.30	n.a.	n.a.
NB	Ag-Ni-Co-Fe-As	MB12	calcite I	c7	4	11	-70	-52	-26.6	265.1	-5.1	27.2	0.30	n.a.	n.a.
NB	Ag-Ni-Co-Fe-As	MB12	calcite I	p1	1	12	-70	-52	-26.6	273.6	-5.9	27.1	0.30	none	none
NB	Ag-Ni-Co-Fe-As	MB12	calcite I	p1	2	12	-70	-52	-26.6	273.6	-5.8	27.1	0.30	none	none
NB	Ag-Ni-Co-Fe-As	MB12	calcite I	p1	3	12	-70	-52	-26.6	273.6	-6.1	27.1	0.30	none	none
NB	Ag-Ni-Co-Fe-As	MB12	calcite I	p1	4	12	-70	-52	-26.6	273.6	-5.8	27.1	0.30	CH_4, N_2	none
NB	Ag-Ni-Co-Fe-As	MB12	calcite I	p1	5	12	-70	-52	-26.5	273.6	-5.8	27.1	0.30	none	none
NB	Ag-Ni-Co-Fe-As	MB12	calcite I	p1	6	12	-70	-52	-26.6	273.6	-5.8	27.1	0.30	none	none
NB	Ag-Ni-Co-Fe-As	MB12B	calcite I	c3	1	10	-86	-52	-27.0	203.3	-11.4	26.8	0.33	n.a.	n.a.
NB	Ag-Ni-Co-Fe-As	MB12B	calcite I	c3	2	10	-87	-52	-26.9	208.3	-11.5	26.7	0.33	n.a.	n.a.
NB	Ag-Ni-Co-Fe-As	MB12B	calcite I	c3	3	10	-87	-52	-27.1	208.3	-11.5	26.8	0.34	n.a.	n.a.
NB	Ag-Ni-Co-Fe-As	MB12B	calcite I	c3	4	10	-87	-52	-27.1	208.3	-11.5	26.8	0.34	n.a.	n.a.
NB	Ag-Ni-Co-Fe-As	MB12B	calcite I	c3	5	10	-88	-52	-27.1	206.3	-11.5	26.8	0.34	n.a.	n.a.
NB	Ag-Ni-Co-Fe-As	MB12B	calcite I	c3	6	10	-88	-52	-27.1	206.3	-11.5	26.8	0.34	n.a.	n.a.
NB	Ag-Ni-Co-Fe-As	MB12B	calcite I	c3	7	10	-88	-52	-27.1	206.3	-11.4	26.8	0.34	n.a.	n.a.
NB	Ag-Ni-Co-Fe-As	MB12B	calcite I	c3	8	10	-88	-52	-27.1	203.3	-11.4	26.8	0.34	n.a.	n.a.
NB	Ag-Ni-Co-Fe-As	MB12B	calcite I	c3	9	10	-88	-52	-27.2	203.3	-11.4	26.8	0.34	n.a.	n.a.
NB	Ag-Ni-Co-Fe-As	MB12B	calcite I	c3	10	10	-88	-52	-27.2	203.3	-11.5	26.8	0.34	n.a.	n.a.
NB	Ag-Ni-Co-Fe-As	MB12B	calcite I	c3	11	10	-88	-52	-27.2	203.3	-11.3	26.9	0.34	n.a.	n.a.
NB	Ag-Ni-Co-Fe-As	MB12B	calcite I	c4	1	8	-78	-52	-26.6	149.7	-10.9	26.7	0.31	n.a.	n.a.
NB	Ag-Ni-Co-Fe-As	MB12B	calcite I	c4	2	8	-78	-52	-26.6	149.7	-10.9	26.7	0.31	n.a.	n.a.
NB	Ag-Ni-Co-Fe-As	MB12B	calcite I	c4	3	8	-78	-52	-26.6	149.7	-10.8	26.7	0.31	n.a.	n.a.
NB	Ag-Ni-Co-Fe-As	MB12B	calcite I	c4	4	8	-78	-52	-26.8	149.7	-10.9	26.8	0.32	n.a.	n.a.
NB	Ag-Ni-Co-Fe-As	MB12B	calcite I	c5	1	8	-78	-52	-26.3	205.3	-13.2	26.4	0.30	n.a.	n.a.
NB	Ag-Ni-Co-Fe-As	MB12B	calcite I	c5	2	8	-78	-52	-26.8	206.3	-13.3	26.6	0.33	n.a.	n.a.
NB	Ag-Ni-Co-Fe-As	MB12B	calcite I	c5	3	8	-78	-52	-26.7	205.3	-13.2	26.5	0.32	n.a.	n.a.

Table A2.4

Locality	Vein type	Sample	Mineral	FIA	Number	Vapour	T_{freeze}	$T_{1stmelst}$	T_{mice}	T_h	Tm_{HH}	Salinity	Ca/(Na+Ca)	Other components	
						vol. %	°C	°C	°C	°C	°C	wt.%	(molar)	Vapour	Liquid
NB	Ag-Hg-barite	MB59	calcite I	s1	1	4	-70	-52	-26.9	135.9	-13.4	26.6	0.33	n.a.	n.a.
NB	Ag-Hg-barite	MB59	calcite I	s1	2	4	-70	-52	-27.0	135.9	-11.8	26.7	0.33	n.a.	n.a.
NB	Ag-Hg-barite	MB59	calcite I	s1	3	4	-70	-52	-27.0	135.9	-7.1	27.1	0.32	n.a.	n.a.
NB	Ag-Hg-barite	MB59	calcite I	s1	4	4	-70	-52	-26.9	135.9	-13.1	26.6	0.33	n.a.	n.a.
NB	Ag-Hg-barite	MB59	calcite I	s1	5	4	-70	-52	-26.9	135.9	-14.0	26.5	0.33	n.a.	n.a.
NB	Ag-Hg-barite	MB59	calcite I	s1	6	4	-70	-52	-26.8	135.9	-13.0	26.6	0.33	n.a.	n.a.
NB	Ag-Hg-barite	MB59	calcite I	s1	7	4	-70	-52	-26.9	135.9	-13.6	26.6	0.33	n.a.	n.a.
NB	Ag-Hg-barite	MB59	calcite I	s1	8	4	-70	-52	-26.9	135.9	-13.4	26.6	0.33	n.a.	n.a.
NB	Ag-Hg-barite	MB59	calcite I	s1	9	4	-70	-52	-26.9	135.9	-13.3	26.6	0.33	n.a.	n.a.
NB	Ag-Hg-barite	MB59	calcite I	s1	10	4	-70	-52	-27.0	135.9	-13.2	26.6	0.34	n.a.	n.a.
NB	Ag-Hg-barite	MB59	calcite I	s1	11	4	-70	-52	-26.9	135.9	-13.3	26.6	0.33	n.a.	n.a.
NB	Ag-Hg-barite	MB59	calcite I	s1	12	4	-70	-52	-27.0	135.9	-13.7	26.6	0.34	n.a.	n.a.
NB	Ag-Hg-barite	MB59	calcite I	s1	13	4	-70	-52	-26.9	135.9	-13.6	26.6	0.33	n.a.	n.a.
NB	Ag-Hg-barite	MB59	calcite I	s2	1	4	-70	-52	-27.0	135.9	-13.2	26.6	0.34	n.a.	n.a.
NB	Ag-Hg-barite	MB59	calcite I	s2	2	4	-70	-52	-26.9	135.9	-13.4	26.6	0.33	n.a.	n.a.
NB	Ag-Hg-barite	MB59	calcite I	s2	3	4	-70	-52	-26.9	135.9	-13.6	26.6	0.33	n.a.	n.a.
NB	Ag-Hg-barite	MB59	calcite I	s2	4	4	-70	-52	-27.0	135.9	-13.4	26.6	0.34	n.a.	n.a.
NB	Ag-Hg-barite	MB59	calcite I	s2	5	4	-70	-52	-26.9	135.9	-13.6	26.6	0.33	n.a.	n.a.
NB	Ag-Hg-barite	MB59	calcite I	s2	6	4	-70	-52	-26.9	135.9	-13.4	26.6	0.33	n.a.	n.a.
NB	Ag-Hg-barite	MB59	calcite I	s4	1	4	-75	-52	-27.1	135.0	-11.5	26.8	0.34	n.a.	n.a.
NB	Ag-Hg-barite	MB59	calcite I	s4	2	4	-75	-52	-27.1	136.0	-11.6	26.8	0.34	n.a.	n.a.
NB	Ag-Hg-barite	MB59	calcite I	s4	3	4	-75	-52	-27.0	136.0	-11.6	26.8	0.33	n.a.	n.a.
NB	Ag-Hg-barite	MB59	calcite I	s4	4	4	-75	-52	-27.2	135.0	-11.6	26.8	0.34	n.a.	n.a.
NB	Ag-Hg-barite	MB59	calcite I	s4	5	4	-75	-52	-27.0	135.0	-11.6	26.8	0.33	n.a.	n.a.
NB	Ag-Hg-barite	MB59	calcite I	s4	6	4	-75	-52	-27.1	136.0	-11.6	26.8	0.34	n.a.	n.a.
NB	Ag-Hg-barite	MB59	calcite I	s4	7	4	-75	-52	-27.1	136.0	-11.6	26.8	0.34	n.a.	n.a.
NB	Ag-Hg-barite	MB59	calcite II	c1	1	4	-75	-52	-26.6	135.9	-13.4	26.5	0.32	n.a.	n.a.
NB	Ag-Hg-barite	MB59	calcite II	c1	2	4	-80	-52	-26.7	136.9	-13.1	26.5	0.32	n.a.	n.a.
NB	Ag-Hg-barite	MB59	calcite II	c1	3	4	-80	-52	-26.6	135.9	-13.1	26.5	0.32	n.a.	n.a.
NB	Ag-Hg-barite	MB59	calcite II	c1	4	4	-80	-52	-26.6	135.9	-13.2	26.5	0.32	n.a.	n.a.
NB	Ag-Hg-barite	MB59	calcite II	c1	5	4	-80	-52	-26.7	136.9	-13.2	26.5	0.32	n.a.	n.a.

Table A2.7

Locality	Vein type	Sample	Mineral	FIA	Number	Vapour	T_{freeze}	$T_{1stmelst}$	T_{mice}	T_h	Tm_{HH}	Salinity	Ca/(Na+Ca)	Other components	
						vol. %	°C	°C	°C	°C	°C	wt.%	(molar)	Vapour	Liquid
NB	Ag-Ni-Co-Fe-As	MB19	calcite I	c3	5	5	-80	-52	-26.2	166.2	-14.0	26.3	0.30	n.a.	n.a.
NB	Ag-Ni-Co-Fe-As	MB19	calcite I	c3	6	5	-80	-52	-25.9	167.2	-13.1	26.3	0.28	n.a.	n.a.
NB	Ag-Ni-Co-Fe-As	MB19	calcite I	c3	7	5	-80	-52	-26.0	167.2	-13.6	26.3	0.29	n.a.	n.a.
NB	Ag-Ni-Co-Fe-As	MB19	calcite I	c3	8	5	-80	-52	-25.9	167.2	-13.7	26.2	0.28	n.a.	n.a.
NB	Ag-Ni-Co-Fe-As	MB19	calcite I	c3	9	5	-80	-52	-26.2	167.2	-14.0	26.3	0.30	n.a.	n.a.
NB	Ag-Ni-Co-Fe-As	MB19	calcite I	c3	10	5	-80	-52	-25.9	167.2	-14.0	26.2	0.28	n.a.	n.a.
NB	Ag-Ni-Co-Fe-As	MB19	calcite I	c6	1	9	-80	-52	-26.3	218.9	-14.0	26.3	0.30	n.a.	n.a.
NB	Ag-Ni-Co-Fe-As	MB19	calcite I	c6	2	9	-80	-52	-26.2	220.9	-13.9	26.3	0.30	n.a.	n.a.
NB	Ag-Ni-Co-Fe-As	MB19	calcite I	c6	3	9	-80	-52	-26.3	219.9	-14.1	26.3	0.30	n.a.	n.a.
NB	Ag-Ni-Co-Fe-As	MB19	calcite I	c6	4	9	-80	-52	-26.1	220.9	-14.0	26.3	0.29	n.a.	n.a.
NB	Ag-Ni-Co-Fe-As	MB19	calcite I	c6	5	9	-80	-52	-25.9	220.9	-13.9	26.2	0.28	n.a.	n.a.
NB	Ag-Ni-Co-Fe-As	MB19	calcite I	c6	6	9	-80	-52	-26.0	219.9	-14.0	26.2	0.29	n.a.	n.a.
NB	As-Ag-Fe	MB61	calcite I	c1	1	8	-80	-52	-26.9	170.7	-10.7	26.8	0.33	n.a.	n.a.
NB	As-Ag-Fe	MB61	calcite I	c1	2	9	-70	-52	-27.0	208.4	-10.1	26.9	0.33	n.a.	n.a.
NB	As-Ag-Fe	MB61	calcite I	c1	3	9	-70	-52	-26.6	181.6	-11.4	26.7	0.31	n.a.	n.a.
NB	As-Ag-Fe	MB61	calcite I	c1	4	9	-70	-52	-26.6	177.6	-10.0	26.8	0.31	n.a.	n.a.
NB	As-Ag-Fe	MB61	calcite I	c2	1	2	-70	-52	-26.3	114.1	-19.3	25.8	0.32	n.a.	n.a.
NB	As-Ag-Fe	MB61	calcite I	c2	2	2	-70	-52	-26.3	117.1	-19.2	25.8	0.32	n.a.	n.a.
NB	As-Ag-Fe	MB61	calcite I	c2	3	2	-70	-52	-26.2	111.2	-19.3	25.8	0.31	n.a.	n.a.
NB	As-Ag-Fe	MB61	calcite I	c3	1	2	-80	-52	-26.5	94.3	-19.3	25.9	0.33	n.a.	n.a.
NB	As-Ag-Fe	MB61	calcite I	c3	2	2	-80	-52	-26.5	104.2	-19.3	25.9	0.33	n.a.	n.a.
NB	As-Ag-Fe	MB61	calcite I	c3	3	2	-80	-52	-26.5	100.2	-19.3	25.9	0.33	n.a.	n.a.
NB	As-Ag-Fe	MB61	calcite I	c3	4	2	-80	-52	-26.5	98.3	-19.3	25.9	0.33	n.a.	n.a.
NB	As-Ag-Fe	MB61	calcite I	c4	1	3	-70	-52	-26.6	134.0	-13.6	26.5	0.32	n.a.	n.a.
NB	As-Ag-Fe	MB61	calcite I	c4	2	3	-70	-52	-26.6	132.0	-13.5	26.5	0.32	n.a.	n.a.
NB	As-Ag-Fe	MB61	calcite I	c5	1	11	-67	-52	-26.8	235.2	-13.3	26.6	0.33	n.a.	n.a.
NB	As-Ag-Fe	MB61	calcite I	c5	2	12	-67	-52	-26.8	282.8	-13.1	26.6	0.33	none	none
NB	As-Ag-Fe	MB61	calcite I	c5	3	12	-67	-52	-26.6	276.8	-13.2	26.5	0.32	none	none
NB	As-Ag-Fe	MB61	calcite I	c5	4	12	-67	-52	-26.8	285.8	-13.3	26.6	0.33	none	none
NB	As-Ag-Fe	MB61	calcite I	iso1	1	12	-67	-52	-26.9	284.8	-13.3	26.6	0.33	none	none

Table A2.6

Locality	Vein type	Sample	Mineral	FIA	Number	Vapour	T_{freeze}	$T_{1stmelst}$	T_{mice}	T_h	Tm_{HH}	Salinity	Ca/(Na+Ca)	Other components	
						vol. %	°C	°C	°C	°C	°C	wt.%	(molar)	Vapour	Liquid
NB	Ag-Ni-Co-Fe-As	MB12B	calcite I	c5	4	8	-78	-52	-26.8	206.3	-13.3	26.6	0.33	n.a.	n.a.
NB	Ag-Ni-Co-Fe-As	MB12B	calcite I	c6	1	8	-78	-52	-26.8	206.3	-13.3	26.6	0.33	n.a.	n.a.
NB	Ag-Ni-Co-Fe-As	MB12B	calcite I	c6	2	8	-78	-52	-26.8	207.3	-13.3	26.6	0.33	n.a.	n.a.
NB	Ag-Ni-Co-Fe-As	MB12B	calcite I	c6	3	8	-78	-52	-26.7	206.3	-13.4	26.5	0.32	n.a.	n.a.
NB	Ag-Ni-Co-Fe-As	MB12B	calcite I	c6	4	8	-78	-52	-26.8	206.3	-13.3	26.6	0.33	n.a.	n.a.
NB	Ag-Ni-Co-Fe-As	MB12B	calcite I	iso1	1	13	-64	-52	-26.8	272.8	-12.5	26.6	0.33	n.a.	n.a.
NB	Ag-Ni-Co-Fe-As	MB12B	calcite I	iso1	2	13	-64	-52	-26.8	273.8	-12.5	26.6	0.33	none	none
NB	Ag-Ni-Co-Fe-As	MB12B	calcite I	iso1	3	13	-64	-52	-26.8	273.8	-12.5	26.6	0.33	none	none
NB	Ag-Ni-Co-Fe-As	MB12B	calcite I	iso1	4	13	-64	-52	-26.8	277.8	-12.6	26.6	0.33	none	none
NB	Ag-Ni-Co-Fe-As	MB12B	calcite I	iso1	5	13	-64	-52	-26.8	274.8	-12.5	26.6	0.33	none	none
NB	Ag-Ni-Co-Fe-As	MB12B	calcite I	iso1	6	13	-64	-52	-26.8	273.8	-12.5	26.6	0.33	n.a.	n.a.
NB	Ag-Ni-Co-Fe-As	MB12B	calcite I	iso1	7	13	-64	-52	-26.8	277.8	-12.4	26.6	0.33	n.a.	n.a.
NB	Ag-Ni-Co-Fe-As	MB12B	calcite I	iso1	8	13	-64	-52	-26.8	272.8	-12.6	26.6	0.33	n.a.	n.a.
NB	Ag-Ni-Co-Fe-As	MB12B	calcite I	iso1	9	13	-64	-52	-26.8	272.8	-12.4	26.6	0.33	n.a.	n.a.
NB	Ag-Ni-Co-Fe-As	MB12B	calcite I	iso1	10	13	-64	-52	-26.8	274.8	-12.5	26.6	0.33	n.a.	n.a.
NB	Ag-Ni-Co-Fe-As	MB12B	calcite I	iso1	11	13	-64	-52	-26.8	274.8	-12.5	26.6	0.33	n.a.	n.a.
NB	Ag-Ni-Co-Fe-As	MB12B	calcite I	iso2	1	13	-64	-52	-27.2	282.8	-12.4	26.8	0.35	n.a.	n.a.
NB	Ag-Ni-Co-Fe-As	MB12B	calcite I	iso2	2	13	-64	-52	-27.3	282.8	-12.4	26.8	0.35	n.a.	n.a.
NB	Ag-Ni-Co-Fe-As	MB19	calcite I	c1	1	3	-80	-52	-26.4	119.4	-10.1	26.7	0.30	n.a.	n.a.
NB	Ag-Ni-Co-Fe-As	MB19	calcite I	c1	2	3	-80	-52	-26.4	119.4	-10.2	26.7	0.30	n.a.	n.a.
NB	Ag-Ni-Co-Fe-As	MB19	calcite I	c1	3	3	-80	-52	-26.4	121.4	-10.1	26.7	0.30	n.a.	n.a.
NB	Ag-Ni-Co-Fe-As	MB19	calcite I	c1	4	3	-80	-52	-26.3	120.4	-11.4	26.6	0.30	n.a.	n.a.
NB	Ag-Ni-Co-Fe-As	MB19	calcite I	c1	5	3	-80	-52	-26.2	119.4	-14.3	26.3	0.30	n.a.	n.a.
NB	Ag-Ni-Co-Fe-As	MB19	calcite I	c1	6	3	-80	-52	-25.7	120.4	-14.9	26.1	0.27	n.a.	n.a.
NB	Ag-Ni-Co-Fe-As	MB19	calcite I	c1	7	3	-80	-52	-26.4	120.4	-14.1	26.4	0.31	n.a.	n.a.
NB	Ag-Ni-Co-Fe-As	MB19	calcite I	c1	8	3	-80	-52	-26.5	119.4	-9.9	26.8	0.30	n.a.	n.a.
NB	Ag-Ni-Co-Fe-As	MB19	calcite I	c1	9	3	-80	-52	-26.5	121.4	-9.7	26.8	0.30	n.a.	n.a.
NB	Ag-Ni-Co-Fe-As	MB19	calcite I	c3	1	5	-80	-52	-26.0	167.2	-14.0	26.2	0.29	n.a.	n.a.
NB	Ag-Ni-Co-Fe-As	MB19	calcite I	c3	2	5	-80	-52	-25.9	166.2	-14.4	26.2	0.28	n.a.	n.a.
NB	Ag-Ni-Co-Fe-As	MB19	calcite I	c3	3	5	-80	-52	-26.1	167.2	-14.4	26.2	0.29	n.a.	n.a.
NB	Ag-Ni-Co-Fe-As	MB19	calcite I	c3	4	5	-80	-52	-26.3	167.2	-11.4	26.6	0.30	n.a.	n.a.

Table A2.8

Locality	Vein type	Sample	Mineral	FIA	Number	Vapour	T_{freeze}	$T_{1stmelst}$	T_{mice}	T_h	Tm_{HH}	Salinity	Ca/(Na+Ca)	Other components	
						vol. %	°C	°C	°C	°C	°C	wt.%	(molar)	Vapour	Liquid
NB	Pb-Zn-Cu-S	MB97	calcite I	c1	1	12	-80	-52	-26.9	287.1	-11.4	26.8	0.33	s.m.e.	s.m.e.
NB	Pb-Zn-Cu-S	MB97	calcite I	c1	2	12	-80	-52	-26.9	284.2	-11.4	26.8	0.33	s.m.e.	s.m.e.
NB	Pb-Zn-Cu-S	MB97	calcite I	c1	3	12	-80	-52	-26.9	284.2	-11.4	26.8	0.33	none	none
NB	Pb-Zn-Cu-S	MB97	calcite I	c2	4	12	-80	-52	-26.8	280.2	-11.4	26.7	0.32	none	none
NB	Pb-Zn-Cu-S	MB97	calcite I	c2	5	12	-80	-52	-26.9	292.1	-11.4	26.8	0.33	none	none
NB	Pb-Zn-Cu-S	MB97	calcite I	c2	6	12	-80	-52	-26.8	282.2	-11.4	26.7	0.32	s.m.e.	s.m.e.
NB	Pb-Zn-Cu-S	MB97	calcite I	c4	1	12	-80	-52	-27.1	280.2	-11.4	26.8	0.34	n.a.	n.a.
NB	Pb-Zn-Cu-S	MB97	calcite I	c4	2	12	-80	-52	-27.1	278.2	-12.8	26.7	0.34	n.a.	n.a.
NB	Pb-Zn-Cu-S	MB97	calcite I	c4	3	12	-80	-52	-27.1	279.2	-12.7	26.7	0.34	n.a.	n.a.

NB = Nieder-Beerbach; MH = Mackenheim

FIA = fluid inclusion assemblage

iso = isolated; c = cluster; p= primary; ps = pseudo-secondary

s.m.e. = none due to strong matrix effects; none = excludes H_2O; n.a. = not analysed